Novus Scientia 2024

21. Medzinárodná vedecká konferencia doktorandov strojníckych fakúlt technických univerzít a vysokých škôl

Novus Scientia 2024

Zborník príspevkov z XXI. Medzinárodnej vedeckej konferencie doktorandov strojníckych fakúlt technických univerzít a vysokých škôl

25.01.2024

Strojnícka fakulta

Technická univerzita v Košiciach

Zameranie konferencie:

- Automatizácia, mechatronika a robotika
- Technologické a materiálové inžinierstvo
- Manažment, priemyselné a digitálne inžinierstvo
- Konštrukčné a procesné inžinierstvo
- Špeciálne inžinierske procesológie

Vedecký a organizačný výbor konferencie

Patronát konferencie

Dr.h.c. mult. prof. Ing. Jozef Živčák, PhD., MPH

Technická univerzita v Košiciach, Slovensko

Garant konferencie

prof. Ing. Ján Slota, PhD.

Technická univerzita v Košiciach, Slovensko

Vedecký výbor konferencie

prof. Ing. Jozef Bocko, CSc., Technická univerzita v Košiciach, Slovensko

prof. Ing. Radovan Hudák, PhD., Technická univerzita v Košiciach, Slovensko

prof. Ing. Michal Kelemen, PhD., Technická univerzita v Košiciach, Slovensko

prof. Ing. Ervin Lumnitzer, PhD., Technická univerzita v Košiciach, Slovensko

prof. Ing. Emil Spišák, CSc., Technická univerzita v Košiciach, Slovensko

prof. Ing. Tomáš Brestovič, PhD., Technická univerzita v Košiciach, Slovensko

doc. Ing. Ján Kráľ, PhD., Technická univerzita v Košiciach, Slovensko

prof. Ing. Peter Frankovský, PhD., Technická univerzita v Košiciach, Slovensko

prof. Ing. Michal Hatala, PhD., Technická univerzita v Košiciach, Slovensko

prof. Ing. Eva Tillová, PhD., Žilinská univerzita v Žiline, Slovensko

prof. Ing. Stanislav Ďuriš, PhD., Slovenská technická univerzita v Bratislave, Slovensko

prof. Ing. Peter Šugár, CSc., Slovenská technická univerzita v Bratislave, Slovensko

doc. Ing. Jaroslav Katolický, Ph.D., Vysoké učení technické Brno, Česká republika

doc. Ing. Miroslav Mahdal, Ph.D., VŠB Technická univerzita Ostrava, Česká republika prof. Ing. Tomáš Jirout, Ph.D., ČVUT Praha, Česká republika

doc. Ing. Petr Lepšík, Ph.D., Technická univerzita v Liberci, Česká republika

doc. Ing. Václav Vaněk, Ph.D., Západočeská univerzita v Plzni, Česká republika

dr hab. inż. Andrzej Burghardt, prof. PRz, Politechnika Rzeszowska, Poľsko

Dr inż. Tomasz Jachowicz, Politechnika Lubelska, Poľsko

Dr inż. Jacek Rysiński, Uniwersytet Bielsko – Bialski, Poľsko

Organizačný výbor

prof. Ing. Ján Slota, PhD.
Ing. Jaroslav Melko
Ing. Samuel Sivák
Ing. Matúš Lavčák
Ing. Matúš Kačír
Ing. Pavol Tarbajovský
Ing. Lucia Žuľová
Ing. Matúš Vírostko

Recenzovaný zborník z vedeckej konferencie

Príspevky v zborníku z vedeckej konferencie boli recenzované dvoma recenzentmi prostredníctvom anonymného recenzného konania.

Novus Scientia 2024

Zborník príspevkov z XXI. Medzinárodnej vedeckej konferencie doktorandov strojníckych fakúlt technických univerzít a vysokých škôl

Názov:	Novus Scientia 2024
Editor:	© prof. Ing. Ján Slota, PhD.
	© Ing. Lucia Žuľová
	© Ing. Jaroslav Melko
Vydavateľ:	Technická univerzita v Košiciach,
	Strojnícka fakulta, Letná 1/9, 042 00 Košice-Sever
Rok:	2024
Náklad:	75 výtlačkov
Rozsah:	444 strán
Miesto konania:	Strojnícka fakulta, Technická univerzita v Košiciach
Dátum konania:	25.01.2024

ISBN 978-80-553-4690-8

OBSAH

Research on ultrafine particles in the environment and their impact on humans

Miroslava Badidová [1*], Lýdia Sobotová [2] and Kristián Pástor [3,]

[1] Technical University of Košice, Faculty of Mechanical Engineering, Department of Environmental Engineering ; miroslava.badidová@gmail.com
[2] Technical University of Košice, Faculty of Mechanical Engineering, Department of Environmental Engineering ; lydia.sobotova@tuke.sk
[3] Technical University of Košice, Faculty of Mechanical Engineering, Department of Environmental Engineering ; kristian.pastor@tuke.sk
* Correspondence: miroslava.badidová@gmail.com, tel .: +421 0905 343 891

Abstract: The paper deals with the problem of ultrafine particles (UFP) in the environment. Selected methods of UFP measurement in the working environment, their basic principles, but also UFP properties and factors that influence on UFP are presented. The article points out the possible toxic effects of exposure to UFP on the human body. The authors present the conducted experiment focused on the research of emitted UFP emission's during the process of vacuuming with a vacuum cleaner with a wet (water tank bag) and dry (paper bag) filter. The results of the experiment demonstrated that a vacuum cleaner with a water filter emits significantly less UFP into the environment, especially in the initial phase of vacuuming. The issue UFP is intensively dealt with by the EU, several legislative documents are being prepared in the subject area.

Keywords: environment; aerosols; measurement; particles; filtration

1. Introduction

Pollutants, which are made up of particles, vary in size and composition according to the sources of contamination. Fine particles (PM $_{2.5}$) and ultrafine particles (PM $_{0.1}$) are part of normal human life. In the past, they occurred mainly in natural form and came, for example, from volcanic eruptions. With the development of human society, their origin and concentration began to change. People began to use fine and ultrafine particles in several industrial areas, such as in the glass industry, construction and the like. In recent times, there has been a rapid development of nanotechnologies and their application in industry, medicine, engineering, energy, etc. [1,2,3]. On the other hand, it is necessary to realize that nanoparticles and ultrafine particles have a very negative effect on the human body and thus also on the health of workers who are exposed to these particles for a long time. Therefore, it is important to determine the safety and health risks related to the development of nanotechnology [4,5].

The collective of authors [6] presents five critical measures that should decisively influence the responsible development of nanotechnologies. These include:

- identification and monitoring of dangerous particles in the workplace,
- assessment of exposure and reporting of potential danger to workers,
- manage risks for health and safety at work and
- to support the safe development of nanotechnologies.

Figure.1 shows the primary sources of emissions, which can be natural or of anthropogenic origin.

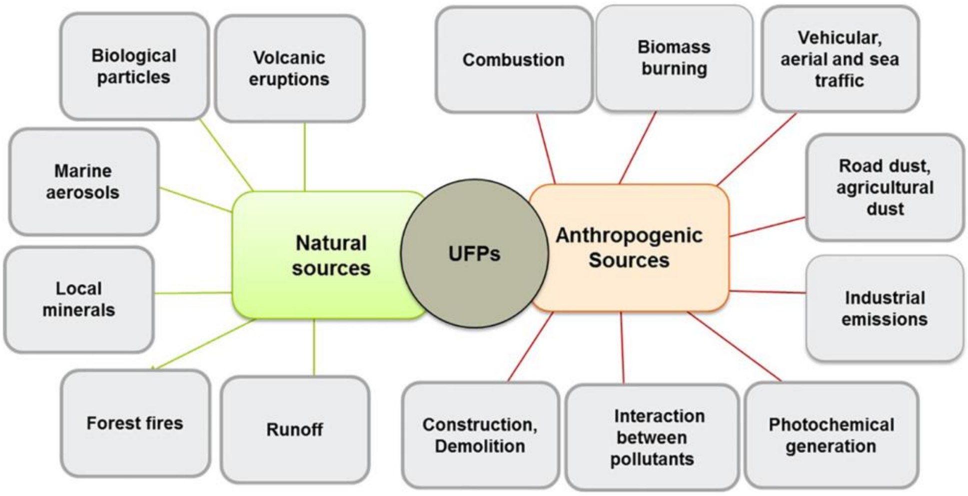

Figure 1. Potential sources of emissions (emissions) of ultrafine particles [3]

In technical practice, dust particles are defined as those particles which, after a short acceleration, reach a steady fall velocity of less than 300 cm.s^{-1} (at a pressure of 760 torr and a temperature of 20 °C). The fall speed of the dust particle depends on the specific weight and shape (lamellar, fibrous, corpuscular) [3].

Solid and liquid particles of natural origin include:

- cosmic dust
- dust from meteorites,
- inorganic dust from volcanic activity carried by the wind,
- ash and soot from forest fires,
- organic dust,
- water mist aerosol.

Solid and liquid particles of anthropogenic origin include:

- dust as a by-product of processing activities,
- dust originating from the transport of raw materials, transport and transport machines,
- of worn machine parts (brake lining, corrosion products),
- combustion products – soot and ash,
- aerosols from combustion or industrial processes.[2]

Solid particles are defined on the basis of their physical and chemical properties and dimensional parameters, they are subject to high variability in terms of properties, concentration levels and composition, which vary depending on the season, climate, space and source, while in technical practice it is often they refer to solid particles dispersed in the environment as dust, which was created by grinding, crushing, abrasion, etc. These particles are divided according to aerodynamic diameters and thus are classified as coarse (2.5—10 μm), fine (0.1—2.5 μm) and ultrafine (< 0.1 μm). A more detailed specification is given in table 1 below [4].

Table 1. Description of solid particles [4]

Title	Size [um]	Emergence	A more accurate description
Thick smoke	0,10-1,00	oxidation processes, condensation of substances evaporated under heat	e.g. welding smoke, metal melting
Fine smoke	0,01-0,50	incomplete combustion	they mostly contain carbon
Fine ash	1,00-100	escape from combustion devices	a product of coal combustion
Aerosóle	0,01-1.00	chemical reactions of water vapor and gases	a mixture of fine solid particles and gas

The shape of solid particles in the air is mostly irregular and the size also varies. These parameters significantly affect the rate of settling of particles in a gravitational, centrifugal or electrostatic field.

According to the shape, there are 3 basic types of dust particles, as follows:

- **Isometric** - they have approximately the same size in all directions, their size is often approximated by a sphere or a cube.
- **Laminar (flat)** - two of the three dimensions are significantly larger. Their shape can be compared to a plate.
- **Fibrillar (fibrous) –** one dimension is significantly larger than the others. These particles have the shape of fibers, needles [5].

The shape of the particles depends mainly on the method of their formation. The ideal shape of a particle is a sphere. This shape is created by the condensation and solidification of a few substances. If they are formed during mechanical operations, they have a much more complex shape. The particles that are created in the combustion process have cavities of different sizes [4]. The size of the particles is defined according to their size - the diameter of the particle and is given in μm. The Ferret diameter is determined as the largest dimension of a particle in a given direction. Ultrafine particles are PM (particulate mass) with an aerodynamic diameter of less than 0.1 μm. UFPs (ultra-fine particles) are typically described in terms of surface area per particle, weight or number of particles (PN - particular number), or the concentration of one of them per volume. [3]

Figure 2 shows the main properties of ultrafine particles (UFP) and the factors that influence them. The size of the particle can also be determined by the diameter of the (graticular) circle, the surface of which is as close as possible to the surface of the particle's projection (Figure 3). These dimensions are determined using a microscope [6]. Examples of particles captured on the air filter of a vacuum cleaner are shown in Figure 4.

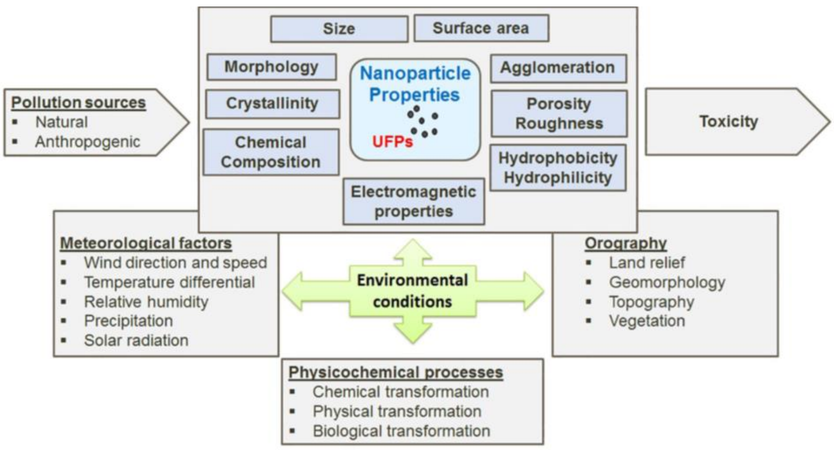

Figure 2. Properties of ultrafine particles and factors affecting them

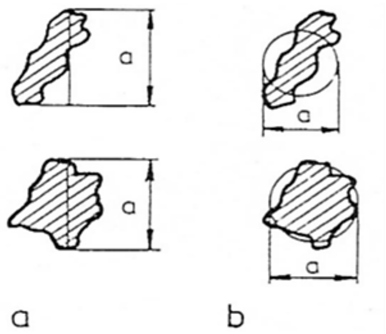

a – Feret's diameter, b – graticule circle [4]
Figure 3. Particle dimensions

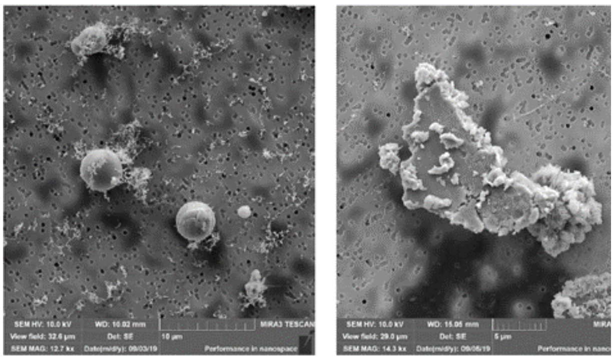

Figure 4. Particles on the air filter [6]

2. Methodology of dust measurement in the working environment

The development of a suitable methodology for measuring fine particles (FP) and ultrafine particles (UFP) is very demanding. The health effect of these particles is determined by their several properties, not only by their concentration. Unlike particles with larger dimensions, the level of sedimentation of UF (ultra-fine) and UFP in the air due to gravity is very low or negligible [5], [6].

Current related legislation: SR Government Regulation 355/2006 on the protection of employees from risks related to exposure to chemical factors at work and SR Government Regulation 121/2024 on the protection of employees from risks related to exposure to carcinogenic and mutagenic factors. This government regulations establishes requirements to protect employees from risks related to exposure to chemical factors at work and to prevent these risks, it applies to all activities in which employees are or may be exposed to chemical factors at work.

The employer must monitor dangerous chemical substances, and if they are present in the workplace, he must:

1. qualify any risk arising from these factors,
2. request additional health information necessary to assess any risk from suppliers or other available sources.

Figure 5 summarizes the main effect and mechanisms of toxicity associated with UFP exposure.

Among the related mechanisms with exposure to UFP ultrafine particles and their components (BC – bio composites, metals, ions, organic compounds, etc.), oxidative stress can lead to inflammatory processes and cardiovascular diseases, carcinogenicity, epigenetics, genotoxicity, mutagenicity, neurotoxicity and even teratogenicity [3].

Currently, many methods of measuring the concentration of dust in the air are leading: [6]

- gravimetric method of measuring dust concentration in the environment,
- optical measurement method – transmission principle of dust concentration measurement,
- optical measurement method – measurement of dust concentration based on light scattering,
- method based on the triboelectric phenomenon and others.

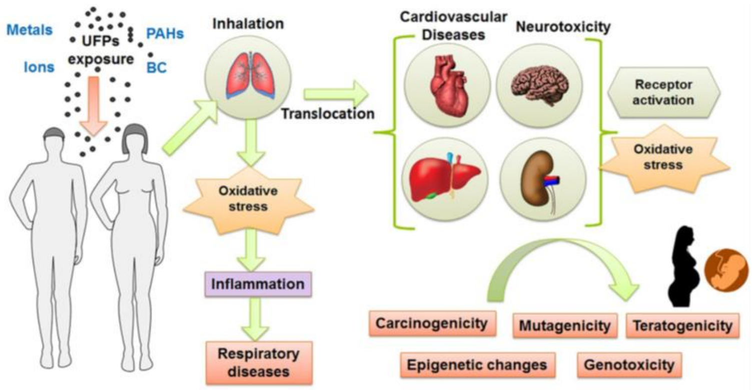

Figure 5. Toxicological effects of exposure to UFP [3]

Figure 6 presents a general diagram of the operation of typical methodologies used to measure UFP. In the CPC (Condensation Particle Counting) methodology, the particles are initially enlarged by condensation vapors until the size is determined and then counted as they pass through the laser beam. Particle detection is performed by optical methods [8].

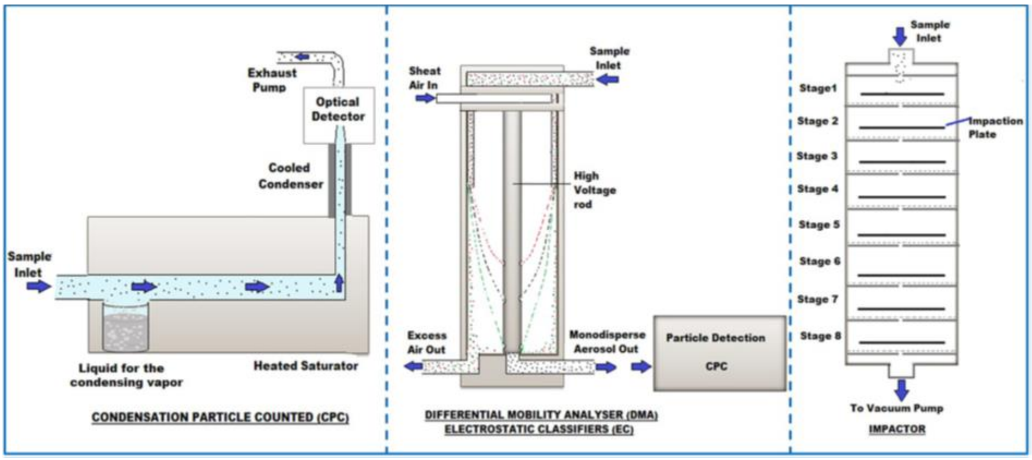

Figure 6. Principles of operation of selected methodologies used for measurement and capture and UFP [3]

Other types of equipment used are UFP monitors, laser aerosol spectrometer (LAS) with optical detection, and instruments manufactured by GRIMM Aerosol Technik Ainring GmbH & Co.KG, which include combinations of DMPS (Differential mobility particle sizer) or SMPS (scanning mobility particle sizer) systems. , DMS (differential mobility spectrometers) and CPC (condensation particle counter) for measuring particles (5 – 1110 nm), low-pressure electric impactors (ELPI - Low-pressure electric impactors), aerodynamic.

Mass concentration, defined as the mass of dust particles in a unit volume of gas (i.e. in units of mg/m^3 or $\mu g/m^3$), or in some cases number concentration, is most often used to quantify the amount of dust in the environment.

3. Experimental example

In addition to measuring aerosol emissions outdoors, it is very important to measure and control emissions indoors, not only in the work environment, but also in homes. An example is the measurement of aerosols during vacuuming (Figure 7 and Figure 9) and while smoking (Figure 8).

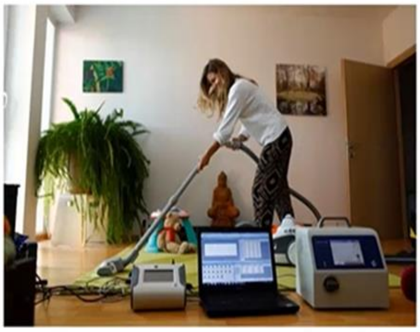

Figure 7. Vacuum cleaner using a paper bag

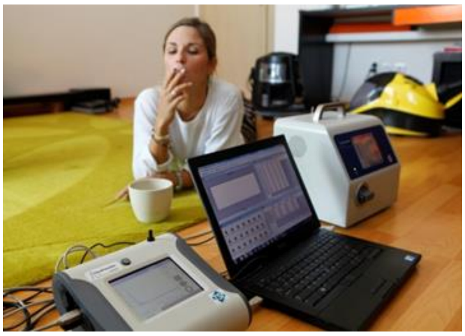

Figure 8. Experiments with cigarette smoke

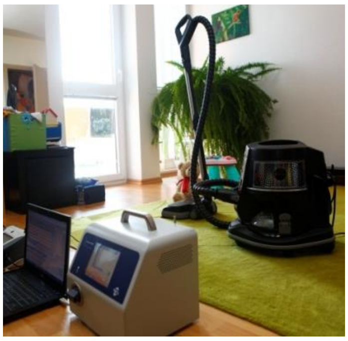

Figure 9. Vacuum cleaner using a water tank bag

Results from the experiment - 2 types of commercial vacuum cleaner:

- general vacuum cleaner,
- water tank to collect the dust – manufacturer claims the vacuum cleaner purifies the air in the meantime.

Experiments:

- nominal indoor air after 20 min. of ventilation,
- experiment with vacuum cleaner using a paper bag,
- open the windows for 20 min – ventilation,
- experiments with vacuum cleaner using a water tank bag,
- open the windows for 20 min. – ventilation,
- experiments with cigarette smoke,
- purified air measured after two hours.

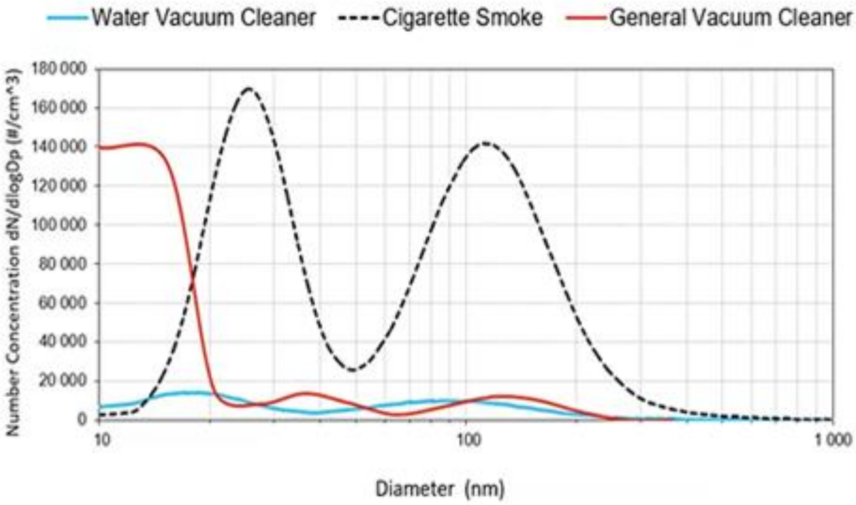

Figure 10. Results of measurements of two types of vacuum cleaners (wet and dry vacuuming method)

We found that the total number concentration and size distribution varied based on the type of vacuum cleaner used. The vacuum cleaner using a paper bag show one dominant peak at 13 nm, vacuum cleaner using a water tank show a bimodal shape and main peaks at 19 and 87 nm. We observed the total number concentration during experiments with a vacuum cleaner using a paper bag was four times higher than the number concentration of a vacuum cleaner using a water thank.

5. Conclusions

Findings reported in various literatures highlight the importance of continuing to conduct studies on UFPs as they are related to various human health conditions that contribute to the worldwide increase in morbidity and mortality. Among the problems identified are respiratory problems such as asthma and chronic obstructive pulmonary disease, pulmonary fibrosis, neuro-degenerative diseases, cardiovascular diseases, and carcinogenic activity. However, there are several mechanisms for measuring and controlling atmospheric UFP, it is necessary to continue studying the various effects of particulate matter in order to obtain sufficient evidence that leads to the creation of new public policies and measures for effective pollution prevention and control. [8]

An example was an experiment where two portable devices for measuring the size of particles, NanoScan SMPS and OPS were used to determine the size and concentration of particulate emissions generated in households by vacuuming. During the measurements, it was observed that the total number of concentrations during experiments with a vacuum cleaner using a paper bag was four times higher than the numerical concentration of a vacuum cleaner using a water tank. The conclusion follows that some types of vacuum cleaners increase the concentration of nanometer and ultrafine particles in the indoor environment. However, more experiments will be needed to analyze this effect and its cause in more detail.

Over the past decades, the occurrence of nanoparticles, ultrafine particles and micrometric particles has increased significantly, mainly due to the increase in transport, the use of nanotechnologies in industry, pharmaceuticals, medicine and research.

With our contribution, we wanted to point out the possible occurrence of particles in nano and micro dimensions in workplaces and living spaces. It is important to reduce the risk of exposure to the lowest possible level.

The analyzes showed that it is important in the field of public health to continue conducting research in the field of exposure to nanoparticles in the workplace or in the environmental environment and to obtain information about their occurrence.

Acknowledgments: This contribution was created based on the solution of the project KEGA 013TUKE-4/2022 and project VEGA 1-0485-2022.

References

1. KÖBÖLOVÁ, J.; ADAMEC, V.; URBÁNEK,M.; ZEMAN, Z.;DRBOHLAVOVÁ ,J.:Methodology for decreasing the level of risk in workplaces with the occurrence of fine and ultrafine particles.,In: Nanocon 2021, October 20 - 22, 2021, Brno, CZ , ISBN 978-80-88365-00-6
2. RUMAN,P.; DZURO,T.; KRUPA,M.: Prašnosť a jej vplyv na človeka v pracovnom prostredí In:15-th International Scientific Conference Trends and Innovative Approaches in Business Processes 2012, s. 1-6, ISBN 80-7078-136-X.
3. MORENO-RÍOS,L.A.; BEJEDA-BENÍTEZ.L.P,; BUSTILLO-LECOMPTE, C.F.: Sources, characteristics, toxicity, and control of ultrafine particles: Geoscience Frontiers 13 (2022) 101147
4. NOVÝ, R.: Technika prostředí. Vyd. 2., přeprac. V Praze: Nakladatelství ČVUT, 2000. ISBN 80-01-03492-5.
5. RICHTER, M.: Technologie ochrany životního prostředí. Vyd. 1. Ústí nad Labem: Fakulta životního prostředí Univerzity J.E. Purkyně v Ústí nad Labem, 2004. ISBN 80-7044-585-8.
6. ADAMEC,V;KÖBÖLOVÁ, K.; URBÁNEK, M.; ČABANOVÁ, K.; BENCKO, V.;TUČEK, M.: The presence of fine and ultrafine particulate matter in the work environment, Cent Eur J Public Health 2020; 28 (Suppl): S31–S36
7. BUSTIN, L.V.; TRITSCHER, T.; SPIELVOGEL, J.; BISCHOF, O.F.; SCHECKMAN, J.; KRINKE, T.: CEN standard "Harmonized counting of atmospheric ultrafine particles" and UFP monitoring initiatives in Europe, Journal of Physics 1420 (2019) 012010, doi:10.1088/1742-6596/1420/1/012010
8. BUSTIN, L.; TRITSCHER, T.; BISCHOF, O. F.; HEE-SIEW HAN.: Particle emission sizing during household vacuum cleaning TSI GmbH, Neuköllner Str. 4, 52068 Aachen, Germany, 2015,
9. FRIČ, M.; SCHWARZ, M.; DADO, M.; BUSTIN, L.: Analýza nanočastíc a mikročastíc v pracovnom ovzduší pri spracovaní kovového materiálu, Hygiena 2017,6(24) s. 112-118,
10. BADIDA, M.; LUKÁČOVÁ, K.; SZABÓ, R.: Pevné aerosóly v pracovnom prostredí, 1. vyd. – Košice, SjF TU, 2015, 209 s.. - ISBN 978-80-553-2458-6.
11. FRIČ, M.; SCHWARZ, M.; DADO, M.; BUSTIN, L.: Analýza nanočastíc a mikročastíc v pracovnom ovzduší pri spracovaní kovového materiálu, Hygiena 2017,6(24) s. 112-118,

TECHNICKÁ UNIVERZITA V KOŠICIACH
Strojnícka fakulta

Experimental testing of material in the form of filament based on PLA/PHB

Tomáš Balint [1], Jozef Živčák [1]

[1] Faculty of Mechanical Engineering, Technical University of Košice, Slovakia; tomas.balint@tuke.sk jozef.zivcak@tuke.sk

Corresponding author: tomas.balint@tuke.sk

Abstract: This scientific study brings significant results in the field of material testing. The problems consisted in the production of filament based on PLA/PHB with the help of innovative single-screw extrusion on the filament maker device. The entire production process was optimized using a constructed laminar box, thanks to which we optimized the production conditions. Also we can say that this scientific work deals with the production of a medically certified filament based on PLA/PHB and its testing using non-destructive tests on a metrotome device. The goal of this effective non-destructive scanning on a metrotome from Carl Zeiss was to detect various sample defects that cannot be detected by ordinary aspect. These defects have an impact on the resulting values of the samples for determining the mechanical properties. The porosity of the samples, the internal structure and the quality of the layers were monitored. Individual aspects were evaluated using VGStudio MAX software. A total of 40 different PLA/PHB samples were evaluated after and before mechanical testing, where up to 80 scans had to be evaluated. The results in this study yield significant findings that have implications for future research in the field.

Keywords: Polymer testing, materials, extrusion, filament, polymers, PLA, PHB

1. Introduction

Biomedical filaments must meet standards and standards of hygiene, quality and safety in order to be applied in the field of tissue engineering and regenerative medicine. The ISO 14644-7:2015 (ISO 7) standard specifies the classification of air cleanliness and minimum requirements for the design and construction of laboratories intended for production. Laboratories according to the ISO 7 standard are certified according to EU GMP C. These laboratories are used for production processing and work with materials for the preparation of solutions where filtration is required. Furthermore, the ISO 13485:2016 standard is used in the production of medical devices. This standard includes requirements for sterile properties and principles that must be met by production and handling facilities. The standard includes all quality standards adopted by the European Union [1]. The key factor for the long-term and reliable effect of the implant is the correct choice of biomaterial. The biological environment will not accept any material. Therefore, in order to optimize biological efficiency, implants should be selected in such a way as to reduce the negative biological response while maintaining adequate function. To ensure the therapeutic effectiveness of the implant, control of the parameters is essential, while it is necessary to take into account three main factors: structure, mechanical and biological properties. With this in mind, manufacturing parameters must be optimized to ensure maximum mechanical functionality. The use of polymers in biomedical applications is very attractive, especially in soft tissue applications, because polymers have the potential to induce an appropriate host tissue response. The concepts of polymer blending or polymer composites have been introduced to overcome the shortcomings of using a single polymer [2,3]. By mixing polymers, implants made of two or more polymers can provide better properties resembling human bone tissue. Implants intended for replacement are used for a variety of medical abnormalities, from heart valves, vascular grafts and stents in cardiology to bone and joint replacements [4,5]. The basic mechanical requirements of implants include: modulus of elasticity, tensile, compressive and shear strength, yield strength, fatigue strength, hardness and toughness. Non-destructive metrotome testing of samples from the given materials approximates the structure at the macroscopic level [6,7].

2. Extrusion of medically certified filament

The advantage of single-screw extruders is their simplicity of construction, but they are more likely to become clogged with material than twin-screw extruders [8,9]. Furthermore, the single-screw extruder is the most common type of extruder and offers relatively low investment costs for companies dealing with the extrusion of materials intended for biodegradable purposes [10]. If higher production and higher performance are required, twin-screw extruders are used. The easiest way to increase the throughput of the extruder is to increase the speed of the screw. This easy solution usually results in poor melt quality caused by exceeding the melting capacity of the screw design and degradation caused by high melt temperature. Using a smaller diameter screw can offer several advantages to achieve higher throughput at a higher screw speed. One of the important advantages of a smaller diameter extruder is better heat transfer characteristics. Higher output at higher screw speed can be achieved by using a smaller diameter extruder. This offers better heat transfer characteristics. A well-designed, developed screw design improves product quality and reduces the time needed to design and optimize the extrusion process, resulting in lower costs. The goal was a filament based on PLA/PHB. The production process itself took place on equipment from the 3devo company. Filament maker Composer 450 is a device for the production of filaments, on which it is possible to mix several materials. Production took place in an air-conditioned room at a temperature of 18°C, in sterile laboratory conditions. Using HDPE transit material, we cleaned the device before the actual extrusion. The cleaning process of the device itself took several hours and is necessary for the optimal course of filament extrusion. We then poured the medical granulate into the extruder hopper. During the production of the first medical filament, we set the melting temperature in the temperature range of 160°C to 180°C at 100% fan power (Figure 1). We achieved these temperatures by combining knowledge about the melting temperature of PLA/PHB materials. After the filament flow stabilized, we placed the extruded fiber in a sensor that measured the diameter of the filament. Following and optimizing all production parameters, the filament was wound into a coil.

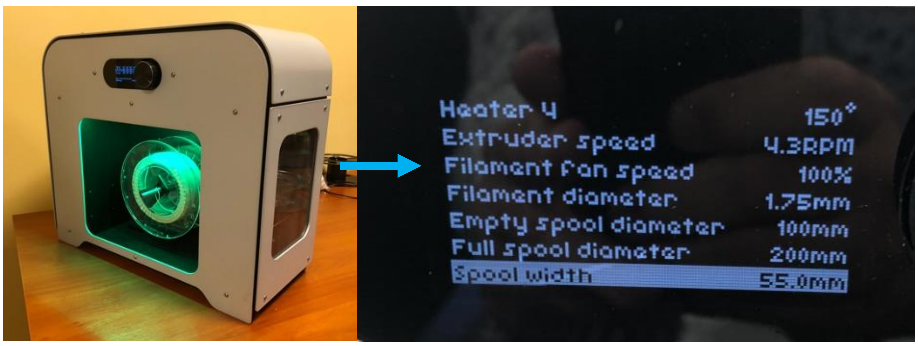

Figure 1. Extrusion setting parameters.

2.2. Optimization of laboratory conditions during filament extrusion

When extruding filaments, we optimized the working environment by using a laminar box based on the technical drawing (Figure 2). This laminar box was developed at the Department of Biomedical Engineering and Measurement at the Technical University. The compact laminar box system, made of components designed specifically for this type of laminar box, is characterized by the fact that its construction is designed for an extrusion system meeting the requirements of filament production (Figure 3). The laminar box is prepared for the installation of additional elements related to the optimization of the production process, and its design allows the configuration and change of preparations intended for the production process of biomedical filaments.

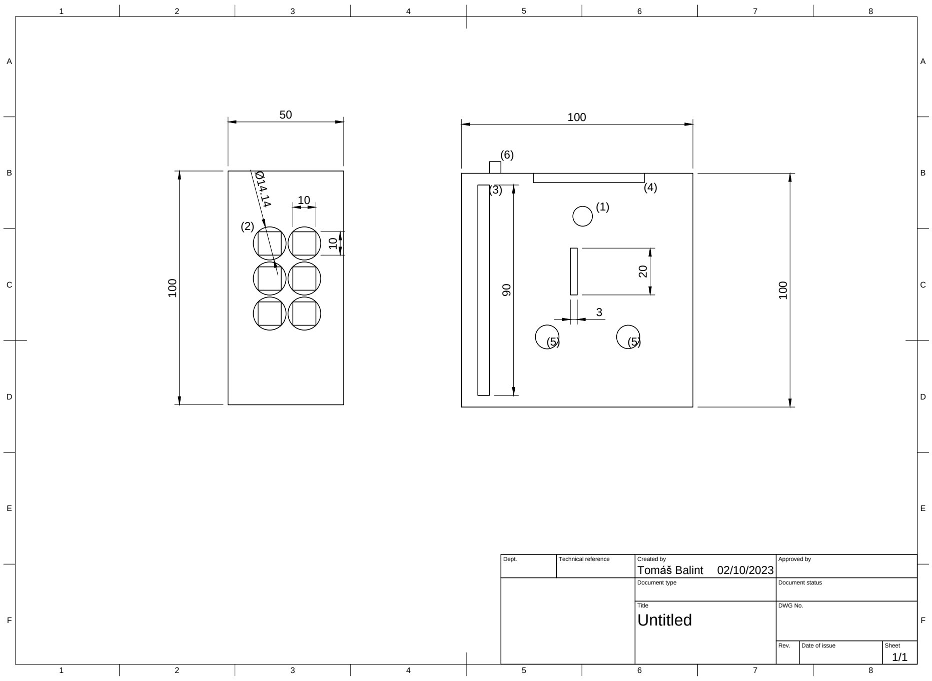

Figure.2. Technical specifications in of laminar box.

Figure.3. Technical solution of the laminar box.

3. Evaluation of non-destructive tests on a Carl Zeiss metrotome

Non-contact non-destructive measurement on a Carl Zeiss metrotome (Figure 4) was performed on PLA/PHB material samples before the tensile test and after the tensile test.

Figure.4. Taking samples in a metrotome.

The goal of this effective non-destructive scanning on a metrotome from Carl Zeiss was to detect various sample defects that cannot be detected by ordinary aspect. These defects have an impact on the resulting values of the samples for determining the mechanical properties. The porosity of the samples, the internal structure and the quality of the layers were monitored. Individual aspects were evaluated using VGStudio MAX software. A total of 40 different PLA/PHB samples were evaluated after and before mechanical testing, where up to 80 scans had to be evaluated. The total porosity of the samples gives us more accurate values, where sample no. 18 from PLA/PHB material had the largest value of 3.71%. When examining individual layers of sample no. 18 from the PLA/PHB material showed layering defects that cannot be detected with the naked eye (Figure 5). This defect can affect the resulting ROI and mechanical testing results.

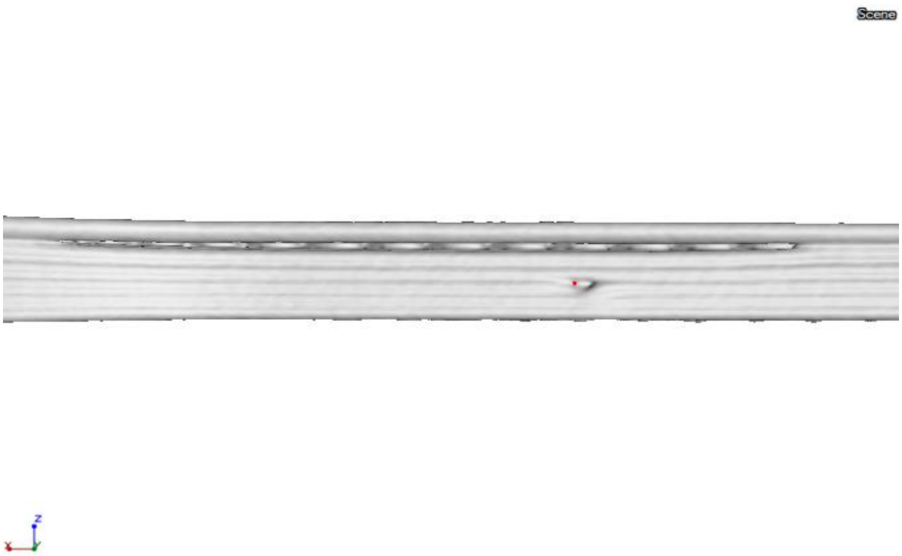

Figure.5. Layering errors of sample No. 18.

Sample No. 18 made of PLA/PHB material broke (Figure 6) in the place of interest marked before testing due to high porosity (3.71%) and the occurrence of a defect, which can be seen in (Figure 7) in cross section of the tested sample.

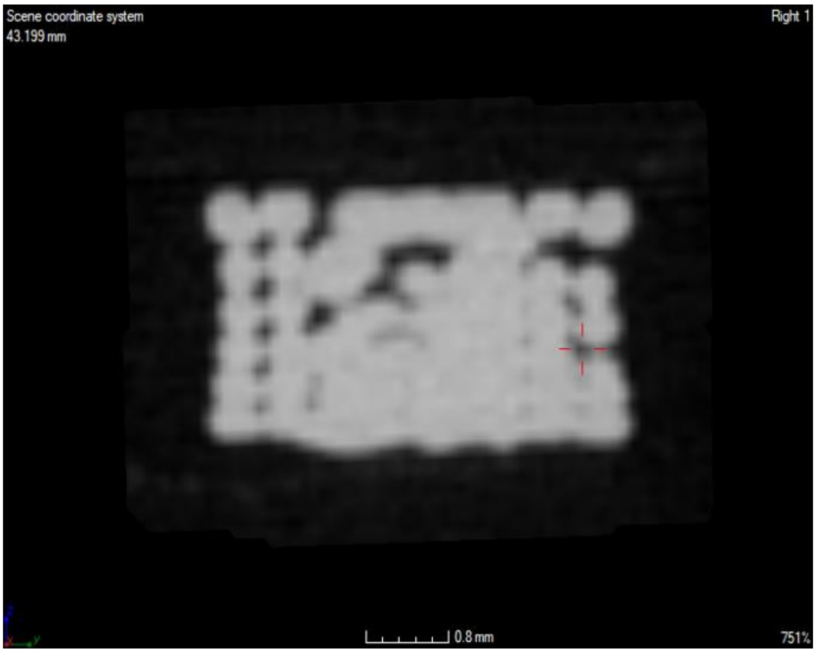

Figure.6. Cross section of sample no. 18 from PLA.

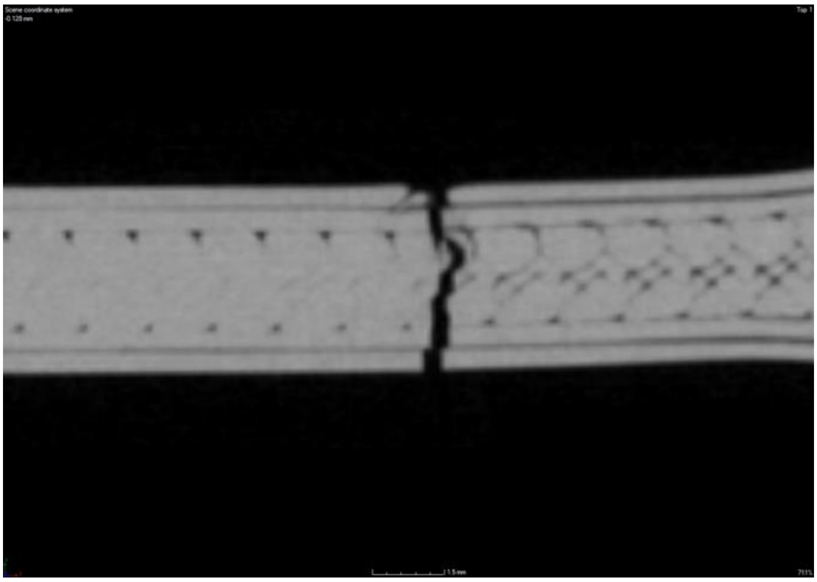

Figure.7. Sample No. 18 from PLA material after tensile test.

5. Conclusion

This scientific study stands out for its specificity in the given issue. It is therefore more difficult to discuss hypotheses and the starting points of other studies. At the beginning of the research, it is necessary to be aware of the components of the material. In our case, it was biodegradable materials such as PLA/PHB/THERMOPLASTIC STARCH AND PLASTICIZER. At the beginning of the study, the characteristics of the individual components of PLA/PHB mixtures should be mentioned. The study, which dealt with the composition and miscibility of the mentioned components, is based on the fact that PLA is the most used biopolymer in the field of application when determining places with low pressure on the human body. The study addressed several strategies to improve the properties of PLA to expand its applications. Melt mixing approaches are gaining considerable interest because they are simple, cost-effective, and readily available. Also, as our findings suggest, (PHB) is a good candidate for blending with PLA. The ability of PHB to act as a nucleating agent for PLA improves its mechanical resistance. In order to improve the processing of PLA/PHB and obtain deformable materials, plasticizers are often added. Current trends to increase the miscibility of PLA-PHB are focused on the development of composites and nanocomposites. On the basis of this knowledge, the theoretical findings of the mentioned studies can be continued and the achieved mechanical as well as biological properties of PLA/PHB components, published in this work, can be brought closer together.

Acknowledgment: This scientific study was created thanks to support under the Op-erational Program Integrated Infrastructure for the project: Open Scientific Community for Mod-ern Interdisciplinary Research in Medicine (OPENMED), code ITMS2014 +: 313011V455, co-financed by the European Regional Development Fund and thanks to support under the Opera-tional Program Integrated infrastructure for the project: Center for Advanced Therapies of Chronic Inflammatory Diseases of the Musculoskeletal System (CPT ZOPA), code ITMS2014 +: 313011W410, co-financed by the European Regional Development Fund and APVV SK-CZ-RD-21-0056 Bioresorbable materials for additive manufacturing of vessel substituents and their biomechanical characterization and thank to project VEGA 1/0599/22 - Design and biomechanical analysis of personalized instruments for arthroscopic applications and KEGA K-22-014-00 Implementation of progressive technologies in prosthetics and orthotics education and support integration with practice.

References

1. ISO 13485:2016 Medical devices — Quality management systems — Requirements for regulatory purposes [online]. [cit. 2021-8-30]. Dostupné z: https://www.iso.org/standard/59752.html.
2. M.S. SINGHVI, S.S. ZINJARDE, GOKHALE, G. V., 2019. Polylactic acid: synthesis and biomedical applications. In: Journal of Applied Microbiology. Vol. 127, no. 6.
3. ZEERATKAR, M., D. DE TULIO, M., PERCOCO, G., 2021. Fused Filament Fabrication (FFF) for Manufacturing of Microfluidic Micromixers, an Experimental Study on the Effect of Process Variables in Printed Microfluidic Micromixers. In: Micromachines. Vol. 12(8), pp. 858.
4. MIRÓN, V., FERRÁNDIZ, F., JUÁREZ, D., MENGUEL, A.: Manufacturing and characterization of 3D printer filament using tailoring materials. Procedia manufacturing. 2017. Available on the internet: https://www.sciencedirect.com/science/article/pii/S2351978917307886.
5. Tagliavini G., Solari F., Montanari R., 2016. CFD simulation of a co-rotating twin-screw extruder: Validation of a rheological model for a starch-based dough for snack food. In: Proceedings of the International Food Operations and Processing Simulation Workshop, FoodOPS.
6. KARTHIK, T., UDAYABHANU, J., WEISMAN. A. J., 2019. 3D Printing Custom Bioactive and Absorbable Surgical Screws, Pins, and Bone Plates for Localized Drug Delivery. In: J. Funct. Biomater. Vol.10(2), no. 17.
7. Wilczyński, K., Lewandowski, A., Wilczyński, K., J., 2012. Experimental study for starve-fed single screw extrusion of thermoplastics. In: Polym. Eng. Sci. 2012;52:1258–1270. doi: 10.1002/pen.23076.
8. ÇANTI, E., AYDIN, M., YILDIRIM, F.: Production and Characterization of Composite Filaments for 3D Printing. Journal of Polytechnic. 2018. Available on the internet: https://www.researchgate.net/publication/322903568_Production_and_Characterization_of_Composite_Filaments_for_3D_Printing.
9. MENČÍK, P., PŘIKRYL, R. et al., 2018. Effect of Selected Commercial Plasticizers on Mechanical, Thermal, and Morphological Properties of Poly(3-hydroxybutyrate)/Poly(lactic acid)/Plasticizer Biodegradable Blends for Three-Dimensional (3D) Print. In: Materials. Vol. 11, no. 10.
10. Tofail, S., A., M., Koumoulos EP, Bandyopadhyay A, Bose S, O'Donoghue L, Charitidis C., 2018. Additive manufacturing. In: scientific and technological challenges, market uptake and opportunities. Vol. , pp. 21:22–37.

Characteristic electric and electromagnetic properties of materials used for rotor and stator laminations within electric motor based on energy losses

Martin Matej Benda [1*], Emil Spišák [1]

[1] Technical University of Košice, Faculty of Mechanical Engineering, Košice, Slovakia
* Correspondence: - martin.matej.benda@tuke.sk, Department of Mechanical Engineering Technologies and Materials, Technical University of Košice, Letná 9, 042 00 Košice, Slovakia

Abstract: Electric automobiles gained popularity in recent years, and it reflected in increased interest in the research of electric motors which are used as their propulsion. This paper presents a short review on electric and electromagnetic properties affecting energy losses generated during electric motor work cycle. Conclusion contains recommended variations of these properties for minimalization of energy losses.

Keywords: electric motor; laminations; iron core losses; eddy currents, hysteresis effect

1. Introduction

Electric motors are devices used to convert electrical energy into motion. Over the years of automotive development, a lot of electromotors found their place in the design of automobiles and today we can find dozens of them inside their construction. They were used for applications which increased the comfort of automobiles and added additional features while the propulsion was solved through the use of a combustion engine [1,2].

This is changing today as increasing ecological awareness is forcing the industry to find alternative solutions to decrease current emissions of automobiles produced mostly by their combustion engine. A lot of people see electric motors as solution to this problem either by completely replacing the combustion engine with electric motor or by using both electric motor and combustion engine in the form of a hybrid car. These electric motors produce rotational movement out of electric energy which can be acquired from renewable sources to decrease overall emissions which improves its impact on the environment [1,2].

Basic parts of every electric motor are its stator and rotor. In the case of the typical rotational motor, stator is its stationary part while the rotor is its rotating part that is placed inside of the magnetic field. The basic part of the rotor and stator is their iron core, which is made by the separate laminations connected into integral shape which is called a stack. These laminations are made out of electrical steel with its characteristic properties many of which help in reducing of iron core energy losses [3,4].

2. Analysis of the iron core loss

Iron core loss is term describing energy losses in electric motor laminations which are generated during its demagnetization and magnetization work cycle.

Two most significant types of iron core losses are eddy currents and hysteresis effect [5].

2.1. Eddy currents

Eddy currents are currents induced inside of conductive iron core exposed to the changing magnetic field. These constantly circulating eddy currents are encountering resistance of the material, transforming the electrical energy into heat. Another negative characteristic of the eddy current is that they can generate their own magnetic field which can interact in negative way with main magnetic field and decrease the performance of electromotor [5,6].

Laminations are greatly helping with the issue of eddy currents by separating the core into isolated parts that allows us to control and isolate them into smaller loops reducing the overall energy losses [5,6].

Main properties that affect eddy currents in laminations are electrical resistance and magnetical permeability [7].

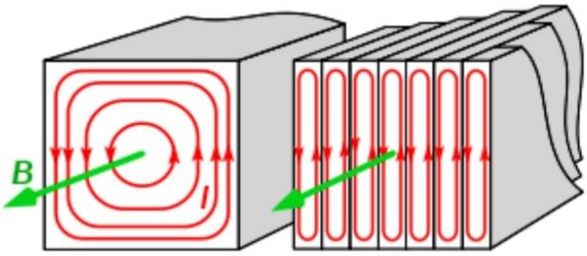

Figure 1. Ilustration of eddy currents in full and laminated material [8].

2.2. Hysteresis effect

When external magnetic field affects material, the magnetic domains within the material align with affecting magnetic field leading to magnetization of the material. When the magnetic field is reversed, the domains retain residual magnetization and don't return fully into their original random state. To overcome this residual magnetization during the reversing of the external magnetic field we need to expend energy which is decreasing the performance of the electric motor. The electric energy is transformed into heat during this process [9,10].

Laminations are decreasing the hysteresis losses by separating the core into isolated sections that are specifically constructed to concentrate the magnetic flux into smaller paths, which helps us to minimize hysteresis losses while increasing our control over the magnetization and demagnetization process [9,10].

Main properties that affect Hysteresis effect in laminations are coercivity, saturation flux density and magnetic permeability [9,10].

2.3. Magnetostrictive hysteresis losses

Magnetostriction and hysteresis are related effect, and it is property of a material defined as mechanical deformation under the influence of the changing external magnetic field. This effect is reversible by removing the object from the changing magnetic field [11].

Simplified, magnetostriction in laminations occurs within magnetic material with crystal lattices. Groups of ions and electrons organize themselves into domains and their unpaired electrons align under the influence of their small magnetic moments. Because of energetic reasons, these domains are small. However, under the influence of an external magnetic field, domains aligned with magnetic field increase while others reduce. Based on the orientation of crystal, some of the orbitals of electrons are not able to align with external magnetic field because of distances between electrons and ions. These distances need to grow for orbitals to get aligned with magnetic field. These changes result in elongation of crystal lattice in the direction of magnetic field, or they can be elongated in different directions in right angles to the magnetic field. In some cases, there may be even contraction [11].

Magnetostriction can create iron core losses by mechanical deformations which can lead to internal friction, stress, and vibrations [11,12].

3. Results

Analyzation of iron core losses determined which properties influence these energy losses the most, but these properties need to be analyzed further to determine how exactly are they positively impacting the performance of electric motor.

3.1. Magnetic permeability

Magnetic permeability (μ) is property defining its capacity for passage of magnetic flux lines , which define ability of the material to be magnetizied under the influence of the magnetic field. Magnetic permeability unit of measuremenet is – H/m [13].

There are two basic types of magnetic permeability:

- Absolute magnetic permeability (μ) – It is the ratio of magnetic flux saturation (B) to the strength of the magnetic field (H), expressed by the formula $\mu = B/H$.

- Relative magnetic permeability (μ_r) – It is ratio of absolute magnetic permeability (μ) of the material to the permeability of vacuum (μ_o), expressed by the formula $\mu_r = \mu/\mu_o$ [13].

Based on the permeability we can separate materials into three categories:

- Paramagnetic materials – Their magnetic permeability is slightly positive. Their magnetic moments tend to align with magnetic field resulting in weak atraction.

- Diamagnetic materials – Their magnetic permeability is slightly negative. Their magnetic moments are negative to the magnetic field resulting in weak repulsion.

- Ferromagnetic materials – Their magnetic permeability is greatly positive and they can be strongly magnetizied. Their magnetic moments easily align with magnetic field and they have strong atraction to it [13].

3.2. Saturation flux density

Saturation flux density (B_s) is closely tied to magnetic permeability. It is a property that defines the maximal capacity of magnetic flux within material that can be proportionately received as response to increasing magnetic field. A material that reaches saturation no longer increase magnetic flux density proportionately to the increasing magnetic field [14].

3.3. Electrical Resistance

Electrical resistance (R) is material characteristic defining how much is a material opposing the flow of electrical current, just like friction oppose movement in mechanical systems. Electrical resistance is opposite of electrical conductivity [15].

Ohm law – Voltage (V) = Current (I) x Resistance (R) (Ω) [15].

3.4. Coercivity

Coercivity (H_c) is a property measuring material resistance to demagnetization under the influence of the external magnetic field. It is an intensity of external magnetic field (H) required for demagnetization of material after we put it in fully flux saturated state [16,17].

There are three types of coercivity:

- Normal coercivity (H_{CN}) – Intensity of magnetic field required to reduce the magnetic flux (B) to 0.

- Intrinsic coercivity (H_{CI}) – Intensity of magnetic field required to reduce the magnetization (M) of material to 0.

- Remanence coercivity (H_{CR}) – Intensity of magnetic field required to reduce the remanence magnetization to 0. This means that after removing material from external magnetic field both magnetic flux and magnetization stays at 0 [16,17].

4. Discussion

After careful analysis of the iron core losses and main properties influencing them, I came upon these conclusions:

High magnetic permeability is allowing magnetic flux to pass through material more easily improving our control over magnetic flux line concentrating them within laminations, reducing the generation of the eddy currents and minimizing the hysteresis losses. It is also improving our control over the magnetization and demagnetization process which happens on smaller hysteresis loop. This in turn help with decreasing hysteresis losses [7,9,10,13]. Therefore, rotor and stator application require high magnetic permeability.

High saturation flux density allows a material to receive larger magnetic flux which in combination with permeability leads to improved magnetization and demagnetization cycles resulting in a smaller hysteresis loop. This in turn help with decreasing hysteresis losses [9,10,14]. Therefore, rotor and stator application require high saturation flux density.

High electrical resistance of material opposes flow of eddy currents in laminations decreasing the iron core losses and improving the performance of electric motor. Therefore, rotor and stator application require high electrical resistance [7,15].

Low coercivity materials have an advantage in optimizing the effectiveness of the electric motor because demagnetization and magnetization cycles of laminations need less energy. This allows for smaller hysteresis loop which in turn reduce the hysteresis loss [9,10,16]. Therefore, rotor and stator application require low coercivity of the materials.

While right choice of materials in consideration to these properties may greatly improve the performance of the electric motor, they themselves are still strongly affected by technology which is used in manufacturing of laminations. Most common technology used for production of laminations is shear cutting which can affect these properties because of plastic and elastic deformations produced during this process and disruptions of the crystal lattice of the material. These deformations lead to residual stress of the cutting segment which is induced next to the cutting segment. A lot of research has been done in this area and residual stress around the cutting area is still highly topical subject of research [18,19,20].

Acknowledgments: This work was supported by by the project APVV-21-0418.

Conflicts of Interest: "The authors declare no conflict of interest."

References

[1] Murat Yilmaz., Limitations/capabilities of electric machine technologies and modeling approaches for electric motor design and analysis in plug-in electric vehicle applications. *Renewable and Sustainable Energy Reviews 52 (2015) 80-99*

[2] Racz, Andrea Aurora, Ionuţ Muntean, and Sergiu-Dan Stan. "A look into electric/hybrid cars from an ecological perspective." *Procedia Technology* 19 (2015): 438-443.

[3] Petro, John. "Advanced Materials for Motor Laminations: Past, Present and Future." *9th International Conference on Energy Efficiency in Motor Driven Systems*. 2016.

[4] de Almeida, Anibal T., et al. "Electric motor standards, ecodesign and global market transformation." *2008 IEEE/IAS Industrial and Commercial Power Systems Technical Conference*. IEEE, 2008.

[5] Mi, Chunting, Gordon R. Slemon, and Richard Bonert. "Modeling of iron losses of permanent-magnet synchronous motors." *IEEE Transactions on Industry applications* 39.3 (2003): 734-742.

[6] Lamprecht, Erik, Martin Hömme, and Thomas Albrecht. "Investigations of eddy current losses in laminated cores due to the impact of various stacking processes." *2012 2nd International Electric Drives Production Conference (EDPC)*. IEEE, 2012.

[7] Hamzehbahmani, Hamed, et al. "Eddy current loss estimation of edge burr-affected magnetic laminations based on equivalent electrical network—Part II: Analytical modeling and experimental results." *IEEE transactions on power delivery* 29.2 (2013): 651-659.

[8] Introduction to Design Laminated Cores [online]. 2023-14-12. Available on internet: https://frenetic.ai/magnetic-notes/introduction-to-design-laminated-cores

[9] Price, Edward. "MAGNETIC DIPOLES, HYSTERESIS AND CORE LOSES." *Enviromental potentials white paper.–2006* (2006): 1-9.

[10] Narod, B. B. "The origin of noise and magnetic hysteresis in crystalline permalloy ring-core fluxgate sensors." *Geoscientific Instrumentation, Methods and Data Systems* 3.2 (2014): 201-210.

[11] Fiorillo, Fausto, et al. "Hysteresis in magnetic materials." *The Science of Hysteresis* 3 (2006): 1-190.

[12] Ebrahimi, Hassan, et al. "Effects of stress and magnetostriction on loss and vibration characteristics of motor." *IEEE Transactions on Magnetics* 52.3 (2015): 1-4.

[13] Undestanding Magnetic Permeability [on-line] 2023 [cit. 2023-14-12]. Available on internet: https://idealmagnetsolutions.com/knowledge-base/magnetic-permeability-table/

[14] Permeability and Saturation [on-line] 2023 [cit. 2023-14-12]. Available on internet: https://www.allaboutcircuits.com/textbook/direct-current/chpt-14/permeability-and-saturation/

[15] What is electrical resistance [on-line] 2023 [cit. 2023-14-12]. Available on internet: https://www.electricityforum.com/what-is-electrical-resistance

[16] Bertotti, Giorgio. *Hysteresis in magnetism: for physicists, materials scientists, and engineers*. Gulf Professional Publishing, 1998.

[17] Givord, Dominique, Michel Rossignol, and Vitoria MTS Barthem. "The physics of coercivity." *Journal of magnetism and magnetic materials* 258 (2003): 1-5.

[18] Roháľ Vladimír, Spišák Emil, Mulidran Peter, Majerníková Janka. Basic classification and processing of electrical steels. The International Journal of Engineering and Science. Roč. 9, č. 7 (2020), s. 1-6 . - ISSN 2319-1813

[19] Spišák, Emil, et al. "The impact of shear gap size on the quality of the sheared surface in electrical steel sheet blanking." *Acta Met. Slovaca* 26 (2020): 49-53.

[20] Slota, J., E. Spišák, and J. Majerníková. "Experimental and finite element analysis of the shear cutting process of electrical steel sheets under various process conditions." *IOP Conference Series: Materials Science and Engineering*. Vol. 651. No. 1. IOP Publishing, 2019.

Distance measurement using the ultrasonic sensor

Ondrej Benedik [1], Katarína Paľová [2], Ivana Koláriková [3] and Tatiana Kelemenová [4,*]

[1] Technical University of Kosice, Faculty of Mechanical Engineering; ondrej.benedik@tuke.sk
[2] Technical University of Kosice, Faculty of Mechanical Engineering; katarina.palova@tuke.sk
[3] Technical University of Kosice, Faculty of Mechanical Engineering; ivana.kolarikova@tuke.sk
[4] Technical University of Kosice, Faculty of Mechanical Engineering; tatiana.kelemenova@tuke.sk
* Correspondence: tatiana.kelemenova@tuke.sk; Tel.: +421 55 6022361

Abstract: The article deals with the methodology of distance measurement using an ultrasonic sensor. Verification of the sensor is very important, because the principle of measurement is based on the time-of-flight principle, which is sensitive to the temperature and humidity of the environment through which the ultrasonic wave propagates. Determining the measurement uncertainty is an integral part of expressing the measurement result, while talking about the reliability of the measurement result.

Keywords: ultrasonic; measurement; uncertainty, deviation

1. Introduction

Distance measurement is a measured quantity quite often, and a non-contact method of measurement is frequently required to determine the distance if the measured object or sensor carrier is moving or there is another obstacle that does not allow the use of contact distance sensors. Of the non-contact forms of measurement, optical, radar, capacitive or ultrasonic principles are often used. For longer distances, it is cost-effective to use the ultrasonic principle.

Ultrasonic distance sensors are designed for non-contact distance measurement and these types consist of transmitter and receiver or transceiver which is able to transmit and to receive ultrasonic sound (Fig. 1). The main idea is to measure the travel time of the ultrasonic sound wave from the sensor to the detected object. The ultrasonic transmitter sends a sound frequency of above 18 kHz in the air at the speed of 344 meter per second (at 20°C) and the receiver receives the reflected sound from the object. Distance between the transmitter and the object can be calculated by simple calculation by considering the time taken by the ultrasonic wave to travel from transmitter and received back (reflected) by the receiver. Measurement range is up to several meters.

The ultrasonic principle of the sensor can reliably detect transparent materials and materials with different color, roughness and surface gloss. However, the disadvantage of sensors based on the principle of ultrasound is the sensitivity to the environment in which the ultrasound propagates. The speed of ultrasound propagation depends on the density of the material or medium through which it propagates, on temperature and humidity if it is a gaseous environment.

In order to measure the distance, it is necessary to determine the time of the ultrasound path, and this can be a problem when a fast measurement is required, because the speed of sound is much smaller compared to the speed of light. If quick measurements are needed and this measurement is followed by quick action, then the use of this sensor should be considered.

Low cost ultrasonic sensors and more expensive sensors for industrial use, which already have a higher ingress protection level, are available for distance measurement. Industrial ultrasonic sensors with a higher ingress protection level can therefore also be used in environments with high humidity and dust and in environments with the presence of aggressive substances and with the presence of smoke and fog. However, the reliability of these sensors needs to be verified.

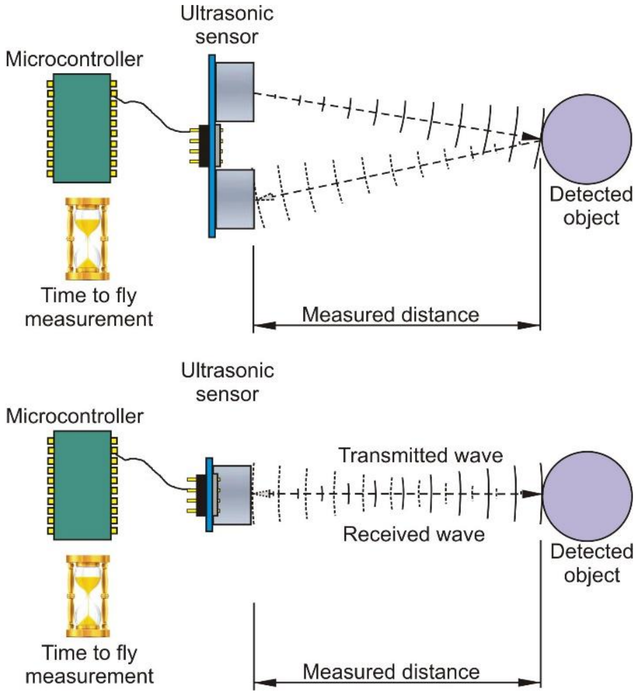

Figure 1. Principle of ultrasonic distance sensor.

2. Experimental verification of distance sensor

Ultrasonic distance sensor with analogue output 0 – 10V has been selected for testing. The sensor uses 300 kHz sound frequency. Measurement range is from 120 mm up to 1000 mm and it has linear characteristic. Repeat accuracy is ±0.15% and resolution is 0.037 mm.

Next step is to examine properties of the sensor. Experimental stand (Fig. 2) has been designed for testing and set of length gauges (Fig. 2) have been used for sensor testing.

Figure 2. Experimental testing of sensor and length gauges.

Gauge lengths – blocks (Fig. 2) have been used as etalon of length and desired value of length or distance has been composed from these blocks. Two sets of gauges have been used for testing and it is possible to compose every possible etalon of length with resolution 0.001 mm in range 0 to 1000 mm.

Some materials are not suitable for distance measurement. Vibration absorbents may cause problems with measurement. For this reason, testing of distance with this material has been executed.

Experimental testing has been executed with solid and soft (vibration absorbent) material. Results from these experiments are visible in Fig. 3.

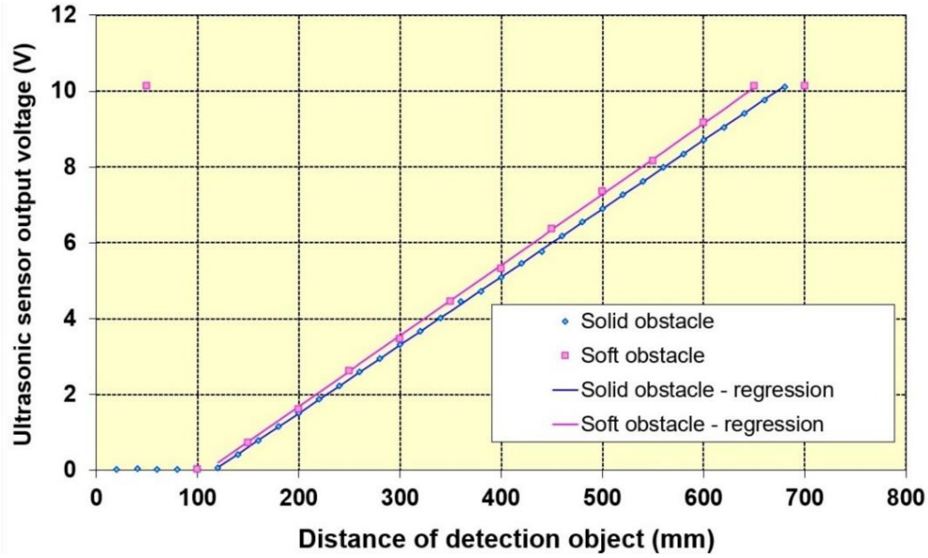

Figure 3. Verification of ultrasonic distance sensor on various material of detected object.

As it is visible (Fig. 3), the sensor has linear characteristic with dead zone, it means that it is not able to measure distances less than 120 mm. Total measurement range is up to 700 mm and after this value sensor has constant value of output voltage. There is also visible difference (change of slope of the characteristic) between the measurement realized with solid material and soft compliant material.

Calibration characteristic from the measurement to solid obstacle is shown in Fig. 4.

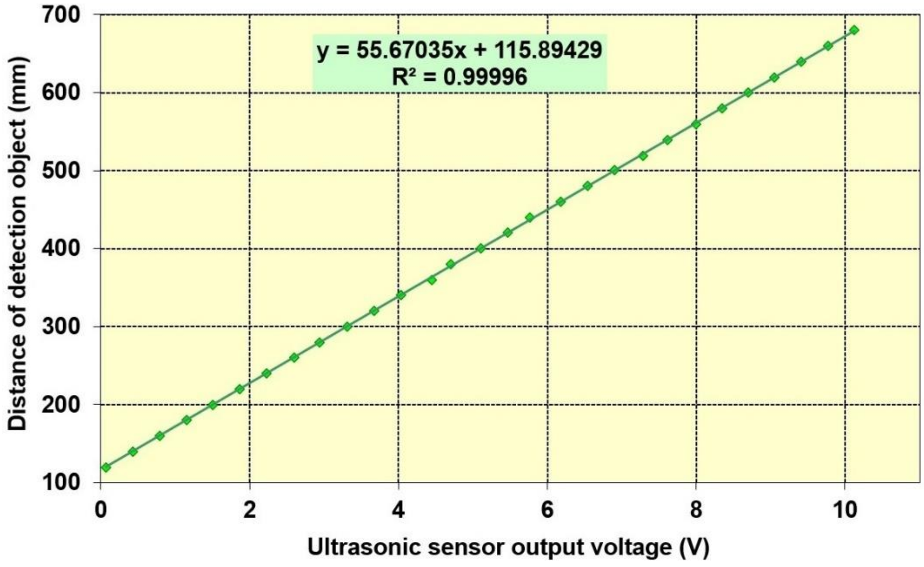

Figure 4. Measurement result of ultrasonic sensor – calibration characteristic.

Math model obtained from regression of calibration characteristic define the equation (Fig. 4), which can be used for recalculation of measured output sensor voltage to requested information about position measurement. For practical usage of the sensor, it is necessary to analyze the uncertainty of measurement.

3. Determination of the standard uncertainty of measurement

By determining the measurement uncertainty, we are trying to determine the degree of trustworthiness of the obtained measurement value. The measurement value should always be presented together with the measurement uncertainty. The reliability of the determination of the measurement value can have a serious impact on the functionality of the device or even on the safety of using the device. Therefore, the goal is to determine or estimate the uncertainty of the measurement under all circumstances.

Calibration characteristic (Fig. 4) is made for set of values (x_i - sensor output voltage, y_i – distance of detected object). The calibration curve is approximated with linear model $y = b_0 + b_1 \cdot x$, where regression coefficients also have uncertainty of determination expressed with equations:

$$u^2{}_{(b1)} = \frac{n}{n\sum_{i=1}^{n} x_i^2 - \left(\sum_{i=1}^{n} x_i\right)^2} \cdot \sigma^2 . \tag{1}$$

$$u^2{}_{(b0)} = \frac{\sum_{i=1}^{n} x_i^2}{n\sum_{i=1}^{n} x_i^2 - \left(\sum_{i=1}^{n} x_i\right)^2} \cdot \sigma^2 . \tag{2}$$

Covariance between these regression coefficients estimation is defined with equation:

$$u_{b0,b1} = \mathrm{cov}(b0, b1) = \frac{-\sum_{i=1}^{n} x_i}{n\sum_{i=1}^{n} x_i^2 - \left(\sum_{i=1}^{n} x_i\right)^2} \cdot \sigma^2 . \tag{3}$$

Where σ is standard deviation of distance (y_i) it is possible to estimate with residual variance:

$$\sigma_{MSE}^2 = \frac{1}{n-2}\sum_{i=1}^{n}\left[w_i - \left(b_1 \cdot x_i + b_0\right)\right]. \tag{4}$$

For general math model described with polynomial of p degree $y = b_0 + b_1 \cdot x + b_2 \cdot x^2 + ... + b_p \cdot x^p$ overall standard uncertainty is defined as:

$$\begin{aligned} u_y = &\sum_{j=0}^{p} x^{2\cdot j} \cdot u_{bj} + \left(\sum_{j=1}^{p} j \cdot x^{j-1} \cdot b_j\right)^2 \cdot u_x^2 + \\ &+ 2 \cdot \sum_{j=0}^{p-1} \sum_{k=j+1}^{p} x^j x^k u_{bj,bk} \end{aligned} . \tag{5}$$

For our linear model equation (5) can be simplified:

$$u_y = (u_{b0}^2 + x^2 \cdot u_{b1}^2) + b_1 \cdot u_x^2 + 2\left(x \cdot u_{b0,b1}\right). \tag{6}$$

Standard uncertainty (Fig. 5) is obtained by applying the equation (6) for measurement chain with ultrasonic distance sensor. These values represent collected uncertainty for all parts of measuring chain (ultrasonic sensor, multimeter, length gauges, positioning table etc.)

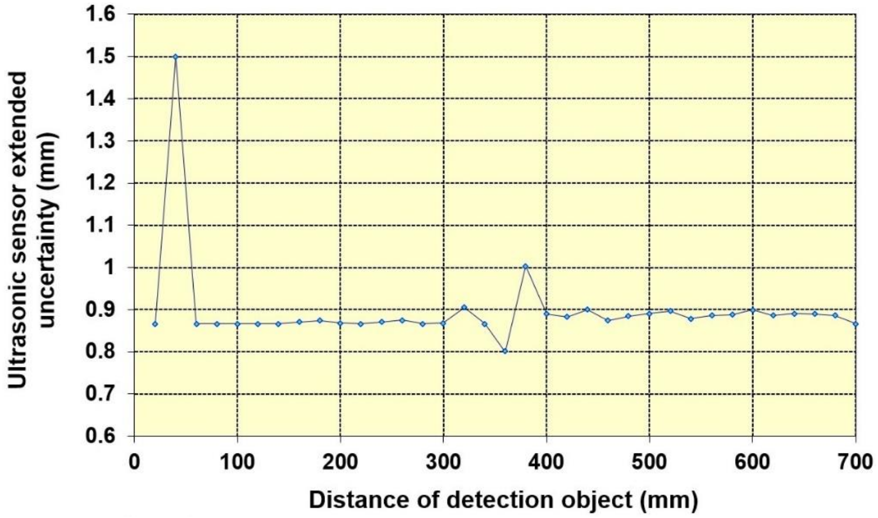

Figure 5. Standard uncertainty of measurement using the ultrasonic sensor.

Larger value of uncertainty occurs because it is out of the useful range of the sensor. All other uncertainties are less than 1 mm. Consequently, standard uncertainty depends also on more factors (not only on sensor).

4. Conclusions

Extended uncertainty of ultrasonic sensor measurement is less than 1.5 mm. However, this value is extreme and occurs only at a distance of 40 mm. This value is probably related to the minimum value of the distance that the sensor is probably capable of measuring, so we can exclude this value from the set of measurements and the measurement range will be limited by this value. In this case, the extended uncertainty is less than 1 mm when considering the uniform law of distribution of measured values with probability P = 0.95. In further research, the influence of environmental parameters on the measurement uncertainty of this sensor will be investigated.

Acknowledgments: The authors would like to thank the Slovak Grant Agency - project VEGA 1/0191/24 and KEGA 004TUKE-4/2024.

Conflicts of Interest: The authors declare no conflict of interest.

References

1. Kelly, N.: A Guide to Ultrasonic Sensor Set Up and Testing Instructions, Limitations, and Sample Applications. Application Note. Michigan State University. available online: http://www.egr.msu.edu/classes/ece480/capstone/fall09/group05/docs/ece480_dt5_application_note_nkelly.pdf.
2. Carullo, A.; Parvis M.: An Ultrasonic Sensor for Distance Measurement in Automotive Applications. In: IEEE SENSORS JOURNAL, vol. 1 n. 2, 2001. pp. 143-147. - ISSN 1530-437X.
3. Henning, B., Rautenberg, J.: Process monitoring using ultrasonic sensor systems, Ultrasonics, Volume 44, Supplement, 22 December 2006, Pages e1395–e1399.
4. Taylor, B.N. and Kuyatt, C.E., 1994, Guidelines for Evaluating and Expressing the Uncertainty of NIST Measurement Results, NIST Technical Note 1297.
5. [EA-4/02 1999] Expression of the Uncertainty of Measurement in Calibration. European co-operation Accreditation Publication Reference. December 1999.
6. [JCGM 100 2008] JCGM 100 – Evaluation of measurement data – Guide to the expression of uncertainty in measurement (ISO/IEC Guide 98-3). First edition September 2008. Available online: http://www.iso.org/sites/JCGM/GUM-JCGM100.htm.
7. [JCGM 104 2009] Evaluation of measurement data – An introduction to the "Guide to the expression of uncertainty in measurement" (ISO/IEC Guide 98-1). First edition July 2009. Available online: http://www.bipm.org/en/publications/guides/gum_print.html.

TECHNICKÁ UNIVERZITA V KOŠICIACH
Strojnícka fakulta

Methodology for measuring pressure and air flow

Leo Brada [1,*], Lubica Mikova [2] and Erik Prada [3]

[1] Technical University of Košice, Faculty of Mechanical Engineering, Department of Power Engineering, Vysokoškolská 4, 042 00 Košice; leo.brada@tuke.sk
[2] Technical University of Košice, Faculty of Mechanical Engineering, Department of Power Engineering, Vysokoškolská 4, 042 00 Košice; lubica.mikova@tuke.sk
[3] Technical University of Košice, Faculty of Mechanical Engineering, Department of Power Engineering, Vysokoškolská 4, 042 00 Košice; erik.prada@tuke.sk
* Correspondence: leo.brada@tuke.sk

Abstract: This article focuses on the design and testing of pressure and air flow measurement systems. Verification of measurement principles and sensor testing is an important part of engineering practice. This article discusses the principles of air flow measurement as well as methods of testing measuring apparatus for air pressure measurements in a given system. This procedure can be used for further testing and measuring in the future.

Keywords: pressure, air flow, pressure sensors

1. Introduction

Measuring fluid parameters in industry is an essential part of the production process. Whether it is pneumatic and hydraulic machines, air quality in the workplace or lubricant and coolant parameters. These measurements are very necessary not only in mechanical engineering but also in the food, aerospace, medical, chemical and agricultural industries. This article focuses on the measurement of air parameters intended for pulmonary ventilation, which has been quite sought after and needed for the past years.

2. Air parameters

Most commonly measured air parameters are: temperature, pressure, humidity, oxygen concentration, air quality and the content of pollutants and unwanted gases in the air. Depending on the application, only selected parameters necessary for the task are measured. In the case of pulmonary ventilation, the 3 main parameters to be monitored are: pressure, flow rate and humidity. Specialized measuring instruments are used for sensing the individual parameters, but some measuring instruments can measure multiple parameters at the same time. Such instruments tend to be relatively expensive, and some professional instruments are unavailable to the general public. Therefore, there is a need for a simpler and more cost-effective way to measure the required parameters. In engineering practice, stationary measuring instruments that are mounted on an existing system and perform a continuous measurement of a given section, for example a pipeline, are most used. Such instruments are varied not only in design but also in quality, availability and price. High quality and accurate measuring instruments are usually not available to the general public as they are specialized instruments for industry. For the purpose of simple but effective pulmonary ventilation this is unacceptable as the necessary sensors must be as cheap and accessible as possible in case of failure and need for replacement. The second most used group of measuring devices are portable measuring devices. Portable instruments are advantageous because of their weight, size and the possibility of measuring several parameters with one instrument. These instruments are mainly used for fault inspection.

In the end, the best decision was to use MEMS sensors, which are essentially miniaturized measuring units. Such a unit contains 3 main components: a measuring sensor, a communication interface and a data processing unit [1]. The output data is sent using SPI and I2C communication protocols depending on the module in question. Such measurement modules are relatively small, inexpensive, affordable, easy to operate and to process data from. For data processing, microcontrollers such as Arduino or Raspberry Pi are used, which can receive the signal from the sensors and thus visualize the data from them or further process it according to the need of the task. Most MEMS modules have built-in sensors that can measure not just 1 parameter but several at once. An example of such a sensor is the BME680 from Bosch, which can measure not only pressure but also humidity and air temperature, and in addition can detect organic substances with carbon in the air [2].

3. Air pressure measurement

Pressure measurement can be approached in several ways, for example with a bellows manometer, an aneroid manometer, a resistance strain gauge or a piezoelectric pressure sensor. These sensors work on the principle of air acting on the measuring mechanism, which deforms and thus changes its physical properties. Based on this change, the amount of pressure applied to the measuring instrument can be determined with a high degree of accuracy. These gauges are mounted on an existing pipeline or other fluid distribution system and measure the fluid parameters continuously. However, robust mechanical measuring devices are unsuitable for use in this type of lung ventilation as, apart from their size and weight, they do not provide data in a suitable manner. Therefore, it is more appropriate to use MEMS sensors that can be easily applied to the existing air distribution system. Also, data collection is simple and fast. Another advantage is the I2C and SPI communication itself. These communication protocols operate on a so-called master/slave system. This means that the microcontroller is in the master role, collecting data from slave sensors, and other components, and controlling them. The sensors themselves and other necessary components are in the slave role which means that they cannot control other devices on the communication link and serve only as input/output devices. Both communication protocols can control more than 1 slave device on 1 communication line at the same time. The difference between SPI and I2C is that SPI can only have 1 master device and multiple slave devices on 1 line, unlike I2C which can have multiple master devices on 1 line. There is also a difference in the wiring and the speed of sending data as SPI requires 4 data channels and is faster as opposed to I2C which only requires 2 data channels and is slower. For this case Arduino is very suitable as it is very easy to visualize data from it and also its wiring is very simple [3].

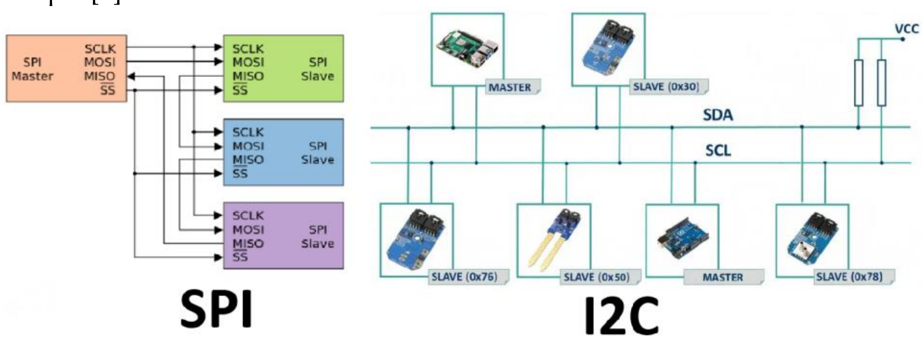

Figure. 1 Comparison of SPI and I2C communication [3, 4]

As for the measurement itself, it is necessary to create a closed measuring system with given properties such as air tightness outside the measuring system, the possibility of measuring with several sensors simultaneously and an opening for air to be blown into the measuring system. A blow hole is needed to change the air pressure inside the measuring system. The temporal change in pressure will be recorded by the individual sensors.

The sealing and surface treatment of the system surface are very important due to the permeability of the walls. The measurement system is most easily created using 3D modelling software and then printed on a 3D printer. In this way, it is possible to create a customized measurement system with precise dimensions and openings for the components under test. The measurement system thus created needs to be surface-treated with clear spray paint or clear nail polish. Without this surface treatment, air would leak through the individual layers of plastic, which would have adverse effects on the measurement. The data obtained from the pressure sensors should then be processed into a table of values at a given time interval. This method is simple and efficient. The measured values need to be compared with a pressure standard reference, which in this case can be a high-end precision sensor. The standard gives the pressure value with very high accuracy and thanks to it we can determine the accuracy of the tested pressure sensors.

For this case, 3 MEMS sensors and 1 reference sensor were selected. The first 2 sensors are manufactured by Bosch, BME680, BMP280. These sensors are sufficiently accurate and inexpensive however their stability varies ±1 hPa over time. This means that preventive testing of the accuracy of the sensors is necessary. However, the advantage is their cost which means that in case of damage, replacement is inexpensive. In addition to these sensors, the differential pressure sensor MPXV7002DP was selected. This sensor has 2 input openings for differential pressure measurement. Its accuracy is 2.5%. The last sensor selected was the testo 510i, which would be used as a benchmark for pressure measurement. It is suitable as a standard as it is possible to measure the pressure difference with an accuracy of ±0.2 hPa using this instrument. The exact parameters are listed in the datasheets [2, 5 - 7].

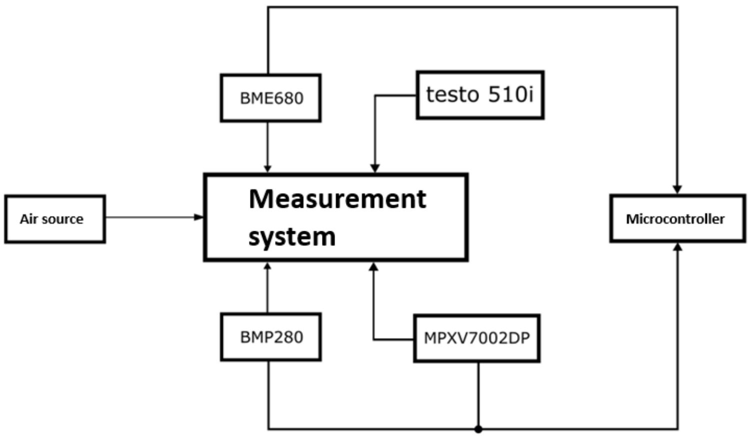

Figure 2. Pressure measurement wiring block diagram

The measuring system can be used to test pressure sensors as well as to measure air flow depending on the dimensions and shape of the measuring system. In this case, the system was designed as a section of piping with a standardized pipeline orifice and openings for the connection of measuring instruments. From the front side there is an opening for air injection by means of, for example, a syringe or ambu bag, which can change the magnitude of the pressure in the measuring system for a short period of time and relatively quickly. The entire measurement system was 3D printed using PLA filament.

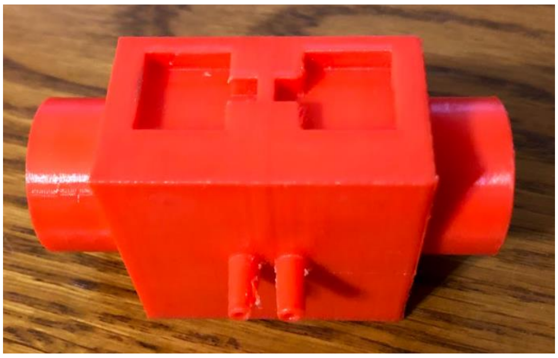

Figure 3. Measuring system with openings for placing measuring instruments

4. Air flow measurement

Flow rate is defined as the amount of fluid flowing through a pipe in a given time. In practice, 2 types of flow are distinguished: volumetric and mass flow. Volumetric flow is defined as the fraction of the volume of a substance passing through a pipe of a given cross-section in a given time. Mass flow is defined in the same way as volumetric flow, but unlike volume flow, mass flow is measured as a proportion of the mass of the substance passing through the pipe. The measurement is highly dependent on the type of fluid flow in the pipe. There are 3 types: laminar, transitional and turbulent flow. The type of flow is influenced by several factors such as the shape of the pipe profile, the characteristics of the pipe surface, the presence of control elements, the presence of sensing elements, etc. Both types of flow can be measured using instruments called flow meters. There are 8 types of flowmeters namely: volumetric flowmeters, velocity flowmeters, flowmeters using pressure loss of fluid, flowmeters using dynamic fluid action, ultrasonic, magnetic induction, special and mass flowmeters. An important factor influencing the selection of a suitable flowmeter is the filling of the pipe with the fluid to be measured. Not all flowmeters can operate efficiently when the pipe is partially filled [8].

This article is mainly devoted to flowmeters using fluid pressure loss. These flowmeters are the most widely used in practice due to their simple design. They are divided into cross-sectional and elbow flowmeters. Both groups use a throttling body to measure fluid flow. The pressure change is measured just at the throttling organ. The essence of this flowmeter is to apply a sudden change in the cross section of the pipe in the form of a throttling organ and then observe the pressure change upstream and downstream of the throttling organ. The volumetric flow rate is calculated using the relationship:

$$= \frac{*}{\sqrt{1 - \ ^2 - \ ^2}} * \ _2 * \sqrt{\frac{2 * \Delta}{}} \tag{1}$$

where Δp is the pressure difference measured upstream and downstream of the throttling organ, ϱ is the density of the measured fluid, μ is the dynamic viscosity value of the measured fluid, ξ represents the influences affecting the actual fluid flow velocity, and S_2 is the cross-sectional area of the throttling organ. The throttling organs used include normalized pipeline orifice, normalized nozzle, double and segmented pipeline orifice, measuring capillary, normalized and Venturi tube. An important fact to keep in mind is the occurrence of permanent pressure loss of the measured fluid due to the placement of the throttling organ in the system [8].

The normalized pipeline orifice is the simplest and most commonly used throttling organ in practice, exploiting the pressure loss of the fluid. It is basically a flat disk of circular diameter placed in the manifold. This disc has an pipeline orifice in the center which changes the diameter of the flow and thus the pressure of the fluid being measured at that point. This change in pressure is then recorded by the measuring channels. Factors influencing the implementation and design of a standardized pipeline orifice are the type of fluid to be measured, the diameter and material of the pipe, the temperature of the measured fluid, the physical and chemical properties of the measured fluid, and so on [8].

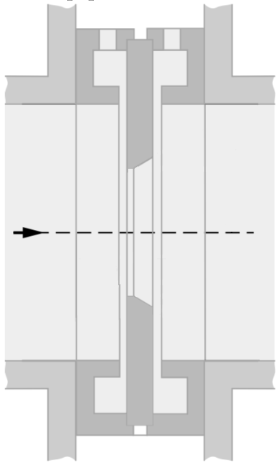

Figure 4. Cross-section of a standardized pipeline orifice

For this particular application, a measurement system was created, the dimensions and shape of which were given according to a standardized pipeline orifice, together with openings for differential pressure measurements before and after the measurement orifice.

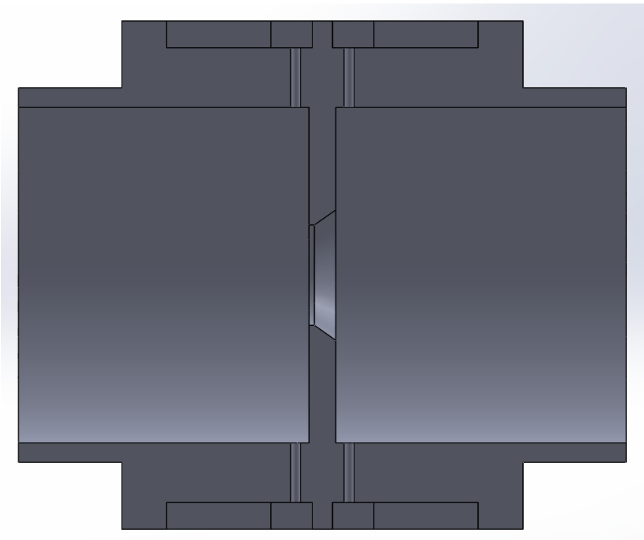

Figure 5. Cross-section of the Solidworks model of a measurement system with a normalized pipeline orifice

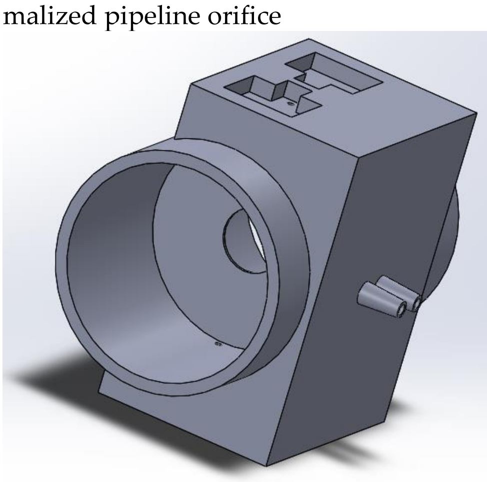

Figure 6. Model of the measuring system in Solidworks

The standardized nozzle has a more complicated shape compared to the standardized orifice and is not so often used in practice. The inlet part of the nozzle is formed by a rotating surface that smoothly transitions into a cylindrical surface with a sharp edge at its end. It is mainly used in cases where greater precision is emphasized, such as in the power industry when measuring steam flow [8].

The standardized Venturi exists in two embodiments namely as a tube and a nozzle. A standardized Venturi tube consists of 3 parts: a confuser, a throat and a diffuser. The Venturi nozzle consists of a normalized nozzle and a diffuser. Both designs are complicated to manufacture and their dimensions make them not very suitable for practice [8].

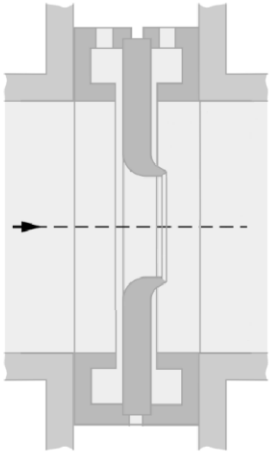

Figure 7. Cross section of the standardized nozzle

The double pipeline orifice works on the principle of gradually decreasing and increasing the diameter of the pipe. Unlike the standardized pipeline orifice and nozzle, this change in diameter is carried out gradually and not abruptly by the orifice. The gradual narrowing is provided by a conical confuser and the subsequent widening by a conical diffuser [8].

The segmented pipeline orifice is mainly used to measure the flow of contaminated fluids. Unlike previous throttling organs, this one is formed by a circular cut-out with a free lower bottom part, which prevents the orifice from becoming clogged with impurities [8].

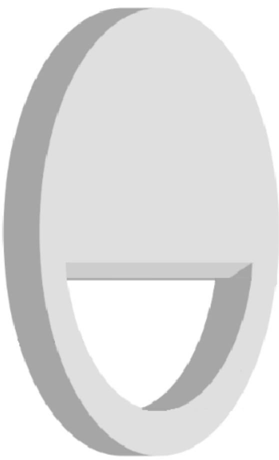

Figure 8. The segmented pipeline orifice

The measuring capillary is mainly used for measuring very small flow rates and is simple to design. It consists of a straight tube embedded in a pipe otherwise known as a capillary. This creates resistance to the flowing fluid and thus creates pressure loss. Using the magnitude of this pressure loss, the value of the fluid flow rate is calculated [8].

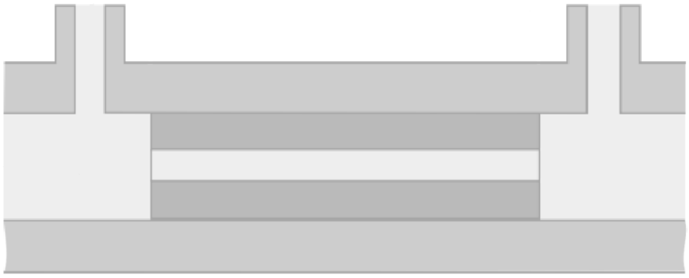

Figure 9. Cross-section of the measuring capillary

5. Conclusions

Measuring air parameters is very useful not only in industry but also in the home environment. In industry, air parameters such as pressure, temperature and humidity are often measured using various sensors. This paper has highlighted the possibilities of measuring the pressure and air flow in the working duct. The use of new MEMS technologies is very advantageous and feasible for implementation with existing methods and procedures for measuring air parameters as well as other working fluids. By combining old and new technologies, it is possible to improve existing operations more cheaply and achieve better output parameters.

Acknowledgments: This article was created thanks to the project support: VEGA 1/0436/22 Research on modeling methods and control algorithms of kinematically redundant mechanisms.

References

1. Pressure sensors: The design engineer´s guide, [online] [cit. 14. Október 2023]. Dostupné na internete: <https://www.avnet.com/wps/wcm/connect/onesite/fe01dc51-8967- 4f18-869c-97f3e36970a6/Pressure_Sensors-Design_Engineers_Guide_USAV2.pdf?MOD=AJPERES&attachment=false&id=1564101777976>
2. Gas sensor BME680, [online] [cit. 14. Október 2023]. Dostupné na internete: < https://www.bosch-sensortec.com/products/environmental-sensors/gas-sensors/bme680/>
3. I2C vs SPI: Difference Between I2C and SPI, 2. Marec 2021 [online] [cit. 14. Október 2023]. Dostupné na internete: <https://prodigytechno.com/i2c-vs-spi/>
4. Rajbir Singh, Difference between I2C and SPI (I2C VS SPI), 7. Február, 2020 [online] [cit. 14. Október 2023]. Dostupné na internete: <https://medium.com/@rjrajbir24/difference-between-i2c-and-spi-i2c-vs-spi-c6a68d7242c4>
5. Pressure sensor BMP280, [online] [cit. 14. Október 2023]. Dostupné na internete: <https://www.bosch-sensortec.com/products/environmental-sensors/pressure-sensors/bmp280/ >
6. MPXV7002DP, [online] [cit. 14. Október 2023]. Dostupné na internete: <https://www.mouser.sk/ProductDetail/NXP-Semiconductors/MPXV7002DP?qs=N2XN0KY4UWXOkdT07YYQaw%3D%3D>
7. testo 510i - diferenční tlakoměr ovládaný chytrým telefonem, [online] [cit. 14. Október 2023]. Dostupné na internete: <https://www.testo.com/sk-SK/testo-510i/p/0560-1510 >
8. Chudý, P. a kol. 1999. Meranie technických veličín. 1. vyd. Bratislava: STU, 1999. 688 s. ISBN 80-2271275-2

TECHNICKÁ UNIVERZITA V KOŠICIACH
Strojnícka fakulta

Machining nickel-chromium alloy with modified inserts

Jozef Brindza [1]*, Michal Demko [1], Ján Kušnír [1], Marek Vrabeľ [1] and Peter Ižol [2]

[1] Prototyping and Innovation Centre, Faculty of Mechanical Engineering, Technical University of Kosice, Slovak republic
[2] Department of Technology, Materials and Computer Supported Production, Faculty of Mechanical Engineering, Technical University of Kosice, Slovak republic
* Correspondence: jozef.brindza@tuke.sk; Tel.: 0556023364

Abstract: Nickel-chromium alloys, exemplified by Inconel 718, pose challenges in machinability due to their inherent toughness and high-temperature resistance. This study addresses the machinability of nickel alloys, focusing on the turning of Inconel 718. The essence of the experiment involves comparing the performance of an unmodified cutting insert with two textured cutting inserts, each featuring distinct coating, under constant cutting conditions. The experiment evaluates the size of wear on the major flank of the inserts and assesses the surface roughness of the machined workpiece.

Keywords: Turning, Texturing, Coating

1. Introduction

Nickel-chromium based alloys find broad applications in industries such as aerospace, energy, the petrochemical sector, and medicine. These materials are sought after for their exceptional properties, including high corrosion resistance, high-temperature stability, strength, and good formability. In the aerospace industry, they are utilized in the manufacturing of engine components and turbines. In the energy sector, nickel-based alloys are employed in the production of heat exchangers and turbine blades. In the petrochemical sector, they are used for durable components in aggressive environments. In medicine, these alloys are utilized, for example, in the production of implants due to their biocompatibility and resilience [1].

The machinability of nickel-chromium alloys is one of the critical properties that influences their processing capabilities and applications in the industry. Among the most used nickel-chromium alloys is Inconel 718, which was selected for the experiment. Inconel 718 faces poor machinability due to its high strength, hardness, and low thermal conductivity, leading to significant heat generation during machining. The material work-hardens quickly, resulting in increased tool wear, and its abrasive nature further challenges tool durability. Specialized cutting tools and optimized machining parameters are crucial to overcoming these challenges and improving the machinability of Inconel 718 [2].

The modification of cutting inserts used in the experiment will involve the texturing of the insert's face and flank, followed by subsequent coating.

Texturing cutting inserts is a specialized technique aimed at enhancing their performance and capability to machine difficult-to-process materials. This method involves the application of grooves, structures, or surface modifications on the surface of cutting inserts. The objective of texturing is to optimize chip removal, minimize friction, and address issues related to thermal impact during machining.

The advantages of texturing cutting inserts are diverse. Texture creation on the insert surface improves lubrication, minimizing friction between the insert and the machined material. Consequently, it leads to reduced chip formation. Well-designed texturing enables better chip evacuation from the cutting zone, lowering the risk of tool and workpiece damage. Additionally, texturing contributes to increased wear resistance of cutting inserts, thereby extending their lifespan. Textured surfaces also exhibit enhanced heat dissipation capability, helping to minimize thermal damage during the machining process [3].

Coating cutting tools is a prevalent practice in machining, offering multifaceted advantages. These coatings act as protective layers, significantly increasing tool hardness to resist wear and extend lifespan. Additionally, they enhance lubricity, reducing friction between the tool and workpiece, leading to smoother cutting operations and less heat generation. Improved thermal stability allows coated tools to endure higher temperatures during machining without compromising performance. Coated tools also resist adhesion and built-up edge formation, ensuring consistent cutting efficiency. The combination of increased hardness, better lubricity, and thermal stability results in extended tool life, reducing the need for frequent changes and enhancing overall machining efficiency. Common coating materials include titanium nitride, titanium carbonitride, and various diamond-like carbon coatings, chosen based on specific machining requirements and materials [4].

The article focuses on investigating the turning of Inconel 718 using textured and coated inserts. The study aims to measure and evaluate wear on the major flank and the surface roughness of the machined area.

2. Description of experiment

The essence of the experiment involved machining three cylindrical samples of Inconel 718 using turning. The first sample was produced using the original unmodified turning insert CNMG 120408E-SM, while the others had stochastically textured rake face, major and minor flank, subsequently coated with nACRo4 and TiXCo coatings. In this experiment, only conventional cutting fluid was used without the use of solid lubricant. Each sample underwent a constant cutting path, i.e., the helix described by the cutting tool tip during longitudinal turning. The length of the helix was calculated using the formula: [mm],
where: d – turned diameter [mm],
l – turned length [mm],
f – feed [mm.ot.$^{-1}$] [5].

The final cutting path was set at 240 m, with scanning of the machined surface and cutting insert performed after every 80 m, at 80 m, 160 m, and the final 240 m of cutting. The initial diameter of the workpiece was 50 mm, and the final diameter was 16 mm. As the machined diameter decreased, the length of the helix for one pass also decreased. Hence, 4 passes were sufficient for the first 80 m, 5 passes for the next 80 m, and a total of 8 passes were required for the last 80 m of cutting.

The following cutting conditions were used during turning:

- cutting speed: v_c= 30 m.min^{-1},
- feed: f = 0,2 mm.ot^{-1},
- depth of cut: a_p = 1 mm.

To produce the samples, a CNC turning and milling center, DMG MORI CLX 450 TC, available at the Prototyping and Innovation Center at the Faculty of Mechanical Engineering, Technical University of Kosice, was utilized. The machine is controlled by the Sinumerik 840D control system from Siemens.

For surface profiling of the machined samples and the major flank of the cutting insert, a confocal microscope ZEISS Smartproof 5 was employed. The accompanying software used for data analysis included ZenCore and ConfoMap.

3. The modification of cutting inserts

To conduct the experiment, C-type turning inserts with a corner radius of 0.8 mm, identified as CNMG 120408E-SM Grade 902 from the manufacturer Dormer Pramet, designed for machining difficult-to-cut materials, were used. These inserts had a stochastically textured rake face, as well as the major and minor flank surfaces achieved through laser texturing. The major flank of the insert before and after texturing is depicted in Figure 1.

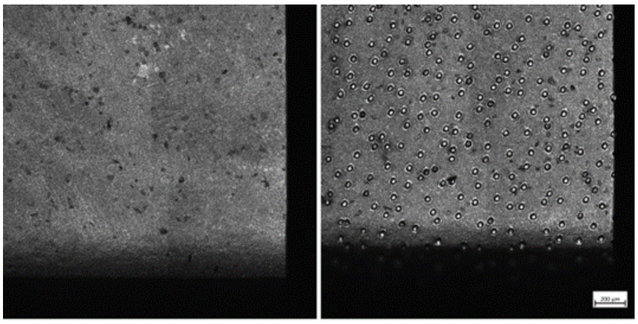

Figure 1. The major flank of the cutting insert before and after texturing

To enhance the lifespan of textured cutting inserts, after texturing, one insert was coated with the nACRo4 coating, and the other with the TiXCo coating. These coatings are commonly applied to cutting tools for machining challenging materials. Each of these coatings has its own unique properties and advantages that contribute to the improved performance of the tools [6].

4. Results

During the experiment, after completing 80, 160, and the final 240 m of the cutting path (helix) traced by the cutting edge during turning, the major flank of the cutting insert was captured using a confocal microscope. Figure 2 displays the major flank of the cutting insert after the first 80 m of cutting. The highest wear is observed on the non-textured original insert with a length of 450 µm, while the textured insert with the TiXCo coating exhibits the least wear, measuring only 120 µm.

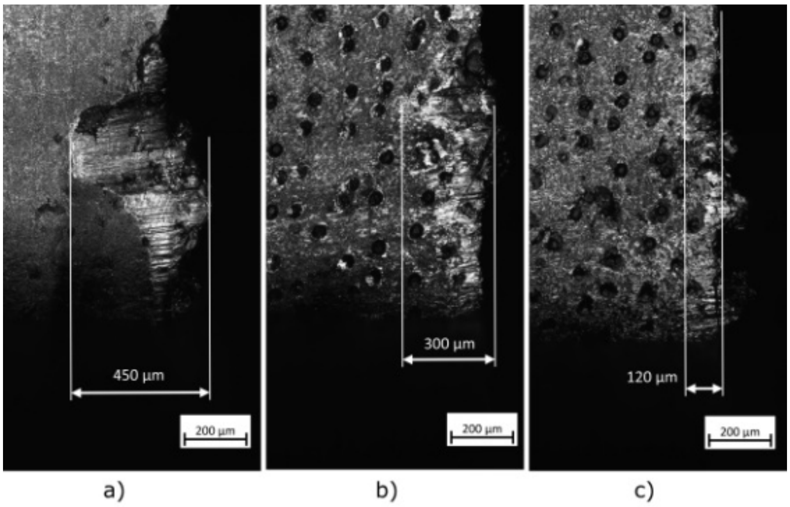

Figure 2. Wear on the major flank after 80 m of cutting:
a) non-textured (original) insert, b) textured insert with nACRo4 coating,
c) textured insert with TiXCo coating.

The condition of the major flank after completing the final 240 m of cutting is depicted in Figure 3. In all inserts, a significant volume of material has already been fractured, reaching a size of 1105 µm for the non-textured insert, 837 µm for the textured insert with nACro4 coating. Abrasive wear on the non-textured insert reached a value of 675 µm, 790 µm on the textured insert with nACro4 coating, and 640 µm on the insert with TiXCo coating.

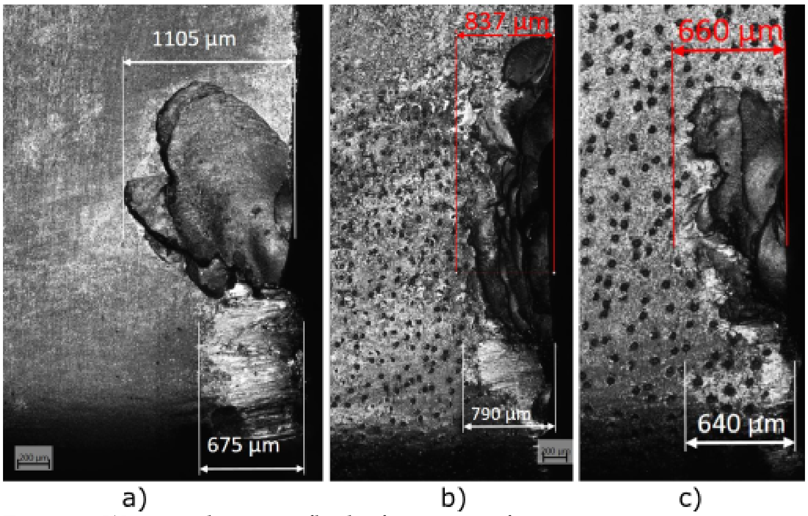

Figure 3. Wear on the major flank after 240 m of cutting:
a) non-textured (original) insert, b) textured insert with nACRo4 coating,
c) textured insert with TiXCo coating

The evolution of abrasive wear without material notching on the major flank is presented in Table 1 and graphically depicted in Figure 4. In terms of abrasive wear, the textured insert with the TiXCo coating performs the best, and it also exhibits the smallest notched area on the flank.

Table 1. The sizes of wear on the major flank:
a) non-textured (original) insert, b) textured insert with nACRo4 coating,
c) textured insert with TiXCo coating

Cutting length [m]	a) [µm]	b) [µm]	c) [µm]
80	450	300	120
160	590	760	390
240	675	790	640

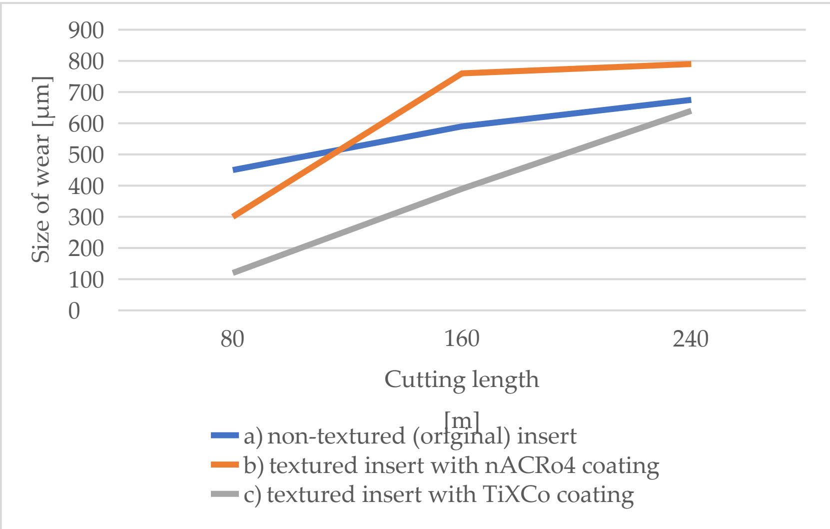

Figure 4. The progression of wear on the major flank

After every 80 meters of cutting, in addition to the major flank of the cutting insert, the machined surface of the workpiece, with an area of 4 x 0.5 mm, was also scanned using a confocal microscope. Based on these scans, 2D sections were created at the center, as depicted in Figure 5, to obtain the 2D roughness profile and evaluate the 2D roughness parameters.

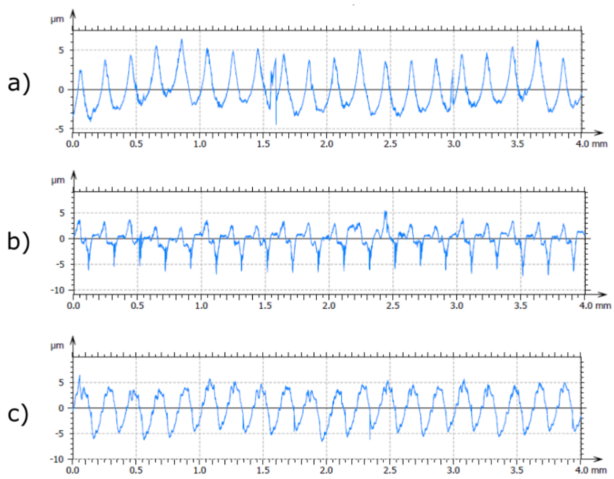

Figure 5. Surface roughness profiles after 80 meters of cutting:
a) non-textured (original) insert, b) textured insert with nACRo4 coating,
c) textured insert with TiXCo coating

As evident in Figure 5, individual profiles exhibit significantly different trends, even though precisely the same cutting conditions were employed for each sample. The measured roughness values (Ra) of the machined surface after 80, 160, and 240 meters of cutting are presented in Table 2 and visually represented in Figure 6.

Table 2. The Ra parameters of the machined surface
a) non-textured (original) insert, b) textured insert with nACRo4 coating,
c) textured insert with TiXCo coating

Cutting length [m]	a) [µm]	b) [µm]	c) [µm]
80	1.81	1.33	2.69
160	1.86	1.58	2.44
240	1.83	1.19	1.58

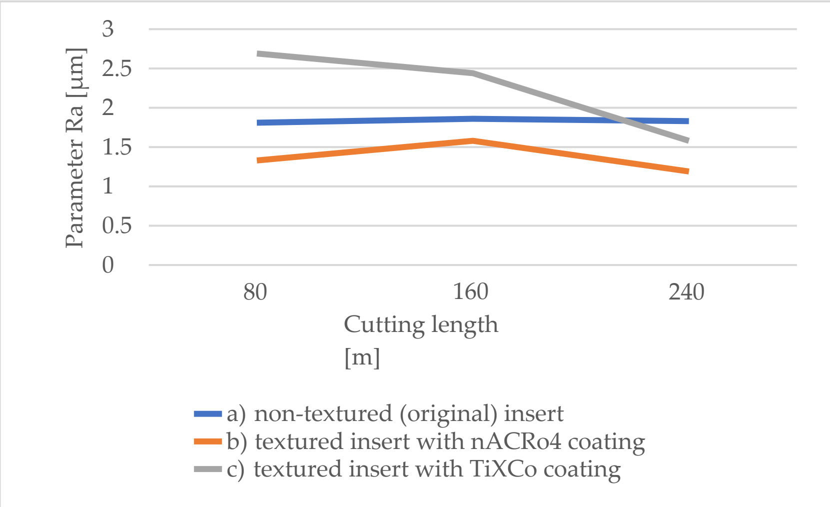

Figure 6. The evolution of the surface roughness parameter Ra

As evident from the table and graphs, the best surface roughness throughout all stages is achieved with the textured insert with the nACRo4 coating, with the roughness deteriorating after 160 meters of cutting to Ra = 1.587 µm and subsequently improving to Ra = 1.192 µm. The worst surface roughness at 80 meters of cutting is observed with the textured insert with the TiXCo coating, with a value of Ra = 2.696 µm, but the roughness gradually improves with the largest improvement occurring between 160 and 240 meters of cutting, reaching a value of Ra = 1.588 µm. The surface roughness for the non-textured insert hardly changes during the experiment and reaches a final roughness of Ra = 1.835 µm. To confirm these results, it would be necessary to conduct multiple samples with the same production parameters to eliminate random influences and validate repeatability.

5. Conclusions

This research aims to contribute to the evolving field of machining nickel alloys by investigating the synergies between textured cutting inserts, advanced coating technologies, and surface analysis techniques. The insights gained from this study have the potential to guide future developments in the quest for enhanced tool performance and superior machined surface quality in the machining of nickel alloys.

This was the initial experiment in machining nickel-based materials, and the research will continue using solid lubricants based on disulfides. The use of solid lubricants based on disulfides in machining offers several advantages. These lubricants create a protective coating on the cutting edges of tools, significantly reducing friction and wear during the machining of difficult-to-process materials. This contributes to the extended tool life and minimizes the need for frequent tool changes, resulting in improved overall performance and productivity in manufacturing processes. The lower friction and more efficient use of tools allow for higher efficiency, ultimately enhancing production outputs [7].

Acknowledgment

The paper was created within the solution of the projects VEGA 1/0457/21 Efficiency improvement in machining nickel based super alloys by texturing cutting tools and utiliztion of solid lubricants, and KEGA 050TUKE-4/2023.

Conflicts of Interest: The authors declare no conflict of interest.

References

1. Y. Guo: Nickel-based Superalloys for Advanced Turbine Engines: Chemistry, Microstructure and Properties. Woodhead Publishing Series in Metals and Surface Engineering, Elsevier, 2015.
2. A. Çaydaş: Machinability of Nickel-Based Superalloys: A Review. Materials and Manufacturing Processes, vol. 30, no. 12, 2015. pp. 1558-1566.
3. G. R. Liu, et al.: Laser Surface Texturing on Cemented Carbide Cutting Tools. Applied Surface Science, vol. 254, no. 22, 2008. pp 7315-7319.
4. K. Holmberg, A. Matthews: Coatings Tribology: Properties, Mechanisms, Techniques, and Applications in Surface Engineering. Elsevier, 2017.
5. Mujsolidworks.cz. Available online: https://www.mujsolidworks.cz/wp-content/uploads/2018/07/Skrutkovice.pdf (accessed on 9.12.2023).
6. L. F. P. Conceição, et al.: Texture and Lubrication: A Review. Lubricants, vol. 5, no. 2, 2017.
7. M. Babic, S. Hladnik, M. Kalin: Solid Lubricants and Coatings in Forming Processes—A Review. Tribology International, vol. 34, no. 6, 2001. pp. 389-396.

TECHNICKÁ UNIVERZITA V KOŠICIACH
Strojnícka fakulta

The evaluation of modern steels innovation potential when used for the parts of the car's deformation zones

Marek Buber [1*]. Emil Evin [1] and Miroslav Tomáš [1]

[1] Department of Automotive Production, Faculty of Mechanical Engineering, Technical University of Košice, Mäsiarska 74, 040 01 Košice; emil.evin@tuke.sk, miroslav.tomas@tuke.sk
[*] Correspondence: marek.buber@tuke.sk, Tel. +421 55 602 3519

Abstract: Nowadays, a lot of emphasis is placed on the car safety. It's very difficult to ensure the highest possible body strength using conventional tests. The correct testing method is the basis for the safety of the car bodies. It is less expensive and time-consuming to apply deformation characteristics testing to selected types of steel than to produce a complete body and then test its deformation properties. The three-point bending test makes it possible to determine the absorption potential of the selected sheet metal. The purpose of this article is to evaluate innovation potential of the dual phase steel HCT600X and austenitic steel AISI 304, which can be used in the automotive industry for the body-in-white structural components, and deformation parts mainly.

Keywords: 3-point bending test, energy absorption, deformation work, stiffness constant

1. Introduction

In car safety, many passive elements have supplemented and even replaced by active safety elements. The brake systems were supplemented with electronic control units that ensure better brake operation and vehicle controllability in skidding [1]. However, even active members in combination with passive ones will not ensure the complete safety of the vehicle crew. Therefore, scientists and car developers had to focus on the materials used for the construction of the car [2-5].

It was necessary to focus on the deformation zones, their construction, and the material from which they are made. The deformation zone is not responsible only for the safety of passengers but also pedestrians. An intersection between the strength of the material and the ability to absorb energy on the deformation path had to be found. In modern cars a "controlled" course of deformation needs to be ensured. The deformation of the front part of the vehicle should have a graded course consisting of 5 stages: 1. protection at low speeds - parking maneuvers; 2. compatibility - protection of a co-participant in a traffic accident; 3. self-protection - the necessity to comply with biomechanical criteria; 4. space for crew survival; 5. pedestrian protection.

In modern cars, deformation zones are distributed around the entire cabin of the vehicle. That means the space for the crew is sufficiently protected. While at a frontal impact of a vehicle there is enough space for deformation, the side of the car must be sufficiently rigid to withstand the side impact (Fig. 1). [6-9]

Compared to the front or rear of the vehicle, where there is sufficient length to create deformation zones, the side parts of the vehicle have minimal space to absorb deformation energy. A collision with a vehicle from the side is the most dangerous for the crew, as most vehicles are very vulnerable from the side. Therefore, the greatest number of modern materials are used for these areas, which are able to absorb a significant amount of energy in a side impact. [7-9]

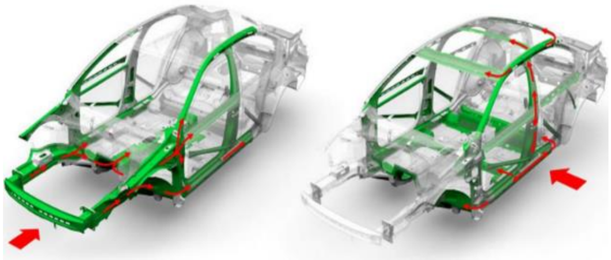

Figure 1. Distribution of deformation forces in frontal and side impact [8].

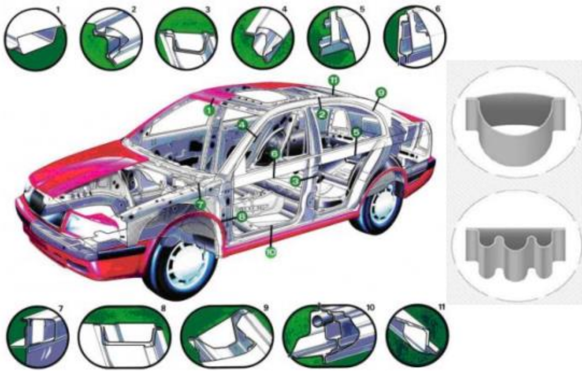

Figure 2. Pre-Safe structure and side reinforcements of the car. [9]

A novelty on the market in the area of safety elements of deformation zones is the Pre-Safe structure - Fig. 2. They are actually special metal profiles, stored in the reinforcements of the body. In the event that the sensors of the vehicle's control unit detect an impact, the charge is activated and the struts are inflated. The duration of inflation is a few milliseconds. The pressure in these reinforcements reaches 1-2 MPa. The braces can hold a load of 100 kg (1 kN). Their function is similar to the function of an airbag, but with the difference that they are made of metal material and the reinforcements do not inflate, which can also appear as a disadvantage. [7-9]

Research of modern steels used in the body-in-white has a great importance from many points of view. Mihalikova et al [4] performed dynamic testing of DP 600 steel by two testing methods. They found increasing of both, the yield and tensile strength due to significant microstructure changes during dynamic conditions, which lied in increasing the density of dislocations. Thus, increasing the strain rate the time for overcoming of local obstacles in the slip plane is shorter. Rodríguez-Martínez et al. [10] researched AISI 304 steel and analyzed its behaviour when subjected to perforation under a wide range of impact velocities. Due to transformation of austenite into martensite during mechanical loading, this process leads to an increase in strength and ductility of the material. Thus, makes this steel attractive for engineering applications, such as structural elements responsible for absorbing energy under fast loading. Cotterell et al [11] investigated the mechanical properties of the undeformed part of the specimen after a tensile test. They found that there were changes in microhardness in the entire measured length of the sheet metal. However, the most deformed grains are in the specimen with a rolling direction 0°. It follows that the strengthening of the material in the given area is also correlated with the size of the deformation. In the case of deep-drawing DC steels, where large deformation is expected both during the crash and during the forming of the part itself, deformation strengthening is useful and has an effect on the stiffness of the part made of this type of sheet metal. Sommer et al [12] focused on the dynamic deformation properties of austenitic stainless steel in a tensile test with deformation rates of 1000 s^{-1}. They investigated the distribution of deformation during the test using digital image correlation. They found that at such a high rate of deformation, pores appear in the structure of the material. They discovered that these pores could come directly from production, where dust particles or impurities were rolled into the material. An increased concentration of such "cavities" can cause a violation of the material in this area.

The article is focused to the research of deformation properties of deep-drawing, dual phase and austenitic stainless steel by the modified three-point bending test, when the specimen's ends are fixed. The loading of the beams, bumper, roof reinforcement and doors can be tested with this test, where can be measured the bending strength (material resistance), deformation work, stiffness, etc. [13]

2. Materials and methodology of experiment

2.1 Three-point bending test with stretching

The experimental test was performed at predetermined strain rate, using a combination of three-point bending and stretching. The absorption potential of the material was determined from the force required to deform a specimen with a width of 26 mm and a length before deformation L_0 = 300 mm (length of the loaded part of the specimen $L_0 = 2.X_0$ = 2x110 mm) and the thickness of the specimen a_0 = 0.75 mm (Fig. 3).

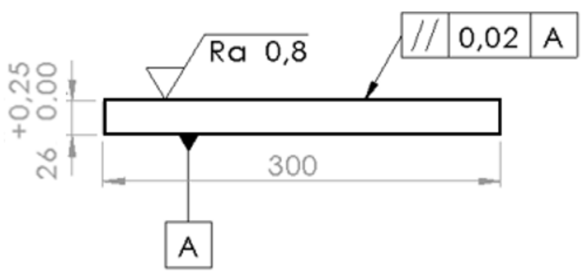

Figure 3. Dimensions of the tested specimen.

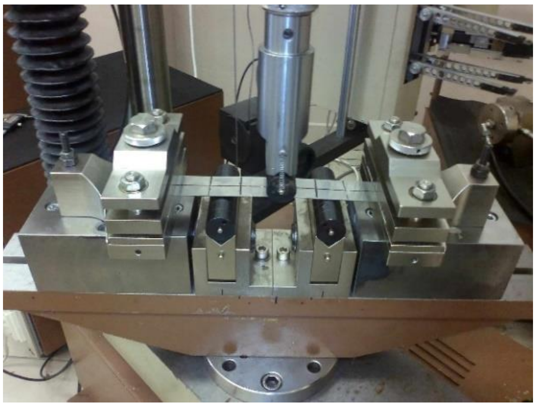

Figure 4. Three-point bending test with stretching [10].

The three-point bending test was performed on a TiraTEST 2300 testing machine. equipped with the necessary fixtures for holding the specimen and also with a sensor measuring the magnitude of the load force. The tested specimens were fixed with jaws into the machine in such a way that there was no movement of the specimen during the test. The specimen was loaded by force through the roller mounted on the end of the strain gauge sensor. With such a combination of clamping the specimen and its bending, a combined bending and tension stress occurs. TiraTEST 2300 allows you to record the measured force and traversed path of the crossbar to the computer. The support rollers on which the specimen was positioned were at a distance of 110 mm from each other and their diameter was d = 30 mm. The specimens were stressed until failure (Fig. 4).

2.2 Materials and their properties

Steel sheets made of drawing quality steel DC 05, dual-phase steel HCT600X (DP600) and sheets made of austenitic stainless steel AISI 304 were used for the experiment, the chemical composition of which is shown in Tab. 1.

Tab. 2 shows the material properties of the investigated materials. The properties were evaluated in the 90° directions. The mechanical properties were determined by a tensile test according to STN EN ISO 6892-1. The normal anisotropy coefficients (Lankford coefficients) were determined according to STN EN ISO 10 113. The strain hardening exponent and the material constant were determined according to STN EN ISO 10 275.

Table 1. Chemical composition of the experimental materials.

Material	Chemical composition %								
	C	**Si**	**Mn**	**P**	**S**	**Cu**	**Al**	**Ni**	**Ti**
DC 05	**0.03**	0.01	0.18	0.009	0.010	-	0.044	0.003	0.002
HCT600X	**C**	**Si**	**Mn**	**P**	**S**	**Cu**	**Al**	**Cr**	**Mo**
	<0.111	0.279	1.963	0.026	<0.002	0.019	0.031	0.206	<0.002
	Ni	**V**	**Ti**	**Nb**	**Co**	**W**	**Fe**		

	<0.002	0.012	<0.002	0.02	0.017	<0.005	97.31		
AISI 304	**C**	**Si**	**Mn**	**P**	**S**	**Cu**	**Al**	**Cr**	**Mo**
	0.055	0.592	1.597	0.018	<0.002	0.029	0.009	18.30	0.015
	Ni	**V**	**Ti**	**Nb**	**Co**	**W**	**Fe**		
	7.79	0.040	0.007	0.049	0.062	0.015	71.42		

Table 2. Mechanical properties of the experimental materials.

Material	**$R_{p0.2}$ [MPa]**	**R_m [MPa]**	**A_g [%]**	**A_{80} [%]**	**K [MPa]**	**n [-]**	**r [-]**	**Eps**	**Wpl [J]**
DC 05	166	280	27	49	502	0.241	1.9	0.0081	**86.26**
HCT 600X	371	627	19.3	30.7	1095	0.22	0.81	0.0053	**133.99**
AISI 304	305	750	61	67	1614	0.491	1.01	0.0316	**448.00**

2.3 Methodology of experiment evaluation

The evaluation of elongation, bending path and springback of the specimens was carried out according to the scheme in Fig. 5, when the path of the bender is 25 mm, and the individual quantities are: h - bend path; h´ - path of the bender after unloading force; α' - angle after unloading force; α''- angle under load; X_0´- length of half of the examined part of the specimen in the unloaded state; X_0''- length of half of the examined part of the specimen under load.

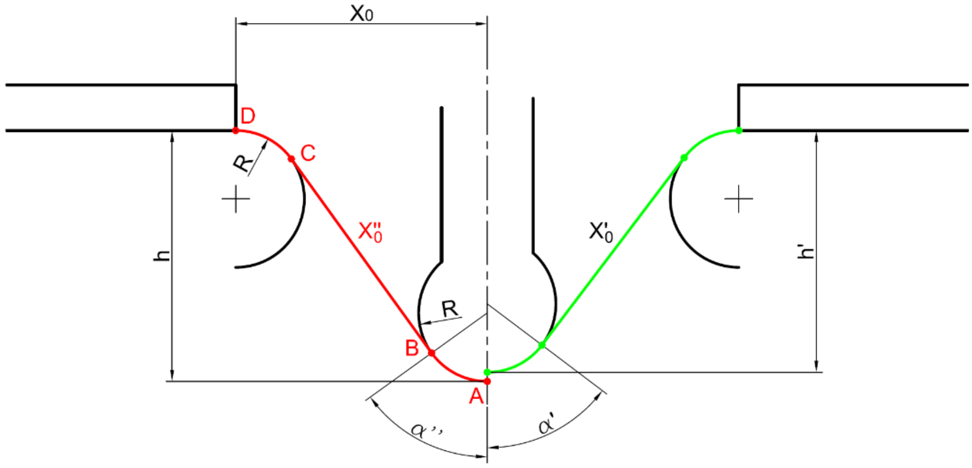

Figure 5. Scheme of the three-point bending test with fixed ends.

The deformation of the examined part of the specimen was calculated based on relations (1) and (2). The assumption was that the free part of the specimen is deformed uniformly depending on the path of the bender h until the moment when a narrowing, i.e. neck occurs. In the initial position of the bender h=0, the length of the specimen was 110 mm. The size of the angle α can be expressed as:

$$(h) = -2.tan^{-1}\left(\frac{_0-\sqrt{h^2-4.\ .h+\ _0^2}}{h-4.}\right), \tag{1}$$

After the sum of the lengths of the arcs AB and CD and the addition of the section EC, we express the half length of the specimen x after deformations as:

$$(h) = -2.tan^{-1}\left(\frac{_0-\sqrt{h^2-4.\ .h+\ ^2_0}}{h-4.}\right), \tag{2}$$

The total length of the specimen is twice the x obtained from equation (2).

The magnitude of the deformation work was evaluated from the maximum force and path of the bender when the specimen broke according to the relationship:

$$_{de} = \frac{\cdot}{2}, \tag{3}$$

The stiffness constant c can be determined from the record of the bending force Fmax depending on the path of the bender x_{max}. With the assumed linear course of the dependence, the stiffness constant c will represent the direction of the straight line indicated in the dependence (Fig. 6).

3. Reached results and their evaluation

Based on the bending test scheme shown in Fig. 6 and relations (1) and (2) the angles during loading and unloading and the total length of the specimen were calculated, the values of which are given in Tab. 3.

Table 3. Extensions of the tested specimens – path of the bender 25 mm.

Material	DC 05	HCT 600X	AISI 304
Force [kN]	5.201	10.453	7.619
Path of the bender in the loaded state h [mm]	25	25	25
The path of the bender in the unloaded state h´ [mm]	23.55	22.26	22.15
Angle α'' in the loaded state [°]	27.71	27.71	27.71
Angle α' in the unloaded state [°]	26.11	24.68	24.56
Free part length of the specimen in the loaded state 2.X_0''[mm]	121.75	121.75	121.75
Free part length of the specimen in the unloaded state 2.X_0'[mm]	120.440	119.33	119.241
The difference after unloading (springback) X_0''- X_0' [mm]	1.31	2.42	2.51

The length of the free part of the specimen in the loaded state, with the traveled path of the bending punch of 25 mm for the reference steel DC 05, was 121.75 mm. After the specimen was unloaded, the material contracted by 1.31 mm, which was 1.11 mm less than that of the HCT600X steel and 1.2 mm less than that of the austenitic steel AISI 304. The force required to deform the specimen by 25 mm reached a value of 5.201 kN for the reference steel DC 05, which was half as much as for the HCT600X steel, where the force reached a value of 10.453 kN. For AISI 304 steel it was 7.619 kN, which was 2.418 kN more than the reference steel.

Table 4. Stiffness constant and measured deformation work at 3-point bending test.

Material	DC 05 (ref)	HCT 600X	AISI 304
Deformation work W_{def} [J]	246.3	269.6	620.1
Stiffness constant c [N.m^{-1}]	0.207	0.450	0.324
W_{def}/ $W_{def\ ref}$	1.00	1.28	2.94
c / c_{ref} = a / a_{ref}	1.00	2.17	1.57

The deformation work W_{def} needed to deform the specimen until the moment of its failure reached the value of 246.3 J for the reference steel DC 05. The similar deformation work needed to deform the specimen was for the HCT600X steel and reached the value of 269.6 J. For the AISI 304 steel, the force needed to deform the specimen was 2.5 multiplied and reached the value of 620.1 J.

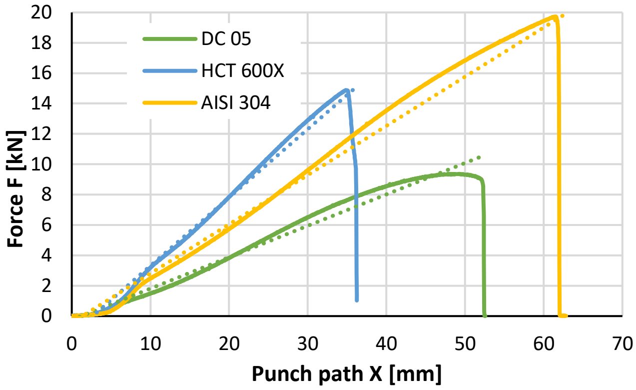

Figure 6. Record of the dependence of the bending force on the path traveled by the bending punch.

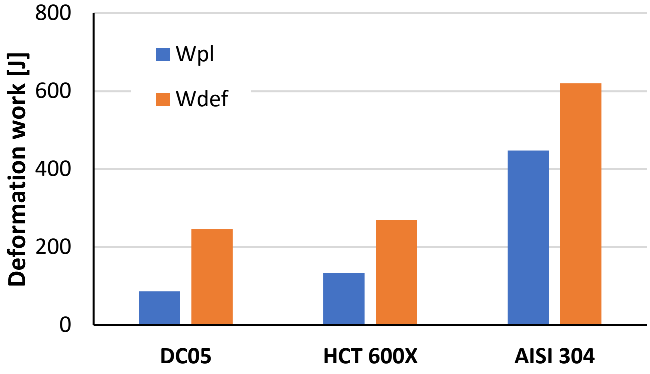

Figure 7. Comparation of deformation work in tension test and tri-point bending with fixed ends.

On Fig. 7 is a comparison of the deformation work during the tensile test (Tab. 2) and the three-point bending test with fixed ends (Tab.4). W_{pl} represents the amount of force required to deform the specimen until failure in tensile test. W_{Def} represents the work required to deform the specimen until failure in three-point bending with fixed ends. According to the graph, we can conclude that the material AISI 304 is able to absorb the largest amount of energy even in the tensile test as well as in three-point bending with fixed ends.

From the point of view of the protection of the vehicle crew, it is very important to take into account the deceleration of the safety cage. In Euro NCAP, the prescribed frontal impact speed is 64 km/h^{-1} and in EHK it is 56 km/h^{-1}. At such speeds, the maximum acceleration (deceleration of the vehicle) is a limit coming out from the biomechanical limits of the human body. Overload at such speeds reaches a value of around 20g. However, not only the acceleration but also the track on which such an overload occurs determines whether the passenger is able to survive an impact. The deformation path is closely related to the structure of the deformation zones, the material from which they are made and the geometry of the deformation zones themselves. At the moment the vehicle hits an obstacle, it is possible to write the energy balance condition in the form:

$$= \;_{de} \quad => \quad \frac{\cdot \;_0^2}{2} = \int_{=0} \quad . dx, \tag{4}$$

where W_k is the kinetic energy, W_{def} is the deformation work that is consumed to absorb (absorb) the kinetic energy during the impact, V_0 is the initial speed at the moment of the impact, m is the mass of the vehicle, X is the deformation path on which W_K is absorbed.

Even if the deformation elements of the car are deformed first elastically and then plastically, we consider only the plastic deformation of the deformation elements in the event of an impact. Assuming that the force required for deformation grows linearly, we can write the relation:

$$\frac{\cdot \;_0^2}{2} = \int_{=0} \quad . dx, \tag{5}$$

It is possible to express the strength of resistance by the ratio of the stiffness constant and deformation zones and deformation path:

$$_{max} = \; \cdot \quad , \tag{6}$$

where F_{max} represents the maximum force value on the maximum deformation path x_{max} from the moment when the elastic deformation ends and plastic deformation begins. From the action-reaction law it follows that at every moment of the collision, the resistance force of the structure is equal to the multiple of the vehicle's weight and its acceleration:

$$ {}_{SV} = \quad {}_{max,Veh} \quad , \tag{7}$$

or

$$ \cdot \quad = \quad \cdot \quad {}_{,max}, \tag{8}$$

If we consider that there will be a collision of vehicles with the same weight and the same geometry of deformation zones but made of different material, then it is possible to write the equation for a vehicle made of a reference material:

$$ \cdot \quad = \quad \cdot \quad {}_{1,max}, \tag{9}$$

and for a vehicle structure made of a different material than the reference material:

$$ \cdot \quad = \quad \cdot \quad {}_{,max}, \tag{10}$$

After comparing the deformation forces on the same path, we get the equation for the improvement ratio when changing the reference material to another:

$$ \frac{\quad ,\quad}{\quad ,\quad} = \frac{\quad}{1,}, \tag{11}$$

It follows from equation (11) that the ratio of the stiffness constants of the considered and reference material is proportional to the ratio of their decelerations or body overload. This means that if we change the material used for the construction of the deformation zones while maintaining the same geometry and deformation path, we can predict the amount of overload on a person in a vehicle collision based on the stiffness constant of the material. With such a material change, it is necessary to ensure that there is no increase in overload. Therefore, when using a material with a higher stiffness constant, it is possible to reduce its thickness while maintaining the same deformation characteristics and at the same time reducing the weight of the component.

4. Conclusions

The aim of the experiment was to compare the absorption characteristics of drawing quality steel DC 05, dual-phase steel HCT 600X, and austenitic steel AISI 304 with a nominal thickness of 0.8 mm for their use in the deformation zones of the car body. The deformation characteristics were evaluated by a three-point bending test with. Based on the experiments and their evaluation, it is possible to state:

- when replacing drawing quality steel DC 05 with dual-phase steel HCT 600X, an increase in absorption capacity by 1.28x was found;
- when comparing the stiffness constants between the reference steel DC 05 and steel HCT600X, there was an increase of 2.17x;
- when replacing drawing quality steel DC 05 with austenitic steel AISI 304, an increase in absorption capacity by 2.94x is possible;
- whereas when comparing the stiffness constants between the reference steel DC 05 and the austenitic steel AISI 304, there was an increase of only 1.57x.

It was found that with the application of the stronger HCT 600X material of the same thickness, there would be an increase in passenger overload at the same time. Therefore, in order to maintain the same level of overload, when applying a stronger material, it is necessary to reduce its thickness. The ideal choice of material for front deformation zones of the body in white would be AISI 304 austenitic steel, which, with a slightly increased value of the stiffness constant, provides us with a very good absorption potential. However, such steel is too expensive for application in the car structure, it could increase the price of the vehicle to such an extent that it would become unattractive for the consumer.

On the contrary, HCT 600X steel, which has the ability to absorb a large amount of energy over a short distance, is suitable for side reinforcements where there is not enough space for the application of defo-elements that would absorb the impact over a sufficiently long distance. Therefore, when designing the deformation zones of the body, it is necessary to take into account many factors such as the path of deformation, the space required for the survival of the crew in the event of an impact, the magnitude of the overload and then find their balance. The right choice of material can save many lives and also save production costs for the manufacturer.

Acknowledgments: The article was prepared with the support of the project VEGA 1/0238/23 "Implementation of CAx systems and virtual engineering techniques in the redesign of parts of the deformation zones of the car body".

References

1. Sun, C. - Zheng, S. - Ma, Y. et al: An active safety control method of collision avoidance for intelligent connected vehicle based on driving risk perception. *J. of Intell. Manuf.*, *Vol. 32*, **2021**, p. 1249–1269; doi: 10.1007/s10845-020-01605-x.
2. Čada, R.: Formability of Deep-Drawing Steel Sheets. In: Proc. of Conference EUROMAT 97: Volume 4 - Characterization and Production/Design. Netherlands Society for Materials Science, **1997**, s. 463-466. ISBN 90-803513-4-2.
3. Moor, E.: Advanced High-Strength Sheet Steels for Automotive Applications. *High-Performance Ferrous Alloys*, 1st ed., Springer Cham, Springer Nature Switzerland AG **2021**, 624 p., ISBN 978-3-030-53824-8.
4. Mihalikova, M. – Német, M. – Girman, V.: DP600 Steel Research of Dynamic Testing. *Metalurgija*, *Vol. 54*, No. 1, **2015**, p. 211-213.
5. Valeš, M. – Novák, V. – Tatíček, F. – Šanovec, J. – Chrášťanský, L.: Outer car body panels made of dual-phase steel. Proceedings of the 28th Conference on Metallurgy and Materials, **2019**, pp. 507- 512.
6. Vlk, F.: Motor vehicle bodywork: ergonomics: biomechanics: passive safety: collisions: structure: materials. Brno: VLK, **2000**, ISBN 80-238-5277-9.
7. Passive Body Safety Features [online]. [cit. 2015-11-15]. Available on the internet: <https://www.bezpecnecesty.cz/cz/bezpecnost-automobilu/pasivni-prvky-bezpecnosti/karoserie>
8. Schwarz, T. - TSchritter, A. - Köppel, T. et al.: Active and passive safety, *ATZextra Worldwide*, *Vol. 15*, no. 5, **2010**, p. 72-75; doi:10.1365/s40111-010-0203-1
9. Deformation zone of the car and its testing. [online]. [cit. 2015-11-18]. Available on the internet: http://auto.ihned.cz/c1-17237000-deformacni-zona-vozu-a-jeji-zkousky
10. Rodríguez-Martínez, J.A. – Rusinek, A. – Pesci, R.: Experimental survey on the behaviour of AISI 304 steel sheets subjected to perforation. *J. Thin-Walled Structures., Vol. 48 Iss 12* **2010**, p. 966-978; doi.org/10.1016/j.tws.2010.07.005
11. Cotterell, M. – Schambergerova, J. et al: Dependence of micro-hardness on deformation of deep-drawing steel sheets. *J of Materials Processing Technology., Vol 124. Iss 3.* **2002**, p. 293-296; doi.org/10.1016/S0924-0136(02)00203-0
12. Sommer, N. – Lee, S. et al: Dynamic tensile deformation behavior of AISI 316L stainless steel fabricated by laser-beam directed energy deposition. *J. of Materials Research and Technology., Vol 27*. **2023**, p. 5896-5909; doi.org/10.1016/j.jmrt.2023.10.251
13. Evin, E. - Tomáš, M. - Kmec, J. et al: The Deformation Properties of High Strength Steel Sheets for Auto-body Components. *Procedia Engineering*, *Vol. 69*, **2014**, p.1-1568; doi: 10.1016/j.proeng.2014.03.052

TECHNICKÁ UNIVERZITA V KOŠICIACH
Strojnícka fakulta

Biocompatibility evaluation of porous titanium scaffolds

Jana Demeterová [1*], Marianna Trebuňová [1], Darina Bačenková, Viktória Rajťuková[1] and Jozef Živčák [1]

[1] Technical University of Košice, Košice, Slovakia; email: jana.demeterova@tuke.sk

Abstract: Biomaterial sciences and tissue engineering have emerged as novel areas of science in the recent decade, with rising demands for regenerative treatments. Tissue regeneration utilizing stem cells has been achieved since direct cell transplantation into tissues that have been damaged. However, monitoring the transplanted stem cells while maintaining them in one location is challenging. As a result, new technologies, such as the cultivation of stem cells on scaffolds, are currently under development. This paper assesses the cytotoxic impact and biocompatibility of titanium scaffolds with porosity of 0,5, 0,9, and 1,3 mm, using chorion-derived mesenchymal stem cells (CMSCs), while analyzing their viability and proliferation using the colorimetric MTT test. CMSCs displayed strong adherence to surfaces and high vitality on titanium scaffolds, depending on the pore size.

Keywords: biocompatibility, stem cells, scaffolds, regenerative medicine

1. Introduction

Tissue engineering is an interconnected field of study that uses technical and biological principles to repair damaged tissues. Chorion-derived mesenchymal stem cells (CMSCs) have caught the interest of tissue engineers as a source of cells due to their ability to proliferate in an undifferentiated form for an extended period of time and later specialize into specific cell types. Mesenchymal stem cells are being studied in clinical trials for a variety of inflammatory and regenerative diseases [1]. This study focuses on the cultivation of placental stem cells, specifically chorionic mesenchymal stromal cells (CMSCs). The typical source of human mesenchymal cells is bone marrow, but the placenta appears to provide a more easily accessible source. The placenta is a tissue that retains fetomaternal immunological tolerance during pregnancy, which may indicate that cells have immunomodulatory properties. The studies of cells that originate from the placenta indicates that they have greater immunosuppressive properties than adult mesenchymal stem cells. Large quantities of these cells can be obtained from the placenta without intrusive procedures or ethical issues. Furthermore, mesenchymal stem cells from amniotic and chorionic membranes are pluripotent, which means they can differentiate not only into mesodermal cells but also into ectodermal and endodermal cells [2].

As a substrate that can imitate the natural extracellular matrix, the scaffold plays a significant role in tissue engineering, as its features have been demonstrated to influence cell behaviors such as cell attachment, proliferation, and differentiation. A variety of qualities should be present in ideal scaffolds for tissue engineering. Scaffold should be highly biocompatible and not cause immunological or clinical symptoms, nor should show negative body reactions to a foreign body, such as an inflammatory process [3]. A very important requirement for the development of a scaffold is its structure, as it should be highly porous with an interconnected pore network available for cells growth, movement of nutrients and metabolic waste. Porosity and pore size are thought to be one of the most important factors in affecting cell proliferation and viability. In 2016, Wang et al. published in the paper that the pore size to accelerate proliferation should be in the range of 0.1– 0.9 mm [4].

2. Materials and Methods

2.1. Preparation of Titanium Scaffolds

This paper examines the testing of cylindrical samples constructed of the titanium alloy Ti-6Al-4V - rematitan CL, while having a distinct porous structure with pore diameters of 0.5mm, 0.9mm, and 1.3mm (Figure 1). Titanium Ti-6Al-4V is made up of 90% titanium, 6% aluminum, 4% vanadium, 0.25% iron (max.) and 0.2% oxygen. It has extraordinary strength, a low modulus of elasticity, high corrosion resistance, good weldability, and the ability to be heat treated. Inserting aluminum and vanadium increases the hardness of the material in the alloy matrix, improving its mechanical and physical qualities [5].

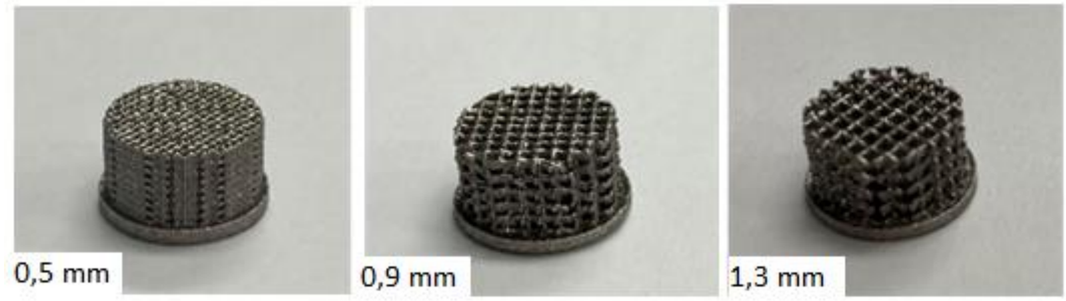

Figure 1 Titanium samples produced by SLM technology - porosity of 0.5 mm, 0.9 mm, and 1,8 mm**.**

For the production of porous test samples, additive manufacturing technology SLM (selective laser melting) 3D printer Mlab cusing R (*GE Additive*, *USA*) was used. This device is beneficial for the manufacturing of metal parts with complex structures, as well as reactive materials such as titanium. It operates on the basic idea of selective laser melting. Table 1. shows the basic device settings in the SLM production process used to create the test samples.

Table 1 parameters of the production a sample

Parameter	Value
Diameter [mm]	15,0
Height [mm]	15,0
Grid dimensions [mm]	0,5 / 0,9 / 1,3
Lamella thickness [mm]	0,2
Internal structure	grid
Pores	square

2.2. Preparation and Cultivation of Chorionic Mesenchymal Stromal Cells

The biocompatibility and potential cytotoxicity of titanium scaffolds were assessed using chorionic mesenchymal stem cells (CMSCs) obtained from fetal membranes. Stem cells obtained from the chorion were sufficiently sensitive to determine the potential cytotoxic effect of the analyzed material. After the expected termination of the pregnancy, with the approval of the obstetricians, the fetal envelopes had been preserved in collaboration with the AGEL Košice- Šaca hospital's gynecology-obstetrics clinic. MSCs were extracted enzymatically from the amniotic membrane, in Dulbecco's modified eagle's medium (DMEM) with antibiotics using the enzyme dispase and then type II collagenase (1 mg/mL, Gibco). The disintegrated chorion pieces - cell suspension containing tissue remains - were filtered through a 40 m cell strainer, and the cells went through a centrifuge for 10 minutes at 1300 rpm. These cells are known as chorionic mesenchymal stromal cells (CMSCs). Isolated washed cells went into cultivation in a concentration approximately

4000 cells/cm². This was followed by *in vitro* cultivation in an incubator at 37° C and 5% CO_2. As a complete culture medium, DMEM with 10% FCS and 1% antibiotics/antimycotics was used. The entire culture medium was changed two to three times per week. After two weeks, cells were released from the monolayer using enzyme trypsine – EDTA 0,25% where they formed a suspension suitable for biocompatibility testing on the scaffolds.

2.3. Cytotoxicity testing of titanium scaffolds

The titanium scaffolds were washed in distilled water and sterilized. They were tested on a 24-well plate using seeded CMSCs. Scaffolds together with prepared CMSCs suspension were cultured *in vitro* (37° C, 5% CO_2) using DMEM medium with 10ˇ% fetal bovine serum and 1% antibiotic solution for 20 days. Every 2 to 3 days was the culture medium changed. On 2nd, 4th, 8th, 10th, 13th, and 15th day the MTT test was performed. The MTT assay is used to determine cell viability, proliferation, and cytotoxicity by measuring cellular metabolic activity. This colorimetric assay is based on reduction of a yellow tetrazolium salt to purple formazan crystals by metabolically active cells. MTT is reduced to formazan by NAD(P)H-dependent oxidoreductase enzymes in active cells. The insoluble formazan crystals are dissolved in a solubilization solution, and the solution is evaluated by measuring absorbance at 500-600 nanometers with a multi-well spectrophotometer. The darker the fluid, the more live, metabolically active cells there are (Figure 2.).

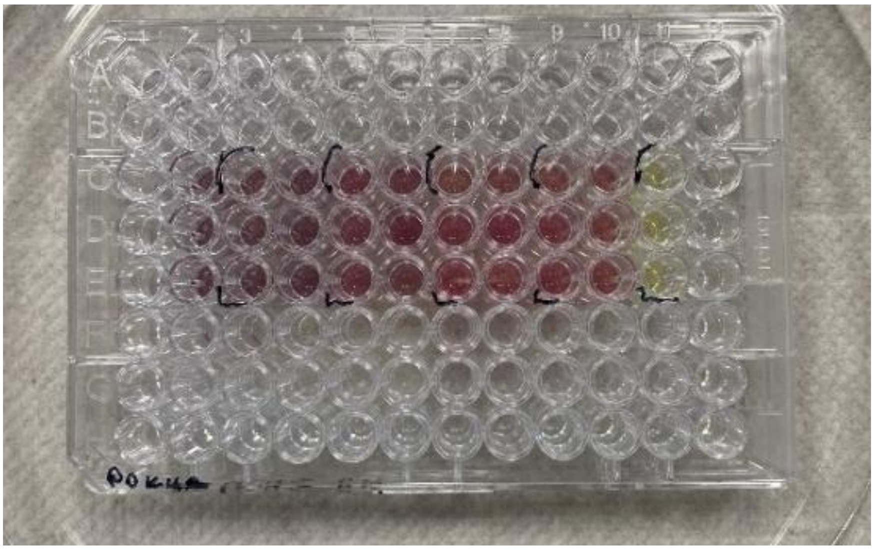

Figure 2 The MTT test before spectofotography measurement at a wavelength of 490 nm

3. Results

3.1. Cultivation on scaffolds

Cell adhesion was measured 48 hours after cell seeding on a transparent plate of a 24-well culture plate (Figure 3.). Proliferation was visually observed in all comparing groups for 15 days. Cells in all monitored wells were morphologically typical spindle-shaped and were visually compared to control CMSCs sample.

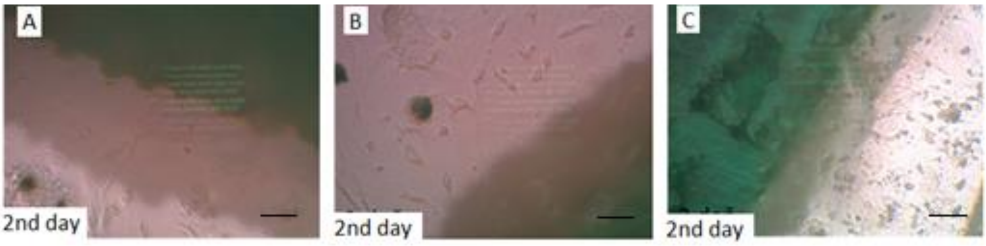

Figure 3 : Titanium matrix, pore size A 0.5 mm; B 0.9 mm; C 1.5 mm on the second day of culture of CMSCs. Scale bar 50 μm.

3.1. MTT test evaluation

The percentage degree of compatibility and the minimal cytotoxicity effect of the titanium scaffolds were observed by the MTT test (Figure 4). Proliferation and cell viability were visually confirmed in all samples. The highest viability was observed in sample of 0,5 mm porosity, with steadily increasing viability and peak at 63 % on day 15. Sample with 0,9 mm porosity showed a good viability throughout the measuring days with peak 42 % on day 15. Sample with 1,3 mm pore size showed some degree of comparable proliferation in the first days of cultivation, however the concentration of cells during the testing days increased insignificantly and after the peak at 10^{th} day with 15 % viability - regression in number of viable cells occurred.

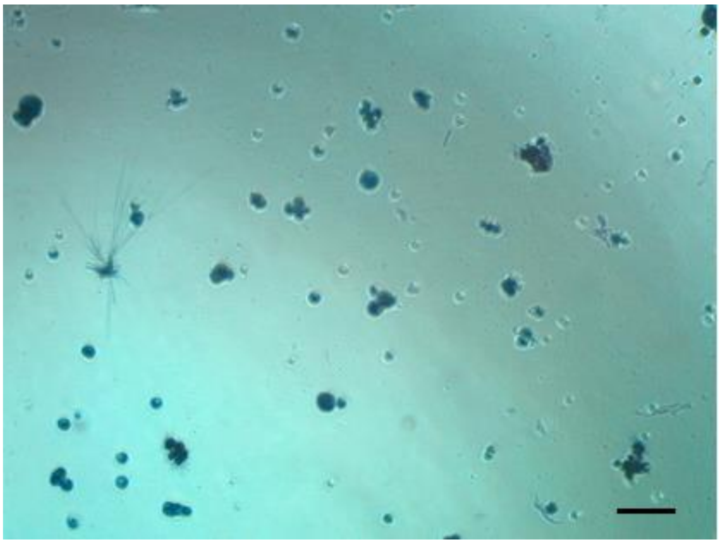

Figure 4 MTT test in the reaction phase of vital CMSCs formation, NAD(P)H-dependent oxidoreductase enzymes reduction to formazan. Scale bar 100 μm.

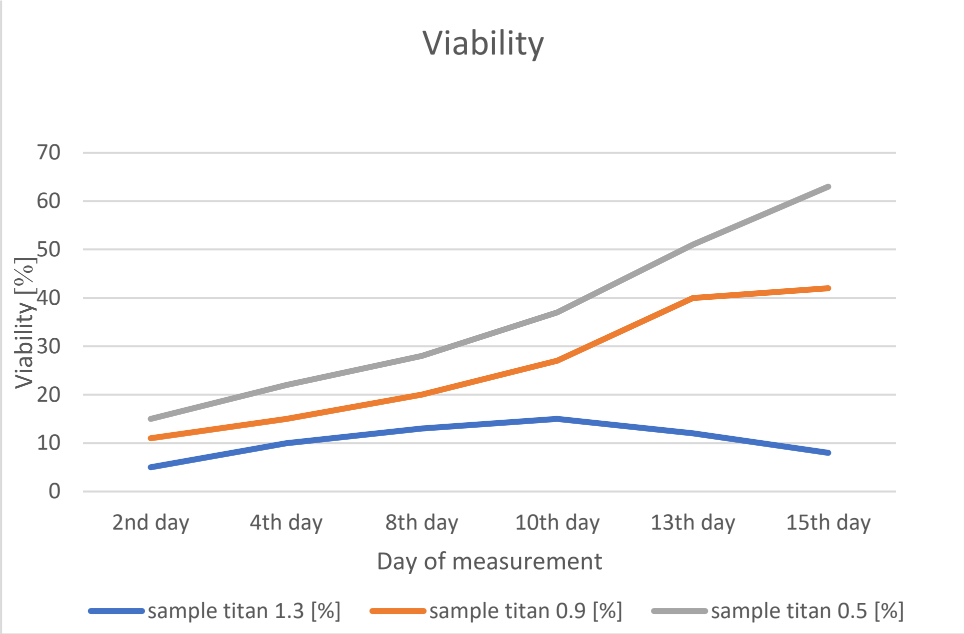

Figure 5 Viability of titan samples with 0,5; 0,9 and 1,3 mm pore size during 15 days of MTT measurement. Viability is expressed as a percentage relative to the control with pure cells (100%) without the scaffold.

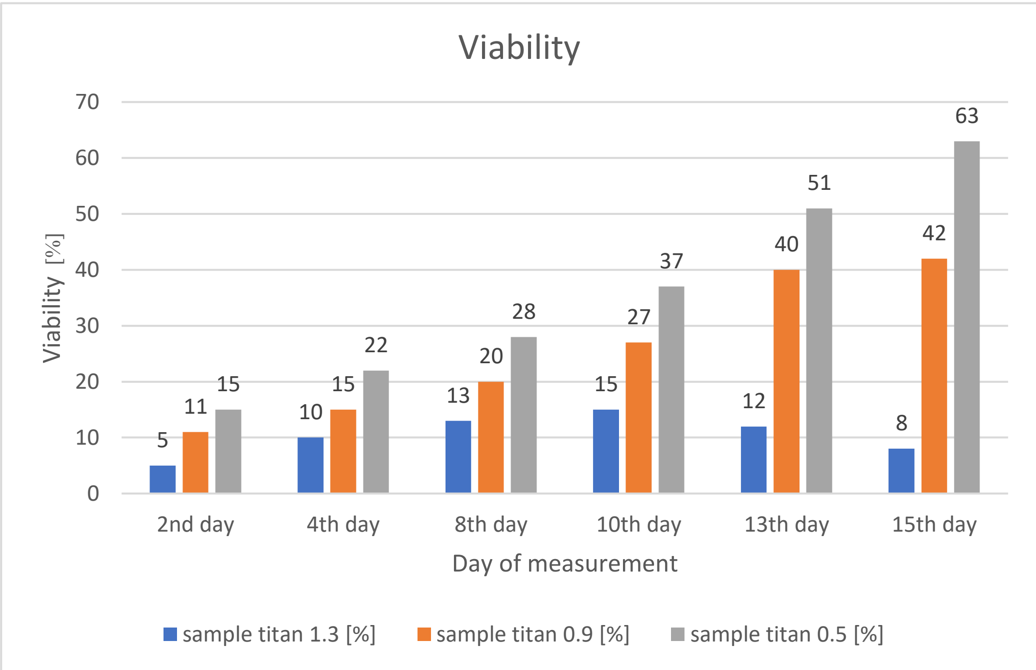

Figure 6 Comparation of viability of each sample on different days of measurement. Viability is expressed as a percentage relative to the control with pure cells (100%) without the scaffold.

5. Conclusions

Scaffolds for tissue engineering applications must be designed to meet a number of criteria that are specific to their particular use. Ideal scaffolds for tissue engineering should include several properties. They should be highly biocompatible and should not cause immunological or clinical manifestations, nor should they show negative reactions to a foreign body, e.g. inflammatory process. In this paper, we tested the biocompatibility of titanium alloy Ti-6Al-4V scaffolds with porosity of 0,5; 0,9 and 1,3 mm. Using the MTT test we observed a viability of CMSCs seeded on scaffolds for 15 days. Highest viability was measured with 0.5 mm sample, where the viability was rising thorough the 15 days of measurement with peak 63%. Second sample with porosity of 0,9 mm showed its highest viability at 42%. The lowest viability was observed in sample with 1,3 mm porosity, where there was a 15% peak at the day 10 and then the viability started to decrease. Previously published research by Wong et. al suggest the range of porosity to enhance the viability to be 0.1– 0.9 mm [3]. The reason of lower viability and proliferation in samples with higher porosity could be a poor cell to cell interaction due bigger gaps. Overall the titanium alloy showed a good biocompatibility and low cytotoxicity, as we suppose the lower viability values in sample 1.3 mm were due the higher porosity and not the material itself, as it was previously tested and confirmed to be biocompatible by many researchers [6,7,8].

Funding: KEGA 018TUKE – 4/2023

Conflicts of Interest: "The authors declare no conflict of interest."

References

1. Abou-Saleh, H., Zouein, F.A., El-Yazbi, A. et al. The march of pluripotent stem cells in cardiovascular regenerative medicine. Stem Cell Res The. 2018, 9, 201.
2. Darina Bačenková, Ján Rosocha, Timea Tóthová, Ladislav Rosocha & Marek Šarisský. Isolation and basic characterization of human term amnion and chorion mesenchymal stromal cells, Cytotherapy, 2011, 13, 1047-1056
3. Modrák, M.; Trebuňová, M.; Balogová, A.F.; Hudák, R.; Živčák, J. Biodegradable Materials for Tissue Engineering: Development, Classification and Current Applications. *J. Funct. Biomater*. **2023**, 14, 159.
4. Wang X, Xu S, Zhou S, Xu W, Leary M, Choong P, Qian M, Brandt M, Xie YM. Topological design and additive manufacturing of porous metals for bone scaffolds and orthopaedic implants: A review. *Biomaterials*. **2016**, 1:127-41.
5. Richbourg, NR, Peppas, NA, Sikavitsas, VI. Tuning the biomimetic behavior of scaffolds for regenerative medicine through surface modifications. J Tissue Eng Regen Med. **2019**; 13: 1275–1293.
6. Sidambe AT. Biocompatibility of Advanced Manufactured Titanium Implants-A Review. *Materials*. **2014**; 7, 8168-8188.
7. Trevisan F, Calignano F, Aversa A, et al. Additive manufacturing of titanium alloys in the biomedical field: processes, properties and applications. *J Appl Biomater Funct Mater*. **2018**; 16, 57-67.
8. da Costa Valente ML, de Oliveira TT, Kreve S, et al. Analysis of the mechanical and physicochemical properties of Ti-6Al-4 V discs obtained by selective laser melting and subtractive manufacturing method. *J Biomed Mater Res B Appl Biomater*. **2021**, 109, 420-427.

Estimating tangential cutting force in turning operations through analysis of internal CNC control data

Michal Demko[1,*], Marek Vrabeľ[1], Jozef Brindza[1], Peter Ižol[2] and Ján Kušnír [1]

[1] Technical University of Košice,Faculty of Mechanical Engineering, Prototyping and Innovation Centre, Park Komenského 12A, 040 01 Košice, Slovakia
[2] Technical University of Košice, Faculty of Mechanical Engineering, Department of Computer Aided Production, Mäsiarska 74, 040 01 Košice, Slovakia
* Correspondence: michal.demko@tuke.sk; Tel.: +421 55 602 3362

Abstract: This study explores using internal CNC data to calculate tangential cutting force during turning operations, aiming to detect tool wear and demonstrate its potential for optimization of tool life and cutting parameters. As part of the study, an experiment was conducted in which the torque and power of the CNC lathe spindle drive were recorded. The experiment consisted of turning different cutting lengths every time with a new insert, and the tangential cutting force was calculated based on the recorded data. In conclusion, the computed tangential cutting force values affirm the viability of monitoring tool wear through internal CNC data. The noted rising trend in cutting force corresponds with the tool wear curve, offering supplementary validation; however, future studies must ensure the accuracy by validating these values using a dynamometer.

Keywords: CNC internal data; cutting force; tool wear

1. Introduction

Modern manufacturing processes, particularly those involving Computer Numerical Control (CNC) machining, have seen significant advancements in recent years. Precision and efficiency are paramount in these processes. Understanding and optimizing cutting forces play a crucial role in achieving these goals. Among the components of cutting force, the tangential cutting force is a key parameter influencing tool wear and overall machining performance. Tool wear then is one of the crucial problems in a turning process since it can cause worse roughness onto workpiece surface and inaccurate shapes. [1,2]

Traditionally, the calculation of tangential cutting force during turning operations relies on empirical models and measurements with dynamometers [3-5]. However, with the increasing integration of internal sensors and data collection capabilities within CNC systems, there exists an opportunity to refine and enhance the accuracy of tangential cutting force estimation and other parameters [6].

This research focuses on harnessing internal CNC control data to develop methodology for calculating tangential cutting forces during turning operations. By delving into the wealth of data generated within the CNC system itself, there is an aim to improve the understanding of dynamic machining conditions and subsequently optimize tool life and cutting parameters.

2. Machine setup and experimental plan

The objective of the experiment detailed in this article was to assess the feasibility of identifying cutting insert wear using internal data from a CNC machine, without the need for additional external sensors. The assumption was that wear on the cutting insert increases with the overall cutting length, which is the total length traveled by the tip of the tool along the helix during longitudinal turning. This leads to a rise in the tangential cutting force F_t, which should be evident in the increased torque of the spindle drive. To validate the potential for calculating and comparing tangential cutting force Ft, an experiment was devised. It involved progressively turning a sample made of austenitic chrome-nickel steel 1.4305 in three trials, with simultaneous recording of power and spindle drive torque. The experiment was conducted on a CNC lathe, specifically the DMG ecoTurn 510 equipped with the SINUMERIK 840D sl control system. Figure 1 depicts the workpiece clamped in the chuck before experiment.

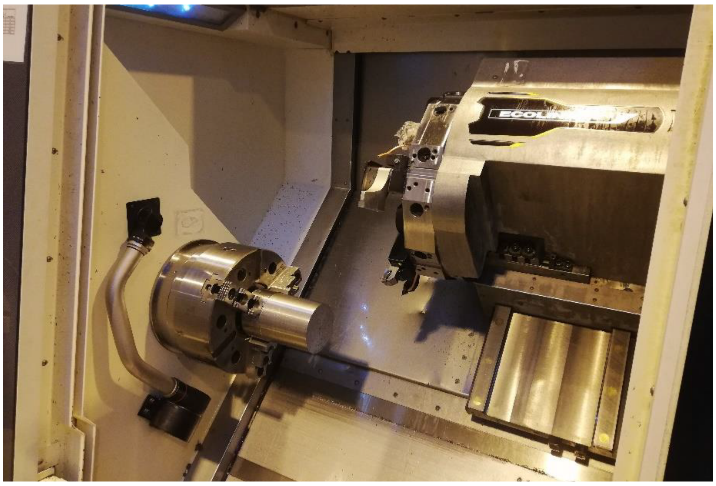

Figure 1 Clamped raw material before experiment

In the first trial, the cutting length was 150 m, and the workpiece radius r was 58 mm. In the second trial, there were 2 passes of 150 m cutting length each, with radii of 57 mm and 56 mm. In the third trial, there were 3 passes of 150 m cutting length each, with radii of 55 mm, 54 mm, and 53 mm. Each trial commenced with a new cutting insert, and the specified cutting conditions were: cutting speed v_c = *120 m/min*, feed rate f = *0,25 mm/rev*, and depth of cut a_p = *1 mm*. The radial rake angle γ_0 defined by the tool body was 6°, and the lead angle κ_r was 95°.

To record data from the machine, a custom-developed application utilizing OPC UA communication was employed, and parameters were logged every 100 ms. The torque profile recorded in the application after completing the experiment is depicted in Figure 2.

Figure 2 OPC UA client app

3. Results and discussion

In Figure 3, the spindle drive power is illustrated, recorded throughout the entire experiment. From this profile, the average power values P_D were calculated each time the last 150 m cutting length were removed (refer to Table 1).

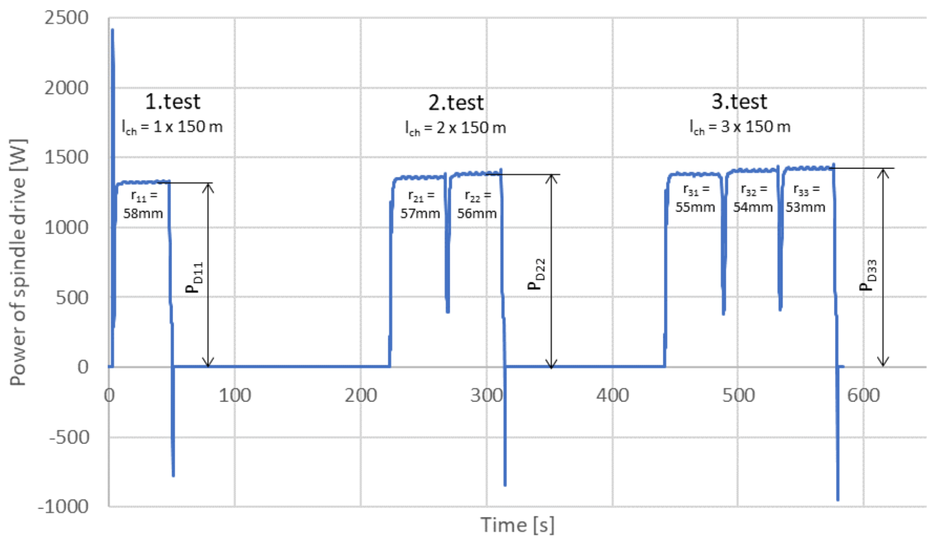

Figure 3 Spindle drive power during experiment

As the machine spindle is driven using a belt drive system (Figure 4), determining the gear ratio was a prerequisite for calculating the tangential cutting force from the torque. This information was derived from the available data.

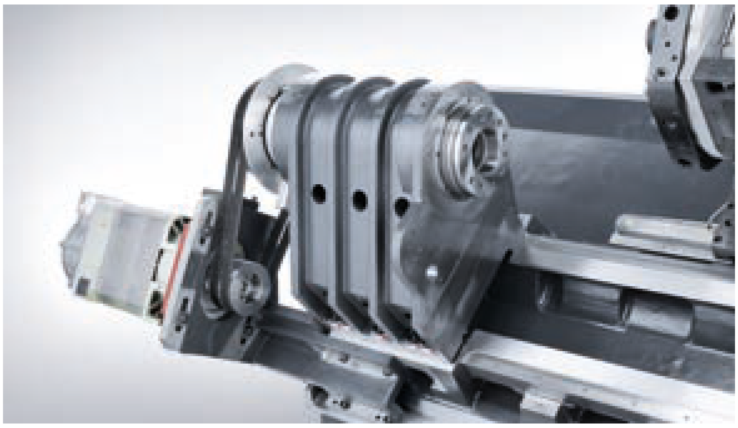

Figure 4 Belt drive system of DMG ecoTurn 510 spindle

If we neglect losses in the belt drive system, the recorded power of the drive P_D is equal to the power of the spindle P_S.

$$P_S = P_D \tag{1}$$

Given that we know the spindle speed S, which can be calculated from the set cutting speed v_c in the program using the formula:

$$S = \frac{1000\ v_c}{2\pi r} \tag{2}$$

Thus, we can determine the spindle torque Ms using the equation:

$$M_S = \frac{P_S}{2\pi S} \tag{3}$$

Subsequently, the gear ratio n is expressed as the ratio of the calculated spindle torque M_S to the recorded drive torque M_D.

$$n = \frac{M_S}{M_D} \tag{4}$$

In this manner, the gear ratio n=2 was calculated, and it was later verified directly on the machine. All computed values are presented in Table 1.

Table 1 Calculated torque values

Trial	$P_D = P_S$ [W]	r [mm]	S [rpm]	S [rps]	M_S [Nm]	M_D [Nm]	n
1	1323	58	329,3	5,49	38,4	18,99	2,02
2	1382	56	341,0	5,68	38,7	19,45	1,99
3	1421	53	360,4	6,01	37,7	18,94	1,99

By applying the gear ratio, the spindle torque profile M_S was subsequently generated from the recorded drive torque M_D as depicted in Figure 5. To compute the tangential cutting force F_t, the torque value $M_{S0} = 11{,}8\ Nm$, representing the state when the workpiece was rotating without any machining, was initially subtracted from the profile when machining. This subtraction from the average torque M_S ensured that the torque M_{SC} exclusively reflected the values associated with the tangential cutting force.

(5)

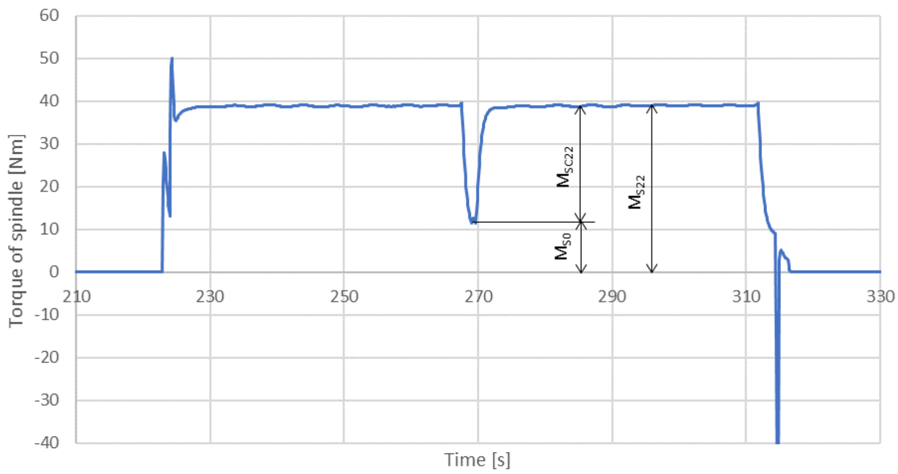

Figure 5 Profile of spindle torque during 2nd trial

From this point, the calculation of the tangential cutting force F_t was feasible using the following formula:

$$F_t = \frac{M_{SC}}{r} \tag{6}$$

The computed values of tangential cutting force F_t are presented in Table 2.

Table 2 Calculated tangential cutting force values

Trial	r [mm]	M_{SC} [Nm]	F_t [N]
1	58	26,6	458
2	56	26,9	480
3	53	25,9	488

These results validate the hypothesis that it is viable to detect tool wear based on internal machine data during turning. When converted to tangential force, a noticeable increment is observed between consecutive operations, correlating with the length of the machined chip. The larger discrepancy between F_{t1} and F_{t2} compared to F_{t2} and F_{t3} can be attributed to the wear curve, where the initial wear phase occurs up to a cutting length of 300 m, followed by a transition to the normal wear phase beyond 300 m. Although the tangential force calculation was manual in this case, future automation is feasible, as all essential parameters can be extracted from the internal data of the CNC machine.

For the theoretical validation the tangential cutting force values, a calculation was performed using the specific cutting force k_{C1} = 2150 N/mm² for the given material, as per the formula:

$$F_C = k_C . b . h \tag{7}$$

Where chip width b is:

$$b = \frac{a_p}{\sin \kappa_r} = \frac{1}{\sin 95} \cong 1mm \tag{8}$$

Chip thickness h is:

$$h = f . \sin \kappa_r = 0{,}25 . \sin 95 \cong 0{,}25\ mm \tag{9}$$

and the specific cutting force k_C s is calculated using the formula:

$$k_C = k_{C1} . h^{-m_C} . \left(1 - \frac{\gamma_0}{100}\right) = 2150 . 0{,}25^{-0{,}2} . \left(1 - \frac{6}{100}\right) = 2669\ N/mm^2 \tag{10}$$

Then the tangential cutting force is:

$$F_C = 2669 . 1 . 0{,}25 = 667{,}2\ N \tag{11}$$

However, this calculated value is based on a simplified model of the cutting wedge, which inadequately represents the geometry of the used cutting insert. Therefore, the difference of around 200 N between the recorded cutting force values and the calculated one is not an actual error in the results but rather reflects the limitations of the simplified model. This calculation serves to confirm the order of magnitude of the values, indicating that they are within a realistic range. Furthermore, it is evident that the calculated value of 667,2 N cannot be accurate, as even when the force value is computed from the spindle torque M_{S1}, the total torque in the first trial where M_{S0} is not subtracted, results in a value of 661 N, which is still lower than the calculated value.

4. Conclusions

Utilizing internal CNC machine data, it was successfully estimated the tangential cutting force. The values of the tangential cutting force demonstrate the feasibility of monitoring tool wear based on internal CNC data. The observed increasing trend in cutting force aligns with the tool wear curve, providing additional validation to our findings.

In future studies, it is crucial to validate the calculated cutting force values using a dynamometer. This step will ensure a comprehensive understanding of the accuracy and reliability of the internal CNC data for tool wear monitoring. Additionally, exploring the determination of other components of cutting forces from the drives on the linear axes of the machine holds promise for further insights into machining dynamics.

Considering the insights gained, practical applications of the obtained information can be highly valuable. Implementation of a monitoring system in machining processes that leverages internal CNC data for real-time tool wear assessment could enhance tool life, optimize machining parameters, and minimize downtime.

In conclusion, this research underscores the potential of internal CNC data as a valuable resource for tool wear and workpiece quality monitoring, paving the way for more efficient and informed machining practices.

Acknowledgments

This work was supported by the Slovak grant research project VEGA 1/0457/21 and KEGA 050TUKE-4/2023.

Conflicts of Interest

The authors declare no conflict of interest.

References

1. Sawangsri, W., & Wattanasinbumrung, P. (2022). A model approach for in-process tool condition monitoring in CNC turning using machine vision. International Journal on Interactive Design and Manufacturing (IJIDeM), 16(4), 1439–1456.
2. Tangjitsitcharoen, S., & Lohasiriwat, H. (2017). Intelligent monitoring and prediction of tool wear in CNC turning by utilizing wavelet transform. The International Journal of Advanced Manufacturing Technology, 99(9–12), 2219–2230.
3. Mohamed, A., Hassan, M., M'Saoubi, R., & Attia, H. (2022). Tool Condition Monitoring for High-Performance Machining Systems—A review. Sensors, 22(6), 2206.

4. Sahu, N. K., Andhare, A. B., Andhale, S., & Abraham, R. R. (2018). Prediction of surface roughness in turning of Ti-6Al-4V using cutting parameters, forces and tool vibration. IOP Conference Series: Materials Science and Engineering, 346, 012037.
5. Ingle, S. V., & Raut, D. N. (2023). Monitoring Tool Wear with Sensors and Arduino in CNC Metal Cutting Turning Operation of Titanium Alloys (Ti6Al4V). In Lecture notes in mechanical engineering (pp. 101–109).
6. Alomari, Yazan & Ando, Matyas. (2023). An analysis of OPC UA communication with CNC turning machines: Emphasis on synchronized data acquisition. 55 (2023). 175-190.

TECHNICKÁ UNIVERZITA V KOŠICIACH
Strojnícka fakulta

Numerical modelling of passenger car foam for pedestrian protection

Erika Dubňanská [1]*, Martina Hančinová [1] and Róbert Huňady [1,]

[1] Department of Applied Mechanics and Mechanical Engineering, Faculty of Mechanical Engineering, Technical University of Košice, Letná 9/B, 042 00 Košice, Slovakia; erika.dubnanska@tuke.sk; martina.hancinova@tuke.sk; robert.hunady@tuke.sk;
* Correspondence: erika.dubnanska@tuke.sk

Abstract: The paper deals with the numerical modelling of foam, which, as part of the crash management system (CMS) of a passenger car, is becoming an increasingly important aspect in the protection of pedestrians, as well as ensuring the reduction of damage to individual parts in low-speed car crashes. The aim of the paper is to investigate the possibilities of tuning the numerical model in order to improve the current state and to approach the results obtained in physical crash tests. The RCAR (Research Council for Automobile Repairs) association develops and administers global standards for assessing the level of damageability and repairability of vehicles in low-speed impacts where the vehicle structure is damaged but the passengers are not injured. Attention is paid to RCAR frontal low-speed structural impacts (hereafter referred to as RCAR 10°). Numerical model tuning was performed using the ANSA pre-processor, the META post-processor and the PAM-Crash solver. The FEM simulations of the impact tests in PAM-Crash used a non-linear material model of the foam with strain-rate dependency (material type 45) and a non-linear contact (contact type 10). The essence was to investigate the appropriate setting of the EPSI parameter at the material type 45 and the EDGLN, FSVNL parameters at the contact type 10. The influence of the investigated parameters on the contact force curves and the time step was shown within the created variants of the numerical model BIF_001 to BIF_006. Among these variants, variant BIF_006 exhibited the highest correlation with the reference curve, and this configuration of the numerical model was also reflected in the time step.

Keywords: RCAR low-speed structural impacts, crash management system, foam impact absorber, numerical modelling, PAM-Crash

1. Introduction

Minor collisions occurring at low speeds of up to 15 km/h are accompanied by damage to some components, leading to the need for servicing or an increase in the insurance premium. In order to reduce these costs, as well as to increase pedestrian protection, RCAR frontal low-speed structural impact tests (hereafter referred to as RCAR 10°) are implemented. For these tests, the focus is primarily on the development of the front CMS, which is mounted in the front crumple zone of the car. The foam impact absorber, as part of the CMS, is made of expanded polypropylene (EPP). The outstanding properties of EPP include recyclability, light weight, the ability to absorb kinetic energy almost without breaking, and the ability to regain its original shape [1][2][3].

To ensure the least number of crash tests needed, finite element method (FEM) analyses and simulations are applied in practice. Since the car impact is a complex occurrence, its complexity is also reflected in the numerical model tuning tasks.

Ramaswamy et al. [4] investigated the differences in mechanical properties of EPP foams depending on different material suppliers. Murata et al. [5] outlined some approaches to designing pedestrian safe bumper systems using EPP. The concepts were tested on a full vehicle system, illustrating how soft initial contact can be combined with a high energy absorbing capacity.

The main focus of this paper is to investigate the influence of the EPSI parameter at the foam material model and the EDGLN, FSVNL parameters at contact type 10 on the response of the numerical model in order to approach the experimentally obtained results.

2. Materials and Methods

The RCAR test procedures assessing the level of damageability and repairability of a vehicle are based on a series of tests carried out and experience gained. In the front low-speed tests, the test vehicle impacts into a rigid barrier at a speed of 15 km/h with a tolerance of +1/-0 km/h. The height of the barrier exceeds the height of the front of the test vehicle. The front face of the barrier is vertical to within ± 1° and oriented with its front face 10° (±1°) relative to the perpendicular of the longitudinal axis of the test vehicle. The front of the vehicle also overlaps the front of the barrier by 40 % ± 25 mm [2].

The scheme of the initial position of the test vehicle and the rigid barrier in the RCAR 10° low-speed frontal impact test is shown in Figure 1.

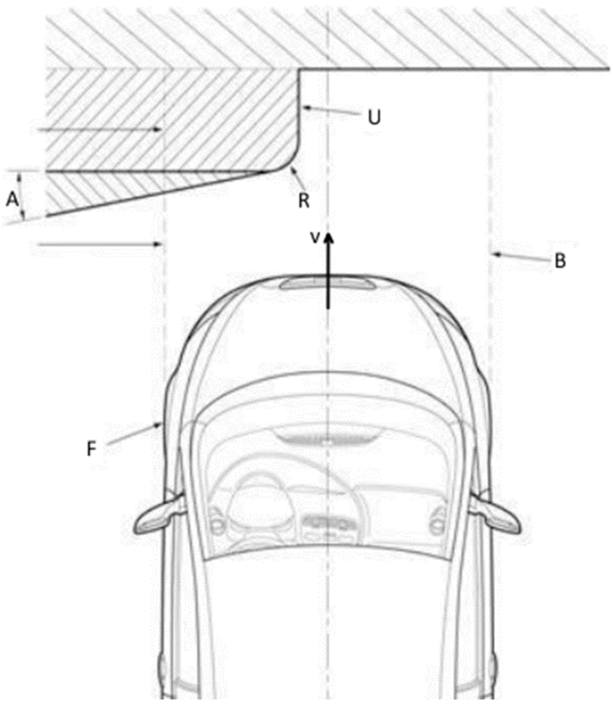

Figure 1. Scheme of the RCAR 10° low-speed frontal impact test. F – test vehicle, B – vehicle width (front), U – rigid barrier with 40% overlap, A – barrier front face angle 10°, R – 150 mm radius, v – velocity of the test vehicle [2].

The finite element method (FEM) is applied to a significant extent in the investigation of these processes, whereby the behaviour of the structure is investigated in a virtual environment through analyses and simulations, thereby reducing the number of crash tests performed and the associated costs of prototyping and the time required.

In order to adequately define the material in the FEM analysis, it is necessary to appropriately specify the behaviour of the material. For a linear static analysis, its elastic behaviour may be sufficient, while more complex analyses, such as structural impact of a car, require the inclusion of additional behavioural models [6].

In the PAM-Crash software, material type 45 was used to describe the behaviour of the foam impact absorber. Material type 45 corresponds to a highly compressible nonlinear elastic foam material with strain-rate dependency, where the geometric nonlinearity is accounted for in the analysis step.

Since foam materials have a limited tensile strength where they can easily fail under excessive tensile loads, it is possible to define a limiting value for the maximum tensile stress at which the material will remain intact.

For easier modelling of material failure, the element elimination from the simulation was activated. Element elimination is piloted with a strain value limit ε_{elim}, also referred to as EPSIelim (EPSI), when the IFAILIC = 1. This value is compared at each cycle to the principal strains. If the strain limit is reached for one of the principal directions, the failure process starts and the element is eliminated after 100 cycles [7].

The prevention of numerical problems that could arise due to heavy compression and distortion of the solid elements was ensured by the use of an internal solid contact, which is represented in the PAM-Crash software by a contact type 10.

This option helps to reduce excessive compression and avoids, therefore too large drops in the stable solution time steps. The option also helps to avoid very large element distortions that may lead to ill-defined elements (negative volume) [7].

The parameter EDGLN, representing a fraction of the initial edge length of the body element, was defined to activate the contact. For defining the EDGLN value to activate the contact thickness for each contact area, the recommended range was used [7]

$$0.1 < EDGLN < 0.3. \tag{1}$$

To avoid perforations in severe contact problems, such as large elastic deformations, large kinetic of impact pairs, etc., it is possible to activate non-linear contact stiffness. In solving this problem, a nonlinear penalization stiffness parameter FSVNL was defined. That is the force scaling factor for penetration equal to the contact thickness. The values used for this FSVNL parameter were chosen within the recommended range [7]

$$10 < FSVNL < 100. \tag{2}$$

In order to achieve the most accurate outputs representing the frontal impact behaviour of the foam absorber, its numerical modelling was performed within the overall FEM model of the car.

The numerical modelling was based on experimentally obtained results from crash tests according to RCAR test procedures.

The reference was the prototype test, denoted as EIF, whose results were closest to the results of the numerical simulation performed on the FEM model, denoted as BIF.

The BIF model is considered in this paper as the initial numerical model based on which new variants were successively created and subsequently analyzed in order to investigate the influence of the EPSI parameter at the foam material model and the EDGLN, FSVNL parameters at type 10 contact. The monitored parameter was the contact force in the x-axis direction (X force) on the barrier generated at impact. The x-axis direction represents the longitudinal axis of the car. The second monitored parameter was the time step, used to assess the stability of the explicit analysis in terms of convergence.

The ANSA pre-processor was used to modify the numerical model, the results were processed using the META post-processor from BETA CAE Systems and the solver was represented by the PAM-Crash software.

3. Results

Figure 2 shows a plot of the X force obtained experimentally (EIF) and a plot of the X force obtained by FEM analysis from the initial numerical model (BIF). Figure 3 plots how the time step varied over the course of the analysis. As can be seen, the time step for the initial model is stable.

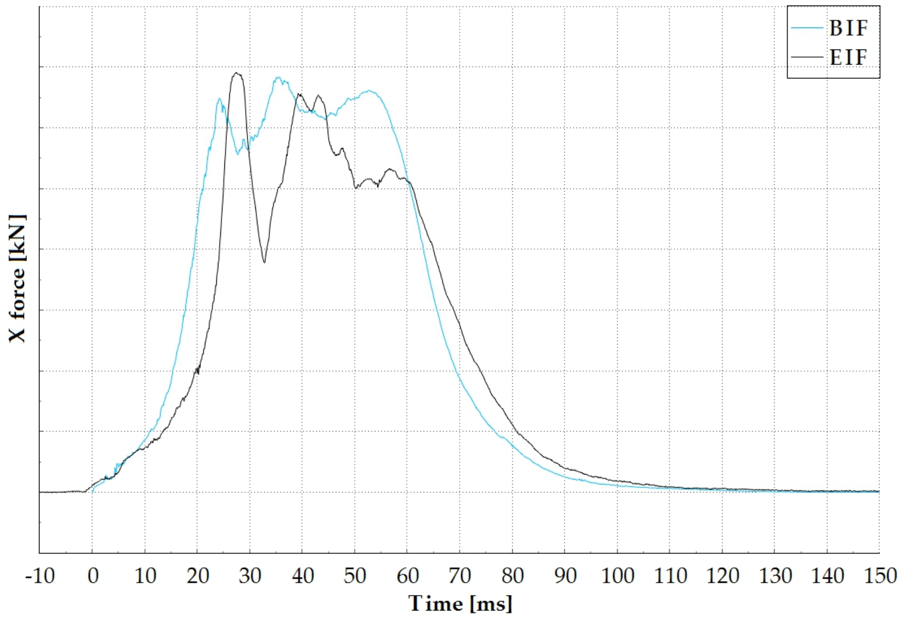

Figure 2. X force – EIF (experiment), BIF (initial numerical model).

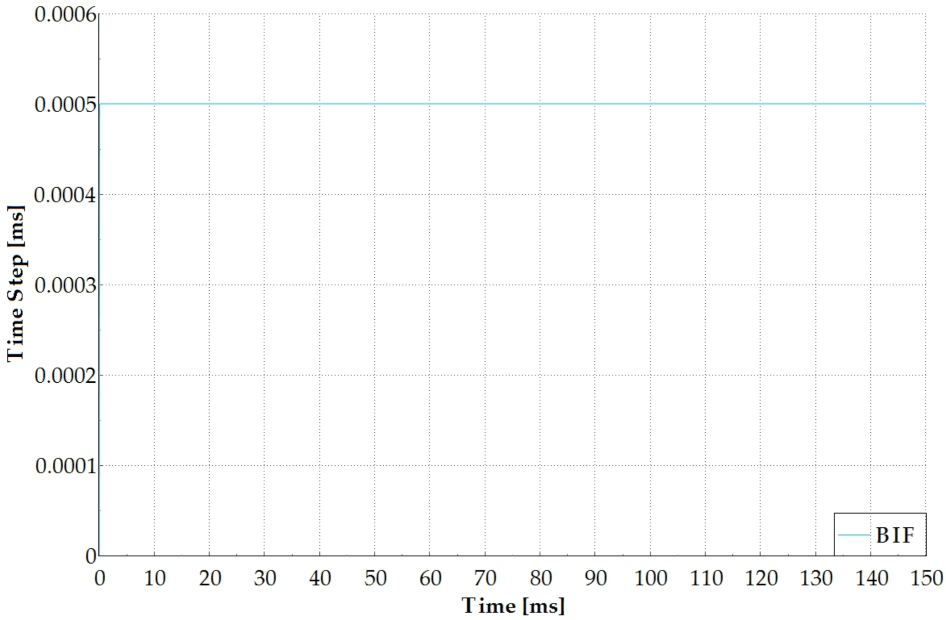

Figure 3. Time step – BIF.

Variants BIF_001 to BIF_005 were created from the initial BIF model, where the values of the EDGLN and FSVNL parameters were changed within contact type 10. Furthermore, a variant BIF_006 was created from variant BIF_005, where the values of the parameters EDGLN and FSVNL remained unchanged, however, the foam material model was modified to include the EPSI parameter.

The configuration of the numerical model including the chosen values of the investigated parameters is listed in Table 1.

Table 1. Numerical model configuration – variants BIF_001 to BIF_006.

Variant	Parameter		
	EDGLN	*FSVNL*	*EPSI*
BIF_001	0.1	30	-
BIF_002	0.1	50	-
BIF_003	0.3	80	-
BIF_004	0.3	30	-
BIF_005	0.2	10	-
BIF_006	0.2	10	0.05

In Figure 4, can be seen a plot of the X force for variants BIF_001 to BIF_006, and also BIF and EIF for comparison. Figure 5 shows the time step progression of the initial BIF variant and the created variants.

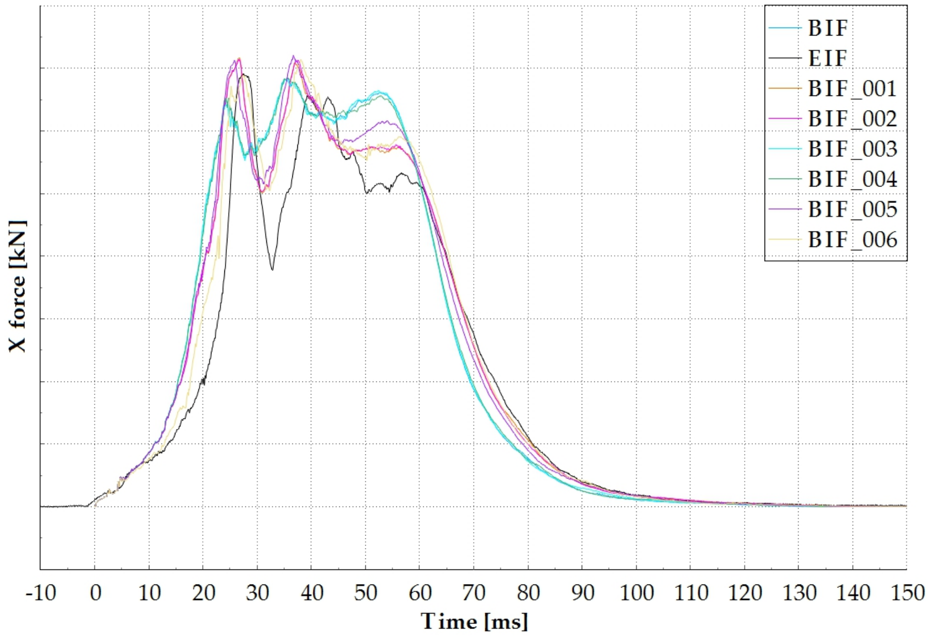

Figure 4. X force – variants BIF_001 to BIF_006.

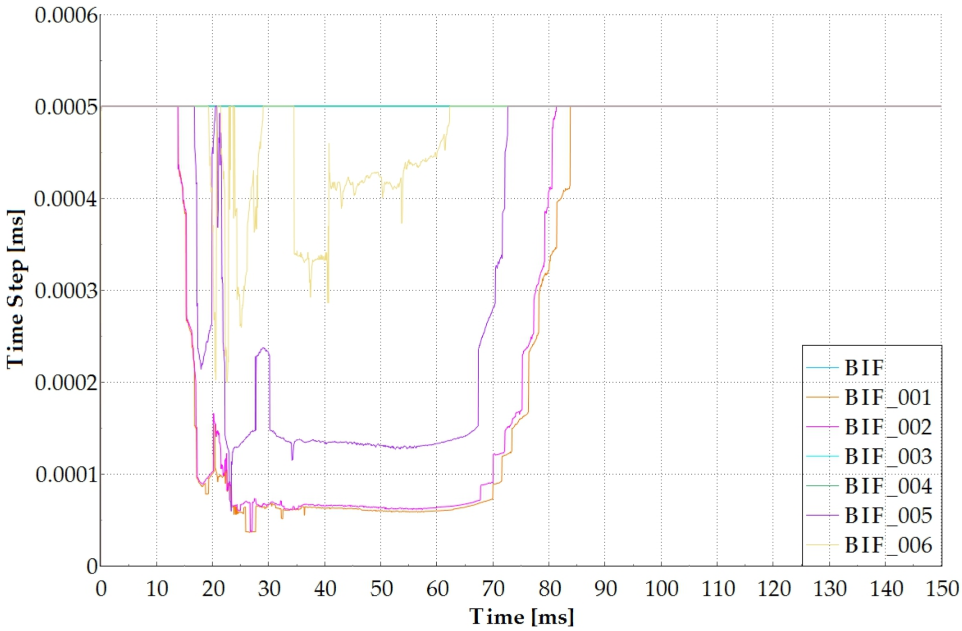

Figure 5. Time step – variants BIF_001 to BIF_006.

4. Discussion

The effect of the investigated parameters related to the contact type 10 and the material model is visible for the created variants. By changing the values of these parameters, the course of the X force curve was changed. As the value of the EDGLN parameter approaches its lower recommended limit, representing earlier contact activation, the first and second peaks on the curve increased, while the third peak decreased. However, this made the solution unstable as the time step decreased. Another parameter with effect on the obtained results is the EPSI parameter, which is used in the PAM-Crash software to control the elimination of elements during the failure process. By defining this parameter within the foam material model, the progression of the X force curve for the BIF_006 variant converged to the results obtained from the experiment. In addition to the decrease in the first and third peaks on the X-force curve, the effect of this parameter was also apparent on the time step.

Since tuning a numerical model is a complex task, the fact that the resulting curve approximates the experimentally obtained results, but with a certain degree of inaccuracy, may be due to several factors. In addition to examining other values of these parameters, there is also the possibility of examining the effect of other factors, such as the quality of the parts mesh, the refinement of the impact velocity of the vehicle, etc.

Acknowledgments: This work was supported by the Slovak Research and Development Agency under the grant project VEGA No. 1/0500/20 and VEGA No. 1/0516/22.

References

1. European Aluminium Association: Applications – Car body – Crash Management Systems. The Aluminium Automotive Manual. 2013. Available online: https://european-aluminium.eu/wp-content/uploads/2022/11/4_aam_crash-management-systems1.pdf.
2. Midas NFX: Low-speed crash test (RCAR bumper test). Automotive. Available online: https://www.scribd.com/document/396794187/12-Low-speed-Crash-Test-Standard-RCAR-Process.
3. RCAR: RCAR Low-speed structural crash test protocol. 2023. Available online: https://www.rcar.org/images/papers/procedures/RCAR_low_speed_structural_crash_test_procedure_V2_4.pdf.
4. Ramaswamy, K., Virupaksha, V., Polan, J., and Tripathy, B.: Validation of Expanded Polypropylene (EPP) Foam Material Models for Low Speed Bumper and Pedestrian Protection Applications. SAE Technical Paper 2017-01-0363. 2017. Available online: https://www.researchgate.net/publication/315859680_Validation_of_Expanded_Polypropylene_EPP_Foam_Material_Models_for_Low_Speed_Bumper_and_Pedestrian_Protection_Applications.
5. Murata, S., Shioya, S., and Suffis, B.: Expanded Polypropylene (EPP) - A Global Solution for Pedestrian Safety Bumper Systems. SAE Technical Paper 2004-01-1703. 2004. Available online: https://saemobilus.sae.org/papers/expanded-polypropylene-epp-a-global-solution-pedestrian-safety-bumper-systems-2004-01-1703.
6. Dassault Systemes: User Assistance. 2023. Available online: https://help.3ds.com/2023x/english/dsdoc/FrontmatterMap/DSDocr-Abaqus.htm?contextscope=cloud&id=e6787ef8445e4e069ee7ce05f33de099.
7. ESI: Virtual performance solution. Solver Reference Manual. 2022. Available online: https://myesi.esi-group.com/webhelp/VPS_2022-0_UserDocumentation/VPS_2022-0_SolverReferenceManual/Default.htm#Standard_Content/Online/home_page.htm?TocPath=_____1.

TECHNICKÁ UNIVERZITA V KOŠICIACH
Strojnícka fakulta

Design of an efficient cooling system for a non-standard hydrogen storage tank

Filip Duda [1*], Natália Jasminská [2]

[1] Technical University of Košice, Faculty of Mechanical Engineering Department of Energy Engineering filip.duda@tuke.sk
[2] Technical University of Košice, Faculty of Mechanical Engineering Department of Energy Engineering natalia.jasminska@tuke.sk
* Correspondence: filip.duda@tuke.sk

Abstract: The article in deals with the structural design and strength calculation of a low-pressure metal hydride storage tank of a non-standardized shape for mobile applications, and at the same time it deals with the design of an effective cooling system of the designed storage tank, which needs to be cooled during the process of hydrogen absorption into the metal alloy structure.

Keywords: Metal hydride, hydrogen, pressure tank, internal intensifier

1. Introduction

Due to the growing demand for energy and the reduction of stocks of primary energy sources, the intensity of using alternative energy sources on a larger scale to reduce the carbon footprint is increasing. Suitable alternative fuel candidates include hydrogen. Hydrogen provides several advantages as an energy carrier [1], [2], [3]. It can be used in various applications, whether mobile, stationary or portable, and will play an important role, for example, in transport, where it can contribute to the diversification of fuel sources [5], [6]. The fundamental advantage of hydrogen is the wide range of substances from which it can be produced, and it has three times the calorific value of diesel or gasoline. The disadvantage is that, under normal conditions, hydrogen is in a gaseous state, and therefore compression or condensation. A big problem for the use of hydrogen as an alternative fuel is its storage. The most common methods of hydrogen storage are high-pressure, cryogenic and low-pressure based on the storage of hydrogen in the structure of a metal alloy. High-pressure storage of hydrogen gas is currently the most used method in mobile applications and is under considerably high pressure, ranging from 30 MPa, which is not the best alternative from the point of view of safety. Cryogenic storage of hydrogen or storage of hydrogen in the liquid state is an energy-intensive process where it is necessary to reduce the temperature of hydrogen below the boiling point of 20.39 K (-252.76 °C). Therefore, for common mobile applications such as cars, buses, tractors and the like, it makes no sense to use this type of hydrogen storage [6].

Low-pressure storage of hydrogen based on absorption into the metal alloy structure represents a suitable alternative for mobile applications, as it is possible to store hydrogen at ambient temperature and pressure from 1 MPa to 3 MPa. Compared to the high-pressure method of storage, the geometry of the containers is relatively flexible. Cylindrical or spherical tanks are most often designed and constructed. The biggest disadvantage of this storage is that an exothermic reaction occurs during the absorption of hydrogen, which increases the temperature of the metal hydride alloy, thereby reducing the amount of absorbed hydrogen. For example, with an alloy based on LaCeNi, up to 1 MJ is released for

1 m3 of stored hydrogen. Therefore, it is necessary to design an effective cooling system that effectively removes the generated heat and cools it at the same time.

The aim of this article is to design an efficient low-pressure hydrogen storage system based on the absorption of hydrogen into the metal alloy structure using a tank of a non-standardized shape, which will meet the operational parameters in terms of strength, and at the same time to design an effective cooling system of the tank during the process of hydrogen absorption into the metal alloy structure.

2. Structural design of non-standardized metal hydride tank and strength calculation

The tank consists of three main parts, namely the bottom of a non-standardized shape with holes and flanges with 1/4 NPT" thread, which serve to supply hydrogen to the tank, three cylindrical seamless pipes and a non-standardized bottom as a tank closing. The material from which the mentioned parts are made is stainless steel type 316L-1.4404. It is a type of steel that is compatible for hydrogen applications listed based on the STN EN 13322-2 standard, which describes the transport cylinders for gases, structural design and strength calculation. The tank is designed to be manufacturable, and therefore production and assembly drawings were made [8].

A heat transfer intensifier is inserted in the cylindrical seamless pipes, which serves to effectively remove the generated heat from the core of the tank to the inner wall, where this heat is effectively cooled by the cooling liquid that flows around the outer wall of the designed tank. The material from which heat transfer intensifiers are made is aluminium AlMg3 and it is mainly due to very good thermal conductivity ($= \mathbf{237} \; . ^{-} . ^{-}$).

Table 1 shows the design parameters of the designed metal hydride tank.

Table 1. Parameters of the designed metal hydride tank of non-standardized shape

Weight of empty metal hydride tank	**5.71 kg**
Weight of metal hydride	**8.5 kg**
Total weight of tank with metal hydride	**14.2 kg**
Metal hydride volume	**$3 \cdot 10^{-3}$ m^3**
Hydrogen weight	**0.116 kg**
Hydrogen volume	**1.38 m^3**
Generated heat	**13867.8 kJ**

The designed storage tank was subsequently subjected to operational requirements and the boundary conditions used for the simulation are [9], [10]:

1. Defining the material properties of the selected stainless steel 316L-1.4404 according to the manufacturer.

2. Load with a maximum operating pressure of 3 MPa, which acts on the inner walls of the designed non-standardized metal hydride tank. Subsequently, the internal pressure

changed to a value of 4.7 MPa, which represents the maximum test hydraulic pressure above atmospheric.

3. The load by the weight of the metal hydride, which is replaced by the hydrostatic pressure function at a density of 7000 kg·m-3 and acts on the inner walls of the designed tank.

4. Temperature condition 60°C, which represents the maximum temperature at which the metal hydride can absorb hydrogen into its structure.

5. Setting the Earth gravity on metal hydride tank.

6. Application of cylindrical bonds on cylindrical seamless tubes of the tank, which simulate storage of the tank in real operation.

Based on strength calculations and simulation, it was found that the maximum stress according to von Misses theory is not higher than the yield strength of the selected steel 316L-1.4404 (205 MPa) set by the manufacturer. At a maximum operating pressure of 3 MPa, the stress in the tank reached a value of 125 MPa, and at the same time, even at a maximum test hydraulic pressure above atmospheric of 4.7 MPa, the stress reached a value of 142 MPa. It is possible to state that the designed tank meets the strength operating parameters and is therefore suitable for use. The result of the strength simulation is shown in Figure 1.

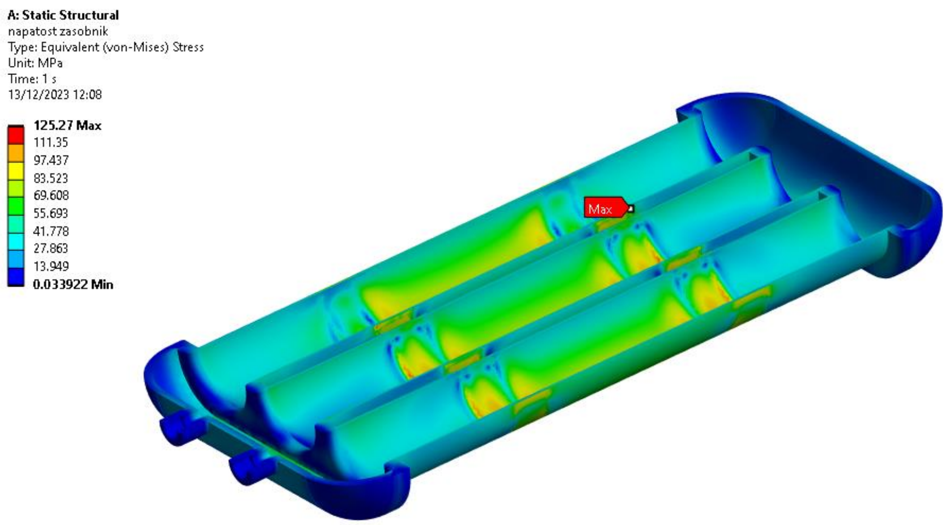

Figure 1 Generated stress fields according to von Misses theory on the designed metal hydride tank

Next part of the work is the design of effective cooling of the designed metal hydride tank of a non-standardized shape.

3. Design of efficient cooling of metal hydride tank

The cooling system consists of an active and passive cooling module. The active cooling module is represented by a cooling liquid that flows around the outer walls of the designed metal hydride tank. The passive cooling module represents the internal intensifiers of heat transfer, which are in the cylindrical seamless pipes of the tank. The intensifier serves to effectively remove the generated heat from the core of the storage tank to the inner wall, where this heat is subsequently effectively cooled by an active cooling module. Heat removal can be optimized, for example, by changing the geometric shape of the heat transfer intensifier.

The designed heat transfer intensifier consists of 3 primary and 3 secondary fins, which describe the shape of a circle whose diameter is 52 mm. The gap between the heat transfer intensifier and the inner wall of the seamless cylindrical pipe is 1 mm. The angle between individual fins is 120 °.

The design of the internal heat transfer intensifier is shown in Figure 2.

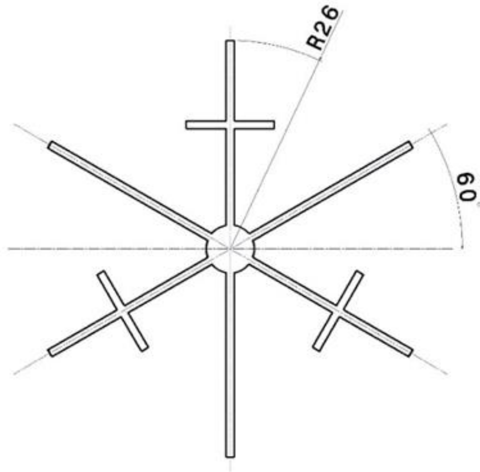

Figure 2. Design of the internal heat transfer intensifier for the designed tank

Next task is the examination of the generated temperature fields in the tank, where the tank will be examined without cooling at the beginning, and then in the second simulation, passive and active cooling will be applied to the tank.

4. Heat transfer simulations of the designed metal hydride tank

In the first simulation, the maximum temperature in the tank during the hydrogen tanking process into the metal alloy structure is investigated. The entire process of refuelling the tank takes approximately 20 minutes, which will also represent the simulation time. Before the simulation itself, it is necessary to generate a 3D simulation model of the designed tank consisting of non-standardized bottoms, cylindrical seamless pipes, metal hydride and internal heat transfer intensifiers, which represent the domains of the simulation model that need to be defined before the start of the simulation [7]. In the second simulation, it is also necessary to model the cooling liquid in which the tank is immersed. The simulation model can be seen in Figure 3.

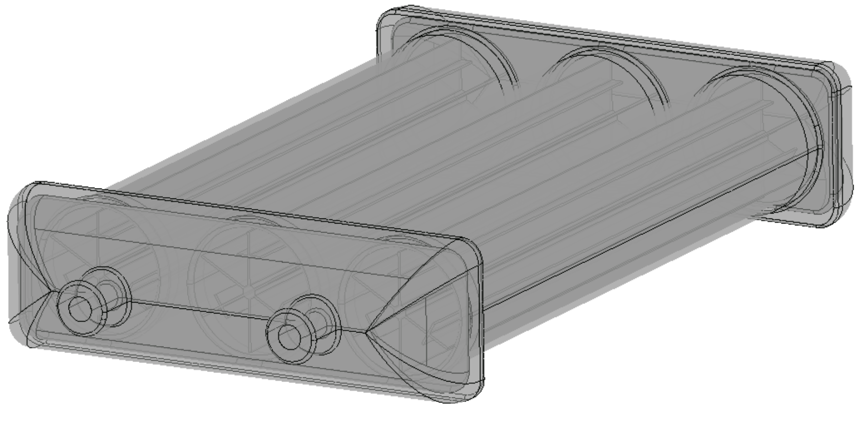

Figure 3. Simulation model of the designed tank

The next step is to generate the finite element mesh. The simulation model consists of 1,200,000 volumetric finite elements with quadratic approximation and 6,000,000 nodes. The initialization temperature of the simulation model is 20 °C. Another boundary condition of the simulation is the generated heat output of the metal hydride alloy, which is defined as W·m-3. After setting up the boundary conditions of the simulation model it is possible to run the simulation and get results.

The result of the first simulation showed that after 20 minutes the maximum temperatures in the tank reached 49.5°C. The simulation result is shown in Figure 4.

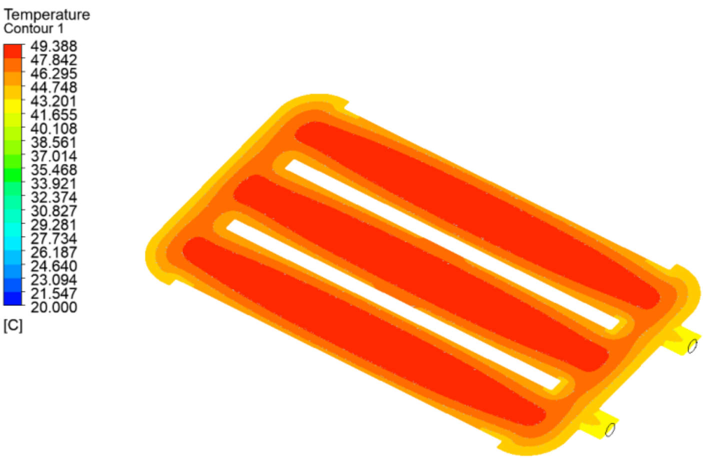

Figure 4. Maximum temperatures in the tank during hydrogen refuelling without the use of a cooling system.

For the kinetics of hydrogen absorption and at the same time for a larger amount of hydrogen to be absorbed, it is necessary to cool the designed tank. In the second simulation, temperature fields will be investigated using a cooling system.

In the second simulation, the simulation model consists of 1,500,000 volumetric finite elements with quadratic approximation and 6,700,000 nodes. It was necessary to model the cooling liquid itself to the simulation model. Figure 5 shows the result of the simulation using active and passive cooling.

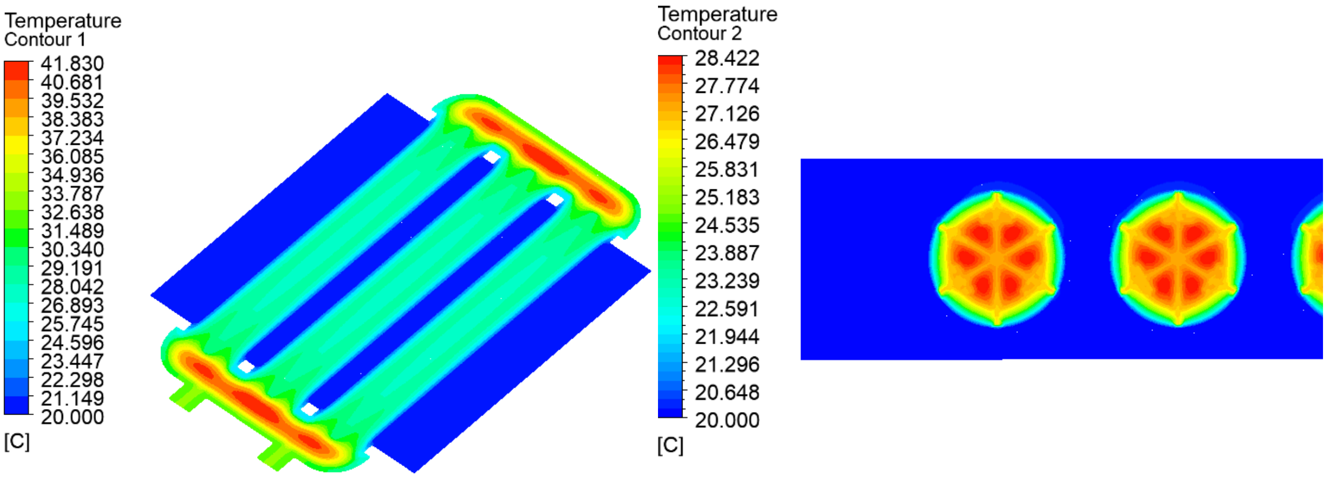

Figure 5 Simulation result using active and passive cooling module

The maximum temperature in the seamless pipes was reduced to a temperature of 28.4 °C, which significantly increased the kinetics of hydrogen absorption.

5. Conclusion

The task of this article was to design an effective low-pressure hydrogen storage system based on the absorption of hydrogen into the metal alloy structure using a non-standardized tank shape. The designed tank was subsequently tested for strength, which found that it meets the operating parameters and can be used in practice.

Another part of the contribution was the investigation of the maximum temperatures that arose because of the absorption of hydrogen into the structure of the metal alloy, which released heat. In the first part, the tank was investigated without the use of active and passive cooling modules, which revealed that the maximum temperatures in the tank reached values of approximately 50 °C. Since the temperature is so high, the kinetics of hydrogen absorption is significantly lower, and therefore it is necessary to cool the tank. In the next part, an internal heat transfer intensifier was designed, which serves as a passive cooling module. The active cooling module is the cooling liquid in which the tank is immersed. Based on the results, it was found that the maximum temperatures occurred at the bottom of the tank, where the maximum temperature reached a value of approximately 41 °C. In the cylindrical seamless pipes, where the internal heat transfer intensifiers were located, the maximum temperatures were approximately 28 °C, which significantly increased the kinetics of hydrogen absorption. The maximum temperature in seamless pipes can be further reduced, for example, by suitable optimization of the geometric shape of the internal intensifier, which will be another research task.

Acknowledgments: This paper was written with financial support from the VEGA granting agency within the projects no. 1/0224/23 and no. 1/0532/22, from the KEGA granting agency within the project no. 012TUKE-4/2022 and with financial support from the APVV granting agency within the projects no. APVV-15-0202, no. APVV-20-0205 and no. APVV-21-0274.

References

1. Afzal, M. Mane, R. Sharma, P.: Heat transfer techniques in metal hydride hydrogen storage: A review. International Journal of Hydrogen Energy 42, 2017.
2. Chibani, A. Bougriou, Ch. Merouani, S.: Simulation of hydrogen absorption/desorption on metal hydride LaNi5-H2: Mass and heat transfer. Applied Thermal Engineering 142, 2018.
3. Valizadeh, M. Delavar, A, M. Farhadi, M.: Numerical simulation of heat and mass transfer during hydrogen desorption in metal hydride storage tank by Lattice Boltzmann method. International Journal of Hydrogen Energy 41, 2016.
4. Jurczyk, Mieczyslaw.: Handbook of Nanomaterials for Hydrogen Storage. Singapore: Pan Stanford Publishing Pte. Ltd, 2018. ISBN 978-1-315-36444-5.
5. Lipman, E. T., Weber, Z, A. Fuel Cells and Hydrogen Production. New York: Springer Science+Business Media, 2018. ISBN 978-1-4939-7789-5.
6. Stolten, D. (2010). Hydrogen and Fuel Cells, Weinheim: Wiley, 2010, 908 p. ISBN 978-3-527-32711-9.
7. Brestovič, T., Jasminská, N. Numerické metódy a modelovanie v energetike, Košice, SjF TU v Košiciach, 2015. ISBN 978-80-553-0223-2.
8. STN EN 13322-2, Prepravné fľaše na plyny. Navrhovanie a výroba znovuplniteľných oceľových fliaš na plyny. Časť 2: Nehrdzavejúce ocele, 2003
9. Bocko, Jozef; Lengvarský, Pavol; Huňady, Róbert; Delyová, Ingrid. Simulácia v programe ANSYS. Stojnícka fakulta, Technická Univerzita v Košiciach, 2020.
10. Ravinger, Ján. Numerical methods in theory of structures, Slovenská technická univerzita v Bratislave 2014.

TECHNICKÁ UNIVERZITA V KOŠICIACH
Strojnícka fakulta

Innovating technological processes through simulation

Richard Duda [1,*], Matúš Matiscsák [2], Michal Baluch [3] and Peter Trebuňa [4]

[1] Department of Industrial and Digital Engineering, Technical University of Košice, Park Komenského 9, 04001 Košice; richard.duda@student.tuke.sk
[2] Department of Industrial and Digital Engineering, Technical University of Košice, Park Komenského 9, 04001 Košice; matus.matiscsak@tuke.sk
[3] Department of Technology and Quality of Animal Products, Slovak University of Agriculture in Nitra, Trieda Andreja Hlinku 2, 949 01 Nitra: baluch@taurisgroup.sk
[4] Department of Industrial and Digital Engineering, Technical University of Košice, Park Komenského 9, 04001 Košice; peter.trebuna@tuke.sk
* Correspondence: richard.duda@student.tuke.sk; Tel.: +421 55 602 3243

Abstract: The goal of the scientific article is the synergistic combination of practical operations in the field of production with the use of simulation techniques, with the primary aim of identifying problematic aspects of the technological production process and subsequently formulating the potential for improvement in this process. To improve the accuracy of the analysis, we implemented a simulation model using the TX Plant Simulation software. This model includes us in detail below and identifies bottlenecks and deficiencies in the overall production chain. After implementing the proposed changes in the simulation environment, we prepared a detailed report that demonstrated an increase in the efficiency of the overall production process by 33.06%.

Keywords: Technological process, Digital technologies, Simulation

1. Introduction

The need for efficiency in the manufacturing industry is becoming more important as the cost of materials, transportation and labor increases every year [1]. Successful companies must ensure that costs associated with time, equipment and other investments are accounted for and optimized. Manufacturing simulations inherently offer a cheaper and more efficient way to test anything from simple improvements to large-scale improvements, always with the goal of achieving production goals at the lowest possible cost [2,3].

For this reason, simulation in production is extremely important and preferred nowadays. The results of the simulations allow us to identify potential improvements without stopping production, which could lead to significant losses [4]. Simulation also gives us the opportunity to introduce and test new elements in production before they are physically installed, during which operations would need to be either curtailed or completely stopped. In addition, simulation can facilitate large-scale research without requiring significant financial investment.

2. Research Methodology

In the framework of this scientific paper, we have carried out an analysis of the gas production process based on the data obtained by the companie concerned. We then used this data to run a simulation created using TX Plant Simulation software.

After running the simulation, the software provided us with a statistical report, which we discussed and subsequently reviewed with engineers from the company. Based on this discussion and detailed analysis of the simulation, graphs, and results, we identified a bottleneck in the manufacturing process. Having identified this bottleneck, we proposed the most effective solution, which we simulated again using TX Plant Simulation software.

We again discussed the results with engineering from the company and based on the individual graphs and results we arrived at the final solution. With the industrial engineering tools, we were able to minimize the shutdown of the entire plant and minimize the financial loss that such would cause.

3. Concise technological overview of the production process

In this part of the article, we describe a simplified technological procedure for processing gas condensate. With the help of which we will then create a simulation necessary for the subsequent analysis of the entire production process. The technological procedure consists of 5 points.

1. Condensate separation: Unstable gas condensate is separated from tanks E801-1 to E801-8 and fed to pipe space T-102, where it is heated to 38°C.
2. Condensate cleaning: The condensate passes through the T-101-1 exchanger and TDG-101 thermodehydrator, where water, dissolved salts, and mechanical impurities are removed. The collected water is discharged into the sewer, and the rest of the condensate passes through the F-101 filter to remove mechanical impurities.
3. Condensate heating and further cleaning process: Condensate cleaning continues in distillation columns and evaporators, where the products are separated, and the condensate is distributed to different parts of the installation depending on the temperature and other parameters.
4. Main components involved in the process: Additionally, the main components include distillation columns, radiant convection ovens, viscin filters, tubular heat exchangers, and others. Each of these components has a specific role in the process of cleaning and separating condensate.
5. Principle of operation of the individual components: Distillation columns enrich the condensate with various components with a boiling point, radiant convection ovens increase the temperature of the flue gas to radiating heat rays, viscin filters remove mechanical impurities, and tubular heat exchangers enable heat exchange between two liquid streams.

3.1. Simulation and evaluation of the current production process

In this part of the article, based on the technological procedure from chapter 3, a simulation was made in the TX Plant Simulation program. In Figure 1., you can see the 2D layout of the production process.

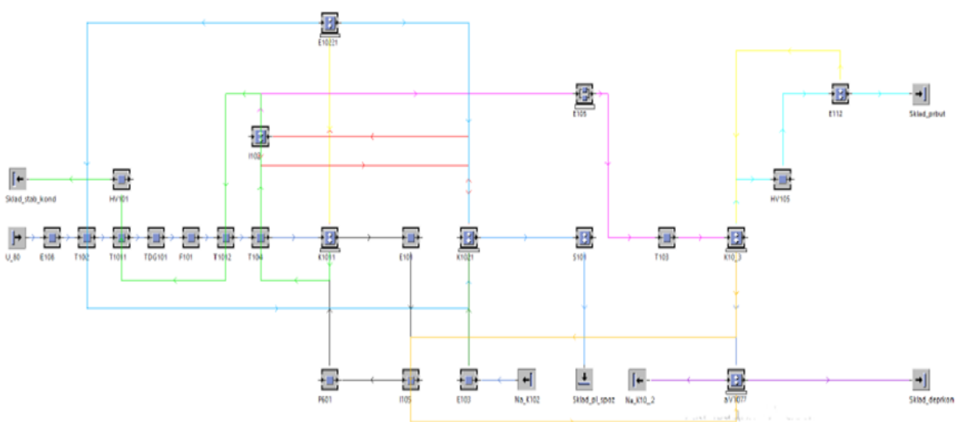

Figure 1. 2D layout of the current production process

In the process of working in the enterprise, communicating with engineers and operators, as well as studying technical documentation and simulating this technological process, it was found that the operation of the furnace in the form it is now slows down the production process and consumes more gas for its work than it could in current conditions. This fact was also confirmed by the documentation and the opinion of the engineering staff. During a more detailed analysis of the operation of the furnace itself, it was found that the burners that are currently installed there, due to moral and physical obsolescence, reduce the economic and production efficiency of the furnaces in the entire process.

4. Proposal and implementation of a solution to the chosen issue

In connection with the above, it is considered necessary to study and offer the possibility of replacing an outdated burner, since the furnace plays one of the key roles in the chosen technological procedure, and therefore the amount of the output product and the price of its costs will largely depend on the efficiency of the burner's work Currently, a GEVK-500 type burner (intended for hydrocarbon heating) with the following technical characteristics is installed:

- Condensate heating temperature from 180 °C to 270 °C.
- Furnace transition from 500 °C to 770 °C.
- Working pressure of raw materials in the furnace from 15 kgf / cm2 to 25 kgf / cm2.
- Heat output of the furnace 11600 kW.

Figure 2. Burner GEVK-500

The proposal to improve production is to replace the burner with a Weishaupt WM-G30/4 A, ZM burner.

Brief description of its operation: air dampers regulate the volume of air required for combustion. The flaps are controlled by the combustion manager via a servomotor. When the burner stops, the manager automatically closes the dampers. This reduces unnecessary cooling of the heat source. The fan wheel draws air from the air intake cover into the combustion head. Depending on the setting of the flame tube, the air gap between the flame tube and the holding plate is changed, thereby adjusting the mixing pressure and the volume of combustion air. A brief description of the technical characteristics of the burner:

- Mains voltage - mains frequency 230 V / 50 Hz.
- Mains voltage / mains frequency 380 ... 415 V / 50 Hz (burner motor).
- Permitted fuels: Natural gas, LPG.
- Condensate heating temperature from 250 °C to 320 °C.
- Furnace transition from 600 °C to 850 °C.
- Working pressure of raw materials in the furnace from 15 kgf / cm2 to 35 kgf / cm2.

- Heat output of the furnace 12500 kW.

Figure 3. Burner Weishaupt WM-G30

In the simulation, the characteristics of the burner change option were adjusted, which in the normal case reduced the time that the raw materials spend in the furnace. These changes can also be observed in the final statistics after the simulation.

5. Result

Initial values of the current production process after 12 hours of simulation.

Simulation time:12:00:00.0000

Object	Name	Mean Life Time	Throughput	TPH	Production	Transport	Storage	Value added	Portion
WH stable condensate	stable gas condensate	20.0000	186	16	100.00%	0.00%	0.00%	50.00%	
WH gas to consumers	gas stabilization	15.1681	238	20	100.00%	0.00%	0.00%	65.93%	
WH propane butane	propane butane	12.5000	1904	159	100.00%	0.00%	0.00%	80.00%	
WH deetane propane butane con.	deet prop but cond	1:29.4538	476	40	100.00%	0.00%	0.00%	11.18%	

Figure 4. The result of the simulation, the current state

Final values after applying the proposed simulation changes after 12 hours of simulation.

Simulation time:12:00:00.0000

Object	Name	Mean Life Time	Throughput	TPH	Production	Transport	Storage	Value added	Portion
WH stable condensate	stable gas condensate	20.0000	246	20	100.00%	0.00%	0.00%	50.00%	
WH gas to consumers	gas stabilization	15.1258	318	26	100.00%	0.00%	0.00%	66.11%	
WH propane butane	propane butane	12.5000	2536	211	100.00%	0.00%	0.00%	80.00%	
WH deetane propane butane con.	deet prop but cond	1:07.3502	634	53	100.00%	0.00%	0.00%	14.85%	

Figure 5. Simulation results optimized state

For greater clarity, a table has been created to compare the current production with the upgraded production (see Table 1.). The table also shows the improvement compared to the current production in percentage.

Table 1. *Table showing performance changes before and after improvement*

Object	Throughput (per hour)		Improvement	Throughput (shift)		Improvement
	Current	Innovated	%	Current	Innovated	%
Stable gas condensate	16	20	25,00	186	246	32,26

Gas stabiliza-tion	20	26	30,00	238	318	33,61
Propane-bu-tane	159	211	32,70	1904	2536	33,19
Deetane-pro-pane-butane condensate	40	53	32,50	476	634	33,19
Result	**235**	**310**	**30,05**	**2804**	**3734**	**33,06**

After changing the burner, we can observe an increase in the production process. From the table we can see that production in the overall production process increased by 30.05% per hour and 33.06% per shift

6. Conclusions

To optimize the manufacturing process, it is essential to engage in a comprehensive examination of all relevant influencing variables [5]. A careful analysis of the genesis of bottlenecks, coupled with the formulation of strategies aimed at improving them, is essential, while at the same time assessing the likely consequences on production dynamics in a preventive manner. Attention to the markers is of paramount importance to avoid operational adverse effects and to ensure that optimization results are achieved without problems [6,7].

Based on the detailed results obtained through simulation, the overall production process has increased by 30.05% per hour. This increase is even more pronounced during the working shift, where it reaches a value of 33.06%, representing an increase in the overall production process.

Acknowledgments: This article was created by the implementation of the grant project APVV-17-0258 Digital engineering elements application in innovation and optimization of production flows, APVV-19-0418 Intelligent solutions to enhance business innovation capability in the process of transforming them into smart businesses, KEGA 020TUKE-4/2023 Systematic development of the competence profile of students of industrial and digital engineering in the process of higher education and VEGA 1/0508/22 Innovative and digital technologies in manufacturing and logistics processes and system.

Conflicts of Interest: The authors declare no conflict of interest.

References

1. KLIMENT, M.: Production efficiency evaluation and products' quality improvement using simulation. International Journal of Simulation Modelling, Vol. 19, No. 3, pp. 470-481, 2020. https://doi.org/10.2507/IJSIMM19-3-528...
2. KOVALČÍK, J., BALOG M., "AUTOMATIC IDENTIFICATION SYSTEMS FOR MANAGEMENT - MATERIAL FLOW CONTROL AND STOCK STATUS." Acta logistica 8, no. 1 (March 31, 2021): 55–64. DOI:10.22306/al.v8i1.202.
3. DURICA, L.; GREGOR, M.; VAVRIK, V.; MARSCHALL, M.; GRZNAR, P.; MOZOL, S.: A Route Planner Using a Delegate Multi-Agent System for a Modular Manufacturing Line: Proof of Concept. Appl. Sci.-Basel, 9 (21), 4515, (2019). DOI: 10.3390/app9214515.
4. MOZOL Š., GRZNÁR P., KRAJČOVIČ M., DESIGN OF SYSTEM FOR MORE EFFECTIVE DATA ACTUALISATION IN SIMULATION, Acta Simulatio, Vol. 6, No. 4, pages 19-22, (2020) DOI: 10.22306/asim.v6i4.58
5. CHROMJAKOVA, F., BOBAK, R., HRUSECKA, D.: Production process stability – core assumption of Industry 4.0 concept, 5 th International Conference on Manufacturing, Optimization, Industrial and Material Engineering, 2017, pp. 143-154Author 1, A.B.; Author 2, C.D.; Author 3, E.F. Title of Presentation. In Title of the Collected Work (if available), Proceedings of the Name of the Conference, Location of Conference, Country, Date of Conference; Editor 1, Editor 2, Eds. (if available); Publisher: City, Country, Year (if available); Abstract Number (optional), Pagination (optional).
6. Lai X, Shui H, Ding D, Ni J., Data-driven dynamic bottleneck detection in complex manufacturing systems. J Manuf Syst :662–75, (2021). DOI: 10.1016/j.jmsy.2021.07.016.
7. Lin L.., A systematic-theoretic analysis of data-driven throughput bottleneck detection of production systems. J Manuf Syst ; 47:43–52, (2018). DOI: 10.1016/j.jmsy.2018.03.001.

TECHNICKÁ UNIVERZITA V KOŠICIACH
Strojnícka fakulta

Implementation of overhead crane model, controlled by using an IoT network

Pavol Dzurňák[1]*, Martin Mantič[2]

[1] Faculty of Mechanical Engineering, Technical university of Košice, Slovakia; dzurnak@tuke.sk
[2] Faculty of Mechanical Engineering, Technical university of Košice, Slovakia; martin.mantic@tuke.sk
* Correspondence: dzurnak@tuke.sk; Tel.: +421 55 602 7654

Abstract: This article describes implementation of overhead crane model, where will be an IoT network used for its control. Following that, IoT sensors that collect all necessary on real time data for crane control are discussed in detail. The purpose of deploying crane control is briefly described with the aim of harmonizing various tasks in overhead crane control as well as harmonizing the selection of suitable sensors for effective control of the crane model. The overhead crane model is used for a fast and cost-effective testing management procedures, which can later be applied to a real overhead crane in productive operation.

Keywords: IoT network; sensors; overhead crane

1. Introduction

Overhead cranes are widely used in manufacturing, construction, shipyards, warehouses, construction facilities and other industrial settings where heavy and bulky materials need to be lifted and moved with precision. They offer efficiency, versatility, and the ability to cover a large working area. The lifting capacity, span, and features of an overhead crane can vary based on the specific application and requirements of the user.

To be able to effectively create new processes for managing real cranes in productive operation, to test new technological elements designed for data collection and processing, it is suitable to have a crane model, within of which are the implementation, testing processes and technologies easier, faster and therefore more effective. For this reason, a new crane model which is using new IoT network elements was developed.

During the process of overhead crane control implementation, it is necessary to coordinate several tasks that need to be performed at each moment of the overhead crane control. There were tree tasks considered:

- three-dimensional control (anti-sway process)[1][2]
- elimination of crane skew
- container logistic.

From mechanical point of view, it is very important to prepare suitable construction design, especially some mechanical parts where IoT sensors will be installed. For proper overhead crane container future functionality, the well-designed spreader is crucial. That combine different functionalities as an effective container catching process and reliable rope system usable for antisway control, data collecting from camera and catching sensors. All of them will support to implement the antisway system.[3] In the context of control systems are used microcontroller ESP32 that are capable of taking actions based on their measured data using IoT sensors. One of the basic conditions for the control design is real-time data processing. This requirement is crucial for the correct design of IoT network components. Other crane control systems are also used in the world, e.g. based on fuzzy logic [4][5], but these solutions are preliminary aimed at finding methods for determining the skewing forces on bridge cranes and trolleys.

2. The implementation of overhead crane model

2.1 The definition of crane activity goals

Defining the activity goals of the model was the first step in the creation of the test crane module, during which the requirements for future tests were analyzed, with the main requirement being the possibility to test processes/methods for determining the skewing forces. At the same time, however, the operator had to perform some specific activity so that the conditions of the activity were as close as possible to the conditions in real operation. For this reason, a crane model, whose main activity is container logistics, was chosen. This task results in the requirement for the skewing forces determination as well as the minimization of load swinging, respecting forbidden zones, identification of containers, their location as well as the precise guidance of the crane during their movement. Because of requirements defined in this way, it will be possible to effectively test several management methods while respecting the achievement of diverse goals.

2.2. The crane construction

For the construction of the crane, the MB modular system from the company Item was chosen, while the basic structural element was an aluminum profile with dimensions of 30x30 mm. The given profile guaranties sufficient stiffness and resistance of the construction, so that it is possible to carry out tests with the greatest possible degree of accuracy.

2.3. Design *definition*

The overall design of the crane model solution was designed and implemented so that it was possible to perform tests as efficiently as possible, under the conditions of the most accurate simulation of the productive environment and the minimization of ideal laboratory conditions. At the same time, the model fulfills the condition of solving logistic tasks, when the handling of containers is controlled by valid logistics processes. The model has electrical equipment, the basis of which is a DC 24 V power source. The crane bridge girder consists of aluminum profiles with dimensions of 15 x 15 mm, while the rest of the construction is made on a 3D printer from PLA filament. As per request, model containers are used in the modeling scale G, where each of the containers has an adjusted interior so that it can be held by an electromagnet, and at the same time, the weight of the container is adjusted. In this way, it is possible to simulate various operational conditions when handling the load. The Figure 1 shows the whole concept of overhead crane with railroad and containers.

Figure 1. The railroad model within overhead crane

3. IoT network implementation

IoT stands for "Internet of Things," which refers to the network of physical objects — "things" — that are embedded with sensors, software, and other technologies for the purpose of connecting and exchanging data with other devices and systems over the Internet.

Due to IoT network functions are establishing connections among devices, sensors, and systems to the exchange of data and perform data processing. IoT can generate some new information, which can be useful from different point of view. The main components of IoT network are:

IoT sensors play a crucial role in connecting the physical world with the digital world, enabling a vast array of smart applications. These sensors are the key components in IoT devices, responsible for collecting data from their environment and sending it for processing, analysis, or action.

IoT connectivity refers to the various methods and technologies used to connect IoT devices with each other and to the internet or other networks. This connectivity is critical for enabling these devices to collect, send, and process data, making IoT systems function effectively.

IoT processing refers to the methods and technologies used to handle and process the data collected by IoT devices. This processing can happen at different levels within an IoT system, each with its own characteristics and use cases. Mostly used processing are: Edge Computing, Cloud processing, Fog computing and Hybrid models which combine edge, fog and cloud computing.

3.1 Microcontroller ESP32 as an agent role

At least two basic requests were made to the system agent. The first was the ability to read measured data in real time, the second was the ability to process the data through defined processes, and the third was to have suitable communication interfaces so that the result could be sent to another agent or receive a result from another agent in real time. From the point of view of affordability and efficient creation of the necessary software, microcontrollers of the Arduino Nano 33 vs. ESP32 can be considered. A comparison of both types of micro-controllers is shown in Table 1.

Table 1. Features and parameters of Arduino Nano 33 vs. ESP32

Feature	Arduino Nano 33	ESP32
Processor	ARM Cortex-M4F	Dual-core Tensilica Xtensa LX6
Clock Speed	64 MHz	Up to 240 MHz
Flash Memory	256 KB	4 MB (external)
SRAM	64 KB	520 KB (on-chip), 8 MB (external)
Connectivity	BLE	Wi-Fi (802.11 b/g/n), Bluetooth v4.2, BLE
Operating Voltage	3.3V	3.3V
Digital I/O Pins	14	34 (GPIOs)
PWM Pins	11	16
Analog Input Pins	8	18
Analog Output Pins	N/A	2 (DACs)
Dimensions	45 mm x 18 mm	Typically 51 mm x 21 mm
Special Sensors	Multiple (BLE Sense variant)	Hall sensor, temperature sensor, capacitive touch sensors
Security	None	Hardware encryption, secure boot, flash encryption

Development Environment	Arduino IDE	Arduino IDE, ESP-IDF, PlatformIO
Low Power Modes	Yes	Yes, with ultra-low power coprocessor
Special Interfaces	SPI, I2C, UART, ADC	SPI, I2C, I2S, UART, ADC, DAC, touch sensors

The comparison clearly shows that it seems optimal to use the ESP32 microcontroller, to which individual sensors will be gradually connected, and at the same time the electric motors will be controlled by means of ESP32, when the electrical power required for the motor will be solved by means of so-called H-bridges. The L298N type was used in this solution. The L298N is a dual full-bridge driver, designed to drive inductive loads such as DC and stepping motors. Driver contains two H-Bridge circuits which can be used to control two DC motors independently in both clockwise and counter-clockwise directions. Individual modules will use WiFi for mutual communication, later communication via 5G and LoraWAN network will also be tested.

3.2 Sensors

The choice of sensors had to first of all fulfill the condition of compatibility with ESP32, both from the HW and SW perspectives, i.e. the availability of necessary libraries and drivers, that made it possible to write the necessary functional SW, were requested. The current range of used sensors includes:

Accelerometer MPU6050, which is a widely used motion tracking device. It combines a 3-axis gyroscope and a 3-axis accelerometer on the same silicon die, along with an onboard Digital Motion Processor™ (DMP™), which can process complex 9-axis MotionFusion algorithms. 3-Axis Gyroscope can measure rotational velocity along three perpendicular axes (X, Y, and Z). This is useful for determining container orientation. 3-Axis Accelerometer measures acceleration along three axes, It's useful for detecting container motion, tilt, and orientation in space. Digital Motion Processor (DMP) can perform complex calculations with the sensor data, enabling the MPU-6050 to offload computation from the main processor. The MPU-6050 communicates to ESP32 via the I2C protocol.

RFID RC522 is used RFID (Radio-Frequency Identification) module that operates at 13.56 MHz frequency. It's designed for communication with RFID cards, tags, and other devices that use a similar frequency for wireless data transmission. We plan to use it for the recognition and identification of containers, so the system will know which containers are managed due to model. The module communicates with ESP32 microcontrollers using the Serial Peripheral Interface (SPI).

ESP32-CAM is a small camera module based on the ESP32 microcontroller, combining WiFi and Bluetooth connectivity with image processing capabilities. It's a versatile and cost-effective solution for various applications involving wireless image or video transfer. It typically comes with an OV2640 camera module, which is a 2MP camera capable of capturing images and video. Based on captured image will be recognized required object. So can be process of contain-er capturing very fast and fully automated. On the same principles can be container placed on required place.

Tensiometer is a passive electrotechnical component, used as a sensor to indirectly measure mechanical stress on the surface of parts by measuring of resistance, which depends on material deformation. The sensor is attached to the object to be measured so that the inner side of the metal foil bends with the object.

3.3 Implementation of IoT sensors

There were RFID, ESP32-CAM, accelerometer and tactil pressure sensors implemented on existing model. The location of all sensors is shown in Figure 2.

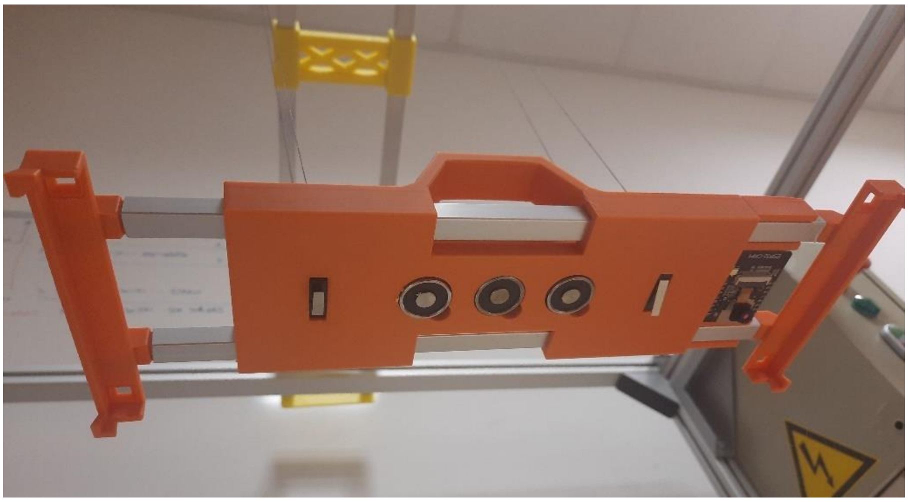

Figure 2. The sensor location on the spreader

There are 3 magnets in the middle of the spreader, which should catch the container. There is a module ESP32-cam located on the right side of spreader and it is capturing the image. The image is proccesing using methods for recogniton of container edges. The image capturing process continues until a correct capture is successfully detected. Based on this information the final result is generated for main controller ESP32 that executes signal for spread engine to move in x, y or z axis [6]. There is an accelerometer MPU6050 located on the top of spreader as it is shown in Figure 3.

Figure 3. The accelerometer MPU6050 located on right side of spreader

Based on all these information can main controller control all three engines to lift container to desired place. All sensors are connected to the local controller on the spread, which is able to communicate with main controller over wifi, 5G, LoRaWAN or another protocols used in the IoT networks. RFID sensor, type RC522 is located on the frame of crane. Location was designed based on the measurement results of RFID tag reading. Reliable results of reading where achieved when distance between sensor and RFID tag was less than 30 mm. Implementation of RFID sensor is shown in Figure 4.

Figure 4. The RFID sensor reading of container tag

4. Conclusion

A rail-road terminal within an overhead crane model requires solving a complex of tasks. This will make it possible to verify different control processes, efficiency, and functionality of various types of IoT sensors implementation, respectively to test different overhead crane model controls. The tests implementation in the environment of the crane model is significantly faster and cheaper than similar tests provided on a product overhead crane.

Acknowledgments: This article was elaborated in the framework of the Grant Projects KEGA 029TUKE-4/2021 and VEGA 1/0528/20.

References

1. N.Q.Hoang,S.-G.Lee,H.Kim,S.-C.Moon,Trajectory planning for overhead crane by trolley acceleration shaping, J.Mech. Sci. Technol. 28 (2014) 2879–2888, http://dx.doi.org/10.1007/s12206-014-0641-1
2. Li, G., Ma, X., Li, Z. et al. Optimal trajectory planning strategy for underactuated overhead crane with pendulum-sloshing dynamics and full-state constraints. Nonlinear Dyn 109, 815–835 (2022). https://doi.org/10.1007/s11071-022-07480-w
3. Tuan, Le & Cuong, Hoang & Lee, Soon-Geul & Cong, Nho & Moon, Kee. (2014). Nonlinear feedback control of container crane mounted on elastic foundation with the flexibility of suspended cable. Journal of Vibration and Control. 22. 10.1177/1077546314558499
4. YU, W.; MORENO-ARMENDARIZ, M. A.; RODRIGUEZ, F. O. Stable adaptive compensation with fuzzy CMAC for an overhead crane . Information Sciences. 2009, ISSN doi:10.1016/j.ins.2009.06.032.
5. LIU, Diantong, et al. Adaptive sliding mode fuzzy control for a two-dimensional overhead crane. Mechatronics. 2005, Nr. 15, pp. 505-522
6. Shengzeng Zhang, Xiongxiong He, Haiyue Zhu, Xiaocong Li, Xinggao Liu,PID-like coupling control of underactuated overhead cranes with input constraints, Mechanical Systems and Signal Processing,Volume 178,2022,109274,ISSN 0888-3270,https://doi.org/10.1016/j.ymssp.2022.109274

Unveiling the Future: Thermal Imaging Drones in Scientific Applications

Valéria Eiben [1] *, Ružena Králiková [2]

[1] Kokopelli, s.r.o.; lilly.eiben@gmail.com
[2] Technical University of Kosice; ruzena.kralikova@tuke.sk
* Correspondence: Ing. Valeria Eiben, Kokopelli, s.r.o, Lomonosovova 36, 040 01 Kosice, lilly.eiben@gmail.com; Tel.: +421 905 357 097

Abstract: Thermal imaging technology, coupled with the versatility of drones, has revolutionized scientific research, industrial applications, and various fields requiring advanced data acquisition. The article explores the transformative impact of thermal imaging drones, examining their technological features, applications, and the novel insights they provide across different disciplines. This article delves into the convergence of drone technology and thermal imaging, exploring the synergies that have given rise to an array of innovative applications.

Keywords: thermal imaging; drones; modelling; simulation; infrared radiation

1. Introduction

Thermal imaging, once relegated to the realm of science fiction and military applications, has evolved into a versatile and widely used technology with applications ranging from industrial processes and medical diagnostics to search and rescue operations. Drones, or Unmanned Aerial Vehicles (UAVs), equipped with thermal imaging sensors have become a game-changer in scientific research. Drones have become more comma and it is important to understand how they work, especially since they entered the civilian sphere. Practice shows how drones are increasingly being used in many applications [8].

2. Thermal Imaging

Nowadays, many other sectors are using the systems of the thermal imaging, as they offer multiple benefits [4]:

- Quality control of industrial processes;
- Error and failures detection in critical and strategic installations and facilities;
- Mining, petrochemical, and construction industry;
- Civil, mechanical, electro technical engineering;
- Environmental monitoring;
- Industrial automation systems;
- Protection and rescue operations;
- Automobile industry – to prevent traffic accident;
- Medicine - to prevent the spread of disease, to diagnostic human health etc.

Temperature as a very frequently measured physical parameter provides information about the objects' internal energy and its regulation or control is important in many industrial processes and in the various fields of living [7]. Measurement of temperature can be provided by standard contact temperature sensors or non-contact.

Infrared temperature sensors, which are currently at a very high technical level, provide a wide range of applications for non-contact temperature measurement. These sensors use a unique measuring principle, consisting in measuring the energy reflected by each body in a space with a temperature higher than absolute zero. Technological advances in thermal imaging systems are increasingly making this technology available to the general public in its day-to-day use.

Technology operates by capturing the emissions of an electromagnetic spectrum - infrared emitted as heat by a body or object (living or inert), making it possible to observe these elements and/or create images from them. The principle of an infrared IR thermal imaging by the thermal camera receiving radiation is illustrated in Figure 1.

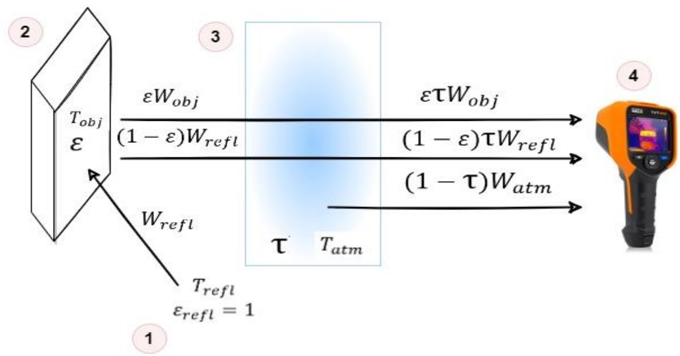

Figure 1. The principle of scanning an object.

Legend to Figure 1:

1 – environment (heat source e.g. Sun, lamp etc.),

2 – object;

3 – atmosphere;

4 – camera.

For different types of measurements is important to observe the conditions, depending on the measurement location. If the measurement takes place outdoors, atmospheric conditions are also important. The object temperature T_{obj} is calculated according to equation (1). Other parameters must be set up in the camera [3].

$$T_{obj} = \sqrt[4]{\frac{-\ (1-\ )\cdot\tau\cdot\sigma\cdot\ ^{4}\quad -(1-\ )\cdot\ \cdot\ ^{4}}{\cdot\ \cdot}} \qquad (1)$$

Where:

σ - Stefan Boltz. Constant, σ = 5,67.10^{-8} W.m^{-2}K^{-4}

$\mathcal{E}$ - Object emissivity

τ - Atmospheric transmission

ω - Relative humidity

T_{atm}- Atmospheric temperature

D_{obj}- Distance of the camera from the measured object

T_{refl}- Effective ambient or reflected temperature.

3. Technological Features

3.1. Hight-Resolution Thermal Sensors

Thermal imaging drones are equipped with high-resolution sensors capable of capturing detailed thermal data, allowing for precise temperature measurements and thermal mapping.

3.2. Real-time Data Transmission

Advanced thermal imaging drones are designed with real-time data transmission capabilities, enabling researchers to monitor and analyze thermal changes on-site [2].

3.3. Integrated GPS and Navigation Systems

Integrated GPS and navigation systems enhance the precision of thermal imaging drones, allowing for accurate spatial mapping and the creation of thermal models.

3.4. Autonomous Flight Capabilities

Many thermal imaging drones are equipped with autonomous flight capabilities, enabling pre-programmed flight paths and facilitating efficient data collection over large areas [2].

4. Applications

4.1. Environmental Monitoring

Thermal imaging drones contribute to environmental studies by providing real-time thermal data for assessing ecological health, monitoring biodiversity, and identifying changes in vegetation patterns.

4.2. Agricultural Practices

In agriculture, these drones aid in crop management, enabling farmers to assess crop health, identify irrigation needs, and detect pest infestations based on temperature differentials.

4.3. Search and Rescue Operations

Thermal imaging drones are invaluable in search and rescue missions, helping locate missing persons, identify survivors in disaster-stricken areas, and conduct nighttime operations [1].

4.4. Industrial Inspections

For industrial applications, thermal imaging drones facilitate inspections of structures, electrical systems, and pipelines, identifying potential faults, leaks, or structural issues.

4.5. Wildlife Conservation

In wildlife conservation efforts, thermal imaging drones assist in monitoring animal populations, tracking migration patterns, and combating poaching activities [1].

5. Advancements in Technology

Manufacturers are continually improving the resolution, sensitivity, and overall performance of both thermal cameras and drones. Most applications take advantage of the following trends [5]:

1. Integration with Artificial Intelligence and Machine Learning - There are developments in the integration of Artificial Intelligence (AI) and Machine Learning (ML) algorithms with thermal imaging. This could improve the analysis and interpretation of thermal data for various applications. This involves the development of systems that can analyze thermal data on the fly, enabling drones to make informed decisions during missions. Drones equipped with thermal imaging cameras have proven invaluable in search and rescue missions, especially in locating missing persons in difficult terrain or at night.

The artificial intelligence (AI) component of a drone for monitoring and patrolling tasks associated with disaster relief missions. The AI component uses deep learning models for environment recognition and object detection. Semantic segmentation or pixel-based labeling is used for environment recognition based on the RGB images in Figure 2. Object detection is key for detecting and locating people in need. Since people are relatively small objects from the drone perspective, we use both RGB and thermal images [5].

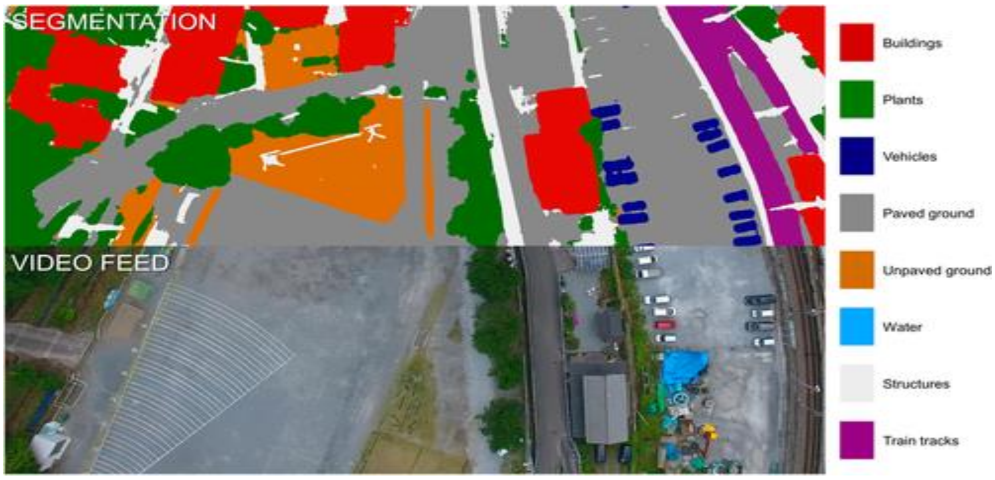

Figure 2. Sample frame from the semantic segmentation model.

Drones are scanning the disaster area to detect and locate people. An even more important task is to determine and compute a ground route leading to the detected people. Roads blocked by landslides or fallen trees must be identified, as these could prevent rescue vehicles from reaching people in distress.

The system uses three cameras: two RGB cameras and one thermal camera. While one RGB camera, pointed downwards, is used as input for the semantic segmentation component, the person detector component uses both RGB cameras and the thermal camera, which are pointed at 45°. The cameras are mounted on a gimbal shaft, as seen in Figure 3, which keeps them stable, independent of the drone's motion [5].

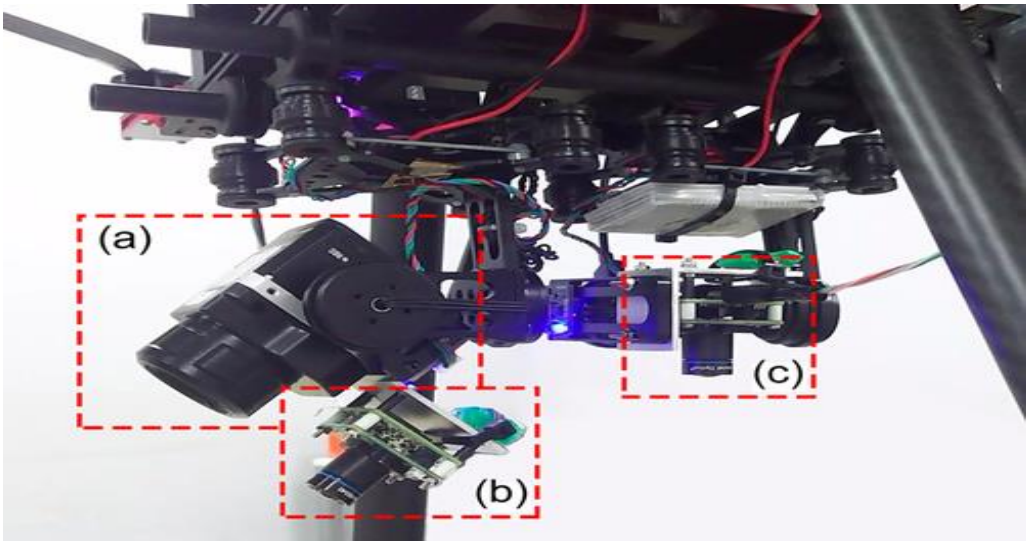

Figure 3. FLIR Vue Pro 640 thermal camera (a) mounted on a gimbal system under the drone. Two e-con Systems See3CAM cameras installed: one (b) fixed to the FLIR camera with a 45° forward tilt angle and the other (c) pointing 90° downwards for the segmentation task. Cameras (a) and (b) were used for human detection.

2. Research and Development Initiatives - News about research initiatives, collaborations, or partnerships between drone manufacturers, thermal camera producers, and research institutions could indicate upcoming breakthroughs in thermal imaging technology. Partnerships between drone manufacturers, thermal camera manufacturers, and research institutions can include the development of sophisticated image processing algorithms and analysis software. This will increase the ability of drones to interpret thermal data, providing more meaningful insights in real time. Collaborations often focus on integrating advanced sensors into smaller and lighter drones. Miniaturization of thermal imaging technology is key to expanding the range of applications and improving drone performance. Research institutions may collaborate with drone manufacturers and thermal camera producers to develop specialized systems for environmental monitoring and climate studies. This involves the collection of high-resolution thermal data for analyzing temperature variations in ecosystems [5].

Ongoing advancements in thermal imaging drone technology include improvements in sensor resolutions, increased flight times, and the integration of artificial intelligence for enhanced data analysis. Future prospects involve the continued integration of these technologies in diverse scientific and industrial applications [8].

6. Discussion

The benefits of thermography have been verified many times. In many cases, thermo - diagnostics are irreplaceable or difficult to replace with other diagnostic methods. Heat transfer and temperature visualization can be used in various engineering applications through a modeling and simulation approach. By providing initial data, it paves the way for in-depth analysis and penetration into the technical intimacies of problem solving. Its use became more important and popular especially after the introduction of computer simulation techniques [6]. The use of thermal imaging is one of the possible sources of input data that can be used via simulation and modeling of heat transfer and possibly for further processing. Several software tools like FLUENT, Modelica, FEMLAB, APROS (Performance Dynamic Simulation), BALAS (Conceptual Process Design), Chem Sheet (Process Chemistry), Kiln Simu (Rotary Furnace Simulator) etc. are often used to model and simulate process engineering parameters of various operations and for other applications where thermal imaging is required.

7. Conclusions

The fusion of thermal imaging capabilities with drone technology represents a leap forward in scientific research and applications. Thermal imaging drones provide researchers with unprecedented access to real-time thermal data, unlocking new possibilities for understanding and addressing complex challenges across various disciplines. As technology continues to evolve, the full potential of thermal imaging drones in scientific endeavors is yet to be fully realized, promising continued innovation and transformative insights.

Acknowledgments: This work was supported by the Cultural and Educational Grant Agency of the Ministry of Education, Science, Research, and Sport of the Slovak Republic under project KEGA No. 011TUKE-4/2021 titled "Implementation of current scientific-research, technical and methodological solutions in the environmental engineering field into the educational process at universities".

Conflicts of Interest: "The authors declare no conflict of interest."

References

1. Niranjan, S.K. Proceedings of the International Conference on Smart Technologies in Computing Electrical and Electronics (ICSTCEE 2020), October 9-10, 2020.
2. Alsamhi, S.H.; Almalki, F.A.; Afghah, F.; Hawbani, A.; Shvetsov, A.V.; Lee, B. "Drones' edge intelligence over smart environments in B5G: Blockchain and federated learning synergy", IEEE Trans. Green Commun. Netw., 2022, Volume 6, pp. 295-312.
3. Brzezinski, R.Y.; Rabin, N.; Lewis, N. Automated processing of thermal imaging to detect COVID-19, Scientific Reports, 2021, Volume 11, pp. 1-10.
4. Manullang, M.C.T.; Lin, Y.-H.; Lai, S.-J.; Chou, N.-K. Implementation of Thermal Camera for Non-Contact Physiological Measurement: A Systematic Review, Sensors, 2021, pp. 21.
5. Liu, L.; Ouyang, W.; Wang, X.; Fieguth, P.; Chen, J. Deep learning for generic object detection: a survey. International Journal of Computer Vision, 2020, pp. 261–318.
6. Vollmer, M.; Mollmann, K.P. Infrared Thermal Imaging: Fundamentals, Research and Applications, Wiley: Weinheim, Germany, 2011, pp. 612.
7. Petrocelli, S.; Sentenac,T.; Yannick Le Maoult: 3D Thermal Imaging: An approach towards true field temperature measurement, QIRT 2014 - 12th International conference on Quantitative Infrared Thermography, 10 p, Bordeaux France, 2014.
8. Nguyen, T. X. B. K.; Chahl, J. A review of modern thermal imaging sensor technology and applications for autonomous aerial navigation, J. Imag., 2021, Volume 7, pp. 217.

TECHNICKÁ UNIVERZITA V KOŠICIACH
Strojnícka fakulta

Depth-based Anomaly Detection in Real-time Using Morphological Filters

Maksym Grytsiv [1*], Marek Sukop [1], Dávid Kovaľuk

1 Technical University of Kosice, Department of Production Technology and Robotics.
• Contact: maksym.grytsiv@tuke.sk; Tel.: +421 55 602 3156

Abstract: This study focuses on real-time anomaly detection in depth-sensed images using morphological filters and computer vision techniques. Depth sensing technology captures depth information, allowing the detection of anomalies or defects within the captured scenes. The utilization of morphological filters enables preprocessing of depth images, emphasizing the identification of irregularities. The study explores the integration of these filters within a real-time processing environment, enabling efficient and accurate anomaly detection. The proposed methodology showcases the potential for enhancing quality control in various industries, particularly in identifying defects, irregularities, or anomalies for immediate corrective action. The findings highlight the efficacy of using depth-sensed data and morphological filters for robust anomaly detection in computer vision applications.

Keywords: Depth Sensing, Anomaly Detection, Real-time Processing, Morphological Filters, Computer Vision.

1. Introduction

In recent years, the advancement of computer vision and image processing technologies has opened wide possibilities for detecting anomalies and defects in real-time. [8] One of the key technologies used for this purpose is depth sensing in conjunction with morphological filters. Depth sensing provides additional measurements that allow gathering information about the depth of objects in an image, while morphological filters enable effective processing and extraction of this valuable data. This area of research has gained significant importance in fields such as automation, quality control, and monitoring, particularly in the industrial sector. Real-time anomaly detection has become a crucial task to reinforce control over production processes, medical research, technical maintenance, and more. [11]

The advent of depth-sensing cameras like the Intel RealSense 435i has significantly contributed to advancing this field. RealSense 435i offer high-resolution depth maps and sophisticated sensing capabilities, allowing for precise depth perception and improved image quality. These cameras have become integral tools for applications requiring accurate depth information, including robotics, and anomaly detection in various industries. [7] The utilization of Intel RealSense 435i in depth sensing not only enhances the accuracy of anomaly detection but also enables real-time processing, providing a robust framework for efficient anomaly identification and analysis. Therefore, this study aims to explore the effectiveness and potential applications of the Intel RealSense 435i in depth-based anomaly detection using morphological filters.

2. Technologies of depth perception

Depth perception is a technology that allows obtaining information about the distance to objects within an image. Intel RealSense 435i employs infrared light or laser emissions to create precise depth maps that indicate the distance to each pixel in the image. This capability enables the detection of objects, their shapes, and sizes.

Morphological filters, in turn are utilized for image processing and modification of their structure to highlight or obscure specific details. [9] In anomaly detection, morphological filters are employed to isolate unusual or outlying areas within the image. They can detect abnormal patterns that may indicate defects or malfunctions in industrial environments.

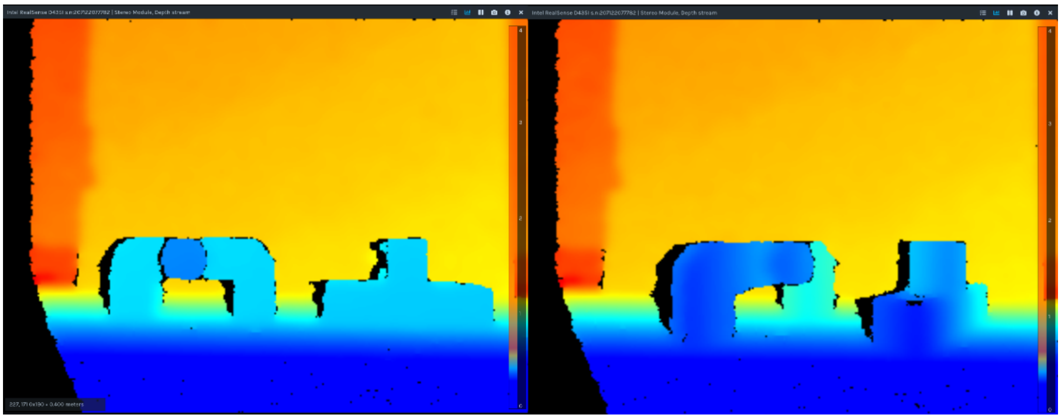
Figure 1 2D Depth perception with Stereo Module

The Bag format (ROS bag) is used to store various data types, including depth information from a camera, within data fragments that are easily saved and replayed. Intel RealSense 435i can store this data in Bag format by mapping depth images to timestamps associated with the video stream.

The camera generates specific messages or topics containing depth data for each video frame. Upon reading data from the Bag file, the depth information can be identified and reproduced as images or numerical depth values.

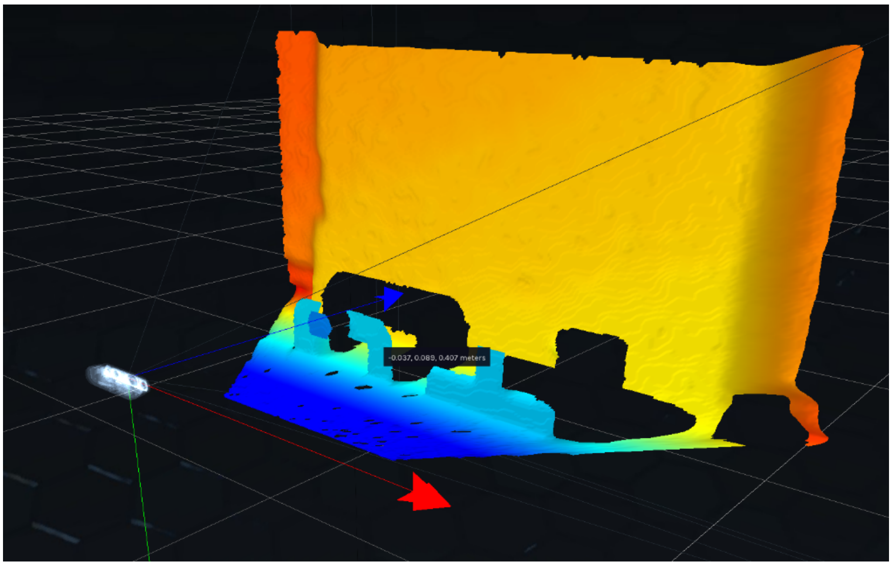

Figure 2 3D Depth perception with Stereo Module

Stereoscopic 3D scanning, through the use of dual-camera systems, offers enhanced depth accuracy and robustness in depth sensing. By capturing scenes from multiple viewpoints simultaneously, it delivers precise depth perception, enabling better resilience against environmental variations like lighting changes and textureless surfaces. [12]

3. Anomaly detection process

To compare a sample set of objects with a main dataset to detect anomalies in size, shape, and color of objects.

1. Imports:

```
# Import necessary libraries
import numpy as np
import cv2
```

Figure 3 Import libraries.

2. Find_anomalies Function:

- This function takes two lists of objects: sample_data (your sample dataset) and main_data (the main dataset for comparison). [13]
- It compares the objects' size (width, length, depth), shape, and color between the sample_data and main_data.
- Anomalies are detected based on predefined thresholds (e.g., a difference in size greater than 10%).
- Anomalies are appended to different lists (size_anomalies, shape_anomalies, color_anomalies).
- Finally, these anomaly lists are returned.

```python
# Function to compare a sample with the main dataset
def find_anomalies(sample_data, main_data):
    # Checking size (width, length, depth)
    size_anomalies = []
    for sample_object in sample_data:
        for main_object in main_data:
            if abs(sample_object['width'] - main_object['width']) > 0.1 * main_object['width']:
                size_anomalies.append("Anomaly: Different width detected")
            # Add checks for length and depth similarly

    # Checking object shape
    shape_anomalies = []
    for sample_object in sample_data:
        for main_object in main_data:
            if sample_object['shape'] != main_object['shape']:
                shape_anomalies.append("Anomaly: Different shape detected")

    # Checking color
    color_anomalies = []
    for sample_object in sample_data:
        for main_object in main_data:
            if sample_object['color'] != main_object['color']:
                color_anomalies.append("Anomaly: Different color detected")

    return size_anomalies, shape_anomalies, color_anomalies
```

Figure 4 Find_anomalies Function.

3. Sample Objects and Main Dataset:

- sample_objects and main_objects are lists of dictionaries, where each dictionary represents an object.

```python
# Sample objects
sample_objects = [
    {'width': 5.2, 'length': 8.3, 'depth': 3.1, 'shape': 'rectangle', 'color': 'blue'},
    # Add other sample objects
]

# Main dataset
main_objects = [
    {'width': 5.0, 'length': 8.0, 'depth': 3.0, 'shape': 'rectangle', 'color': 'blue'},
    {'width': 5.5, 'length': 8.5, 'depth': 3.2, 'shape': 'circle', 'color': 'red'},
    # Add other objects for comparison
]
```

Figure 5 Sample Objects and Main Dataset.

- Each object is represented as a dictionary containing information about width, length, depth, shape, and color. These values are examples; you should replace them with actual measurements and properties of your objects.

4. Finding Anomalies:

- The find_anomalies function is called with the sample_objects and main_objects as arguments.
- Anomaly lists (size_anomalies, shape_anomalies, color_anomalies) are populated based on the differences detected between the sample and main datasets.
- The detected anomalies are printed to the console.

```python
# Finding anomalies
size_anomalies, shape_anomalies, color_anomalies = find_anomalies(sample_objects, main_objects)

# Printing the results of the checks to the screen
print("Size Anomalies:", size_anomalies)
print("Shape Anomalies:", shape_anomalies)
print("Color Anomalies:", color_anomalies)
```

Figure 6 Finding Anomalies.

Erosion used to shrink objects in the image. cv2.erode() reduces the size of objects by removing pixels at the object boundaries. Dilation, cv2.dilate() enlarges objects in the image. This operation expands the object areas by adding pixels at the object boundaries. Opening: The morphological operation opening using cv2.morphologyEx() is employed to remove noise and small objects from the image area. It combines a sequence of erosion followed by dilation. In contrast to opening, the morphological operation closing with cv2.morphologyEx() aims to fill small holes and gaps between objects. It also consists of a sequence of dilation followed by erosion.

Here are code examples for each morphological operation: erosion, expansion, opening, and closing, using the OpenCV library in Python.

```python
import cv2
import numpy as np

# Reading an image
img = cv2.imread('image_path.png', 0)

# Creating a kernel for morphological operations
kernel = np.ones((5, 5), np.uint8)

# Erosion
erosion = cv2.erode(img, kernel, iterations=1)

# Dilation
dilation = cv2.dilate(img, kernel, iterations=1)

# Opening
opening = cv2.morphologyEx(img, cv2.MORPH_OPEN, kernel)

# Closing
closing = cv2.morphologyEx(img, cv2.MORPH_CLOSE, kernel)

# Displaying the original and processed images
cv2.imshow('Original Image', img)
cv2.imshow('Erosion', erosion)
cv2.imshow('Dilation', dilation)
cv2.imshow('Opening', opening)
cv2.imshow('Closing', closing)
cv2.waitKey(0)
```

Figure 7 morphological operations

These morphological operations are widely used in image processing to enhance quality, highlight objects, or diminish them, as well as to prepare data before applying analysis and anomaly detection algorithms.[1]

4. Conclusion

The convergence of stereo modules, depth-sensing cameras like Intel RealSense, and advanced morphological algorithms has markedly transformed anomaly detection and spatial analysis across diverse domains. This integration facilitates precise depth perception, spatial understanding, and the ability to identify anomalies effectively. The application of morphological algorithms enhances image processing capabilities, extracting vital features, and aiding in the precise identification of irregularities and anomalies.[2]

This Work opens avenues for further research in this field, including algorithm optimization, leveraging more sophisticated image processing methods, and expanding the scope of detectable anomalies. Overall, this approach holds broad applicability in automation, quality assurance, and safety across diverse industrial environments.

5. Acknowledgment

This research was supported by project KEGA: 020TUKE-4/2022 Development and implementation of new approaches in teaching industrial and collaborative robotics and project VEGA: 1/0215/23 Research and development of robotic workplaces equipped with industrial and collaborative robots.

References

1. Song, H., Yang, J., & Kim, J. (2020). "Real-time Anomaly Detection Using Depth Sensing and Morphological Filters." IEEE Transactions on Image Processing, 29(7), 3245-3258.
2. Szeliski, R. (2010). "Computer Vision: Algorithms and Applications." Springer.

3. Christer Ericson, 2005, "Real-Time Collision Detection", CRC Press, ISBN: 978-1558607323
4. Liu, W., et al. (2018). "Real-time Object Detection for Autonomous Driving." Proceedings of the IEEE Conference on Computer Vision and Pattern Recognition (CVPR).
5. Zhang, Z. (2012). "Microsoft Kinect Sensor and Its Effect." IEEE Multimedia, 19(2), 4-10.
6. Gonzalez, R. C., & Woods, R. E. (2017). "Digital Image Processing." Pearson, ISBN-13: 978-0133356724
7. Guo, S., et al. (2019). "A Review of Real-time Depth Sensing Techniques and Applications." Sensors, 19(19), 4315.
8. Li, J., et al. (2016). "Real-time Image Processing in Depth Sensing Systems." Proceedings of the International Conference on Image Processing (ICIP).
9. Liao, H. Y. (2018). "Real-time Object Detection Using Morphological Filters." Computer Vision and Image Understanding, 172, 60-71.
10. Cheng, M. M., et al. (2015). "Global Contrast based Salient Region Detection." IEEE Transactions on Pattern Analysis and Machine Intelligence, 37(3), 569-582.
11. Varun Chandola, Arindam Banerjee, Vipin Kumar, 2009, "Anomaly Detection: A Survey", ACM Computing Surveys, doi:10.1145/1541880.1541882
12. Konstantinos Daniilidis, Reinhard Klette, David C. Gibson, 2011, "Stereo Vision", Springer, ISBN: 978-1848829343
13. Rafael C. Gonzalez, Richard E. Woods, 2017, "Digital Image Processing", Pearson, ISBN: 978-0133356724
14. Christer Ericson, 2005, "Real-Time Collision Detection", CRC Press, ISBN: 978-1558607323

TECHNICKÁ UNIVERZITA V KOŠICIACH
Strojnícka fakulta

Numerical simulation of deep-drawing in Simufact Forming.

Július Hajduk[1]*, Janka Majerníková[1], Samuel Vilkovský[1]

[1] Technical University of Košice, Faculty of Mechanical Engineering, Department of Technologies, Materials and Computer Aided Production, Mäsiarska 74, 040 01 Košice, Slovakia,
* Email: julo.hajduk@centrum.sk,

Abstract: This research entails conducting experiments on the HX420 sheet to assess its formability in the creation of ears through a cupping test performed on a metal sheet with a 63 mm diameter. The validation of experimental findings was achieved by employing Simufact software. Simulations utilized a 0.7 mm thick HX420 metal sheet. The primary goal of this study is to confirm the formability of HX420 material in earing formation and to compare experimental outcomes with simulations employing varying numbers of elements per thickness. The evaluative parameter for the simulations was height of ears on the deep-drawn cup.

Keywords: Deep-drawing, earing, Simufact Forming, optimization

1. Introduction

Deep-drawing is a form of sheet metal forming and is one of the most commonly used technologies for sheet metal processing. It is utilized in various industrial sectors, such as the automotive and aerospace industries, among many others. This technology, as part of sheet metal forming, stands as one of the most crucial processes for reshaping sheet metal. It is extensively used in mass production, primarily due to benefits such as low manufacturing costs, high surface quality, reduced weight, and rigidity.

The process of sheet drawing is performed using a drawing press consisting of a drawer and a die (fig. 1). The press blank is placed above the die cavity. The drawer, along with a retainer that prevents the edges of the drawn part from improper deformation and cup wrinkling, presses on the surface of the drawn part, which is then drawn through the die opening. This opening is rounded with a radius rp. Simple and shallow shapes are created in a single operation, while deeper and more complex drawn parts are drawn in two or more stages [1,2].

Computer simulation significantly shortens the production preparation stage from the component drawing to tool manufacturing. It reduces the costs of preparing complex component production, optimizes the use of material properties, replaces costly experiments, reveals design errors in forming processes, enhances dimensional and geometric accuracy of products, and allows for rapid verification of varied procedures. The results obtained from computer simulation must be validated based on prototype and model experimental test outcomes [3].

Numerical simulation can predict the influence of material properties, friction conditions, tool geometry, and the drawing press on the drawing process. Over time, numerous methods have been developed to evaluate the formability of sheets.

2. Materials and Method

In the experimental research, the material HX420 (micro-alloyed steel) with a sheet thickness of 0.7 mm was used. The mechanical properties of the examined material are presented in Table 1.

Table 1 Mechanical properties of HX420 material

RD (°)	Yield strength (MPa)	Ultimate Tensile strength (MPa)	Ultimate Strain (MPa)	r_{90} (-)	Δr (-)	n_{90} (-)	K (MPa)
0	462.2	518.4	29.0	0.599	- 0.402	0.151	791

Strengthening Model

In numerical simulation, input data includes the Hollomon hardening curves. The Hollomon hardening curve describes material behaviour under plastic deformation between the yield point and tensile strength. The specific index n is the strain hardening exponent characterizing hardening processes initiated during cold plastic deformation. The Hollomon hardening curve is defined by the equation:

$$\sigma = K(\varepsilon_P)^n \tag{1}$$

where:
ε_P – plastic deformation,
n – strain hardening exponent,
K – material constant [4].

Plasticity condition

Considering the advantages and disadvantages of various plasticity conditions, recommendations for industrial application of these programs are provided. The theory of plasticity according to Hill48 was used for our experiment. [5,6].

Cupping test

Figure 1. Hydraulic press ZD-40

The experimental part of the study consisted of a cupping test performed on the hydraulic device ZD-40 (Figure 1).

Circular blanks of size D = 63 mm were produced from the examined material HX420. From these blanks, cylindrical cups with a flat bottom were subsequently drawn using an experimental drawing tool. The dimensions of the drawing tool are shown in Table. 2.

Table 2 Dimensions of the deep-drawing tool

Parameters	Dimensions (mm)
Punch diameter	31.71
Die diameter	33.46
Punch radius	4.5
Die radius	5.5
Clearance between punch and die	1.75

To assess the susceptibility of the sheet to earing formation during deep drawing, the height of the ears of the cylindrical cups was chosen as the parameter for evaluation. Figure 2 presents the average measured height values of the cups in the directions of 0°, 45°, and 90°, relative to the rolling direction.

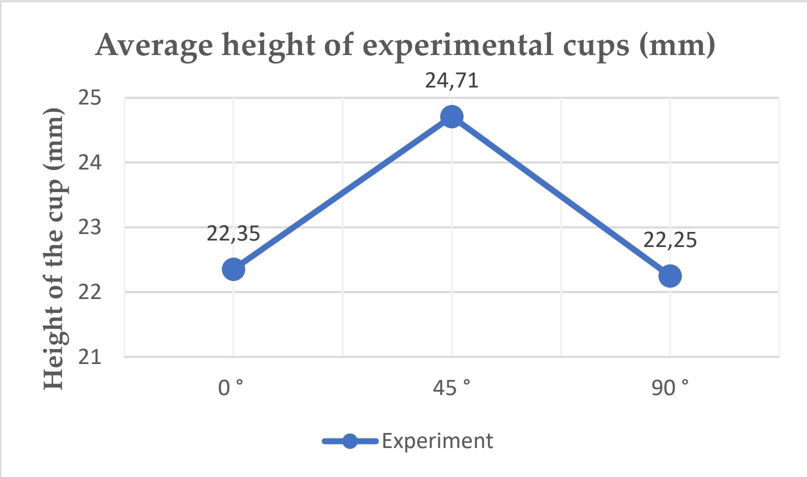

Figure 2. Measured values of ears height

The deep drawing process simulation was conducted in the Simufact Forming simulation environment. The dimensions of the CAD model (Fig.3) matched those of the used experimental tool (see Table 2). In the simulation, the Hollomon hardening model and the yield criteria according to Hill were employed.

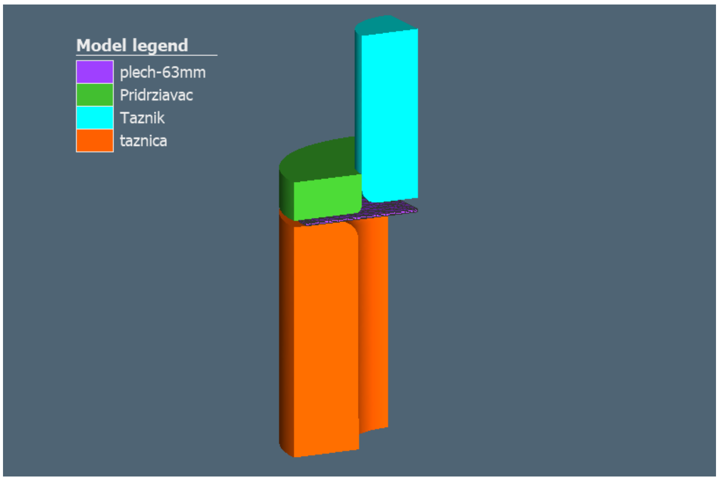

Figure 3. CAD model of deep-drawing tool

The cylindrical blank was meshed using hexahedral elements with a size of 0.25 mm. During the experiment, the number of elements through the thickness of the sheet was varied. The accuracy of the calculation was verified with different counts of elements through the sheet thickness: 3, 5, 7 and 11. The simulation results are shown in Figures 4-7.

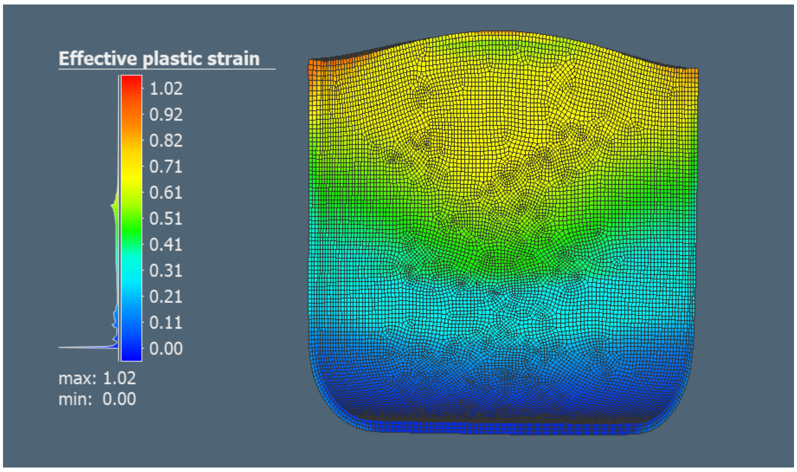

Figure 4. Simulation of deep-drawing using 3 elements per thickness

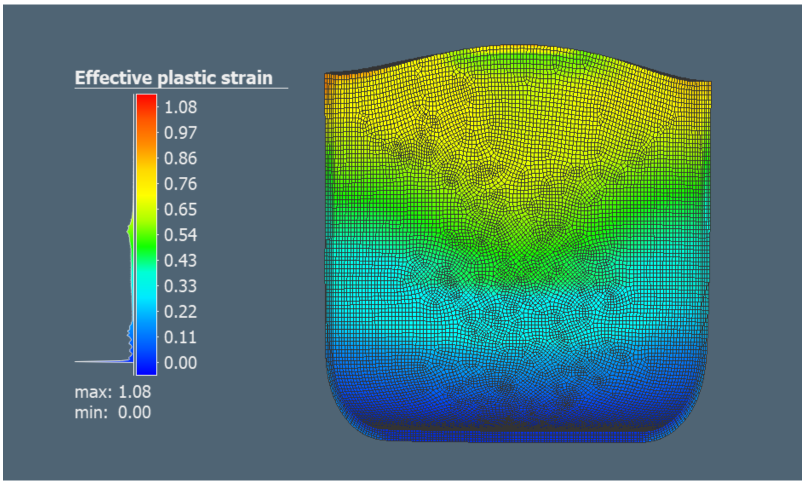

Figure 5. Simulation of deep-drawing using 5 elements per thickness

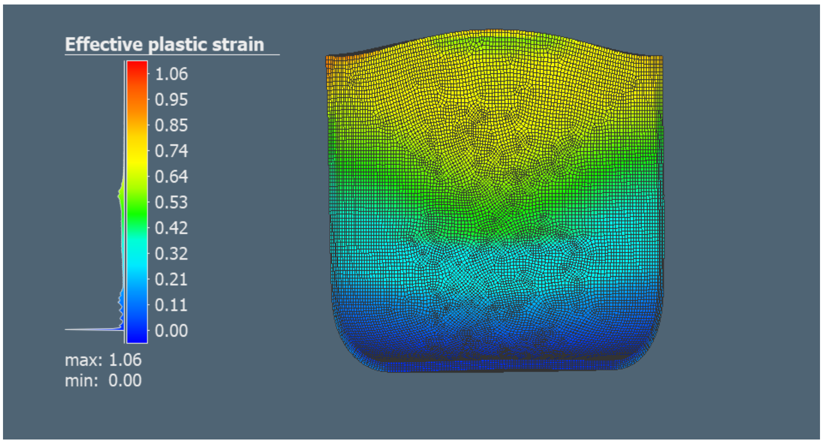

Figure 6. Simulation of deep-drawing using 7 elements per thickness

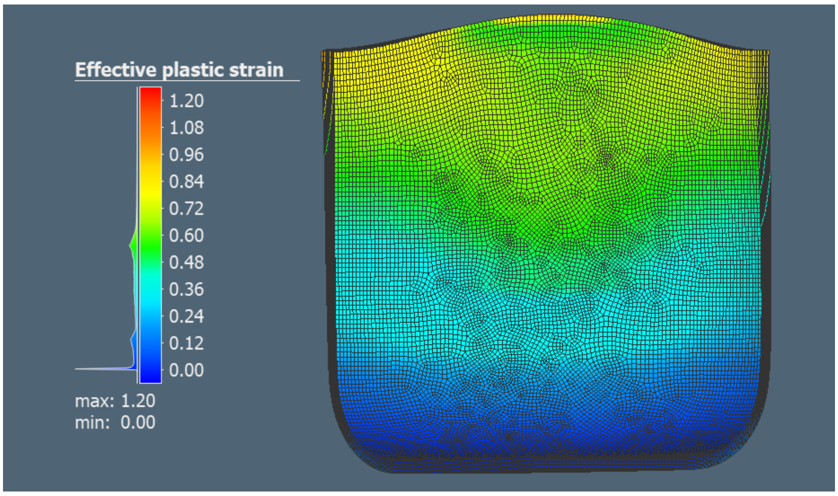

Figure 7. Simulation of deep-drawing using 11 elements per thickness

Comparison of ears height obtained by simulations with experimental results is shown in Fig. 8.

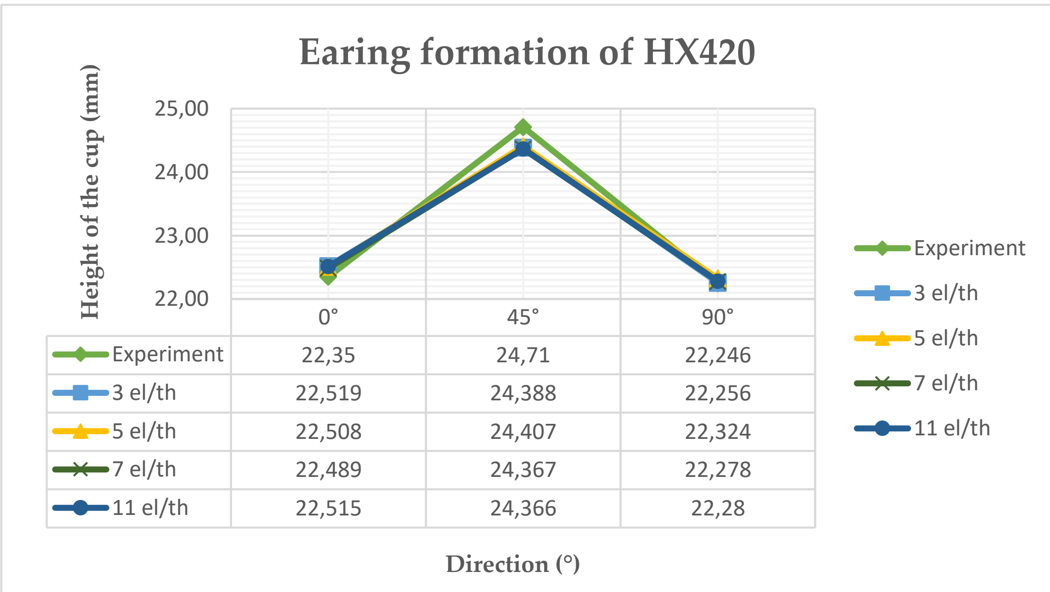

	0°	45°	90°
Experiment	22,35	24,71	22,246
3 el/th	22,519	24,388	22,256
5 el/th	22,508	24,407	22,324
7 el/th	22,489	24,367	22,278
11 el/th	22,515	24,366	22,28

Figure 8. Comparison of experimental results with simulations

3. Results

In summary, this paper investigates the formability of the HX420 material. The study reveals that ears on the HX420 material develop in a 45° direction, consistent with predictions derived from planar anisotropy. The cupping test's experimental findings were corroborated through simulations conducted with the Simufact Forming software. These simulations employed the Hollomon hardening model and yield criteria based on Hill. In the simulations, hexahedral elements with size of 0.25 mm were used. However, the number of elements varied with the thickness of the sheet, leading to a reduction in the height of the elements and an increase in the number of elements. As depicted in Figure 8, it can be noted that in the simulation of drawing the HX420 material, the number of elements does not have a significant impact on the accuracy of the simulation concerning the height of the cup. However, as indicated in Figures 4-7, the value of effective plastic strain differed in each case, with a maximum variation of 0.18.

Acknowledgments: The authors are grateful to VEGA 1/0384/20.

References

1. SPIŠÁK, E. Mathematical modelling and simulation of technological processes -Drawing. Košice: TYPO Press, 2000. 156 p. ISBN 80-7099-530-0
2. ČADA, Radek. Technology of forming and casting - theoretical basis: sheet metal drawing [online]. Ostrava: University of Mining and Metallurgy - Technical University of Ostrava, 2013 [cit.2018-03-30]. ISBN 978-80-248-3015-5.
3. BOŽEK, P.; KUZNETSOV, A. P.: Analýza účinnosti technologického zariadenia v stratégii štruktúry strojárstva. In: Manažment priemyselných podnikov. ISSN 1336-5592. Roč. 6, č. 1 (2009), s. 5 – 12
4. Ch.A.R. Saleh, A.R. Ragab, in Current Advances in Mechanical Design and Production VII, 2000
5. ARWIDSON, C.: Numerical Simulation of Sheet Metal Forming for High Strenght Steels: Luleâ University of Technology, Department of applied physics and mechanical engineering. Sweden 2005. 93s. ISSN: 1402-1757
6. SLOTA, J. – OLEXOVÁ, M.: The formability limits of shape-complicated cups from trip steel. MTeM 2010, ISBN: 978-80-553-0560-8.

TECHNICKÁ UNIVERZITA V KOŠICIACH
Strojnícka fakulta

Polymer material calibration using the Parallel Rheological Framework model

Martina Hančinová [1*], Erika Dubňanská [1] and Róbert Huňady [1]

[1] Department of Applied Mechanics and Mechanical Engineering, Faculty of Mechanical Engineering, Technical University of Košice, Letná 9/B, 042 00 Košice, Slovakia; martina.hancinova@tuke.sk; erika.dubnanska@tuke.sk; robert.hunady@tuke.sk;
* Correspondence: martina.hancinova@tuke.sk

Abstract: Finite element method simulations have a significant role in modern engineering development. For the most realistic simulations in commercial software, a properly developed material model is essential. This paper describes the calibration of an advanced PRF material model that is implemented in the commercial software Abaqus. Data measured in uniaxial tensile tests and relaxation tests were used for calibration of the material model. The coefficients, which were initially calculated in Excel, were used as input values for creating the material model in Abaqus. A simplified model of the specimen, which is a unit cube, was used for the simulations. For the most accurate results, the coefficients were optimized in Isight software. The optimization of the material model coefficients ensured the specification of the results obtained from the simulations. The calibration resulted in material model coefficients that can be used in the simulations in representation of the PPC3TF2 material properties.

Keywords: PRF; Abaqus; Isight; optimization

1. Introduction

When designing components and products that contain polymers, it is important to consider that their mechanical behaviour significantly differs from conventional engineering metals [1]. One of the most notable characteristics of polymers is the ability to undergo large and reversible elastic deformations. Depending on the temperature and experimentally chosen time scale, polymers can exhibit behaviors ranging from an elastic solid to a viscous liquid [2].

The viscoelastic behavior of polymers is rate-dependent and can be represented by a rheological model combining a dashpot and a spring. The viscous component (dashpot) causes a time delay in the mechanical response. A perfectly elastic material obeys Hooke's law, behaving like a perfect spring, storing the energy it gains as it elongates and releasing it as the material returns to its original shape [3]. Hyperelasticity is a generalization of linear elasticity, it is non-linear and suitable for the prediction of large deformations [1]. The hyperelastic model for rubber-like materials enables the simulation of nearly incompressible elastomers undergoing significant elastic deformations [4]. To accurately simulate such specific material behaviors, it is necessary to use a suitable constitutive model in finite element analysis [5].

The Parallel Rheological Framework (PRF) has been implemented in the commercial software Abaqus since version 2013 [5]. PRF is a material model that consists of multiple parallel viscoelastic networks and optionally an elastoplastic network in parallel [6]. Unlike conventional models, PRF can capture the non-linear viscoelastic behavior of materials, as well as the Mullins effect and permanent set in elastomers [7]. The PRF model allows

the material behaviour of polymers (elastic, plastic, and viscous) to be represented comprehensively, thus allowing more realistic simulations [1]. However, the advantages of the PRF model come with the need for more complex methods to calibrate the model coefficients [5].
In this paper, the calibrated material is PPC3TF2, a polypropylene copolymer grade, filled with 20% talc by weight, supplied by Washington Penn Plastic Co. Inc. PPC3TF2 finds applications in the production of HVAC (heating, ventilation, and air conditioning) components and in the automotive industry as interior trim [8].

2. Materials and Methods

The PPC3TF2 calibration data consists of uniaxial tensile test data and relaxation test data. The number of viscoelastic networks of the model is (due to the number of parameters) generally appropriate to choose N=3 for the calibration of plastics. The chosen PRF model (Figure 1) consists of one equilibrium elastoplastic network 0 and three viscoelastic networks 1, 2, 3.
The elastic part of the response is specified for all networks by using a hyperelastic material model. For each of the networks, the same definition of the hyperelastic material is used. As a result, the model requires only one definition of hyperelasticity along with the stiffness ratio for each network.

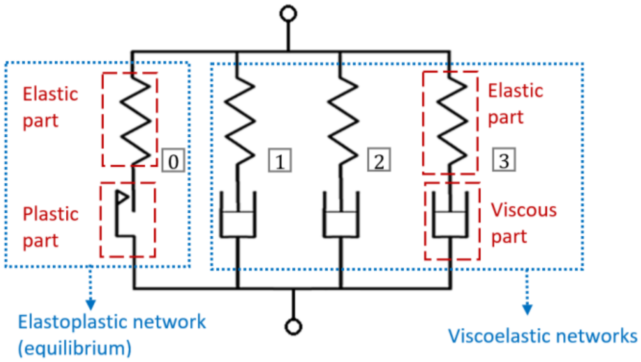

Figure 1 Used PRF model.

In general, the Yeoh model was chosen to describe the hyperelastic behaviour in Abaqus. For this model, due to the limited amount of data from the material tests, only two members, C_{10} and D_1, were defined. Using viscoelasticity, the behaviour of the viscous dampers is defined as well as the ratio of stiffness of individual springs to the total stiffness.

Hyperelasticity parameters

Since the material is isotropic, two material constants are required to represent the material properties. Based on the Young's modulus of elasticity determined from the stress-strain curves and the Poisson's number for polypropylene, the constraints C_{10} and D_1 of the Yeoh model were calculated.

Viscoelasticity parameters

Relaxation test data were used to estimate the viscoelasticity parameters and the Prony series was defined. The Prony series parameters were then converted to the PRF model parameters.

Table 1 Estimated parameters of PRF model.

Hyperelasticity	$_{10} = 474.87\ \text{MPa}$	$_{1} = 0.000309\ \text{MPa}^{-1}$
	$_{20} = 0\ \text{MPa}$	$_{2} = 0\ \text{MPa}^{-1}$
	$_{30} = 0\ \text{MPa}$	$_{3} = 0\ \text{MPa}^{-1}$
Viscoelasticity	$SR_1 = 0.0228$	$_{1} = 0.0154\ \text{MPa}^{-1}$
	$SR_2 = 0.0876$	$_{2} = 0.000236\ \text{MPa}^{-1}$
	$SR_3 = 0.154$	$_{3} = 0.0000144\ \text{MPa}^{-1}$

Using the coefficients from Table 1. and for n=1, m=0 for each of the three networks, the PRF model is linearly viscoelastic, which corresponds to the response of the model defined by the Prony series.

Material model

The material model, defined by using the PRF model keywords, was created in Abaqus. It includes the definition of hyperelasticity, and viscoelasticity and the parameters listed in Table 1. Specification in Abaqus looks like:

```
*Material, name=M1;PPC3TF2
*Hyperelastic, yeoh, moduli=INSTANTANEOUS
 <C10>, <C20>, <C30>, <D1>, <D2>, <D3>.
*Viscoelastic, Nonlinear, NetworkId=1, SRatio= <SR1>, Law=STRAIN
<A1>, <n1>, <m1>
*Viscoelastic, Nonlinear, NetworkId=2, SRatio=<SR2>, Law=STRAIN
<A2>, <n2>, <m2>
*Viscoelastic, Nonlinear, NetworkId=3, SRatio=<SR3>, Law=STRAIN
<A3>, <n3>, <m3>
```

Two types of material tests were used in the Isight material coefficient fitting process. In the calibration scheme (Figure 2), one network for uniaxial test and three networks for relaxation tests are used.

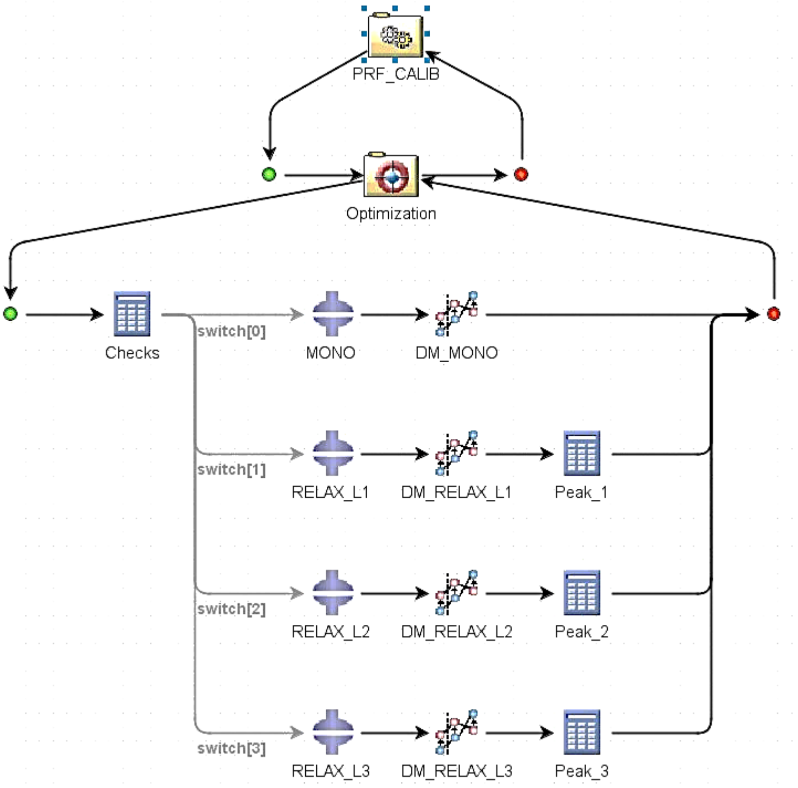

Figure 2 Optimisation scheme.

3. Results

A unit cube was used as a simplified model of the specimen in the simulations.
A comparison of the results of the first simulation (using the estimated coefficients from Table 1) with the curves obtained from the material tests is shown in Figure 3 and Figure 4. From the comparison of the responses, the need for the adjustment of the model parameters is evident. The optimization requires modification of the shape of the tensile stress-strain curve, which can be done primarily by changing the hyperelasticity parameter C_{10}. At earlier times, stress relaxation also needs to be emphasized. This can be achieved by optimizing the n, m parameters.

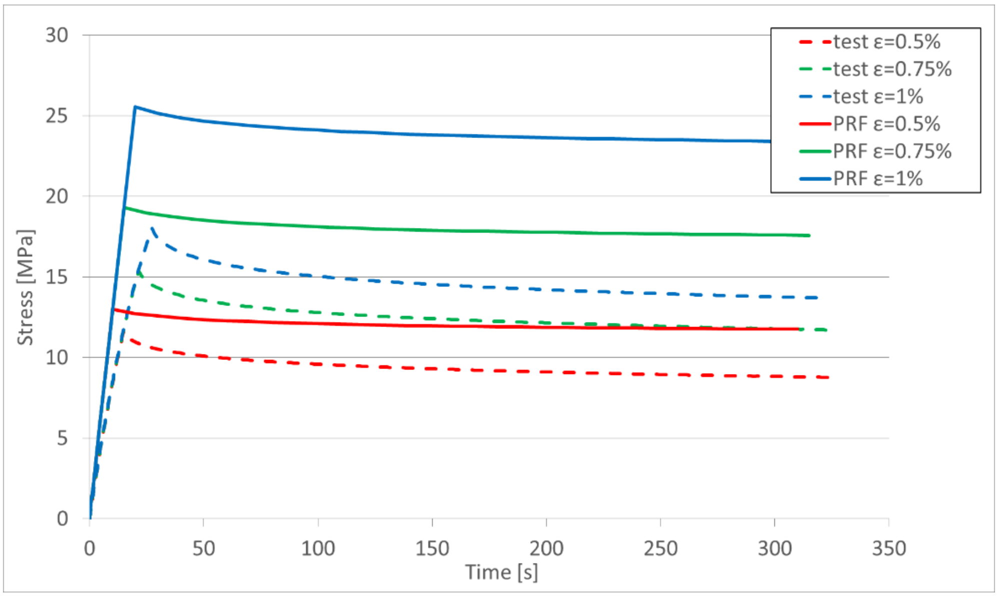

Figure 3 Material response compared to experimental data, in dependence stress – time.

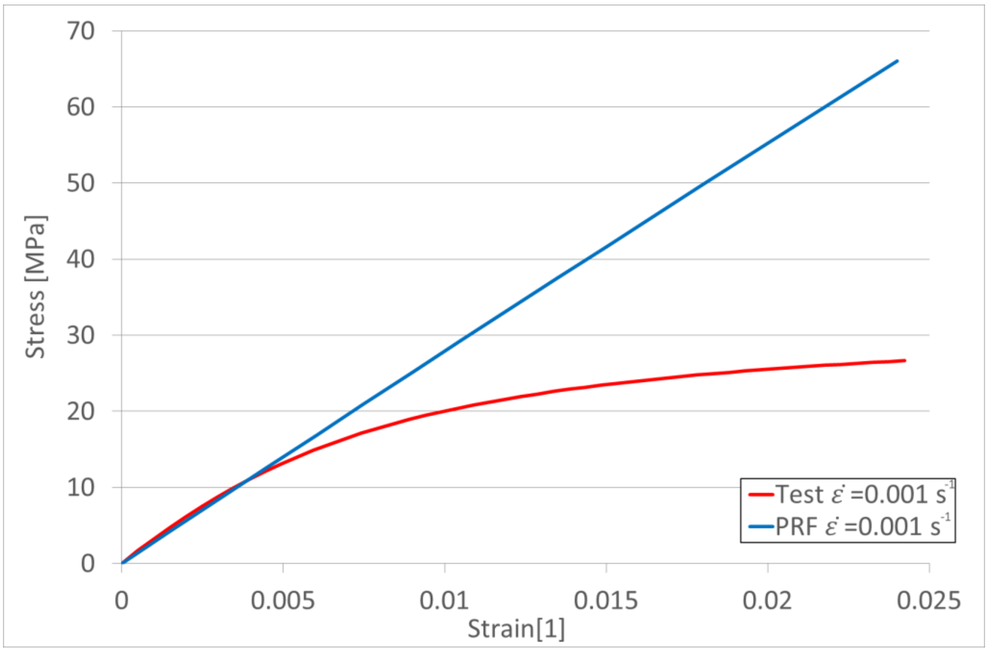

Figure 4 Material response compared to experimental data, in dependence stress – strain.

The optimization algorithm AMGA - Archive based Micro Genetic Algorithm was used to optimize the coefficients in Isight. The hyperelasticity parameter C_{10} is optimized first. In the next optimization the viscoelasticity parameters SR_1, SR_2, SR_3, $_1$, $_2$, $_3$, $_1$, $_2$, $_3$, $_1$, $_2$, $_3$ are refined. Out of ten thousand calculated solutions, the optimal solution for which the objective function in the form of squared error takes the lowest value, was selected. The results from the simulation using the final coefficients of the model are shown in Figure 5 and Figure 6 and the used values are written in Table 2.

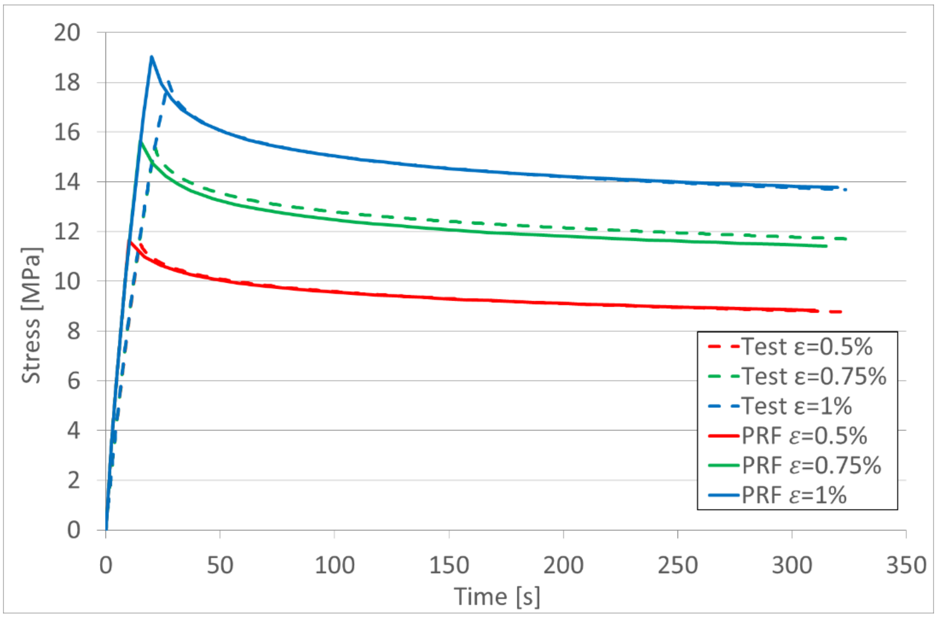

Figure 5 Comparison of relaxation curves.

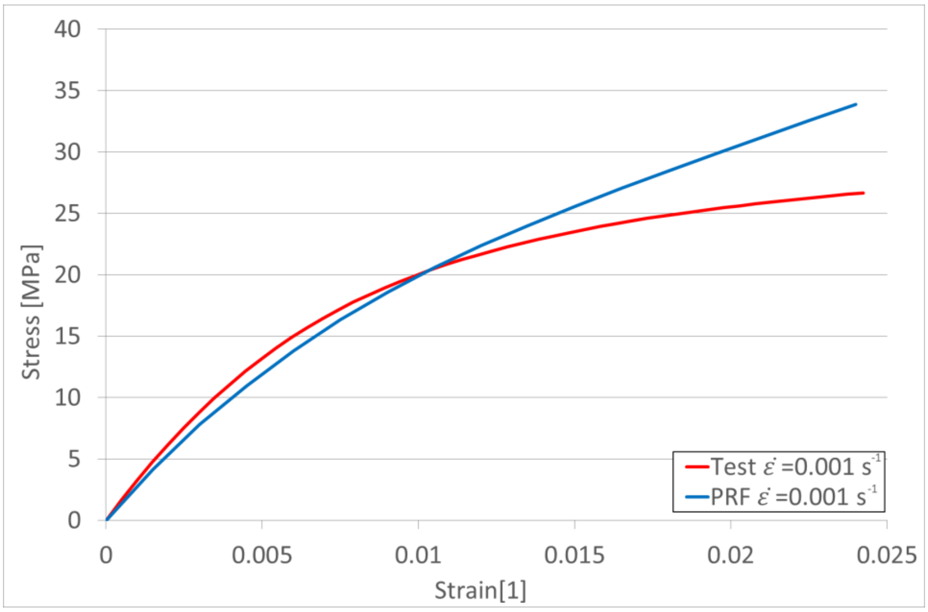

Figure 6 Comparison of stress-strain curves.

Table 2 Final parameters of PRF model.

Hyperelasticity	$_{10} = 493.62\ \text{MPa}$			
	$_{1} = 0.000309\ \text{MPa}^{-1}$			
Viscoelasticity	$SR_1 = 0.0979$	$_{1} = 4.708$	$_{1} = -0.335$	$_{1} = 0.0000226\ \text{MPa}^{-1}$
	$SR_2 = 0.372$	$_{2} = 3.47$	$_{2} = -0.524$	$_{2} = 0.0000151\ \text{MPa}^{-1}$
	$SR_3 = 0.247$	$_{3} = 4.45$	$_{3} = -0.369$	$_{3} = 2.15 \cdot 10^{-7}\ \text{MPa}^{-1}$

4. Discussion

By calibration with the use of the PRF material model, a material model of the PPC3TF2 plastic was created for use in FEM calculations in Abaqus. Optimization of the proposed coefficients in Isight ensured the approximation of the relaxation and stress-strain curves. To further improve the model, it would be possible to build on this work and extend the material model to include plasticity parameters. It would also be feasible to make the material model strain rate dependent and temperature dependent.

Acknowledgements: This work was suppoeted by the Slovak Research and Development Agency under the grant project VEGA No. 1/0500/20 and VEGA No. 1/0516/22.

References

1. Bergström, J. In *Mechanics of Solid Polymers. Theory and Computational Modeling.* Elsevier Inc., 2015. ISBN 978-0-323-31150-2.
2. Ward, I. M. ; Sweeney, J. Mechanical Properties of Solid Polymers. 3rd Edition. 2013. John Wiley & Sons, Ltd. 2013. ISBN 978-1-444-31950-7.
3. Yousefzadeh, M. Modeling and simulation of the electrospinning process. In Electrospun Nanofibers, Woodhead Publishing, 2017. ISBN 978-0-081-00907-9.
4. Hyperelastic Behavior of Rubberlike Materials. Dassault systems, user assistance R2022x. Available online: https://help.3ds.com/2022x/English/DSDoc/SIMA3DXMATRefMap/simamat-c-hyperelastic.htm?contextscope=cloud&id=5e85ce5f9b0b40c88eb15b286fb2abec. (accessed on 07. December 2023).
5. Karim, M. R.; Zhang, Z.; Zhu, Y. Prediction of Nonlinear Viscoelastic Recovery of Thermoplastic Polymers using Abaqus Parallel Rheological Framework (PRF) Model. In Science in the age of experience, 2016.
6. Ruano, P. C. et al. Innovative Fiber Reinforced Elastomeric Isolation Devices. In Proceedings of the IABSE Conference - Structural Engineering: Providing Solutions to Global Challenges, Geneva, Switzerland, 23-25. September 2015.
7. Hurtado, J.A.; Lapczyk, I.; Govindarajan, S.M. Parallel Rheological Framework to Model Non-linear Viscoelasticity, Permanent set, and Mullins Effect in Elastomers. In Constitutive Models for Rubber VIII.; Gil-Negrete, N., Alonso, J., Eds.; Taylor & Francis Group: London, UK, 2013; pp. 1-138. ISBN 978-1-138-00072-8.
8. Nexeo Plastics. WPP PP PPC3TF2-Black. Available online: https://www.nexeoplastics.com/types/plastics-database-datasheet/?id=16006&product=WPP+PP&grade=PPC3TF2-Black. (accessed on 05. December 2023).

Optimizing Heat Dissipation in Metal Hydride Hydrogen Storage Systems: Strategies and Solutions

Šimon Hudák [1,*], Marián Lázár [2]

[1] Technical University of Košice, Faculty of Mechanical Engineering, Department of Energy Engineering, Vysokoškolská 4, 042 00 Košice, Slovakia; simon.hudak@student.tuke.sk
[2] Technical University of Košice, Faculty of Mechanical Engineering, Department of Energy Engineering, Vysokoškolská 4, 042 00 Košice, Slovakia; marian.lazar@tuke.sk
* Correspondence: simon.hudak@student.tuke.sk

Abstract: Hydrogen, an alternative energy carrier, poses storage challenges. Metal hydrides offer promise, but effective heat management is crucial. This article reviews strategies for enhancing heat dissipation, concluding that cylindrical tanks with optimal cooling and annular-shaped heat exchangers show promise for efficient heat transfer in low-pressure hydrogen storage systems. Additionally, methods to minimize heat losses are discussed.

Keywords: Hydrogen; Metal Hydride tank, thermal management, intensifier

1. Introduction

Hydrogen stands as a promising alternative energy carrier. Throughout the past century, the chemical energy of hydrogen has been utilized in aviation, space exploration, defense industries, and fuel cell vehicles. With its high calorific value and minimal environmental impact when harnessed through oxidation-reduction reactions in fuel cells, hydrogen holds potential as a carbon-neutral substitute for fossil fuels. Globally, the hydrogen energy system is an extensive and intricate engineering mechanism encompassing production, storage, and utilization of hydrogen. However, integrating it into industrial spheres poses numerous challenges. One of the key challenges for widespread adoption of hydrogen as a fuel in the economy is its efficient and safe storage.

Chemical storage methods present themselves as promising alternatives to high-pressure hydrogen storage. In recent decades, scientific institutions have studied a vast array of materials and compounds capable of storing hydrogen. The primary advantage of storing hydrogen in chemical compounds like ammonia, methanol, or other cycloalkanes lies in their high volumetric density. Transforming hydrogen into liquid chemical compounds simplifies its transportation and storage under normal conditions. However, a major drawback of storing hydrogen in liquid compounds lies in the limitations or lack of material reusability and the need for specialized equipment for processing and recovering pure hydrogen.

Porous adsorption materials offer another alternative for hydrogen storage. These materials store hydrogen via physisorption due to their high surface area-to-volume ratio and hydrogen's ability to adsorb onto internal and external surface areas. Examples of porous materials for hydrogen storage include carbon nanomaterials, aerogels, zeolites, and metal-organic frameworks (MOFs). While this method provides safe storage, it's relatively energy-intensive. Absorption storage of hydrogen involves various metals and their alloys, which, under certain conditions, form metal hydrides with hydrogen. This storage method offers certain advantages in terms of safety while often providing comparable hydrogen volumes per unit compared to liquid hydrogen storage.

The aforementioned benefits of metal hydrides have led to their increasing importance as an alternative for safe and long-term hydrogen storage. Alloys based on rare earth metals, titanium, zirconium, magnesium, and other metals forming hydrides serve as the basis for new hydrogen storage materials. Depending on specific applications and operational parameters, appropriate alloys can be chosen from a portfolio of commercial and prototype metal hydride alloys. For instance, LaNi5 can absorb approximately 1.4 wt.% of hydrogen at room temperature, forming LaNi5H6 hydride, while some magnesium-based MH alloys can absorb up to 7.6 wt.% of hydrogen at temperatures in the hundreds of degrees Celsius.

Storing hydrogen in metal hydrides necessitates effective temperature management. During absorption, heat generated within the alloy volume due to molecular hydrogen cleavage and chemical bond formation needs to be dissipated. Conversely, desorption process kinetics rely on the amount of heat introduced into the alloy volume, which cools during desorption at the expense of its internal energy, significantly reducing hydrogen release kinetics. Effective heat transfer within the metal hydride bed can enhance the operational characteristics of MH storage systems and their competitiveness in the market. Commercial MH alloy storage systems are often equipped with active (using coolants for flow cooling) or passive cooling systems (fins, ribs, etc.), or a combination of both. Despite various solutions, heat exchangers are widely applied to address heat transfer issues in metal hydride beds due to their simplicity and efficiency. The cylindrical shape of MH storage systems allows for optimizing the number of pipes and selecting specific heat transfer structures. Extensive studies focus on selecting heat exchanger configurations and optimizing their performance.

2. Current state of knowledge in the field of cooling MH alloys

Systems for hydrogen absorption storage in metals and alloys face three main heat transfer problems. The first arises at the gas-solid interface during hydrogen absorption. Heat is generated due to the splitting of hydrogen molecules and their storage in the MH alloy structure as a result of ongoing chemical reactions. The second issue, and simultaneously a challenge for research, is the inefficient heat transport within the volume of the MH alloy due to its low thermal conductivity. The final question concerns the impact of the temperature of hydrogen-stored material particles on the equilibrium pressure.

The irregular shape of MH powder material particles introduces additional thermal resistance, especially with fine powders (average size ~10 microns), characterized by low thermal conductivity. Current research thus focuses on increasing the thermal conductivity of MH powder alloys, aiming for more effective thermal management during the cooling (hydrogen absorption phase) and heating of reservoirs (hydrogen desorption phase).

The local thermal effect of hydrogen absorption/desorption reactions can lead to a temperature spike, slowing down the kinetics of hydrogen storage and release. Consequently, during absorption, hydrogen consumption at the tank inlet decreases, extending the time required for the system to effectively fill with hydrogen. MH alloys operating at high temperatures may also face particle sintering, losing their ability to store hydrogen. Desorption is also dependent on operational conditions of the storage system and thermal management. In the absence of sufficient heat supply to the MH alloy volume, hydrogen desorption slows down, potentially halting entirely in extreme cases.

Enhancing heat transport within the volume of MH alloy can be achieved by improving the thermophysical properties of the MH alloy (e.g., mixing the alloy with expanded graphite or thermally conductive materials such as aluminum or copper) or expanding the surface of heat exchange areas in contact with the powder alloy (e.g., application of aluminum or copper fins, installation of a cooling fluid distribution system placed in the core of the MH alloy, placing a smaller volume of alloy into a more robust heat exchanger system capable of accumulating large amounts of heat - not recommended as it significantly reduces the practicality of the technology).

3. Shapes of MH containers

The shape of the metal MH storage vessel influences heat regulation within the metal hydride bed. A common high-pressure cylindrical-shaped tank is a suitable solution from both structural and strength perspectives for accommodating active and passive cooling elements within the volume of the metal hydride alloy [1]. Cylindrical terminations of the tanks can be easily manufactured and meet the strength requirements placed on the tanks. Tank production can be achieved through material forming and drawing processes (compact tanks) or by assembling individual parts using welding techniques. The most common construction design of an MH storage tank is depicted in Figure 1. In the case of the construction design shown in Figure 1a, above the metal hydride bed, there is free space from which hydrogen gradually diffuses under pressure into the volume of the MH alloy, where it is stored in its structure during absorption. Heat energy generation is not uniform throughout the volume of the MH alloy, with 100% saturation of the alloy with hydrogen occurring first in the upper layers, closer to the tank throat. A more even distribution of heat can be achieved with the tank design shown in Figure 1b, where hydrogen is transported along the entire length of the tank through a perforated tube, reaching the MH bed. From the perspective of their utility, a tank design with perforated tubes within the volume of the MH alloy is a more ideal solution for storing a larger quantity of hydrogen.

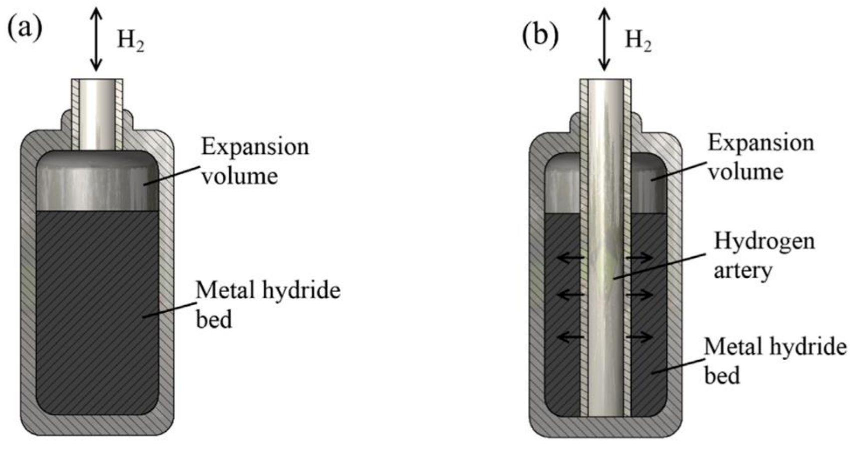

Figure 1. Basic Construction Designs of MH Storage Tanks:
a) Compact Tank, b) Tank with Perforated Inlet Pipe

The auxiliary active and passive cooling elements significantly influence the uniform distribution of the thermal field in the tank and MH bed, aiding in efficient heat dissipation during absorption and heat supply during desorption. These elements also impact the overall filling and emptying time of the tank.

During absorption, the MH alloy absorbs hydrogen and releases heat. Heat exchangers are responsible for efficiently dissipating this heat to maintain the desired operational temperature in the tank and ensure continuous absorption without an increase in tank or operating pressure levels. Heat exchange surfaces typically consist of bundles of tubes (or utilize an active cooling system circulating a cooling medium), or appropriately placed fins in contact with the metal hydride bed. In active cooling, a fluid circulates through these tubes (liquid or gas) to absorb heat generated during absorption. Conversely, during desorption, where hydrogen is released from the metal hydride, an external heat source is usually required to provide the necessary energy for the endothermic reaction. The heat exchanger facilitates heat transfer from the external source to the MH alloy volume, promoting hydrogen desorption and maintaining the ideal temperature for efficient hydrogen release.

Effective heat exchange between the tank and the surroundings is crucial for the overall efficiency and performance of the hydrogen storage system in MH materials. Thermal management ensures that the system operates within the desired temperature range for optimal hydrogen absorption and desorption kinetics. In most cases, cooling systems circulate a cooling fluid, and the thermal energy released or required for desorption is dissipated or supplied to/from the MH alloy volume through a tubular or plate heat exchanger. Heat exchangers are designed to increase the overall efficiency of the hydrogen storage system in the hydride bed by dissipating or supplying heat from/to the MH alloy volume based on recorded temperature changes in the tank.

Shell-and-tube heat exchangers: This type consists of a shell (large container) through which tubes pass. The metal hydride material can be placed in the tubes, and the cooling fluid flows around the heat exchange surfaces of these tubes (less commonly used cooling method). Alternatively, tubes can be placed within the MH alloy volume, and a heat transfer fluid (liquid) circulates in the tubular heat exchanger.

Plate heat exchangers: These exchangers consist of pressed flat plates with good thermal conductivity, defining the size of the heat exchange surface. The alloy and cooling fluid are alternately placed in the exchanger. The design is compact and efficiently transports heat but has a disadvantage of low gravimetric density of stored hydrogen.

Coil-in-tank heat exchangers: In this configuration, coil pipes are placed inside a tank containing the metal hydride bed. Heat transfer fluids flow through the tubular heat exchanger, facilitating heat exchange. Heat exchangers with active cooling often include control systems to monitor and control the temperature of the metal hydride bed during hydrogen absorption and desorption. This control helps optimize the hydrogen storage and release process.

Passive cooling elements rely on natural heat conduction and convection without the need for an external energy source to ensure their reliable operation. They may have a simpler design compared to flow-through cooling systems but have lower operational efficiency.

Fin heat exchangers: These exchangers have fins in direct contact with the hydride bed, typically absorbing heat generated within the volume and directing it from the core of the MH alloy towards the tank shell, which is usually cooled by a cooling fluid. Fins increase the heat exchange surface area and promote better heat transport through natural convection. Passive heat exchangers do not require external energy sources for operation, making them simpler and potentially more reliable in certain applications.

Tubular heat exchangers circulate cooling fluid in the tank during hydrogen absorption. Research primarily focuses on the possibility of using straight and helical tubes, or U-tubes. Many studies aim to optimize the number of tubes required for effective temperature management inside the tank. Based on previous research, it's noted that using a helical heat exchanger significantly increases the heat transfer coefficient compared to a similarly sized straight tube heat exchanger. The potential application of helical heat exchangers in cylindrical metal hydride storage tanks was studied by Mellouli S. et al. [2]. The authors considered the mass flow rate, cooling fluid temperature, applied pressure, and volume of the hydrogen tank. The study results demonstrate that the absorption and desorption times of cylindrical metal hydride tanks are significantly reduced when using a helical heat exchanger (Fig. 2).

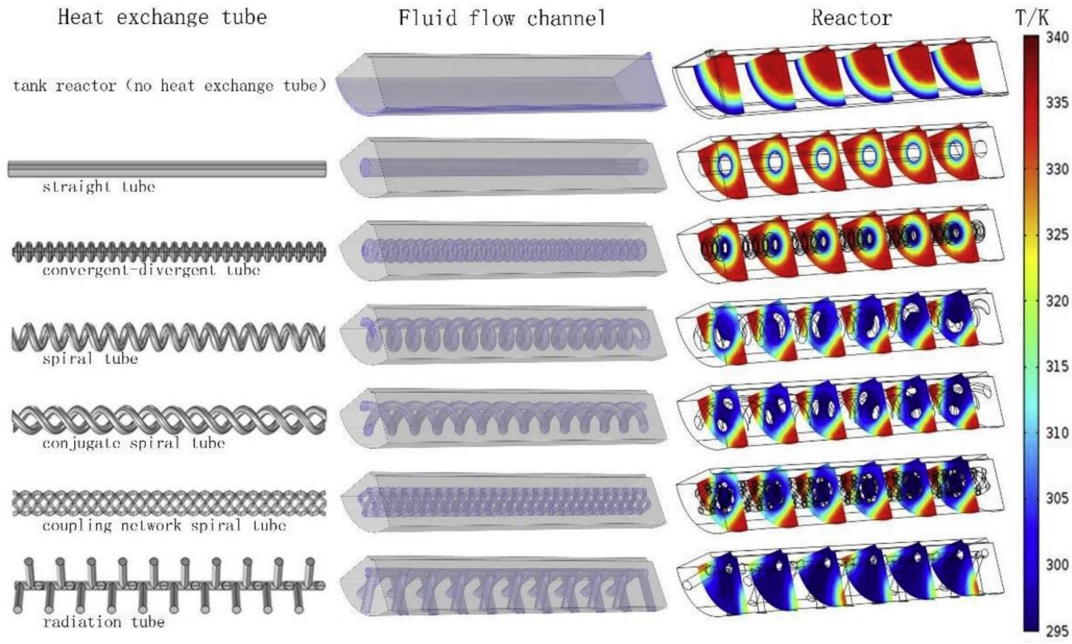

Figure 2. Designs of heat exchangers and the influence of the design on the average temperature of the bed.

Mohan G. et al. [3] investigated the impact of various material properties on the performance of a metal hydride storage unit equipped with multiple cooling tubes. It was found that the hydrogen absorption process is primarily influenced by the absorption rate constant, activation energy, and thermal conductivity.

Mahmoodi F. et al. [4] explored a finned U-shaped heat exchanger in a solid-state hydrogen storage system. The study revealed that increasing the diameter of the tube enhances the heat transfer performance. Additionally, the authors examined the influence of the number and thickness of fins on the storage unit's properties.

Further geometry modifications for the tubes were proposed by Larpruenrudee P. et al. [5]. They numerically studied a magnesium-based metal hydride storage unit with a modified semi-cylindrical spiral as a heat exchanger. Hydrogen absorption time was reduced by 60% compared to a simple spiral tube construction. The authors also observed that decreasing the axial rise of the spiral reduced the hydrogen absorption rate.

Keith M. D. et al. [6] conducted numerical simulations on several configurations of a Ti1.1CrMn-based metal hydride storage unit with a single cooling tube passing through it multiple times. The cooling tube fins were made of aluminum with a wall thickness of 1 mm, evenly distributed around the central part of the storage unit. Tested configurations included 2, 3, 4, 5, 6, 9, 12, and 18 tube heat exchangers. The criterion for determining the optimal number of fins was the ratio of fin length to its width. Adding fins significantly reduced the hydrogen refueling time by 56% to 68%. The authors also concluded that using more than nine cooling tubes in the storage unit is inefficient for hydrogen refueling.

4. Heat transfer through ribs

The use of internal or external fins is a common method to enhance heat transfer in metal hydride alloys. External fins facilitate natural convection. It is evident that compared to cooling tubes, external fins exhibit inferior heat transfer performance, and this solution is less efficient than internal finning. Internal fins provide a larger heat exchange surface area. Typically, internal fins are used in conjunction with cooling tubes. This approach significantly increases the heat transfer area, divides the metal hydride bed into separate domains, and provides better local thermal conductivity. Fins can have various shapes and can be arranged in different ways within the cylindrical metal hydride bed, enabling researchers to design a vast array of configurations.

The combination of external and internal fins was utilized in a storage tank model proposed by Nyamsi S.N. et al. [7]. Through numerical methods, the authors investigated the dehydrogenation performance of a cylindrical metal hydride storage tank filled with 300 g of ground Mg90Ti10 + 5 wt.% °C. By employing a pan-finned heat exchanger without internal cooling tubes, the authors achieved power outputs ranging from 100 to 250 W with nearly constant flow rates.

Parida A. and Muthukumar P. [8] proposed a numerical model to compare the performance of three different fin configurations (longitudinal, transverse, and spiral finning). The authors found that longitudinal fins provide better heat dissipation during the initial absorption phase. Conversely, transverse finning showed superior results during hydrogen desorption. However, all fin configurations exhibited similar performance during simulation at various operating temperatures.

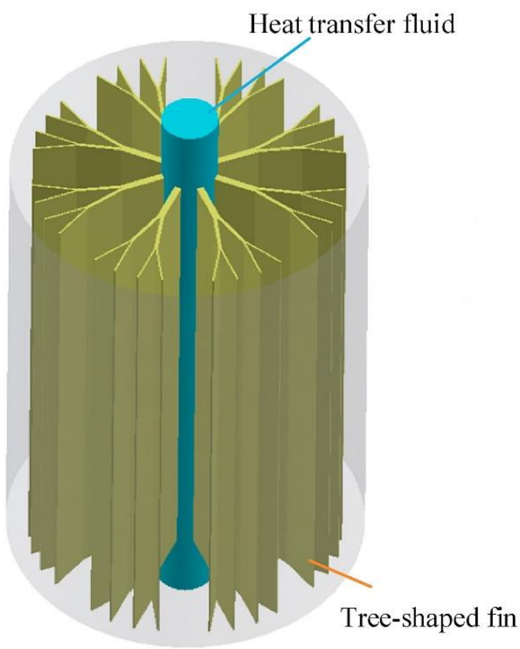

Figure 3. A tree-shaped finned heat exchanger designed by Bai et al. [12]

The design and investigation of a metal hydride storage tank inspired by leaf veins were conducted by Krishna K. V. et al. [9], while Bai X. S. et al. [12] proposed longitudinal tree-shaped fins (Fig. 3). A genetic algorithm was employed to optimize structural parameters (length, width, and branch angle). The authors compared the optimized tree-shaped fin heat exchanger with a radially finned heat exchanger. The tree-shaped fin heat exchanger exhibited superior absorption efficiency compared to the radially finned one.

Simulation results showed a 20% increase in absorption and desorption rates with the optimized tree-shaped fins compared to conventional longitudinal fins.

5. Conclusions

In the development of low-pressure hydrogen storage systems, addressing heat exchange issues in metal hydride alloys is pivotal. Numerous studies have focused on enhancing heat dissipation through the application of various passive and active cooling elements. Several conclusions can be drawn from the analysis of scientific literature. Spherical-shaped tanks exhibit slightly higher hydrogen storage efficiency compared to cylindrical ones, although the difference is negligible, making both suitable for hydrogen storage. However, cylindrical tanks are more practical, leading to their significant prevalence in reviewed literature.

Another method to improve heat transfer in metal hydride storage tanks is the utilization of metallic foams. While their integration can impede hydrogen diffusion and notably reduce tank capacity, metallic foam additives have proven effective for small-scale laboratory hydrogen storage systems and mobile applications. However, their suitability diminishes for medium and large hydrogen storage systems. Combining metallic foams with finning or cooling tubes leads to significantly more efficient heat dissipation during hydrogen absorption.

When selecting the number and configuration of cooling tubes in metal hydride storage tanks, overall geometric dimensions must be considered. Increasing the number of cooling tubes positively impacts heat transfer within the metal hydride alloy, and hydrogen absorption rate due to enlarged heat exchange surface area. However, excessive augmentation of cooling tubes doesn't yield significant improvements. Spiral cooling tubes generally outperform straight tubes in heat dissipation from the tank, with tube diameter and spiral size being critical factors influencing heat transfer.

Implementing annular-shaped heat exchangers proves to be an effective choice for enhancing cooling or heating performance compared to standard solutions. Optimal performance is achieved when the ring symmetrically divides the tank volume, halving the thickness of the metal hydride layer. Larger contact areas of passive cooling elements with the metal hydride alloy increase heat transport efficiency from the core of the MH alloy towards the tank casing. Increasing the number, thickness, and diameter of fins generally facilitates more efficient heat dissipation. In the case of longitudinal fins, straight and tapered fins demonstrate good performance.

Ensuring effective thermal contact between the cooling medium and MH alloy is crucial for successful cooling. Implementation of highly conductive materials and efficient structures is necessary to minimize conductive heat losses.

- Conductive losses arise due to direct heat transfer between the MH tank and the cooling medium.
- Convection losses result from the movement of the cooling medium and its interaction with the surface of the MH tank. Expertly designed flow of the cooling medium and the use of special surface treatments can significantly reduce convection losses.
- Radiative losses are associated with the emission and absorption of heat flow between the MH tank and the surrounding environment. The use of insulation materials and techniques is crucial for minimizing radiative losses to a minimum.

Acknowledgments: This paper was written with financial support from the VEGA granting agency within the projects no. 1/0224/23 and no. 1/0532/22, from the KEGA granting agency within the project no. 012TUKE-4/2022 and with financial support from the APVV granting agency within the projects no. APVV-15-0202 and no. APVV-21-0274.

References

1. Sreeraj, R.; Aadhithiyan, A.K.; Anbarasu, S. Integration of Thermal Augmentation Methods in Hydride Beds for Metal Hydride Based Hydrogen Storage Systems: Review and Recommendation. J. Energy Storage 2022.
2. Mellouli, S.; Askri, F.; Dhaou, H.; Jemni, A.; Ben Nasrallah, S. A Novel Design of a Heat Exchanger for a Metal-Hydrogen Reactor. Int. J. Hydrogen Energy 2007.
3. Mohan, G.; Prakashmaiya, M.; Srinivasamurthy, S. Performance Simulation of Metal Hydride Hydrogen Storage Device with Embedded Filters and Heat Exchanger Tubes. Int. J. Hydrogen Energy 2007.
4. Mahmoodi, F.; Rahimi, R. Experimental and Numerical Investigating a New Configured Thermal Coupling between Metal Hydride Tank and PEM Fuel Cell Using Heat Pipes. Appl. Therm. Eng. 2020.
5. Larpruenrudee, P.; Bennett, N.S.; Gu, Y.; Fitch, R.; Islam, M.S. Design Optimization of a Magnesium-Based Metal Hydride Hydrogen Energy Storage System. Sci. Rep. 2022.
6. Keith, M.D.; Kukkapalli, V.K.; Kim, S. Phase Change Cooling of a Metal Hydride Reactor for Rapid Hydrogen Absorption. Energies 2022.
7. Nyamsi, S.N.; Wu, Z.; Zhang, Z.; Kolesnikov, A.; Lototskyy, M.V.; Pasupathi, S. Dehydrogenation Performance of Metal Hydride Container Utilising MgH2-Based Composite. Appl. Therm. Eng. 2022.
8. Parida, A.; Muthukumar, P. Reactor Design and Numerical Study on Metal Hydride Based Finned Reactor Configurations for Hydrogen Compression Application. Int. J. Hydrogen Energy, 2023.
9. Krishna, K.V.; Pandey, V.; Maiya, M.P. Bio-Inspired Leaf-Vein Type Fins for Performance Enhancement of Metal Hydride Reactors. Int. J. Hydrogen Energy 2022.
10. Xiao-Shuai Bai, Wei-Wei Yang, Xin-Yuan Tang, Fu-Sheng Yang, Yu-Hang Jiao, Yu Yang. Optimization of Tree-shaped Fin Structures Towards Enhanced Absorption Performance of Metal Hydride Hydrogen Storage Device: A numerical study, Energy 2021.
11. Yuan, J.; Yao, M.; Zhao, B.; Lv, Y.; Huang, H.; Chen, J.; Liu, B.; Zhang, B.; Wu, Y. Influence of Heat Exchanger Structure on Hydrogen Absorption-desorption Performance of Storage Vessel. Prog. Nat. Sci. Mater. Int. 2022.
12. Bai, X.S.; Yang, W.W.; Tang, X.Y.; Yang, F.S.; Jiao, Y.H.; Yang, Y. Optimization of Tree-Shaped Fin Structures towards Enhanced Absorption Performance of Metal Hydride Hydrogen Storage Device: A Numerical Study. Energy 2021

TECHNICKÁ UNIVERZITA V KOŠICIACH
Strojnícka fakulta

Technical cleanliness audit - a tool for eliminating risks resulting from unwanted contamination

Róbert Jánošík

Certified Auditor of Technical Cleanliness; info@cleanlinessaudit.com
* Correspondence: janosik@cleanlinessaudit.com
Tel.: +421 911 868 200)

Abstract: Technical cleanliness in industry is an increasing problem due to the growing trend towards clean environments and the demands on technology, and therefore appears as standard in the specifications of manufacturers in the electronics industry, the automotive industry as well as the aerospace industry.

Several methods have been defined to control contamination, but none is universal enough to eliminate the risks of contamination. The aim is to eliminate possible risks to the functionality of manufactured products so that possible contamination during manufacture or operation does not lead to failure and possible safety hazards for consumers and users of the products in question.

Using the right methodology to detect unwanted contamination can effectively reduce the cost of manufacturing errors and defects and significantly eliminate potential failure risks. Using the right methodology to detect unwanted contamination can effectively reduce the cost of manufacturing errors and defects and significantly eliminate potential failure risks. However, which is the right contamination detection methodology is questionable and much depends on what we want to achieve with the right detection. So what is the goal of clean manufacturing plant analysis?

Keywords: Technical cleanliness in processes, Technical cleanliness audit, Sedimentation analysis in processes, Sedimentation coefficient determination, Clean environment, Verification of a clean environment, Validation of a clean environment, Cleanroom, Clean zone

1. Introduction

In the field of modern industry, the concept of technical cleanliness is of paramount importance. Precision, accuracy, and reliability are paramount for ensuring the quality of products. Technical cleanliness, defined as the absence of foreign particles and residues that can affect the functionality, reliability or durability of a product, goes beyond mere order. It is a rigorous standard followed in a variety of industries including automotive, aerospace, medical and electronics. This article discusses the nuances of technical cleanliness, its importance, methodologies, and emerging trends.

The importance of technical cleanliness:

Technical cleanliness is not just about aesthetics, but also about ensuring optimum performance, durability and product safety. In industries such as automotive and aerospace, where precision and reliability are a priority, even minute contaminants can cause catastrophic failures. Nowadays, with the demand for electrification of transport and the demand for the production of electric vehicles growing significantly, as well as the trend towards the use of electricity as one of the propulsion alternatives in both the automotive and aerospace industries to reduce emissions, the risk of potential contamination and non-compliance with technical cleanliness requirements poses a huge safety problem. For example, in car manufacturing, contaminants such as dust, metal shavings or lubricants can damage electrical components or engine parts, which can lead to problems with vehicle quality, reliability and safety. More widespread failures lead to costly recalls or even the loss of a company's reputation. Similarly, in the aerospace sector, a dust storm can compromise sensitive instruments or machinery, jeopardizing mission success and passenger safety. Therefore, Technical Cleanliness needs to start to be seen as a system made up of multiple, interrelated factors. On a global scale, the state of cleanliness of the component itself, as well as the state of cleanliness of the surrounding environment, should be seen as the fulfilment of the requirements for Technical Cleanliness.

Why component cleanliness and how to influence it positively?

Contamination of products can lead to their deterioration. Therefore, it is necessary to constantly check the purity of the product and choose the correct method to control contamination through sampling. From Picture no. 1 it is possible to see one of the methods of separating the contamination from inside the parts, by means of flushing the part in special cabinets. With correctly set parameters of the rinsing cabinet, it is possible to increase the efficiency of the extraction of dirt from the surface of the component [1].

If, based on risk management and the assumption of possible product failure, we can predict the outcome - the failure - it is possible to determine with a high probability the appropriate methodology for detecting contamination on the product. In fact, it is important to determine the appropriate detection method so that, based on the detection of contamination, we can focus on the factors that affect the purity of the product and can then determine appropriate and effective measures to potentially eliminate the contamination of the product.

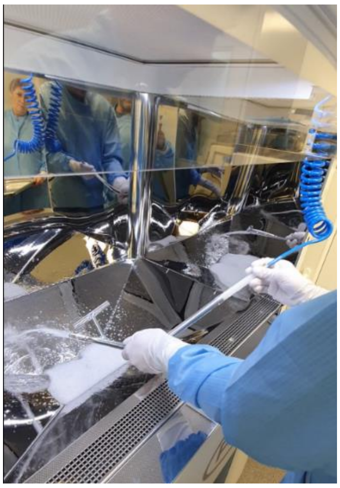

Figure 1 - Extraction of contamination from the product

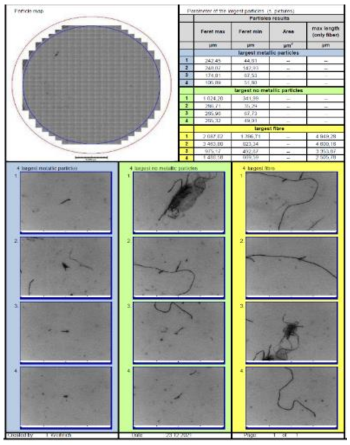

Figure 2 - Results from the extraction of impurities

As can be seen from Picture 2, solid particles as well as fibers were detected after extraction. If the particles were soft and non-conductive, such contamination would not pose as great a risk to us as conductive and hard particles. With hard and conductive particles, there is a risk of electrical components being knocked out, which can have fatal consequences when incorporated into the safety features of cars or aeroplanes. The results from the extraction of impurities are used to detect the causes of pollution [2].

Our task is to set up and implement knowledge-based tools that enable us to positively influence the reduction of product contamination and thus positively influence the level of risk affecting product quality, reliability and safety. However, we must also take into account the environment that surrounds the products during production and use.

Why environmental cleanliness and how to influence it positively?

Another important factor influencing technical cleanliness is the environment itself. Many factors enter into our technical cleanliness system, such as handling, human factor, surrounding environment, maintenance and condition of production lines, component packaging and transportation system, storage and assembly. To single out any one of these factors would be to focus on a narrow potential of possible causes, and we often end up missing the next sequence of significant disagreements. It often happens that under the term clean space in organizations, they imagine cleanliness at the 5S level and the provision of clean air through the regular replacement of air conditioning filters. Many times, after the filters have been replaced, the air-conditioning system is checked and possibly the representatives of the construction companies approve the cleanliness of the installed space based on the measurements taken by the contractor himself. Often times, "only" control of the operation of the air conditioning is carried out and, based on the results, a clean environment is declared. Unfortunately, we do not take into account:

- sedimentation,
- air flow of air in an empty room,
- air flow in the room where machines and equipment are already installed,
- introduction of contamination by personnel,
- introduction of contamination by packaging.

This was the reason to think about a control methodology that would be more appropriate and possibly also take into account the probability of possible contamination in a clean environment.

2. Materials and Methods

Based on knowledge from the past and practical implementations, we came to the opinion that it would be beneficial if, with the aim of building a clean space and regulating a clean zone, clients could independently assess the state before the introduction of the clean zone and the state after the introduction of the clean zone with a simple tool. Nowadays, it is a great benefit if it is possible to assess the state of operation directly in production and at the same time the results can be shared with the management of the organization. It is important that the assessment of the reviewed state is based on evidence and that it is possible to proactively reveal weak points in the system with one tool. Alternatively, under one tool, also apply corrective measures in the event of undesirable conditions.

For the sake of prevention and deployment of flexible tools, simple software was developed to perform Technical Cleanliness checks with the aim of:

- check the current status in the verified operation,
- document and visualize the current status of the inspected operation,
- determine the probability of the possible level of contamination in the inspected operation, which may result in the production of contaminated and defective products,
- determine critical factors affecting technical purity and the degree of increased contamination,
- make it possible to define and share the results of the system inspection and proposed corrective measures in the online space.

An effective tool to detect potential increased contamination in the work environment is the performance of Technical Cleanliness audits [3]. Part of the combined audit of Technical cleanliness is also the measurement of contamination of light particles in the air, as can be seen in picture no. 3

Figure 3 - Technical cleanliness audit

Figure 4 shows the results of the Technical Cleanliness audit, according to which it is possible to predict the potential level of contamination in the checked area of the clean zone.

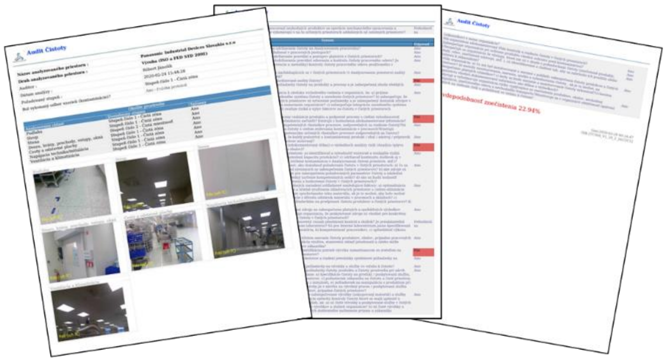

Figure 4 - Output from the Technical Cleanliness Audit

The output from the complex audit, including the output from the analyzes of sedimentation samples, is a detailed report indicating the state of contamination in the inspected environment, and at the same time it is possible to detect risk factors in the inspected area. In the case of sampling, it is possible to analyze the type of contamination, from which the cause and origin of pollution can be determined through standard analyzes or additional spectral analyses [4].

3. Results

If we want to prevent disagreements and have the production of products in new, technologically demanding processes under control, it is necessary to introduce effective tools for monitoring the status of processes. Nowadays, when the production of precise and technologically demanding products is coming to the fore, which are supposed to make our everyday life easier and help in progress and development, it is necessary to have every step of the production and assembly under control. We are surrounded by more technologically sophisticated products that help us in making difficult decisions, therefore it is necessary to have these technologies under control, and the production of hardware for each of the technically advanced devices today requires constant and controlled monitoring of conditions that could negatively affect their reliability and quality. Efficiency and profitability still need to be taken into account. Therefore, timely prevention in the implementation of regular checks in combination with the evaluation and analysis of risks results in high reliability, which helps us maintain client satisfaction and a good reputation on the market. But the most important parameter is the effective prevention of non-conformities directly in the production process, where with a simple approach such as the Technical Cleanliness Audit, we significantly reduce the risks of unwanted contamination and increase the reliability of our production. The results of a study where Technical Cleanliness Audits were deployed through our software showed that the cost of complaints and non-delivery due to contamination was lower by more than 80% compared to regular checks and measurements of air conditioning in clean rooms.

4. Discussion

Since the issue of technical cleanliness and clean rooms in industry is a relatively new topic, it is still necessary to leave room for discussion in a wider context. It will be important to ensure the necessary awareness in companies as soon as possible about the possible consequences of not securing the specifications related to the observance of the parameters of a clean environment and Technical cleanliness. The risks related to the uncontrolled contamination of the space as well as the components have not only an economic dimension but also a security dimension, where the biggest risk is system failure with fatal consequences. It is essential to give this issue enough space for professional discussion.

Conflicts of Interest:
"The authors declare no conflict of in-terest."
"The funders had no role in the design of the study; in the collection, analyses, or interpretation of data; in the writing of the manuscript, or in the decision to publish the results".

References

[1] Extraction of contamination from the product – InterTribodia s.r.o.

[2] Results from the extraction of impurities – CRL Silesia, s.r.o.

[3] Audit performance of Technical cleanliness in electrotechnical operations – Cleanliness Certification Center s.r.o.

[4] Output from the Technical Cleanliness Audit – Cleanliness Certification Center s.r.o.

TECHNICKÁ UNIVERZITA V KOŠICIACH
Strojnícka fakulta

Technologies increasing torsional vibration of the crankshaft and methods of their elimination

Matúš Kačír[1], Lucia Žuľová[2], Robert Grega[3]

[1] Technickáuniverzita v Košiciach, Strojníckafakulta, Katedra konštrukčného a dopravnéhoinžinierstva, matus.kacir@tuke.sk
[2] Technickáuniverzita v Košiciach, Strojníckafakulta, Katedra konštrukčného a dopravnéhoinžinierstva, robert.grega@tuke.sk
[2] Technickáuniverzita v Košiciach, Strojníckafakulta, Katedra konštrukčného a dopravnéhoinžinierstva, robert.grega@tuke.sk

Abstract: Torsional oscillation of the output shaft of the combustion engine occurs as a result of fluctuating torque. Therefore, the designers of internal combustion engines try to minimize torsional vibration of the crankshaft as much as possible and reduce vibrations in vehicle. Along with torsional vibration, the risk of failure of the powertrain components also increases. In order to comply with emission standards, technologies to reduce the production of emissions were applied to cars. However, emissions reduction effects in the form of increased torsional vibration of the crankshaft. Therefore, it is necessary to deal with the origin and possibilities of elimination the torsional oscillation of combustion engines as best as possible. Torsional oscillation eliminators applied to vehicles are at the limit of their possibilities and this leads to the need to consider other options that will be more suitable for the current requirements of torsional oscillation elimination. The most common component for eliminating torsional vibration is a dual-mass flywheel. The proposed possibility is a change in the flexible components of the dual-mass flywheel to achieve higher torsional vibration damping efficiency.

Keywords: dual mass flywheel, torsional vibration, elimination of torsional vibration

1. Introduction

Four-stroke combustion engines work in four periods: intake, compression, expansion, and exhaust. During the operation of the engine, due to the influence of the exhaust gas pressure and the position of the crankshaft, there are changes in the speed of the movement of the piston and a change in the speed of rotation of the crankshaft. Changing the speed of rotation of the crankshaft creates torsional oscillations, which are manifested as vibrations. From Otto's ideal cycle, it is obvious that the pressure above the piston changes, which also affects the speed of rotation of the crankshaft. [1]

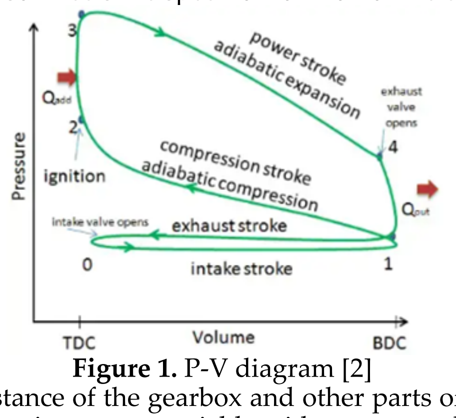

Figure 1. P-V diagram [2]

If we consider the resistance of the gearbox and other parts of the drive mechanism to be irrelevant, then the most important variable with respect to the speed of rotation of the crankshaft is the force acting on the piston caused by the expansion. The analysis of the rotation of the engine crankshaft with respect to the acting forces is shown in fig. 2. From the graph, we can see the tangential load due to gas pressure above the piston, the inertia forces and the resulting tangential force acting on the connecting rod of the crankshaft at an engine speed of 2000 rpm. [3, 4]

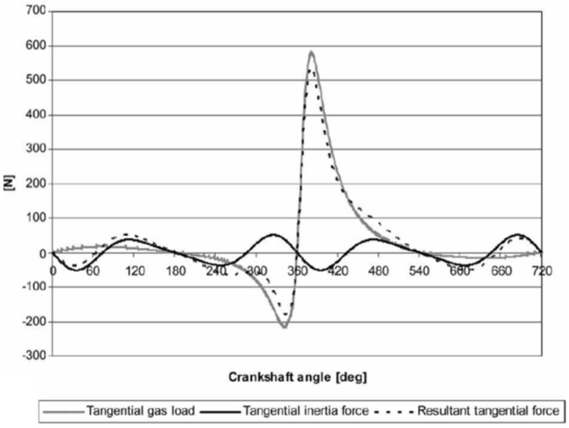

Figure 2. Force diagram of tangential forces at engine speed of 2000 rpm [4]

Vibrations caused by irregular rotation of the crankshaft can cause damage to vehicle components in the drivetrain. That is why the designers try to eliminate these torsional oscillations or vibrations as much as possible for the sake of driving comfort, but also to reduce the wear of individual components of the drive system. Maintaining torque and engine power with a smaller number of cylinders is only possible if we increase the pressure on the piston during expansion, which causes a lower frequency but higher amplitude of torsional oscillations [3, 4].

2. Technologies increasing torsional oscillation

Due to the environmental pressure on the production of emissions, engine designers proceeded with structural and technological changes in internal combustion engines, which caused an emphasis on the torsional vibration of the crankshaft. Those technologies are, for example:

Downsizing

The main idea of downsizing is construction of an engine with a smaller number and volume of cylinders while maintaining power and torque. This technology will guarantee a reduction in heat losses, a reduction in friction, which results in a reduction in fuel consumption. Figure no. 3 shows the change in torsional oscillation frequency for engines with different number of cylinders. [5]

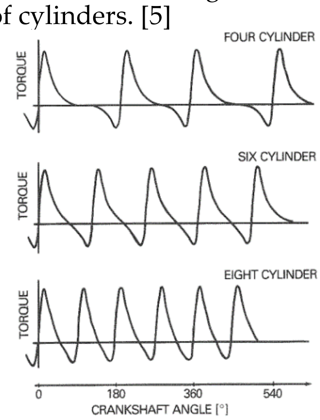

Figure 3. Torque course for engines with different number of cylinders with the same displacement [5]

Engine supercharging

Engine supercharging is directly related to downsizing in order to maintain engine performance. The task of supercharging is to get the largest possible volume of air into the cylinder space, respectively to increase the pressure in the cylinder. The result is a higher torque compared to atmospheric combustion engines of the same volume. A larger volume of air when injecting the same amount of fuel means an increase in performance while maintaining fuel consumption. The principle of supercharging the engine using a turbocharger is shown in fig. 4.[6]

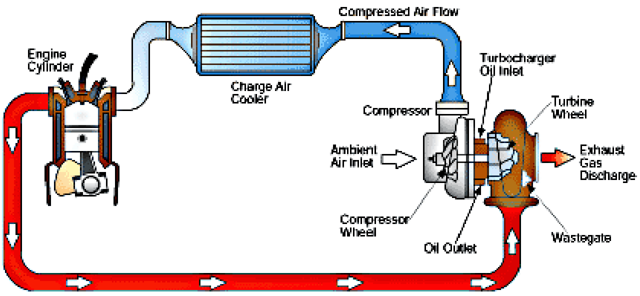

Figure 4. Supercharging the engine with a turbocharger [6]

Cylinder deactivation

Cylinder deactivation is carried out by turning off (closing) the valves, blocking the injector or ignition. When the cylinders are deactivated, the smoothness of the engine's operation changes and the occurrence of torsional oscillations increases, as the characteristics of the engine also change. During the deactivation of the cylinders, the resonance area moves to the engine's operating speed, while the torsional oscillation eliminators cannot respond appropriately to this fact. The displacement of the resonance when deactivating the cylinders is shown in fig. 5. [7, 8]

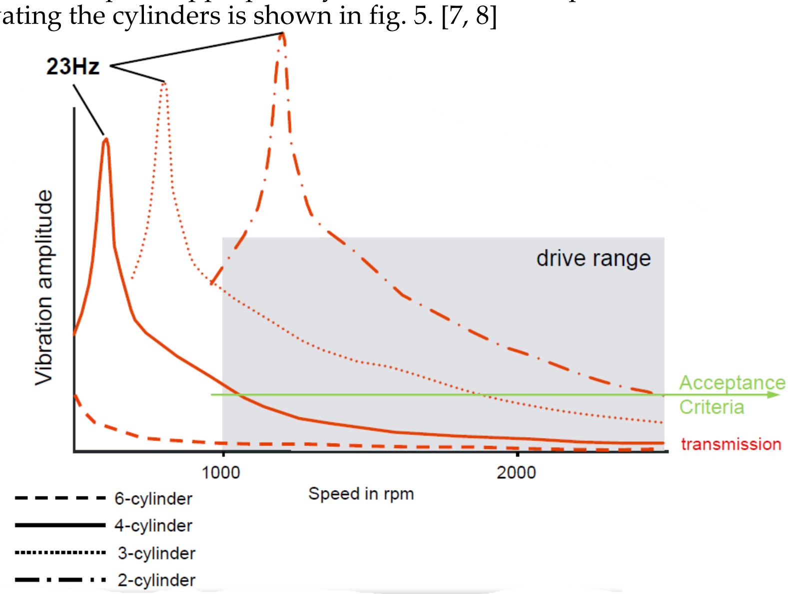

Figure 5. Changing the position of resonance when deactivating cylinders [7]

3. Elimination of torsional vibrations using a dual-mass flywheel

A dual-mass flywheel (DMF) is a rotating mass that is divided into two separate disks. The pair of disks is connected to each other by a damping element designed to eliminate torsional oscillations originating from the crankshaft. The difference between two-mass flywheels is in flexible elements. [9, 10]

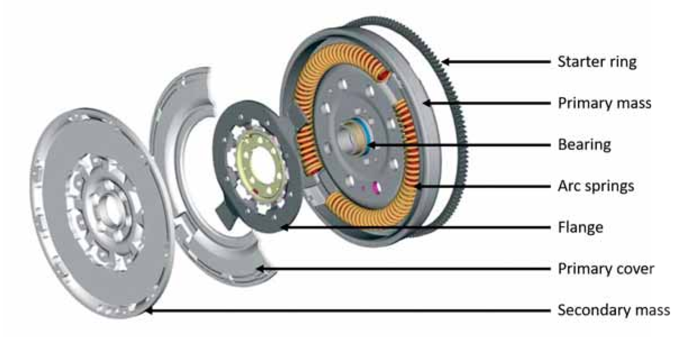

Figure 6. Components of a dual-mass flywheel[10]

The springs placed between the masses of the flywheel also determine its characteristics. By combining different numbers of compression springs with different stiffnesses, better DMF properties can be achieved. The soft initial run-up ensures excellent engine behavior when starting and shutting down. The harder grades provide effective torsional vibration elimination and sufficient overload protection at normal driving speeds. In fig. 6 is a comparison of the load characteristics between the DMF with two spring rates (blue curve) and three spring rates (red curve). [11, 12]

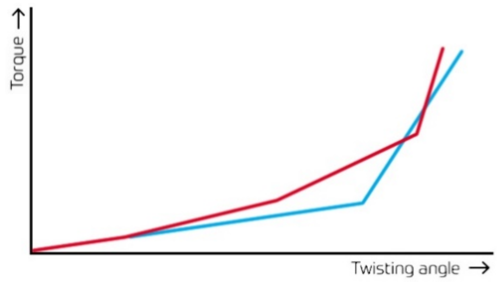

Figure 7. Characteristics of dual mass flywheels [12]

4. Proposal to change the design of the dual-mass flywheel

All currently used two-mass flywheels have a linear characteristic, or a characteristic consisting of several linear characteristics. In any case, all dual-mass flywheels are produced and applied at the same time and they are tuned to a certain type of engine according to its main parameters (power, volume, maximum torque). Modern low-emission engines work in several modes. In addition to driving modes such as ECO, normal or sport, one or more cylinders can be deactivated while the engine is running, while the engine characteristics also change. However, dual-mass flywheels produced at the same time cannot react to this fact due to their characteristic, which is not possible during engine operation. We cannot influence the changes during engine operation; therefore it would be advisable to change the characteristics of the dual-mass flywheel when changing the engine mode.

One of the alternatives to reduce the torsional vibration of the crankshaft is to replace the dual-mass flywheel while driving, or to connect them while driving, but this is not possible with the current design of the engine and gearbox.

The second of the alternatives is to change the characteristics of the two-mass flywheel, or to change the stiffness of the elastic element so that the compression is not dependent on the force acting on the given elastic element. This means that the twist angle of the two-mass flywheel would not depend on the torque created between the individual flywheel masses. In such a case, DMF characteristic would not be a curve, but by changing the stiffness of the elastic element, it would be possible to change the characteristic according to the requirements. The elimination of torsional vibrations using a pneumatic coupling was discussed in the articles [13, 14, 15] Examples of characteristic changes are shown in fig. 8.

Figure 8. Possibilities of changing the characteristics of the dual-mass flywheel

If the constant stiffness springs were changed to an adjustable stiffness component, it would be possible to change the stiffness characteristic of the dual-mass flywheel according to the required conditions while the engine is running. Figure no. 9 shows the proposed change to the dual mass flywheel components.

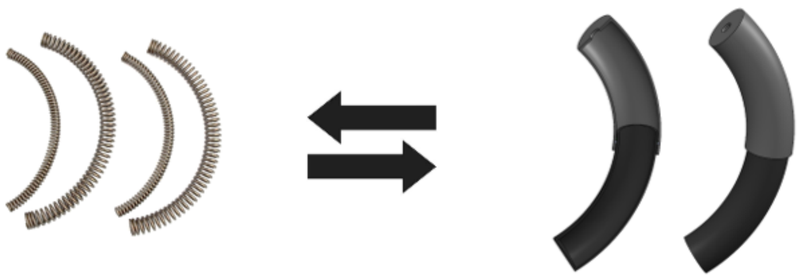

Figure 9. Proposal for changing the flexible components of the dual-mass flywheel

5. Conclusions

The comfort of traveling in car is constantly increasing and the requirements for eliminating vibrations are increasing, also as the requirements for the service life of the components are increasing. One of the components for eliminating vibrations is a dual-mass flywheel. From the investigation so far, it seems that the possibilities of conventional two-mass flywheels are probably exhausted, therefore it is necessary to think about the possibilities of applying new elements to the drive train of cars.

Technologies that are applied to vehicles due to requirements to reduce emissions have an adverse effect on the comfort of travel. Therefore, our aim is to propose options for ideally adaptation to conditions in real time during engine operation and thereby ensure more optimal engine operation, increased travel comfort and reduced wear and tear of vehicle drivetrain components.

Acknowledgments: This paper was written in the framework of Grant Project VEGA: "1/0528/20".

Conflicts of Interest: "The authors declare no conflict of interest."

References

1. HLAVŇA, Vladimír, Pavol KUKUČA, Rastislav ISTENÍK, Róbert LABUDA a Štefan LIŠČÁK. Dopravný prostriedok - jeho motor [online]. Žilina: Žilinská univerzita, 2000 [cit. 2023-06-23]. ISBN 80-710-0665-3. Dostupné z: http://katalog.utc.sk/e-books/books/pdf/Hlavna_Vladimir__Dopravny_prostriedok_joho_motor/dopravny_prostriedok_joho_motor.pdf
2. Seminář aplikované termomechaniky, [online]. 2009. [cit. 2023-11-26]. Dostupné z: https://www.vutbr.cz/elearning/course/view.php?id=80270>
3. TANG X., HU X., YANG W., YU H.: Novel Torsional Vibration Modeling and Assessment of a Power-Split Hybrid Electric Vehicle Equipped With a Dual-Mass Flywheel, 2018
4. MENDES, A. S., P. S. MEIRELLES a D. E. ZAMPIERI. Analysis of torsional vibration in internal combustion engines: Modelling and experimental validation. Proceedings of the Institution of Mechanical Engineers, Part K: Journal of Multi-body Dynamics [online]. 2008, 222(2), 155-178 [cit. 2023-06-23]. ISSN 1464-4193Author 1, A.B.; Author 2, C. Title of Unpublished Work. Abbreviated Journal Name stage of publication (under review; accepted; in press).
5. Solving the Powertrain Puzzle: 10th Schaeffler Symposium April 3/4, 2014 [online]. 10. Herzogenaurach, Nemecko: Springer Vieweg Wiesbaden, 2014 [cit. 2023-06-23]. ISSN 3-658-06430-3.

6. Janco, Marcel. Preplňovanie motora: Čo je to turbodúchadlo a ako funguje mechanický kompresor. Marcel Janco sudny znalec odbor cestna doprava [online]. 27.08.2017 [cit. 2023-06-23].Author 1, A.B. Title of Thesis. Level of Thesis, Degree-Granting University, Location of University, Date of Completion.
7. IHLEMANN, Arndt a Norbert NITZ. Cylinder Deactivation: A technology with a future or a niche application?. Schaeffler Symposium 2014 [online]. 2014, 172-187 [cit. 2023-06-23].
8. FRIDRICHOVÁ, K., DRÁPAL, L., VOPAŘIL, J. and DLUGOŠ, J. Overview of the potential and limitations of cylinder deactivation. Renewable and Sustainable Energy Reviews. 2021. Vol. 146, p. 111196. DOI 10.1016/j.rser.2021.111196
9. CHEN, L., ZENG, R. and JIANG, Z. Nonlinear dynamical model of an automotive dual mass flywheel. Advances in Mechanical Engineering. 2015. Vol. 7, no. 6p. 168781401558953. DOI 10.1177/1687814015589533
10. VALEO. Transmission Systems Dual-Mass Flywheel DMF valeoscope product focus. 2016
11. Long C, Wen-ku S, Song L, Zhi-yong C, Yuan-bin Y. Modeling of multistage nonlinear Dual Mass Flywheel torsional damper based on smoothing function fitting. Proceedings of the Institution of Mechanical Engineers, Part D: Journal of Automobile Engineering. 2021;235(1):32-42. doi:10.1177/0954407020951318
12. ZF Friedrichshafen AG. Clutch Systems. 2017
13. GREGA R, KRAJŇÁK J, BARAN P.: The Reduction of Vibrations in A Car - The Principle of Pneumatic Dual Mass Flywheel. In: Zeszyty naukowe Politechniki Śląskiej. No. 84. ISSN 0209-3324 (2014)
14. HOMIŠIN J[et al.]: Continuous tuning of ship propulsion system by means of pneumatic tuner of torsional oscillation. In: International Journal of Maritime Engineering: Transactions of The Royal Institution of Naval Architects. Vol. 158, no. Part A3. ISSN 1479-8751 (2016) GREGA R [et al.]: Analysis of the impact of flexible couplings on gearbox vibrations. In: Zeszyty naukowe politechniky Śląskiej: Seria Transport. Vol. 91, ISSN 0209-3324 (2016)
15. GREGA R [et al.]: Analysis of the impact of flexible couplings on gearbox vibrations. In: Zeszyty naukowe politechniky Śląskiej: Seria Transport. Vol. 91, ISSN 0209-3324 (2016)

TECHNICKÁ UNIVERZITA V KOŠICIACH
Strojnícka fakulta

Elements of the early warning system in business management in the pre-production PHASE

Štefan Kandráč [1], Jaroslava Kadárová[2, *]

[1] Technical University of Kosice, Faculty of Mechanical Engineering. Hlavna 9, 042 00 Kosice; stefan.kandrac@tuke.sk
[2, *] Technical University of Kosice, Faculty of Mechanical Engineering. Hlavna 9, 042 00 Kosice; jaroslava.kadarova@tuke.sk

Abstract: The issue of implementing a manufacturing activity from its initial stages through pre-production activities to actual production and post-production activities is a topic that can bring investors and managers several unforeseen obstacles. After the decision to implement the activity, the pre-production phase comes into play, which is addressed in this article based on a real investment plan. It shows how to navigate the individual activities of the pre-production phase from the perspective of risk anticipation and incorporating solutions into enterprise management. It discusses the individual phases of manufacturing activity in the production of composite materials with an emphasis on the pre-production phase. It addresses the threats of the pre-production phase and the stability of the system with a focus mainly on the scenario method and the use of lean management elements, the outputs of which it recommends being applied in management. The scenario method in its essence brings three alternatives for the development of the pre-production phase of the activity. Each of the scenarios assumes different development alternatives in the external and internal areas and, based on them, proposes a further course of action for the implementation of the activity in order to achieve the goal. The output of each scenario is recommendations for management and measures to prevent the occurrence of threats and disruption of the stability of the system, which will probably be more beneficial for achieving the goal of the activity than just focusing on specific risk events and their resolution.

Keywords: risk management; scenario; pre-production phase

1. Introduction

An enterprise in a market economy is a fundamental entity of entrepreneurship with precisely defined goals. It is influenced by both the internal and external environment. It is necessary to monitor key indicators at all times that may indicate a crisis [1].

Currently, the market environment is very difficult to predict with a high degree of uncertainty in planning. Developments in the political and economic spheres do not give much hope for early stabilization, which motivates investors and managers to be more cautious. This uncertainty emphasizes the need to deal with risk anticipation in every phase of manufacturing activity and to incorporate risk management insights directly into enterprise management principles. According to the results of the Institution of Risk Management [2], the interest in risk management in any sphere is growing every year.

For managers, it should be important to set a strategy to strengthen resilience and pay much more attention to risk assessment, monitoring symptoms of corporate crises, and proposing measures to reduce them. Risk anticipation and management is a high priority for new investments, in the pre-production phase, when it is appropriate to verify pre-investment calculations and timetables, as well as meeting the assumptions for the implementation of the production phase. Both external and internal. According to research by the American Institute for Crisis Management [3], more than half of corporate crises are caused by poor and ineffective problem solving by managers.

Serious corporate problems are caused by both managerial decisions and employee behavior.

2. Materials and Methods

One of the risk management methods that managers can use for early risk identification is scenario analysis [4,5]. Using this method, companies can reflect on the future development of the company from an optimistic, pessimistic and realistic perspective. Based on a thorough analysis, they can predict risks, their consequences and propose measures to minimize the expected changes. When applying the method, it is necessary to take into account the quality and quantity of changes in the internal and external environment of the company's development. Identification of symptoms, indicators and reaction to them should be an important part of strategic enterprise management.

Stages of Manufacturing Enterprise Management [6]:

- pre-production phase – definition, preparation;
- production phase – start, implementation;
- post-production phase – guarantees, claims, service, waste disposal.

Pre-production phase – the task of this phase is to explore the opportunities and assess the feasibility of the given intention. It also includes the processing of various analyzes and studies. Its contents usually include two types of documents:

- study of opportunities - its task is to determine whether the time is right for the implementation of the given intention, to evaluate the situation in the organization, on the market, the expected development of the market, the company, etc.;
- feasibility study - if the organization has decided to implement the given project, this study should determine the most suitable way to implement the project, specifies the content, planned dates of individual milestones, costs, necessary resources, opportunities, threats.

And after evaluating the documents from these documents:

- the start of trial operation - the start-up part of this phase, the need to verify and specify goals, required outputs, conditions and implementation procedures, staffing, competencies, etc.
- Production phase:
- start of production – after carrying out the preparatory phase in the stage of securing production documentation for individual selected products and secured material and energy inputs, as well as personnel and financial security of production, ownership of all decisions regarding the operation itself, it is possible to start trial production, the aim of which is is to make and test individual products. Subsequently, after possible corrections, the products can be certified;
- start of serial production – After certification of the products and ensuring their sales through contracts, it is possible to start serial production. In this phase, the company mainly manages and controls material inputs, deadlines and quality of outputs and the level of costs – elements of lean management ensuring the optimization of expenses. There is a sale of manufactured products and other development, business and marketing activities. The company manages inputs and outputs and monitors, among other things, selected indicators warning of possible threats and risks.

How to behave and navigate in the prevention or solution of risk situations in the pre-production phase?

The tasks of the early warning system can be identified with the risk management process. Risk management represents the coordination of management and control activities of the organization with regard to risks. From an early warning system perspective, risks can be seen as sources of early warning signals, if not as the signals themselves. Therefore, it is possible to start from the principles and structure of risk management when creating an early warning system [7].

An important methodological starting point is the assumption that frequent unpredictable changes in the external and internal environment are a source of risks and cause a greater need for resistance and prevention in the company than before. Based on this, it is possible to make the assumption that despite the negative effects of the environment, it is necessary to identify potential risks and reduce the consequences of adverse situations. This is possible mainly through the effective application of risk management using some proven methods and techniques, e.g. by analyzing scenarios. The comparison of previous knowledge and approaches to the management of risks and corporate crises confirms the high topicality of the issue being addressed.

The key methodological tool is the processing of the company's own management study in the conditions of the pre-production, production and post-production phase using scenario analysis in an effort to optimize processes based on the expected development in the external and internal environment of the company. New techniques related to systemic issues, assumption testing and scenario-based SRA are likely to be more beneficial to processes than just focusing on specific risk events.

For this, it is possible to use, for example, methods:

- analysis of relevant sources, studies, current knowledge and approaches,
- analysis of own experience from practice and from the academic environment in the form of solving scientific projects,
- analysis of scenarios (optimistic, realistic and pessimistic),
- analysis of cash flows,
- examination and assessment of processed results,
- synthesis of proposed measures and prediction of cash flow and management systems after taking corrective measures.

When processing the study, we can use the procedure of business management in crisis [8]: 1. Identification of symptoms and causes of the crisis, 2. Analysis of scenarios and taking measures with regard to the short-term survival of the business (management of cash flow to overcome the crisis), 3. Taking measures with regard to long-term development of the company (defining the strategy and adopting the operational plan), 4. Implementation of measures with regard to the long-term development of the company (change management) (see Figure 1).

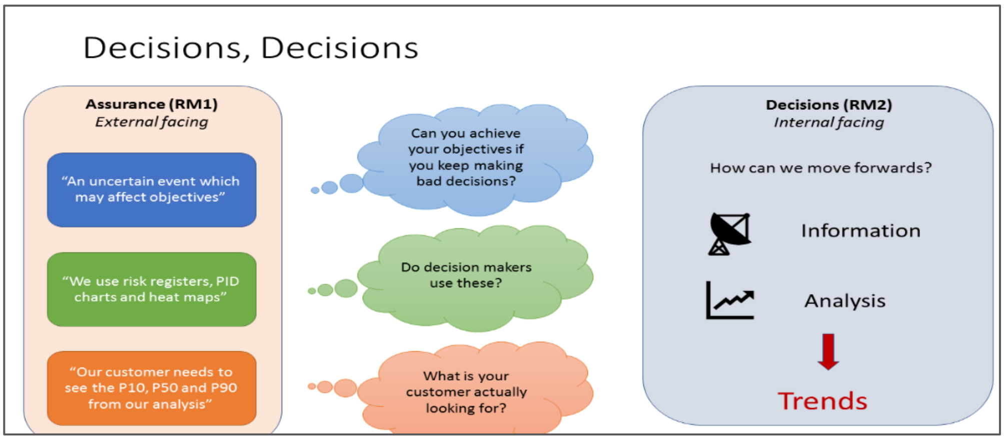

Figure 1. Procedure of business management in crisis.

3. Results

A case study of the creation of scenarios of the possible development of risks in the pre-production phase. The owner decided to finance the creation of a company for the production of composite materials in 2021 from his own funds and funds from grants. For this purpose, he created a business plan and also tried to get a co-investor. The implementation of the project began with the preparation of project documentation for the construction and other activities of the pre-production phase. The company specified these activities in the Summary of Pre-Production Activities and assigned a weight to them in the risk assessment.

In total, there are 24 risks associated with the pre-production phase. This clearly points to the fact how important the preparatory - pre-production phase is for the success of the project. However, this does not mean that the production phase is less important. Vice versa, production activity is a set of activities for which the pre-production phase was carried out and is directed towards the meaning of business - to the creation of profit. The better risk management is managed in the pre-production phase, the faster the production phase will be optimized and the faster the return on investment will be.

The investor is currently exposed to many internal and external risks resulting from his activity in the technical-economic-social environment. There are also contact circles of danger, arising from the contact between investors, suppliers and customers, while the nature of their contractual relations is important. Currently, new products, technologies and processes are already being used in the pre-production phase, which increases the demands for professional training of interested parties. For this reason, the risk management system and the transfer of its outputs to the management of the company are very important in all phases of the activity.

Financial resources for the start-up of the company are planned at a minimum amount, as no significant co-investor is part of the activity. Therefore, it is all the more desirable to implement risk management together with the application of lean management elements already in pre-production activities.

From the aforementioned analysis, the following symptoms were identified:

- impossibility of invoicing for the sale of products before the start of production and certification of own products,
- insufficient cash for investing in own infrastructure (the company has its own premises - need for investment) - temporary lease of production premises with the necessary expenditure on construction costs adjustments and rent,
- the necessity of approval of the production premises in the shortest possible time,
- immediate installation of the technological line and start of trial operation – start-up cycle,
- immediate certification of the products of the first phase of production and contracting of production,
- simultaneously with the mentioned production activities, implement all sales and marketing activities for the purpose of speeding up the contracting of products and their sale,
- realize the sale of products with the highest possible added value (minimize the cost) and thus obtain financial resources for investing in your own premises.

Since these are cash flow problems, it can be concluded that in order to prevent an acute financial crisis, the company needs to implement all the activities of the pre-production phase without significant time delays so that the possibility of selling and invoicing the finished products is possible in the shortest possible time. It is necessary to take measures to optimize processes and, in a pessimistic scenario, to rehabilitate the company - the implementation of all steps in accordance with the prepared schedule.

Ultimately, however, there is a real need for a fundamental shift in thinking and behavior in and around the discipline of risk management and competences, and what is very important from the customer's point of view, understanding the exam question and being able to derive clear, indisputable and relevant answers by adopting new and innovative techniques and approaches that deliver what is really needed.

Optimistic scenario: In order for the company to achieve product sales and profit as soon as possible, it is necessary to start production on April 15, 2024 and to certify the products of the first phase of production by August 31, 2024. Due to the fact that the company has, in addition to production technology, a laboratory, it is possible to ensure contractual sales of production production already during the certification by commercial activities, which means invoicing and obtaining income from 9/2024. This would enable the circulation of funds in accordance with the business plan. However, the development of prices on the market must be monitored and the costs for 2024 and 2025 must be analyzed accordingly. According to this scenario, the company will start producing income and making a profit in 2024.

Proposed measures for an optimistic scenario:

- the company will carry out all the necessary steps of the pre-production phase in the relevant dates and achieve the start of production and certification of products in the required date,
- the company will take measures for contracting production and selling products to customers,
- for the year 2024, the company will set a price list of products with prices ensuring income and profit in the expected amount.

Realistic scenario: If the company started production on 15/05/2024 and it would take until the end of 2024 to certify the products of the first phase, this would mean that it would produce a loss for the year 2024. The start date of the return on the investment would be postponed. The sale of products and the generation of income from sales would thus only take place in January 2025, when, along with production activity, the development of new products would take place in the laboratory. This would enable the circulation of funds for 2025 in accordance with the business plan for this year. However, the development of prices on the market must be followed and the costs for 2025, as well as the costs of 2024, must be analyzed accordingly as part of the start of production, product certification and other processes. In terms of lean management, it is desirable to ensure only necessary material stocks just in time, only necessary operating expenses and necessary staffing of production and other positions. In 2025, the company will start generating revenue and making a profit.

Proposed measures for an realistic scenario:

- the company will carry out all the necessary steps of the pre-production phase in the relevant dates and will achieve the start of production and certification of products in the required date,
- the company will take measures for contracting production and selling products to customers,
- for the year 2025, the company will set a price list of products with prices ensuring income and profit in the expected.

Pessimistic scenario: It is based on the assumption that product certification will not be achieved by 12/31/2024, which would mean a postponement of the start of product sales. In this case, the company would have to provide additional resources to cover expenses for the year 2025 until the start of product sales and revenue generation. The "benefit" is more time for the development and testing of new products, which can positively affect the composition of the future production program.

Proposed measures for the pessimistic scenario:

- Optimizing the state of production and development employees.
- Optimization of all costs related to development, testing, production and business-marketing activities,

- The company sets the same goal for income from the sale of goods and services to other customers as in the business plan for 2024 to 2025.
- For 2025, the company sets the price list for the sale of products with updated prices based on assumptions from the business plan and the real situation on the market.

4. Discussion

The problem of investment production activity in the pre-production phase is a view of what is happening in the company after the decision to implement the plan has been made. It is accompanied by activities that influence the realization of the intention dynamically, by changes in external and internal conditions. By specifying these activities with financial and time limits, the company has an analytical basis for determining the development assumption already in the pre-production phase and can thus identify threats, evaluate them and process the expected development in this phase of the investment activity using elements of lean management using the scenario method.

5. Conclusions

The proposed measures for each of the scenarios are actually guidelines for the implementation of measures and the execution of management decisions ensuring the feasibility and success of the investment plan in terms of the applied scenario. Current knowledge of science and technology predetermines digital technologies, and Technologies combined in the form of Industry 4.0, or even the Industry 5.0 standard to introduce PLM software solutions for assessment and evaluation of pre-production phases from the point of view of risk management also in the form of digital tools [9,10]. These tools will be described and scientifically solved in the next continuation of my research work.

Conflicts of Interest: “The authors declare no conflict of interest.”

References

1. Göbel, M., Araújo, T. Indicators of economic crises: a data-driven clustering approach. In: *Appl Netw Sci* **5**, 44 (2020). https://doi.org/10.1007/s41109-020-00280-4.
2. Institute of Risk Management. Available online: https://www.theirm.org/media/6827/arms_2002_irm (accessed on 23 May 2023).
3. Institute of Crisis Management. Available online: https://crisisconsultant.com/ accessed on 23 June 2023).
4. Huss, W. R. A move toward scenario analysis. In: *International journal of forecasting*, 1988, 4.3: 377-388.
5. Postma, T., Liebl, F. How to improve scenario analysis as a strategic management tool?. In: *Technological Forecasting and Social Change*, 2005, 72.2: 161-173.
6. Kukartsev, V. V., et al. Model of production resource management for manufacturing enterprise. In: *Journal of Physics: Conference Series*. IOP Publishing, 2020. p. 012178.).
7. Pačaiová, H., J. Sinay, and A. Nagyová. "Development of GRAM–A risk measurement tool using risk based thinking principles." *Measurement* 100 (2017): 288-296.
8. Lockwood, N. R. Crisis management in today’s business environment. In: *SHRM Research Quarterly*, 2005, 4: 1-9.
9. Marion, T. J., & Fixson, S. K. The transformation of the innovation process: How digital tools are changing work, collaboration, and organizations in new product development. In: *Journal of Product Innovation Management*, 2021, 38(1), 192-215.
10. Zaverzhenets, M., & Łobacz, K. Digitalising and visualising innovation process: comparative analysis of digital tools supporting innovation process in SMEs. In: *Procedia Computer Science*, 2021, 192, 3805-3814.

Comparison of evaluation systems for 4x4 vehicles during a driving test

Martin Kočan [1] and Ján Semjon [2,*]

[1] TESTEK, a.s., P.O.BOX 42, 820 17 Bratislava 217, Slovakia, martin.kocan@testek.sk
[2] Technical University of Košice, Faculty of Mechanical Engineering, Department of Production Technology and Robotics, Park Komenského 8, 042 00 Košice, Slovakia, jan.semjon@tuke.sk
* Correspondence: jan.semjon@tuke.sk; Tel.: +421 55 602 2625

Abstract: Currently, the Slovakian-developed application "Testek expert" is used at technical vehicle inspection stations, which, however, does not take into account deviations from a straight path during the vehicle's sudden braking during the driving test. The mentioned issue is not only interesting from a technical point of view, but also affects the fate of vehicle crews, which, based on an incorrect evaluation of the state of the braking system, can lead to traffic accidents. This problem was investigated by modifying the braking system on the test vehicle, so that it was possible to induce individual states when some of the wheels have a weak effect or no braking at all. The brake system on the test vehicle was specially modified so that it was possible to simulate different conditions (the brake system on each wheel of the vehicle could be controlled independently). The implemented modification of the vehicle made it possible to measure, evaluate and, based on the obtained data, to design and test a mobile application based on the conducted experiments, which allows during the driving test to also monitor "the deviation of the 4x2 and 4x4 vehicle from the straight line during the sudden braking of the vehicle".

Keywords: verification; mobile application; brake system

1. Introduction

In practice, a methodology based on European as well as Slovak standards and methodological procedures is used to verify (check) the correct functionality of the brake systems of vehicles moving on various types of roads. Currently, checking the state of the braking system is handled on the basis of Act 106/2018 Coll. and Methodological Instruction No. 71/2018 (performance of control of the braking effect and proportionality of the action of the service brake of vehicles of categories L, M, N, T and PS by driving test during technical inspections) [1,2].

The stated methodological instruction is primarily used by technical inspection stations (STK) so that they can carry out state-mandated vehicle inspections.

The principles below apply to all vehicles subject to inspection at technical inspection stations with 4x4 drive:

The driving test according to this procedure can only be performed on an area suitable for this purpose. During the test, the area must be appropriately marked and secured against the possibility of intrusion by persons, vehicles, animals, etc. There must be no objects, objects or other obstacles on the surface that could endanger the safety of the driving test. The surface of the area must be made of asphalt, concrete or other material with similar properties; during the test, the surface of the surface must not have significantly impaired adhesion properties (e.g. muddy, wet, icy, snowy, oil-contaminated, etc.).

When checking the effect and proportionality of the operation of the vehicle's service brake by a driving test, it is necessary to observe the relevant principles of safety and health protection at work. During the test, no one may stay in the immediate vicinity of the vehicle or its expected trajectory.

During the driving test, the vehicle is driven by a technical inspection technician, or according to his instructions and under his supervision, the driver (owner) of the vehicle. In that case, the driver of the vehicle must be familiar with the safety principles that must be observed during the driving test.

In the case of an air-pressure or mixed brake system (air over liquid), before the driving test, the pressure in the brake system must be topped up to a level corresponding to the prescribed operating pressure (the required air pressure is generally reached at the moment when the pressure regulator releases excess overpressure).

The vehicle deceleration meter (decelerograph, mobile phone with the given application) is placed or attached in the vehicle according to the meter's operating instructions;

The driving test can only be carried out after all other inspection items of group 1 (brakes) and all inspection items of groups 2 (steering) and 5 (axles, discs, tires) relating to the vehicle in question, which are part of the technical inspection, have been carried out. If any dangerous defect (C) is detected in these inspection items on the vehicle, the driving test will not be carried out and the relevant dangerous defects (C) will be marked [3].

2. Driving test procedure at "STK" stations

In the case of vehicles with switchable front axle drive, the front axle drive must be switched off before the driving test. In the case of vehicles with a differential lock, the differential lock must be switched off.

A preliminary test of the service brake is carried out without measuring the deceleration achieved by at least two brakings from a low speed. Its goal is to familiarize the technician with the characteristics of the tested vehicle. If, during the preliminary test, another undetected dangerous error (C) or other fact is detected that threatens the safety of the further course of the test (e.g. the vehicle is not steerable safely or the service brake is clearly not working, etc.), the driving test is interrupted and errors are marked and record.

The vehicle accelerates to the initial measurement speed after starting from the starting point. The magnitude of the initial speed is determined according to the immediate conditions of the measurement and the condition of the surface so that the safety of the test is not compromised and the vehicle can be safely stopped before the end of the test surface. A speed higher than 20 km·h-1 is considered a sufficient initial speed.

The moment (location on the test surface) at which braking begins after the vehicle has started to the initial speed is determined so that the vehicle can be safely stopped before the end of the surface.

Immediately before the start of braking, the technician (vehicle driver) disengages the clutch (in the case of vehicles with a manual transmission) and intensively depresses the service brake pedal, making sure that the vehicle, if the circumstances allow, brakes just before the wheel locking limit. The vehicle brakes until it comes to a complete stop.

The mean full braking deceleration or braking of the vehicle achieved by the service brake (measured with the vehicle deceleration gauge) and possible deviation from the direct direction of travel during braking are determined [1,2].

Evaluation of the effect of the service brake: From the value of the average full braking deceleration detected, the equivalent braking value is calculated by the relation [1].

$$Z=a/g.100\ (\%), \tag{1}$$

where:

a - mean full braking deceleration of the vehicle achieved by the service brake ($m{\cdot}s^{-2}$),

g - gravity acceleration (9,806 $m{\cdot}s^{-2}$).

If the vehicle deceleration meter directly indicates the braking value, then the indicated value is used and the calculation is not performed.

If for braking Z determined according to paragraph 1 compared to the prescribed minimum braking Z_{min} for the service brake applies:

$$Z \geq Z_{min} (\%), \tag{2}$$

then it is proven that the vehicle is able to achieve the prescribed minimum braking effect with the service brake. Otherwise, if:

$$Z < Z_{min} (\%), \tag{3}$$

the vehicle does not achieve the minimum braking effect prescribed by the service brake [1].

If the vehicle does not deviate from the straight line of travel during the driving test of the service brake, then it is proven that the effect of service braking acts on the wheels of all vehicle axles symmetrically to the longitudinal median plane of the vehicle. Otherwise, if the vehicle has clearly deviated from the straight line of travel, the service braking effect does not act proportionally to the longitudinal median plane of the vehicle. The degree of deflection is judged subjectively. In the case of a one-track vehicle of category L, deviation from a straight direction is not assessed [2].

If possible, the fulfillment of the other prescribed conditions of the control item, such as e.g. gradability, or a delay in the start of the operation brake [1].

3. Mobile applications used in brake testing

The mobile application called "mSTK" is intended exclusively for the purpose of carrying out technical inspections at technical inspection stations (STK), its use is therefore linked to the national information system of technical inspections. Without access to this information system, the application cannot be used [4]. A mobile application derived from mSTK, but intended for commercial use, is named TESTEK expert, Figure 1a, and can be installed via the Google Play service. Using the accelerometer built into the smart phone, the mobile application measures the acceleration components from the x, y and z axes, from which it calculates the total longitudinal acceleration of the vehicle. In order to achieve an accurate measurement of the vehicle's longitudinal acceleration, it is necessary to firmly attach the smart phone to the vehicle using a mobile phone holder. The advantage is that it is not necessary to additionally correct the correct position of the smart phone, this position correction takes place automatically immediately after starting the measurement. The smart phone can therefore measure correctly in any position. However, it is not recommended to measure in a horizontal position, because it is from this acceleration component (z-axis) that the application determines the arithmetic sign of the resulting acceleration, whether it is acceleration or deceleration. For accurate measurement, it is sufficient to fix the smart phone in the holder in the usual user position [5]. The mobile application immediately after the end of the measurement calculates the results of the driving brake test, namely the average full brake deceleration defined by EHK regulation No. 13 and the effect of the service brake, the so-called braking. These measurement results are essential parameters for evaluating the vehicle's ability to operate on land roads in terms of braking effect. In the mSTK version for technical inspections, after sending the measured data, the course and results of the driving test are transferred to the national information system of technical inspections, from which it is possible to reconstruct in detail the course of the entire measurement even with GPS coordinates. In case of incorrect measurement, which may be caused by e.g. by undesired movement of the smart phone or a large change in the slope of the road, the application will show an error message and the measurement cannot be sent to the national information system of technical controls.

In this case, the measurement during the technical inspection must be repeated in correct conditions. In Figure 1b, a view of the TESTEK expert application environment is shown.

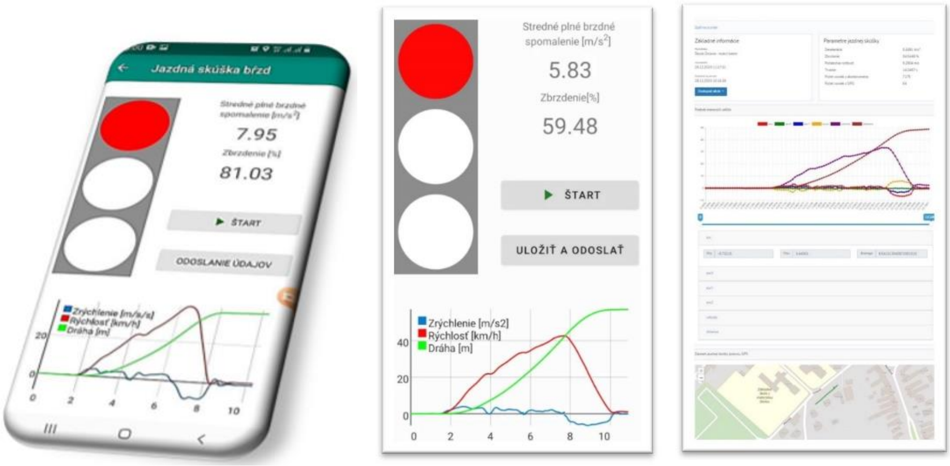

(**a**) (**b**)

Figure 1. Mobile application Testek expert

4. Measurement results

In order to be able to use the mobile application in the mSTK version during technical inspections as a device replacing the deceleration meter, or to verify the accuracy of the accelerometer used in the TESTEK expert version, it is possible to subject the accuracy of the smart phone accelerometer to metrological control - calibration using standard inclinometer and flat surface with variable inclination [5].

Comparative measurements with a calibrated decelerometer - during the development and optimization of the calculation algorithms of the mobile application, a number of measurements were performed on different vehicles, different road surfaces and with different smart phones in different positions of attachment to the vehicle. The final developed algorithm with automatic position correction and with direct evaluation of the measured results was verified by comparative measurements, which prove the high accuracy of the measurement in comparison with the calibrated type of decelerograph used in technical inspections. To illustrate the accuracy of the measurement, two measurements with different braking intensities are shown below. The accuracy of measurement with a commercial decelerometer is strongly dependent on the correct location and setting of the decelerometer to the correct measuring position. Before each measurement, the decelerometer must be set in a horizontal position and exactly aligned with the direction of travel of the vehicle. During comparative measurements, it is necessary to ensure the correct position of the comparative decelerometer [6]. This disadvantage of decelerometers is eliminated by the automatic correction of the position of the smart phone by the mobile application. The measurements below are taken with the decelerograph properly positioned and the smart phone in different positions. Figure 2 shows a graph comparing the measured data of two vehicles on the smart phone "Samsung S10e" and the decelometer "Inventure XLmeter"[7,8].

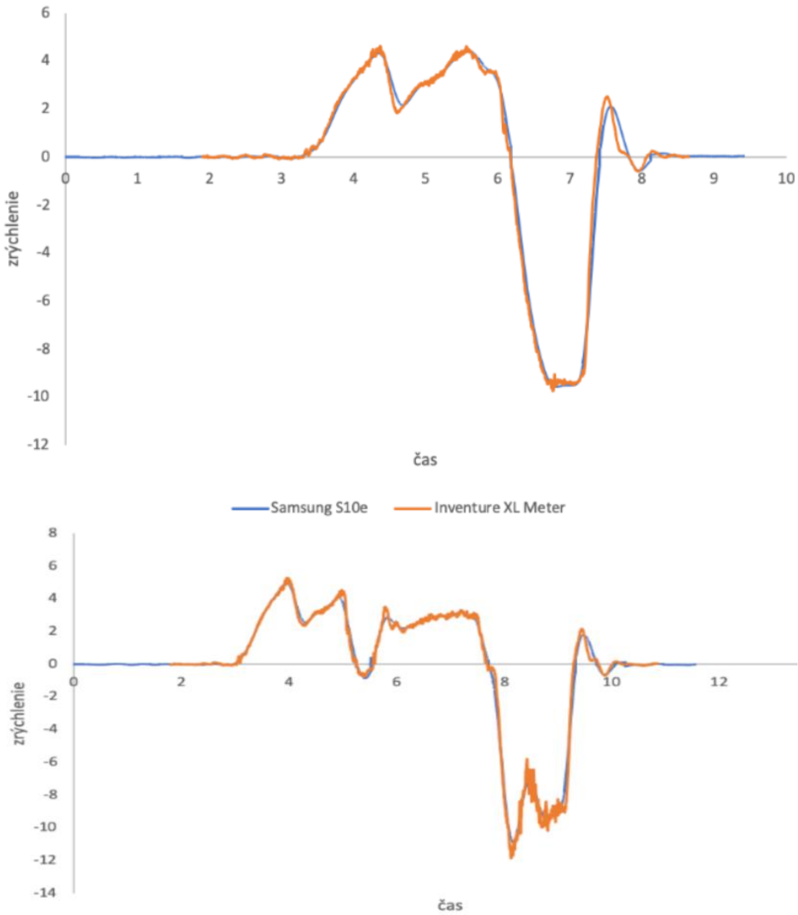

Figure 2. Decelometer and mobile application graph - vehicle 1 and 2

Table 1 shows ten measurements from a total of 30 measurements on different types of 4x4 cars.

Table 1. Measurement results between the XL meter device and the TESTEK expert application

	XL meter		TESTEK expert		Difference	
Measurement No.	Full braking deceleration ($m.s^{-2}$)	Braking (%)	Full braking deceleration ($m.s^{-2}$)	Braking (%)	Full braking deceleration ($m.s^{-2}$)	Braking (%)
1	8.54	87	8.59	87.6	-0.05	-0.6
2	4.25	43.3	4.21	43	0.04	0.3
3	8.88	90.5	8.85	90.27	0.03	0.23
4	7.97	81.3	7.99	81.54	-0.02	-0.24
5	9.25	94.3	9.2	93.89	0.05	0.41
6	8.73	89	8.64	88.16	0.09	0.84
7	8.54	87.1	8.78	89.6	-0.24	-2.5
8	3.82	38.9	3.78	38.56	0.04	0.34
9	7.89	80.4	7.94	81.04	-0.05	-0.64
10	7.81	79.6	7.89	80.46	-0.08	-0.86

From the given example of the measurement process on vehicles 1 and 2 and the measurements shown in Table 1, it follows that the calculation algorithm used in the mobile application is sufficiently accurate to fully replace the currently approved deceleration meters used in technical inspections. In the aforementioned sixteen consecutive measurements, the application shows in the measurement results an average deviation of the measured values of the mean full braking deceleration -0.01625 m.s^{-2}, respectively, an average deviation of the measured values converted to braking -0.2425 percentage points compared to the approved decelerometer.

The results of comparative measurements are repeatable with deviations within similar limits only if the strict conditions of correct use of the comparative decelerometer are met.

The calculated value of the correlation coefficient using the additional function Analytical tools - Correlation of the MS Excel program between Inventure XL meter and TESTEK Expert in the Samsung S10e smart phone is 0.999066793.

5. Conclusions

Based on the verifications carried out on 30 different vehicles equipped with a 4x4 drive, it can be concluded that the use of the developed Testek expert application at technical control stations is possible. By direct comparison of the measured data with a calibrated decelometer used as a standard for measuring braking, it is possible to conclude that the Textek expert application is sufficiently accurate. At the same time, the use of a mobile application in a smartphone does not require complicated and precise positioning in the vehicle, as was the case with the use of a decelometer. Operating a decelometer and calibrating it is also more financially demanding than using a suitable smart phone.

Acknowledgments: This article was created thanks to the support of the KEGA project: 020TUKE-4/2022 Development and implementation of new approaches in the teaching of industrial and collaborative robotics and VEGA project: 1/0215/23 Research and development of robotic workplaces equipped with industrial and collaborative robots.

References

1. Act No. 106/2018. Available online: https://www.slov-lex.sk/pravne-predpisy/SK/ZZ/2018/106/20180501.html (accessed on 19-02-2024).
2. Methodological instruction No. 71/2018. Available online https://www.testek.sk/files/meto/MP_71_2018.pdf (accessed on 19-02-2024).
3. Pan, M.; Chen, S.; Huan, R.; Wang, F; Liu, Y. Research on the Parameters Measurement of Vehicle Brake Performance in Driving, ICAIIS 2021: 2021 2nd International Conference on Artificial Intelligence and Information Systems, May 2021Article No.: 13, Pages 1–9, https://doi.org/10.1145/3469213.3469226
4. mSTK. Available online: https://testek.sk/files/mSTK-navod.pdf (accessed on 19-02-2024).
5. Testek expert. Available online: https://testekexpert.testek.sk (accessed on 19-02-2024).
6. Šarkan, B.; Holeša, L.; Ivánek, P. Measurement of the braking distance in dependence on the momentary vehicle weight. In. *Transport and Communications*, 2013; Vol. I. ISSN: 1336-7676
7. Samsung. Available online: https://www.samsung.com/sk/support/model/SM-G970FZYDORX/?sv1=affiliate&sv_campaign_id=922583&awc=18739_1708429424_34019ac78165a7ef30f16d0851033157 (accessed on 20-02-2024).
8. Inventure XLmeter. Available online: https://www.nehodar.cz/docs/XLMPUSRCZ.pdf (accessed on 20-02-2024).

TECHNICKÁ UNIVERZITA V KOŠICIAH
Strojnícka fakulta

Research on the influence of the parameters of the measuring chain of the inclined tribometer

Ivana Koláriková [1]*, Tatiana Kelemenová [1] and Katarína Paľová [1]

[1] Technical University of Košice, Faculty of Mechanical Engineering, Department of Biomedical Engineering and Measurement, Letná 9, 042 00 Košice, Slovak Republic
* ivana.kolarikova@tuke.sk, tatiana.kelemenova@tuke.sk, katarina.palova@student.tuke.sk

Abstract: Friction's role in mechanical engineering demands precise regulation, prompting the development of an inclined tribometer to measure both static and dynamic coefficients of friction. However, before delving into coefficient measurements, this research rigorously examines the influential parameters of the measuring chain within the complex tribometer setup. The measuring chain is scrutinized for its impact on measurement accuracy. Key components, including a regulated power supply, gear motor, position sensors and inclinometer, are systematically evaluated to ensure adherence to standards. Results from angle measurements using digital protractors and the inclinometer demonstrate accuracy, with acceptable standard deviations and type A standard uncertainties. The inclinometer's calibration reveals a reliable linear relationship between voltage and angle. Functional tests on components, such as photoresistor and relay highlight successful integration within the measuring chain. This research contributes foundational insights for optimizing the inclined tribometer, providing valuable guidance for engineers and researchers seeking enhanced accuracy in friction coefficient measurements for diverse mechanical systems. Future work should address challenges associated with different material pairs and refine measurement filters for comprehensive tribological investigations.

Keywords: tribometer, coefficient of friction; uncertainty; angle; speed

1. Introduction

Friction is ubiquitous and plays an important role in mechanical engineering. Sometimes friction is desirable, it needs to be regulated, or vice versa, it is often necessary to minimize this friction, because friction is an obstacle for the proper functioning of the system. The unstable nature of the basic underpinnings of friction has not prevented scientists from compiling tables of coefficients of friction and publishing them for general use. However, problems often arise when engineers attempt to use tabulated friction coefficients to solve specific problems in mechanical design or failure analysis. This is where the idea to build a tribometer that would detect the actual coefficients of friction came from, since there is no affordable and commercially available device that would measure both the static and the dynamic coefficient of friction between different material pairs. But before these coefficients of friction are going to be measured by the inclined tribometer, it is necessary to research the influence of the parameters of the measuring chain of the inclined tribometer, as it is a complex device with various components.

2. Measuring Chain of the Inclined Tribometer and Measurement Methodology

The inclined tribometer (Figure 1) consists of an aluminum structure with an articulated replaceable platform, sensors, a motor and its power supply, a computer and many other parts. All of the sensors are connected to the computer and for programming and measuring is used Matlab – Simulink.

First of all, the aluminum structure needed to be built long enough to be able to measure friction. According to TAPPI T 815 inclined plane should be at least 25 mm long for measuring static coefficient. For dynamic coefficient it needs to be long enough for an object - a sled to reach a constant speed [1].

According to the same standard the angle of plane should smoothly increase at a rate of 1.5°± 0.5°/s [1]. To move the plane the gear motor 25GA-370 D [2] is used and it can make 60 revolutions per minute. To change the speed of the motor to match the rate of 0.5°/s 1°/s and 1.5°/s, it is connected to a regulated power supply 9 V – 24 V.

The length of the operating part of the inclined plane is 500 mm. On upper end of the plane there is placed linear position sensor Panasonic HG – C1400- P which was chosen to measure traveled distance of the sled according to its results from previous article. The regression equation from this article is used in Simulink, thus constant speed of the sled moving down the plane can be determined and calculated [3]. On the plane there are installed five sensors - Autonics BJ300-DDT-P which can sense when the object passed in front of them so they can measure the distance too [4].

In order to measure static coefficient, it is essential to know when the movement of the sled is initiated. This purpose is fulfilled by relay Songle SRD-05VDC-SL-C photoresistor and a LED light [5].

On the side of the plane there is the inclinometer 8.IS40.14121 KÜBLER which is used to measure the angle of the plane. It is the best fit for measurements of the angle as reported in the article from 2 years prior to this experiment. Its output is not in arc degrees but in volts so there is a need to calculate an equation which can be later used in Simulink for purpose of the precise angle measurement. In order to get that equation, there are performed 10 measurements with step every 5 degrees from horizontal plane to 45°. Those reference degrees are given from working standard of the angle - digital protractor AG-82413B (which was used as the reference before) and there is another digital protractor - Level box. The reference is placed in the middle of the plane [6].

As the sled there is used a steel prism and as replaceable platform there is used a steel plate.

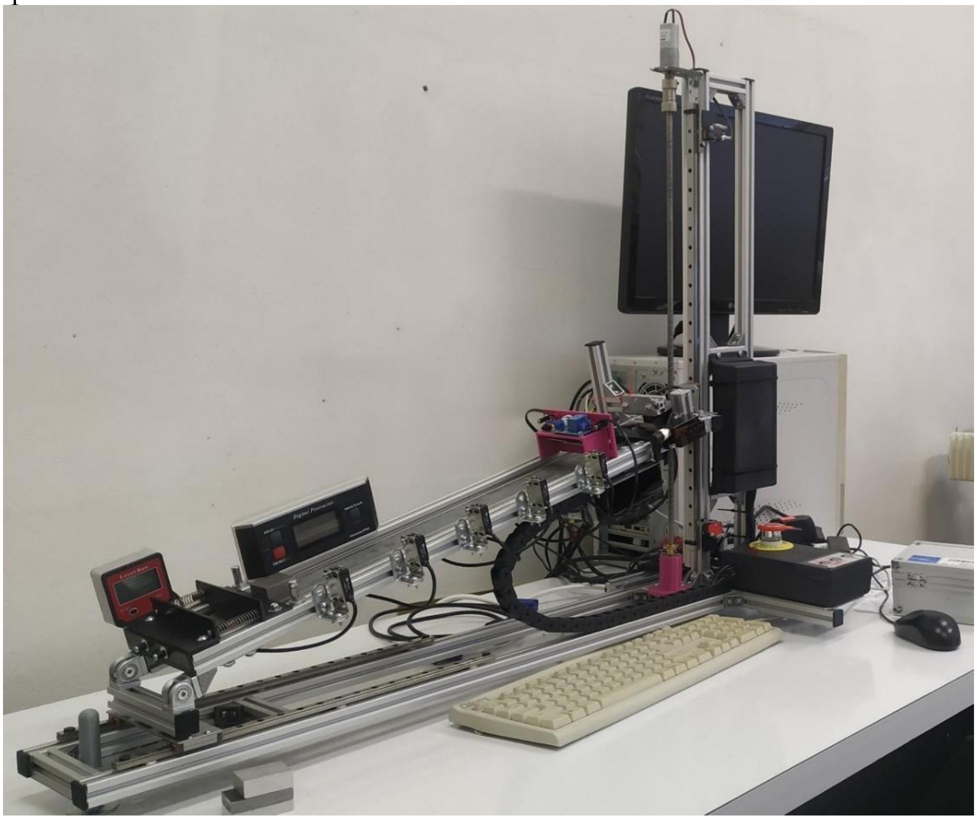

Figure 1. The inclined tribometer.

3. Results

There were performed 100 measurements of the different angles with the protractors and inclinometer 8.IS40.14121 KÜBLER. An example of how the measurement was done with the digital protractors can be seen in Figure 2. It is obvious that the level box is off by 0,4° in this measurement. It was always higher degree and it varied from 0.35° to 0.5°.

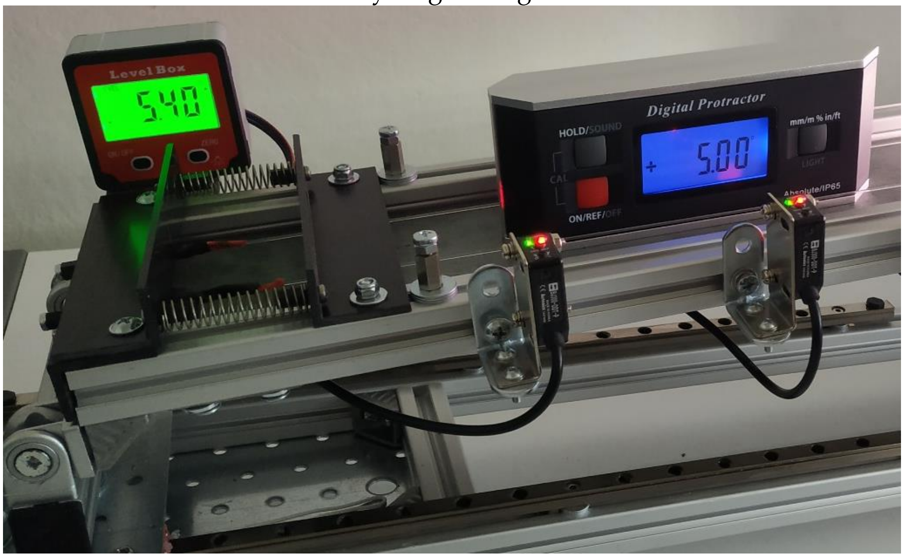

Figure 2. The digital protractors on the inclined plane.

The voltage of the inclinometer was measured in Simulink (Figure 3).

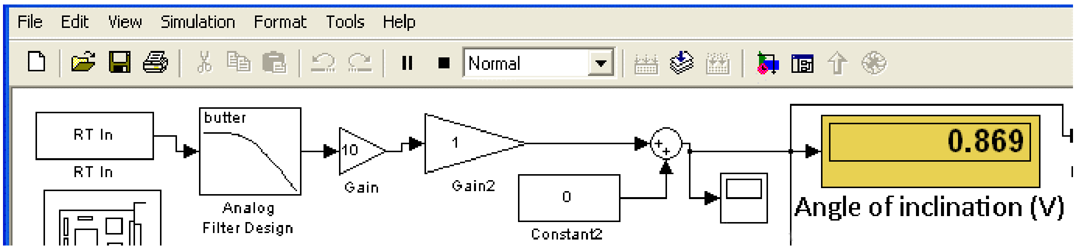

Figure 3. The angle of inclination in Volts.

There were calculated average voltages from 10 measurements of each angle. The lowest angle the plane can get is 0.85° and the average voltage is -0.011 V. At 45° the average voltage was 2.03 V. It rose in linear manner. The calibration characteristic, regression equation and model can be seen in Figure 4. Regression model was close to 1.

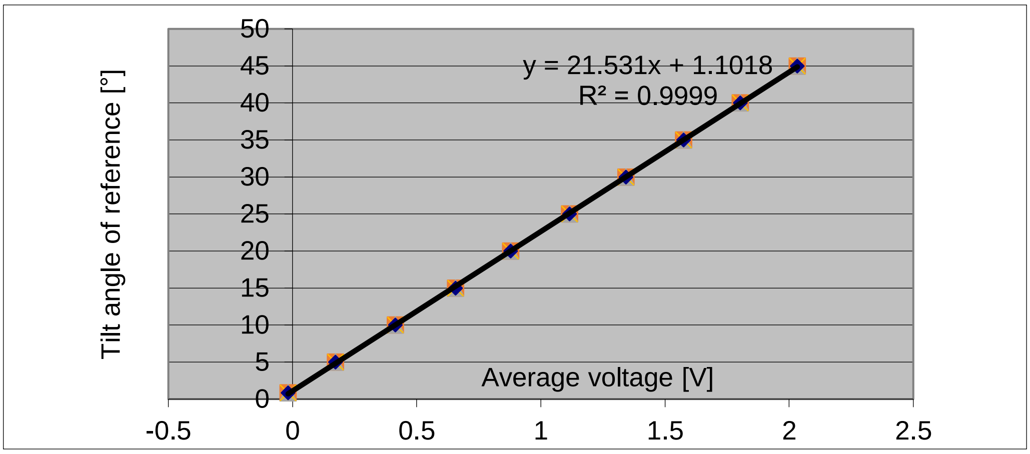

Figure 4. Dependence of the tilt angle of reference on the average voltage of KÜBLER.

There were calculated standard deviations from measurements, and they varied from 0.006 V to 0.014 V. Then type A standard uncertainty was calculated and its values were between 0.0019 V and 0.0046 V. These results can be seen in Figure 5.

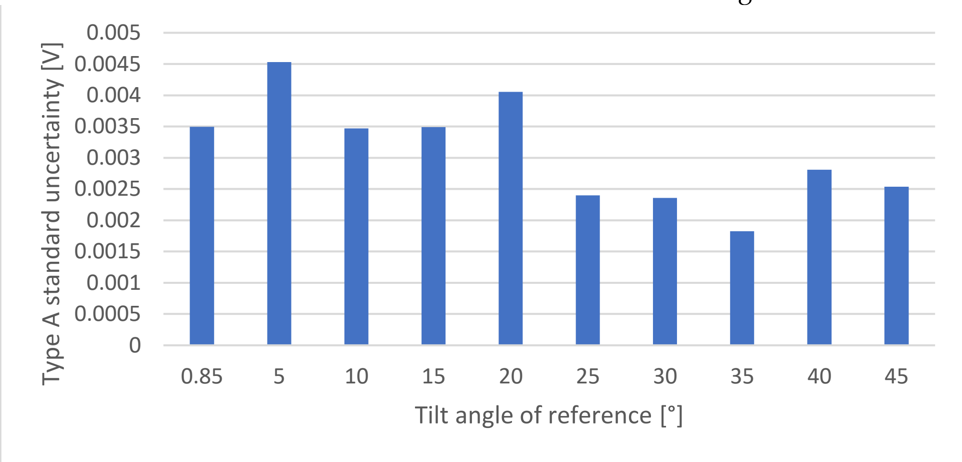

Figure 5. Type A standard uncertainty of KÜBLER.

The function of the photoresistor and the relay was tested. The sled was placed in the chamber in such way that it covered the photoresistor so that the led light did not penetrate into it and the motor started moving plane upwards. The photoresistor was connected to the relay and at the moment when the sled in the chamber moved, the led light shined on the photoresistor, thereby reducing its resistance, which subsequently turned off the engine and tilting of the plane. It worked immediately.

The linear position sensor Panasonic HG – C1400- P measured the traveled distance of the sled and with Simulink the constant speed of the sled was calculated. The plane was set to 21° when the sled started its way down. The graph of its progression and when it was at a constant speed can be seen in Figure 6. The constant speed was 0.425 m/s.

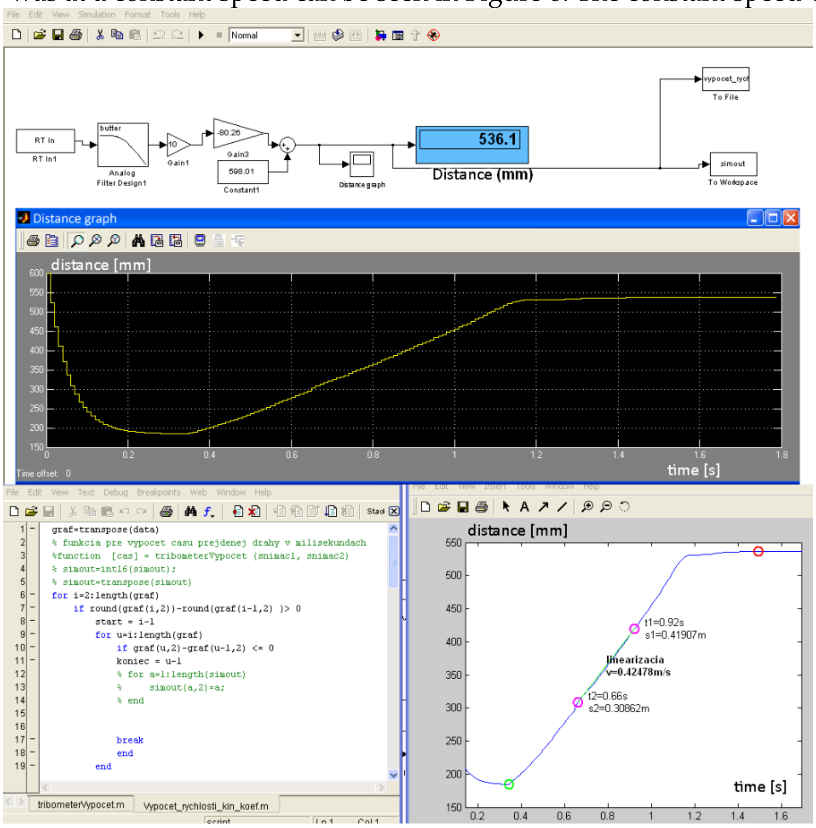

Figure 6. Dependence of the distance on the time and constant speed of the sled

Photoelectric sensors - Autonics BJ300-DDT-P that can sense when the object got in front of them were tested and placed on the plane in a way that it is exactly 250 mm between the first and the last (fifth) sensor which were tested in this article.

Regulated power supply of the gear motor was set up to match closest the rate of increasing the plane by 0.5°/s 1°/s and 1.5°/s. The measurement of speed of the inclination started at about angle of 10° when it was shown true speed. The speed of 0.5°/s can be reached by setting the power supply to 9.37 V, speed of 1°/s can be reached by setting the power supply to 19.1 V and speed of 1°/s can be reached by setting the power supply to 24 V as can be seen in Figure 7.

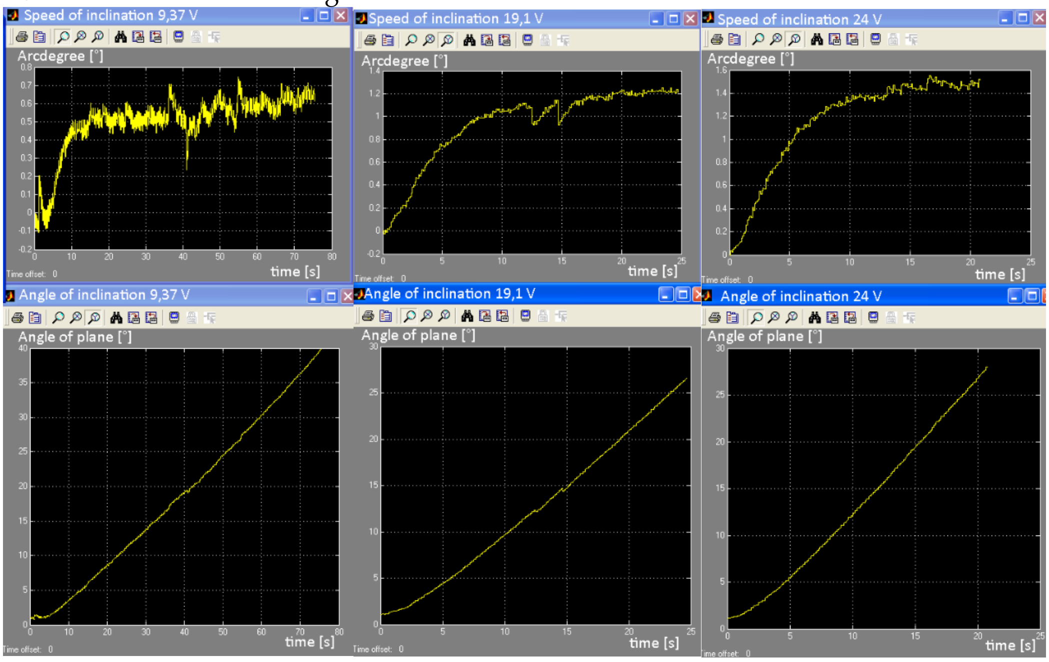

Figure 7. Speed of inclination and angle of inclination at 9.37 V; 19.1 V and 24 V (left to right)

4. Discussion

Measurement of the angle triggered many topics to discuss. The difference between two protractors is caused by the different position of both on the plane and also Level box (Figure 2 left) is less precise. The regression equation $y = 21.531x + 1.1018$ (Figure 4) is going to be used in Simulink in order to calculate angle in degrees for the inclinometer KÜBLER and this will be further used to calculate the coefficients of friction. The standard deviations and type A standard uncertainty were low values, so the measurement was precise. The distance between Autonics sensors should be enough to measure dynamic coefficient of friction. Due to the used filter when measuring speed of inclination (Fig- ure 7), it seemed that the speed was for the first seconds increasing rapidly, but that was not true. For steel object and steel plane the static coefficient of friction did not start earlier than at 10°, so the filter was not the problem, but when the material pairs switch, it could become a problem, therefore it needs to be addressed in further work.

Acknowledgments: This study was supported by projects VEGA 1/0191/24 Development, optimization, and application of coordinate measurement strategies of geometric parameters and structure of additive products and KEGA 004TUKE-4/2024 Innovative methods of implementing students' digital skills in length metrology.

Conflicts of Interest: The authors declare no conflict of interest. The funders had no role in the design of the study; in the collection, analyses, or interpretation of data; in the writing of the manuscript, or in the decision to publish the results.

References

1. Coefficient of static friction (slide angle) of packaging and packaging materials (including shipping sack papers, corrugated and solid fiberboard) (inclined plane method). Available online: https://www.tappi.org/content/sarg/t815.pdf (accessed on 20. 11. 2023).
2. 25GA-370 DC 12V Electric Gear Motor Reduction Motor. Available online: https://www.amazon.com/Metal-Electronic-Electric-Curtain-25GA-370/dp/B097QSP2PK (accessed on 20. 11. 2023).
3. Ivana Koláriková, Tatiana Kelemenová, Barbora Hudáková. Verification of the properties of linear position sensors. In: Novus Scientia 2023. - Košice (Slovensko) : Technická univerzita v Košiciach s. 94-100 [online]. - ISBN 978-80-553-4369-3
4. BJ300-DDT-P. Available online: https://www.autonics.com/model/A1650000198 (accessed on 20. 11. 2023).
5. Relé SRD-05VDC-SL-C. Available online: https://www.ampul.eu/sk/rele-magneticke-kontakty/2687-rele-srd-05vdc-sl-c-5v-dc-250v-ac-10a (accessed on 20. 11. 2023).
6. Ivana Koláriková, Tatiana Kelemenová, Eduard Jakubkovič. Verification of the properties of tilt angle sensors. In: Novus Scientia 2022. - Košice (Slovensko) : Technická univerzita v Košiciach s. 280-289 [online]. - ISBN 978-80-553-4085-2

Ultrasonic liquid indicator for blind people

Petra Kolembusová [1,*], Veronika Sedláková [1], Norbert Ferenčík [1], and Radovan Hudák [1]

[1] Department of Biomedical Engineering and Measurement
* Correspondence: petra.kolembusova@tuke.sk

Abstract: This research deals with the issue of assessing the quality of sensing individual liquids using an ultrasonic sensor for application to a liquid detection aid for the blind. The life of the blind is very problematic. For a person with healthy eyesight, figuring out how much liquid to put in a glass is natural, but it creates a problem for people with partial or complete loss of eyesight. For this reason, the goal of this paper was to emulate liquid indicators that help users determine when to stop pouring. A common self-help technique used by blind people is to stick their finger in the glass and stop pouring when they feel it is wet. However, the mentioned technique isn't suitable for pouring hot drinks. First, we analyze the operation of the Arduino and the ultrasonic sensor to understand which factors affecting the sensing need to be considered. Subsequently, we will present the concept of an auxiliary device detecting liquid using an ultrasonic sensor with a sound signal. At the end of the document, we present cases of assessment of the quality of sensing of individual liquids.

Keywords: Arduino UNO, ultrasonic sensor, liquid detection

1. Introduction

An open-source platform called Arduino is used to build and program circuits. It can communicate with the majority of gadgets both directly and through the internet to control the particular electronic equipment. It programs the board using a software application (Simplified C++) and a hardware device called an Arduino Uno circuit board. Pouring drinks is more challenging for the visually impaired and is challenging to determine the exact level of the liquid inside. This paper presents the design and development of an assistive device to assist the visually impaired handle liquids safer [1].

2. Materials and Methods

2.1 Hardware

2.1.1 Arduino UNO

board The Arduino board hardware consist of many components that combine to make it work, but we are going to discuss the main component on the board such as follows [3]:

- USB plug,
- external power supply,
- reset button,
- microcontroller,
- analog pins (0–5),
- digital I/O pins (2–13),
- in–circuit programmer,
- digital and analog ground pins and
- power pins.

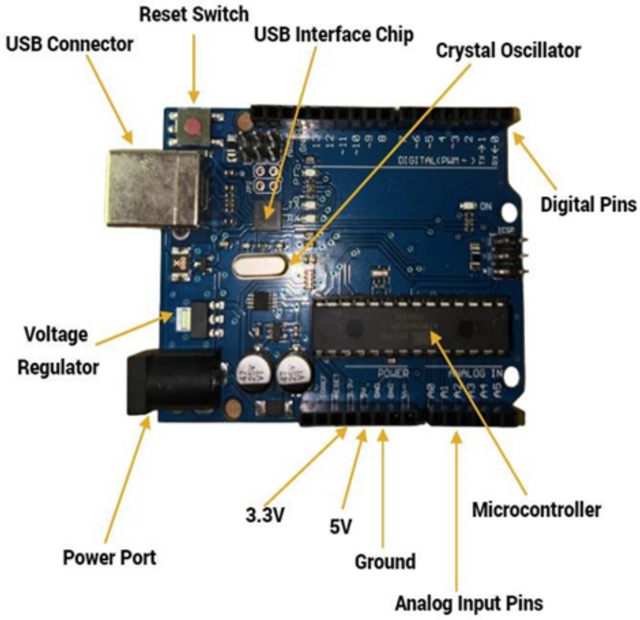

Figure 1. Arduino UNO board

2.1.2 Ultrasonic sensor HC-SR04

Similar to how bats utilize SONAR, the HC-SR04 ultrasonic sensor uses it to measure an object's distance. The sensor provides outstanding non-contact range detection from 2 cm to 400 cm with high precision and reliable readings [2][6][7].

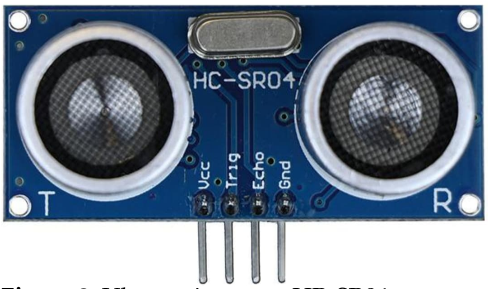

Figure 2. Ultrasonic sensor HR-SR04

The basic composition of the sensor are two ultrasonic transducers. One is a transmitter that pulses out ultrasonic sound, while the other is a receiver that listens for reflected waves. At 40,000 hertz, it releases an ultrasonic wave that travels through the air and returns to the module when encountering an object or obstruction. You may compute the distance by considering the sound speed and the travel time. [5] Sunlight or black material has no effect on the operation, although, soft materials such as cloth may be hard to detect acoustically [2][4][5].

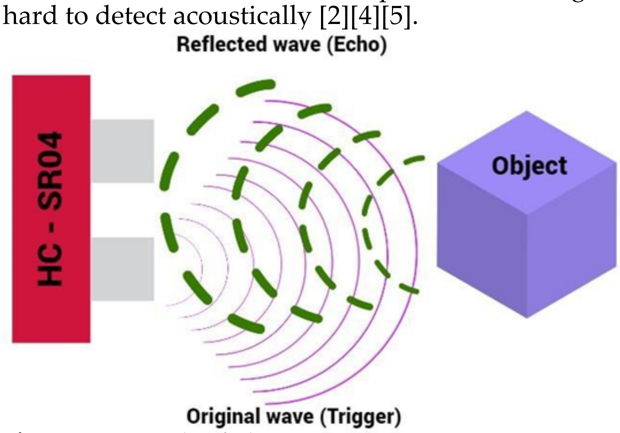

Figure 3. Principle of ultrasonic sensor

2.1.3 Liquid-Crystal display (LCD)

Figure 4 illustrates a liquid-crystal display (LCD), which is a flat-panel display or other electronically controlled optical device that makes use of polarizers and liquid crystals' ability to modulate light. Liquid crystals use a backlight or reflector to create color monochrome pictures rather than emitting light directly. LCDs are available to show fixed graphics with minimal information content that can be shown or hidden, including preset words, numerals, and seven-segment displays, as in a digital clock, or arbitrary visuals, like in a general-purpose computer display. LCDs can be configured to be either normally on (positive) or off (negative) biased, based on the polarizer

Figure 4. Liquid-crystal display

2.1.4 Piezo buzzer

Figure 5 shows an example of a simple gadget that produces simple tones and beeps - piezo buzzer. A piezo crystal, a unique substance that alters shape in response to voltage, is how they function. A pressure wave that the human ear perceives as sound can be produced when the crystal presses up against a diaphragm, such as a miniature speaker cone. They work on the principle of a changed voltage applied to a piezo, which quickly changes shape and starts producing sounds. It is an affordable device that is able to transform mechanical energy into sound energy. By applying varied frequency electric pulses to the buzzer, it is possible to generate various tones [8][10].

Figure 5. Piezo buzzer

The designed prototype of the liquid distance detector was assembled from the following components: Computer for programming, USB cable for connecting the computer with the microprocessor, Arduino Uno, breadboard, several jumping wires, ultrasonic sensor (HC- SR04), piezo buzzer, I2C LCD display (16x2), 200Ω – resistor [8] [10].

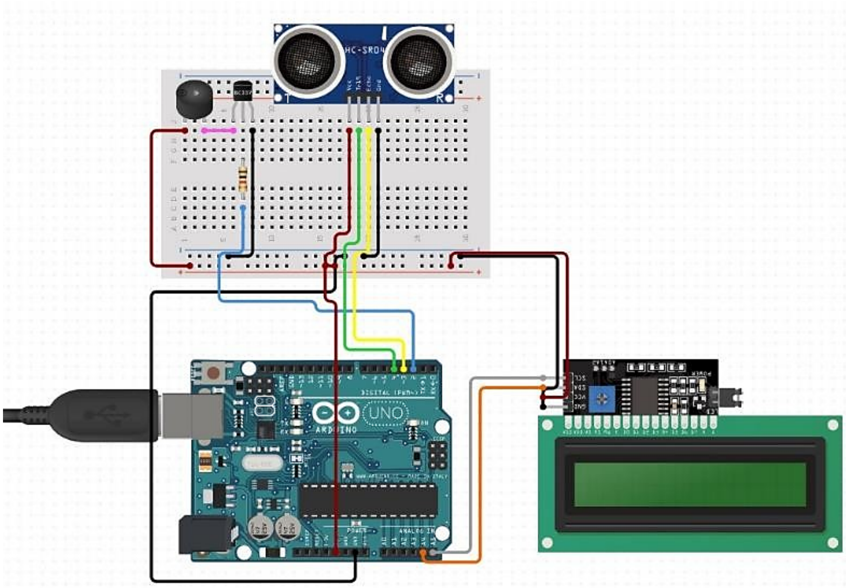

Figure 6. Hardware connection scheme

2.2 Software

Arduino is an open-source physical computing platform built on a microcontroller board and a development environment that uses the processing programming language. Arduino can be used to create interactive things with inputs controlling outputs. Arduino projects can be standalone or can communicate with software running on a computer. The Arduino IDE, which uses the C programming language, is the most commonly used programming approach. This offers access to the vast Arduino Library, which is constantly expanding thanks to the open-source community [10][11][12].

The components were connected using jumper wires as follows. The Arduino Uno was attached to the breadboard using jumper cables as it is possible to see in the previous picture. A jumping wire comes out of the 5V pin on the Arduino, which is connected to the plus channel of the breadboard. Another jumping wire from the GND (ground) pin on the Arduino is connected to the negative channel of the breadboard. The ultrasonic sensor consists of 4 pins: VCC - connected to the positive channel on the breadboard, GND - connected to the negative channel on the breadboard, ECHO pin - connected to digital pin 7 on the Arduino, TRIGG - connected to digital pin 6 on the Arduino. Piezo buzzer consists of two ends. Both positive and negative. The positive pin is connected to digital pin 3 of the Arduino, while the negative pin is connected by using 200Ω resistor to the negative channel of the breadboard. The project also used an LCD display that comes from 4 pins. As in the case of the ultrasonic sensor, the VCC and GND pins are connected to the positive and negative pins. The SDA pin is connected to analog pin A4 and the SCL pin to A5 [1][9][10][11][12].

3. Results

The code we generated was sent to the Arduino microcontroller using a computer with the appropriate Arduino IDE to execute the circuit. The working principle of the prototype consists in detecting the distance of the liquid in the cup, on which the ultrasonic sensor is placed. The liquid distance is also shown on the LCD display. After reaching the limit determined by us, 3 cm from the upper edge of the glass, an audio warning will sound. This audio signal signals to blind people that they have reached the optimal amount of liquid in the glass.

The final prototype consisted of a sensor that was placed on top of a cup using cardboard paper. We cut this cardboard paper precisely so that it does not interfere with scanning. We tested the final prototype on two types of liquids - water and milk.

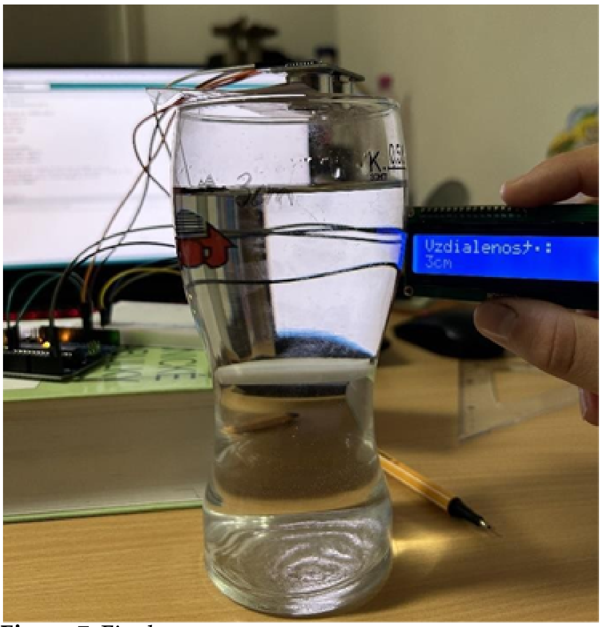

Figure 7. Final prototype – water

Figure 8. Final prototype – milk

4. Discussion

During our research we dealt with the most suitable stabilization of the sensor in a position that corresponded to the distance determined by us. We managed to hold the sensor above the glass using cardboard paper that was precisely cut to the shape of the sensor. Paper could not get in the way of the sensor, because it would not detect the measurements correctly. We also focused on the comparison of sensor feedback for individual liquids. We compared 2 different colored liquids - water and milk. We assumed that water would be harder for the sensor to detect, but we were wrong. Both liquids were recorded right by the sensor, but with milk the sensor started reading just before the specified distance. This may have been caused by bubbles on the surface of the milk that are created during pouring.

5. Conclusions

The goal of paper was to help blind people with pouring liquids into a glass while using an ultrasonic sensor that recorded the distance and a buzzer that alerted blind people with a sound when the glass was filled with the optimal amount of liquid. In the continuation of the project, we could create a sensor stabilizer from another material, for example by additive manufacturing (using 3D printing). Such a stabilizer could have a stronger grip on the glass, but at the same time it would take up less space on the glass, this would allow easier pouring of the liquid. By continuing the project, we could focus on comparing other types of liquids, or liquids of different temperatures.

Acknowledgments: In this section, you can acknowledge any support given which is not covered by the author contribution or funding sections. This may include administrative and technical support, or donations in kind (e.g., materials used for experiments).

References

1. Galadima, A. A. (2014). Arduino as a learning tool. In 2014 11th International Conference on Electronics, Computer and Computation (ICECCO). 2014 11th International Conference on Electronics, Computer and Computation (ICECCO). IEEE. https://doi.org/10.1109/icecco.2014.6997577
2. Mutinda Mutava Gabriel. (2020). Arduino Uno, Ultrasonic Sensor HC-SR04 Motion Detector with Display of Distance in the LCD. In International Journal of Engineering Research and (Vol. V9, Issue 05). ESRSA Publications Pvt. Ltd. https://doi.org/10.17577/ijertv9is050677
3. Louis, L. (2016). Working Principle of Arduino and Using it as a Tool for Study and Research. In International Journal of Control, Automation, Communication and Systems (Vol. 1, Issue 2, pp. 21–29). Academy and Industry Research Collaboration Center (AIRCC). https://doi.org/10.5121/ijcacs.2016.1203
4. DEJAN, Ultrasonic Sensor HC-SR04 and Arduino – Complete Guide, 8.11.2023 [ONLINE] https://howtomechatronics.com/tutorials/arduino/ultrasonic-sensor- hc-sr04/
5. Kadhim, R. A., Raheem, A. K. K. A., & Gitaffa, S. A. H. (2017). Implementing of liquid tank level control using Arduino-LabView interfaceing with ultrasonic sensor. *KUFA journal of engineering*, *8*(2).
6. Karwati, K., & Kustija, J. (2018). Prototype of Water Level Control System. In IOP Conference Series: Materials Science and Engineering (Vol. 384, p. 012032). IOP Publishing. https://doi.org/10.1088/1757-899x/384/1/012032
7. Aryanti, A., Lin, W.-C., Lin, C.-Y., Brian Henriquez, B., Mekongga, I., & Raymond See, A. (2020). Smart Cup Holder For Visually Impaired People. In Journal of Physics: Conference Series (Vol. 1500, Issue 1, p. 012095). IOP Publishing. https://doi.org/10.1088/1742-6596/1500/1/012095
8. Jawale, R. V., Kadam, M. V., Gaikawad, R. S., & Kondaka, L. S. (2017). Ultrasonic navigation based blind aid for the visually impaired. In 2017 IEEE International Conference on Power, Control, Signals and Instrumentation Engineering (ICPCSI). 2017 IEEE International Conference on Power, Control, Signals and Instrumentation Engineering (ICPCSI). IEEE. https://doi.org/10.1109/icpcsi.2017.8391846
9. Chaudry, A. M. (2020). Using Arduino Uno Microcontroller to Create Interest in Physics. In The Physics Teacher (Vol. 58, Issue 6, pp. 418–421). American Association of Physics Teachers (AAPT). https://doi.org/10.1119/10.0001841
10. Halim, D. K., Ming, T. C., Song, N. M., & Hartono, D. (2019). Arduino-based IDE for Embedded Multi-processor System-on-Chip. 2019 5th International Conference on New Media Studies (CONMEDIA). https://doi.org/10.1109/conmedia46929.2019.8981862
11. Amestica, O. E., Melin, P., Duran-Faundez, C., & Lagos, G. (2019). An Experimental Comparison of Arduino IDE Compatible Platforms for Digital Control and Data Acquisition Applications. 2019 IEEE CHILEAN Conference on Electrical, Electronics Engineering, Information and Communication Technologies (CHILECON). https://doi.org/10.1109/chilecon47746.2019.8986865
12. Pan, T., & Zhu, Y. (2017). Getting Started with Arduino. Designing Embedded Systems With Arduino, 3–16. https://doi.org/10.1007/978-981-10-4418-2_1

TECHNICKÁ UNIVERZITA V KOŠICIACH
Strojnícka fakulta

Effect of UltiMaker Cura support and fill settings on the 3D model

Ján Kopec [1], Miriam Pekarčíková [2] and Juraj Kováč [3]

[1,2,3] Department of industrial and digital engineering, Technical University of Košice, Park Komenského 9, 04001 Košice,
* Correspondence: jan.kopec@tuke.sk; Tel.: 0556022714

Abstract: This paper investigates the effect of support and fill settings in UltiMaker Cura software on the quality of three-dimensional models created using 3D printing technology. The use of optimal support and fill settings is critical to achieving high-quality results when printing. Different combinations of support and fill values were tested within the setup using UltiMaker Cura. The results show that proper settings can improve support removability, minimize deformation, and achieve optimal fill uniformity [1]. We also discuss practical recommendations and best practices for support and fill settings in UltiMaker Cura concerning the specific needs of printed projects. This research contributes to a better understanding of the impact of these factors on 3D printing quality and guides users in optimizing settings for their specific applications. The final section of the paper discusses possible directions for further research in print setups and 3D printing technology in general.

Keywords: UltiMaker, 3D printing, fill, support

1. Introduction

With the rapid development of 3D printing technology, it is becoming an increasingly important aspect of computer-aided design (CAD) printing. In this context, it is crucial to set the print parameters correctly, especially support and fill, to achieve optimal results. This paper focuses on the analysis of the impact of support and fill settings in UltiMaker Cura software on the quality of 3D models [2].

Our research aimed to investigate how different combinations of values of these parameters affect material consumption and time considerations. We focus on a specific software, UltiMaker Cura, widely used in the 3D printing community.

In this introduction, we present the issues faced by 3D printing users and emphasize the importance of proper support setup and padding for optimal results.

For the average user, UltiMaker Cura is an affordable solution for creating models for 3D printing in .gcode format. Once installed, UltiMaker Cura offers many brands of 3D printers with supported printer models from the respective brands. This facilitates the process of defining the axes (X, Y, Z), the shape of the work surface, support for heating the work surface, and many other settings down to the start and end G-code. This part is very essential in determining the print quality [3]. For the printers in the supported list, this G-code is defined and in the Machine Settings section, it is available for viewing, and possibly redefining. It is true that as printers are diverse, the G-code at the beginning and end of the 3D printing process must match the dimensions of the printer, otherwise damage can occur, whether to the extruder, the work surface, or the printer drive. Once the initial settings have been defined, the program is ready to 3D model in the corresponding format, i.e. STL.

Fused Filament Fabrication (FFF), also known as Fused Deposition Modeling (FDM), is one of the most popular and affordable 3D printing technologies. This technology works on the principle of melting a thermoplastic material that is in the form of a filament (filament) and then depositing the molten material layer by layer until the object is complete.

The FFF process starts with a 3D model created in a computer program, which is then processed into a printer-readable format (often G-code). This file contains information on how and where the printer should apply the material. The printer has an extruder that melts the filament and applies it through a nozzle to the printing substrate. The movement of the nozzle is controlled by stepper motors that allow the material to be accurately deposited according to the submitted model.

The advantage of FFF technology is its affordability and the wide range of materials available. The most commonly used materials are PLA (polylactic acid) and ABS (acrylonitrile butadiene styrene), but there are many others, including PETG, TPU and nylon. Each of these materials has its own properties that make it suitable for different applications. PLA, for example, is biodegradable and easy to print, making it ideal for beginners. ABS, on the other hand, is more durable and has a higher heat resistance, making it advantageous for functional prototypes and parts.

STL (STereoLithography) is a file format used in the field of 3D computer graphics and three-dimensional modeling. This format is widely used to represent geometric data of three-dimensional objects using a network of triangles. STL files contain the information needed to define the surface and geometry of an object in 3D space. Figure 1. in part (a) shows the model in its actual full texture and in part (b) the identical model is rendered using a network of triangles [4].

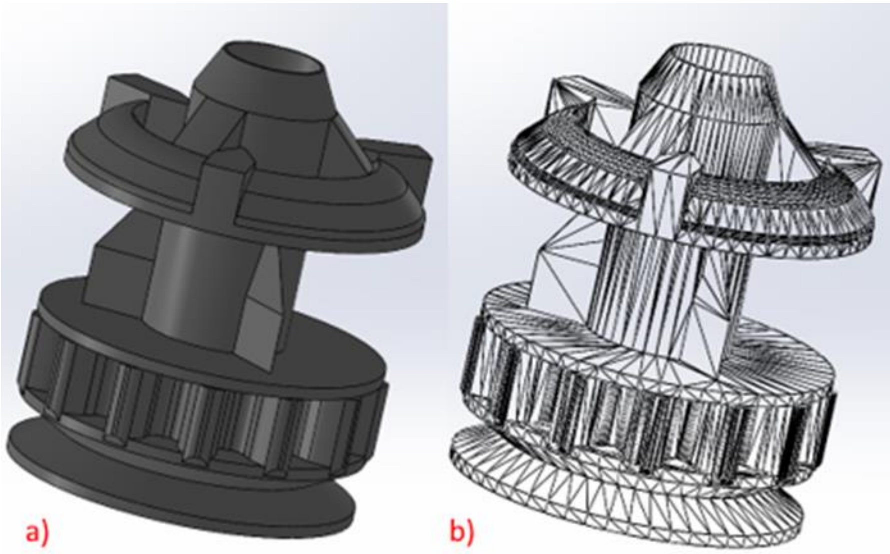

Figure 1. a) view of a 3D model formed by a classical structure, b) model formed by a network of triangles

2. 3D model color definitions

The STL model format is already applicable for all types of slicers. After uploading to UltiMaker Cura (Fig.2 a)), the model is colored in the appropriate colors. Each color has its meaning, and it is necessary to recognize it, in some cases to define new settings.

Table 1. Color model definition

Color	Description	Note
	This is the color of the borders of the model. It represents an auxiliary part for better visualization of the model for the user.	
	Color generated by UltiMaker Cura. The program used the Generic PLA option, which has a yellow color when setting up. To change it, you need to define the filament.	It does not affect the quality; it only serves as a visual element. It can be changed in Preferences, under Materials.
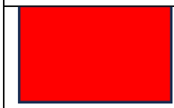	Color indicating the error. The model with the settings used fails to print this area or warns the user of possible deformations until they change the print settings. In most cases, this is to create support. In the Preview section, this color defines a model without support material.	For print quality this color is essential, until the user makes changes, they run the risk of print quality being reduced.
	It is located at the bottom of the model and is only created if the model is accurately positioned on the work surface and there is no gap between the model and the work surface. Defines the first layer. In the Preview section, this color shows the support material.	As soon as the user creates a gap between the model and the surface, the color switches to red. This is to indicate that the model is misplaced.
	If the model is shifted to negative values on the Z-axis, the part below the print area will not be printed and will be rendered in dark blue.	This step simply defines the part of the model that needs to be printed without using modifications in the 3D modelling software.
	Represents the wall thickness defined in the settings.	

3. Generating support

If the user encounters a red render, support needs to be generated because the printer is unable to store material in the blank space. For a model with cone shapes, even without support material, the printer can create an area and thus produce a model with the desired quality for detail and shape [6]. However, the generated print image with supporting materials has a different color distribution (Fig. 2(b)).

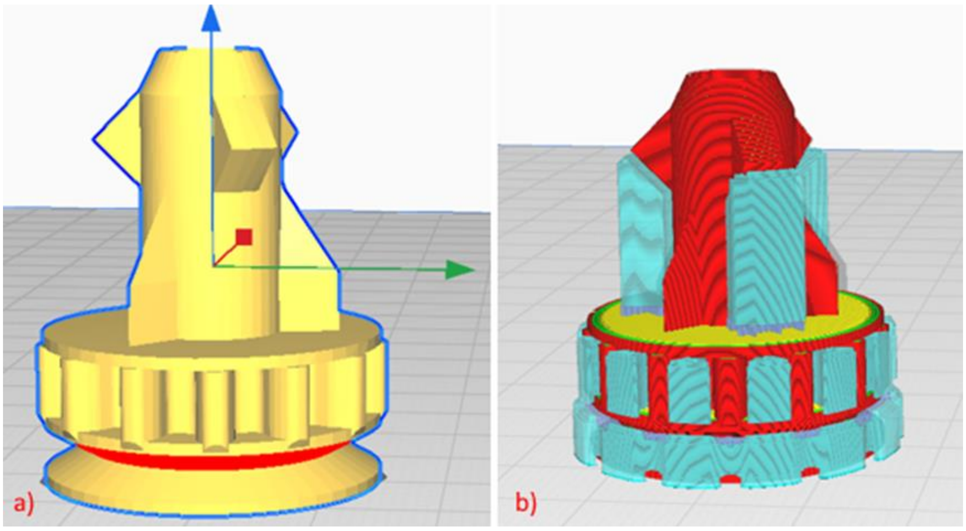

Figure 2. a) classic 3D model without support b) model with generated support

In the settings section, there is a Support section that needs to be activated. Afterwards, various settings can be defined:

- **Support Structure**: UltiMaker Cura offers 2 options (Normal, Tree). Normal generates support directly under the model and is predefined in each printer. The alternative is Tree. In this case, as in nature, the Tree will create branches growing around the 3D model. The advantage of Tree support is shorter printing time and less disruption to the structure of the model.

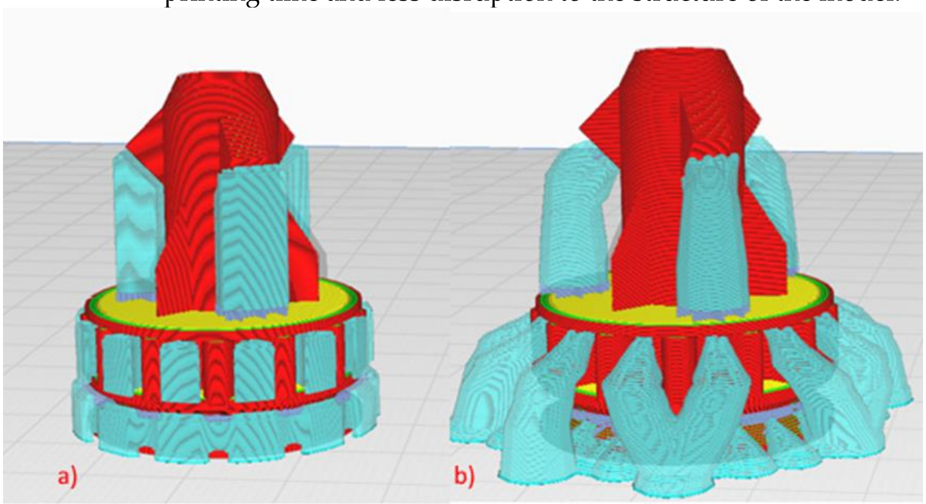

Figure 3. a) model with generated support Normal b) tree support

- **Support Pattern**: the support is also allowed to have a defined shape. Support shape options include Lines, Grid, Triangles, Concetric, Zig Zag, Cross, and Gyroid. Examples are shown in Figure 4. Different types also have different amounts of material they need to create it. The numerical representation is worked out in Table 2. The model in Figure 1 is used to quantify the semi. Grid and Infill Density of 20% and print speed of 80mm/s were chosen as the fill type [5].

Figure 4. graphic examples of filling type options

Table.2 time and material calculations for different types of support

Support Structure	Support Pattern	Support Placement	Support Over-hang Angle	Values
Normal	**Lines**	Everywhere	45°	**1 hour 27 minutes/ 3.11m**
Normal	**Grid**	Everywhere	45°	**1 hour 26 minutes/ 3.09m**
Normal	**Triangles**	Everywhere	45°	**1 hour 26 minutes/ 3.12m**
Normal	**Concetric**	Everywhere	45°	**1 hour 18 minutes/ 3.01m**
Normal	**Zig Zag**	Everywhere	45°	**1 hour 27 minutes/ 3.31m**
Normal	**Cross**	Everywhere	45°	**1 hour 29 minutes/ 3.27m**
Normal	**Gyroid**	Everywhere	45°	**1 hour 23 minutes/ 3.15m**
Tree	**Lines**	Everywhere	45°	**1 hour 22 minutes/ 3.06m**
Tree	**Grid**	Everywhere	45°	**1 hour 23 minutes/ 3.06m**
Tree	**Triangles**	Everywhere	45°	**1 hour 22 minutes/ 3.06m**
Tree	**Concetric**	Everywhere	45°	**1 hour 22 minutes/ 3.06m**
Tree	**Zig Zag**	Everywhere	45°	**1 hour 22 minutes/ 3.06m**
Tree	**Cross**	Everywhere	45°	**1 hour 23 minutes/ 3.08m**
Tree	**Gyroid**	Everywhere	45°	**1 hour 23 minutes/ 3.08m**

4. Filler adjustment options

The quality of the model and its final properties are also influenced by the type of slow fill. UltiMaker Cura offers the possibility to define Infill Density in percentage and Infill Pattern (Fig.5). It all depends on the use of the model, for more loaded models a higher infill percentage or 100% is recommended. An increase in infill requirements will be reflected in printing time and material consumption.

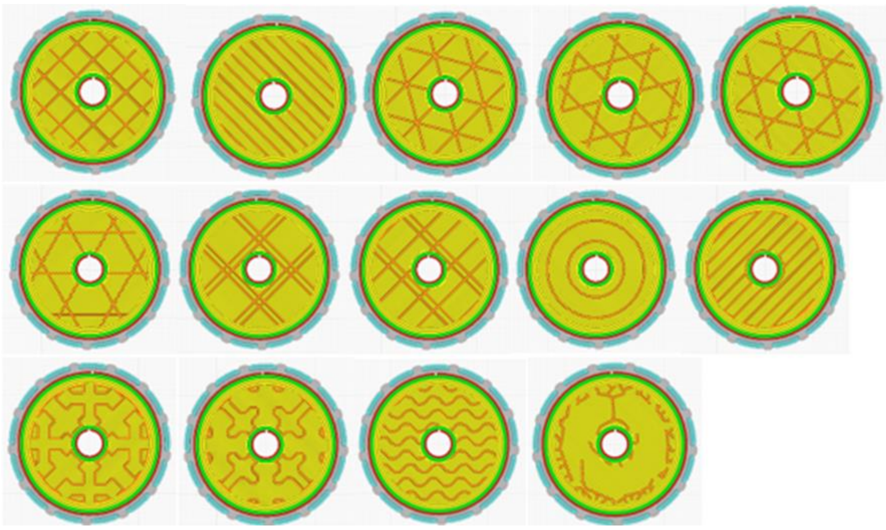

Figure 5. Examples of fill options in UltiMaker Cura

In Table 3 the values are quantified according to the type of filling. For the authenticity of the results, the print speed (80mm/s), support type (Normal), and Infill Density (20%) are preset.

Table.3 Generated values for different fill types

Infill Pattern	Values
Grid	**1 hour 23 minutes/ 3.08m**
Lines	**1 hour 24 minutes/ 3.07m**
Triangles	**1 hour 21 minutes/ 3.09m**
Tri-Hexagon	**1 hour 20 minutes/ 3.07m**
Cubic	**1 hour 21 minutes/ 3.08m**
Cubic Subdivision	**1 hour 20 minutes/ 3.03m**
Octet	**1 hour 21 minutes/ 3.07m**
Quarter Cubic	**1 hour 22 minutes/ 3.07m**
Concertic	**1 hour 18 minutes/ 2.99m**
Zig Zag	**1 hour 23 minutes/ 3.08m**
Cross	**1 hour 21 minutes/ 3.27m**
Cross 3D	**1 hour 23 minutes/ 3.16m**
Gyroid	**1 hour 24 minutes/ 3.08m**
Lightning	**1 hour 18 minutes/ 2.90m**

5. Conclusions

This article shows that 3D printing is a complex technology that is modifiable for the user. Different settings, from basic to advanced ones where knowledge of the technology is required give the possibility of creating models of different shapes, quality to detail, and speed of printing. The article describes the types of supports that directly affect the quality of the printout. On the other hand, the environmental footprint also needs to be considered, as more complex models need more support material, which represents waste and has no added value for the user [7].

The filler, which is the subject of the remainder of this article, is also fundamental to the resulting properties of the print model. The percentage fill of the model must be considered. It is pointless to use 100% fill for models that will only serve as display pieces. There is a direct proportion, the more material used the longer the model takes to print, the more electricity is consumed and the longer the print time the greater the likelihood of errors. In the tables, the numerical values for the types of supports and filler are worked out. The values do not vary much as this is a small and simple model, but even from the results, it can be concluded that the changes are still visible.

This paper is a part of further research where we will look at the properties of the models by support and infill type, whether from a mechanical, temporal, visual, or environmental impact perspective.

References

1. Ahmed,GH, A review of "3D concrete printing": Materials and process characterization, economic considerations and environmental sustainability, Journal of building engineering, doi 10.1016/j.jobe.2023.105863. 2023
2. Xiao,JZ, Study on preparation and mechanical properties of 3D printed concrete with different aggregate combinations https://www.webofscience.com/wos/woscc/full-record/WOS:000805982900001, doi 10.1016/j.jobe.2022.104282
3. Zhao, ZF, A critical review on reducing the environmental impact of 3D printing concrete: Material preparation, construction process and structure level, https://www.webofscience.com/wos/woscc/full-record/WOS:001111262500001, doi 10.1016/j.conbuildmat.2023.133887
4. UltiMaker, UltiMaker Cura, [Online], Available on: https://ultimaker.com/software/ultimaker-cura/
5. UltiMaker, Support settings, [Online], Available on: https://support.ultimaker.com/s/article/1667417606331
6. GEBHARDT, A.; KESSLER, Julia a THURN, Laura. 3D printing: understanding additive manufacturing. 2nd edition. Munich: Hanser Publishers, [2019]. ISBN 9781569907023.
7. HORVATH, J. C. a CAMERON, R.. Mastering 3D printing: a guide to modeling, printing, and prototyping. Second edition. Technology in action. New York: Apress, [2020]. ISBN 978-1-4842-5841-5.

Innovation of the method of controlling the robotic cell using the GUI environment

Dávid Kovaľuk [1] and Ján Semjon [2,*]

[1] M-D-J, spol. s r. o., Rampová 6, 040 01 Košice, Slovakia, david.kovaluk@mdj.sk
[2] Technical University of Košice, Faculty of Mechanical Engineering, Department of Production Technology and Robotics, Park Komenského 8, 042 00 Košice, Slovakia, jan.semjon@tuke.sk
* Correspondence: jan.semjon@tuke.sk; Tel.: +421 55 602 2625

Abstract: During the period when there was a lack of various components intended for the automation and robotization of processes, it was necessary to use the components and software solutions that were available to complete the tasks in progress. For this reason, there was also a need for the design, production and revival of a robotic cell, where the nailing of parts of wooden pallets was carried out. The robotic cell was specific in that it used its own control and software solution to create its own graphical operator interface. The use of a GUI interface made it possible to simplify the work of workers working with a robotic cell and at the same time created a prerequisite for further expansion or modification of the cell.

Keywords: innovation; robotic cell; palletization

1. Introduction

In addition to the significant impact on our health, the covid 19 disease worldwide affected not only the production of precious metals and other basic materials, but also the production of microprocessors and other products dependent on them. Even before the pandemic, great pressure was exerted on production (microprocessors, microcontrollers, motherboards, etc.), even though there were already limitations in terms of production capacity. The pandemic has added further pressure to an already busy segment, as production and distribution bottlenecks have met with increased demand due to pandemics [1].

Not so long ago, the interruption of the production of microchips had an impact only on the manufacturers of smartphones, tablets, computers, external drives and also the manufacturers of televisions. However, it has now affected almost all industries, not excluding the automotive industry and also manufacturers of PLC and HMI components. The delivery times of individual components began to gradually increase, which disrupted not only the development and construction of new robotic cells, but also the maintenance of older ones. In the case of smaller companies that did not have some spare components in stock, they had to look for alternative solutions. These solutions required in most cases increased maintenance costs [2,3].

Companies that had to modify their production portfolio to a greater extent during the pandemic and immediately after it, whether due to a change in customers or the current market orientation and demand, were forced to start more dynamic production. The ever-increasing use of robotic systems in production lines requires an improvement in their accuracy. In this direction, the proposed approach leads to an increase in accuracy by means of a closed-loop robot dynamic parameter estimation system [4]. Such a change in production also requires a more innovative and flexible approach to the logistics of storage and subsequent distribution of production to customers. One such warehouse innovation is a robotic workplace for the production of pallets of various dimensions. Pallets are produced in different sizes and in different numbers. Some pallets are used to transport products intended for the food industry and these must not be made for storage. Therefore, it is necessary to ensure a flexible and quick change in the production of the type of pallet. Last but not least, such a robotic cell not only makes production more efficient, but also protects human health, by minimizing the need to produce pallets manually with nailing equipment.

During the development of the new workplace, the delivery times of individual components and their price were also taken into account. Another important parameter was the simple implementation of individual parts of the workplace, as well as the subsequent adjustment and additional implementation of new types of pallets for production, without unnecessary downtime.

GUI automation can transform a system's GUI into an API in a non-intrusive way, allowing users to apply software systems in ways that were not envisioned by their original creators. For example, GUI elements can be packaged as objects [5] and used in other programs and models for purposes that may go beyond testing.

The graphical operator interface is the basis for simple operation of the robotic cell. A properly designed interface offers an adequate amount of information at the right time and in a format understandable to the operator. Operator error is cited as a major factor in many accidents. Many errors stem from a misunderstanding of the situation caused by an inappropriate HMI design. It's not just that people make bad decisions or act incorrectly, but they often just don't understand the situation they're in [6]. Therefore, comments and the level of experience of the operator were also taken into account when designing the HMI.

Modern GUI automation tools use computer vision and machine learning algorithms to process the visual elements in the GUI in near real time and to emulate the user interactions required to respond to these events [7].

The benefit of the solution to the described problem is the use of a GUI for simplifying the operation of the robotic workplace by the operator, the possibility of making simple adjustments when changing production, reducing the cost of purchasing and shortening the time for putting the workplace into operation.

2. Workplace requirements and workplace realization

As part of the innovation, certain requirements were specified that the workplace must meet on the basis of dynamic production and also taking into account the knowledge level and experience of the operator in controlling such robotic cells. The technical solution must minimize costs after the start of the proposed technology. And that, by minimizing the staffing of operation and maintenance by maximizing the automation of individual elements and subsystems. Also by minimizing the overall maintenance costs (the smallest possible number of different components), downtimes and minimization of the costs of energy, media, chemicals, etc.

The workplace must not exceed the maximum built-up area of 6x11m. In this space, a supply point for input material for the production of pallets and a space for finished and correctly nailed pallets must be provided.

The robotic cell must also meet production requirements with at least two types of nail lengths according to the type of pallet produced. Pallets differ in size, and for initial implementation, 7 of the most commonly used types were selected, ranging from 800x800mm to 1500x3000mm. Automatic detection of running out nails in the magazine and detection of incorrectly shot (protruding) nails is also required. For the needs of automatic stacking of manufactured pallets, the minimum load capacity of the robotic arm was defined as 100 kg, regardless of the weight of the effector itself.

Based on production and technical parameters, a palletizing robot with four degrees of freedom IRB 760-450/3.2 from ABB [8] was selected. This robotic manipulator is intended only for mounting on the floor, and therefore it is not possible to anchor the robot in an inclined direction around the X and Y axes. Its maximum load is 450 kg and a reach of up to 3.18 m. Figure 1 shows a view of the IRB 760 robot and the values of the maximum load of the end flange depending on the center of gravity of the end effector.

The robotic manipulator is equipped with an IRC 5 control system with a Flex-Pendant control panel. The control system can control up to 36 moving axes. The main axes of the robotic manipulator can be coordinated with external mechanical units such as positioners, linear motions and motion tracking devices.

The effector of the robotic manipulator was designed for nailing pallets and their subsequent stacking in predetermined places without the need to change the effector either automatically or manually.

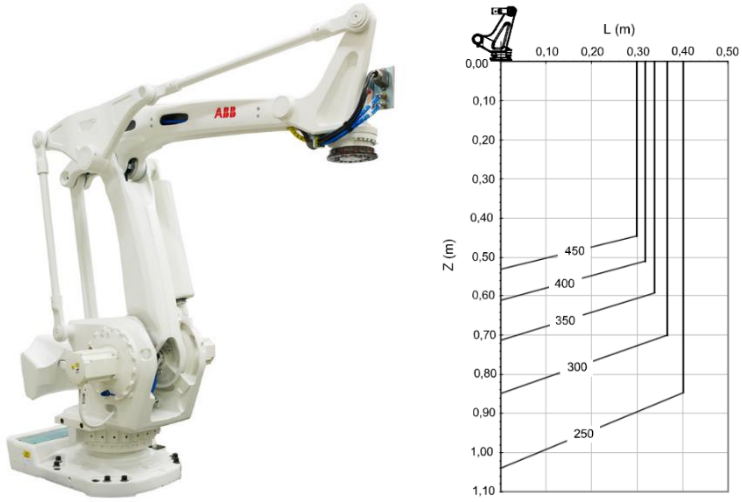

Figure 1. ABB palletizing robot and robot flange load course [9]

For nailing, two nailers [10] placed on a sprung frame are used to compensate for the differences in the thickness and curvature of the boards used for the production of pallets and thus to prevent the direct transfer of the pressure of the robotic manipulator to the pallet and the rotary table. Both have a precisely and statically set inclination and distance between them so that they can both nail at the same time according to the pre-defined distance of both nails. The nailers are supplied from "jumbo" magazines, the supply of which is up to 1000 nails. Each of the nailers has its own valve on the effector, which is activated only before nailing the given nail.

The rotary table (positioner) is divided into two halves, Figure 2. In one half the operator loads the parts of the pallet and in the other half the pallets are nailed by the robot. The rotary table allows changing the inclination of the loading surface for better ergonomics of the operator. Tilting is ensured by air pneumatic pistons with a brake in case of a drop or total loss of air pressure. An ABB MID 1000 motor unit was used for the rotary movement, which is controlled by the robot as an external axis [7]. The maximum load capacity of the unit is 3300 kg. The maximum rotation speed is 90°/s and the emergency stop time of the unit at full load is 0.9 s.

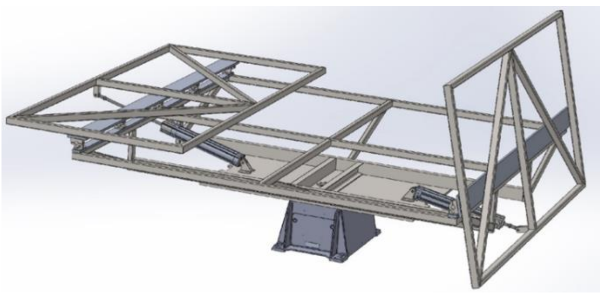

Figure 2. Turntable with the possibility of tilting the loading surface

3. Design and implementation of the program at the workplace

ABB robotic manipulators are programmed using the RAPID language. The ABB RobotStudio software was used as a programming IDE, which allows off-line programming [11]. It enables the programming of the robotic arm on a PC without the need to stop production. An exact copy of the real software that runs on the robotic manipulator is used. The entire management of the workplace is divided into three logical units that run in a separate task (thread).

All movement commands must be in the task of the mechanical unit of the robot. That is, all subprograms that execute commands associated with the control of the mechanical unit and their logic. The basic structure of the program is designed so that it is possible to easily implement other types of pallets in the future.

Individual types of pallets are therefore in their own subprograms (modules), which are named according to the pattern PM_[height]x[width]x[thickness].

Each palette type subroutine has its own set of variables, which have the same nomenclature as the palette types, but followed by an underscore and the variable name.

The most essential data type of each pallet module is the custom "PALETA" structure of all pallet-nailing points, Figure 3.

```
CONST PALETA p_1100x950x100_offset{50} := [
    [[0,0,0],0,1],
    [[0,15,0],0,1],
    [[0,145,0],0,3],
    [[0,285,-2],0,3],
    [[0,435,-5],0,3],
    [[0,580,-7],0,3],
    [[0,0,0],0,0]
]
```

Figure 3. Position structure for pallet nailing

Since the RAPID programming language cannot dynamically allocate the size of an object (array), it is necessary to define the size in advance. The proposed structure consists of the object position (pos), orientation (num) and ID of the nailer (num).

From the thus defined structure, we can determine the nailing position, which has X, Y and Z values. This position is defined as an offset from the first pallet nailing point, Figure 4.

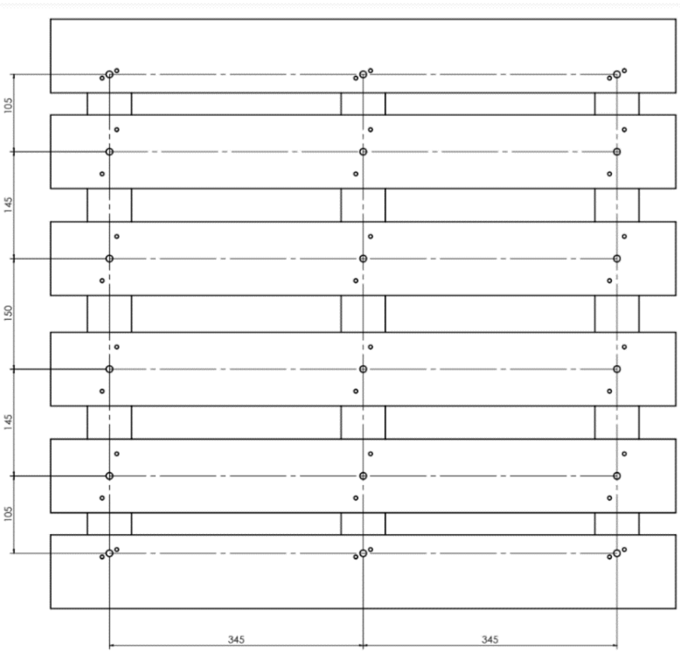

Figure 4. The position of the nails on the pallet

The orientation is entered as the offset of the effector rotation angle in the Z axis of the first defined point. The value "A nailer" or "B nailer" is a numerical expression of which nailer is active at a given nailing point. Both nailers on the effector have their own identifier, so a value of 1 or 2 in the "nailer" variable activates only the particular nailer. A value of 3 activates both nailers and a value of 0 disables both nailers. The value 0 is also used to end nailing.

Each pallet module also contains constant values that cannot be changed programmatically, such as the number of columns in the unloading zone into which pallets can be stacked, the number of pallets in one column and also the height (thickness) of the pallet in the column.

In this way, it is possible to lay out the entire module from the production drawing of the pallet and upload it between programs without having to stop production in any way. Subsequently, it is necessary to verify and possibly adjust the initial nailing position. This action is the only one that requires production suspension.

4. Use of GUI in the robotic cell program

Given that the robotic cell does not use a PLC controller, it was also necessary to find an alternative to classic HMI panels. One solution is to use the existing control panel (FlexPendant) of the robotic manipulator. This enables the operator's graphical interface to be displayed directly on the panel. This functionality is available as RobotWare option “617-1 FlexPendant Interface”. To develop such a graphical interface, the "ScreenMaker" tool included in RobotStudio can be used without the need for knowledge of application development in the Visual Studio environment.

The ABB FLexPendant has limited CPU and memory performance compared to a classic PC. The generated GUI application must be placed in the specified folders before it can be loaded into memory. If it is already loaded, it will appear as the next item in the ABB menu. By clicking on the item, this application is launched.

Since the controller controls the robotic manipulator and its other peripherals using the RAPID program, the GUI application needs to communicate with the RAPID server in order to read and write values and control inputs and outputs.

ScreenMaker only offers basic functionality for each graphic element, such as visibility, value, etc. Each of these properties can be assigned a RAPID variable, an application variable of a specific task or an I/O signal directly. In the case of using more complex functionalities, or logical connections, or enabling buttons, it is necessary to create such logic in the RAPID program. For these cases, a second task was created, which runs cyclically in the background in "semi static" mode. This task is responsible, for example, for displaying the current status of "safety zones", checking the logged-in user and controlling the effector.

Sometimes interaction with the operator is necessary even during production itself. For example, if the nail magazine is empty, the robotic manipulator stops working, goes to the position designated for refilling the magazines and prompts the operator to refill. The operator must first confirm with the OK button that he has been informed of the reason for the interruption of production, and then confirmation of the operator and replenishment of the nail reservoirs is expected. If a non-standard situation occurs during production that cannot be evaluated by the sensors, the operator is notified of this situation. Subsequently, it is possible to evaluate the current state of the workplace or material based on a series of questions asked to the operator and their answers. This eliminates downtime associated with manual guidance of the robotic manipulator from a collision situation, the need for the operator to be trained in manual operation of the robotic manipulator, and subsequent possible collisions during manual control.

5. Conclusions

This article describes the basic design and implementation of a robotic cell without a superior system and with the possibility of using the FlexPendant control panel as a replacement for HMI panels. The design of the workplace took into account the delivery times of individual components as well as the subsequent difficulty of implementation. The entire system was designed in such a way that its extensibility by other types of dimensions was easy and, above all, that the implementation limited production as little as possible. The design and implementation of the HMI in the FlexPendant robotic panel simplified the programming work and the time required to assemble the entire cell. Last but not least, such a control and visualization approach accelerated the training of the operator, since each step is interaction with the user in the form of information windows and questions. Therefore, if a situation arises that requires operator intervention, it can be resolved quickly and with a high degree of awareness of the situation and its possible solution.

Acknowledgments: This article was created thanks to the support of the KEGA project: 020TUKE-4/2022 Development and implementation of new approaches in the teaching of industrial and collaborative robotics and VEGA project: 1/0215/23 Research and development of robotic workplaces equipped with industrial and collaborative robots.

References

1. The conversation. Available online: https://theconversation.com/the-covid-19-pandemic-has-revealed-that-global-supply-chains-are-a-huge-house-of-cards-164821 (accessed on 22-02-2024).
2. Kovaľuk, D.; Semjon, J.; Syč - Krivaň, M.; Sabol, M. Design of the educational workplace for working with a collaborative robot. In: Technical Sciences and Technologies: Chernihiv National University of Technology Roč. 29, č. 3 (2022), s. 37-44. - ISSN 2411-5363.
3. Kovaľuk, D.; Semjon, J.; Kočan, M.; Demko, R. Inovácia spôsobu pripojenia koncových efektorov na robot Motoman. In: Scientific Letters of Academic Society of Michal Baludansky. - Košice (Slovensko): Roč. 10, č. 1 (2022), s. 64-68. - ISSN 1338-9432.
4. Aivaliotis, P.; Papalitsa, E.; Michalos, G.; Makris, S. Identification of dynamic robot's parameters using physics-based simulation models for improving accuracy, Procedia CIRP, Vol. 96, 2021, p. 254-259, ISSN 2212-8271, https://doi.org/10.1016/j.procir.2021.01.083.
5. Tudor, B.I. Leveraging Graphical User Interface Automation for Generic Robot Programming, Robotics 2021, 10, 3. https://doi.org/10.3390/robotics10010003.
6. Gruhn, P. Human Machine Interface (HMI) Design: The Good, The Bad, and The Ugly (and what makes them so), In. 66th Annual Instrumentation Symposium for the Process Industries January 27-29, 2011.
7. Yang, X.; Miao, Y.; Zhang, Y. Model-driven GUI Automation for Efficient Information Exchange between Heterogeneous Electronic Medical Record Systems. In Information Systems Development; Springer: New York, NY, USA, 2011; pp. 799–810.
8. ABB Robot. Available online: https://new.abb.com/products/sk/3HAC020536-020/irb-760 (accessed on 21-02-2024).
9. APACH. Available online: https://www.apach-tools.com/product-Automate-Modular-For-Jumbo-Coil-Nails-Automate.html (accessed on 21-02-2024).
10. ABB Robot. Available online: https://library.e.abb.com/public/d091a804eb9e45d7820d948609b67671/3HAC040147%20PS%20MU%20GU-en.pdf?x-sign=0LEL+Yfn07JAwrQqawr4BEFziIoMCcm5bKN3gPlge/tGchB6ETyNtXmc50QUncbn (accessed on 21-02-2024).
11. ABB Robot Studio. Available online: https://new.abb.com/products/robotics/robotstudio (accessed on 22-02-2024).

Cell Lines for the Formation of Cartilage Tissue Using 3D Bi-oprinting

Zuzana Kovářová [1]

1 Faculty of Mechanical Engineering, Technical University of Košice, Slovakia; Zuzana.kovarova@student.tuke.sk

Abstract: Human cartilage tissue can be categorized into three types: hyaline cartilage, elastic cartilage and fibrocartilage. Each type of cartilage tissue possesses unique properties and functions, which presents a significant challenge for the regen-eration and repair of damaged tissue. [1] Cell lines based therapy represents a promising treatment strategy for defect cartilage. Cells, scaffolding biomaterials and 3d bioprinting open many new avenues for cartilage tissue engineering. However, the choice of the optimal cell source is not that straightforward. Currently, various types of differentiated cells (articular and nasal chondrocytes) and stem cells (mesenchymal stem cells, induced pluripotent stem cells) are being researched to objectively assess their mer-its and disadvantages with respect to the ability to repair damaged cartilage. [2] This review presents foundational in-formation about different cell types used in cartilage treatment. We compare and analyze the advantages and disad-vantages of these cell types and offer a potential outlook for future research.

Keywords: Cell lines, bioprinting, cartilage, tissue engineering, scaffolds, bioink

1. Introduction

Cartilage tissue engineering has emerged as a promising field for addressing the limitations of conventional treatments for cartilage defects and injuries. Among the innovative techniques, 3D bioprinting stands out as a revolutionary meth-od for precisely fabricating complex tissue structures. Central to this process are specialized cell lines that play a pivotal role in the formation of functional cartilage tissue. Traditionally, cartilage repair strategies have faced challenges due to the limited regenerative capacity of cartilage. However, the advent of 3D bioprinting technology has provided new ave-nues for overcoming these hurdles. By combining biocompatible materials known as bioinks with living cells, research-ers can create intricate 3D structures that mimic the native tissue's architecture and properties. The selection of an ap-propriate cell line is crucial for successful cartilage tissue formation via 3D bioprinting. Factors such as cell viability, proliferation capacity, and ability to produce cartilage-specific ECM components must be carefully considered. Addi-tionally, optimizing the bioink composition and printing parameters is essential to ensure cell survival and maintain tissue integrity during and after bioprinting. Recent advancements in bioprinting technologies have enabled the fabrica-tion of complex, multi-layered cartilage constructs with precise control over micro-architecture and mechanical proper-ties. By incorporating bioactive molecules, growth factors, and mechanical stimuli into the bioprinting process, re-searchers aim to further enhance the functionality and integration of engineered cartilage implants.

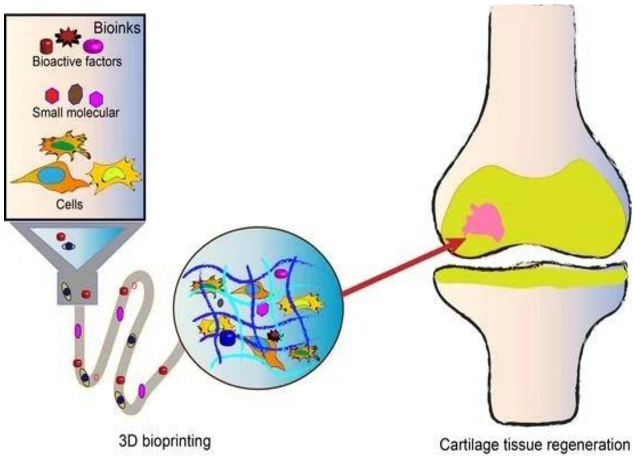

Figure 1 Graphical abstract [3]

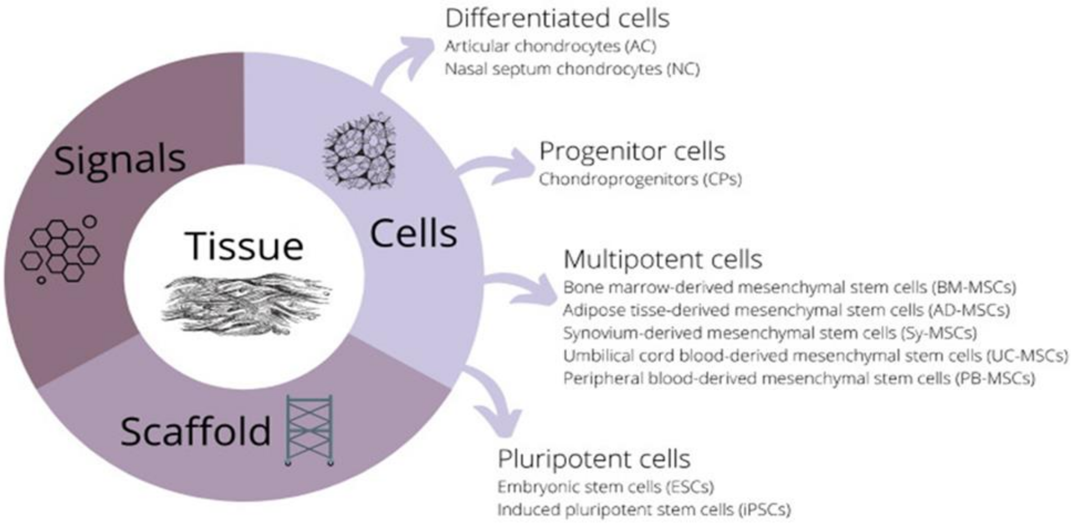

Figure 2 Three essential components of new strategies for cartilage treatment: cells, scaffold, signals [2]

2. Sources of Cells for Cartilage Tissue Bioprinting

The choice of cells is a central problem to any modality of tissue engineering. For cartilage bioprinting, several factors need to be taken into consideration when choosing suitable cell sources:

(i) cells must be robust enough to survive any shear stress and pressure during the printing process;

(ii) cells must proliferate well;
(iii) cells must possess biosynthesis levels (e.g., of proteoglycans, Collagen type II) comparable with native chondrocytes so they can maintain their biological functions.[4]
Cartilage is produced by the chondrocytes, and that makes them the key cells for the development of cell-based cartilage repair and regeneration strategies. Often, these procedures require culture expansion of cells with chondrogenic poten-tial. That property can be attributed to several cell types from the categories of differentiated cells and their unipotent progenitors, as well as multipotent and pluripotent stem cells.[3]

2.1. differentiate cells, the well-known sources of cells with chondrogenic capacity are:
2.1.1. articular chondrocytes -many studies have focused on the use of articular chondrocytes as a viable cell source for cartilage repair. However, the harvesting of joint cartilage is a highly invasive procedure accompanied by the potential for donor site morbidity and loss of function. In addition, low cell yields, low mitotic rates, and low bioactivity can fur-ther limit the use of articular chondrocytes in a clinical setting.[1]
2.1.2 auricular chondrocytes is an elastic cartilage found in the ear and epiglottis. In a study by van Osch et al, human auricular chondrocytes were investigated for their potential use in cartilage repair. Compared to articular cartilage, au-ricular chondrocyte isolation resulted in cell yields 2-fold higher and cell proliferation rates 4 times faster, while retain-ing chondrogenic potential when cultured in alginate beads. With in vivo culture, constructs exhibited proteoglycan-rich matrices with positive type II collagen staining and faint elastin staining. In addition, auricular chondrocyte samples produced neocartilage with greater biochemical and histological similarity to that of native cartilage than articular counterparts when implanted in vivo . [1]
2.1.3. nasoseptal cartilage is a hyaline cartilage that has received attention for applications in craniofacial and plastic surgeries. Adult nasal chondrocytes are capable of generating a matrix with high collagen II/I ratio and GAG accumula-tion. In addition, nasal chondrocytes proliferate 4 times faster than articular chondrocytes in monolayer. Also, nasal chondrocytes have been successfully cultured in number of scaffold system including alginate, methylcellulose and hyaluronic acid. [6]
2.2.unipotent progenitor cells, chondroprogenitors (CPs), are descendants of stem cells , can be isolated from various tissue sources such as cartilage, synovium, meniscus, and infrapatellar pad. They don´t require autologous cartilage, but show limited abundance.
2.3. multipotent stem cells with chondrogenic capacity:
mesenchymal stem cells (MSCs) from different sources such as bone marrow, adipose tissue, synovial fluid, amniotic fluid, umbilical cord blood, and peripheral blood. Mesenchymal stem cells display strong self-renewal, proliferation, and differentiation potential, but with high donor site morbidity. MSCs remain the most largely investigated sources of chondrogenic cells for cartilage repair. These stem cells can be differentiated to undergo chondrogenesis with the sup-plement of specific growth factors, such as transforming growth factor beta family and therefore they have been ex-plored to be used in cartilage tissue engineering.
2.4.pluripotent stem cells :
pluripotent embryonic stem cells (ESCs) is inner cell mass from the blastocyst and induced pluripotent cells (iPSCs) can be derived from differentiated cells using reprogramming techniques.
It is an ongoing challenge to produce enough regenerative-non-immune cells that maintain their unique biological ac-tivity in the transplanted areas. For example, cartilage provides limited donor tissue for chondrocytes, while allogeneic or heterogeneous chondrocytes are often rejected due to the immune response of the human body. Various conditions, such as dedifferentiation and loss of cell phenotype, are prone to occur in the process of in vitro expansion. However, stem cell-based 3D printing may result in enhanced tumorigenesis risk as well as genetic instability and chromosomal aberrations [3] and cell reprogramming.

3. Cartilage Tissue Bioprinting

In tissue engineering, cells are generally seeded onto a scaffold, whose primary objective is to replicate the characteris-tics of the target-tissue extracellular matrix (ECM), which is comprised mainly of proteoglycans, glycoproteins, collagen fibers, and water.[10] By mimicking the ECM, biomaterials provide cells with an environmental structure able to sup-port cell viability, proliferation and secretory activities. Many ECM-like

scaffolds are available and have been considered for cartilage tissue engineering. Traditional cartilage scaffold materials mainly choose natural biomaterials or artificial materials.
Natural biomaterials, including gelatin, alginate, collagen, silk fibroin, sodium hyaluronate, chitosan, etc.[1] which are easily accessible and possess a variety of growth factors that can allow chondrocytes to attach to scaffolds and enhance their survival capacity, but the resulting scaffolds have poor mechanical properties [9].Artificial polymer materials, such as polylactic acid, polycaprolactone, polyethylene glycol, and polyglycolic acid etc., have been also utilized [1], the ad-vantages of which can be based on the demand, obtaining scaffolds of different porosity, different mechanical properties of scaffolds, and different degradation rates due to different materials, but the disadvantages are the hydrophobic sur-face of synthetic polymers, lack of bioactive factors, poor cell adhesion, and acidic metabolites are generated during the degradation process after implantation into humans, which causes a local pH reduction and will cause inflammatory immune responses. [9]
Inorganic materials are also sometimes added to scaffold material; these include nano-hydroxyapatite, tricalcium phosphate, graphene oxide, carbon nanotubes, nano-cellulose, iron oxide nano particles, and silver nanoparticles.
However, cartilage has excellent mechanical properties due to its complex ultrastructure, which is difficult to replicate artificially. The use of nanotechnology can provide a solution in simulating the structure of cartilage tissue. Studies have proved that carbon nanotubes manufactured using 3D bioprinting technology can enhance the physical properties of cartilage scaffolds. In another study, carboxylated cellulose nanocrystals (cCNCs) were prepared using ammonium persulfate as hydrogel inks, and stable cell-free and cell-loaded hydrogel inks with the best physicochemical properties and biocompatibility were developed magnetic nanoparticles (Fe_2O_3) were used as a bioink to generation magnetic nanocomposite hydrogel for cartilage tissue engineering . [3] As a technology that initially appeared at the end of the 20th century, 3D printing can manipulate the structure of engineered tissue scaffolds with high resolution and accuracy. In the recent decade, the 3D printing technique has been increasingly applied in the repair of articular cartilage, which is usually unable to self-regenerate as it lacks vessels and nerves. [12]
Hydrogels play an important role in 3D bioprinting . Their excellent water absorption makes the hydrogel as the first choice for 3D applications. Nutrients and growth factors are encapsulated in the hydrophilic hydrogel to form a hydro-gel network that mimics the microenvironment of natural tissues, allowing for high biocompatibility. Gelatin, alginate, hyaluronic acid, collagen, fibrin/fibrinogen, hyaluronic acid, chitosan, decellularized extracellular matrix (dECM), and polyethylene glycol (PEG) are commonly used bioinks, as they are natural materials with biocompatibility properties. Additionally, some of these materials can be easily photo-crosslinked in their modified form. Furthermore, there are some specific honeycomb integrins found within the hydrogel matrix that can enhance cell adhesion, migration, prolif-eration, and differentiation. [10]
The ideal biomaterial should be biocompatible to prevent inflammatory and immunological reactions. It must provide a favorable environment for the 3D maintenance of chondrocyte phenotype and be adhesive to enable attachment of the cells within the lesion. It must be permeable to allow the diffusion of molecules, nutrients and growth factors. Finally, it should be biodegradable enough to be integrated in the physiological processes of tissue remodeling and ideally, should be injectable, thereby allowing for implantation by minimally invasive surgery.

4. Conclusions and Future Perspectives

Many different cell lineages of various potencies and sources have been studied; advantages and disadvantages of the types are outlined in Table 1.

Potency	Type of cells	Advantages	Disadvantages
unipotent	chondroprogenitor cells	doesn´t require autologous cartilage to obtain	limited abundance
multipotent stem cells MSCs	mesenchymal	self renewal autologous abundant	donor site morbidity
pluripotent stem cells	embryonal ESCs	indefinite self renewal multiple cell lines	ethical problems immune rejection
	induce IPSCs	autologous	tumorigenicity cellular reprogramming
chondrocytes	articular	low immunogenicity	low mitotic rates
	nasoseptal	fast proliferation	donor site morbidity
	auricular	fast proliferation	donor site morbidity

Research results show, that mesenchymal stem cells (MSC) have emerged as a major line with respect to cartilage engi-neering and show excellent chondrogenic potential. [11]

Hydrogels have become the most used resources for bioinks used in 3D bioprinting due to their elastic property and ECM-mimetic crosslinked network structure. [13].The mechanical and structural properties of printed constructs can be tuned by manipulating their printing process or crosslinking with other materials. In addition, cells, drugs, and other bioactive factors such as cytokines, can also be combined with 3D-printed tissue scaffolds to enhance the repair and regeneration of cartilage [7]. The potential applications of 3D bioprinting cartilage constructs extend beyond regenera-tive medicine to drug screening, disease modeling, and personalized medicine. However, challenges such as vasculari-zation, long-term stability, and immune response need to be addressed to translate these innovations into clinical thera-pies successfully.3D bioprinting combined with specialized cell lines offers a promising approach for the formation of cartilage tissue with remarkable structural and functional properties. Continued research and collaboration between scientists, engineers, and clinicians are essential to unlock the full potential of this transformative technology in carti-lage regeneration. [14]. Overall, the future of 3D bioprinting is promising and it is expected to drive major advancements both within research and the clinical environment in the future, including in areas of reconstructive surgery, medical imagery, drug development and delivery, and cancer research. Ultimately, 3D bioprinting is expected to become an es-sential tool in the treatment of cartilage injury and disease, and overall will improve the quality of life for patients. [15]

Conflicts of Interest: "The authors declare no conflict of interest."

References

1. Jian Zhou , Qi Li , Zhuang Tian , Qi Yao , Mingzhu Zhang Recent advances in 3D bioprinted cartilage-mimicking constructs for applications in tissue engineering ScienceDirect Published December 2023
2. Inga Urlič, Alan Ivkovič : Cell Sources for Cartilage Repair—Biological and Clinical Perspective PMC PubMed Central Published 16 September 2021
3. Jianghong Huang, ,Jianyi Xiong ,Daping Wang, Jun Zhang,Lei Yang, Shuqing Sun and Yujie Liang 3D Bioprinting of Hydrogels for Cartilage Tissue Engineering MDPI Open Access Journal Published:16 September 2021
4. Fu You , B. Frank Eames and Xiongbiao Chen: Application of Extrusion-Based Hydrogel Bioprinting for Cartilage Tissue Engineering MDPI International Journal of Moecular Science Published: 23 July 2017
5. Cindy Chung and Jason A. Burdick Engineering Cartilage Tissue PMC Published October 2007
6. Marta Anna Szychlinska, Fabio Bucchieri, Alberto Fucarino, Alfredo onca, and Ugo D'Amora : Three-Dimensional Bioprinting for Cartilage Tissue Engineering: Insights into Naturally-Derived Bioinks from Land and Marine Sources PMC PubMed Central Published 12 August 2022.
7. Qiushi Liang, Yuanzhu Ma,Xudong Yao, and Wei Wei Advanced 3D-Printing Bioinks for Articular Cartilage Repair Published: April 2022
8. Matai I., Kaur G., Seyedsalehi A., McClinton A., Laurencin C.T. Progress in 3D bioprinting technology for tissue/organ regenerative engineering. Biomaterials. 2020;226:
9. Research on Cartilage 3D Printing Technology Based on SA-GA-HA by Yong Chen,Youping Gong,Lijun Shan,Chou Yong Tan,MS Al-Furjan,Huipeng Chen,Xiangjuan Bian,Yanda Chen,Yunfeng Liu and Rougang Zhou MDPI Published:28 July 2023
10. SophieMcGivern, Halima Boutouil, Ghayadah Al-Kharusi, Suzanne Little, Nicholas J. Dunneand Tanya J. Levingstone Translational Application of 3D Bioprinting for Cartilage Tissue Engineering PMC Published: 18 Oct 2021
11. Sam L.Francis, Claudia Di Bella, Gordon G.Wallace, Peter F.M.Choong Cartilage Tissue Engineering Using Stem Cells and Bioprinting Technoogy – Barriers to Clinical Translation Frontiiers in Surgery Published: 27 Nov.2018
12. Dijkgraaf L.C., de Bont L.G.M., Boering G., Liem R.S.B. Normal cartilage structure, biochemistry, and metabolism. A review of the literature
13. A.T.Mohammadi, N.S.T.Gohari,S.Shafagh,H.Bagheri Stem Cell Book Published: Oct 2022 ISBN: 971-8843740580
14. Matai, I.; Kaur, G.; Seyedsalehi, A.; McClinton, A.; Laurencin, C.T. Progress in 3D bioprinting technology for tissue/organ regenerative engineering. Biomaterials 2020,
15. Thayer, P.; Martinez, H.; Gatenholm, E. History and Trends of 3D Bioprinting. Methods Mol. Biol. 2020, Derby, B. Inkjet Printing of Functional and Structural Materials: Fluid Property Requirements, Feature Stability, and Resolution.

TECHNICKÁ UNIVERZITA V KOŠICIACH
Strojnícka fakulta

Data Digitization in an Industrial Enterprise

Peter Krajny [1]* and Jaroslava Janekova [1]

[1] Institute of Industrial Engineering, Management, Environmental Engineering and Applied Mathematics, Faculty of Mechanical Engineering, Technical University of Košice, Park Komenského 5, 040 02 Košice, Slovakia; peter.krajny@student.tuke.sk (P.K.); jaroslava.janekova@tuke.sk (J.J)
* Correspondence: peter.krajny@student.tuke.sk; (P.K.)

Abstract: In a world that is progressively becoming more digital, the modeling and handling of data have gained high significance. This is especially true as we transition from conventional data management, pass through the era of big data, and enter into the current phase of digitization. This paper describes the study of the digitization of various data types and the interconnections between multiple data sources from a real automotive assembly line. The model is designed for a specific production line, with a focus on analyzing the efficiency of the line and optimizing maximum output. The results of this study include the evaluation of stations and applications that can alert common users when any deviation in production is detected.

Keywords: data digitization; production data; digitization; industry

1. Introduction

Digitization has been recognized as one of the prominent trends reshaping society and business in the immediate and long-term future [1]. The impact of digitization will be substantial; several authors have linked it to the industrial revolution [2-5]. The term "digitization" specifically refers to "the action or process of digitizing; the conversion of analogue data (especially in later use, images, video, and text) into digital form." According to the literature, digitization, or digital transformation, denotes "the changes associated with the application of digital technology in all aspects of human society" [6]. Digitization is also recognized as the "ability to turn existing products or services into digital variants, and thus offers advantages over tangible products" [7,8].

Certainly, numerous challenges are linked to the effective management of various data types. Beyond addressing the substantial volume of big data, there is a necessity to identify and comprehend patterns. Historical data management has consistently prioritized the acquisition of precise depictions of business activities.

The evolution of data management has transitioned from crafting tools and methodologies for conventional, structured data to handling big data, thereby opening avenues for innovative applications of data derived from emerging technologies. Effective data management, along with the archival of data for future utilization [9], is of paramount importance. This paper focuses on digitization of data transformation from the production environment to Cloud Application, using analytical techniques to merge data from multiple sources to obtain one analytical output.

2. Methods and Materials

One of the criteria for measuring the level of factory digitization is also the evaluation of the method for recording and processing data. Data can come from various sources and can be processed by different tools. This study focuses on an example problem from an automotive company that specializes in the production of car seating systems.

2.1 Case study description

Observed in the long term, on the assembly line, consisting of 16 assembly stations (see Figure 1), a prolonged cycle time consequently reduces maximum output from the line. This issue leads to delays in deliveries and requires overtime work to meet customer demands. In addition to the increased cycle time, higher failure rates were identified, resulting in more products requiring rework and further burdening the production process.

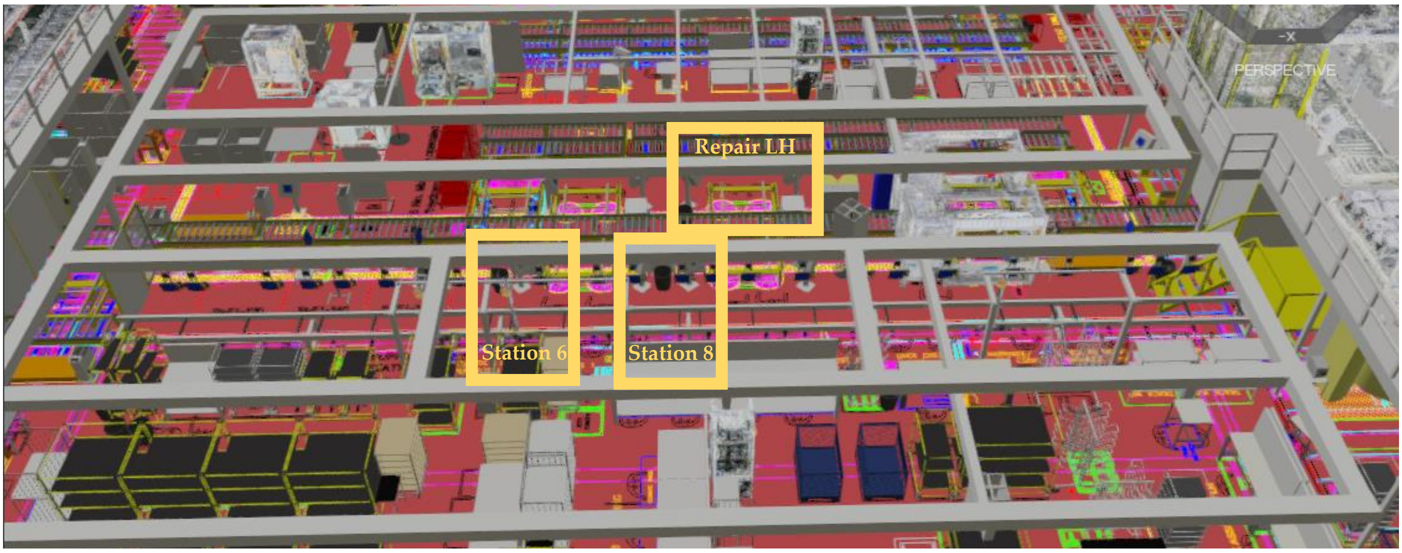

Figure 1. Line snapshot from 3D Digital Twin model with marking of the most problematic stations.

The mentioned issue burdened the company with one extra shift per month, involving 14 operators classified as Direct Labor (DL) on the assembly line. The annual salary for such an operator amounts to EUR 33,750. It is also necessary to consider Indirect Labor (IDL) representing additional costs. IDL activities are connected with all additional production activities, such as logistics. Therefore, when calculating the impact of the issue for a year, the total loss for DL overtime hours is EUR 28,300.

2.2 Case study solution process

As an analytical tool, Palantir Foundry software was chosen, which allows the evaluation of a huge amount of data provided as outputs from the line. This technical solution enables filtering and processing of all production data, providing a comprehensive overview of assembly operations at individual stations.

To process data with the given software, it is necessary to transfer data from the assembly line to the Cloud Server. Some data from the line are processed by an internal information system and serve for traceability. This data includes information about completed operations and general details about whether they were executed correctly and completely. However, for a comprehensive analysis of the assembly line, this is not sufficient. Therefore, additional data has to be collected, such as the time of individual operational tasks, repeatability of scanning, documentation of product defects etc. To obtain such data, it was essential to directly connect the assembly line to the Cloud Server and set up automatic data uploads to the Cloud Server.

All the data that was received from the specific assembly line and the company's information system on the Cloud Server is referred to as raw data. In the next stage, it is necessary to filter and cleanse this data to retain only the necessary information. Since this data comes from multiple sources, in addition to the cleaning process itself, it is also necessary to interconnect and map this data. This allows the system to associate times, defects, and other operational findings with individual car sets. Such data is referred to as raw datasets. Subsequently, these datasets need further modification and definition of the type of information they carry (such as date and time, value, number, etc.). The modified data with properly defined values is called preprocessed datasets.

Correctly sorted data from multiple sources is mutually linked, thereby creating clean datasets. These clean datasets serve as our input databases for our analysis—input data.

After creating and processing datasets, the next step involves defining how the system should process and evaluate gathered data. This step focuses on the creation of Data Lineage and the formation of a Pipeline (see Figure 2). A Pipeline illustrates the network of connections between individual phases of the process and datasets, culminating in one or more outputs. This final output represents the conclusion of our analysis.

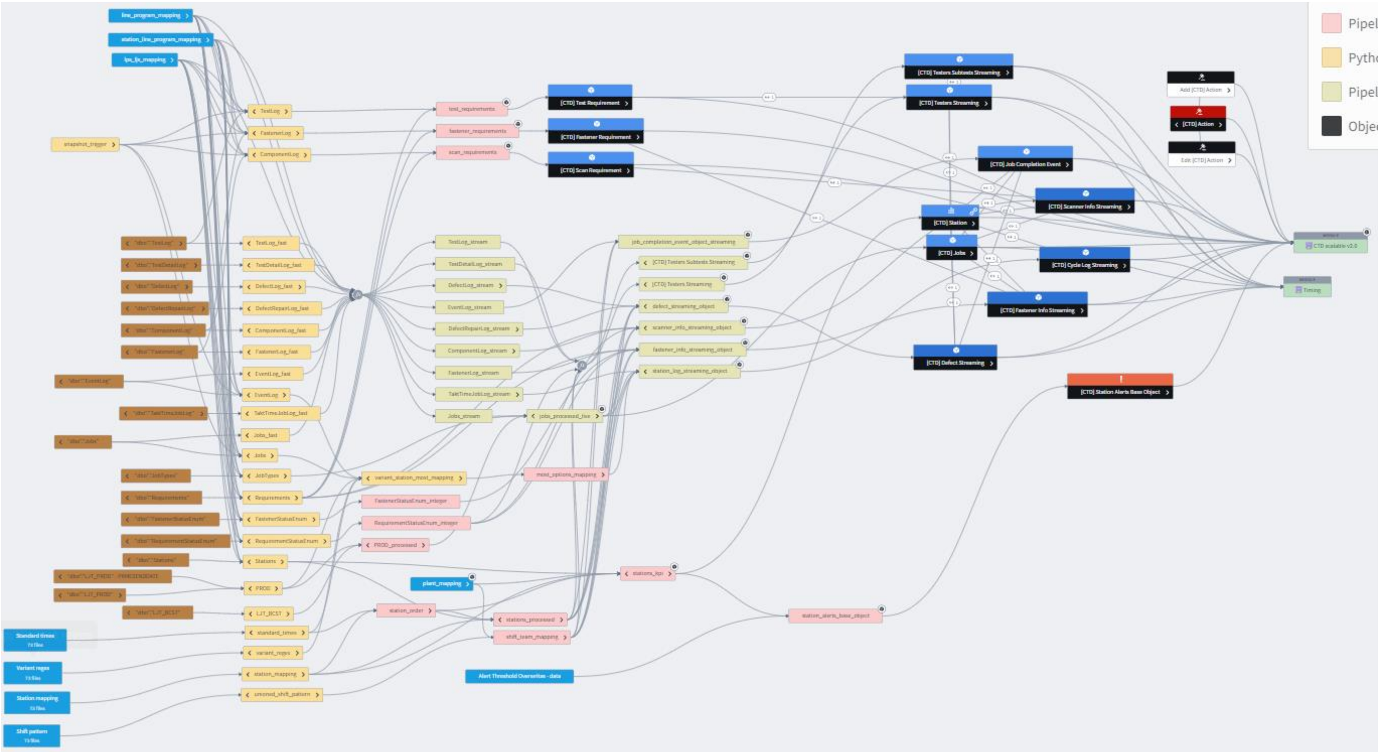

Figure 2. Pipeline snapshot from Palantir Foundry.

The Data Lineage built with the Pipeline, as shown in Figure 2, provides a quick snapshot of how the data are processed. In the left part of the figure, we can see raw data uploaded to the Palantir Foundry platform and the data transformation in the middle part. The right part of the Data Lineage consists of the Ontology layer, which describes internal processes and processed data as the final output shown in the front-end application.

The application allows the programmer to create a user interface using the Contour module, where it is possible to monitor the process in real-time (see Figure 3). The user interface created in this way can quickly inform users about current events on the assembly line. The display for the end user is called the Workshop, enabling them to enter individual stations and analyze the process.

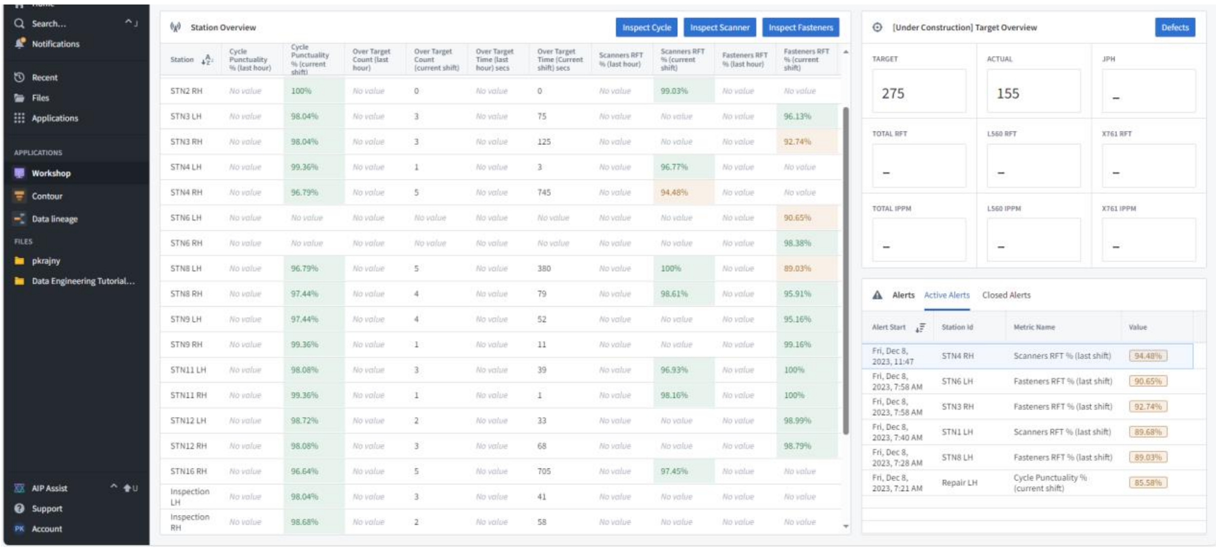

Figure 3. User interface snapshot from Palantir Foundry workshop module.

3. Results

By collecting raw data from the assembly line and subsequently processing it, it was possible to analyze and diagnose weak points on the line over a period of 3 weeks.

During the evaluation of this analysis, two shortcomings were identified in the fastening process. Extended fastening times were detected at stations 6 and 8 (see Figure 4). To find the root cause of the fastening process it will be necessary to conduct additional analysis to identify the root cause in the initial analysis.

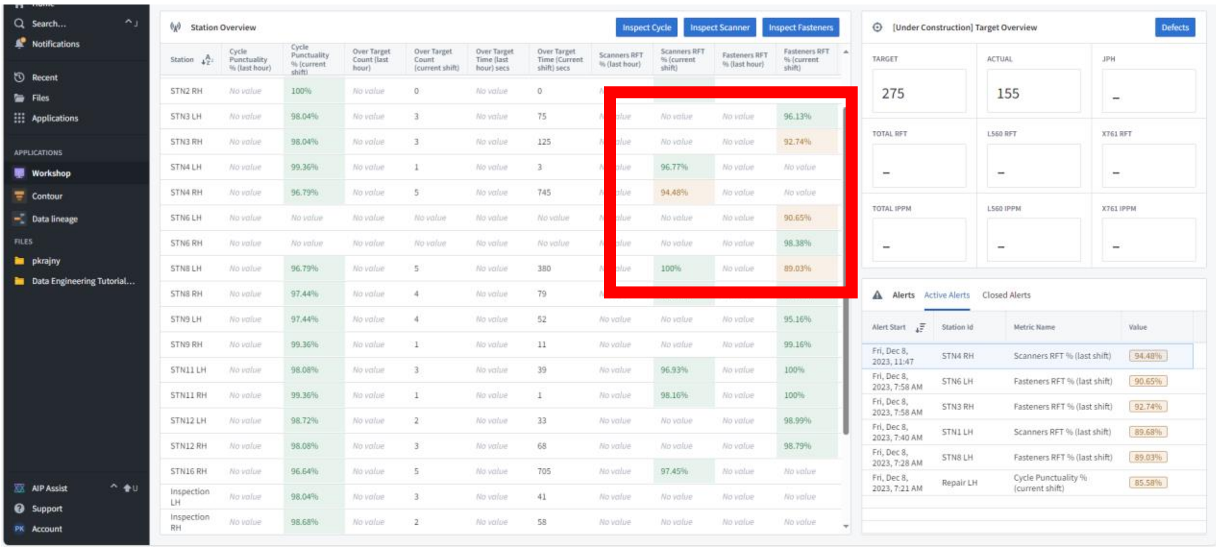

Figure 4. Detection of cycle time deviation in fastening operations.

At the Inspection LH station, it was detected that the most common defect occurs in zone 27 (See Figure 5).

Figure 5. Defect identification by the system

Due to the more demanding rework at the Repair LH station, the station's efficiency decreased to 85 % (see Figure 6).

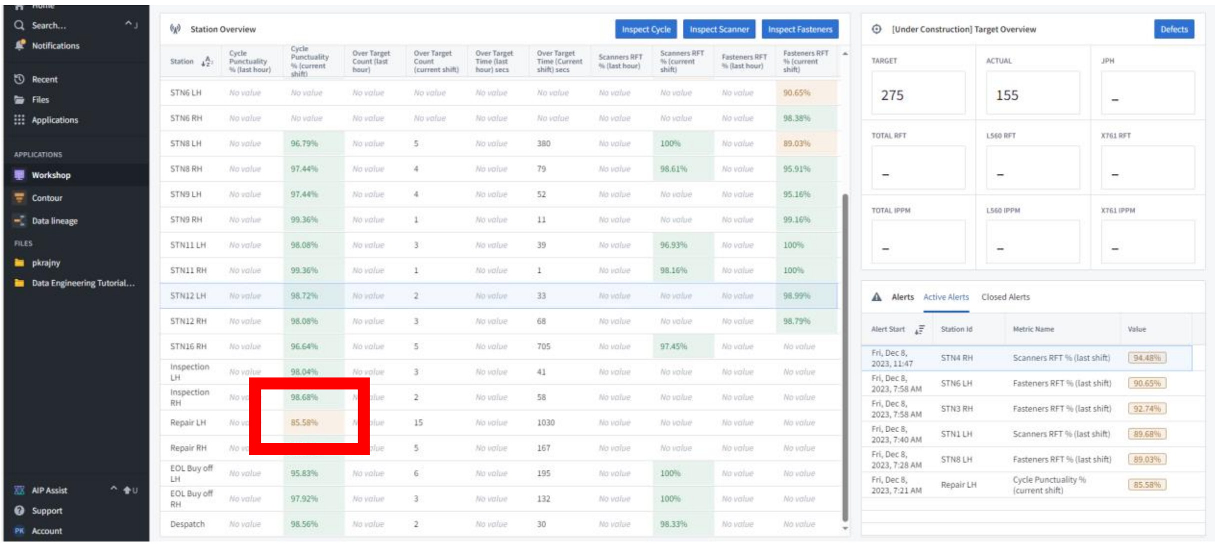

Figure 6. Deviation in cycle time from the standard time due to a higher scrap rate.

In addition to analyzing the efficiency of the assembly line at station Repair LH, it is possible to monitor defects and the system can analyze and categorize them into groups. It is also possible to automatically assign defects to specific zones and visualize them.

The Palantir Foundry application collaborates with artificial intelligence, and the longer it runs, the more it learns and understands the process. This capability can enable us to achieve better process monitoring and utilize early warning systems in the future.

If there are some improvements in efficiency at these three stations, it will be possible to meet customer requirements without the need for overtime and realize potential annual savings in the amount of EUR 28,300.

In addition to process analysis a monitoring interface was created for real-time production monitoring and an application for an early warning system was prepared. This may help in tracking the process with automatic alerts in case of any deviation.

4. Discussion

Data digitization, as described in these pages, brings us to another level of evaluation and data analysis. Implementing automated data analytical tools using artificial intelligence may help us better understand the processes and save time for additional big data analysis.

We can see similarities with authors Storey and Woo (2018) as they describe in their papers focused on the data challenges in the digitalization era, particularly the issues related to data quality and integration from multiple sources. Our approach of filtering and cleansing data, and the subsequent creation of preprocessed datasets, reflects a similar concern for data quality. Both studies emphasize the critical role of data integrity in achieving accurate and reliable analytical outcomes.

Based on this case study and future research, we aim to define the classification and evaluation of the level of digitalization in industrial enterprises.

5. Conclusion

The digitization of data within an industrial enterprise, as exemplified by this case study, underscores the transformative potential of advanced data management techniques. By integrating cloud-based solutions and sophisticated analytical tools like Palantir Foundry, the study effectively highlights how comprehensive data collection, cleansing, and analysis can optimize production efficiency and reduce operational costs. The ability to identify and address inefficiencies in real-time through automated systems not only enhances productivity but also promises significant financial savings. This case study lays a foundation for future research aimed at developing standardized measures for evaluating the level of digitization in industrial enterprises, further contributing to the ongoing digital transformation in the manufacturing sector.

Acknowledgments: This paper was developed within the projects implementation: VEGA 1/0340/21 "The impact of a pandemic and the subsequent economic crisis on the development of digitization of enterprises and society in Slovakia"

Conflicts of Interest: The authors declare no conflict of interest.

References

1. Beck, R.; Avital, M.; Rossi, M.; Thatcher, J.B. Blockchain technology in business and information systems research. *Business & Information Systems Engineering*. **2017**, 59(6), 381–384.
2. Chen, H.; Chiang, R.H.; Storey, V.C. Business intelligence and analytics: from big data to big impact. *MIS Q*. **2012**, 36(4), 1165–1188.
3. Chen, P.P.S. The entity-relationship model—toward a unified view of data. *ACM Trans. Database Syst*. **1976**, 1(1), 9–36.
4. Delcambre, L.M.L.; Liddle, S.W.; Pastor, O.; Storey, V.C. A reference framework for conceptual modeling. In: *Conceptual modeling, ER 2018*, Trujillo, J.C., et al. (eds.) ER 2018. Springer, LNCS, Cham, 2018; Volume 11157, pp. 27–42.
5. Embley, D.W.; Liddle, S.W. Big data—conceptual modeling to the rescue. In: *Conceptual modeling, ER 2013*, Ng, W., Storey, V.C., Trujillo, J.C. (eds.) ER 2013. Springer, LNCS, Heidelberg, 2013; Volume 8217, pp. 1–8.
6. Goes, P.B. Editor's comments: big data and IS research. *MIS Q*. **2014**, 38(3), iii–viii.
7. Gupta, M., George, J.F. Toward the development of a big data analytics capability. *Information & Manage*. **2016**, 53(8), 1049–1064.
8. Larsen, H. The crisis of public service broadcasting reconsidered: commercialization and digitalization in Scandinavia. Crisis Journal. 2016. Reconsidered: Democ. Cult. Prof. Codes, Digital Future 43–58.
9. Storey, V.C.; Woo, C. Data challenges in the digitalization era. In: Proceedings of the 28th Workshop on Information Technologies and Systems, Santa Clara, California, 2018.

TECHNICKÁ UNIVERZITA V KOŠICIACH
Strojnícka fakulta

Evaluation of Nakazima test results obtained by the Aramis system and comparison with numerical simulations

Juliy Martyn Kulya [1]* and Miroslav Tomáš [1]

[1] Department of Automotive Production, Faculty of Mechanical Engineering, Technical University of Kosice; miroslav.tomas@tuke.sk
* Correspondence: juliy.martyn.kulya@tuke.sk; Tel.: +421 55 602 3528

Abstract: This study investigates the effectiveness of the Nakazima test in evaluating the formability of dual-phase high-strength steel DP800. Mechanical testing was conducted to characterize material anisotropy, and Nakazima tests were performed using a Erichsen 145-60 universal deep-drawn sheet metal testing machine equipped with an Aramis 3D optical system for deformation analysis. The simulation model, incorporating Hill 48 anisotropic plasticity and Hollomon hardening, showed good agreement with the experimental results. The experimental setup and simulation model provide valuable insights into the formability of DP800, highlighting its potential in light-weight automotive design. The findings emphasize the importance of precise deformation analysis and the utility of simulation in predicting sheet metal behavior.

Keywords: Nakazima test, stretching force, punch path, experiment, simulation

1. Introduction

In pursuit of reducing emissions during the operation of automobiles, there is a growing demand for lightweight vehicle designs while ensuring the safety of passengers. This drive towards weight reduction has led to the implementation of advanced high-strength steel (AHSS) grades in the body structure, such as dual-phase steels known for their optimal combination of strength, ductility, and cost-effectiveness [1].

The formability of sheet metal, a critical aspect in the manufacturing of automotive components, plays a pivotal role in achieving desired structural integrity. Formability, defined as the ability of sheet metal to undergo stamping without fracture, involves a complex interplay of material and process-related factors [2]. While material formability can be assessed through simple tensile or compression tests, process formability requires a comprehensive evaluation of various factors associated with the manufacturing process [3].

Numerous simulative tests are employed to assess formability, including but not limited to Erichsen, Engelhardt, Cup test, Limit Dome Height (LDH), and the Nakazima test [2-4]. The Nakazima test, an influential evaluation method, is designed to simulate fracture conditions under specific deformation scenarios, offering insights into sheet metal behavior during plane-strain deformation [5]. Its importance has grown as it addresses a substantial portion of stamping failures, making it a valuable tool in the automotive industry.

The Nakazima test, originally introduced by Nakazima and subsequently modified by various researchers, has seen adaptations to accommodate diverse materials, sheet thicknesses, and even laser-welded dissimilar materials [5,6]. Researchers like Sahu [7], Xie and Nakamachi [8], Kuramae et al [9], Katragadda et al [10], and Bandyopadhyay et al [11] have applied the Nakazima test to study and analyze the deformation properties, formability, and fracture predictions of various materials, including high-strength steels and dissimilar material combinations.

In this article, our focus is on comparing the experimental results obtained from Nakazima tests conducted on dual-phase steel DP800 with the outcomes predicted through numerical simulations. Additionally, major and minor strains will be quantified using Aramis system, and compared to strains calculated through simulation software like Pam-Stamp.

2. Materials and Methods

2.1 Material – DP800

The formability assessment of dual-phase high-strength steel DP800 with a thickness of 1.5 mm was conducted using the Nakazima test. To characterize the mechanical properties of the experimental material, standard testing procedures were employed, including ISO 6892-1 for tensile testing, ISO 10113 for plastic strain ratio evaluation, and ISO 10275 for determining the strain hardening exponent. Samples for the mechanical tests were extracted in three directions: 0°, 45°, and 90° relative to the rolling direction, aiming to comprehensively describe material anisotropy. Each direction underwent testing with three specimens, and the resulting average values are presented in Table 1. The experimental tests were performed on a TIRA test 2300 testing machine, equipped with both longitudinal and transversal extensometers with a precision of 0.001 mm. The plastic strain ratio was assessed at the uniform elongation level, while the strain hardening exponent was determined within the range of 5% to uniform elongation. This comprehensive characterization aims to capture the material behavior under different loading conditions, providing valuable insights into the anisotropic properties of the dual-phase steel under consideration.

Table 1. Mechanical properties of dual-phase steel DP 800, thickness 1.5 mm

	$R_{p0,2}$ [MPa]	R_m [MPa]	A_{80} [%]	r [-]	r_m [-]	n [-]	n_m [-]
0°	527	828	19.9	0.873		0.126	
45°	508	830	18.2	0.907	0.917	0.125	0.125
90°	496	838	18.4	0.979		0.123	

2.2 Nakazima Test

The Nakazima test, a significant method for evaluating sheet metal forming properties, particularly ductility, was employed in our experiments using the Erichsen 145-60 universal deep-drawn sheet metal testing machine. This machine, with a maximum force capacity of 600 kN, was equipped with Nakajima tooling setup for precise control during the tests. The Nakazima test involves subjecting clamped specimens to strains induced by a hemispherical punch until fracture occurs. Various specimen widths, specifically 196, 110 and 30 millimeters, were utilized, as illustrated in Figure 1.

Figure 1. Types of blanks.

For precise measurement of the applied deformation mesh, we utilized the Aramis 3D optical system developed by GOM Metrology, nowadays as a part German company Zeiss. Renowned for its complexity and reliability, Aramis employs digital image correlation (DIC) to track surface deformation. By applying a speckle pattern to the specimen, Aramis captures images during testing with frequency 10 Hz, allowing for detailed analysis of 3D coordinates, strain, and displacement after the test. This comprehensive setup on the Erichsen 145-60 machine with Nakajima tooling provides valuable insights into the formability of dual-phase high-strength steel DP800 under Nakazima test conditions.

The results obtained with Aramis were achieved through the implementation of two key methods: the time-based approach and the cross-section method. The time-based method involves monitoring surface deformation over a specified period, beyond the specimen fracture. Then course of major and minor strains is evaluated and fracture limit is determined based on approximation the major strain in time of fracture. In contrast, the cross-section method evaluates the major and minor strains course in the section performed before fracture. Then approximation by inverse parabola limit strains are determined. Two methods are showed in fig.2.

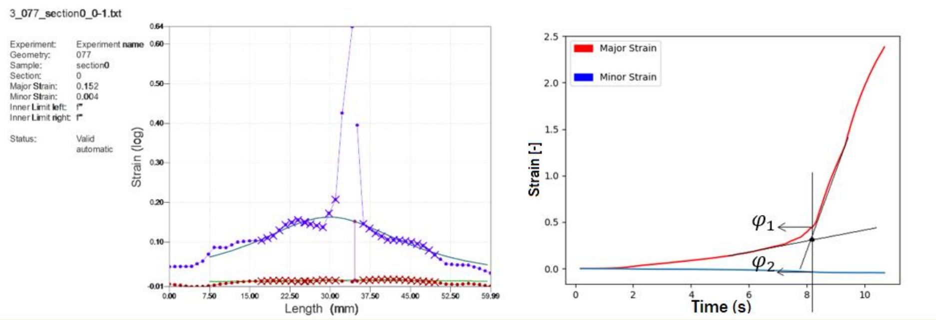

a) b)

Figure 2. Methods of major and minor strains evaluations by Aramis system: a) Section method; b) Time-dependent method.

2.3 Simulation model of Nakazima test

The simulation model is shown in Fig.3. It consists of three parts – die (green), punch (red), blank holder (turquoise), and blank (purple). These parts were meshed during importing CAD model of the tool and set as rigid surface tools. The picture shows one type of blanks with a width of 196mm. Blanks were meshed by square elements 2x2mm.

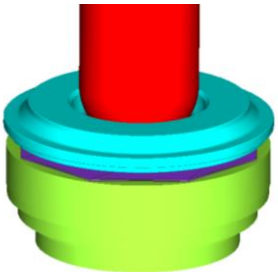

Figure 3. Simulation model.

Yield law and hardening curve describing material behavior were defined as follows: Hill 48 anisotropic plasticity model:

$$ {}_1^2 = \frac{{}_0(1 + {}_{90})}{{}_{90}(1 + {}_0)} \, {}_2^2 - \frac{2 \, {}_0}{1 + {}_0} \, {}_1 \, {}_2 = ({}_1)^2 \qquad (1) $$

Hollomon hardening model (Eq. 2).

$$ = \cdot \; , \qquad (2) $$

where K is material constant, n is strain hardening exponent and r_0, r_{45}, r_{90} are plastic strain ratios (Lankford's coefficients) in specified direction.

3. Results and discussion

The results of the measurement of the maximum tensile forces and the punch path up to the specimen fracture for the individual widths of the samples are given in Table 2. For the individual widths, 3 measurements were carried out and the average value of the maximum force and the average value of the path at fracture were calculated. In the simulation model, this average value of the path was used to define the path of the punch. Table 2 shows the results of the maximum force from the numerical simulation.

Table 2. Measured values of the maximum force and the punch path at fracture

	Experiment			Simulation	
	Max. Force [kN]	Average value	Stroke [mm]	Max. Force [kN]	Stroke [mm]
196	195.9		37.1		
	194.6	201.4	36.9	247.8	37
110	97.7		26.6		
	105.5	101.9	26.9	130.84	26.8
	102.6		26.9		
30	37.2		28.5		
	37.1	37.3	28.4	43.38	28.6
	37.6		28.9		

Fig. 3 shows a representation of the measured data from the table 3. The deformation on the specimen with a width of 196mm obtained from the numerical simulation is slightly higher compared to the deformation obtained from the real experiment (point on the right). The deformation of the 110mm wide specimen obtained from the numerical simulation (point in the middle) is as close as possible to the results of the real experiment, while the deformation of the 30mm wide specimen is slightly lower in the simulation than in the real experiment (point on the left), the deformation measured on the larger blank widths differ more than those of the smaller blank widths. The larger the diameter of the blank, the greater the difference in deformation between the simulation and the experiment.

Table 3. Comparison of major and minor strain values measured experimentally and calculated by numerical simulation

Section method		Time dependent method		Simulation	
Minor	Major	Minor	Major	Minor	Major
-0.133	0.363	-0.145	0.402	-0.096	0.298
0.035	0.171	0.034	0.241	0.044	0.189
0.283	0.287	0.280	0.260	0.418	0.431

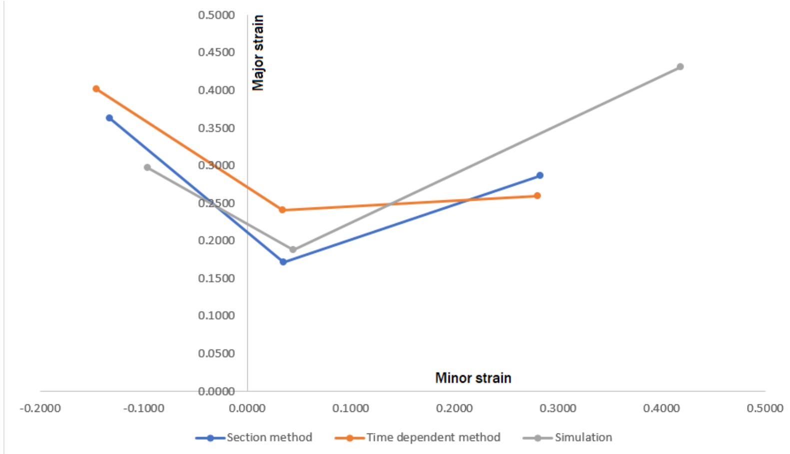

Figure 4. Comparison of FLCs obtained with Aramis and those obtained with numerical simulation

In Figure 3 you can see a comparison of the FLC curves that were obtained from the numerical simulation and the real experiment. The maximum deformations obtained by the time method and the intersection method from the real experiment were used for comparison. This comparison indicates that these data can be predicted by numerical simulation.

The results of the strain distribution measured by the Aramis system and determined by numerical simulation are given in Tab. 4. Major strains of the fracture zone when measured by Aramis were significantly larger than those of the safety zone [14]. Even though the results of numerical simulations depend on yield law-hardening law combination, it is possible to state a good agreement between the results of experimental measurements and numerical simulation.

Table 4. Comparison of major and minor strain measured experimentally and calculated by numerical simulation

	Simulation		Experiment
	Minor strain	Major strain	Time dependent method
030	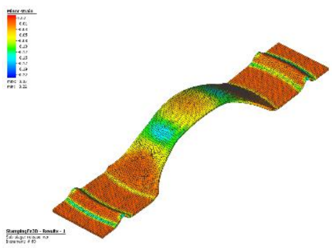	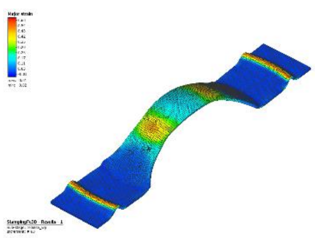	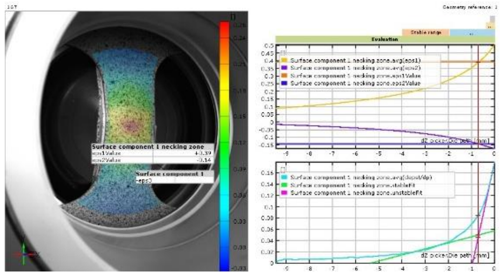

110	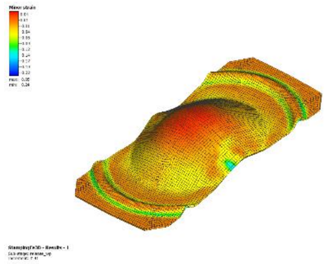	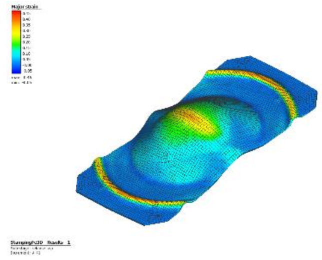	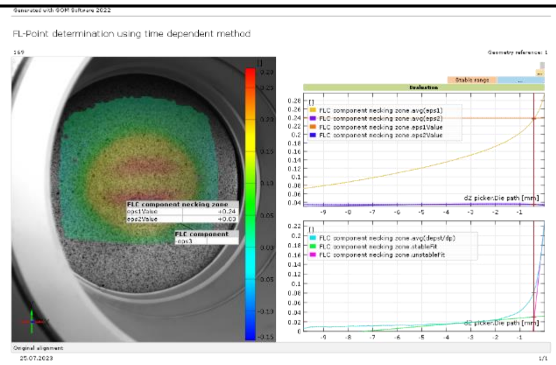
196	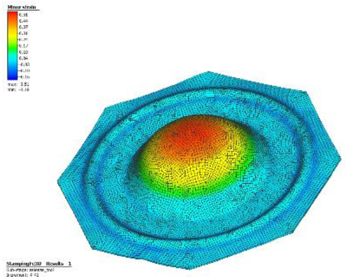	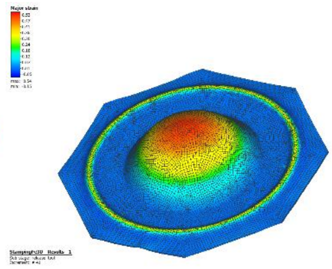	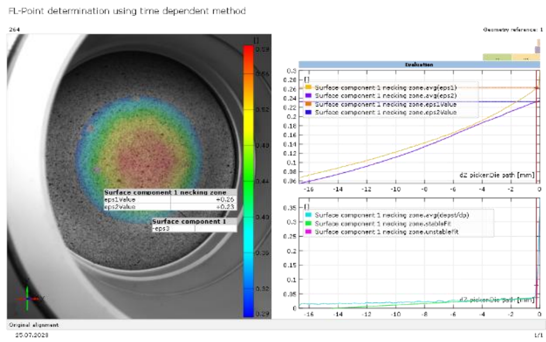

5. Conclusions

The Nakazima test on DP800 steel effectively characterized its anisotropic formability. Using the Aramis system, precise deformation measurements were obtained, highlighting critical strain distributions. The simulation model, which utilized Hill 48 anisotropic plasticity and Hollomon hardening, accurately predicted experimental results, demonstrating strong correlation and reliability. These outcomes confirm that numerical simulations can effectively complement experimental methods for predicting sheet metal behavior, aiding in the design of lightweight automotive structures. This study provides concrete insights into DP800's formability, supporting its application in advanced automotive engineering.

Key results for different specimen widths are as follows:

- For the 196 mm wide specimen, the major strain was 0.402 (time-dependent method), 0.363 (section method), and 0.298 (simulation).
- For the 110 mm wide specimen, the major strain was 0.241 (time-dependent method), 0.171 (section method), and 0.189 (simulation). The best correlation between experimental and simulation results was observed for this size.
- For the 30 mm wide specimen, the major strain was 0.260 (time-dependent method), 0.287 (section method), and 0.431 (simulation).

The time-dependent method consistently produced higher major strain values than the section method, with the simulation results generally falling between the two.

Acknowledgments: The work was done under the grant project VEGA 1-0238-23 "Prediction of weldability and formability for laser welded tailored blanks made of combined high strength steels with CAE support"

References

1. Oliver S., Jones T.B., Fourlaris G., Dual phase versus TRIP strip steels: Microstructural changes as a consequence of quasi-static and dynamic tensile testing. *Materials Characterization*, **2007**, *Volume 58*, p. 390-400.
2. Hrivňák A., Evin E. Formability of metal sheets, 1st ed.; Kosice : Technical University, Slovakia, 2004; pp. 223.
3. Mielnik E.M., *Metalworking Science and Engineering*, McGraw-Hill, 1991, p. 976.
4. Hosford W.F., Caddell R.M., *Metal Forming , Mechanics and Metallurgy*, 3rd edition, Cambridge University Press, 2012.

5. Narasimhan K., Miles M.P., Wagoner R.H., A better sheet-formability test, *Journal of Materials Processing Technology* **1995**, Volume 50, p. 385-394.
6. ASM Handbook, *Forming and Forging*, ASM International, 9th Edition Metals Handbook, 1988.
7. Sahu J., Mishra S., Limit dome height test of very thin brass sheet considering the scaling effect. Journal of Physics Conference Series **2016**.
8. Xie C.L., Nakamachi E., The effect of crystallographic textures on the formability of high-strength steel sheets. *Journal of Materials Processing Technology* **2002**, p. 104-111.
9. Kuramae H., Ikeya Y., Sakamoto H., Morimoto H., Nakamachi E., Multi-scale parallel finite element analyses of LDH sheet formability tests based on crystallographic homogenization method. *International Journal of Mechanical Sciences* **2010**, p. 183-197.
10. Katragadda S.C., Ramulu P., Investigation of forming behavior prediction of different steel grade materials using numerical simulation, 5 th International & 26th All India Manufacturing Technology, Design and Research Conference, India, 2014.
11. Bandyopadhyay K., Panda S.K., Saha P., Padmanabham G., Limiting drawing ratio and deep drawing behavior of dual phase steel tailor welded blanks: FE simulation and experimental validation. *Journal of Materials Processing Technology* **2015**, p. 48-64.
12. AHSS Guidelines, Available online: https://www.worldautosteel.org/projects/advanced-high-strength-steel-application-guidelines/ .
13. Takahashi M., "Development of High Strength Steels for Automobiles," Nippon Steel Technical Report No. 88 (July **2003**).
14. Sun, L.; Cai, Z.; He, D.; Li, L. Aluminum Alloy Sheet-Forming Limit Curve Prediction Based on Original Measured Stress–Strain Data and Its Application in Stretch-Forming Process. Metals 2019, 9, 1129. https://doi.org/10.3390/met9101129

TECHNICKÁ UNIVERZITA V KOŠICIACH
Strojnícka fakulta

Optimizing the milling process through the design of a specialized machining fixture.

Ján Kušnír [1,*], Jozef Brindza [1], Michal Demko [1] and Marek Vrabeľ [1]

[1] Prototyping and Innovation Centre, Faculty of Mechanical Engineering, Technical University of Kosice, Slovak Republic
* Correspondence: jan.kusnir@tuke.sk; Tel.: +421 55 602 3371

Abstract: This article delves into the challenges of machining aluminum, particularly in milling thin-walled components where increased cutting forces and thermal-mechanical bonds present obstacles. The primary focus is on the crucial role of clamping fixtures in mitigating workpiece deformations during milling. The design process involves meticulous planning, considering factors like part dimensions and material specifications. The study emphasizes the significance of optimizing the machining process, addressing challenges such as workpiece displacement. Insights from pre-series production underscore the need for balanced clamping stiffness. The refined fixture design aligns with requirements for workpiece stability. The production process includes roughing, annealing, precise milling, and clamping. The article concludes by affirming the successful implementation of the milling fixture in serial production, emphasizing its transformative impact on efficiency and precision in manufacturing processes.

Keywords: Milling, Thin-walled part, Milling fixture, Optimization

1. Introduction

Machining is a complex process, involves chip formation where tough materials like aluminum lead to large contact areas, thick chips, and increased cutting forces. High-speed machining offers efficient production but faces challenges like thermal-mechanical bonds and tool wear, impacting quality. Deformation hardening during aluminum alloy 6061-T6 machining may increase cutting resistance. Improving edge sharpening or reducing surface roughness can enhance machining quality. Thin-walled components, common in aerospace, favor side milling for efficiency but face challenges with higher cutting forces. Incorrect parameters may even cause tool breakage. Predicting workpiece deformation inside milling is studied, but the clamping device's influence on surface errors is often overlooked, crucial for limiting excessive workpiece deformation, especially in thin-walled components [1-5].

Fixtures are specialized clamping devices crucial in manufacturing for positioning and securing workpieces during operations, commonly used in repetitive and precise production processes. Individually designed for specific tasks, fixtures ensure the stable placement of workpieces throughout operations, enhancing productivity and reducing operational time, especially in milling processes. They utilize positioning elements and clamps to eliminate the need for constant checks and repositioning, contributing to stable and efficient production. The process of designing milling or clamping fixtures involves systematic planning, with the designer managing input data and continually checking for potential changes. Full functionality analysis and consideration of workpiece, machining, tools, and equipment details are essential. Preliminary analysis may take hours to days for complex designs. Fixture design requires creativity, considering factors like part dimensions, material specifications, machining operations, tolerances, production quantity, and surface details. The designer evaluates various options, such as permanent, modular, or universal fixtures, and must consider time and budget constraints [6-8].

2. Preparation and analysis

This study focuses on the serial production of an aluminum component (Figure 1). The aluminum component have to adheres to standard material (6061-T6) specifications and tight dimensional/geometric tolerances. Alongside the customary material specifications and dimensional/geometric tolerances, it is imperative that the aluminum component is manufactured using a CNC milling machine. Main final component dimensions are 398 mm x 211 mm x 101 mm. The workpiece material has dimensions of 407 mm x 217 mm x 110 mm and weighs 26.23 kg.

Figure 1 Aluminium component

In a pre-series production of 6 units at Prototyping and Innovation Centre, Faculty of Mechanical Engineering, the DMG MORI ECOMILL 50 machine was used for the manufacturing of aluminum components. The milling program, generated by CAM software, employed a 3D model from SOLIDWORKS CAD software. Operating the machine required a high level of milling expertise, and the workpieces were secured using modular clamping systems, with frequent dimensional checks ensuring precision. The production of a single piece took approximately 6 hours, underscoring the importance of process optimization.

Insights from pre-series production and consultation with CNC technologists and operators highlight the need for a proper balance in clamp stiffness to prevent workpiece displacement. Specific requirements include a minimum safety clearance of 1 mm, minimum deformation of the workpiece from clamping and a minimum of 70 mm required for side slot machining access.

3. Results

Following the assessment, the design underwent refinement, gained approval, and was then utilized for the development of manufacturing documentation, leading to the subsequent production of the proposed fixture shown in Figure 2.

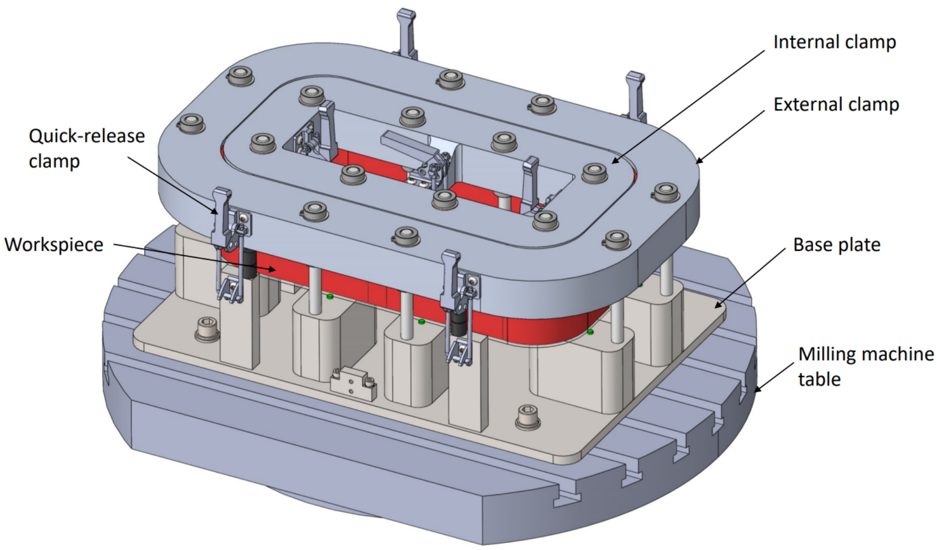

Figure 2 Milling fixture in full composition

The workpiece is securely fastened to the base plate, employing external clamps for the inner contour and internal clamps for the outer contour, while maintaining a specified offset to facilitate groove access (70 mm). The fixture design incorporates a foundational section meticulously crafted for the precise placement of the workpiece, featuring guide bars set 27.5 mm apart. This base component is adjusted to seamlessly integrate with other parts, ensuring the easy insertion and removal of clamps.

Both the internal and external clamps are milled from lightweight aluminum alloy 7075, emphasizing an efficient fixation approach using quick-release elements. These clamps replicate the shape of the workpiece, ensuring a uniform distribution of clamping force. Strategically positioned cylindrical holes accommodate linear bearings, enhancing overall stability and operating. A 0.2mm clearance between the internal clamp and the workpiece accommodates potential deviations from the roughing operation (Figure 3). The simultaneous securement of both internal and external clamps is designed to maintain stability during variations machining operations. A 3D model of the tool with the holder serves as an additional means of spatial verification.

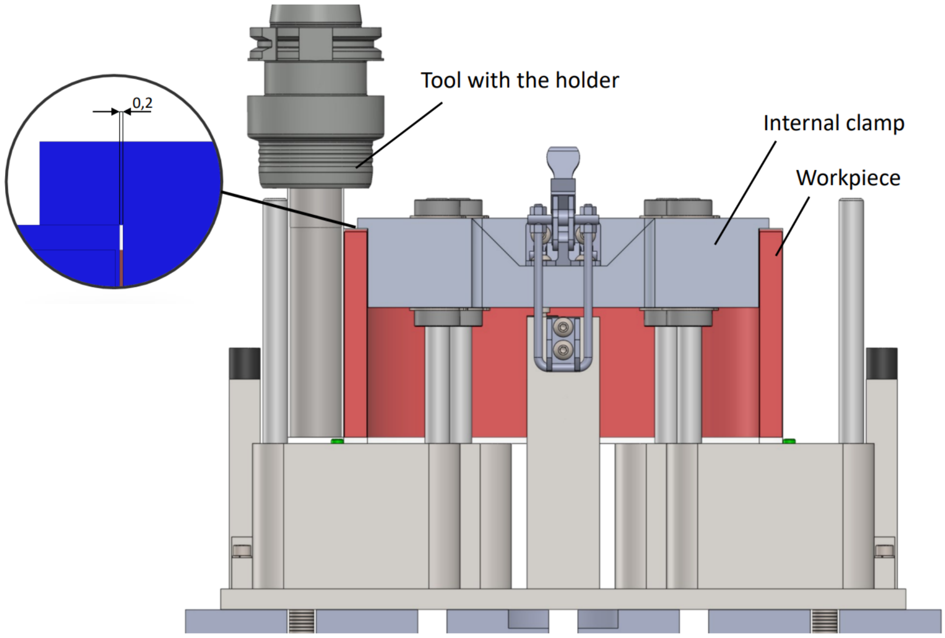

Figure 3 Section view of milling fixture with internal clamp

The technological production process was modified using a milling fixture in the following steps (Figure 4):

1. Initiating the process involves outlining the aluminum component from a semi-finished piece. The roughing operation, guided by CAM software using a 3D model within specified tolerances, utilized a solid tool with a chip breaker suitable for trochoidal milling.
2. The subsequent step entailed optimizing internal stresses arising from the production of the semi-finished product and roughing. This was achieved through an annealing process.
3. Following annealing, the aluminum component was placed in the fixture, with both clamps simultaneously set and tightened to the desired force.
4. After removing the internal clamp, the workpiece was measured using a tool probe and standard cycles. The external clamp remained tightened, enabling the machining of the internal part in the first cycle, which involved a pre-finishing operation. The subsequent steps included releasing and re-clamping the clamp to alleviate stresses and then performing the finishing operation for achieving final dimensions.
5. After completing the internal surface machining, the internal clamp was positioned while the external clamp remained active to prevent unintended

displacement. A similar process of pre-finishing, releasing, and re-clamping was undertaken before initiating the finishing operation.

6. Finally, external grooves were machined by tilting the entire worktable with the fixture in a 5-axis milling machine. The groove dimensions were determined based on the current measured data using a machine probe, stored as variable parameters in the program.

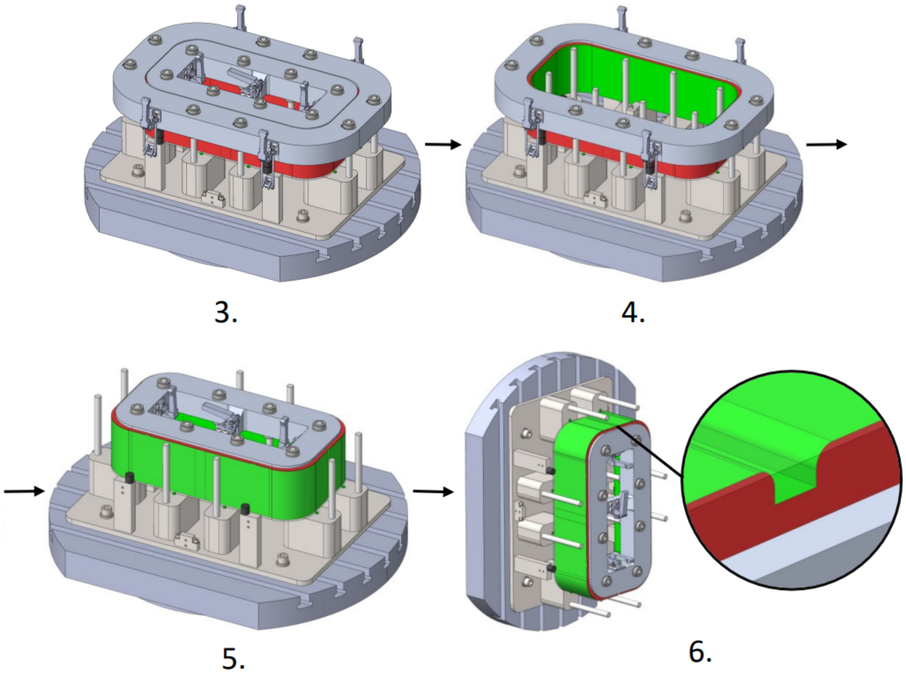

Figure 4 Production process using a milling fixture

4. Conclusions

The milling fixture was fabricated and tested in the production environment following the previously outlined procedure as shown in Figure 4. As a result, the production time for each component was shortened to around 150 minutes (instead of approx. 360 minutes before using developed fixture), inclusive of handling. Annealing was executed concurrently with multiple pieces (minimizing downtime). Beyond the time reduction, the outcome was also an enhancement in the production of superior-quality and more accurate components. Serial production concluded successfully.

Figure 5 Utilization of the milling fixture in production

Acknowledgment: This article was created with the support of project: VEGA 1/0457/21

Conflicts of Interest: The authors declare no conflict of interest

References

1. SANTOS, Mário C. Jr et al. Machining of aluminum alloys: a review. The International Journal of Advanced Manufacturing Technology **2016**, 86.
2. SUYANG, Li. Optimization of Milling Aluminum Alloy 6061-T6 using Modified Johnson-Cook Model. Simulation Modelling Practice and Theory **2021**, 111.
3. Nghiep, T.N., Sarhan, Ahmed A.D. and Aoyama, Hideki. Analysis of tool deflection errors in precision CNC end milling of aerospace. Measurement **2018**, 125.
4. ZAHAOYU, Li et al. Multi-pass adaptive tool path generation for flank milling of thin-walled workpieces based on the deflection constraints. Journal of Manufacturing Processes **2021**, 68.
5. Shaogang, Liu et al. Optimal fixture design in peripheral milling of thin-walled workpiece. The International Journal of Advanced Manufacturing Technology **2006**, 28.
6. Rajkumar, D. Patil et al. Design of Milling Fixture in Mass Production of Pivot Block. Asian Review of Mechanical Engineering **2017**, 1.
7. Hoffman, Edward G. Jig and Fixture Design. New York: Delmar, 2004.
8. Shailesh, S.Pachbhai et al. A Review on Design of Fixtures. International Journal of Engineering Research and General Science **2014**, 2.

Use of Digital Technologies in Enterprises: Slovakia vs EU-27

Laura Lachvajderová*, Milan Fiľo, Dominika Sukopová and Lenka Vyrostková

Department of Business Management and Environmental Engineering, Faculty of Mechanical Engineering, Technical University of Kosice, 040 01 Košice, Slovakia; milan.filo@ecoinvest.sk (M.F.); dominika.sukopova@tuke.sk (D.S.); lenka.vyrostkova@tuke.sk (L.V.)
* Correspondence: laura.lachvajderova@tuke.sk

Abstract: This scientific article focuses on creating a digital index to assess digital transformation in the EU-27 countries. Utilizing data from Eurostat and a multi-objective optimization method based on ratio analysis, we determined the level of digitization in businesses across different countries. Our findings emphasize disparities in investments in ICT technologies, digital skills, job mobility, and innovative activities of small and medium-sized enterprises. To highlight the potential of digital transformation, we propose specific measures, including increased investments in digital infrastructure, support for education, and the digitization of public administration. Overall, our approach to creating a digital index and identifying areas for improvement contributes to a broader understanding of digital transformation in European countries and establishes a framework for further research and policy efforts.

Keywords: digital index; digital transformation; digitalization; European countries; MOORA; descriptive statistics

1. Introduction

The significance of the digitization process for businesses and the entire economy in the European Union members countries (EU-27) is well understood, as it is evident that countries or groups of countries where the process of digital transformation (DT) is at an advanced stage can gain a competitive advantage. Business activities in these regions, based on modern and innovative solutions, have also proven to be more resilient to crises and market changes. Their production flexibility and ability to quickly adapt to customer needs make these companies well-received by customers and generally more efficient than those not utilizing digital solutions. These characteristics were particularly evident during the recent pandemic caused by the SARS-CoV-2 coronavirus [1]. However, the EU-27 faces challenges related to high structural fragmentation (27 countries) and varying levels of economic development and wealth among individual countries. These disparities manifest in significant differences between countries in the process of digitization (using Industry 4.0-related technologies) and the adoption of innovative technologies [2]. Therefore, evaluating the implementation of digitalization across the entire economy of the EU-27 requires consideration of countries where this process has been interrupted.

The main objective of this scientific output is to conduct a comprehensive analysis using a specific method to determine the level of digitization in a selected sample of countries and identify which digital technologies are most widely implemented by European businesses.

2. Materials and Methods

Various levels of economic development among EU-27 member states, and consequently variations in the progression of digital processes and the adoption of digital technologies, legitimately justify conducting research to assess the level of these processes among businesses in individual EU-27 countries. In order to achieve the research objective, it was necessary to address the following research question:

"Which of the digital technologies is the most commonly used in EU-27?"

To answer the research question, we conducted a study based on 10 selected indicators describing the main digital technologies in businesses across the EU-27.

2.1. Data

We obtained the data for our analysis from the statistical office of the European Union (EUROSTAT) [3]. The data were extracted from the years 2021-2022. The following Table 1 serves for a clear overview of ten indicators in the respective years.

Table 1. Indicators for the study

Year	Characteristic	Represented Technology
2021	3D Print	Additive Technology
	Use of industrial/service robots	Robotization
	Internal analysis of big data	Big Data Analytics
	Businesses that use e-invoices	Integration with customers/suppliers
	ICT security - use of VPN (virtual private network)	Cyber security
	The maximum contracted download speed of the fastest fixed Internet connection is at least 100 Mbps but less than 500 Mbps.	Internet connection 100 Mb/s - 500 Mb/s
2022	Enterprises using AI (artificial intelligence) technologies	Artificial intelligence
2022	Use of connected devices or systems that can be monitored or controlled remotely over the Internet	IoT
2022	Purchase of cloud computing services used over the Internet	Cloud Computing
2022	Businesses that have an ERP software package to share information between different functional areas	Internal process integration

The provided data pertains to businesses categorized according to NACE Rev. 2 (Statistical Classification of Economic Activities), excluding the financial sector (with ten or more employees and self-employed individuals). They inform about the percentage of usage of a specific digital technology and the internet connection speed, characterizing the infrastructure domain necessary for implementing Digital Transformation (DT).

2.2 Interpretation of Used Method

After extracting and consolidating the obtained data, we proceeded with the interpretation of the method. Digitalization levels within the context of each EU country were determined using the Multiple Objective Optimization based on Ratio Analysis (MOORA) method. This method falls under the category of Multi-Criteria Decision Optimization and enables the evaluation of alternatives (in this case, the EU-27) based on criteria (indicators). The chosen method integrates various decision-making methods and analytical approaches to address complex problems [4].

To establish the level (index) of digitalization using the MOORA method, the following steps need to be undertaken:

1. Creating a decision matrix X with m number of alternatives and n number of criteria:
(1)
2. Creating a normalized decision matrix:
(2)
3. Calculating a normalized score value for each alternative, taking into account all existing alternatives. The final score of each variant is thus determined by the equation:
(3)

Where represents the MOORA score for the i-th alternative, whereas j=1,2,3...t and j=t+1,t+2...n refer to objectives that must be maximized (beneficial criteria) and minimized (unfavorable criteria). Since the weights are considered in terms of certain criteria when evaluating alternatives, the MOORA score for each alternative is therefore determined by the following equation:

(4)

Where represents the weight of the i-th criterion.

In the final evaluation, the option with the highest score is considered the best option and the option with the lowest score is considered the worst option. The MOORA entropy method was used to determine the weights for the selected digital technologies and DT infrastructure (indicators) and the main steps for determining these weights in this method are as follows:

4. Creating a decision matrix according to (1);
5. Creating a normalized decision matrix as follows:

(5)

6. Determining the value of entropy:

(6)

Where and represents the proportion of samples at time t in the i-th indicator.

7. Determining the level of entropy variation for each criterion (the degree of deviation of ratings with respect to subsequent criteria):

(7)

8. Determining the weight of criteria (indicators):

(8)

We will use the weight values determined from equation (8) in the MOORA method in equation (4).

3. Results of analysis

3.1. Descriptive statistics

In the next phase of our study, we examined whether there is a correlation between the use of digital technologies in businesses in the EU-27 (Table 2). It was found that several technologies exhibit statistically significant correlations with each other. The highest correlation coefficient was observed between AI and robotics, and cybersecurity, additive technology, and cybersecurity, big data analytics, and cybersecurity, and cloud computing and cybersecurity (with correlation coefficients exceeding 0.7). Additionally, we identified a statistically significant correlation between AI and additive technology, robotics and additive technology, big data analytics, and AI, internal process integration and robotics, and internal process integration and AI. The indicator of customer/supplier integration correlated only with robotics and cloud computing.

However, among the set of digital technologies used in businesses, there are also those for which we found no correlations. No correlations were found between AI and the Internet of Things (IoT), additive technology and IoT, and others. The only negative correlation identified was between the use of big data analytics and IoT. All statistically significant relationships are marked in bold in Table 2.

Table 2. Correlation coefficients among the indicators adopted for our study (with a level of statistical significance of $p < 0.005$)

	AI	IoT	Additive technology	Robotization	Big data analytics	Cloud computing	Integration with customers/suppliers	Internal process integration	Cybersecurity	Internet connection
AI	1,000 p= —	0,222 p=0,229	**0,683 p=0,000**	**0,738 p=0,000**	**0,611 p=0,001**	**0,522 p=0,003**	0,361 p=0,059	**0,619 p=0,001**	**0,739 p=0,000**	**0,578 p=0,003**
IoT		1,000 p=—	0,377 p=0,071	0,114 p=0,689	-0.036 p=0,873	**0,438 p=0,024**	0,297 p=0,144	0.309 p=0,131	0,332 p=0,098	0,109 p=0,603
Additive technology			1,000 p=—	**0,699 p=0,000**	**0,537 p=0,009**	**0,632 p=0,002**	0,353 p=0,097	**0,514 p=0,004**	**0,797 p=0,001**	**0,391 p=0,049**
Robotization				1,000 p=—	0,338 p=0,113	0,341 p=0,121	0,464 p=0,011	**0,633 p=0,002**	**0,541 p=0,006**	0,321 p=0,134
Big data analytics					1,000 p=	**0,527 p=0,005**	0,086 p=0,743	**0,415 p=0,038**	**0,756 p=0,000**	0,342 p=0,163
Cloud computing						1,000 p=—	**0,626 p=0,000**	0,295 p=0,128	**0,764 p=0,000**	**0,398 p=0,043**
Integration with customers/suppliers							1,000 p=—	0,087 p=0,604	0,247 p=0,202	0,154 p=0,437
Internal process integration								1,000 p=—	0,565 p=0,002	0,445 p=0,029
Cybersecurity									1,000 p=—	0,461 p=0,024
Internet connection										1,000 p=—

3.2. Multi-Objective Optimization Method by Ratio Analysis (MOORA)

In the next part of this research, using the Entropy-MOORA method, we determined the digitization index and compiled a ranking of the examined EU-27 countries based on their level of digitization in businesses within those countries. We followed the individual steps and equations outlined in section 2.2. The assigned weight values for the indicators used in this analysis are presented in Figure 1.

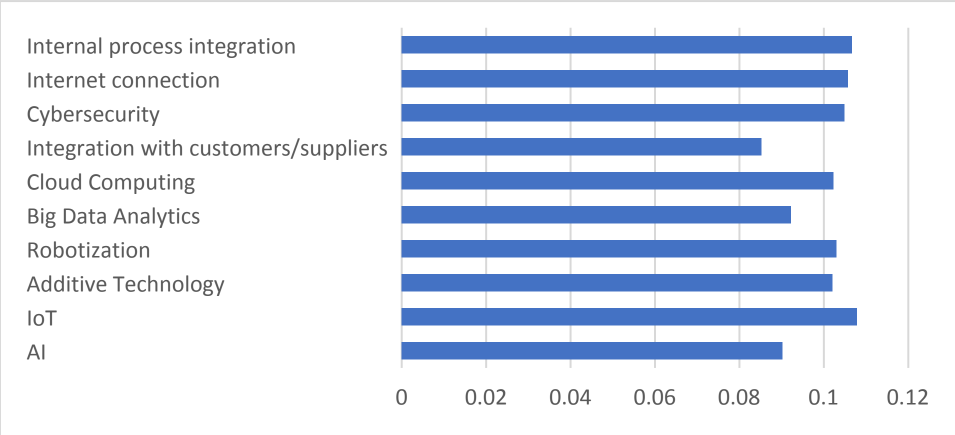

Figure 1. Indicators weight values

The technology with the highest weight value is IoT, whereas the lowest weight is assigned to customer/supplier integration. These weight values are derived from entropy, indicating the level of disorder within the analyzed sample of EU-27 countries. This approach enables us to assess the significance of individual indicators based on the variance in their values.

The highest values of the digital index were found in Denmark, Belgium, and Finland, while the lowest values were identified in Hungary, Bulgaria, and Romania (Figure 2).

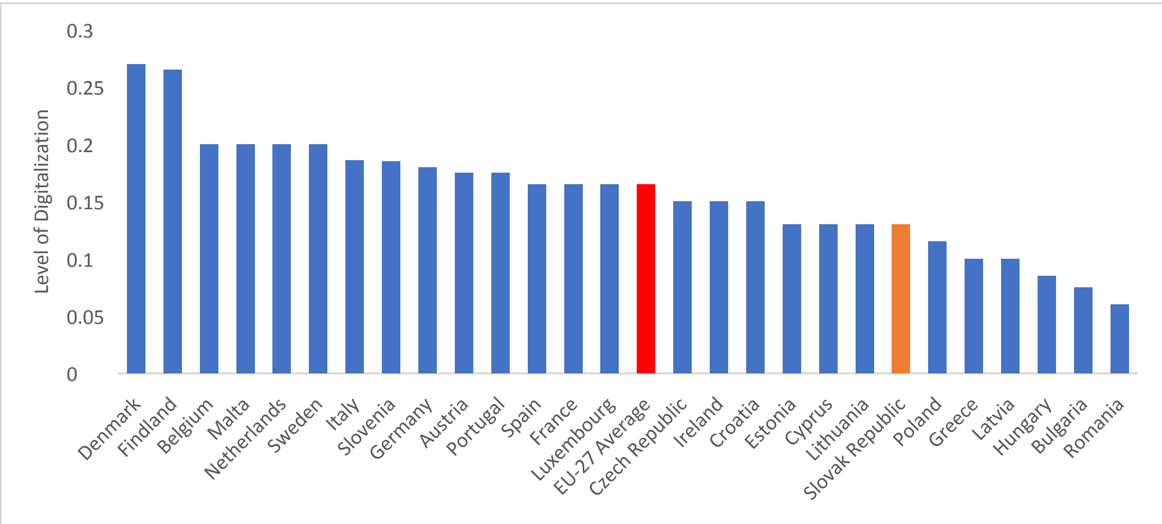

Figure 2. Digitalization index values for EU-27 countries

Overall, up to 13 countries, including Slovakia, did not reach the average values for the EU-27, with 11 of them belonging to the "new union" group, countries that joined the EU after 2004 (Slovakia, Czech Republic, Estonia, Croatia, Lithuania, Cyprus, Poland, Hungary, Latvia, Romania, and Bulgaria). This implies that businesses in these countries are adopting digital technologies at a slower pace than in the so-called "older union" (EU-14) countries. The main reasons for this issue are economic constraints and a lack of qualified personnel. The process of digital transformation requires significant financial investments and substantial economic and social changes. According to the studies [41], only 13% of entities operating in the "new union" declare having a digital transformation strategy for the economic sector, or at least working on its implementation.

4. Discussion

Slovakia lags in digital transformation compared to the EU-27 average, ranking 23rd in the Digital Economy and Society Index (DESI) for 2022. Lower investment in ICT technologies contributes to the limited integration of digital technologies in the business sector. In 2019, only 18% of Slovak businesses exhibited high digital intensity, contributing to an overall lag in digital development compared to the EU and the Czech Republic [5]. Digital transformation requires the strengthening of digital skills and competencies through education. The European Commission has set a target to achieve a 70% rate of individuals aged 16 to 74 with basic digital skills by 2025 [6].

Slovakia is classified as a country with low innovation performance in the Innovation Score 2023, categorized among "new innovators" with a rating below 70% of the EU average. The country does not even reach the level of medium innovators. The European Commission identified "weaknesses" and proposed measures to improve the situation. Slovakia faces challenges in digital transformation due to low investment in ICT technologies, weak digital skills, and limited job mobility. Additionally, there are constraints on research and development investments, insufficient government support, and restricted venture capital. SMEs exhibit innovation struggles, and there's a decline in the sale of innovative products along with reduced interest in doctoral studies [7].

To address these issues, proposed actions include increasing investments in digital infrastructure, particularly overseen by the state. Initial investments in digital technologies are suggested, with a subsequent focus on hiring more qualified labor. The emphasis is on attaining necessary digital capacities through education. Public administration digitization is prioritized, aligned with the Recovery and Resilience Plan [8]. Conditions for utilizing the European Investment Fund to invest in startups will be established. Efforts to strengthen the Slovak Investment Holding and support the Venture to Future Fund, offering financing for SMEs, are recommended. Lastly, the creation of an Innovation Fund is proposed to support scientific research projects in key economic sectors [9].

5. Conclusions

In this study, our focus was on creating a digital index based on data from Eurostat, utilizing the multi-objective optimization method based on ratio analysis. The primary objective was to provide a comprehensive overview of the level of digital transformation in the EU-27 countries. The results revealed various challenges, including low investment in ICT technologies, weak digital skills, and limited innovation activities. Based on identified weaknesses, we proposed specific measures that could contribute to improving digital development, such as increased investments in digital infrastructure, support for education and innovation, and the creation of conditions for developing digital capacities in the business sector. Our conclusions offer a holistic view of the current state of digital transformation in the EU-27, serving as a starting point for further discussions and actions in the realm of the digital economy and society.

Acknowledgments: This paper was developed within the implementation of the project VEGA 1-0340-2021 "The impact of a pandemic and the subsequent economic crisis on the development of digitization of enterprises and society in Slovakia".

Conflicts of Interest: The authors declare no conflict of interest.

References

1. Lachvajderová, L.; Kádárová, J. (2022). Attitude of European SMEs to digitalization and digital transformation during the COVID-19 pandemic. In: Novus Scientia 2022. - Košice (Slovensko) : Technická univerzita v Košiciach s. 101-106. Available on: https://www.sjf.tuke.sk/NovusScientia/Zborn%C3%ADk%20konferencie%20Novus%20Scientia%202022.pdf
2. Lachvajderová, L.; Kadarová, J. Industry 4.0 Implementation and Industry 5.0 Readiness in Industrial Enterprises. Manag. Prod. Eng. Rev. 2022, 13, 102–109. DOI: 10.24425/mper.2022.142387
3. Eurostat Database. Available on: https://ec.europa.eu/eurostat/web/main/data/database
4. Zavadskas, E.K.; Antucheviciene, J.; Kar, S. (2019). Multi-Objective and Multi-Attribute Optimization for Sustainable Development Decision Aiding. Sustainability, 11, 3069. https://doi.org/10.3390/su11113069
5. European Commission. DESI. (2022). Available on: https://digital-strategy.ec.europa.eu/sk/policies/desi
6. Friedrich Ebert Stiftung, E. F. SPRAVODLIVÉ, INOVATÍVNE A TRVALO UDRŽATEĽNÉ SLOVENSKO Návrhy opatrení pre sociálnodemokratický vládny program na obdobie rokov 2023 -2027. Available on: https://www.researchgate.net/publication/374814332_SPRAVODLIVE_INOVATIVNE_A_TRVALO_UDRZATELNE_SLOVENSKO_Navrhy_opatreni_pre_socialnodemokraticky_vladny_program_na_obdobie_rokov_2023_-2027
7. Kádárová, J.; Lachvajderová, L.; Sukopová, D. Impact of Digitalization on SME Performance of the EU27: Panel Data Analysis. Sustainability 2023, 15, 9973. https://doi.org/10.3390/su15139973

8. Kopec, J., Pekarcíková, M., Dic, M., & Lachvajderová, L. (2022). ANALYSIS OF THE BIG DATA CONCEPT AND ITS USE FOR LOGISTICS PROCESSES. Advanced Logistic Systems - Theory and Practice, 16(1), 85–91. https://doi.org/10.32971/als.2022.008

9. European Commission. European innovation scoreboard. Available on: https://research-and-innovation.ec.europa.eu/statistics/performance-indicators/european-innovation-scoreboard_en

Application solution for the use of HCCI technology in motor vehicles

Matúš Lavčák [1,*], Pavol Tarbajovský [2] Michal Puškár [3]

[1] Faculty of Mechanical Engineering, TU Košice, Letná 9, 040 01 Košice, Slovak Republic; matus.lavcak@tuke.sk
[2] Faculty of Mechanical Engineering, TU Košice, Letná 9, 040 01 Košice, Slovak Republic; pavol.tarbajovsky@tuke.sk
[3] Faculty of Mechanical Engineering, TU Košice, Letná 9, 040 01 Košice, Slovak Republic; michal.puskar@tuke.sk
* Correspondence matus.lavcak@tuke.sk; Tel.: 0944 344 186;

Abstract: This article investigates the synergies between HCCI engines and hybrid technology. HCCI engines excel in fuel efficiency but face limitations in their operating range. Conversely, hybrid vehicles, particularly series hybrids, leverage electric propulsion with the internal combustion engine acting as a power generator. By amalgamating these technologies, it becomes plausible to optimize the HCCI engine's efficiency within an ideal speed range for enhanced fuel economy and performance.

Keywords: HCCI, hybrid, vehicles

1. Introduction

HCCI engines are a promising alternative to traditional spark-ignition or compression ignition internal combustion engines, offering many advantages, particularly in terms of combustion efficiency and low fuel consumption, which is closely linked to the low amount of CO2 and NOx emissions produced. Despite these considerable advantages, the introduction into mass production is hampered by problems such as timing of the moment of ignition of the mixture, cold start, high noise levels and others. These factors have a major impact on the performance and emissions of these engines and require sophisticated solutions to achieve optimal results. One such solution is the use of HCCI technology in hybrid vehicles.

2. Definition of HCCI engine and hybrid engine

2.1. Definition of HCCI engine

The HCCI (Homogeneous Charge Compression Ignition) engine is a revolutionary type of internal combustion engine that combines the advantages of petrol and diesel engines. Unlike conventional internal combustion engines, which use either spark (gasoline) or compression (diesel) to ignite the fuel, the HCCI engine uses compression to ignite a homogeneous mixture of air and fuel (Figure 1).

In an HCCI engine, fuel and air are mixed in such a ratio to create a homogeneous mixture with controlled compression. Subsequently, this mixture spontaneously ignites during the compression stroke of the piston, without the need for spark or fuel injection. This process of combining air and fuel takes place under high temperature and pressure, resulting in efficient combustion. [1,2]

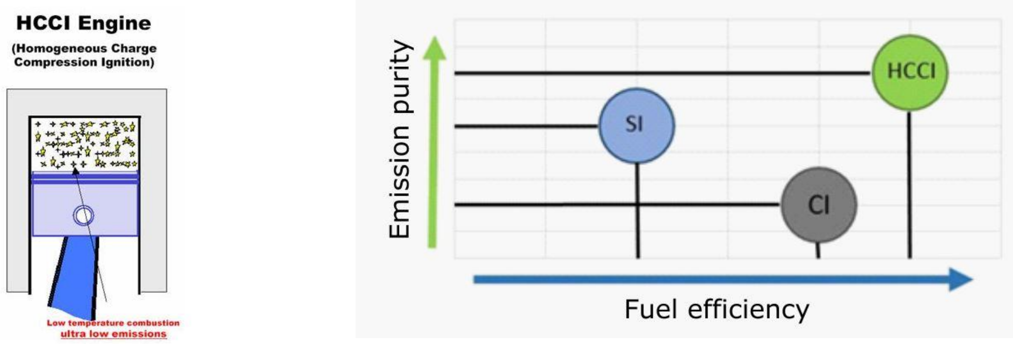

Figure 1 HCCI engine (left side) and fuel efficiency - emissions purity diagram (right side)

The great advantage of HCCI engines is that they achieve high fuel efficiency, which implies that they have the ability to burn fuel more efficiently and therefore can make better use of the energy produced. Another advantage is that the auto-ignition of the mixture allows better combustion control, resulting in lower NOx, CO2 and PM emissions.

Despite its many advantages, HCCI technology also has serious drawbacks, such as the difficulty of controlling the auto-ignition process, as the control itself is influenced by a number of factors (engine temperature, engine load ...). It follows that HCCI engines, or the autoignition and combustion process of the mixture, is strongly dependent on the operating conditions. Moreover, the HCCI engine has a limited speed range (Figure 3), which is not suitable for driving the vehicle in the city. As can be seen in Figure 4, the ideal speed range for an HCCI engine is in the range of 1200-1300 rpm. [1,2,3]

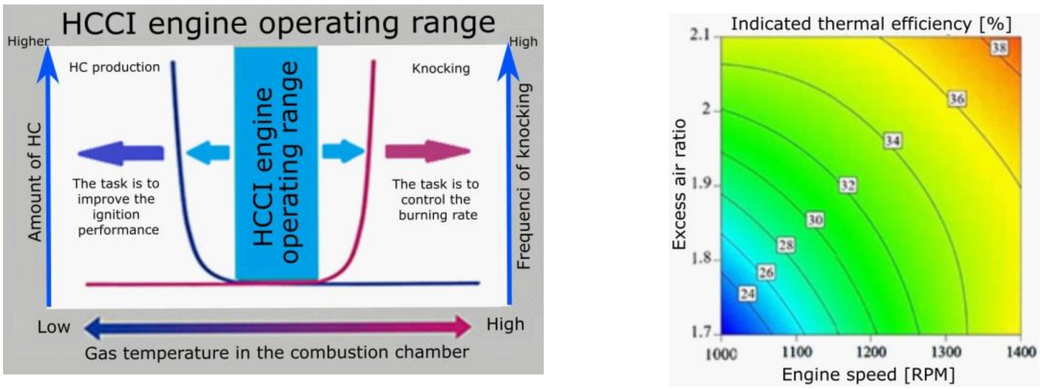

Figure 3 HCCI operating range (left side) and interactive effect of excess air ratio and engine speed on ITE (right side)

2.2. Definition of Hybrid vehicles

In an effort to reduce greenhouse gas emissions and reduce dependence on fossil fuels, the automotive industry is focusing on the development of cleaner alternatives. One of these innovations is hybrid vehicles, which have become increasingly popular in recent years.

A hybrid vehicle is a type of car that uses a combination of multiple propulsion systems, usually an internal combustion engine and an electric drive. There are two main types of hybrid vehicles: parallel and series.

Parallel hybrids (Figure 5) use both powertrains simultaneously, allowing the engine and electric drive to work together to move the vehicle. Series hybrids (Figure 5), on the other hand, are more focused on electric propulsion, with the internal combustion engine serving as the generator of electricity that drives the electric motors. [4-7]

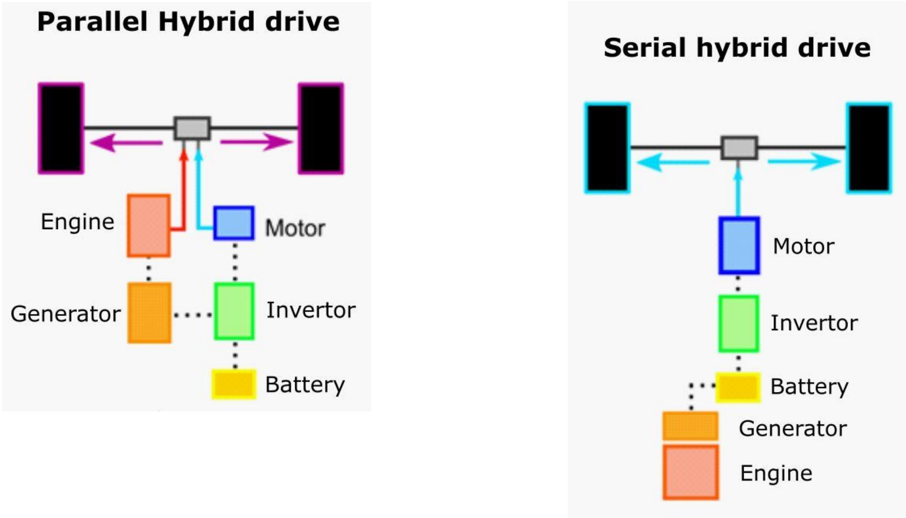

Figure 5 Parallel hybrid (left side) and serial hybrid drive (right side)

4. Discussion

From the above, it is clear that the technologies described have many advantages, which are more or less accompanied by serious shortcomings. However, by fusing the two technologies it is possible to exploit their strengths and at the same time significantly reduce or even eliminate their weaknesses.

As mentioned in Section 2.1, HCCI engines have the ability to use fuel efficiently and achieve high performance with respect to fuel consumption. However, the disadvantage is the very narrow operating range. The limited range of loads means a limited range of use of the HCCI mode in a depower that would only be designed for smooth running.

In Section 2.2, the advantages of hybrid drives were described, in particular the advantages of series drives, where the most significant advantage was that in series hybrid systems the engine is usually only used as a generator of electrical energy, which drives the electric motor of the vehicle itself.

Thus, by combining these facts about the HCCI and the hybrid engine, it is possible to tune the HCCI engine to operate in a speed range where fuel consumption, thermal efficiency, and performance are ideal.

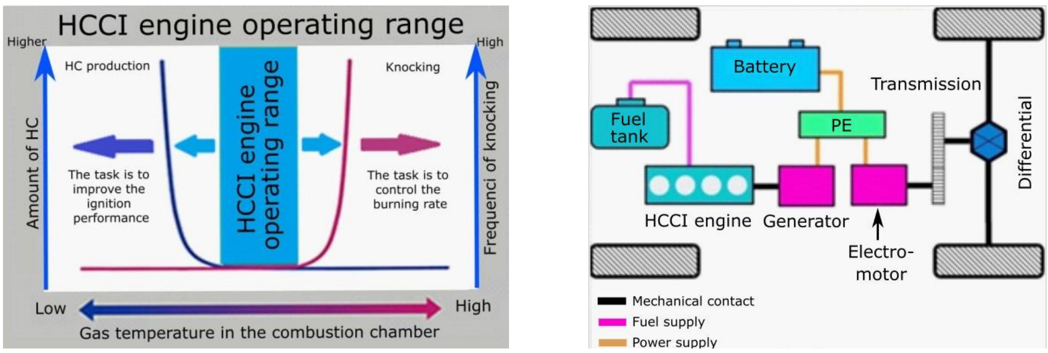

Figure 7 HCCI operating range and Schematic drawing of HCCI hybrid engine

5. Conclusion

In conclusion, the HCCI engine offers several advantages over conventional engines. One of its main benefits is the minimal level of emissions produced, thus promoting environmental sustainability. Reducing emissions is a key priority for the Europe an Union and the HCCI engine appears to be a potential solution to this problem. Across the spectrum of conventional and new innovative engines, the HCCI engine achieves the highest efficiency, with values as high as 55% . Nevertheless, it has its limitations, as it reaches its highest efficiency in the 1200-1300 rpm range and thus cannot directly replace conventional engines. Its best application is in hybrid vehicles, where the choice of the right hybrid powertrain makes it possible to optimize the overall efficiency of the HCCI engine system. The flexibility of the design allows the use of a variety of fuels, including diesel, gasoline, or even non-traditional fuels such as synthetic fuels or hydrogen, in order to achieve zero emissions.

Today, electric vehicles are considered to be among the most efficient in terms of emissions from the conversion of electrical energy to mechanical energy. It is important to realise that most of the world's energy is currently produced in thermal power stations, which are often less than 25-30% efficient. This energy is then used to charge batteries.

Acknowledgments: This work was supported by the Slovak Research and Development Agency under the Contract no. APVV-19-0328. The article was written in the framework of Grant Projects: VEGA 1/0318/21 “Research and development of innovations for more efficient utilization of renewable energy sources and for reduction of the carbon footprint of vehicles” and KEGA 007TUKE-4/2023 “Transfer of innovations and advanced technologies, determined for more ecological and more efficient vehicle drive systems, into the educational process.”

Conflicts of Interest: The authors declare no conflict of interests.

References

1. Enginelabs: Is HCCI the future of the internal combustion engine? [Online]. 16.9. 2016 https://www.enginelabs.com/news/video-hcci-future-internal-combustion-engine
2. Saxena, Samveg-Vuilleumier; David Kozarac; Darko Krieck; Martin Dibble; Robert Aceves Salvador: Optimal operating condizions for wet ethanol in a HCCI engine using exhaust gas recovery. [online]. 20.12.2013 https://reader.elsevier.com/reader/sd/pii/S0306261913009276?token=EA1C4C18553EE0576D4D4259F6D0F45F10750D4ACF663BB967C0AD41A40FA2D10FF834DF706641A7070FA788BAD8E02E&originRegion=eu-west-1&originCreation=20230328181131
3. Puškár, Michal: Pokročilé technol=ogie spaľovania a emisná prioblematika vozidiel. Košice: Strojnícka fakulta Technickej univerzity v Košiciach, 2023. ISBN 978-80-553-4196-5.
4. SFMTA: Hybrid technology Parallel vs, series. [Online]. [Dátum: 27.11.2023]. www.sfmta.com/sites/default/files/reports-and-documents/2021/04/4-28-21_emsc_item_8_bus_propulsion_slide_presentation.pdf
5. Gettozero: Parallel hybrid for motor Coaches, [Online]. [Dátum: 1.12.2023]. https://gettozero.com/parallel-for-motor-coach.php
6. Manigandan S, Gunasekar P, Devipriya J. Emission and injection characteristics of corn biodiesel blends in diesel engine. Fuel 2019;235:723–35.
7. van Niekerk AS, Drew B, Larsen N, et al. Influence of blends of diesel and renewable fuels on compression ignition engine emissions over transient engine conditions. Appl Energy 2019;255:113890.

Control of dynamic systems with non-minimum phase

Lukáš Leštach [1*], Ľubica Miková [2,*]

[1] Technical University of Košice, Faculty of Mechanical Engineering, Department of Industrial Automation and Mechatronics, Park Komenského 8, 042 00 Košice; lukas.lestach@student.tuke.sk
* Correspondence: lukas.lestach@student.tuke.sk; Tel.: +421 944 664 579
2 Technical University of Košice, Faculty of Mechanical Engineering, Department of Industrial Automation and Mechatronics, Park Komenského 8, 042 00 Košice; lubica.mikova@tuke.sk
* Correspondence: lubica.mikova@tuke.sk

Abstract: The aim of this paper is to describe dynamic system with a non-minimum phase. The first introductory part of the paper deals with the actual problem controlling of various dynamic models . The second part deals with the control of dynamic systems. The next part describe formulation of the control problem. The last section deals with the construction of the mathematical model of the manipulator.

Keywords: dynamic system**,** minimal phase, non-minimal phase

1. Introduction

Nowadays, many scientific publications and researches are devoted to the issue of manipulator control, where various dynamic models are used to describe the manipulator instead of the real manipulator. Manipulator is a device that is used for handling work, performing technological tasks in order to facilitate heavy physical work. The problem of robotic manipulators involves solving the position and orientation of manipulator segments. The control of actuators in mechatronic devices and instruments is a very important problem in industrial applications. The biggest problem and challenge is the control of such systems, where the control is affected by less available control inputs as well as degrees of freedom. In this well-known problem, a new intelligent hybrid structure is used in online tuning of PID controllers. The structure is based on two adaptive neural networks that are used to approximate the control signals and handle system deviations. The developed structure and its experimental testing allows us to analyze and monitor the deviation signals in order to significantly minimize the deviation of the signals compared to other controllers. In this form of solution it is recommended to use a highly nonlinear system that operates in the presence of unwanted disturbances [1].

2. Control of dynamic systems

Dynamic systems can be classified according to continuity, linearity, number of inputs and outputs, and time dependence. These divisions are further subdivided into subgroups. SISO is characterized as the simplest type of single-input, single-output system. The simplicity of this system is exploited in the control design by using the Bode diagram, the Nyquist stability criterion and by using frequency analysis. The controller design can be done using polynomial expressions, which have the advantage of being easy to solve [2].

2.1. Minimum phase system:

A transfer function *G(s)* is minimum phase if *G(s)* and *1/G(s)* are causal and stable. That is, the system has neither zeros and poles in the right half-plane and it also has no delay. For a system with minimum phase, Bode discovered that the phase can be uniquely derived from the magnitude slope. Minimum phase systems can be divided into stable and not stable.

Stable minimum-phase regulated systems of 1st and 2nd order, where the gain of the controller is not bounded from above. To control a stable regulated system with 1st and 2nd order minimum phase, the magnitude of the controller gain can be set without any constraints, where the following applies:

$$0 < \quad < \infty \tag{1}$$

For stable regulated systems with a minimum phase higher than 2nd order the gain of the controller K is bounded from above.

In unstable minimum-phase controlled systems, one or more poles occur in the right half-plane, while the other poles and all zeros are located in the left half-plane of the root plane „*s*". For unstable minimum-phase regulated systems, the gain of the controller is bounded both from above and below. For these systems, faster controller responses are required compared to the stable regulated system.

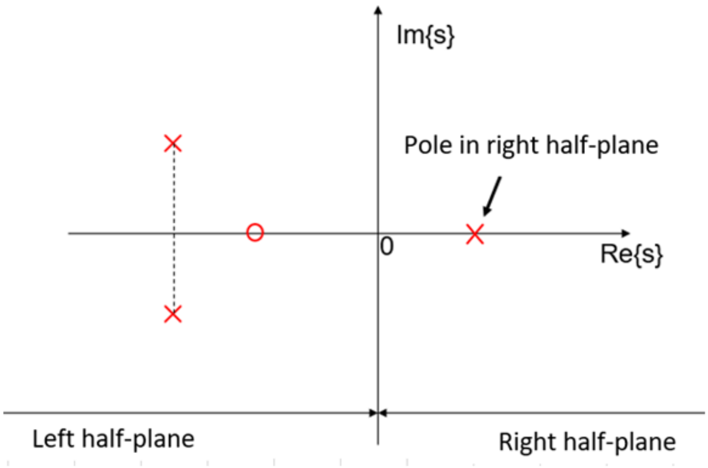

Figure 1. An unstable dynamic system with minimum phase [2]

A minimum phase system has a minimum phase change among all transfer functions that have a graph of the same size. As an example, we can consider a regulated unstable system with minimum phase with transmission:

$$= \frac{1}{(\ -1)(\ +2)(\ +3)} \quad . \tag{2}$$

The Hurwitz rule is used to investigate the effect of controller gain. The characteristic equation and the main Hurwitz determinant are:

$$^3 + 4\ ^2 + \ -6 + \ = 0 \tag{4}$$

$$_3 = \begin{matrix} 4 & -6+ & 0 \\ 1 & 1 & 0 \\ 1 & 4 & -6+ \end{matrix} \tag{5}$$

$$_3 = -6+ \quad 10- \quad > 0 \tag{6}$$

The stability condition is:

$$6 < \quad < 10 \tag{7}$$

A minimum phase system has a minimum phase change among all transfer functions that have a graph of the same size.

2.2 Non-minimum phase system

Non-minimum phase systems are that they have the same Bode magnitude plots as minimum phase systems. The only difference is that the Bode phase plot for a non-minimum system has more phase than for a minimum system. Minimum phase system follows the Bode rules it means that we are able to determine transfer function for such a system from the Bode magnitude plot and we are also able to identify non-minimum phase system from the fact that phase plot is inconsistent with transfer function.

The non-minimum phase system consists of two transfer functions.

$$_1 \quad = 1, \ _2 \quad = \frac{1-}{1+} \qquad (8)$$

The transfer function $G_1(s)$ is the minimum phase until it contains no unstable zeros and poles. The magnitude of the transfer function $G_1(s)$ is 0 dB and the phase is 0°. The magnitude of the transfer function with non-minimum phase $G_2(1)=0$.

It can be verified that $1/ \ _2 \quad = \frac{1+}{1-}$ is unstable.

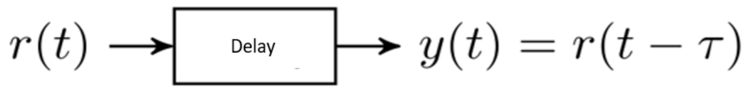

Figure 2. Delay of non-minimum phase dynamic system with r(t) action variable input [1]

Non-minimum phase stable system is a regulated system which has all poles located in the left half-plane „s'', where some zeros may be located in the right half-plane „s''. As an example, we can consider a stable regulated system with a non-minimum phase with transfer function:

$$= \frac{(\ -4)}{(\ +1)(\ +3)} \qquad (9)$$

The characteristic equation is:

$$^2 + \ 4 + \quad + 3 - 4 \quad = 0 \qquad (10)$$

Using the Hurwitz criterion assessing the stability of the system, we can determine the controller gain to determine the stability of the control system.

$$-4 < \quad < \frac{3}{4} \qquad (11)$$

In a stable regulated system with a non-minimum phase, there is a zero in the transmission of the regulated system in the right half-plane „*s*'', so there is a limitation in the gain of the controller.

Non-minimal phase unstable system is a regulated system with a non-minimum phase which is characterized by some poles and zeros being located in the right half-plane of the „*s*'' plane.

We can consider a regulated system with transfer function:

$$= \frac{(\ \ - 4)}{(\ \ - 1)(\ \ + 3)} \tag{12}$$

The characteristic equation is:

$$^2 + \ 2 + \qquad - 3 - 4 \quad = 0 \tag{13}$$

Applying the Hurwitz criterion, we obtain conditions for stability:

$$-2 < \quad < -\frac{3}{4} \tag{14}$$

If a pole from the right half-plane of the roots „s" is in the transmission of the regulated system, the gain of the regulator is bounded from below. In the case of 1st and 2nd order systems, the constant *K* is not bounded from above [3].

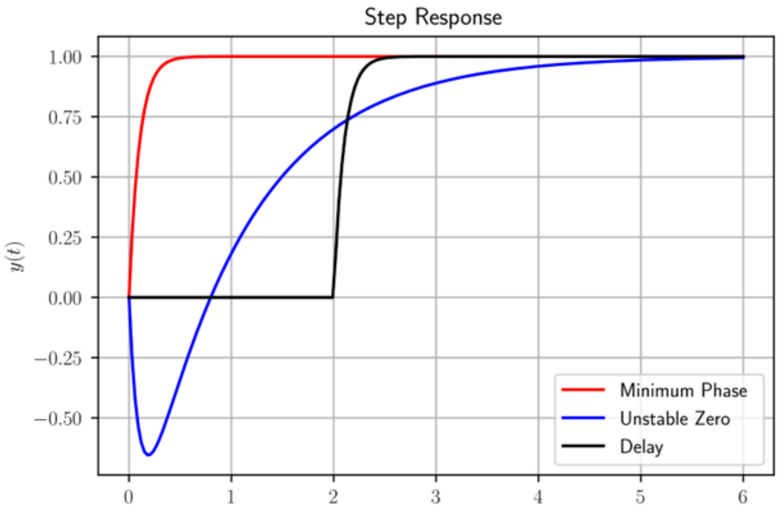

Figure 3. Bode amplitude-frequency diagram for a non-minimum phase dynamic system [2]

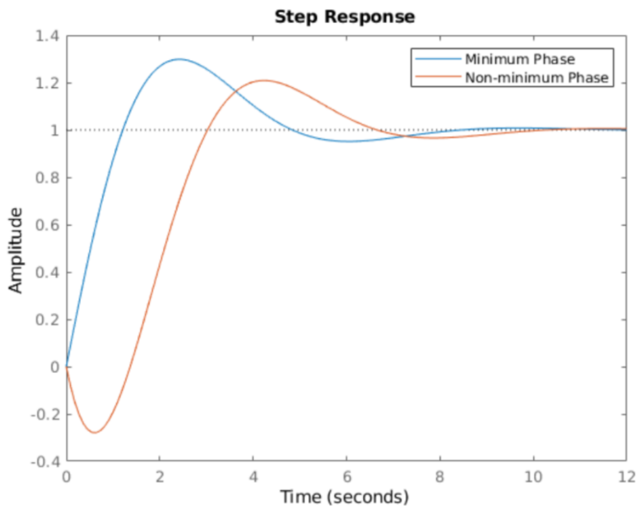

Figure 4. Minimum and non-minimum phase difference [2]

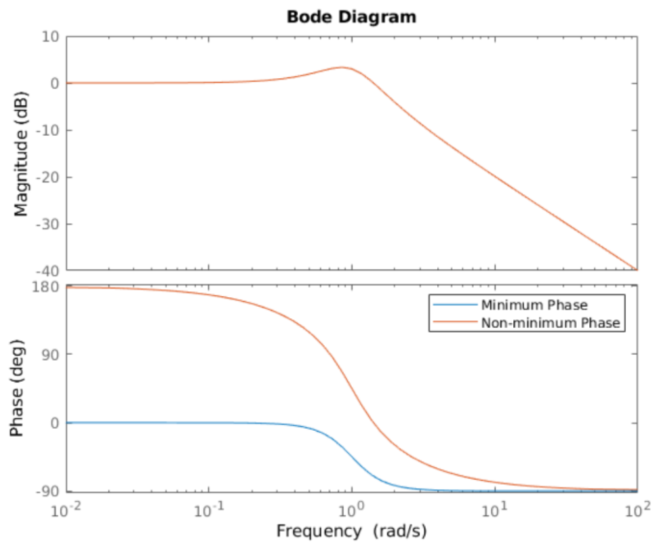

Figure 5. Bode amplitude-frequency diagram for a minimum and non-minimum dynamic system [2]

3. Formulation of the control problem

The aim is to find a feedback controller that generates the control variable:

$$= \quad - (\;) \tag{15}$$

based on the measurement of the controlled variable *y(t)* in such a way that the control objectives are achieved. This concerns the determination of the operator A, which represents the controller as a dynamical system. If the dynamic system is controlled linearly, then operator A is represented by a transfer function. In the search for the controller, the controller is joined to the controlled and together they form the controlled system [4].

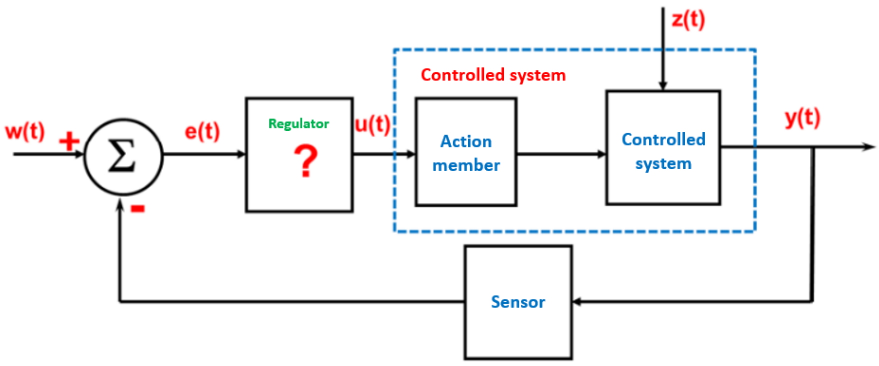

Figure 6. Structure of deviation control [3]

4. Creation of mathematical model

Figure 7 shows a system that is considered to be elastic. It is assumed that a flexible beam is attached to the trolley, when the trolley moves the beam deflects.

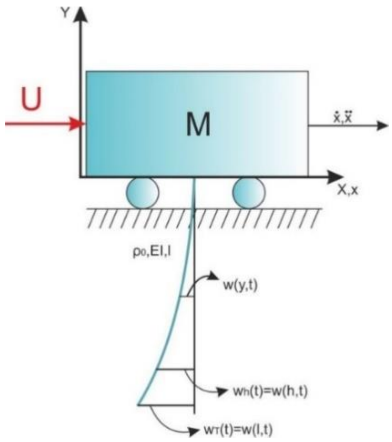

Figure 7. Flexible dynamic system

Under the Euler-Bernolli assumption, the equations of motion are derived from Hamilton's principle:

$$+ \quad {}^{0} \quad + \frac{{}^{2} \quad ,}{{}^{2}} \quad = \; (\;) \tag{16}$$

$$\frac{{}^{4} \quad ,}{{}^{4}} + \quad + \frac{{}^{2} \quad ,}{{}^{2}} = 0 \tag{7}$$

where M is the mass of the trolley, l is the length of the flexible beam, ϱ is the specific gravity of the flexible beam, EI is the bending stiffness of the beam, y is the position of the trolley and w (y, t) is the deflection of the beam.

The boundary conditions can then be written as:

$$0, \quad = \frac{(0,\;)}{} = \frac{{}^{2}\;(\;,\;)}{{}^{2}} = \frac{{}^{3}\;(\;,\;)}{{}^{3}} = 0 \tag{18}$$

As is well known, a moving elastic beam represents a system with a non-minimum phase. For simplicity, only the first eigenmode, i.e. *n=1*, is considered. First, the transfer function between the end position of the beam *(y_2)* and the input *U(t)* must be determined. The position of the beam end is given by the relation:

$$_{2} \quad = \quad + \; _{1}(\;)\; _{1}(\;) \tag{19}$$

Laplace transforming the transfer function is of the form:

$$\frac{_{2}}{(\;)} = \frac{_{1}\;\frac{1}{\frac{2}{1}}\;1 - \frac{_{1}(\;)\;_{1}}{_{1}}\quad {}^{2} + 1}{{}^{2}\quad _{1}\;{}^{2} + \quad _{1}} \tag{20}$$

The value of the non-minimum phase of the system can be determined from the following criterion [5]:

$$= 1 - \frac{_{1}(\;)\;_{1}}{_{1}} \tag{21}$$

5. Conclusions

If *B(r)* is negative, the system is with non-minimum phase If *B(r)* is positive, the system is with minimum phase.

The aim of the paper was to develop a mathematical model of a manipulator of a dynamic system with a non-minimum phase. In the first part, current manipulator control solutions and basic concepts related to the problem are described. In the second part, it was necessary to understand the control theory based on the different characteristics of the dynamic system with minimum and non-minimum phase, where based on the theory, the development of the mathematical model was started. For the selected dynamic system model, an elastic dynamic system of a trolley to which an elastic beam is attached was chosen where deflection occurs during motion. According to the Euler-Bernolli assumption, the equations of motion are derived from Hamilton's principle based on which the boundary conditions were determined. This moving elastic beam represents a system with a non-minimal phase where only the first eigenmode is considered. Based on the mathematical operations, the transfer function of the dynamic system was determined, where the value of the non-minimum phase of the system is determined using the *B(r)* criterion.

Acknowledgments: The authors would like to thank the Slovak Grant Agency -project VEGA 1/0201/21 and project KEGA 027TUKE-4/2022.

References

1. Miroslav B. Milovanovic, Adaptive PID control based on orthogonal endocrine neural newtworks, University of Niš, Faculty of Electronic Engineering, Department of Control Systems, Aleksandra Medvedeva 14, 18000 Niš, Serbia. [online]. [cit. 2023-12-01]. Available on the internet: :< https://www.sciencedirect.com/science/article/abs/pii/S0893608016301162>.
2. Shakhatreh F. et al. THE BASICS OF ROBOTICS, LAHDEN AMMATTIKORKEAKOULU, Tekniikan ala Kone- ja tuotantotekniikka, Mekatroniikka, Opinnäytetyö, Syksy 2011, Available on the internet:: <https://www.theseus.fi/bitstream/handle/10024/37806/Shakhatreh_Fareed.pdf > [cit. 2023-12-04].
3. Gmiterko A. a kolektív et al. Teória dynamických systémov, TUKE, Košice, 2013. 301 pages [cit. 2023-12-02].
4. Gmiterko A., Riadenie technických sústav, TUKE, Košice, 2013. 301 pages. [cit. 2023-12-02].
5. Tzu-Sung Wu et al. Anti-sway tracking control of tower cranes with delayed uncertainty using a robust adaptive fuzzy control, Department of Mechanical Engineering, Texas A & M University at Qatar,Qatar,2015. , Available on the internet:: <http://dx.doi.org/10.1016/j.fss.2015.01.010> [cit. 2023-12-04].

TECHNICKÁ UNIVERZITA V KOŠICIACH
Strojnícka fakulta

Noise effects on human life functions

Elena Lukáč Jurgovská [1*], Ervin Lumnitzer [1]

[1] Technical University of Košice, Faculty of Mechanical Engineering, Department of Business Management and Environmental Engineering
* Correspondence: elena.lukac.jurgovska@tuke.sk

Abstract: The effects of noise on the human body are a long-term researched issue. However, we rarely come across an analysis of the immediate, short-term effects of noise on humans. It is obvious that these influences do not cause (unless it is acoustic trauma) damage to a person's health, but they can affect their attention, the ability to react to unexpected events, or the ability to make the right decisions. The contribution deals with the analysis of the impact of noise on blood pressure, heart rate and the attention of the test respondents. The introduction summarises the knowledge base aimed at assessing the impact of noise on human health, the psychological burden on humans and epidemiological studies. The experimental measurement is aimed at performing and evaluating the dependence of blood pressure and heart rate on the action of the source. The results of the testing show that the most statistically significant is the increase in the frequency of the heart rate during the action of the noise source. The increase in heart rate after exposure to a noise source is also significant. Based on the above experimental results, it is possible to assess the effects of noise on the human body.

Keywords: Noise, Blood pressure, Heart rate, Epidemiological studies

1. Introduction

Exposure to unpleasant and disturbing noise can cause people to become stressed, distracted, focused and reactive. Several epidemiological studies have been carried out in this area. Based on an epidemiological study [1] in the automotive component manufacturing plant, there were significant changes in mean heart rate, systolic and diastolic blood pressure between the exposed group and the control group of the experiment. At the Aligarh plant [2], where employees were exposed to a variety of noise sources (hydraulic press, lathes, grinding, hand press), there was a significant increase in systolic pressure and heart rate for all noise sources. For diastolic pressure and mean arterial pressure, there was an increase in all sources of noise except the handprint and the pulse pressure was increased for the handprint and the hydraulic press. An epidemiological study [3] carried out in Nigeria in a company producing polypropylene sacks showed that systolic blood pressure values during on-call time were lower than systolic blood pressure values during morning and night duty. No significant changes in staff diastolic blood pressure were observed during morning and night duty. There were also no significant differences between diastolic blood pressure values during morning and free time. An epidemiological study [4] carried out in Italy on workers working in the paper industry shows an increase in cases of high blood pressure, diastolic and / or systolic, among workers exposed to noise compared to the two control groups not exposed to noise. Based on the results of a study [5] in the Rubber and Tire Company of Iran, it can be concluded that there was a significant increase in systolic and diastolic blood pressure. The results of the study showed that exposure to noise has a significant impact on the incidence of hypertension.

The negative impact of noise on the human body can also be manifested by an increased level of cortisol, disruption of the immune system, psychological problems, cardiovascular diseases and hearing disorders. Increased cortisol is an indicator of chronic stress and is closely related to immunological changes. The associations between noise and mental health have been studied in terms of mental symptoms and psychiatric illnesses in society [6].

Several studies [6 - 10] of the impact of noise on the cardiovascular system looked at dose-response relationships between noise exposure and cardiovascular diseases. Recent results show that there are individual differences (e.g. gender) in the effect of noise and that the effect of noise may also reflect other environmental features as well as air pollution. In addition to the psychosocial effects of noise on society, there are concerns about the impact of noise on cardiovascular diseases in particular. The effects of noise on health have been studied for several decades using laboratory and empirical methods. These include blood pressure, heart rate, cardiac output, and vasoconstriction, as well as stress hormones (corticosteroids, adrenaline).

Studies [7 - 10] have shown that persistent exposure to noise increases the risk of cardiovascular diseases, including high blood pressure and coronary heart disease:

- Sound or noise is a psychosocial stressor that activates the endocrine system,
- The acute effects of noise occur not only in the working environment but also in the environment.

The importance of public health is due to the high incidence of cardiovascular diseases in developed and industrialised countries. Ischemic heart diseases are one of the main causes of premature death in modern societies.

Noise is the risk factor that most often affects a person's mental well-being at work. Even at relatively low noise levels, environmental noise can be a stressful factor. Exposure to noise affects communication, attention, balance, hearing, sleep, mental status, performance, cardiovascular function, anger, and social behaviour. A study on the effects of exposure to noise on various aspects of the functioning of the human body has shown impaired cognitive development. Noise harms memory, verbal speech, and comprehension already at a noise level of 70-80 dB. Attention is an indicative activity that enables a person to examine objects, phenomena, and the environment, focusing on those that are most important to him or her. The focus is most pronounced in tests where relatively simple, stereotypical work is carried out over a longer period [11 - 12].

The paper deals with conducting an experiment in which we focused on the dependence of blood pressure, heart rate, and attention during short-term noise exposure. We used the proposed methodology in a specific experiment, which we evaluated using statistical methods.

2. Materials and Methods

The first step in the design of the methodology of the experiment on the dependence of blood pressure and heart rate on the noise level is the determination of the measured quantities. The measured quantities are systolic blood pressure, diastolic blood pressure, and heart rate. Depending on the effect of the noise source, these quantities are measured to determine the change in these quantities if the respondent is in an environment without noise and subsequently in an environment with noise.

Subsequently, measuring devices were selected, which are used for measuring systolic blood pressure, diastolic blood pressure, and heart rate. It is important to use a clinically proven digital sphygmomanometer to measure these values. This was followed by the determination of the noise parameters to which the respondents will be exposed during the measurement of systolic blood pressure, diastolic blood pressure, and heart rate.

The next step is to determine the location and conditions of the experiment. It is necessary to choose the place of the experiment so that during the measurement, disturbing environmental influences that could affect the monitored parameters are eliminated to the maximum extent possible. It is also important to ensure the optimal temperature and relative humidity of the environment.

The length of the experiment must be set so that the organism has time to react to the noise and at the same time so that the measurement is not time-consuming for the respondents due to monotony or fatigue. The length of the experiment must also exclude the adaptation of the organism to noise.

In the next step, we selected respondents suitable for the experiment, the number of women and men, and the age range. The homogeneity of the statistical set and the exclusion of respondents with hypertension and other health disorders are important. Since this is a pilot project that was supposed to prove the validity of the experiment, different age categories were not represented.

The last step, after the measurements of the experiment, was its statistical evaluation. Using statistical methods, it was possible to determine whether the values of systolic blood pressure, diastolic blood pressure, and heart rate during short-term noise exposure are higher than the values of systolic blood pressure, diastolic blood pressure, and heart rate without noise exposure.

2.1. Experimental measurements

The total length of measurement of one respondent was 21 minutes. Blood pressure and heart rate were measured throughout the measurement. All parameters were measured in the respondents first before exposure to the noise source (M1). Subsequently, the respondents were exposed to the noise source for 7 minutes (M2). After exposure to the noise source, all parameters were measured in respondents for 7 minutes (M3).

Since this was an initial study, the size of the statistical set is 20 respondents, while the characteristics of the respondents are shown in Table 1.

Table 1. The characteristics of the respondents.

Gender	Number	Age min - max	Weight [Kg]	Height [m]
Woman	12	23-25	49-65	158-172
Man	8	23-25	65-90	170-186

Blood pressure and heart rate were measured while sitting, and during the measurement, the respondent was not allowed to move his hand or communicate with the surroundings. Figure 1 shows the respondent during the measurement.

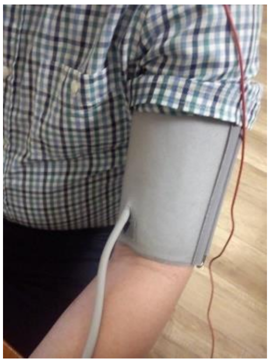

Figure 1. Respondent during the measurement.

Before the beginning of the measurement, each respondent was at rest for at least 20 minutes without physical exertion. Before the measurement, the respondents were familiarized with the course of the measurement to avoid stress that could affect the results of the experiment. Blood pressure and heart rate were measured while sitting, and during the measurement, the respondent was not allowed to move his hand or talk. In fig. 1 shows the respondent's measurement process.

Data evaluation was carried out by testing hypotheses, using a two-sample paired t-test on the mean value and regression analysis. The goal was to determine whether the hypothesis was accepted or rejected at the level of significance but also to determine the smallest possible level at which the hypothesis is still rejected. This value is called the p-value and applies:

- if $p < \alpha$, then we reject the null hypothesis in favor of the alternative hypothesis,
- if $p \geq \alpha$, then we do not reject the null hypothesis

Testing was performed at a significance level of $\alpha = 0.05$. The results of hypothesis testing with a two-sample paired t-test on the mean value are presented in Table 2.

Table 2. Results of hypothesis testing.

Observation quantity	Hypothesis H0	Hypothesis H1	$p < \alpha$	Assessment
systolic blood pressure	SBP1=SBP2	SBP1<SBP2	$2{,}42797.10^{-18} < 0{,}05$	H0 reject, accept H1
	SBP1=SBP3	SBP1<SBP3	$0{,}29285112 < 0{,}05$	H0 do not reject, accept H0
diastolic blood pressure	DBP1=DBP2	DBP1<DBP2	$0{,}001236 < 0{,}05$	Valid, H0 reject, accept H1
	DBP1=DBP3	DBP1<DBP3	$0{,}00245653 < 0{,}05$	Valid, H0 reject, accept H1
heart rate	PP1=PP2	PP1<PP2	$1{,}59889.10^{-21} < 0{,}05$	Valid, H0 reject, accept H1
	PP1=PP2	PP1<PP2	$1{,}00295.10^{-7} < 0{,}05$	Valid, H0 reject, accept H1

Explanations:
SBP1 – systolic blood pressure before exposure to the noise source
SBP2 – systolic blood pressure during exposure to a noise source
SBP3 – systolic blood pressure after exposure to a noise source
DBP1 – diastolic blood pressure before exposure to the noise source
DBP2 – diastolic blood pressure during exposure to a noise source
DBP3 – diastolic blood pressure after exposure to a noise source
PP1 – heart rate before exposure to the noise source
PP2 – heart rate during the action of the noise source
PP3 – heart rate after exposure to a noise source

3. Results

The results of hypothesis testing are presented in the following figures of bar graphs of frequency values of systolic blood pressure in respondents before exposure to the noise source (M1) and during exposure to the noise source (M2).

Figure 2 shows a bar graph of the frequency of systolic blood pressure values of all respondents before exposure to the noise source (SBP1) and during exposure to the noise source (SBP2). The graph shows that lower values of systolic blood pressure are most numerous among respondents before exposure to the noise source, and the greatest frequency is in the interval (107.112> corresponding to the value of 109.5 mmHg. Higher values of systolic blood pressure are most numerous among respondents during exposure to the source noise and the greatest frequency is in the interval (112.117> corresponding to the value of 114.5 mmHg.

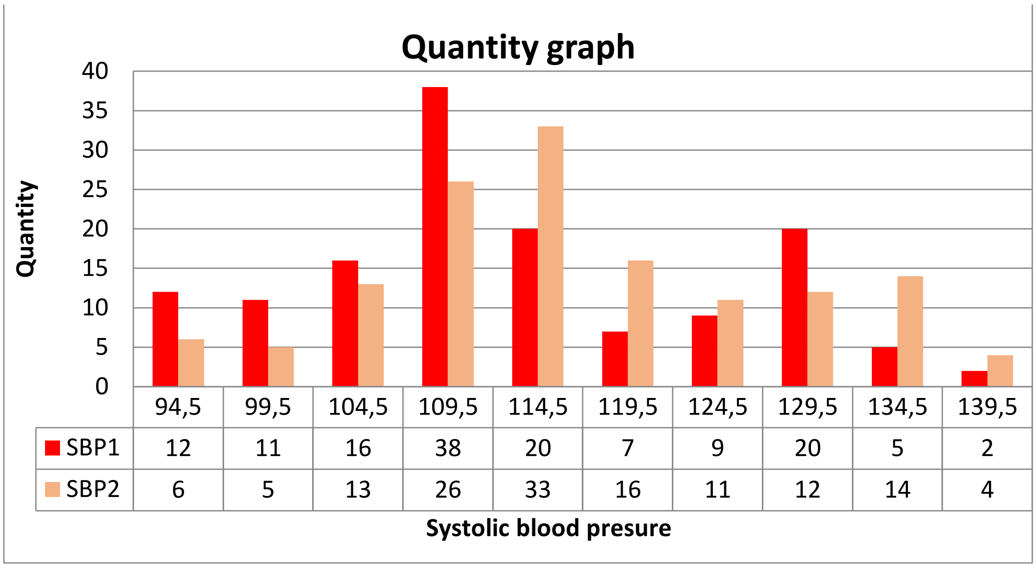

Figure 2. Quantity graph of systolic blood pressure values.

Explanations:

SBP1 – systolic blood pressure before exposure to the noise source

SBP2 – systolic blood pressure during exposure to a noise source

In the following figure, is a bar graph of the frequency of systolic blood pressure values in the respondents before exposure to the noise source (M1) and after exposure to the noise source (M3).

In Figure 3, the bar graph of the frequency of the systolic blood pressure values of all respondents before the exposure to the noise source (SBP1) and after the exposure to the noise source (SBP3) shows that the differences in the frequencies are not significant. The greatest frequency of systolic blood pressure values is after exposure to a noise source in the interval (107.112> corresponding to the value 109.5 mmHg.

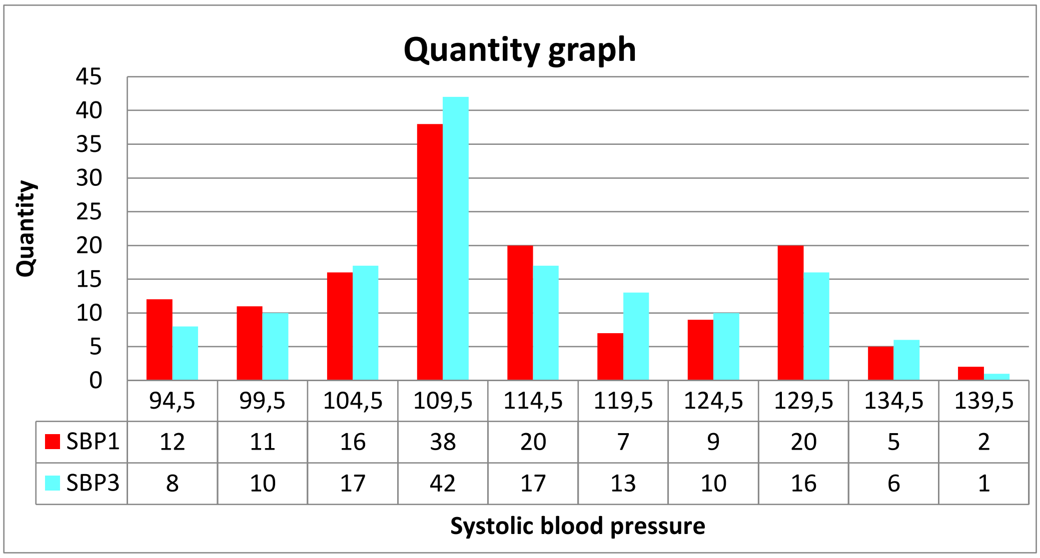

Figure 3. Quantity graph of systolic blood pressure values.

Explanations:

SBP1 – systolic blood pressure before exposure to the noise source

SBP3 – systolic blood pressure after exposure to a noise source

The following results for the frequency of heart rate values of all respondents before exposure to the noise source (PP1) and during exposure to the noise source (PP2) are:

- the greatest number of heart rate values among respondents before the noise source is in the interval (61.66> corresponding to a value of 63.5 mmHg.
- The greatest number of heart rate values among respondents during the noise source is in the interval (81.86> corresponding to a value of 83.5 mmHg.

The following results for the frequency of heart rate values of all respondents before exposure to the noise source (PP1) and after exposure to the noise source (PP3) are:

- The graph shows that the greatest number of heart rate values in respondents before exposure to the noise source is in the interval (62.67> belonging to the value 64.5.
- The greatest number of heart rate values in respondents after exposure to the noise source is in the interval (72.77> belonging to value of 74.5.

Based on our pilot experiment, we agree with epidemiological studies.

5. Conclusions

The results of hypothesis testing show that the most statistically significant is the increase in heart rate during the exposure to the noise source. The increase in heart rate after exposure to a noise source is also significant. The increase in systolic blood pressure during the exposure to the noise source is statistically significant. There was a small increase in diastolic blood pressure during exposure to the noise source, but at the same time there was a decrease in diastolic blood pressure after exposure to the noise source.

When assessing the average values, there was a significant increase in the average value of systolic blood pressure during the exposure to the noise source. The increase in the average value of the heart rate during the exposure to the noise source, the average value of the heart rate after the exposure to the noise source compared to the average value before the exposure to the noise source is also significant. The increase in the average value of diastolic blood pressure during the exposure to the noise source is insignificant.

Acknowledgments: his article was prepared with support from the project titled APVV-21-0120 „Research of an innovative method of monitoring the noise load generated by overhead power lines“.

Conflicts of Interest: The authors declare no conflict of interest.

References

1. Kalantary, S. et al.: The effects of occupational noise on blood pressure and heart rate of workers in an automotive parts industry. *Isfahan Cardiovascular Research Center & Isfahan University of Medical Sciences*, 2014.
2. Singhal, S. et al.: Effects of workplace noise on blood pressure and heart rate. *Aligarh Muslim University*, 2009.
3. Ismaila, S. O. et al.: Noise exposure as a factor in the increase of blood pressure of workers in a sack manufacturing industry. *Abeokuta*: Federal University of Agriculture, 2013.
4. Tomei, F. et al.: Can noise cause high blood pressure? Occupational risk in paper industry. *Società Editrice Universo*, 2014.
5. Attarchi, M. et al.: Effect of exposure to occupational noise and shift working on blood pressure in rubber manufacturing company workers. *National Institute of Occupational Safety and Health*, 2012.
6. Smith, A. P.: Noise and health: Why we need more research. Cardiff University: School of Psychology, 2010.
7. Salazar, MR. Hypertension, a linchpin between environmental noise exposure and the development of cardiovascular disease? *Journal of Clinical Hypertension* **2022,** *Volume 25,* Page 165-167.
8. Babisch, W. Cardiovascular effects of noise. *Noise & Health* **2011,** *Volume 13*, Page 201-204.
9. Chang, T.-Y., Hwang, B.-F., Liu, C.-S., Chen, R.-Y., Wang, V.-S., Bao, B.-Y., & Lai, J.-S. (2013). Occupational Noise Exposure and Incident Hypertension in Men: A Prospective Cohort Study. *American Journal of Epidemiology* **2013**, *Volume 177(8)*, page 818–825.
10. Stokholm, Z. A., Bonde, J. P., Christensen, K. L., Hansen, Å. M., & Kolstad, H. A. (2013). Occupational Noise Exposure and the Risk of Hypertension. *Epidemiology* **20013**, *Volume 24(1),* page 135–142.
11. Hnilica, R. et al.: Noise and health: Intenzita hluku verzus psychická záťaž človeka. *ACTA FACULTATIS TECHNICAE* **2013**.
12. Folscher, L. et al.: Emergency Department Noise: Mental Activation or Mental Stress? *Emergency Medicine Journal*, **2015**.
13. LUMNITZER, Ervin et al.: *Hodnotenie vplyvov fyzikálnych faktorov na zdravie človeka*. TU, 2014.159 s. ISBN 978-80-553-1632-1

Thingspeak platform as a tool for wireless data collection

Ondrej Majerčák [1]*, Marek Vagaš [1]

[1] Technical University of Kosice, Faculty of Mechanical Engineering, Department of Industrial Automation and Mechatronics;
* Correspondence: ondrej.majercak@tuke.sk;

Abstract: The article deals with the possibilities of wireless data collection and their evaluation in the Thingspeak environment. In the introductory chapters are listed devices, which were used in the creation of the measuring circuit with their description. Subsequently, the article focuses on an experiment that tests wireless communication and data transmission using the ESP-8266 module with a sample of the code. In the results of the work, the individual outputs from the Thingspeak platform as well as the possibilities of data processing in the Matlab program are subsequently presented. We can find individual measured values for humidity and temperature visualized there.

Keywords: wireless; collection; ESP-8266 module; Thingspeak

1. Introduction

The collection, processing, protection, and visualization of data are still largely solved nowadays. This article deals with the field of wireless data collection from the temperature and humidity sensor DHT 11 via a wireless and relatively widespread WIFI network based on the ESP module. Wireless data collection and the creation of sensor networks for collecting all kinds of data on different protocols do not bypass the industrial area either. There are many options for collecting data these days. There are many communication protocols and many ways of processing and visualizing the acquired data. The final visualization and data processing is in the result a desired product for the end user, for whom they have a greater informative value. The wireless collection of all kinds of data from production lines is a trend in the industry, where the use of the obtained data and its processing leads to the efficiency of production systems. When switching to wireless data collection, it comes into consideration to use the cheapest and simplest solutions that will not be burdensome for the end user. One such option is the use of the ESP-8266 module, which serves as an adapter to an existing wireless collection solution and offers even greater efficiency when introducing such a wireless collection solution [1,2].

2. Materials and Methods

This chapter describes the individual components that were used in the implementation of wireless data collection with their basic components. The chapter also describes the ESP-8266 communication module and the corresponding adapter for its use in more detail.

2.1. DHT 11 Sensor

One of the most used sensors for application prototyping. It is used to sense the temperature and humidity of the environment with a temperature deviation of ±1°C and humidity of ±1%, which is sufficient for this application of testing the wireless collection using the ESP module. Its supply voltage is from 3.5V to 5.5V with a working current of 0.3 mA. The measured temperature range is from 0°C to 50°C and the measured humidity range is from 20% to 90%. The response time of the sensor to a change in temperature is about 10 seconds, and when measuring humidity, about 6 seconds, as stated by the manufacturer [3,4].

Figure 1 shows the wiring diagram of the DHT 11 sensor with the microcontroller (Figure 1.). From the circuit diagram, we can see that we need one input of the microcontroller to communicate with the microcontroller. This means that the sensor communicates using serial communication based on 16-bit resolution.

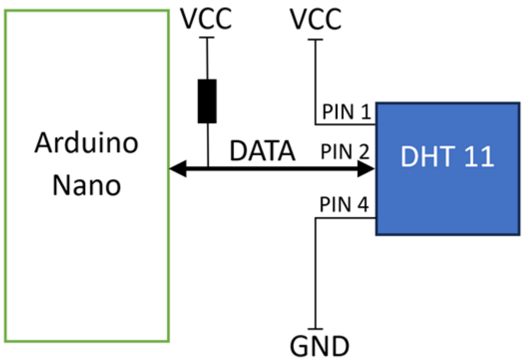

Figure 1. Connecting of DHT 11 sensor to microcontroller.

When connecting the sensor to the microcontroller in a line length of up to 20 m, 5 kΩ pull-up resistors should be used. The temperature and humidity sensor DHT11 has a supply voltage of 3 - 5.5 V. To achieve the purpose of filtering, a 100 nF capacitor can be placed between the VCC and GND pins [5].

2.2. ESP-8266 module

The ESP 8266 is a module used to connect microcontrollers to a WiFi network. It has an integrated TCP/IP protocol and firmware programmed in memory containing commands that make it possible to control it. This communication module has its own built-in processor and memory. The supply voltage is 3.3 V and the maximum drawn current is 300 mA [6]. The use of this module is also advantageous due to the possibility of placing the module further from the microcontroller. This makes it possible to improve the quality of the connection of the module with the communication gateway providing access to the Internet.

The module with a description of its individual parts is shown in Figure 2. The ESP-8266 module ranges in price from 2 - 5 €.

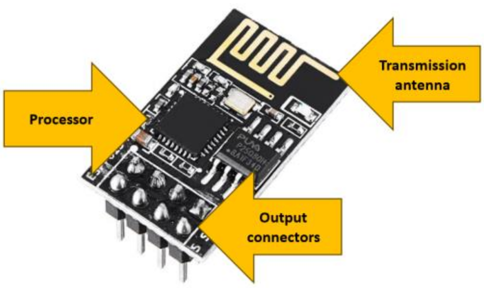

Figure 2. ESP-8266 module.

2.3. ESP-01 Adapter

ESP-01 Adapter is a component that serves to connect the already mentioned ESP module. This adapter, shown in Figure 3, aims to simplify the connection of the ESP module to microcontrollers by reducing the number of pins connected to the microcontroller from eight to four, providing a much simpler connection and occupying fewer microcontroller pins. Among other things, this adapter already has a built-in voltage stabilizer at 3.3 V, which solves the problem of powering the ESP module. The adapter connection is at the standard 5V provided by most microcontrollers. The output of the adapter is the power connectors and the Tx and Rx communication connectors. The ESP module adapter ranges in price from 2 - 5 €.

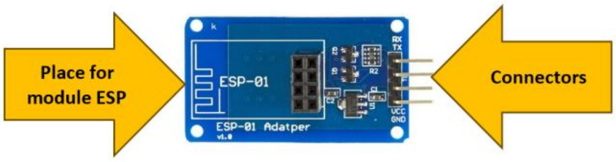

Figure 3. ESP-01 Adapter.

2.4. Thingspeak platform

The Thingspeak platform is an open IoT platform that is used for data collection and visualization, as well as for data analysis. It includes Matlab commands that can be used to analyze the acquired data. Collected data is stored in created channels, where each channel has its own API key. It is possible to set the availability of individual channels. This means that channels can be public, i.e. available to all users, or secret - available only to those who have been granted access. Each channel provides the acquisition of a maximum of 8 data windows [7].

3. Experiment

For testing wireless data collection from the DHT 11 sensor, we choose Arduino Nano as the microcontroller, which provides us with sufficient performance, interface, and software for this purpose and data collection. In the Arduino IDE environment, we created the source code of the microcontroller for the DHT 11 sensor together with the freely available library for the given sensor. We then continued testing the sensor via serial communication and subsequently corrected its parameters by comparing the results sent from the sensor and the thermometer with the built-in hygrometer. The correction of the deviation of the results was carried out in the program by writing the correction value to the result.

Subsequently, the adapter with the ESP-01 module was connected according to the circuit diagram in Figure 4. For the communication of the module, we chose Arduino connectors for serial communication. When uploading the program to the microcontroller, we disconnected the ESP module, and after uploading the program, we reconnected it. It is based on the ability to read and write data using the serial line.

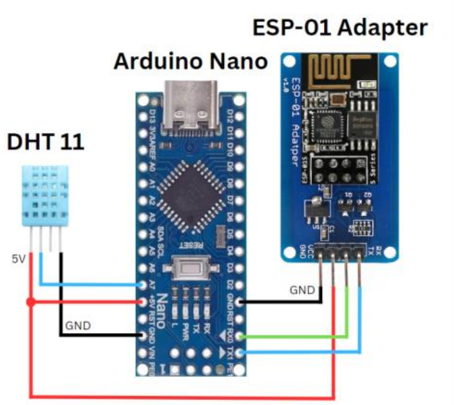

Figure 4. Microcontroller wiring diagram with peripherals.

Subsequently, we continued by modifying the program and creating functions for sending data to the Thinkspeak platform, in which we created our own channel with a unique API key, which we then inserted into our code (Figure 5).

```
#define SSID "WiFi Name"
#define PASS "Password"
#define IP "184.106.153.149"// thingspeak.com ip

String msg = "GET https://api.thingspeak.com/update?api_key";

```

Figure 5. Network parameters setting in the program.

In the program, we set the frequency of sending data about the temperature and humidity of the given room for 15 minutes. This means that in one hour we obtained 4 values of the temperature and humidity of the given environment, which was sufficient for our purposes. We applied the connection and measurement prototype to a room with relatively frequent movement of people to obtain variable temperature and humidity data for further processing.

4. Results

We collected data on temperature and humidity in the room for one month. During this period, we obtained 1496 temperature and humidity records. The Thingspeak platform allows us to directly process this data according to the parameters we specified and visualize it directly. The advantage is also the direct connection with the Matlab program, where we can process and evaluate individual data in more detail.

As part of data processing and visualization, we set the processing of average values of humidity and temperature during the day. The output is the graphs shown in Figure 6, which show us the average value of temperature or humidity in the room for one day in the entire measured period. The advantage of such a solution is very fast data processing and filtering of bad data. As we can see in the above picture, there was a so-called dead period during the data collection, when no data about the measured temperature and humidity was entered into the database. This could have been caused by a signal failure as well as a failure in the power supply of the microcontroller.

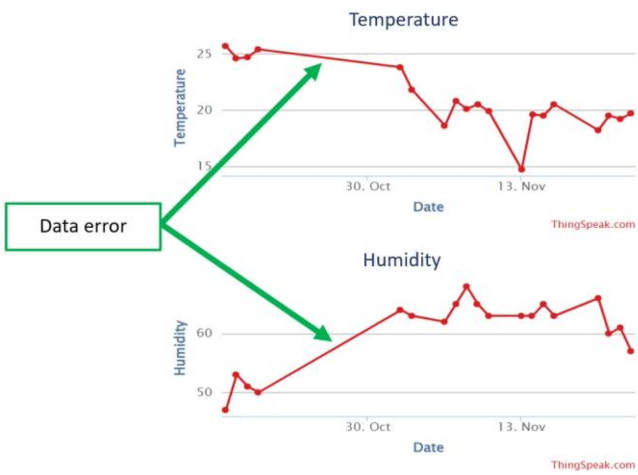

Figure 6. Visual processing of data in the Thingspeak platform

In the following graph, we have visualized the obtained raw data in the Matlab program, which we obtained for the entire test period. In the graphs in Figure 7, we can see individual measurement deviations that occurred and step changes that can be further processed and assessed using Matlab tools.

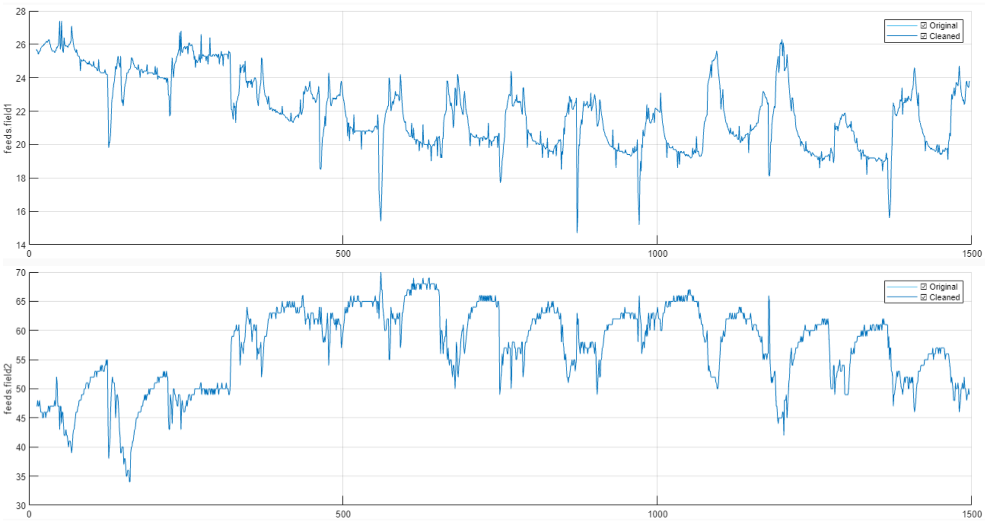

Figure 7. Graphic representation of the obtained raw data

In our case, we were able to process these values more efficiently using the Thingspeak platform. The reason why we processed the data in Matlab was precisely to obtain statistical data from the obtained data, which we can export from the Matlab program directly from the table. The procedure for processing this data is addressed from different sides. A sample of the obtained outputs from the program is shown in Figure 8.

field1	
Type	double
Unique Values	117
Has Duplicates	True
Is Sorted	False
Missing Count	11
Minimum	14.7
Maximum	27.4
Mean	21.9822
Median	21.8
Mode	19.6
Standard Deviation	2.177

field2	
Type	double
Unique Values	48
Has Duplicates	True
Is Sorted	False
Missing Count	11
Minimum	34
Maximum	70
Mean	57.0492
Median	58
Mode	62
Standard Deviation	6.9028

Figure 8. Outputs from Matlab

4. Discussion

Wireless data collection via the ESP-8266 module in combination with an Arduino microcontroller and a DHT 11 temperature and humidity sensor produced the expected outputs. Data collection in this form is relatively reliable and simple for programming and especially for application. Using the ESP-8266 module with the appropriate adapter is more reliable and easier to ensure the correct functionality of the module. Another advantage is the ease of replacing the ESP module without disturbing the corresponding microcontroller connectors. Based on the experiment, this module with an adapter is suitable for use with different microcontrollers, where it occupies fewer inputs of the microcontroller. The final processing of the results and their subsequent visualization with the help of the Thingspeak platform is completely sufficient for wireless data collection in this case. The advantage of this platform is the connection with the Matlab program and the possibility of processing these results in real time.

Acknowledgments: This work has been supported by the Slovak grant VEGA 1/0169/22 New methodics approaches to data from automated and robotized workplaces.

Conflicts of Interest: The author declare no conflict of interest.

References

1. Khaing, K. K. K. Temperature and Humidity Monitoring and Control System with Thing Speak. *International Journal of Scientific Research and Engineering Development, Faculty of Computer System and Technologies, University of Information Technology, Myanmar* **2019**. *Volume 2*. Available online: www.ijsred.com.
2. Pasha, S. Thingspeak based Sensing and Monitoring System for IoT with Matlab Analysis. *International Journal of New Technology and Research (IJNTR)* **2016.** *Volume 2.* pp. 19-23, ISSN: 2454-4116.
3. Datasheet, AOSONG. Temperature and Humidity Module DHT11 Product Manual. 2023. Available online: https://components101.com/sites/default/files/component_datasheet/DHT11-Temperature-Sensor.pdf.
4. Novelan, M. S.; Amin, M. Monitoring System for Temperature and Humidity Measurement with DHT11 Sensor Using NodeMCU. *International Journal of Innovative Science and Research Technology*, **2020**. *Volume 2.* ISSN No:-2456-2165
5. Wang, Y.; Chi, Z. System of Wireless Temperature and Humidity Monitoring Based on Arduino Uno Platform. *Sixth International Conference on Instrumentation & Measurement, Computer, Communication and Control (IMCCC),* China: Harbin, **2016**. pp. 770-773, 10.1109/IMCCC.2016.89.
6. Datasheet, Shenzhen Anxinke Technology CO;LTD. ESP-01 WiFi Module Version 1.0. 2023. Available online: www.ai-thinker.com
7. Malik, H.; Khattak, K. S.; Wiqar, T.; Khan, H.; Altamimi, A. B. Low Cost Internet of Things Platform for Structural Health Monitoring. *22nd International Multitopic Conference (INMIC),* Islamabad, Pakistan, **2019**. pp. 1-7. 10.1109/INMIC48123.2019.9022801.

TECHNICKÁ UNIVERZITA V KOŠICIACH
Strojnícka fakulta

Detection of straightness deviation on a production machine in an automatic cycle

Mateusz Markiefka [1], Artur Zawada [2]

[1] Univeristy of Bilsko-Biala; mmarkiefka4@gmail.com
[2] Univeristy of Bilsko-Biala; artur.zawada88@gmail.com

Abstract: The article presents a method of measuring straightness of a metal flat bar on a production machine in an automatic cycle. The measurement was carried out while the production machine was operating, using a laser profilometer. In order to determine straightness, the measurement results were used along the entire length of the side edges of the flat bar, omitting the support points. Then, using an appropriate algorithm, the maximum deviation was calculated and presented, defining whether the measured part meets production requirements.

Keywords: straightness deviation; algorithm; measurement; laser profilometer;

1. Introduction

In the era of widely available tools and devices, production time and product quality are crucial when choosing a supplier. In order to maintain appropriate quality, control measurements are introduced during production. Performing these measurements is an additional burden for production workers, whose main goal is to produce in accordance to the established quantity standard. Often, the need to produce a given batch within a specific time may result in placing quantity over quality. That is why companies try to automate measurement processes to detect nonconformities and defects at the earliest possible stage of production, while minimizing costs. Due to the number of necessary measurements, automation also relieves employees of this task. [1, 2].

According to that, the main reason for the research was to develop a method for measuring the straightness of metal profiles on a specific machine during the automatic cycle, without a negative impact on the cycle time. Before installing the measuring system on this machine, the straightness of the profiles after the straightening process was checked manually by a company employee on a table dedicated for this purpose.

2. Materials and Methods

The research was carried out on a machine used for straightening steel profiles. The operation of the machine consists in separation of one profile (flat bar) from the batch placed on transport chains, positioning it and subjecting it to the straightening process. Next, the straightened flat bar is moving to the measurement area and measuring of the shape in two axes at a given point starts. Measurement is done using a laser profilometer [3] moving on an additional axis along the entire length of the flat bar. After measuring the profile is transported to unloading zone. During measurement, the profile is transported to specially prepared prisms that position it along its entire length. Then, by simultaneously rotating the prisms, the flat bar is set at a given angle so that the laser beam can measure it in two axes through the measurement holes. The dimensional range of flat bars that can be processed at the station is 3000-6000 mm in length, 16-200 mm in width, 4-20 mm in thickness. The machine elements responsible for measuring straightness are presented in Figures 1 and 2.

Figure 1. Photo of a fragment of a machine positioning a flat bar for measuring straightness.

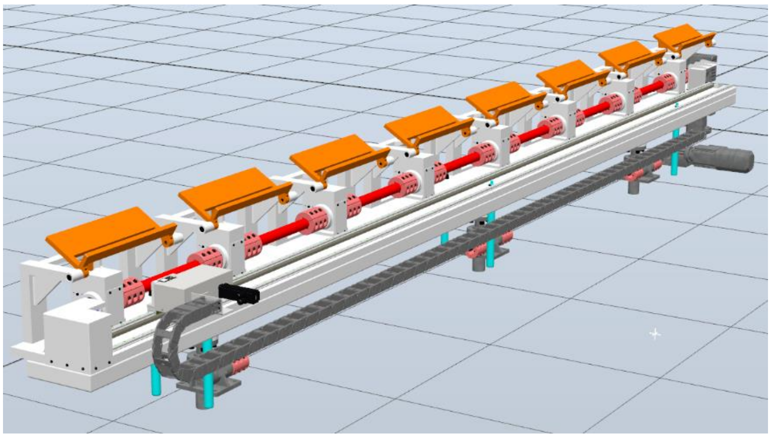

Figure 2. 3D model of the measurement system.

While traveling along the edge of the flat bar, the profilometer is covered by transport chains placed every 0.9 m and by measuring prisms responsible for the orientation of the detail. These elements significantly influence the arrangement of the detail. The plastic deformation that affects the straightness of the flat bar changes with the rotation of the detail. The smallest deformation occurs when the longer wall of the flat bar is perpendicular to the ground. However, in such a case, without proper support, the detail could tip over. The same effect may occur when the dynamics of the ramp movement responsible for the rotation of the detail is too high.

To sum up, in an ideal measurement position, process automation is difficult to implement. On the other hand, with the normal orientation of the flat bar (longer wall parallel to the ground), plastic deformation caused by gravity may distort the measurement. The same will happen if the detail has too much support when rotated. Reducing the number of supports may again cause the detail to give under its own weight. Analyzing the above conditions and based on the preliminary tests, the 60° angle turned out to be the best value. Of course, it is not possible to completely eliminate the influence of gravity and support friction, which may affect the results. However, this angle is sufficient to enable automation of the process. Figure no. 3 shows the positioned flat bar and the forces acting on it. The forces marked Fz and Fx are the plastic deformation of the material in a given axis. The vector Fg, on the other hand, means the gravitational force.

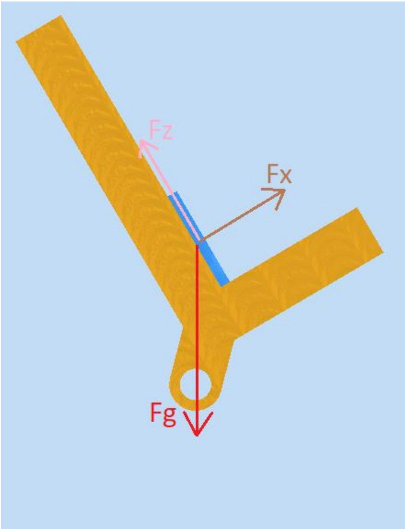

Figure 3. Force vectors influencing flat bar during measurement.

The tested flat bar is located at an angle to the coordinate system of the measuring device, so the displacement of the edges on this plane is the sum of the unevenness of both walls of the flat bar (width and thickness). This problem can be solved using the transformation matrices. For this purpose, three coordinate systems have been introduced in Figure 4:

- X0Z0 – measuring device system,
- XrZr – flat bar rotation system,
- X'Z' – flat bar arrangement.

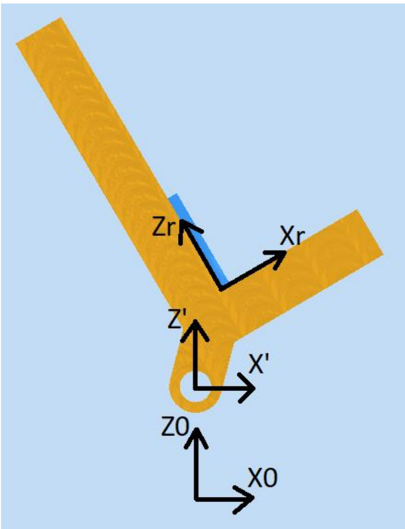

Figure 4. Designated coordinate frames during measurement.

The rotation system of XrZr is shifted relative to the measurement system, which should be taken into account first using the translation matrix (1). The next step is to take into account the rotation of the measurement system. In this way, equation (2) will be created, from which it is possible to determine equations (3) and (4) that determine the actual position of the tested corner point in the XZ plane. [4]

$$\begin{bmatrix} \cos\beta & 0 & -\sin\beta & 0 \\ 0 & 1 & 0 & 0 \\ \sin\beta & 0 & \cos\beta & 0 \\ 0 & 0 & 0 & 1 \end{bmatrix} \times \begin{bmatrix} 1 & 0 & 0 & a \\ 0 & 1 & 0 & b \\ 0 & 0 & 1 & c \\ 0 & 0 & 0 & 1 \end{bmatrix} = \begin{bmatrix} \cos\beta & 0 & -\sin\beta & x \\ 0 & 1 & 0 & y \\ \sin\beta & 0 & \cos\beta & z \\ 0 & 0 & 0 & 1 \end{bmatrix}, \tag{1}$$

$$x = \cos\beta \cdot a + 0 \cdot b + (-\sin\beta) \cdot c = a \cdot \cos\beta - c \cdot \sin\beta, \tag{2}$$

$$y = 0 \cdot a + 1 \cdot b + 0 \cdot c = b, \tag{3}$$

$$z = \sin\beta \cdot a + 0 \cdot b + \cos\beta \cdot c = a \cdot \cos\beta + c \cdot \cos\beta, \tag{4}$$

3. Results

The measuring device allows to read the current values of points on the XZ plane. In the case of the tested flat bar, after taking into account equations (2) and (3), these points determine the position of the edges, while the Y axis is responsible for the absolute position of the measurement system. Figure 5 shows the measurement result in the XY plane after taking into account the orientation of the flat bar.

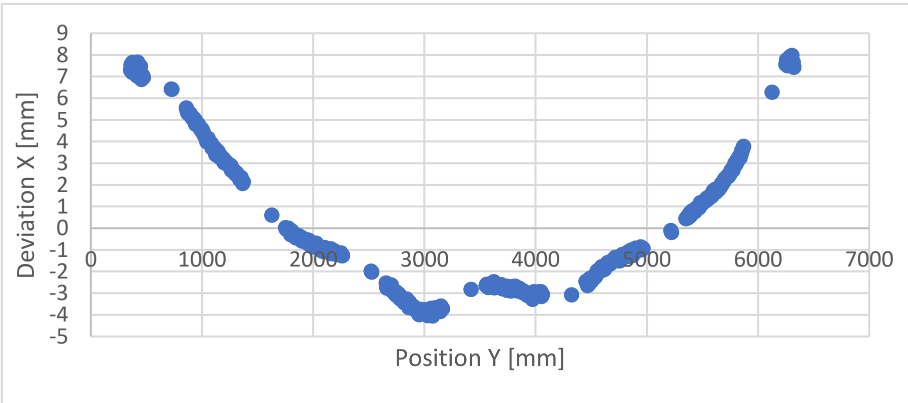

Figure 5. Obtained edge positions in the XY plane.

Analyzing Figure 5, you can notice visible breaks in the measurements. They result from the previously mentioned need to support the flat bar and from the transport chains covering the detail. Another aspect is the parabolic shape of the graph, which could indicate the lack of straightness of the element. If the measurement result refers to the absolute values of the entire flat bar, the deviation is less than 12 mm (-4.04 - 7.65 mm). A different approach should be taken when straightness is tested on a given section. For example, on the section 2600 - 3600 mm (Figure 5) the deviation was 1.4 mm, while for the section 400 - 1400 mm it was as much as 5 mm (2.05 - 7.22 mm). These values represent the corner positions in the XY plane. Straightness determines the way in which individual points are distributed on a given section.

To sum up, when verifying sectional straightness, another operation is necessary: for each measurement point (point A), another point is determined that is a set value away (point B), and the maximum deviation is determined by the distance of the points from the straight line connecting points A and B Using the diagram in Figure 6 for the example in Figure 5, point A will be 400mm (X = 2.05mm) and point B will be 1400mm (X = 7.22mm). The line connecting these two points corresponds to a deviation of 0mm. By performing one iteration of the algorithm from Figure 6 for the given values of A and B, we will obtain a maximum deviation of 0.88 mm at position 728 mm.

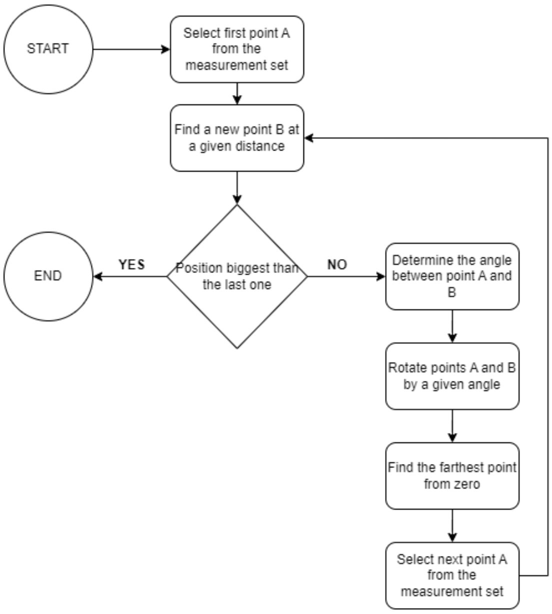

Figure 6. Diagram of the procedure for determining subsequent deviations.

The methodology presented in Figure 6 allows for determining the maximum deviation for subsequent points. The effect of such an algorithm is presented in Figure 6, which shows the actual deviation in relation to the obtained measurement. As you can see, the deviation for the value of 728 mm was ultimately 1.01 mm, because this point was further away for the section 371 - 1370 mm.

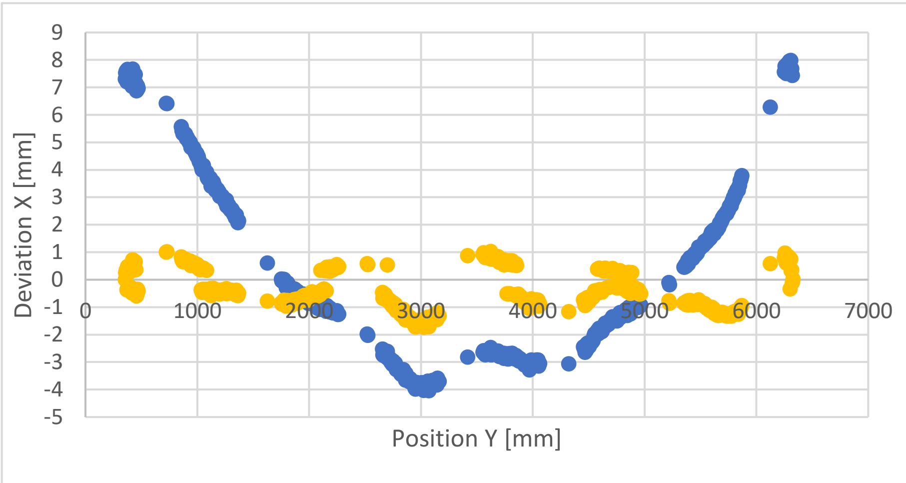

Figure 7. Obtained edge positions in the XY plane taking into account the actual deviation.

In order to achieve full automation of the measurement, it is necessary to draw a tolerance line of ±1 mm/1 m (for a tolerance of ±2 mm/1 m, the detail would obtain the OK status, even though initially, due to its shape, it showed a horizontal deviation of ±8 mm). A similar procedure was performed for the YZ plane, as shown in Figure 8.

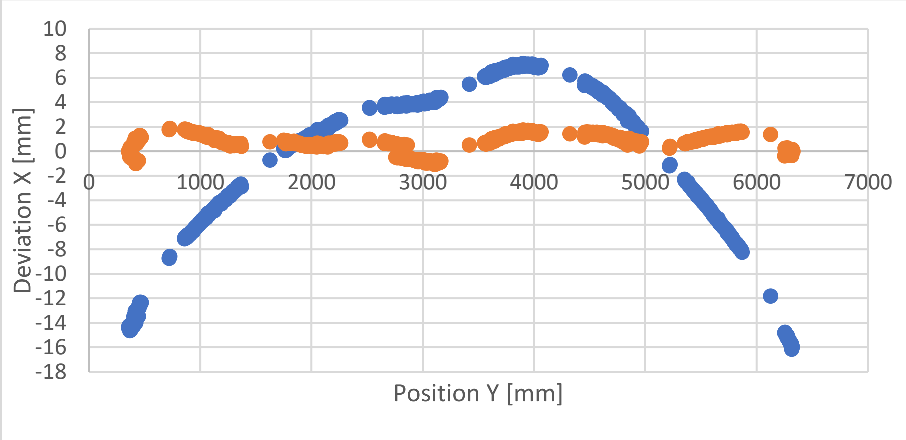

Figure 8. Obtained corner position in the YZ plane taking into account the actual deviation

The largest deviation for the presented flat bar was:

- -1.73mm for position 3028mm relative to points 2520-2620mm on the XY plane,
- 1.87mm for position 728mm relative to points 376-1376mm on the YZ plane.

4. Discussion

In order to verify the repeatability of the measurement, tests were carried out, during which it was found that the maximum measurement error was less than 0.1 mm, which is an order of magnitude smaller than the assumed measurement tolerance. For this reason, this system can be used in an industrial solution ensuring the correctness of the measurement. The use of a laser profilometer presented in the article confirms that with appropriate implementation of the sensor and data processing, using elementary operations on numbers and matrices, an advanced measuring device can be implemented into the production process. The use of machine positioners, which set the profiles at a given angle before the measurement, and the rotation matrix made it possible to perform a measurement reflecting the actual condition. The ability to control the straightness of profiles during series production allows for real-time supervision of the process. It minimizes losses by detecting a deviation in the straightness dimension that exceeds the permissible tolerance, and thus reduces the risk of sending goods to the customer that do not meet the requirements. Automation of the process of feeding flat bars for straightening, measurement and storage allowed a reduction in the number of employees. This would not be possible without a measuring device that would direct the flat bar to the appropriate OK/NOK warehouse. Integrating the measuring system with the machine also makes it possible to archive the measurement results obtained for a given batch of elements. In line with continuous improvement, a potential next modification may be, for example, equipping the station with a detail marking system that will enable the implementation of the Traceability system, i.e. tracking the product and its parameters throughout the process.

Conflicts of Interest: The authors declare no conflict of interest.

References

1. Liker Jeffrey K. The Toyota Way: 14 Management Principles from the World's Greatest Manufacturer; MT Biznes; 2022.
2. Setsuo Mito, Taiichi Ohno. Just-In-Time for Today and Tomorrow; Productivity Pr; First English Edition, 1988.
3. Device datasheet, Wenglor. Available online: https://www.wenglor.com/en/Machine-Vision/2D3D-Sensors/MLSL/2D3D-Profile-Sensor/p/MLSL123 (05.12.2023 r.)
4. Politechnika Wrocławska, Katedra Cybenetyki i Robotyki. Available online: https://kcir.pwr.edu.pl/~jjakubia/PodstawyRobotyki/wyklad2.pdf (05.12.2023 r.)

Optimization of the production process by applying simulation technologies

Matúš Matiscsák [1,*], Michal Baluch [2], Richard Duda [3] and Peter Trebuňa [4]

[1] Department of Industrial and Digital Engineering, Technical University of Košice, Park Komenského 9, 04001 Košice; matus.matiscsak@tuke.sk
[2] Department of Technology and Quality of Animal Products, Slovak University of Agriculture in Nitra, Trieda Andreja Hlinku 2, 949 01 Nitra: baluch@taurisgroup.sk
[3] Department of Industrial and Digital Engineering, Technical University of Košice, Park Komenského 9, 04001 Košice; richard.duda@student.tuke.sk
[4] Department of Industrial and Digital Engineering, Technical University of Košice, Park Komenského 9, 04001 Košice; peter.trebuna@tuke.sk
* Correspondence: matus.matiscsak@tuke.sk; Tel.: +421 55 602 3243

Abstract: The main goal of this work is to optimize the production process on a specific line in an unnamed company. Through a thorough analysis of the production process and the data provided by the company, we were able to simulate the current production process. The simulation using the TX Plant Simulation software showed us the shortcomings in our analyzed production process. Based on these results, we were able to optimize its outputs and propose improvements to increase production, which we applied to our simulation. The results showed us that from the original production, which was around 3300 pieces per shift, we reached a range of 3950 to 4000 pieces per shift.

Keywords: Production optimization, Simulation, Tecnomatix Plant Simulation

1. Introduction

In the 21st century, simulation programs dominate most of the world's leading companies and enterprises as a key manufacturing design tool. These sophisticated simulation tools enable detailed monitoring of the entire production process with high accuracy and flexibility, as the simulation can be easily started and stopped as needed [1]. Thorough analysis within the simulation environment is suitable for identifying bottlenecks, errors and potential deficiencies that may affect real production.

A production process is defined by a set of inputs, outputs, resources and a time frame. Inputs change into outputs during individual activities [2]. Inputs to the production process include materials, raw materials, energy, equipment, tools, and labor [3]. The output of the process is the final product intended for the consumer [4]. Production processes are the main source of profit for companies and represent a great potential for optimization. Companies often try to rationalize their processes, but after a certain time they may reach a limit where further optimization may threaten the continuity of production and product supply if they do not have sufficient know-how to make decisions in this area [5, 6].

Currently, digitization is necessary to achieve high efficiency in the production process [7]. Connecting and improving individual areas of the production process using digitization can significantly increase efficiency and speed up processes. The integration of simulation into process analysis is one of the most effective solutions that offers flexibility, versatility and a number of other advantages [8]. Simulation programs enable the optimization of all processes even before the start of production, minimizing downtime and ensuring maximum efficiency [9]. The TX Plant Simulation software has great potential, which is reflected in its dynamics and hierarchical structure. It allows working with existing models, modifying them and creating new simulation models of material flows that can reflect different logistics and production systems [10].

2. Research Methodology

In this paper, we performed a thorough analysis of the production operations on a specific line in an unnamed company, which allowed us to determine the key factors affecting the current production processes. Our primary goal was to use simulation techniques to model the production process of a particular assembly line to optimize its outputs and propose improvements to increase productivity.

Currently, the average production on the production line is around 3300 pieces per shift. However, the company faces higher demand than its current production capacity can meet, necessitating the development of optimal solutions to ramp up production to 4,000 pieces or more per shift. To achieve this, we employed Tecnomatix Plant Simulation software to conduct comprehensive simulations.

Our methodology involved providing a succinct overview of the current production process on the designated assembly line and subsequently crafting a simulation using TX Plant Simulation software. By simulating the current production process, we were able to analyze the outcomes and devise an optimized solution geared towards enhancing production capacity [11].

3. Current State of the Production Line

Currently, this line can be defined as a semi-automatic production line, which consists of four workstations. The first workstation is manual, where an operator works, while the remaining workstations are automatic, where production is carried out with the assistance of robotic hands and sensors. Production takes place on a conveyor belt, which moves a certain number of pallets with three nests. Components are placed into these nests, and they are then adjusted at various stations according to the type of operations performed at those stations. This production line (see Figure 1.) serves as the pre-production segment of the main line to produce the primary product.

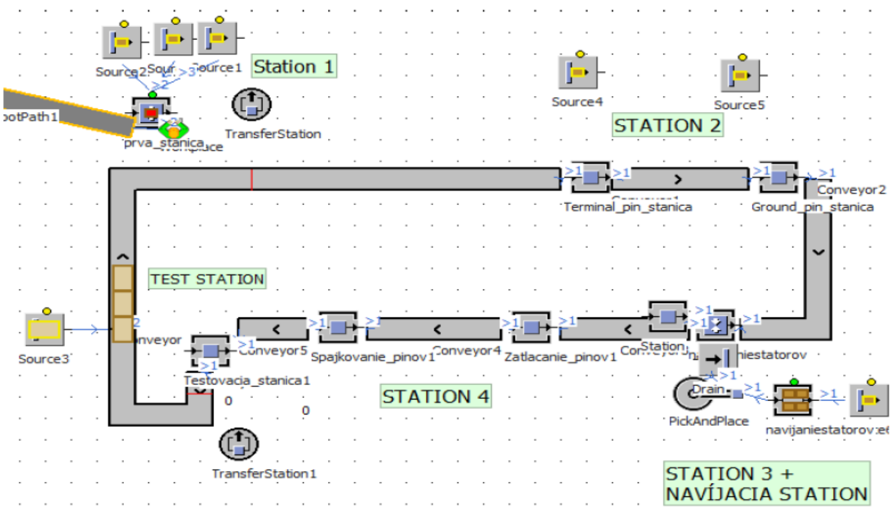

Figure 1. 2D representation of the production line

The product manufactured on this line can be classified as a pre-production component, which we can refer to as a stator. This stator consists of six components that are inserted during its production. The production line operates in two shifts, and the total cycle time at the output of the line is 11 seconds.

4. Optimization of the Production Line

After evaluating the current production process, we have concluded that it is necessary to implement changes at both the first and last stations on the designated line. Firstly, we propose the addition of a small x-ray camera to the tester's station for visual inspection. In addition to the standard electrical and mechanical testing, the Keyence camera will enable us to detect any visual defects or damages in the finished product. While this addition will not directly speed up the cycle time at the last station, it will eliminate the time required for manual inspection by the operator during removal. Each visual inspection by the operator typically lasts about 2-3 seconds. Consequently, implementing this camera will streamline the process by automatically directing defect-free pieces to the finished production box and segregating flawed pieces into a scrap box. Pieces in the scrap box will undergo further inspection by the quality department, which will decide whether to proceed with disassembly or designate them as finished pieces.

Secondly, we propose implementing a KUKA robotic arm to handle the placement of individual components onto the pallets and directly into the nests, a task previously performed by the operator. The robotic arm will be positioned flush with the conveyor belt (see Figure 2.) to minimize downtime between component movements and nest placements, thereby optimizing efficiency.

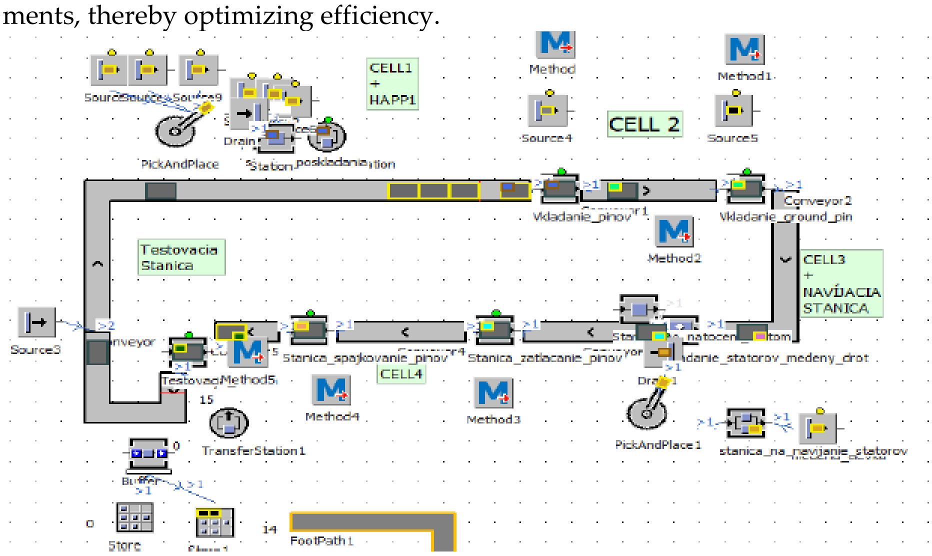

Figure 2. 2D view of the production line after the implementation of the optimization

This implementation will transition the line from semi-automatic to fully automatic, ensuring continuous production over the entirety of a 12-hour shift. Moreover, this change will reduce the cycle time at the first station by approximately 3 to 3.5 seconds, resulting in a higher overall output during a 12-hour shift. Control over the line will be maintained by shift technicians and a designated process engineer, with each station connected to a monitoring system that tracks production, generates reports, and alerts to any unexpected stops or malfunctions.

5. Results

Output from the production process before optimization are presented in the Table 1. below.

Table 1. The result of production during four work shifts at the current state

At the current state	Shift A OK / NOK (pcs)	Shift B OK / NOK (pcs)	Shift C OK / NOK (pcs)	Shift D OK / NOK (pcs)
Per hour / average	306 / 8	294 / 8	285 / 7	294 / 8

Per shift	3367 / 86	3231 / 83	3140 / 81	3232 / 83
Per day	6598 / 169		6372 / 164	
Per 2 days	12 970 / 333			

After incorporating the improvement suggestions into the simulation, we observed notable changes in the production process on the production line. By introducing a robotic arm at the first station, we made slight adjustments to the production time at that station, effectively converting the semi-automatic line into a fully automatic one.

Consequently, we eliminated the necessary break for the operator at the first station, extending the working time in this variant from a net 11 hours to 12 hours. This adjustment resulted in an additional hour of net working time per shift, which subsequently translated into an increased output of finished products. The production times at other stations remained largely unchanged. The Table 2. below depict the values obtained after simulating four work shifts spanning two days.

Table 2. The result of production during four work shifts after the implementation of the optimization

At the current state	Shift A OK / NOK (pcs)	Shift B OK / NOK (pcs)	Shift C OK / NOK (pcs)	Shift D OK / NOK (pcs)
Per hour / average	326 / 8	330 / 9	323 / 6	330 / 6
Per shift	3914 / 100	3960 / 102	3878 / 67	3959 / 69
Per day	7874 / 202		7837 / 136	
Per 2 days	15 711 / 338			

From the analysis of the tables, after the implementation of the optimizations, there was a significant increase in production by more than 600 pieces after each change. This means that in one working day there is an increase in production by more than 1200 pieces. If the operation takes place in four work shifts, the total increase in production reaches exactly 2741 pieces.

However, it is important to emphasize that despite this significant increase in production, the share of unsuccessful or failed pieces almost did not change and remains at approximately the same level.

6. Conclusions

When optimizing the production process, a comprehensive consideration of all influencing factors is paramount [12]. A thorough analysis of bottlenecks is essential, delving into their root causes and strategizing their elimination while anticipating the potential emergence of new bottlenecks [13]. For this reason, it is important to pay attention to details to avoid failure.

Our work shows that by optimizing the production process on a particular line, the line will go from semi-automatic to fully automatic, thereby ensuring continuous production throughout the entire 12-hour shift. In addition, this change will reduce cycle time at the first station by approximately 3 to 3.5 seconds, resulting in higher overall performance over a 12-hour shift.

From the results of current and optimized production, we see that production increased by more than 600 pieces during one shift. It follows that in one working day the production will increase by more than 1200 pieces. In two days, which represents operation for four work shifts, the total increase in production is exactly 2741 pieces. It is important to note that despite the significant increase in production, the proportion defective pieces have hardly changed and remains approximately at the same level.

By using simulations, we avoid unnecessary investments that could be inefficient and costly. We also managed to avoid the unnecessary shutdown of the production process and thereby prevent the financial losses that would have arisen.

Acknowledgments: This article was created by the implementation of the grant project APVV-17-0258 Digital engineering elements application in innovation and optimization of production flows, APVV-19-0418 Intelligent solutions to enhance business innovation capability in the process of transforming them into smart businesses, KEGA 020TUKE-4/2023 Systematic development of the competence profile of students of industrial and digital engineering in the process of higher education and VEGA 1/0508/22 Innovative and digital technologies in manufacturing and logistics processes and system.

Conflicts of Interest: The authors declare no conflict of interest.

References

1. Pekarčíková, M., Trebuňa, P., Dic, M., Král, Š.: Modelling and simulation in the Tecn-omatix Plant Simulation environment, Acta Simulatio, Vol. 7, No. 1, pp. 1-5, (2021). DOI: 10.22306/asim.v7i1.59
2. Rosova, A.; Behun, M.; Khouri, S.; Cehlar, M.; Ferencz, V.; Sofranko, M. Case study: The simulation modeling to improve the efficiency and performance of production process. Wirel. Netw. 28, 863–872. (2020). DOI: 10.1007/s11276-020-02341-z
3. Buckova, M., Krajcovic, M., Edl, M.: Computer simulation and optimisation of transport distances of order picking processes: 12th International Scientific Conference Of Young Scientists On Sustainable, Modern And Safe Transport, Procedia Engineering, Vol. 192, pp. 69-74, (2017). DOI: 10.1016/j.proeng.2017.06.012
4. Kiyko, S., Druzhinin, E., Prokhorov, O., Ivanov, V., Haidabrus, B., Grabis, J.: Logistics control of the resources flow in energy-saving projects: case study for metallurgical in-dustry. Acta Logistica 7(1), 49–60 (2020). DOI: 10.22306/al.v7i1.159
5. Drastich, A., Optimization of material flow by simulation methods, Acta Logistica, Vol. 4, No. 4, 23-26 (2017). DOI: 10.22306/al.v4i4.76
6. Aloini, D.; Dulmin, R.; Mininno, V. Modelling and assessing ERP project risks: A Petri Net approach, European Journal of Operational Research, Vol. 220, No. 2, 484-495 (2012). DOI: 10.1016/j.ejor.2012.01.062
7. Grznár, P., Gregor, M., Gola, A., Nielsen, I., Mozol, S., Seliga, V., QUICK WORKPLACE ANALYSIS USING SIMULATION. International Journal of Simulation Modelling 21(3), 465-476 (2022). DOI: 10.2507/IJSIMM21-3-612
8. Rosova, A., Behun, M., Khouri, S., Cehlar, M., Ferencz, V., Sofranko, M.: Case study: the simulation modeling to improve the efficiency and performance of production pro-cess. Wirel. Netw. 28, 863–872 (2020). DOI: 10.1007/s11276-020-02341-z
9. Straka, M., Khouri, S., et al.: Utilization of computer simulation for waste separation design as a logistics system. Int. J. Simul. Model. 17(4), 83–596 (2018). DOI: https:10.2507/IJSIMM17(4)444
10. Trebuňa, P., Pekarčíková, M., Edl, M.: Digital value stream mapping using the tecno-matix plant simulation software. Int. J. Simul. Model. 18(1), 19–32 (2019). DOI: 10.2507/IJSIMM18(1)455
11. Rosova, A., Behun, M., Khouri, S., Cehlar, M., Ferencz, V., Sofranko, M.: Case study: the simulation modeling to improve the efficiency and performance of production pro-cess. Wirel. Netw. 28, 863–872 (2020). DOI: 10.1007/s11276-020-02341-z
12. Fedorko, G., Vasil, M., Bartosova, M. Use of simulation model for measurement of MilkRun system performance, Open Engineering, vol. 9, no. 1, pp. 600-605 (2019). DOI: 10.1515/eng-2019-0067
13. Lai X, Shui H, Ding D, Ni J. Data-driven dynamic bottleneck detection in complex manufacturing systems. J Manuf Syst :662–75 (2021). DOI: 10.1016/j.jmsy.2021.07.016.

TECHNICKÁ UNIVERZITA V KOŠICIACH
Strojnícka fakulta

Use of motion capture system for reactive robotic manipulations

Tomas Merva[1,*] and Ivan Virgala[1]

[1] Department of Industrial Automation and Mechatronics, Technical University of Kosice
* Correspondence: tomas.merva@tuke.com

Abstract: To bridge the gap between a predictable factory environment and a human-inhabited world, robots need to use reactive motion control methods that would enable autonomous behaviour. The crucial part of the reactive control pipeline is the vision system that captures the sudden changes in the environment. One approach consists of using the motion capture system that provides the exact pose of objects and allows one to completely focus on the development of the motion control part of the original problem. This paper provides a brief guide on how to use such a system with the combination of motion control of a robotic manipulator.

Keywords: motion planning, motion capture, robotics

1. Introduction

The robotic applications within factories consist of very predictable, simple, and repetitive tasks. The control pipeline is applied in an open-loop way, in which there is no feedback from the inferior motion planner to the superior task planner. Another popular approach is to integrate the task and motion planners in order to effectively find a solution for long-horizon sequential tasks [1]. The major drawback of these methods is the high computational time, which makes the replanning not applicable [2],[3]. The replanning is especially required in stochastic, dynamical environments, in which random perturbations can occur. We can distinguish two types of reactiveness in terms of sequential tasks: 1. Reactivity with respect to task planning, 2. Reactivity with respect to motion planning. The reactive task planning methods can quickly adapt to changes on the high action level, whereas they consider the low level as block-box controllers. The reactive motion planning, or motion generators, deals with perturbations with respect to trajectories, such as dynamical obstacles and grasping failures. For the development of these reactive methods, the sudden changes of the environment need to be precisely and quickly detected so a control algorithm can immediately adapt to them. For these reasons, the most used solution is to use an external motion-capture system, such as Vicon [4] or OptiTrack [5].

This paper is organized as follows. In the first part, the general principles and classification of motion capture systems are introduced. The second part is focused on the experimental analysis of the integration of OptiTrack and ROS for the reactive manipulation domain. The contribution of this paper is twofold:

1. General introduction to motion capture systems
2. Integration of the motion capture system with a manipulator

2. Motion Capture System

For indoor motion capturing, optoelectronic measurement systems are considered state-of-the-art systems because of their accuracy and frequency of providing data. The core principle is that a fixed camera detects light to determine the position of a marker in a restricted area. By utilizing more cameras, the position estimation has higher accuracy. Moreover, combining a minimum of three markers provides a pose estimation of a rigid body as well. The main disadvantage of this system is that cameras are fixed, which results in a restricted area. The second limitation is that the received position data are interrupted if the line-of-sight for a given marker is blocked by some obstacle. Both of these limitations can be solved by utilizing more cameras. In practice, it is also recommended to use multiple markers for a rigid body to minimize the risk of losing line-of-sight for the entire rigid body. There are two types of markers: passive and active. Passive markers are made from a reflective material, so they can reflect the light coming from the camera. Active markers are markers capable of producing a light that a camera can capture. Using active markers results in more robust measurements, however, they do require additional electronics, such as batteries. [6]

3. Experiments

For our experiments, we are using three OptiTrack Prime^{x} 13 cameras with a 240 frame rate per second, which results in receiving poses of markers every 4 ms. The accuracy of the cameras was 0.24 mm after the calibration. To avoid using additional cables and electronics, we have decided to use simple passive markers, which have the shape of a sphere with a radius of 9.5 mm. The markers are attached to the end-effector of the robot and the objects within the environment.

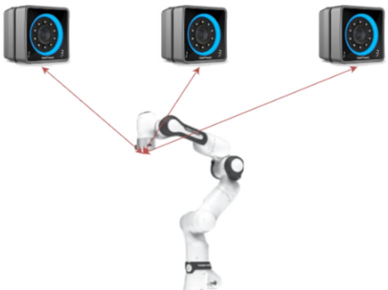

Figure 1. Scheme of the experiment setting using OptiTrack cameras

The OptiTrack cameras are connected to the computer, which has installed the "*Motive*" software that receives all data streams from the cameras. Thereafter, the software determines the poses of all selected markers and rigid bodies within the restricted area. One part of the software is a "*NatNet*" server that provides the poses to the different computers across the network. The other computer, which runs the ROS framework, is connected to the "*NatNet*" server and receives the poses in the form of topics. Each rigid body has a dedicated topic, which a subscriber can listen to. The frequency of incoming messages depends on the predefined frame rate of cameras. The same computer that runs ROS is used to control the seven-degree-of-freedom Franka Emika manipulator. For the communication between the robot and the computer, the "*libfranka*" driver is used, which provides us with a 1000 Hz communication.

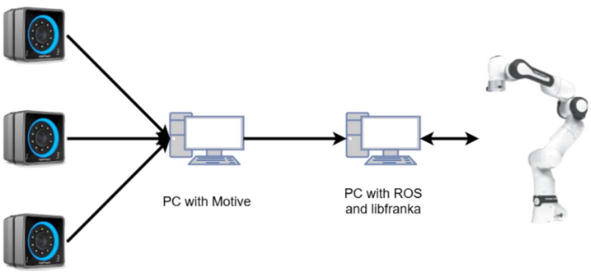

Figure 2: The compute graph that shows the flow of information

The goal of the experiments was to verify the suitability of using the motion capture system. We focused on two aspects: precision and data stream frequency. We attached the passive markers on the gripper of the robot and the base of the robot. The markers around the base served to calculate the transformation matrix between the gripper markers and the gripper itself. Thereafter, the transformation matrix was used to recalculate the coordination frames of other rigid bodies with respect to the gripper's frame. The transformed data stream from OptiTrack was compared with the joint positions of the robot and its end-effector position computed from forward kinematics.

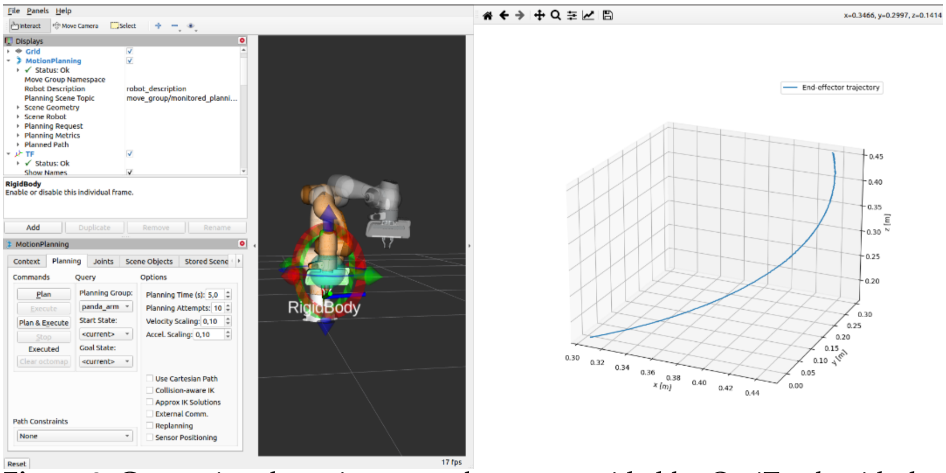

Figure 3: Comparing the trajectory and poses provided by OptiTrack with the kinematic model and joint positions.

4. Conclusions

The objective of this paper was to present a brief introduction to motion capture systems and to test the functionality of one with the intention of using it for the development of reactive motion planning methods. Since task and motion planning methods require high computational time, it is needed to develop methods that would be responsible for reactive behaviour that would execute the original plans. The aim of the first part is to inform a reader about the possibilities of motion capture systems. The second part is dedicated to the integration of the OptiTrack system with the ROS framework. The main goal was to evaluate the suitability of the OptiTrack system for future research within my PhD thesis. The achieved accuracy and the speed of the data stream from cameras is an excellent way to separate the perception part of the problem and purely focus on the reactive TAMP development.

Acknowledgements: The authors would like to thank to the Slovak Grant Agency VEGA 1/0201/21, VEGA 1/0436/22 and KEGA 030TUKE-4/2020. This research was also funded by Research grant for young researchers at TUKE Control of kinematically redundant robots for minimally invasive surgeries.

Conflicts of Interest: The authors declare no conflict of interest. The funders had no role in the design of the study; in the collection, analysis, or interpretation of data; in the writing of the manuscript; or in the decision to publish the results.

References

1. C. R. Garrett, R. Chitnis, R. Holladay, B. Kim, T. Silver, L. P. Kaelbling and T. Lozano-Pérez, "Integrated Task and Motion Planning," *Annual Review of Control, Robotics, and Autonomous Systems,* vol. 4, p. 265–293, 2021.
2. M. Toussaint, "Logic-geometric programming: an optimization-based approach to combined task and motion planning," in *Proceedings of the 24th International Conference on Artificial Intelligence*, Buenos, 2015.
1. C. R. Garrett, T. Lozano-Pérez and L. P. Kaelbling, "PDDLStream: Integrating Symbolic Planners and Blackbox Samplers via Optimistic Adaptive Planning," 2020.
2. Vicon. Available online: https://www.vicon.com/ (accessed on 4.12.2023)
3. OptiTrack. Available online: https://optitrack.com/ (accessed on 4.12.2023)
4. E. van der Kruk, M. M. Reijne, "Accuracy of human motion capture systems for sport applications; state-of-the-art review," *European Journal of Sport Science*, vol. 18, p. 806-819, 2018.
5. K. Hauser and J.-C. Latombe, "Multi-modal Motion Planning in Non-expansive Spaces," *The International Journal of Robotics Research*, vol. 29, p. 897–915, June 2010.
6. M. Toussaint and M. Lopes, "Multi-bound tree search for logic-geometric programming in cooperative manipulation domains," in *2017 IEEE International Conference on Robotics and Automation (ICRA)*, 2017.

Evaluation of Metal Hydride Alloy Activation in the MNTZV-60 Hydrogen Storage Tank

Ivan Mihálik [1,*], Marián Lázár [2]

[1] Technical University of Košice, Faculty of Mechanical Engineering, Department of Energy Engineering, Vysokoškolská 4, 042 00 Košice, Slovakia; ivan.mihalik@tuke.sk
[2] Technical University of Košice, Faculty of Mechanical Engineering, Department of Energy Engineering, Vysokoškolská 4, 042 00 Košice, Slovakia; marian.lazar@tuke.sk
* Correspondence: ivan.mihalik@tuke.sk

Abstract: The paper discusses the possibilities of hydrogen storage, while examining in more detail the possibilities of low-pressure hydrogen storage in metal hydride storage tanks. It also compares the suitability of various metal hydride alloys for mobile applications in terms of their operating temperatures and storage capacity. The article evaluates the experimental measurement of the storage capacity of the Hydralloy C5 alloy during the first three cycles of its activation in the MNTZV-60 storage tank. The thermodynamic parameters of the storage tank measured during activation are also analyzed.

Keywords: Hydrogen; Metal Hydride; Storage Tank; Temperature Management

1. Introduction

In terms of high specific energy per unit mass, hydrogen represents a promising alternative for conventional fuels used in mobile applications. However, one of the obstacles to the application of hydrogen on the market as a fuel for vehicles is its extremely low density. Due to the low density of hydrogen, it is especially problematic to store it in sufficient quantity. Increasing the volumetric energy density in hydrogen storage tanks is currently usually realized in two ways. The first is the compression of hydrogen at a pressure of 350 or 700 bar, the second is the liquefaction of hydrogen at cryogenic temperatures.

An alternative solution is materials-based hydrogen storage. This category includes, for example, adsorption storage of hydrogen on the surface of materials and the use of metal hydride alloys. Adsorption storage takes place through dispersion interactions, which are responsible for the physisorption of hydrogen gas molecules on the surface of a solid substance [1]. During adsorption or desorption from the material surface, dihydrogen, in contrast to other forms of material storage, maintains its molecular form with minimal activation energy all the time. In order to achieve the highest possible storage capacity, it is necessary to ensure the largest possible surface of the material. Due to the porous structure of these materials, the surface of some materials is higher than 5 000 $m^2 \cdot g^{-1}$ [2]. The disadvantage of this method is that due to the weak interaction, significant physisorption can only be achieved at temperatures below 0 °C [1].

The most technologically widespread group of materials for hydrogen storage are metal hydride alloys. Their use is possible, for example, in neutron moderation, thermal storage, purification and separation, heat pumps, compression and more [3-6]. Research into metal hydride alloys focuses mainly on improving storage capacities, hydrogen adsorption and desorption kinetics, cyclic stability and alloy thermodynamics.

2. Metal hydride alloys

Hydrogen storage in metal hydrides is based on the ability of hydrogen to form metal hydrides with metals and alloys. In terms of volumetric storage capacity, it is the most efficient form of hydrogen storage compared to high-pressure and cryogenic tanks, and also compared to adsorption storage of hydrogen on the surface of materials. The disadvantage of this type of storage is the overall higher weight of the system, which partially limits the use of this technology in some mobile applications.

For the application of metal hydride alloys in practice, their reversibility is essential. Reversible alloys include metal hydrides based on magnesium, sodium, lithium, beryllium, or intermetallic alloys, which are currently widespread.

Magnesium-based compounds offer, at a low price, high hydrogen storage percentage at the level of up to 7.66 wt.% while maintaining reversibility and relatively high cyclic stability. Their main disadvantage is the energy-intensive need for high temperatures to achieve desorption. Depending on the elements used in the alloy, these temperatures range from approximately 250 °C to 550 °C. Slow desorption is another disadvantage. These disadvantages can be partially alleviated by adding a suitable catalyst, e.g. palladium or titanium [7,8].

Complex hydrides contain elements such as Na, Li and Be. The biggest advantage of this type of alloy is the very high storage capacity, which in some alloys ($LiBH_4$) reaches a value of up to 18.5 wt.% [9,10]. However, complex hydrides suffer from slow kinetics and poor desorption thermodynamics. When using complex hydrides, reversibility itself and very low cyclic stability are also problematic.

A promising area in the research of suitable metal hydrides for mobile applications is research of intermetallic alloys. Intermetallic hydrides are usually formed by a combination of two members forming a stable and an unstable hydride. The advantages of these alloys are the acceptable operating temperatures and absorption kinetics, which are key to the potential use of the alloys in hydrogen vehicles. However, the limiting factor is still the high price of these alloys and the low energy density per unit weight of the metal compared to other types of metal hydrides, which has an adverse effect on the overall weight of the vehicle.

Recently widespread intermetallic alloys in the field of research are, for example, $LaNi_5$, TiFe or Hydralloy C5. Arslan et. al (2023) investigated hydrogen charge and discharge processes in a $LaNi_5$–H_2 reactor with and without phase change material [11]. Chandra et. al (2023) were dealing with hydrogen sorption characteristics of 5 kg-LaNi5 reactor featuring conical fins and heat transfer tubes [12]. Han et. al (2023) investigated effect of yttrium content on microstructure and hydrogen storage properties of TiFe-based alloy. The activation properties and hydrogen absorption/desorption kinetics were significantly improved by adding different amounts levels of rare earth elements Y to partially replace Ti in TiFe alloys [13]. Kölbig et. al (2021) dealt with the possibility of thermal applications, preheating and air-conditioning, in vehicles using Hydralloy C5 [14]. A two-stage metal hydride compressor for H_2 refueling station was developed by Barale et. al (2023). The compressor employs $La_{0.9}Ce_{0.1}Ni_5$ alloy in the first stage and the Hydralloy C5 in the second one [15].

3. Comparison of alloy storage capacity during the first three absorption cycles

To achieve the maximum storage capacity of a metal hydride alloy, its activation is necessary. The alloy manufacturer declares a grain size of up to 2 mm. During the activation of the alloy, consisting of repeated absorption and desorption of hydrogen, internal stress occurs in the alloy grains. As a result of this tension, the grains are broken into smaller pieces. This allows more hydrogen to be stored in the alloy.

Experimental measurement of the storage capacity of the Hydralloy C5 alloy during the first 3 activation cycles was carried out in the low-pressure hydrogen storage tank MNTZV-60. The measurement results are shown in the Figure 1.

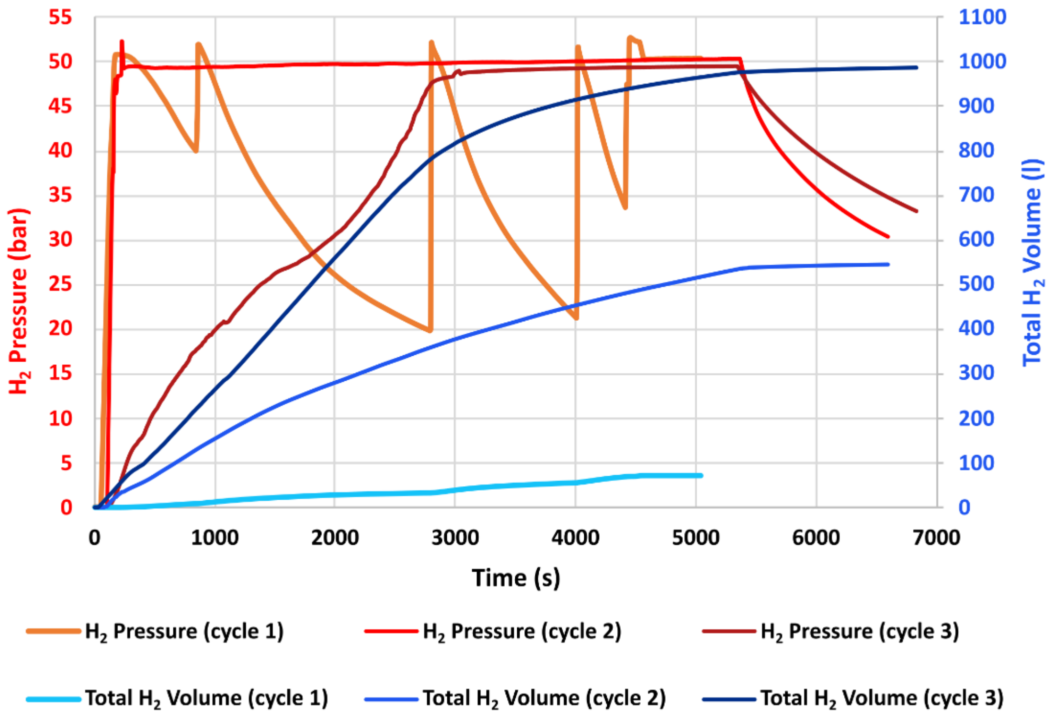

Figure 1. The process of hydrogen absorption during first three cycles.

During the first cycle, approximately 71.6 l of hydrogen was absorbed into the alloy within 84 min. Absorption occurs in the areas of the graph, where it is possible to observe the decrease in pressure after its initial increase. After the first 76 min, hydrogen absorption slowed down significantly, which is evident from the subsequent pressure stagnation.

During the second cycle lasting 110 min, 547.4 l of hydrogen was stored in the alloy. A pressure of around 50 bar was maintained for approximately 90 minutes, during which the hydrogen flow gradually decreased. After the subsequent closing of the valve, it is possible to observe a significantly slow absorption for the remaining 20 minutes at a gradually decreasing pressure, while it can be assumed that with increasing time only a negligible amount of hydrogen will be absorbed into the alloy.

The third absorption cycle lasted 114 minutes. The total amount of hydrogen stored in the alloy stabilized at 985.6 l. For the first approximately 45 minutes, a constant flow of hydrogen was maintained by continuously increasing the pressure in the system. In order not to exceed the limit of 50 bar, after reaching this pressure, the pressure was maintained at an approximately constant value for another 45 minutes. This resulted in a gradual decrease in flow rate and therefore a slowdown of absorption. After this time, the valve was closed, and with the subsequent drop in pressure it is possible to observe a very slow absorption of hydrogen, which remained in the free volume of the system.

The storage tank contained a total of 5.4 kg of alloy. Based on this known mass and hydrogen density of 0.089886 kg·m^{-3} under normal conditions [1], it is possible to determine wt.% of the storage capacity of the alloy during individual cycles according to the equation:

(1)

where V_{H2} is a volume of absorbed hydrogen; is a density of the hydrogen at normal conditions and m_{MH} is a mass of the metal hydride alloy.

The increase in storage capacity between individual cycles is shown in Figure 2.

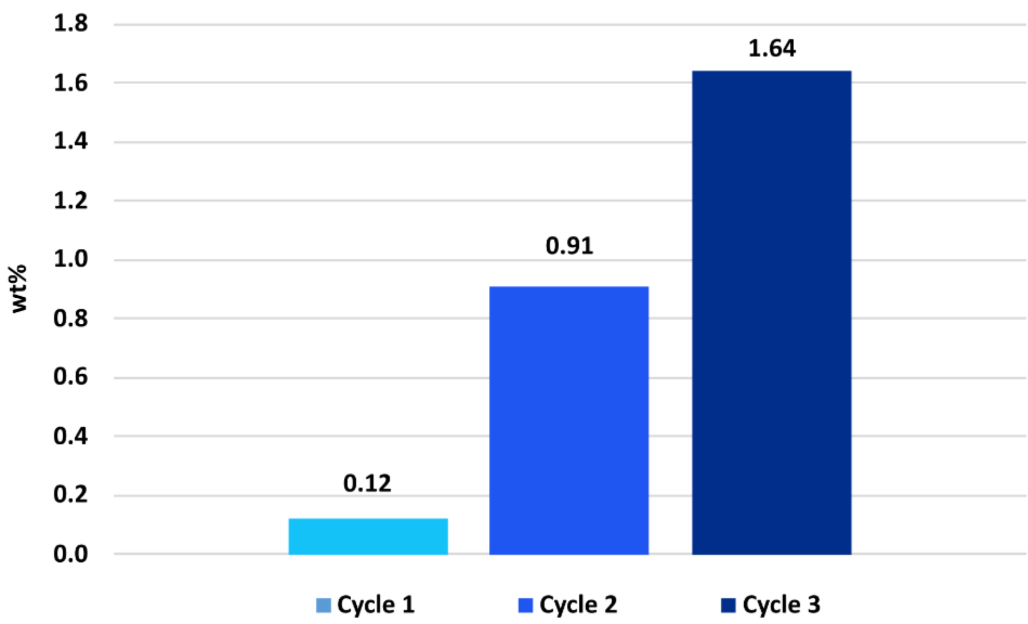

Figure 2. Storage capacity of metal hydride alloy after individual cycles of activation.

The achieved value of the storage capacity after the third absorption cycle is comparable to the capacity stated by the manufacturer of the alloy, so the alloy can be considered fully activated after three cycles of absorption/desorption.

4. Temperature curves measured during the last absorption cycle

Temperature measurement during activation was carried out by surface temperature sensors located on the shell of the tank with a measurement accuracy of 0.5 °C. In order not to influence the measured data by the surrounding environment, the container was covered with a layer of thermal insulation after applying the sensors. The location of individual sensors $t_2 - t_5$ is shown in Figure 3. The temperatures at the inlet were determined as the averages of temperatures t_4 and t_5, the temperatures at the bottom of the tank were determined as the averages of temperatures t_2 and t_3.

Figure 3. Position of individual temperature sensors on the tank.

Figure 4 shows the curves of the measured temperatures at the bottom and at the top of the tank. The data show that the metal hydride alloy heats up more slowly at the bottom of the tank during absorption. At the beginning of the measurement, hydrogen absorption occurs mainly in the area at the inlet to the tank. The temperature of the alloy is also affected by the cooling liquid entering the inter-shell space of the tank in the bottom area. A gradual convergence of the temperatures can be observed in the second half of the measurement, while the temperature at both ends of the tank stabilized at a temperature of approximately 33 °C after 114 min.

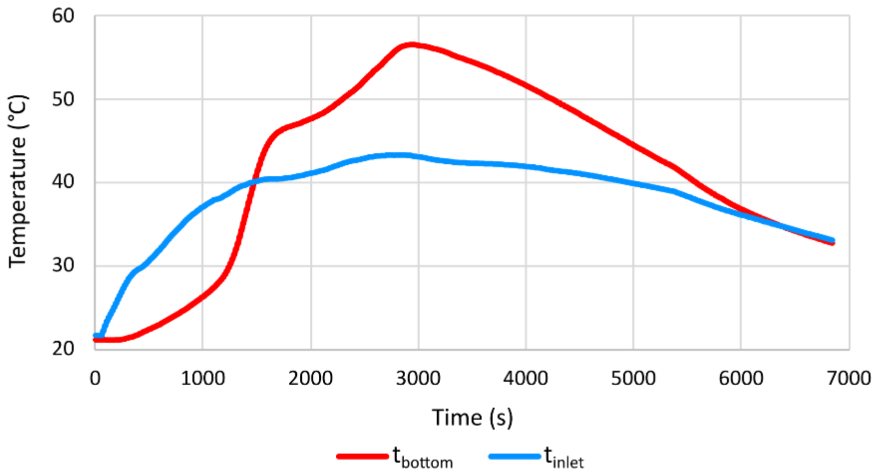

Figure 4. Temperatures at the inlet and bottom of the tank during the third cycle of absorption.

Figure 5 shows the data measured by individual sensors t_2 - t_5. The course of temperatures measured by sensors t_2 and t_3 in the area of the bottom of the container shows very low deviations. On the contrary, the temperatures measured by sensors t_4 and t_5 in the area of the inlet to the tank show significant deviations, especially in the first half of the measurement, while the sensor t_4 located in the upper part of the storage tank recorded lower temperatures during absorption compared to the sensor t_5 located in the lower part of the tank.

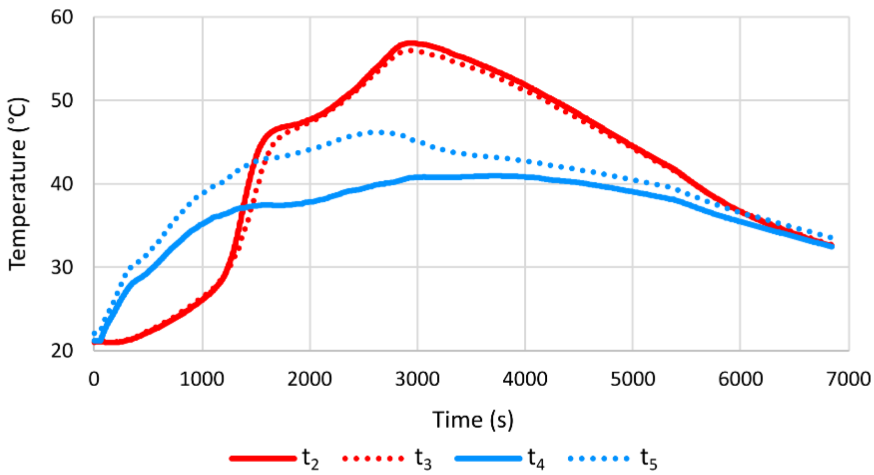

Figure 5. Temperatures measured by individual sensors during the third cycle of absorption.

5. Conclusions

Research into metal hydride alloys and the subsequent development of alloys with a higher storage capacity opens the possibilities of their wider application, for example in mobile applications. The measurement verified that the full storage capacity of the Hydralloy C5 alloy can be achieved after only 3 cycles of absorption. The increase in storage capacity between individual cycles is partly a consequence of the breakdown of the alloy grains under the influence of internal stress. Temperature deviations measured by individual sensors in the inlet area are probably caused by the imperfect technology of filling the tank with a metal hydride alloy before starting the measurement. The storage tank is filled in a vertical position, while the powdered alloy tends to settle in the area of the bottom of the tank due to gravity. After placing the tank in a horizontal position, uneven filling of the tank volume with powdered alloy may occur in the inlet area, while the upper part of the tank may remain partially unfilled. This subsequently affects the heat transfer to the shell of the tank and thus also to the surface sensor t_4, which heats up later than the sensor t_5 located in the lower part of the tank.

Acknowledgments: This paper was written with financial support from the VEGA granting agency within the projects no. 1/0224/23 and no. 1/0532/22, from the KEGA granting agency within the project no. 012TUKE-4/2022 and with financial support from the APVV granting agency within the projects no. APVV-15-0202, no. APVV-20-0205 and no. APVV-21-0274.

References

1. Züttel, A. Materials for hydrogen storage. *Materials Today*. 2003, *Volume 6, Issue 9,* pp. 24-33. DOI: https://doi.org/10.1016/S1369-7021(03)00922-2
2. Zeleňák, V. Uskladnenie vodíka v pórovitých nosičoch. [Online] *engineering.sk.* [2023-12-11] Available at: https://www.engineering.sk/clanky2/stroje-a-technologie/30764-uskladnenie-vodika-v-porovitych-nosicoch
3. Vetrano, J.B. Hydrides as neutron moderator and reflector materials. *Nuclear Engineering and Design*. 1971, *Volume 14, Issue 3*, pp. 390-412. DOI: https://doi.org/10.1016/0029-5493(70)90159-7
4. Felderhoff, M.; Bogdanovic, B. High Temperature Metal Hydrides as Heat Storage Materials for Solar and Related Applications. *International Journal of Molecular Sciences.* 2009, *Volume 10, Issue 1,* pp. 325-344. DOI: https://doi.org/10.3390/ijms10010325
5. Lázár, M. et al. New Design of a Separator Unit with Metal Hydride and an Analysis of Its Potential Application in the Process of Hydrogen Separation from a Binary Mixture of Gases. *Sustainability*. 2023, *Volume 15, Issue 15,* pp. 1-15. DOI: https://doi.org/10.3390/su151511516
6. Lototskyy, M.V. et al. Metal hydride hydrogen compressors: A review. *International Journal of Hydrogen Energy.* 2014, *Volume 39, Issue 11,* pp. 5818-5851. DOI: https://doi.org/10.1016/j.ijhydene.2014.01.158
7. Jasminská, N.; Brestovič, T.; Lázár, M. *Výroba a uskladnenie vodíka;* Publisher: Strojnícka fakulta TU v Košiciach, 2015; 136 p. ISBN: 978-80-553-2378-7
8. Eisapour, A.H. et al. An innovative multi-zone configuration to enhance the charging process of magnesium based metal hydride hydrogen storage tank. *Journal of Energy Storage.* 2021, *Volume 36,* 102443. DOI: https://doi.org/10.1016/j.est.2021.102443
9. Ding, Z. et al. $LiBH_4$ for hydrogen storage - New perspectives. *Nano Material Science*. 2020, *Volume 2, Issue 2,* pp. 109-119. DOI: https://doi.org/10.1016/j.nanoms.2019.09.003
10. Varin, R.A.; Wronski, Z.S. Chapter 13 - Progress in Hydrogen Storage in Complex Hydrides. In *Renewable Hydrogen Technologies;* Gandía, L.M., Arzamendi, G., Diéguez, P.M., Eds.; Publisher: Elsevier, 2013; pp. 293-332. DOI: https://doi.org/10.1016/B978-0-444-56352-1.00013-1
11. Arslan, B.; Ilbas, M.; Celik, S. Experimental analysis of hydrogen storage performance of a $LaNi_5$–H_2 reactor with phase change materials. *International Journal of Hydrogen Energy.* 2023, *Volume 48, Issue 15,* pp. 6010-6022. DOI: https://doi.org/10.1016/j.ijhydene.2022.11.083
12. Chandra, S. et al. Experimental hydrogen sorption study on a $LaNi_5$-based 5 kg reactor with novel conical fins and water tubes and its numerical scale-up through a modular approach. *International Journal of Hydrogen Energy.* 2023, *Volume 48, Issue 96,* pp. 37872-37885. DOI: https://doi.org/10.1016/j.ijhydene.2022.08.098
13. Han, Z. et al. Effect of yttrium content on microstructure and hydrogen storage properties of TiFe-based alloy. *International Journal of Hydrogen Energy.* 2023, *Volume 48, Issue 2,* pp. 676-695. DOI: https://doi.org/10.1016/j.ijhydene.2022.09.227
14. Kölbig, M.; Bürger, I.; Linder, M. Thermal applications in vehicles using Hydralloy C5 in single and coupled metal hydride systems. *Applied Energy*. 2021, *Volume 287,* 116534. DOI: https://doi.org/10.1016/j.apenergy.2021.116534
15. Barale, J. et al. A metal hydride compressor for a small scale H_2 refuelling station. *International Journal of Hydrogen Energy.* 2023, *Volume 48, Issue 87,* pp. 34105-34119. DOI: https://doi.org/10.1016/j.ijhydene.2023.05.155

Possibilities of modification of internal combustion engines for hydrogen fuels

Peter Milenovský[1], **Natália Jasminska** [2], **Lukáš Tóth** [3]

[1] Technical University of Košice, Faculty of Mechanical Engineering, Department of Energy Engineering, Vysokoškolská 4, 042 00 Košice, Slovakia; peter.milenovsky@tuke.sk
[2] Technical University of Košice, Faculty of Mechanical Engineering, Department of Energy Engineering, Vysokoškolská 4, 042 00 Košice, Slovakia; natalia.jasminska@tuke.sk
[3] Technical University of Košice, Faculty of Mechanical Engineering, Department of Energy Engineering, Vysokoškolská 4, 042 00 Košice, Slovakia; lukas.toth@tuke.sk
* Correspondence: peter.milenovsky@tuke.sk

Abstract: The article describes the issue of using hydrogen in conventional combustion engines, discusses the current state of hydrogen combustion units on the market of available cars. Subsequently, this article presents one of the options for theoretically solving the average consumption of hydrogen per 100 km, while relying on the average consumption of selected types of vehicles. At the end of the article, the minimum required volumes of hydrogen for a comfortable range of 600 km are described.

Keywords: hydrogen, internal combustion engine, hydrocarbon fuels, emissions

1. Introduction

The current situation in the world economy and the impact of global warming requires a more vigorous approach to the use of fossil fuels in transport.

Renewable energy sources contribute to the reduction of CO_2 production, but it is not possible to apply them within the entire spectrum of transport.

The use of batteries as well as hydrogen fuel cells in transport brings with it many technological challenges, the need to use precious metals, as well as the development of the necessary infrastructure. One of the possibilities of implementing more ecological transport systems is the use of direct hydrogen combustion in already existing technical equipment. Direct combustion of hydrogen brings with it many challenges, among which the need to store, transport and safely burn hydrogen is inherent. During the processes of direct combustion of hydrogen, technological problems occur due to excessive overheating of local parts of the engine, caused by self-ignition and irregular operation. These problems can be solved by mixing hydrogen with hydrocarbon fuels, where these fuels serve as a combustion moderator, thereby preventing undesirable phenomena.

2. The current state of development of hydrogen combustion engines

In 2003, the Mazda car company was the only one to introduce the Wankel hydrogen combustion engine. It is the only hydrogen combustion engine with a rotary motion of the piston. Mazda uses the Wankel engine in its series models, and therefore the simplest solution was to modify the existing engine for hydrogen fuel.

The engine is equipped with a dual-fuel hydrogen/gasoline switching system called Dual-Fuel, to which two hydrogen injectors were added directly to the combustion chambers. The biggest problem was the too big difference in performance when burning hydrogen and gasoline, but the big positive was running the car without emissions, because the waste is only water vapor. The Wankel engine modified for hydrogen combustion has an advantage over a conventional piston engine in that there is no back-ignition of hydrogen in the intake manifold, because the intake and combustion spaces are separated from each other by a rotating piston. When modifying a conventional engine into a hydrogen combustion engine, the position, number and size of the intake and exhaust holes had to be modified [1].

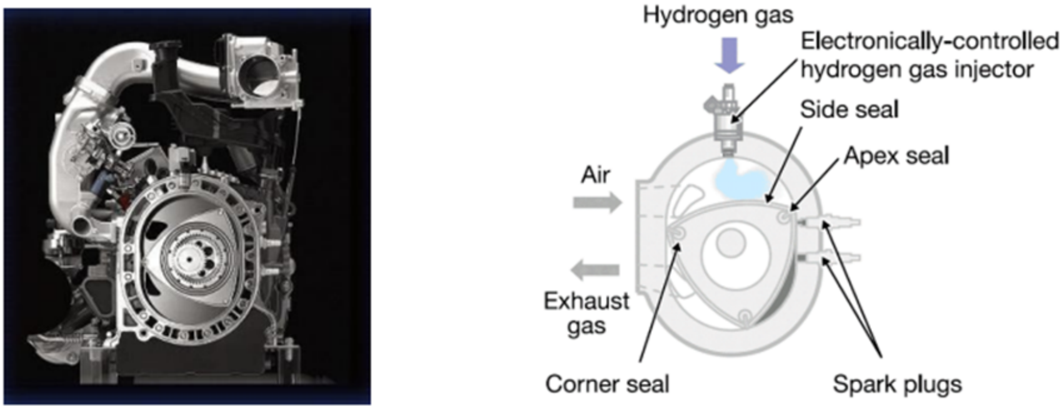

Figure 1 *Motor Mazda RX-8 Hydrogen RE*

BMW also deals with hydrogen combustion engines, which uses modified conventional gasoline engines for the BMW Hydrogen 7. Variable intake and adjustable camshaft timing for intake and exhaust on both sides of the engine make it possible to use valveless Valvetronic cylinder filling. When running on gasoline, gasoline is directly injected into the cylinders, while when running on hydrogen, the mixture is injected outside the cylinder [2].

Another company engaged in hydrogen combustion engine research is FORD, which has developed a prototype Ford F-250 Super Chief engine using the unique Tri-Flex technology, which allows drivers to use the fuel of their choice to power the vehicle. The automaker introduced a new supercharged V-10 engine with a tri-flex fuel system that allows a choice of three different fuels, including gasoline, ethanol E85 or hydrogen. In the tri-flex fuel system, it is possible to use one of the three fuels to drive the car, or even all three types at the same time using the same combustion engine [3].

Aston Martin, in collaboration with Alset Global, has developed a prototype six-litter twin-turbocharged V12 engine that has been implemented into the Hybrid Hydrogen race car, and can run on pure gasoline, pure hydrogen gas, or a mixture of both. Hybrid Hydrogen includes a hydrogen storage system, a hydrogen supply and injection system, a safety system and an engine control unit [4].

In addition to hydrogen-fuelled passenger cars on the market, the H2 Dual Power, the world's first hydrogen-powered tractor, has been developed and is powered by a combination of hydrogen and diesel. It is about mixing hydrogen into the already highly economical Stage V diesel engine. Hydrogen is directly mixed with diesel in the diesel engine. Mixing hydrogen into the diesel mixture significantly affects the reduction of the emission of harmful substances into the air. These engines can be operated exclusively on diesel fuel if hydrogen is not available, or the engine can be run on a mixture of hydrogen and diesel through a simple fuel mixing process. Adaptation of combustion engines for dual-fuel operation requires only minimal modifications. Hydrogen is injected into the hole and drawn into the cylinder during the intake stroke [5].

3. Theoretical proposal of the possibility of rebuilding an internal combustion engine based on the energy balance of fuels

To convert the engine to a hybrid hydrogen system, it is possible to choose from different types of drive units. Power units can be divided into two basic categories:

- spark ignition,
- diesel.

Each of these categories is further divided into subcategories, according to the number of cylinders, volume, compression ratio, etc. In the case of spark-ignition engines, the division by rectilinear movement of the piston and rotating piston is also applied. Currently, rotary piston engines are gaining in importance due to the separation of the combustion chamber by the rotating piston. For classic piston combustion engines, the combination of two different fuels, hydrogen and hydrocarbon fuel, is currently preferred, which reduces the risk of pre-ignition, detonation combustion and other undesirable side effects of direct combustion of pure hydrogen [6]. When hydrogen is combined with hydrocarbon fuel, it is mixed in a ratio of 20% to 90% hydrogen and fuel, while the amount of energy produced by burning the fuel combination must be approximately the same as the amount of energy produced by burning pure hydrocarbon fuel. To determine the amount of energy produced by burning hydrocarbon fuel in an atmosphere with an excess of oxygen, it is necessary to know the amount of fuel introduced into the combustion chamber in one cycle. In Table 1. the amounts of fuel injected into the working space of various types of combustion engines and the amount of heat produced by a range of 100 km are indicated.

Table 1 Fuel consumption for different types of drive units

Car brand	Type of fuel		Combustion heat of diesel MJ/100 km	Combustion heat of gasoline MJ/100 km
	Diesel	Gasoline		
Mercedes Benz	GLE 400d 7,2l/100KM	GLE 400 8,5l/100KM	277,92	290,7
Škoda	Kodiaq 2,0TDI 6,9l/100Km	Kodiaq 2,0TSI 8,5l/100KM	266,34	290,7
Hyundai	Tucson 2,0CRDi 7,77l/100KM	Tucson 1,6TGDi 8,97l/100KM	299,922	306,774
Volkswagen	Touareg 3,0TDI 8,1l/100KM	Touareg 3,0TSI 11,4l/100KM	312,66	389,88
BMW	X6 xDrive30d 6,1l/100KM	X6 xDrive50i 13,13l/100KM	235,46	449,046

The equation can be used to determine the amount of energy released by burning a given amount of fuel:

$$Q = q_s \cdot m \qquad \text{(MJ)} \tag{1}$$

where: q_s is the heat of combustion of the fuel ($MJ \cdot kg^{-1}$), m – the mass of fuel injected into the working space of the cylinder (kg).
In tab. 2 shows the heat of combustion of selected types of fuels, while the heat of combustion of hydrogen per kg is many times higher than the heat of combustion of commercially available hydrocarbon fuels. The main disadvantage of hydrogen is its lower volume density, when 1 m^3 of hydrogen gas under normal conditions accounts for only $3{,}7 \cdot 10^{-3}$ % of the heat of combustion of gasoline and $3{,}3 \cdot 10^{-3}$ % of the heat of combustion of diesel.

Table 2 Combustion heat of fuels

Fuel	Combustion heat $MJ \cdot kg^{-1}$	Combustion heat $MJ \cdot m^{-3}$
Gasoline	46.4	34200
Diesel	45.6	38600
Hydrogen	141.7	12.7

In the case of combining two different fuels based on hydrogen and hydrocarbon fuel, it is necessary to determine the amount of thermal energy released by burning the individual components to determine the total amount of released thermal energy. The equation can be used to calculate the total thermal energy released by burning a multi-component fuel mixture:

$$Q_{celkové} = \sum q_{s,i} \cdot \ m_i \qquad \text{(MJ)} \tag{2}$$

where: $q_{s,i}$ is the heat of combustion of the individual components ($MJ \cdot kg^{-1}$) , m_i – weight of individual components in the fuel (kg).
For the currently solved possibilities of direct use of hydrogen in combustion engines, pure hydrogen in combination with air or mixing hydrogen into a mixture of hydrocarbon fuel and air is being considered. Since the calorific value of hydrogen per unit volume is

significantly different from the calorific value of hydrocarbon fuels, it is necessary to approximately determine the consumption of hydrogen to achieve the same energy level.

4. Theoretical calculation of the necessary amount of hydrogen fuel to determine a comfortable range

The amount of energy obtained by burning a unit volume of fuel determines the power obtained from the drive unit. As the amount of fuel consumed increases, so does the amount of heat produce, and thus the power of the combustion unit. Hydrogen has a significantly lower energy density per unit volume compared to commonly available hydrocarbons.

To determine the consumption of hydrogen to overcome a distance of 100 km during standard driving, it is possible to start from the consumption of ordinary fuels. It is possible to assume that the amount of heat generated must remain approximately the same when using any type of fuel. This assumption also corresponds to the data from Tab. 1, where the amount of heat generated in both the diesel and gasoline versions of the given engine is approximately the same. The only significantly different data is the consumption in the case of the BMW X6, but in its case, the use of additional devices that increase consumption, such as high-performance air conditioning units, may play a role.

In the theoretical calculation of hydrogen consumption in the direct combustion process, hydrogen concentrations in the mixture with hydrocarbon fuel of 25%, 50%, 75% and 100% hydrogen were considered. The amount of heat generated had to be conserved. To determine the volumetric amount of hydrogen needed to supplement the energy level of the fuel mixture compared to pure hydrocarbon fuel, the modified relationship (2) was used:

$$V_{H2} = \frac{Q_{celkové} - q_x \cdot V_x}{q_{H2}} \qquad (3)$$

where: Q_{total} is the amount of heat generated by burning a given amount of pure hydrocarbon fuel (MJ), q_x – heat of combustion of hydrocarbon fuel ($MJ \cdot m^{-3}$), q_{H2} – heat of combustion of hydrogen ($MJ \cdot m^{-3}$), V_x – Volume of hydrocarbon fuel (m^3).

In Tab. 3 shows the requirements for the volume of hydrogen consumed to cover 100 km with different fuel ratios and types of fuel.

Tab. 3 The volume of hydrogen consumed to overcome a distance of 100 KM at different fuel ratios and fuel types

Ammount of H2 in mixture	Brand	Mercedes Benz		Škoda		Hyundai		Volkswagen		BMW	
	Engine	GLE 400d	GLE 400	Kodiaq 2,0TDI	Kodiaq 2,0TSI	Tucson 2,0CRDi	Tucson 1,6TGDi	Touareg 3,0TDI	Touareg 3,0TSI	X6 xDrive30d	X6 xDrive50i
25 %	Volume H2 m^3/100 km	5,471	5,722	5,243	5,722	5,904	6,039	6,155	7,675	4,635	8,839
50 %		10,942	11,445	10,486	11,445	11,808	12,078	12,309	15,350	9,270	17,679
75 %		16,413	17,167	15,729	17,167	17,712	18,117	18,464	23,024	13,905	26,518
100 %		21,883	22,890	20,972	22,890	23,616	24,155	24,619	30,699	18,540	35,358

Now, a distance exceeding 600 km is a comfortable range of a car for one filling of the tank. For this reason, the data in Tab. 3 adjust for the required minimum comfortable range. Considering the requirements of the volume of stored hydrogen, it is necessary to consider an additional high-pressure tank in the vehicle, which will occupy the storage space and increase its weight in the same way as, for example, in case of installation of CNG fuel tanks.

As can be seen in Tab. 3, with the increasing proportion of hydrogen in the mixture with hydrocarbons, the required storage space to ensure the supply of hydrogen during the entire period of operation of the drive unit also increases in direct proportion. The volumes of tanks required to store the required amount of hydrogen to cover a range of 600 km at different concentrations of hydrogen in the fuel mixture are shown in Tab. 4.

Tab. 4 Volumes of tanks needed to store the required amount of hydrogen

Pressure	Concentration of the mixture H	Mercedes Benz		Škoda		Hyundai		Volkswagen		BMW	
		GL	GL	Kodiaq	Kodiaq	Tucson	Tucson	Touare	Touareg	X6	X6
		E 400 d	E 400	2,0TDI	2,0TSI	2,0CRDi	1,6TGDi	g 3,0TDI	3,0TSI	xDrive30d	xDrive50i
Pressure 70 MPa	25 %	0,07	0,07	0,07	0,07	0,08	0,08	0,08	0,10	0,06	0,11
	50 %	0,14	0,15	0,14	0,15	0,15	0,16	0,16	0,20	0,12	0,23
	75 %	0,21	0,22	0,20	0,22	0,23	0,23	0,24	0,30	0,18	0,34
	100 %	0,28	0,30	0,27	0,30	0,31	0,31	0,32	0,40	0,24	0,46
Pressure 35 MPa	25 %	0,12	0,12	0,11	0,12	0,13	0,13	0,13	0,16	0,10	0,19
	50 %	0,23	0,24	0,22	0,24	0,25	0,26	0,26	0,33	0,20	0,38
	75 %	0,35	0,37	0,34	0,37	0,38	0,39	0,39	0,49	0,30	0,56
	100 %	0,47	0,49	0,45	0,49	0,50	0,51	0,52	0,65	0,39	0,75

5. Conclusion

The results of a theoretical analysis of the possibilities of applying hydrogen in direct combustion in the engine units of current cars show that the given technological solution could contribute to the reduction of $CO2$ emissions. However, the burning of hydrogen in heat engines requires a fundamental technological modification of existing vehicles due to the installation of dimensional high-pressure tanks and hydrogen management for rebuilding conventional combustion units. One of the current disadvantages also includes the insufficient infrastructure of networks of hydrogen filling stations.

One of the possibilities for the implementation of direct combustion in vehicles is research in the field of optimization of tank dimensions using progressive metal hydride alloys, or another option is to reduce the power of the power units, which would also reduce the required amount of fuel.

Acknowledgments: This paper was written with financial support from the VEGA granting agency within the projects no. 1/0224/23 and no. 1/0532/22, from the KEGA granting agency within the project no. 012TUKE-4/2022 and with financial support from the APVV granting agency within the projects no. APVV-15-0202, no. APVV-20-0205 and no. APVV-21-0274.

References

1. Wakayama, N., Morimoto, K., Kashiwagi, A., Saito, T.: Development of Hydrogen Rotary Engine Vehicle, WHEC, 2006.
2. Wallner, T.; Lohse-Busch, H.; Gurski, S.; Duoba, M.; Thiel, W.; Martin, D.; Korn, T. Fuel Economy and Emissions Evaluation of a BMW Hydrogen 7 Mono-Fuel Demonstration Vehicle. Int. J. Hydrogen Energy 2008, 33 (24), 7607e7618.
3. Hydrogencarsnow. [Online] Ford Super Chief Truck. 2016, [2023-12-12], Available at: https://www.hydrogencarsnow.com/index.php/ford-super-chief-truck/
4. Racecar ingeneering. [Online] Aston Martin Rapide S Hybrid. [2023-11-30], Avaiable at: https://www.racecar-engineering.com/articles/gt/aston-martin-rapide-s-hybrid/
5. Inhabitat. [Online] New Holland Unveils NH2 Hydrogen Fuel Cell Tractor for Greening Farm Work. 2011, [2023-12-9], Avaiable at: https://inhabitat.com/new-holland-unveils-nh2-hydrogen-fuel-cell-tractor-for-greening-farm-work
6. Gondžár, A. and Gondžár, K. (1990). Automobily a spotřeba paliva. Praha: Nadas.

Autonomous mobile robots and their navigation in an industrial environment

Ing. Dušan Mlinarček [1*], doc. Ing. Rudolf Jánoš, PhD.[1]

[1] Technical University of Kosice, Department of Production Technology and Robotics; Park Komenského 8, 04001 Košice
* Correspondence: dusan.mlinarcek@student.tuke.sk;

Abstract: Traversing unorganized surroundings is a fundamental skill possessed by intelligent beings, making it a topic of great importance in this study. Navigation is an intricate process that depends on creating a mental model of the surrounding environment, based on familiar landmarks and strong visual processing, which can simultaneously provide continual self-positioning and a representation of the destination. This can be accomplished using recent breakthroughs in Artificial Intelligence (AI) and its associated technologies. The proliferation of robots in the manufacturing sector has experienced a significant surge, and this trajectory is expected to persist in the coming years. This is due to the fact that autonomous robots possess the capacity to mechanize a diverse range of labor-intensive activities inside the factory setting, hence enhancing productivity. Several complex technical obstacles must be overcome in order to achieve a fully autonomous multifunctional robotic platform. The objective of this study is to tackle the main issue of guiding self-governing mobile robots in industrial settings. The autonomous robotic platform will drive throughout the factory along a predetermined course, automatically avoiding any obstructions encountered along its route from point A to point B. This research will utilize a JetAcker ROS Education Robot Car, which is equipped with several components such as RGB cameras, motor encoders, and an IMU, to perform robot localization. Additionally, we will use Simultaneous Localization and Mapping (SLAM) to determine the precise location of the robot and utilize a navigation algorithm to direct the robotic platform towards its intended destination.

Keywords: autonomous mobile robot; automated guided robotic system; navigation in industrial environment; vision-based navigation inside the building; SLAM navigation.

1. Introduction

To a significant extent, robotics has assisted humans in automating a variety of tasks that are performed in factories. A number of different industrial processes have been revolutionized by robots in order to mass create things many decades ago; yet these robots are scarcely more than adaptable machines that are operating a complicated but rigid program. The majority of the time, industrial robots do not demonstrate any kind of autonomous intelligence. Apart from fundamental control flow, they are mostly oblivious to their surroundings, and they make use of just a small amount of sensory information while they are operating. For this reason, a considerable deal of effort is made to ensure that the environment in which the robot operates is as predictable as is humanly feasible. For instance, barriers are used to prevent unpredictability from entering the robot's workplace. The lack of autonomy is one of the most significant challenges that must be conquered in order to make it possible for robots to become mobile in an environment that has been previously established. In many instances, robots are subject to human control in order to proceed from their origin to their destination. On the other hand, a number of research have been conducted on autonomous robots, which has contributed to the development of a wide variety of possible applications. The capabilities of autonomous navigation of robots on the factory floor will be bootstrapped. Navigation is a complex task that relies on developing an internal representation of space, which is grounded by recognizable landmarks and robust visual processing. This representation must be able to simultaneously support continuous self-localization and a representation of the destination. The novelty and advantage of this research lie in its investigation of autonomous mobile robots (AMR) and their navigation utilizing simultaneous localization and mapping (SLAM). The study utilizes many types of sensors to develop a comprehensive system suitable for industrial applications.

However, let us also examine the current state of mobile robots. The following are the applications of mobile robots, particularly in the field of services, known as Service robotics, which have either been widely implemented or are now in the prototype phase. Nevertheless, this analysis effectively demonstrates the widespread presence of mobile robots in several domains [1].

- Mobile robotics in agriculture
- Mobile robotics in mining
- Professional cleaning robots
- Robots for inspection and maintenance
- Construction and demolition robots
- Logistics robots
- Rescue and safety robots
- Information and guide robots
- Service applications in households
- Assistance and telepresence robots
- Other applications of service robots

2. Materials and Methods

The AMR will be able to generate a map of the occupied and unoccupied area, and using this map, it will be able to choose the route that would allow it to get from its present location to the destination. Nevertheless, in an industrial setting, there are areas that are not intended to be used by equipment, such as pathways for staff. These areas should be left free. The AMR should be able to determine the space that it can use and the space that it cannot use, and the AMR should be able to design its navigation path based on this knowledge in order to make it compatible with the industrial environment.

LIDAR sensors, time-of-flight (TOF) cameras, and stereo cameras are just few of the many kinds of sensors that may be used to perceive the world around them. These sensors project predefined patterns of light into the surroundings in order to estimate scene depth information. Although TOF cameras offer a faster frame rate and a greater sensing range, their resolution is not as good as other cameras. Although LIDAR sensors have a high level of precision and may be used in outdoor areas when exposed to direct sunshine, their accuracy decreases when exposed to precipitation such as rain or snow. A stereo camera is an alternate method that may be used to feel the environment that is around it. In order to rebuild a disparity map of the scene, it is necessary to use more than one photograph taken from a variety of perspectives. By using camera settings, it is possible to transform a disparity map into a point cloud information. Point cloud data that has been generated may be used for the purposes of route planning and obstacle avoidance [2].

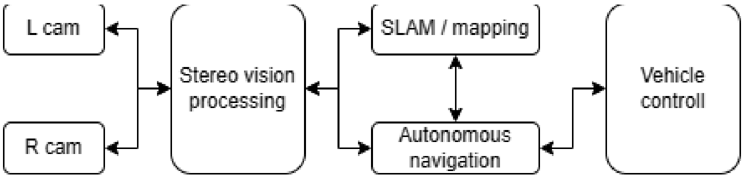

Figure 1. Block diagram of the system of autonomous mobile robot

2.1. Stereo vision for perception

The use of epipolar geometry allows for the creation of depth maps derived from stereo vision. As seen in figure 2, a fundamental configuration is shown below, in which two cameras (OL and OR) capture a picture of the same scene.

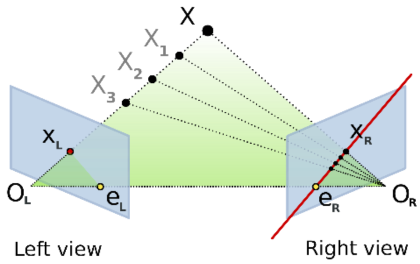

Figure 2. The depth of image using epipolar geometry

We are unable to locate the three-dimensional point that corresponds to the point X in the picture if we just utilize the left camera. This is due to the fact that every point on the line OLX projects to the same position on the image plane. When the picture from the right camera is taken into consideration, it is now possible to see those various places on the line OLX project to different positions in the right plane. We are able to triangulate the proper three-dimensional position by using photos from both the right and left cameras [3].

2.2. Simultaneous localization and mapping

SLAM is an abbreviation for simultaneous localization and mapping of the environment. This refers to the challenge of simultaneously localizing (that is, finding the location or orientation) with regard to its surroundings while concurrently mapping the structure of the environment. SLAM is a notion that brings about a solution to a very significant issue in the field of mobile robots. It is not necessary for SLAM to incorporate any visual information at all, and it is not always an issue that involves computer vision. Despite the fact that it is possible to do this task with just LIDAR and inertial measurement unit (IMU), we have focused on visual SLAM. The SLAM system is composed of two pieces:

- Mapping: The process of creating a map of the environment that the robot is currently in.
- Localization: The robot is able to navigate its surroundings by employing a map while simultaneously maintaining a record of its relative location and orientation [4].

2.3. Cell Decomposition

The fundamental concept underlying the Cell Decomposition (CD) approach is that a route connecting the starting and target places can be created by dividing the unoccupied area of the robot's arrangement into smaller, distinct sections known as cells. The cells can exhibit many shapes, including vertical strips, conventional rectangular grids, and irregular rectangular grids. In order to plan a path from the starting point to the desired destination, only unobstructed cells (cells without any obstacles or barriers) are taken into account during the traversal process. The initial and final cells represent the starting and target positions, respectively. The CD offers the benefit of guaranteeing collision avoidance between a robot with any specific shape and barriers of any shape, regardless of whether they are convex or not. There are two widely recognized forms of the CD approach: exact cell decomposition (ECD) and approximation cell decomposition (ACD), as depicted in Figure 3.

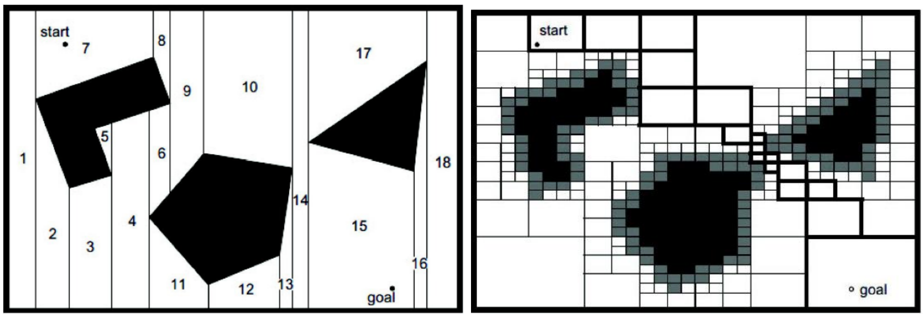

(a) (b)

Figure 3. (a) Exact cell decomposition, (b) Approximate cell decomposition [5].

The first step in the ECD method involves dividing the available space, which is restricted by polygonal obstacles both inside and outside, into trapezoidal and triangular cells. This is done by drawing parallel line segments from each vertex of each interior polygon in the configuration space to the outer boundary. Subsequently, every individual cell, symbolized as a node, is assigned a numerical value in the connectivity graph. Nodes that are neighboring in the configuration space are connected in the graph [6]. A continuous path can be found in this connection graph by sequentially traversing neighboring unoccupied cells from the starting point to the destination. However, this approach may lead to the creation of superfluous minor sub-regions. Proposed techniques for addressing this problem include trapezoidal and boustrophedon decomposition approaches. The Boustrophedon decomposition is an enhanced version of the trapezoidal decomposition that minimizes the overall number of regions by consolidating all the intermediate cells between two crucial points into a single cell. A revised Boustrophedon decomposition approach is suggested, which incorporates contour-following routes within cells and utilizes the corners of cells as starting and ending points for cell coverage.

2.4. Autonomous navigation

During navigation, the objective is to take the AMR from a certain place to a destination while avoiding any and all obstacles that may be in its way. A brief explanation of the most basic algorithm for autonomous navigation is provided below:

- Grid or mesh-based representations are used in the process of creating the map.
- Each cell in the grid represents space as either free (f), occupied (o), or unknown (u), depending on the situation.
- When it comes to navigation, AMR will be able to make advantage of all the free cells in the grid.
- Within the grid, AMR is required to be aware of its present location or cell.
- When the AMR is given a location to travel, it is required to utilize the algorithm for the shortest route.

A depiction of the information offered above may be seen in figure 4, where the location of the robot is denoted by the letter "R" and the destination is denoted by the letter "D." Considering that they are regarded to be static impediments, the enhanced objects are represented by the letter "o."

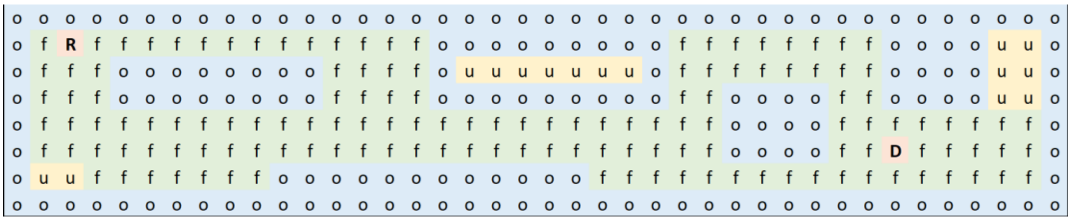

Figure 4. Map after approximate cell decomposition (ACD)

When a dynamic impediment is taken into consideration, the intricacy of this situation grows. In order to handle this situation, global planner that will take into account all of the static impediments, as well as a local planner that will steer clear of the dynamic obstacles and provide the drive train of the robot with information on its velocity. This will assist to have better coordination between AMRs and will have less of an influence on the intended course. In a smart factory, the global map may be shared with numerous AMRs on the factory floor so that they can update their current location and their trajectory to the destination.

The number of cells that are required to navigate the AMR will vary depending on the size of it. If the cells are large, then we need to have a propagation cost associated with each cell to represent the amount of free and occupied space that is associated with the cell. If we consider grid cells to be very small, then the occupancy grid map will generate a clear picture of free spaces [7].

For the purpose of generating AMR trajectory and odometry information, the navigation stack is responsible for receiving data from the IMU and motor encoders. It is necessary to have the sensor transform in order to comprehend the posture and location of the AMRs in relation to the sensor position on AMR. The navigation module and its interaction with other components are shown in figure 5, which provides an overview of the module.

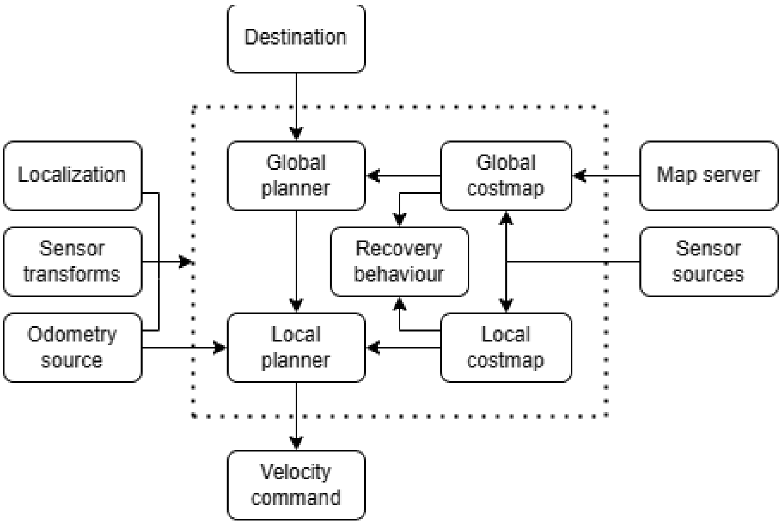

Figure 5. Overview of the navigation of autonomous mobile robot

In order to build an occupancy grid, the cost map makes use of the information obtained from the static map as well as sensor data. Both the addition of obstacle information to the cost map and the removal of obstacle information from the cost map are accomplished via the use of sensors. For the purpose of altering the cost of a cell, an insertion operation is nothing more than an index into an array. A clearing procedure, on the other hand, involves tracing rays across a grid in a direction that extends from the sensor's point of origin to the direction of each observation that is recorded. The obstacle's three-dimensional structure is being projected down and saved as a two-dimensional image, and it is being updated on the cost map [8].

Every global route planner makes use of a planner that is grid-based. The local route planner is responsible for generating a kinematic trajectory that is derived from the global planner. This trajectory allows the AMR to go from its starting point to its destination. Additionally, the local planner is required to have a controller that will make use of the trajectory to ascertain the linear (d_x, d_y) and angular (d_ϑ) velocities that are required to be sent to the AMR drivetrain. It is possible that the AMR may get stuck in a place while it is navigating; thus, we need to have a way to retrieve the AMR from its stuck position [8].

3. Results

The next step in this study will involve simulating the proposed solutions on an actual model to test the validity of the proposed concept. For this particular application, I have selected the mobile robot JetAcker, which is equipped with RGB data and point cloud visualization capabilities. Additionally, it is capable of performing line following tasks and tracking objects as well as human bodies.

Acknowledgments: This article was created thanks to the support of the KEGA project: 020TUKE-4/2022 Development and implementation of new approaches in the teaching of industrial and collaborative robotics.

Conflicts of Interest: This is a declaration that I have independently produced the whole paper by making use of the professional literature that was cited.

References

1. Duchoň František, Tőlgyessy Michal, Dekan Martin, Rodina Jozef, Chovanec Ľuboš, Babinec Andrej: Riadenie mobilnych robotov **2023**, *1st ed.*
2. Georgios Zamanakos, Lazaros Tsochatzidis, Angelos Amanatiadis and Ioannis Pratikakis, Feature Aware Re-weighting (FAR) in Bird's Eye View for LiDAR-based 3D object detection in autonomous driving applications. *Robotics and Autonomous Systems* **2024**, *Volume 175*.
3. Rogério Yugo Takimoto, Thiago de Castro Martins, Fábio Kawaoka Takase and Marcos de Sales Guerra Tsuzuki, Epipolar Geometry Estimation, Metric Reconstruction and Error Analysis from Two Images. *IFAC Proceedings Volumes* **2012**, *Volume 45.*
4. Baofu Fang, Gaofei Mei, Xiaohui Yuan, Le Wang, Zaijun Wang and Junyang Wang, Visual SLAM for robot navigation in healthcare facility. *Pattern Recognition* **2021**, *Volume 113*.
5. R. Siegwart, I.R. Nourbakhsh, D. Scaramuzza: Introduction to Autonomous Mobile Robots. *The MIT Press, Cambridge, MA, USA* ***2011**, 2nd ed.*
6. J.C. Latombe: Exact Cell Decomposition. In: Robot Motion Planning. *The Springer International Series in Engineering and Computer Science* **1991**, *vol 124.*
7. Yu-Cheol Lee, LSMCL: Long-term Static Mapping and Cloning Localization for autonomous robot navigation using 3D LiDAR in dynamic environments. *Expert Systems with Applications* **2024**, *Volume 241*.
8. Sina Tavasoli, Xiao Pan and T.Y. Yang, Real-time autonomous indoor navigation and vision-based damage assessment of reinforced concrete structures using low-cost nano aerial vehicles. *Journal of Building Engineering* **2023**, *Volume 68*.
9. G Uganya, I. Bremnavas, K.V. Prashanth, M. Rajkumar, R.V.S. Lalitha and Charanjeet Singh, Vi Empowering autonomous indoor navigation with informed machine learning techniques. *Computers and Electrical Engineering* **2023**, *Volume 111*.

Investigation of Degradation Properties of the Blends of Polylactic Acid and Polyhydroxybutyrate

Marcel Modrák [1]*, Marianna Trebuňová [1]

[1] Affiliation 1; Department of Biomedical Engineering and Measurement, Faculty of Mechanical Engineering, Technical University of Košice, 042 00 Košice, Slovakia,
* Corresponding author: Marcel Modrák, email: marcel.modrak@student.tuke.sk

Abstract: Polylactic acid (PLA) and polyhydroxybutyrate (PHB) belong to the most studied biobased polymers for degradable hard tissue substitutes. The successful application of biodegradable materials in the development of hard tissue substitutes requires that the rate of their degradation in vivo is consistent with the rate of new tissue formation. The aim of this study was to investigate the degradation properties of three types of PLA-PHB polymer blends with the two different structures. For this purpose, an in vitro research experiment was planned and implemented. The results of this experiment showed that the weights of the examined specimens gradually decreased in accordance with expectations.

Keywords: biodegradation; PLA-PHB polymer blends; in vitro experiment.

1. Introduction

Polymeric biodegradable materials are frequently used for tissue engineering and regenerative medicine. This type of materials can be either natural or synthetic in origin. More about this classification can be found, e.g., in [1]. Natural polymers have some significant advantages, e.g., better interaction between the implant and the cells. On the other hand, their difficult availability in larger quantities and more demanding processing [2] caused an increased interest in the research of synthetic polymers. Among the advantages of the synthetic polymers, it is possible to mention the possibility of adjusting their parameters such as porosity or degradation rate [3], as well as availability in large quantities. Therefore, blends of synthetic and natural polymers can form a new class of materials with improved mechanical properties and biocompatibility [4]. Polymers produced in this way have usually good mechanical and physical properties, such as tensile strength, modulus of elasticity and rate of degradation [5]. This group of polymers also includes mixtures of polymers based on polylactic acid (PLA) and polyhydroxybutyrate (PHB). They are prepared by melt compounding at several different PLA/PHB weight ratios, e.g., 75:25, 60:40, 70:30, 50:50, 25:75. In this work, three different PLA-PHB blends were produced by Fused Deposition Modeling technology. The two of them were plasticized with different concentration of oligomeric lactic acid (OLA), with 5 and 10 wt% of OLA, and the third-one was not plasticized to any extent. The specimens were levelled in two modifications, with a full structure and a porous one. In the in vitro biodegradation experiment, 3 types of solutions were used, in which the tested specimens were immersed. The three distinct solutions were labelled as A, B and C. Saline solution has been denoted as 'A', Hank's balanced salt solution (HBSS) as 'B' and solution 'C' was phosphate buffered saline (PBS). Some details regarding the composition of these solutions are available e.g., in [6]. The experiment was conducted for four months, and the biodegradation process was evaluated by measuring the pH changes and weight loss methods.

2. Materials and Methods

Testing specimens (see Figure 1c and 1d) were manufactured using TRILAB DeltiQ 2 3-D printer (see Figure 1b). This type of printer works with input material in the form of filament. The granules, from which filament was produced, have been dried (to remove water or another solvent) on Airid Polymer Dryer (see Figure 1a).

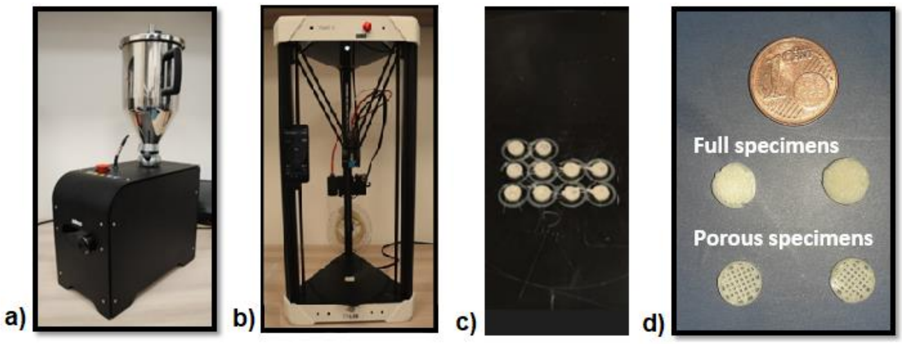

Figure 1. a) Dryer of granules, b) 3D printer c) The specimens after printing, d) The specimens after adjustment for testing.

Further, it is useful to introduce labeling of tested specimens according to the materials from which they were made. The abbreviations used for the three types of materials are listed in Table 1.

Table 1. Characteristics and abbreviations of the materials [7].

Material/Abreviation	Structure of the materials	The amount of added plasticizer - OLA
PLA-PHB 70:30 (MAT #1)	Full	0%
	Porous	
PLA-PHB 70:30 (MAT #2)	Full	5%
	Porous	
PLA-PHB 70:30 (MAT #3)	Full (F)	10%
	Porous	

To make this study easy to follow, the experiment procedure was organized as shown in Figure 2.

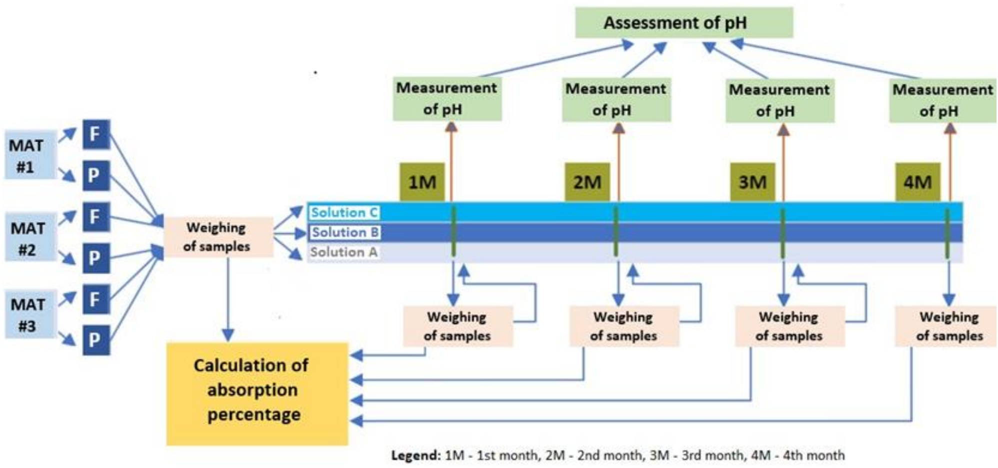

Figure 2. The sequence of the steps followed in the experiment [7].

3. Description and evaluation of the degradation experiments

From the point of view of the type of experiment, natural biodegradation in vitro was chosen, the aim of which is to simulate real processes taking place in the human body after the implantation of the material. The procedure for this method is set out in EN ISO 10993-13 [8], which specifies values such as pH, ambient temperature, duration of the experiment and others. The purpose of the experiments was to monitor the absorption parameters of solutions and changes in pH values in individual solutions. Each type of solution was poured into three closable flasks. A total of 3 flasks with solution A, 3 flasks with solution B and 3 flasks with solution C were prepared. The amount of solution in each flask was the same - 42 ml, the pH value of individual solutions was 7.4. Flasks with solutions and samples (specimens) were placed on the platform of the Orbital Shaker PSU-10i device (see Figure 3a), which simulated the flow of (body) fluids with its movement. The stirring speed was set at 160 rpm.

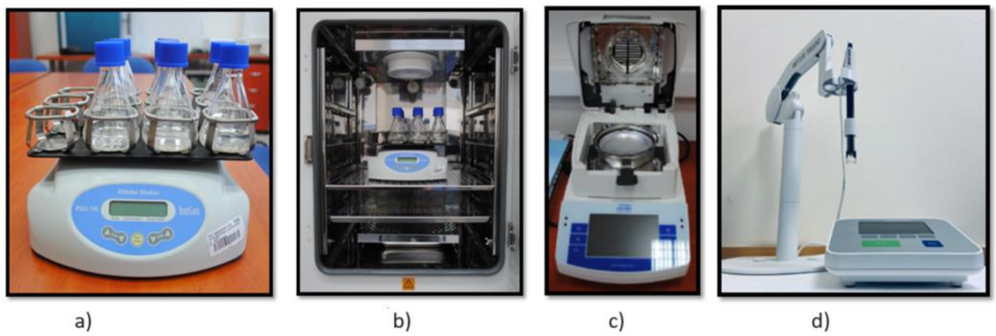

Figure 3. a) Orbital Shaker PSU-10i, b) Esco CelCulture CO2 Incubator, c) Weight measurement Radwag, d) pH measurement equipment.

The Orbital Shaker was placed in the Eeco CelCulture CO2 incubator (see Figure 3b), where a constant temperature of 37 °C was maintained throughout the degradation experiment. The specimens were weighed before the start of the experiment and during the experiment at regular 30-day intervals on the Radwag scale shown in Figure 3c. Excess liquid was removed from the samples with filter paper. In addition to weighing the samples, the pH of each solution was also measured at the same intervals on the Mettler Toledo instrument shown in Figure 3d. The pH value was adjusted to 7.4 after each measurement. The pH values of the solutions after 30-day intervals are shown in Table 2.

Table 2. The obtained pH values [7].

Type of solution	Type of material	Time of interval of measurement of pH values			
		30 days	60 days	90 days	120 days
Saline solution (A)	Material #1	2.36	2.22	2.03	2.13
	Material #2	2.49	2.09	2.04	2.08
	Material #3	2.38	2.41	2.44	2.34
Hank's solution (B)	Material #1	3.85	1.91	1.86	1.85
	Material #2	3.97	2.63	2.41	2.29
	Material #3	4.36	2.15	1.94	2
Phosphate buffered saline (C)	Material #1	6.09	6.13	6.27	6.33
	Material #2	6.27	6.18	6.11	6.48
	Material #3	6.78	6.68	6.56	6.59

The following findings emerge from the measured pH values. For all types of materials and all solutions in which the samples were immersed, there was a shift towards acidity on the pH scale. The differences in pH values between materials that were immersed in the same type of solution did not differ significantly. The pH changes in solution A were the most pronounced, the average pH value of all three materials immersed in solution A was the most acidic. The pH values in solution C turned out to be the most stable, with the smallest decrease in pH, for all types of materials.

The subsequent experiment has been focused to analyze degradation changes of the specimens before and after solutions exposure to them. Weight values of the specimens, measured in accordance with the sequence of procedures outlined in Figure 2, were first processed in a tabular form. Subsequently, absorption percentages of the specimens were calculated using the following formula [9]:

$$Sw = \frac{(\ _{wet} - \ _{dry})}{_{dry}} \quad 100 \tag{1}$$

where w_{dry} is the weight of a specimen prior to biodegradation, wherein W_{wet} is the weight of a specimen on a particular day during the biodegradation. The calculated values are visualized in the form of graphs as depicted in Figure 4.

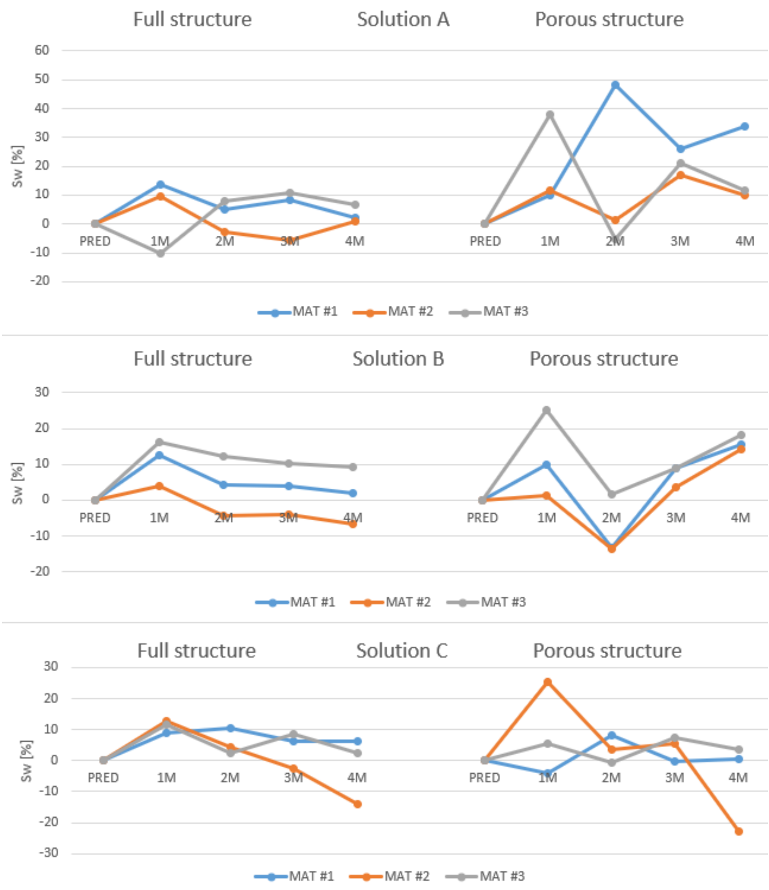

Figure 4. Presentation of absorption changes during the degradation experiment [7].

Graphs in Figure 4 show increasing tendency in absorptions for porous specimens over to full ones. To verify the statistical significance of these differences, statistical testing of the hypotheses was performed using the non-parametric Mann–Whitney U test, the procedure of which is as follows. In the first step, the test statistics U1 and U2 are calculated according to the following two relations:

$$U_1 = n_1 n_2 + \frac{n_1(n_1+1)}{2} - R_1, \quad (2)$$

$$U_2 = n_1 n_2 + \frac{n_2(n_2+1)}{2} - R_2, \quad (3)$$

where n1 and n2 present ranges of the samples; R1 and R2 are the sums of the ranks of the given samples. Then, the smaller value of them is selected U=min (U1, U2), and expected value μ_U is enumerated:

$$\mu \quad = \frac{1\cdot \quad 2}{2}. \quad (4)$$

Subsequently, a standard error SEU is estimated, and after that, z value is calculated:

$$SE \quad = \sqrt{\frac{1\cdot \quad 2\cdot(\quad 1+ \quad 2+1)}{12}}, \quad (5)$$

$$= \frac{U-\mu}{SE}. \quad (6)$$

Finally, z-value is transformed into p-value by using online calculator [10].

Based on the results of the testing, it was not possible to reject the null hypothesis of the difference between the compared medians and at the same time the values from a pair of sets. In a similar way, the influence of individual solutions and materials on the absorption capacity of the specimens was verified. For this purpose, the non-parametric Kruskal-Wallis H test was used. Tables 3 and 4 show p-values from the comparison of differences between solutions and materials.

Table 3. Comparison of the differences between the solutions by Kruskal-Wallis H test.

Type of material		**Compared solutions**
		A ↔ B↔ C
MAT #1	Full	p = 0.4374
	Porous	p = 0.02639
MAT #2	Full	p = 0.5836
	Porous	p = 0.6677
MAT #3	Full	p = 0.1229
	Porous	p = 0.3094

Table 4. Comparison of the differences between the solutions by Kruskal-Wallis H test.

Type of solution	Compared materials MAT #1 ↔ MAT #2↔ MAT #3	
	Full structure	Porous structure
Solution A	p = 0.4374	p = 0.2106
Solution B	p = 0.02178	p = 0.3342
Solution C	p = 0.5004	p = 0.7939

4. Discussion and Conclusions

From Table 3, a statistically significant difference between the solutions was manifested only in the case of material #1 with a porous structure. For this material, it can be argued that solution A had the greatest effect on its absorption. Solution B had the second largest effect on the absorption of this material, while solution C had the smallest effect. Based on the results of the statistical testing of the difference between materials 1 to 3, it can be concluded that the difference between them was found only in the case of comparing materials with a full structure that were immersed in solution B. This also means that these materials have not been confirmed to have a different effect on absorbency.

Finally, it can be stated that for each type of material with both structures and in all three solutions, a positive trend was identified, i.e. the weights of the examined specimens have a predominantly decreasing character from month to month.

Acknowledgements:

This research was funded by KEGA - Cultural and Educational Grant Agency of the Ministry of Education, Research, Development and Youth of the Slovak Republic, grant number KEGA 018TUKE-4/2023.

Conflicts of Interest: The authors declare no conflict of interest.

References

1. Modrák, M., Trebuňová, M., Balogová, A. F., Hudák, R., & Živčák, J. (2023). Biodegradable Materials for Tissue Engineering: Development, Classification and Current Applications. Journal of Functional Biomaterials, 14(3), 159.
2. Iqbal, N.; Khan, A.S.; Asif, A.; Yar, M.; Haycock, J.W.; Rehman, I.U. Recent concepts in biodegradable polymers for tissue engineering paradigms: A critical review. Int. Mater. Rev. 2019, 64, 91–126.
3. Mohanty, A.K.; Misra, M.; Drzal, L.T. Sustainable bio-composites from renewable resources: Opportunities and challenges in the green materials world. J. Polym. Environ. 2002, 10, 19–26.
4. Sionkowska, A. (2011). Current research on the blends of natural and synthetic polymers as new biomaterials. Progress in polymer science, 36(9), 1254-1276.
5. Giusti, P., Lazzeri, L., Cascone, M. G., & Seggiani, M. (1995, October). Blends of synthetic and natural polymers as special performance materials. In Macromolecular Symposia (Vol. 100, No. 1, pp. 81-87). Basel: Hüthig & Wepf Verlag.
6. Findrik Balogová, A., Trebuňová, M., Ižaríková, G., Kaščák, Ľ., Mitrík, L., Klímová, J., Feranc J. Modrák, M., Hudák R., & Živčák, J. (2021). In vitro degradation of specimens produced from PLA/PHB by additive manufacturing in simulated conditions. Polymers, 13(10), 1542.
7. Modrák, M. (2023). Bioaditívna výroba degradovateľných náhrad tvrdých tkanív. Dizertačná práca, Technická univerzita v Košiciach.
8. EN ISO 10993-13:2009 Biological evaluation of medical devices - Part 13: Identification and quantification of degradation products from polymeric medical devices.
9. Guo, Z., Yang, C., Zhou, Z., Chen, S., & Li, F. (2017). Characterization of biodegradable poly (lactic acid) porous scaffolds prepared using selective enzymatic degradation for tissue engineering. RSC advances, 7(54), 34063-34070.
10. Mann Whitney U Test Calculator. Statistics Kingdom. 2017. Available online: http://www.statskingdom.com/170median_mann_whitney.html (accessed on 25th Jan 2022).

TECHNICKÁ UNIVERZITA V KOŠICIACH
Strojnícka fakulta

Development and design of a test bench for detecting the effect of the photocatalytic reaction

Dominik Novotný [1], Ján Kráľ [2]

[1] Technical University of Košice, Faculty of Mechanical Engineering, Department of Manufacturing Technologies and Robotics, Slovakia, dominik.novotny@tuke.sk
[2] Technical University of Košice, Faculty of Mechanical Engineering, Department of Manufacturing Technologies and Robotics, Slovakia, jan.kral.2@tuke.sk

Abstract: The 21st century is also marked by the coronavirus pandemic, which has significantly affected the functioning of society. The deterioration in the health of the population, the significant mortality caused by the virulence and variable mutations of the Covid-19 virus and the way in which it spreads have led to the creation of devices that use photocatalysis to eliminate and destroy pathogens by means of air filtration, which creates a safe environment for the population to function in confined spaces. The purpose of this article is to summarize the basics of photocatalysis, a description of the nature of the test stand and its actual design and development in which the photocatalysis process takes place..

Keywords: Photocatalysis, stand, antimicrobial, filter, core

1. Photocatalytic process

Photocatalysis is the process of chemical decomposition of substances in the presence of a photocatalyst and light radiation. In principle, it is based on photolysis, the natural decomposition of certain substances by the action of light, accelerated by the presence of a photocatalyst. [1]

When a material with photocatalytic properties is exposed to light radiation of a suitable wavelength, its surface is activated and a characteristic reaction is triggered. The free electron-hole pair formed primarily and the hydroxyl radicals formed secondarily by contact between the excited photocatalyst molecule and the water vapour decompose the organic and inorganic substances present. [2]

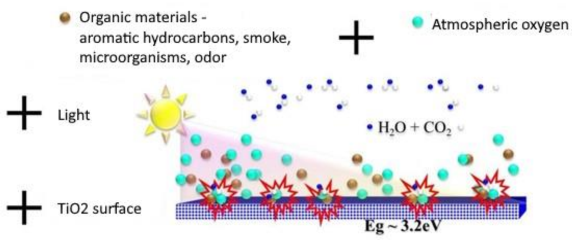

Figure 1 Working principle of photocatalysis

Substances degradable by photocatalysis include, for example, nitrogen oxides (NOx), sulphur oxides (SOx), carbon monoxide (CO), ozone (O3), ammonia (NH3), hydrogen sulphide (H2S), chlorinated hydrocarbons, dioxins, chlorobenzene, chlorophenol, simple hydrocarbons, aromatic hydrocarbons, and also bacteria, viruses, fungi or microplastic particles.

The final product is then usually common and stable compounds. The specific industrial applications of the photocatalysis principle may differ primarily in the type of catalyst. The most commonly used is nanocrystalline titanium dioxide TiO_2, which is activated by UV radiation. [2,3]

2. Technical design of the test stand

The technical solution relates to the design of a device - a test rig for testing photocatalytic efficiency in toluene testing. The technical solution generally belongs to the field of mechanical engineering and the scientific field of biomedical engineering.

It also extends to the fields of measurement, testing and testing or medicine. The technical solution belongs to a group of devices referred to as test devices, which are used for the experimental identification and assessment of the photocatalysis efficiency, the assessment of the filtration efficiency coefficient, the effect of the antimicrobial fibre on the evaporated substance under test.

The photocatalytic efficiency test equipment demonstrates a broad spectrum effect on a variety of organic and inorganic substances.

3. Principle of operation of the test stand

The test device, which operates on the basis of a photocatalytic reaction, houses an antimicrobial core, which consists of a controllable light source and a braid of metal oxide polymer fibers, which are placed in a transparent polymer tube, allowing permanent visual inspection of the device.

In testing the test equipment, the effectiveness of the antimicrobial filter core on the test substance (toluene) is monitored at two points (before entering the filter core, after exiting the filter core of the test equipment) by means of a mass spectrometer, and its effect on the elimination of the evaporated substance, which is located in the lower part of the test equipment.

A fan is used to move the air in the test apparatus and a propeller-shaped mixing unit is used to agitate the air in the pre-filter section of the test apparatus. During testing, the temperature can be continuously controlled for faster evaporation, the level of dust and air pollution by the test substance. In the test rig, we can control the temperature and the filtration rate with a fan controller (fan speed). To determine the effectiveness of the antimicrobial filter core under test, we use a mass spectrometer that can measure the proportion of the test substance in the air at short intervals over a short period of time.

Several parameters can be set before the testing process: volume of air tested per minute, temperature, humidity and dust sensors.

The advantage of this technical solution is the versatility of the test equipment for different variants of photocatalytic substances and their effectiveness in cleaning. Thanks to the use of a mass spectrometer, the process can be evaluated instantaneously with possible control of the volume of air supplied to the core of the test rig.

4. Design of the test stand

A test apparatus designed to determine the photocatalytic performance of an antimicrobial device comprises a test substance generator with thermoregulation to control the evaporation rate, an inlet and mixing arrangement and the antimicrobial core (4) filter section itself.

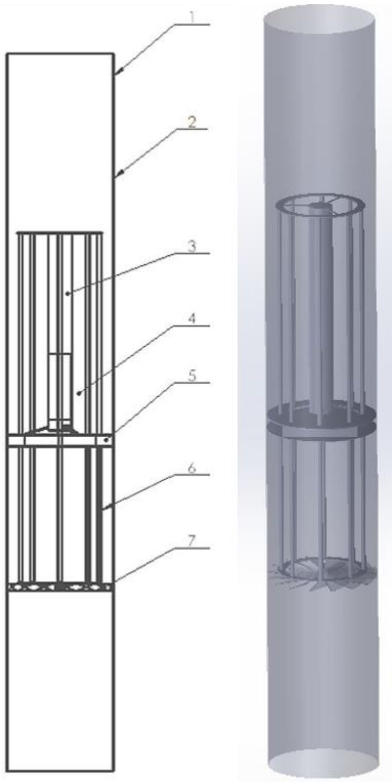

Figure 2 Test stand schematic

The apparatus is housed in a transparent polymer tube (1) with the capability of visually inspecting the process with controlled extraction of excess vapour. The test substance is evaporated into the pre-filter section (6) where the substance is further dispersed by means of a propeller (7). Subsequently, the evaporated substance is drawn by a fan (5) which pushes the test substance into the antimicrobial core (4) of the filter section around the central tube (3) inside the device.

Throughout the various parts of the test device, openings (2) in the tube are accessible for the mass spectrometer probe to accurately quantify the amount of test substance (e.g., toluene) being vaporized.

The industrial applicability of the photocatalytic efficiency test device is apparent from the foregoing description of the gist of the technical solution and the example embodiment. The described embodiment is used to detect the effect of photocatalysis using an antimicrobial filter core comprising a filament and a light source at a controlled temperature.

In addition to the experimental function of the test device, which is of great importance when testing organic but also inorganic substances, we can also investigate the temperature, carry out tests of the lifetime of the core of the antimicrobial filter section where the knitted polymer fibre with metal oxides is applied.

Figure 3 Test stand

5. Sensors

This section is not mandatory but can be added to the manuscript if the discussion is unusually long or complex. For the proper functioning of the bench, air quality and chemical snozors with different focuses were applied.

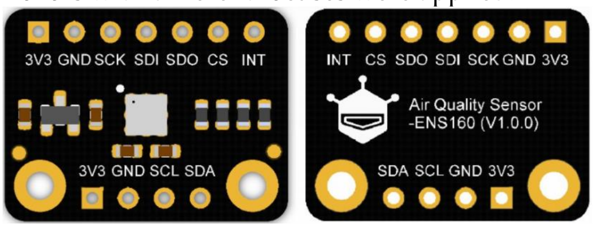

Figure 4 DFROBOT Fermion ENS 160 air quality sensor

For sensing temperature, humidity, and overall air quality, we used the DFROBOT sensor shown in Figure 3, which uses innovative TrueVoc technology with MOX technology to obtain accurate data more quickly and ensure the long-term stability of the sensor.

Figure 5 MQ-2 - methane, butane, LPG and smoke sensor module

This selected module contains a combustible gas sensor, designated MQ-2, and an operational amplifier for simplified use with Arduino boards. The aforementioned MQ-2 sensor can detect the presence of combustible gases, which include, for example, natural gas (LPG), methane, butane, alcohol, propane or hydrogen. The measurement range is 300 - 10 000 ppm.

Figure 6 MQ-3 - Module with sensor for alcohol, ethanol

The MQ-3 sensor has a heating element with an electronic chemical sensor and measures the concentration of alcohol or ethanol. It is possible to measure the concentration of alcohol in the air you breathe. The measurement range of this sensor is 100-1000 ppm.

Figure 7 MQ-7 - Carbon monoxide sensor module CO

The MQ-7 sensor detects CO with a reaction time of 60 seconds and a measurement range of 200 - 2000 ppm.

Figure 8 MQ-8 - Hydrogen sensor module

MQ-8 sensor can detect various kinds of hydrogen containing gas, especially city gas, it is a low-cost sensors for various applications. The measurement range is 100-1000 ppm.

Figure 9 MQ-9 - Module with sensor for carbon monoxide CO and combustible gases

The MQ-9 gas sensor can detect or measure the concentration of combustible gases (LPG, methane) and carbon monoxide (CO). The sensitivity of the sensor can be adjusted using a trimmer. The CO detection range is
10 - 1000 ppm and the combustible gas detection range is 100 - 10,000 ppm.

Figure 10 MQ-131 - Ozone sensor module

The MQ-131 sensor can detect ozone O3 in the measurement range of 100 - 1000 ppm.

Figure 11 MQ-135 - Air quality sensor module, benzene, alcohol, smoke

The sensitive material of the MQ135 gas sensor is SnO2, which has a lower conductivity in clean air. When the target combustible gas exists, the conductivity of the sensors is higher with increasing gas concentration. The measurement range is 10 - 10,000 ppm.

Figure 12 MQ-138 - Module with VOC gas sensor

MQ138 gas sensor has high sensitivity to toluene, acetone, alcohol, methanol, can also detect hydrogen and other organic substances.

All sensors (MQ-3 - MQ-138) are very sensitive and also very accurate, they are very similar, they can only be distinguished by the shape of the sensing module soldered on the top. They operate at 5V and have both digital and analogue output. The sensors are controlled by an arduino.

6. Conclusion

Since we do not have an official certified workplace in Slovakia for testing devices that destroy viruses and we at the school do not have the authorization and do not want to work with viruses, we decided to create a test bench that tests the functionality of the photocatalytic core with inorganic elements in our case with toluene.

The most important part of the bench is the core, which is changeable. The principle of the test bench is simple, at the bottom we produce toluene into the space by evaporation, which is evenly dispersed in front of the filter section and which is forced into the core by a fan.

In the case of successful elimination of toluene in the photocatalytic core, there will be a small concentration of toluene in the upper part relative to that in the lower part. This supports our hypothesis that if photocatalysis can degrade toluene, it can also degrade viruses.

Acknowledgments: This article was written with the support of the project : ITMS2014+ 313011AVF5 INTELTEX - Centre for the Development of Textile Intelligence and Antimicrobial Technologies.

Conflicts of Interest “The authors declare no conflict of interest.”

References

1. A. Yousef, N.A.M. Barakat, K.A. Khalil, A.R. Unnithan, G. Panthi, B. Pant, H.Y.Kim, Photocatalytic release of hydrogen from ammonia borane-complex using Ni(0)-doped TiO2/C electrospun nanofibers, Colloids Surf. A: Physicochem. Eng. Aspects 410 (2012) 59–65, doi:http://dx.doi.org/10.1016/j.colsurfa.2012.06.017
2. Zhixin Chen, Jingjing Xu, Zhuyun Ren, Yunhui He, Guangcan Xiao, High efficient photocatalytic selective oxidation of benzyl-alcohol to benzaldehyde by solvothermal-synthesized ZnIn2S4 microspheres under visible light irradiation, J. Solid State Chem. 205 (2013) 134–141, doi:http://dx.doi.org/10.1016/j.jssc.2013.07.015
3. V. Kuzhalosai, B. Subash, M. Shanthi, A novel sunshine active cerium loaded zinc oxide photocatalyst for the effective degradation of AR 27 dye, Mater. Sci.Semicond. Proc. 27 (2014) 924–933, doi:http://dx.doi.org/10.1016/j.mssp.2014.08.046

TECHNICKÁ UNIVERZITA V KOŠICIACH
Strojnícka fakulta

3D scanning of the maxillofacial area for individual mask production

Bibiána Ondrejová[1*], Branko Štefanovič[1], Lucia Bednarčíková[1], Teodor Tóth[1], Jozef Živčák[1]

[1] Technical University of Košice, Faculty of Mechanical Engineering, Department of Biomedical Engineering and Measurement, Letná 1/9, 04200, Košice, Slovakia
* Correspondence: bibiana.ondrejova@tuke.sk

Abstract: Facial morphology assessment is crucial for surgical planning, fabrication of epithets, and burn masks. This study explores the use of affordable 3D scanning systems for facial morphology assessment, comparing their accuracy against a high-end scanner. Three scanners were evaluated: Artec Eva, CR-Scan 01, and the Scaniverse app on an iPhone 11. Thirty subjects were scanned, and distances between anthropometric points on the face were measured. To ascertain surface accuracy, dimensions between selected anthropometric points on the face were compared in Meshmixer software. Results showed that while the CR-Scan 01 provided measurements comparable to the Artec Eva, the Scaniverse app showed larger deviations with greater variability. Despite this, all devices achieved clinically acceptable accuracy (<1.5 mm).

Keywords: 3D scanning, optical scanners, accuracy analysis, prosthetics, orthotics

1. Introduction

Assessment of facial morphology has important applications for diagnosis and planning of surgical procedures, fabrication of epithets and burn masks. Conventional design and fabrication of such masks involves fabrication of a replica of the face by casting and subsequent moulding of low-temperature thermoplastics. This method is not convenient for patients, as different materials must be applied to the face during the casting process. Moreover, the accuracy of the conventional method is questionable and depends on several factors such as the conditions and setting time of the materials and their properties. An innovative non-invasive non-contact method for taking 3D morphology of the face is the use of 3D scanning systems. [1-3]

While three-dimensional technology is gaining popularity among CPOs (Certified Prosthetists Orthotist), challenges persist, limiting its widespread adoption. The limitation lies mainly in the cost of the equipment and associated software, and unfamiliarity with 3D scanning technology. Consequently, there is a growing demand for a low-cost, user-friendly interface and portable scanning system. However, the price of such a cheap device may reflect on the accuracy of the device. Since the accuracy of these devices as stated by the manufacturer is mostly tested on a static and tangible object, there is a need to test the accuracy of face 3D models acquired by scanning a moving living object - the human body for these purposes. [4-5]

The human face is an anatomically and morphologically complex structure formed with complicated anatomical features that are not easily replicable. The cost of the most used and validated scanning systems typically exceeds €10,000 and is often associated with an additional cost for the associated software.

Therefore, the aim of this study is to compare the surface accuracy of 3D models acquired by 3D scanning of the human face in 30 subjects with more affordable 3D scanning systems (<1,000 €) with a 3D scanner of a higher price category (<15,000 €) and with a higher accuracy reported by the manufacturer (Table 1). One of these is the Scaniverse application that has been installed on the iPhone 11.

Table 1. Parameter comparison of selected 3D scanners.

Device	Approximate price of the device (€)	Technology	Accuracy specified by the manufacturer (mm)
Artec Eva (Artec 3D, Luxembourg,Luxembourg)	13 500	Structured light	±0.1
CR-Scan 01 (Creality 3D Technology Co., Ltd., Shenzhen, China)	700	Structured light	±0.1
iPhone 11 (Apple Inc., Cupertino,CA, USA)	500	Photogrammetry/ LiDAR	±10.0

2. Materials and Methods

The facial parameters of thirty subjects were compared to analyse the accuracy of the scanners. Parameters are understood as the distance between anthropometric points. Anthropometric points are precisely localized points on the head and human body. The points were chosen so that they were relatively stable during scanning and a clear determination of their position on the 3D models was possible.

The anthropometric points taken include (Figure 1):

1. Ektokanthion– a point on the lateral side of the eye at the junction of the two eyelids.
2. Cheilion — the corners of the mouth.

The direct length distances between the outer corners of the eyes, the corners of the mouth and the outer left corner of the eyes and the left corner of the mouth were selected for analysis.

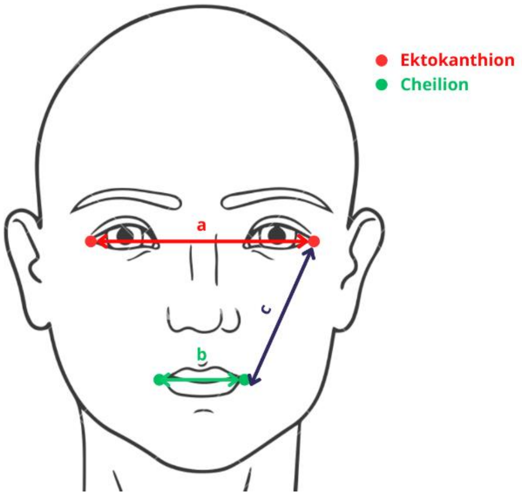

Figure 1. Representation of selected landmarks and their distances.

2.1 Data acquisition

The following scanners were used for scanning: Artec Eva, Creality CR-Scan 01, iPhone 11 with Scaniverse application.

Comparison between the facial scans obtained with the above mentioned 3 devices was performed on 30 subjects (n=90). Scans of a subject with different devices were taken at the same time. In addition, to limit variables related to human scanning that could affect the quality of the 3D scans (i.e., breathing, and micro-movements), all subjects were instructed to sit with their eyes closed, face relaxed, and their back against the backrest. Appropriate room lighting and temperature conditions were set during scanning (Figure 2).

Figure 2. Face scanning of subjects (**a**) Artec Eva; (**b**) CR-Scan 01; (**c**) Scaniverse.

The scanning procedure did not differ significantly between the 3 devices. During scanning with the Artec Eva scanner, sequentially captured portions of the subject are displayed on the surface, on which the colour changes according to the distance of the scanner from the subject. Green indicates the correct distance from the subject (0.6-1 m), red indicates that the scanner is very close to the subject, and blue indicates too far away. When scanning with the CR-Scan 01 scanner, 2 windows are displayed at the same time, with one window showing the image projected from the camera. In this case, only too proximity to the subject is indicated by the red colour map on the camera image. In the second window, a full 3D scan is gradually created during the scanning process. Both devices are connected via a USB cable to the PC, which limits the mobility around the subject. In the case of face scanning, this is not unmanageable as the face area does not need 360° scanning. In contrast, the use of a smartphone is highly advantageous in terms of unrestricted mobility around the subject during scanning. Scanning with a smartphone using the Scaniverse app was not too different from simply shooting a video. After selecting the size of the subject to be scanned, it is necessary to move the smartphone according to the instructions. Areas that are not yet scanned shown in red. Generally scanning a face with these devices took about 3 minutes and the process of generating a 3D model took about a minute.

2.2 Measurements

After the models were generated, the scans were exported in STL format to Meshmixer software (Autodesk, San Rafael, California,USA) to determine the distance between the selected points. It is important to note that the models were not edited or smoothed in any way prior to measurement. Using the Analysis-Units/Dimension function, the distances between the selected anthropometric points were measured. After clicking on one and the other point, the distance is automatically measured. Its value is indicated in the "Real length" line. The unit of the value can be set manually as desired (for example: mm, cm, m). In this case, the length is shown in millimetres. Fig. 3 shows the specified anthropometric points and the measured lengths between them in the software.

Figure 3. Measurement of selected dimensions (**a**) Meshmixer; (**b**) Scaniverse.

3D scans taken in Scaniverse can be measured directly in the application via the "Measure" function. The principle is the same as in the previous software, i.e. after clicking on one and the other point, the distance is automatically measured.

2.3 Data evaluation

The difference in distances obtained from the compared scanners (CR-Scan 01, iPhone 11) with respect to the reference scanner (Artec Eva) was evaluated.

$$= \quad -$$

δ – deviation

R_i – dimension measured by a reference scanner

E_i – dimension measurement by scanner comparison

From the deviations obtained, the average value and standard deviation (SD) were calculated to compare the accuracy of individual devices.

3. Results

Each subject is identified by a number with the chronological order of scanning. Models acquired with the Artec Eva scanner were chosen as the gold-standard models, which means that the parameter values obtained from the models acquired by the CR-Scan 01 and iPhone with the Scaniverse application were compared with the values obtained from models acquired with the Artec Eva 3D scanner.

The average deviations are summarized in Table 2. The CR-Scan 01 deviation represents the average difference between the CR-Scan 01 model parameters and those of the Artec Eva models that were measured using Meshmixer software. The Scaniverse bias represents the average difference between the Scaniverse model parameters and the Artec Eva parameters, also measured with Meshmixer software.

Table 2. Comparison of mean deviations obtained by measuring selected parameters in 30 subjects.

Parameter	**Mean deviation CR-Scan 01 (mm) ± SD**	**Mean deviation Scaniverse (mm) ± SD**
Dimension **a**	0.11 ±0.37	0.49 ±2.10
Dimension **b**	0.16 ±0.37	0.30 ±1.71
Dimension **c**	0.15 ±0.27	0.74 ±0.93

The measured data and their mean deviations show that there are no significant differences in the distances between pairs of landmarks. The results indicate that CR-Scan 01 achieves more accurate and consistent results compared to Scaniverse for the above measurements. Consistency is expressed by the authoritative deviation, which is in tenths of a millimeter for the CR-Scan 01 but in millimeters for the iPhone. Based on the standard deviation, the iPhone has a significantly larger dispersion of measured values and thus less stability of obtaining values.

The largest deviations were observed for the longest distance between anthropometric landmarks, specifically when measuring the distance between the left outer corner of the mouth and the outer corner of the left eye. The iPhone 11 can generate a 3D facial scan with an accuracy that results in an average difference of less than 1 mm when compared to the reference scanner but with a significantly greater dispersion of the measured values.

4. Discussion

The present study investigated the accuracy of new more affordable facial scanning devices compared to the proven ArtecEva 3D scanner commonly used in prosthetics and orthotics. Such deviations may be due to post-movement of the scanning subject (micro-movements, e.g. breathing).

In the study by Hang-Nga Mai et al. they classified the accuracy of a 3D scanner for face scanning into 4 categories: highly reliable (deviation <1.0 mm), reliable (deviation 1.0 mm-1.5 mm), moderately reliable (deviation 1.5 mm-2.0 mm), and unreliable (deviation >2.0 mm) [5]. For clinical use, deviations < 1.5 mm were considered acceptable [7-9]. Considering this classification, it can be concluded that the selected 3D scanner CR-Scan 01 in this study meet the accuracy criteria for clinical use in facial scanning, as the highest mean deviation was (0.16 ±0.37) mm. The mean deviation for the iPhone 11 was less than 1.5 mm, but the standard deviation indicates a larger spread of values.

5. Conclusions

Overall, 3D facial scans taken with a smartphone were not as accurate as those taken with professional scanning systems, but the deviations were within the recommended clinically acceptable range of <1.5 mm. Significant interest in facial scanning using smartphones in recent years has been based on their compactness, wearable-weight, and cost-effective nature; however, the accuracy of facial scans obtained with these scanners has not yet been sufficiently investigated.

Future research will build on this study, which looked at comparing the accuracy of low-cost 3D scanners in the context of facial scanning to produce face masks. The research will include an expanded sample of subjects and scanning systems where surface accuracy will be analysed. This aspect will allow the assessment of the accuracy of scanning devices in the context of manufacturing real products such as personalised face masks. Future research will also address the technical challenges associated with additive manufacturing processes for face masks, with an emphasis on efficiency and convenience. This information will be valuable for the further development of personalized solutions in medical applications and will serve as a basis for improvements in scanning technologies and manufacturing processes.

Acknowledgments: This work was supported by the Slovak Research and Development Agency under the contract No. APVV-22-0340. This research was supported by project KEGA 044TUKE-4/2022 Implementation of progressive technologies in prosthetics and orthotics education and support integration with practice and by project KEGA 021TUKE-4/2022 Implementation of computed tomography in an interdisciplinary technical-natural area.

Conflicts of Interest: The authors declare no conflict of interest.

References

1. Jazayeri HE, Kang S, Masri RM, Kuhn L, Fahimipour F, Vanevenhoven R, et al. Advancements in craniofacial prosthesis fabrication: A narrative review of holistic treatment. J Adv Prosthodont 2018 Dec;10(6):430-439, doi: 10.4047/jap.2018.10.6.430.
2. Zhao YJ, Xiong YX, Wang Y. Three-dimensional accuracy of facial scan for facial deformities in clinics: a new evaluation method for facial scanner accuracy. PLoS One 2017;12(1):e0169402, doi: 10.1371/journal.pone.0169402.
3. Bidra AS. Three-dimensional esthetic analysis in treatment planning for implant-supported fixed prosthesis in the edentulous maxilla: review of the esthetics literature. J Esthet Restor Dent 2011 Aug;23(4):219-236, doi: 10.1111/j.1708-8240.2011.00428.x.
4. Aswehlee AM, Elbashti ME, Hattori M, Sumita Y, Taniguchi H. Feasibility and accuracy of noncontact three-dimensional digitizers for geometric facial defects: an in vitro comparison. Int J Prosthodont 2018;31(6):601-606, doi: 10.11607/ijp.5855.
5. Mai HN, Lee DH. Accuracy of Mobile Device-Compatible 3D Scanners for Facial Digitization: Systematic Review and Meta-Analysis. J Med Internet Res. 2020 Oct 23;22(10):e22228. doi: 10.2196/22228.
6. Luetzenburg, G., Kroon, A. & Bjørk, A.A. Evaluation of the Apple iPhone 12 Pro LiDAR for an Application in Geosciences. Sci Rep 11, 22221 (2021). https://doi.org/10.1038/s41598-021-01763-9.
7. Aung S, Ngim R, Lee S. Evaluation of the laser scanner as a surface measuring tool and its accuracy compared with direct facial anthropometric measurements. Br J Plast Surg 1995 Dec;48(8):551-558. doi: 10.1016/0007-1226(95)90043-8.
8. Secher JJ, Darvann TA, Pinholt EM. Accuracy and reproducibility of the DAVID SLS-2 scanner in three-dimensional facial imaging. J Craniomaxillofac Surg 2017 Oct;45(10):1662-1670. doi: 10.1016/j.jcms.2017.07.006.
9. Ye H, Lv L, Liu Y, Liu Y, Zhou Y. Evaluation of the accuracy, reliability, and reproducibility of two different 3D face-scanning systems. Int J Prosthodont 2016;29(3):213-218. doi: 10.11607/ijp.4397.

TECHNICKÁ UNIVERZITA V KOŠICIACH
Strojnícka fakulta

Methodology for modifying the tensile stress-strain curve of polymer to the flexural modulus

Peter Palička [1,*], Róbert Huňady [1] and Barbara Schürger [1]

[1] Department of Applied Mechanics and Mechanical Engineering, Faculty of Mechanical Engineering, Technical University of Košice, Letná 9/B, 042 00 Košice, Slovakia; peter.palicka@tuke.sk; robert.hunady@tuke.sk; barbara.bacova@tuke.sk.
* Correspondence: peter.palicka@tuke.sk

Abstract: The worldwide production of plastics is approximately 365 million tons per year. Production is steadily increasing and is expected to double in the next twenty years. Plastics and other polymeric materials are an essential part of our daily lives and modern society. For the technical use of plastics, it is necessary to know their response to mechanical loading. The aim of this paper is to highlight the methodology for the evaluation of dynamic mechanical testing of polymers. If the given material tests are used as inputs for numerical models, where it is fundamental to have a correctly described true stress-strain curve, the post-processing of the measured data and the tests evaluation methodology is the important part of the work. If fast events need to be simulated, e.g. impact tests where the material is subjected to fast bending deformation, then the engineering tensile curves can be modified to the bending modulus. This methodology using DMA tests is described in this paper.

Keywords: tensile test; flexural test; dynamic mechanical analysis; stress-strain curve.

1. Introduction

Polymers can be divided according to several criteria, but the basic division of polymers is into plastics and elastomers. Plastics are generally irreversibly deformed by external loads, whereas elastomers are highly elastic with low stiffness, where the deformation can be significant (even in the hundreds of percent in the case of hyperelastic material) and still be reversible. The mechanical properties of polymers have a major role in the usability of the material in engineering practice and are specified by many of the same parameters as metals, i.e. modulus of elasticity, yield stress, ultimate strength and Poisson's number. In the case of polymers, the response to mechanical loading varies to a greater extent with the duration and strain rate, temperature and external environment compared to other materials. Therefore, it is necessary to study the mechanical response of plastics at different strain rates and different temperatures to verify their reliability and usability in various practical applications. In papers [1][2], the authors investigated the effect of mean strain rates and temperatures from -40 °C to T_g (the transition temperature of plastics) on the mechanical properties of plastics. In papers [3-7], the authors investigated the effect of high strain rates from 10^2 s^{-1} to 10^4 s^{-1} on the mechanical properties of plastics using a Split-Hopkinson Pressure Bar (SHPB). In [8], the authors decided to study the suitability of material models for numerical applications. Polymers are mainly used in engineering practice because they are more affordable compared to metals. The ability to create complicated shapes and complex geometries is one of the main advantages of using plastics, which increases their value and importance in industrial applications. In general, polymers behave as viscoelastic materials and exhibit an intermediate behavior between elastic solids and viscous liquids. Elastic solids exhibit linear stress-strain proportionality in accordance with Hooke's law. Polymers at high strain rate or low temperature behave like glassy materials, while at low strain rate or high temperature polymers behave like rubbery materials. In the first case, the mechanical properties are higher, but the polymer becomes brittle, while in the second case the mechanical properties are lower, and the polymer becomes ductile (goes into a rubber-like state). Tensile testing is probably the most widely used method for determining the mechanical properties of various materials, mainly because of its relative simplicity and time efficiency. The tensile diagram gives the relationship between stress and strain, from which the basic mechanical properties of the material, such as Young's modulus and Poisson's number, are derived. The Young's modulus of elasticity describes the linear relationship between stress and strain, which is represented by a linear curve in the tensile diagram. This region of the tensile diagram is also called the elastic region. It is the region of reversible deformation, where the material returns to its original state before loading after unloading. The tensile diagrams in Figure 1 shows that polymers have a wide range of behavior from brittle, to hard and ductile, to incompressible. The effect of strain rate on mechanical behavior may also be important. In general, decreasing the strain rate has the same effect on the stress-strain characteristics as increasing the temperature. This means that the material becomes softer and more ductile [9].

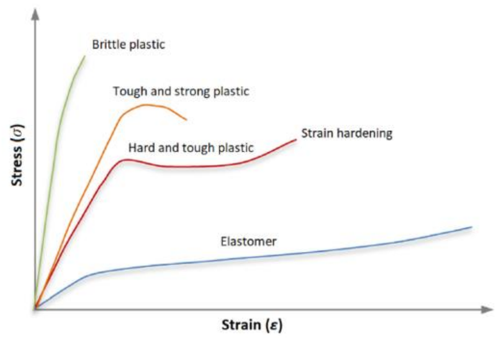

Figure 1. Stress-strain curves for different polymers [9].

2. Material and experimental methods

Acrylonitrile styrene acrylate (ASA) polymer is probably the most widely used amorphous engineering thermoplastic. Like all styrene polymers, ASA is mainly processed by injection moulding. Acrylonitrile provides higher strength, toughness and stiffness compared to standard styrene-based plastics [10][11].

Tensile and bending tests and dynamic mechanical analysis (DMA) were made. Injection moulded plates were produced from ASA polymer granulate. The test specimens were cut with waterjet for tensile tests with dimensions according to Figure 2a and for flexural tests and DMA with dimensions according to Figure 2b.

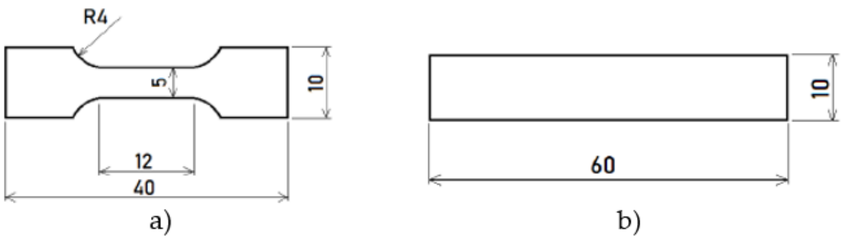

Figure 2. Test specimens for: a) tensile tests; b) flexural tests and DMA.

Tensile and bending tests are standard mechanical tests to determine the basic mechanical properties of a material. The result of the DMA is the frequency dependence of the flexural modulus. If the given material tests are used as inputs for numerical models, where it is fundamental to have a correctly described true stress-strain curve, the post-processing of the measured data and the tests evaluation methodology is the important part of the work. If fast events need to be simulated, e.g. impact tests where the material is subjected to fast bending deformation, then the engineering tensile curves can be modified to the flexural modulus.

The first step was to perform seven tensile tests at a strain rate of 10^{-2} s^{-1} (traverse displacement speed of 10 mm/min) and then evaluate the engineering stress-strain curves. These curves had to be smoothed using Matlab software and polynomial approximation of 6° and above. Then, an averaged curve was created by averaging the measured values over all samples. For plastics, the elastic part of the curve (its slope) is similar, but as can be seen in Figure 3, which shows the curves from the tensile tests and the averaged curve, the plastic part of the curves is over quite a wide range. Each specimen deformed differently in the plastic region.

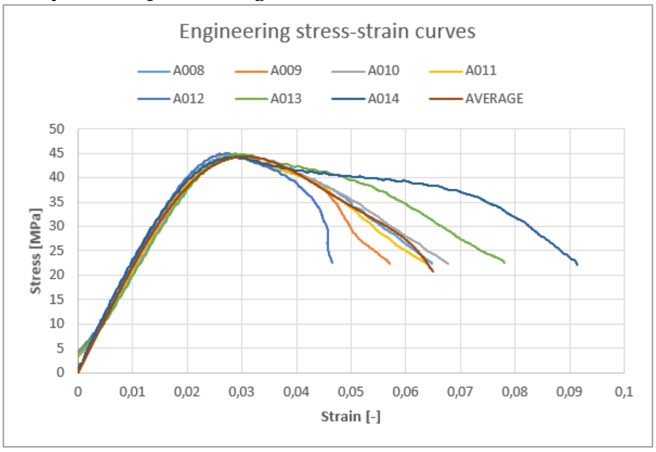

Figure 3. Engineering stress-strain curves with average stress-strain curve.

Flexural tests (three-point bending) were carried out on five specimens at a strain rate of 10^{-2} s^{-1}. The purpose of the bending tests was to obtain flexural modulus values. The results of the bending tests are shown in Figure 4 and the resulting flexural modulus values are given in Table 1.

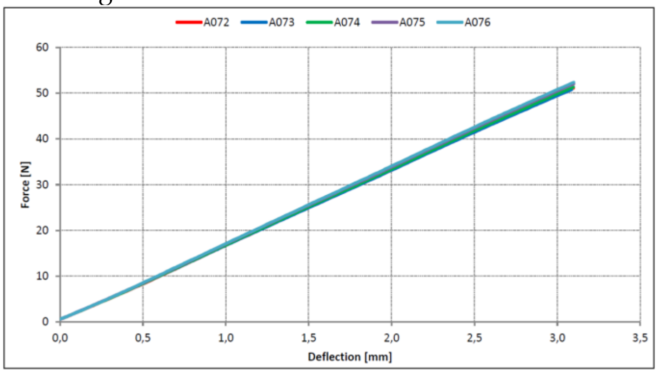

Figure 4. Force-deflection curves from bending tests.

Table 1. Values of flexural modulus from bending tests with strain rate 10^{-2} s^{-1}.

Sample No.	Flexural modulus [MPa]
A072	2689
A073	2673
A074	2691
A075	2729
A076	2729

The last experimental measurement was a dynamic-mechanical analysis (DMA) performed on five specimens at four frequencies of 0.04 Hz, 0.4 Hz, 4 Hz and 40 Hz. During this analysis a sinusoidal force is applied to specimen. The storage modulus (flexural modulus) measures the stored energy, representing the elastic portion, and the loss modulus measures the energy dissipated as heat, representing the viscous portion. The aim of the DMA was to determine the frequency dependence of the storage modulus (see Figure 5). The flexural modulus increases with increasing frequency. A frequency of 0.4 Hz approximately corresponds to a strain rate of 10^{-2} s^{-1}, which was measured by the classical bending test. The resulting value of the flexural modulus from the DMA is 2684 MPa while the average value from the bending tests is 2702 MPa. So it can be said that the correlation of the results is in very good agreement.

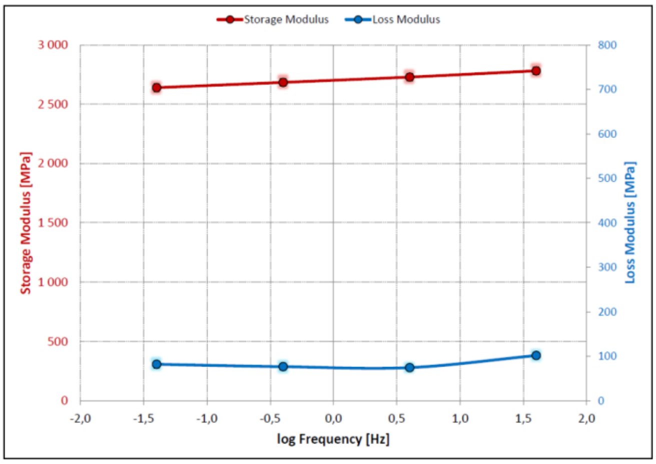

Figure 5. Frequency dependence of flexural modulus from dynamic mechanical analyses.

3. Results

The tensile tests result in an engineering stress-strain curve that shows the relationship between stress and strain in the elastic and plastic region when the specimen is stretched in one direction. However, if we want to simulate e.g. an impact test where the material is loaded in bending, the resulting material curve has to be further optimized. By using the following methodology, it is possible to directly adjust the tensile curve to the flexural modulus and thus obtain a curve that would be much more fitted to solve given problem. The method is the following:

The total deformation (1) of the average engineering stress-strain curve can be written as

$$= \quad + \quad _{pl} \, , \tag{1}$$

where is total deformation of specimen; is elastic deformation of specimen and $_{pl}$ is plastic deformation of specimen. From the average stress-strain curve, only the plastic deformation needs to be expressed according to the equation (2)

$$_{pl} = \quad - - \, , \tag{2}$$

where are stress values and is Young's modulus from tensile test. Using equation (2), all elastic strain values are set to zero, leaving only the plastic strain values. With equation (3)

$$= \quad _{pl} + - \, , \tag{3}$$

where $'$ is flexural modulus, the elastic deformation corresponding to the flexural modulus is added to plastic deformation from previous equation. These steps result in a modified tensile curve for the flexural modulus. The averaged engineering stress-strain curve with an evaluated Young's modulus of 2058.4 MPa can be seen in Figure 6a. In Figure 6b, the modified stress-strain curve to a DMA obtained flexural modulus of 2684 MPa can be seen.

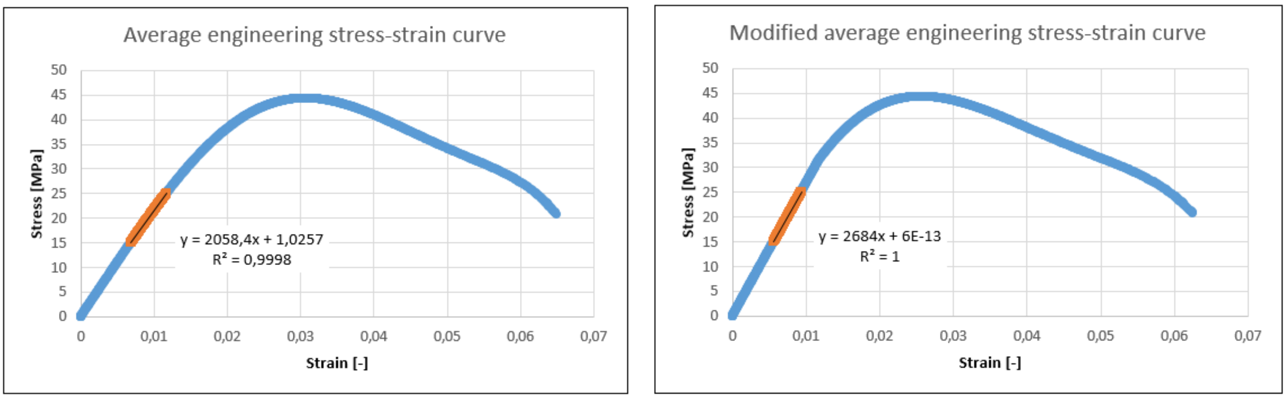

a) b)

Figure 6. a) Average engineering stress-strain curve; b) Modified average engineering stress-strain curve.

The final step for specifying the material curves in the numerical model is to convert the engineering curves into true stress-strain curves. For this, the equations (4) and (5) from the law of conservation of volume are used

$$= \ln(1 + {}_{st}), \qquad (4)$$

$$= {}_{st}(1 + {}_{st}). \qquad (5)$$

The law of conservation of volume is valid only up to the ultimate strength of the material, i.e. up to the moment when the necking of the sample starts. A comparison of the true and engineering curves is shown in Figure 7.

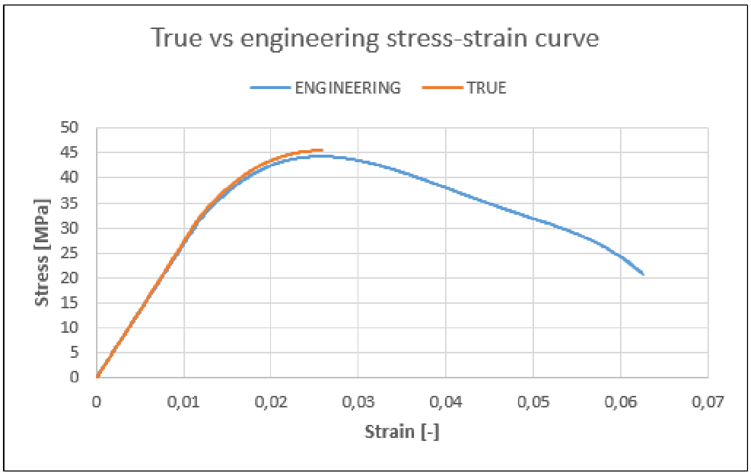

Figure 7. True stress-strain curve in comparison with engineering stress-strain curve.

4. Discussion

Experimental measurements are an important tool in determining material parameters. Tensile test is the most widely used method of determining material constants such as Young's modulus and Poisson's number. It is important to evaluate the measured data correctly when finite element method is used to simulate some kind of mechanical loading. Creating a material card that describes the mechanical response of a material to any type of loading, whether it be tension, compression, bending, etc. is complicated work and numerical model is as good as description of material behavior in material card. If a tensile test is used to obtain a true stress-strain curve and the material card is used to simulate an event in which the material deforms differently than in tension, the material card will not be suitable for the simulation. It is still necessary to do such material tests and adapt the material card to what needs to be simulated. In this paper, a methodology is presented to modify the stress-strain curve, which describes the relationship between stress and strain in a specimen under tensile stress to flexural modulus. If tensile and bending tests were performed and a bending test was simulated with a material card where the stress-strain curve from the tensile test is defined, then of course the numerical and experimental results would not be consistent at all. One possibility would be to changing the slope of the curve in the material card using optimization, so that the material card could be optimized for the bending test. The other possibility which is the content of this paper is to modify the tensile stress-strain curve to the flexural modulus. So, change the slope of the curve according to known mechanics theorems. This process is still just some fitting of the curves, it is not a validation of the material card. Material card validation means simulating a different bending load on the material, where of course one has experimental results, and the goal is to check if the material card correctly describes the mechanical response of the material under different boundary conditions.

Acknowledgments: This work was supported by the Slovak Research and Development Agency under the grant project VEGA No. 1/0500/20 and VEGA No. 1/0516/22.

Conflicts of Interest: The authors declare no conflict of interest.

References

1. M. Zrida et al. High-speed tensile tests on a polypropylene material, Polymer Testing, Volume 29, Issue 6, 2010, pp. 685-692.
2. A.F. Epee; F. Lauro; B. Bennani; B. Bourel. Constitutive model for a semi-crystalline polymer under dynamic loading, International Journal of Solids and Structures, Volume 48, Issue 10, 2011, pp. 1590-1599.
3. B. Jiang; L. Cao; F. Zhu. Dynamic tensile behavior of polypropylene with temperature effect, Composites Part B: Engineering, Volume 152, 2018, pp. 300-304.
4. S. Fu; Y. Wang; Y. Wang. Tension testing of polycarbonate at high strain rates, Polymer Testing, Volume 28, Issue 7, 2009, pp. 724-729.
5. J.T. Fan; J. Weerheijm; L.J. Sluys. Dynamic compressive mechanical response of a soft polymer material, Materials & Design, Volume 79, 2015, pp. 73-85.
6. W. Chen; F. Lu; M. Cheng. Tension and compression tests of two polymers under quasi-static and dynamic loading, Polymer Testing, Volume 21, Issue 2, 2002, pp. 113-121.
7. Y.G. Miao et al. Determination of dynamic elastic modulus of polymeric materials using vertical split Hopkinson pressure bar, International Journal of Mechanical Sciences, Volumes 108–109, 2016, pp. 188-196.
8. P.A. Du Bois et al. Material behavior of polymers under impact loading, International Journal of Impact Engineering, Volume 32, Issue 5, 2006, pp. 725-740.
9. K. Deshmukh et al. Chapter 4 - Mechanical analysis of polymers, Polymer Science and Innovative Applications, Elsevier, 2020, pp. 117-152.
10. C. Bonten. 3 - Plastics Materials Engineering, Plastics Technology, Hanser, 2019, pp. 63-246.
11. S. E. M. Selke et al. 4 - Major Plastics in Packaging, Plastics Packaging (Fourth Edition), Hanser, 2021, pp. 105-164.

TECHNICKÁ UNIVERZITA V KOŠICIACH
Strojnícka fakulta

Uncertainty of roughness parameters

Katarína Paľová [1], Ivana Koláriková [2] Ondrej Benedik [3] and Tatiana Kelemenová [4,*]

[1] Technical University of Kosice, Faculty of Mechanical Engineering; katarina.palova@tuke.sk
[2] Technical University of Kosice, Faculty of Mechanical Engineering; ivana.kolarikova@tuke.sk
[3] Technical University of Kosice, Faculty of Mechanical Engineering; ondrej.benedik@tuke.sk
[4] Technical University of Kosice, Faculty of Mechanical Engineering; tatiana.kelemenova@tuke.sk
* Correspondence: tatiana.kelemenova@tuke.sk; Tel.: +421 55 6022361

Abstract: The article deals with the measurement of surface roughness quantities, namely the mean arithmetic deviation of the surface roughness. An important task is also the determination of measurement uncertainty or determining the value of the mean arithmetic deviation of the surface roughness. Setting the measurement parameters and the measurement methodology itself is also a problem in the measurement process.

Keywords: roughness; measurement; uncertainty, deviation

1. Introduction

Measurement as a scientific activity is an important scientific tool in the identification, verification of properties and states of equipment. Correct handling of the preparation and evaluation of the measurement is as important as the measurement process itself. A poorly prepared measurement or a poorly evaluated measurement is worse than no measurement at all. Measurement results burdened with too large measurement errors and uncertainties degrade this entire process. If, on the basis of these devalued results, an intervention is subsequently carried out in the addressed system, it can have unforeseeable consequences with a huge social and economic impact.

Measurement uncertainties are an integral part of the measurement, so not paying any attention to them when balancing the measurement results would mean a total invalidation of the measurement result, as it would not be determined to what extent it is possible to trust the measurement result. Surface roughness is a surface property that is described by several surface roughness quantities. These quantities are characterized by a high degree of variability of the measured data. This article is focused on the arithmetic mean deviation of surface roughness Ra, which is the most frequently evaluated quantity of surface roughness [1-17].

2. Surface roughness – evaluation and standards

Surface roughness is a geometric property of the surface and there are no direct methods to measure it. The roughness of the surface has a decisive influence on the coefficient of friction of the contacting surfaces. Appropriate characteristics and parameters are usually measured, which are considered as surface roughness criteria. Surface roughness parameters are defined in standards ISO 21920-2:2021 [18] and EN ISO 5436 [19].

Surface texture or the basic surface profile is divided into two components according to the spacing of the respective irregularities, namely the component with the smallest spacing forming the surface roughness profile and the component with the largest spacing of irregularities determined by the basic profile, namely the waviness profile. The basic profile is the complete profile before the application of the short-wave filter (the filter defining the interface between roughness and waviness present on the examined surface).

The basic profile represents the basis for numerical processing of the profile using profile filters and for the calculation of profile parameters.

Waviness profile – as a profile derived by sequentially applying filters (a filter defining the interface between waviness and longer wave components present on the surface) and profile filters to the base profile.

The evaluated length is the length in the direction of the y axis used to assess the evaluated profile. The evaluated length can contain one or more basic lengths.

The profile filter is a tool for dividing the profile into long-wave and short-wave components. The filtration process is carried out in several stages, providing modified profiles.

The basis for measuring surface roughness parameters and characteristics is the unit of length, defined in ENISO standards [18, 19] and realized by a set of micro-length etalons (line depth and line spacing), the conventional true value of line depth is measured by wavelength (on the device – interference microscopes), these etalons are for the area of surface roughness measurement by primary standards.

Secondary standards (Fig. 1) are sets of standards that embody the values of roughness parameters – *Ra*, *Rz* and others. They are used for the calibration of operating meters by the direct measurement method, where a measured standard of the same nominal value is directly calibrated using standard measures.

Figure 1. Secondary standards of surface roughness.

For the practical determination of surface roughness characteristic values, there are a number of methods, the most perfect of which so far is the touch method, which uses a sharp tip that moves over the surface and allows to obtain information about its profile (Fig. 2).

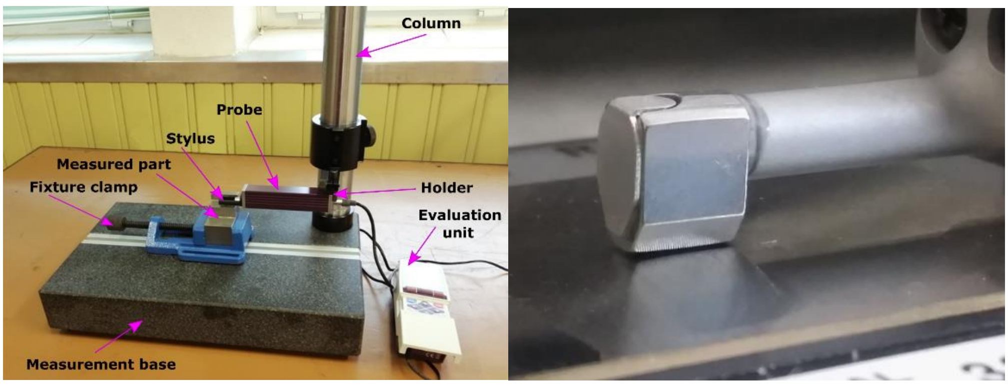

Figure 2. Surface profile sensing method.

Just like the others, the touch method encounters a whole range of limiting factors, which mostly result from the requirements of its specific implementation. Sometimes there are conflicting requirements that require a compromise solution. This method makes it possible to determine the numerical values of normalized and non-normalized characteristics of surface roughness and then to use it for the most modern statistical and spectral assessment of surface unevenness. The implementation of this method is ensured by a touch profilometer, which consists of a mechanical and an electronic part. The measuring chain of the touch profilometer is shown in fig. 2. The mechanical deflection generated by the sensing tip, which monitors the surface irregularities of the measured surface, is transformed into an electrical signal in the inductive position transducer, which is further processed and interpreted as a numerical value of the selected surface roughness characteristic, or as a graphic record of the surface unevenness profile. The sensing system, with its properties, affects the obtained profile.

The roughness values are precisely defined in the standard, but obtaining the correct value of these values by measurement depends on the correct choice of measurement parameters. These include Cut-off filter settings, Evaluation standard, number of base lengths and measurement speed.

The actual measurement of the surface structure usually takes only a few seconds. (Measurement time is determined by feed speed and measured length.) The measurement preparation time is considerably longer. This involves setting the sensor on the measured surface, setting the starting position of the measurement by mechanically moving the sensor in the vertical direction and electrical balancing. To this must be added the time required to obtain a record with the numerical values of the measured parameters, or a graphic record of the profile or graph of some two-dimensional parameters.

An unspecified (due to commercial reasons) stylus-based surface roughness tester was used for experimental measurements. The device allows you to set four different values of the cut-off filter parameter (0.08 mm; 0.25 mm; 0.8 mm; 2.5 mm). However, the manufacturer of the surface tester does not define the maximum permissible error or measurement uncertainty, so it is necessary to determine this uncertainty in some way for measurement purposes.

The surface tester used has a manufacturer-defined resolution for the Z-axis, i.e. for measuring height characteristics with a value of 0.02 μm. This data applies to the largest measurement range that this device has available. Since the device has an automatic selection of the measurement range, for reporting measurement uncertainty we will consider this resolution value as a potential source of measurement uncertainty.

The resolution is not defined for the X-axis, but this data can be determined from the sampling that the device performs at individual settings.

This device for evaluating individual quantities uses the course of the surface roughness profile curve with resolution values for individual measurement axes (X-axis in the horizontal plane and Z-axis in the vertical plane). These are longitudinal measurements, from which the values of individual surface roughness values are then indirectly determined by calculation in accordance with the relevant standards. And so determining the measurement uncertainty for *Ra*, for example, is a rather complicated task beyond the scope of this article. In this article, we will attempt at least an approximate estimation of the measurement uncertainty, because in our opinion, each measurement must have an associated measurement uncertainty in order to be able to evaluate the reliability of the mentioned experimental measurements [20-23].

Therefore, if we consider the differences for measurement in both directions as a significant source of uncertainty, then we can state them as the standard uncertainty determined by method B:

$$u_{BX} = 1.5\ \mu\text{m}. \tag{1}$$

$$u_{BZ} = 0.02\ \mu\text{m}. \tag{2}$$

If we consider that the digital device and the measured quantities follow the uniform distribution law of random values, then we will consider the extended measurement uncertainty with a coverage coefficient with a value of √3 at the significance level of 0.95. Then we will consider the expanded uncertainties of the displacement measurement:

$$u_{BX} = u_{BX} \cdot k_{\mathrm{cov}} = 2.6\,\mu\mathrm{m}. \quad (3)$$

$$u_{BZ} = u_{BZ} \cdot k_{\mathrm{cov}} = 0.035\,\mu\mathrm{m}. \quad (4)$$

It should be emphasized that this is only a very rough estimate, and for a more precise determination of the measurement uncertainty, it is also necessary to consider the uncertainty resulting from the geometry of the measuring tip, the uncertainty resulting from its elastic deformation during measurement, the uncertainty resulting from lateral movements during measurement, the uncertainty resulting from the noise of the device. It is very complicated to identify all components of measurement uncertainty when using such a complex device.

Used surface tester has the function of automatic calibration using Secondary Surface Roughness Standards. Secondary Surface Roughness Standards for surface roughness testers, which is a calibration etalon artefact with unidirectional irregular profile of type D1 (according to ISO 5436-1:2000) [19], is recommended for the calibration of the gauge. For this artefact, the value of *Ra* and *Rz* is defined. In this work, this function is used, and the calibration process is started before each batch of measurements, and after the calibrations, a control measurement was always carried out to verify the calibration process. Likewise, at the end of the measuring dose, a control measurement was carried out to verify the stability of the surface tester calibration. Secondary Surface Roughness Standards for surface roughness testers (Fig. 2) was verified by a superior standard in a certified laboratory and the uncertainty of this used calibration specimen was determined (Fig. 3).

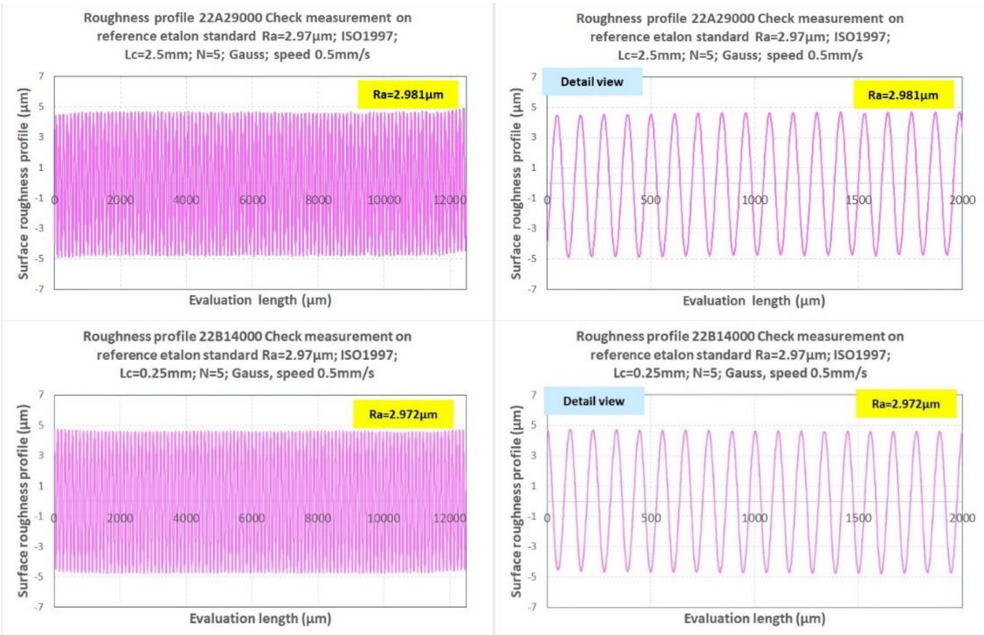

Figure 3. Verification measurements after surface tester calibration.

One way to determine the measurement uncertainty is to look at the gauge as a black box and determine the measurement uncertainty from the statistical evaluation of the data measured on the Secondary Surface Roughness Standards. For this purpose, 100 measurements were carried out at the same place under unchanged measurement conditions on the Secondary Surface Roughness Standard (measured to the standard - ISO1997 [18]; velocity 0.25 mm/s; Cut-off *Lc*=2.5 mm; number of measured lengths *X*=5; Filter - Gauss). From the measured values, histograms of the frequency of individual intervals of arithmetic mean height of the roughness and standard deviations of the measurement were created.

The measurement graph (Fig. 4) shows the variability and range of measured values of the quantity - *Ra* for measurement under the same conditions. From these data, it is possible to create a histogram of the frequency of individual measured data (Fig. 5), from which the nature of the distribution of the measured data is visible, so in further considerations we will assume a uniform law of distribution of the measured data.

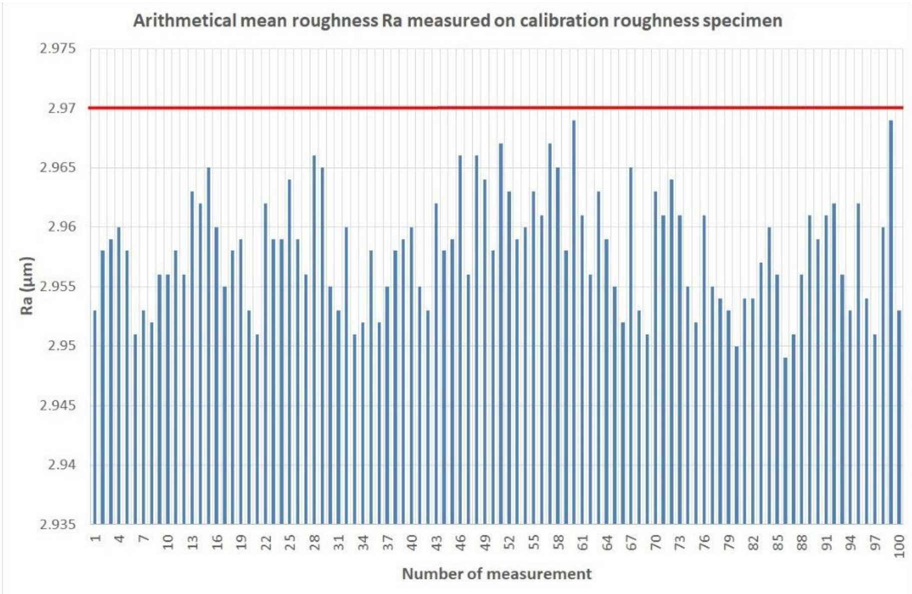

Figure 4. Arithmetical mean height of the roughness Ra values for 100 measurements at the same place under unchanged conditions (measured on Standard - ISO1997 [18]; 0.25 mm/s; *Lc*=0.8; *X*=5; Gauss).

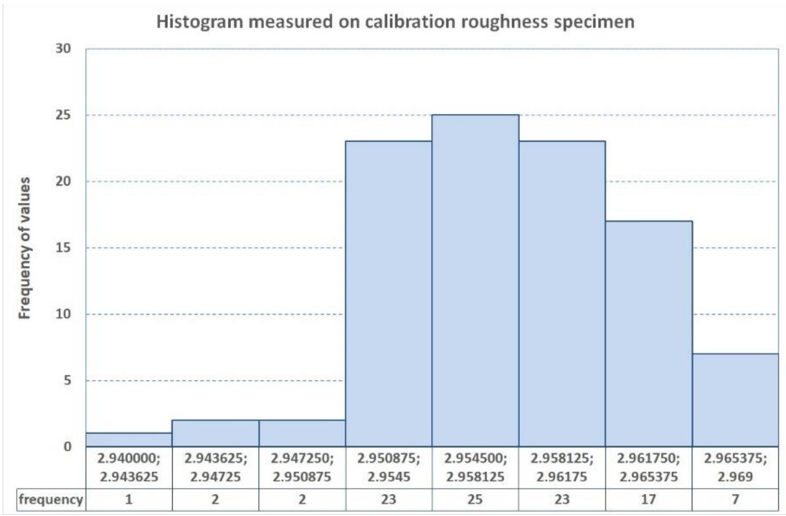

Figure 5. Histogram for values of arithmetic mean height of the roughness *Ra* for 100 measurements at the same place under unchanged conditions.

To assess the number of measurements as an indicator, it will be appropriate to use the standard deviation of a series of measurements. Its value depends on the dispersion of the evaluated values around the mean value. And so the smaller the standard deviation, the smaller the dispersion of the data. The evaluation of the standard deviation is therefore carried out in such a way that the standard deviation of a series of measurements is gradually determined, which is recalculated after the addition of each additional measurement, so we designated it as the cumulative standard deviation (Fig. 6). At the moment when the cumulative standard deviation stops changing, it means that the number of evaluated values has been reached, which will no longer improve the uncertainty of the measurement result. At the same time, these standard deviations give us the answer to the course of the standard deviation with the increasing number of measurements, and thus it is possible to obtain the maximum standard deviation of a series of measurements (Fig. 6).

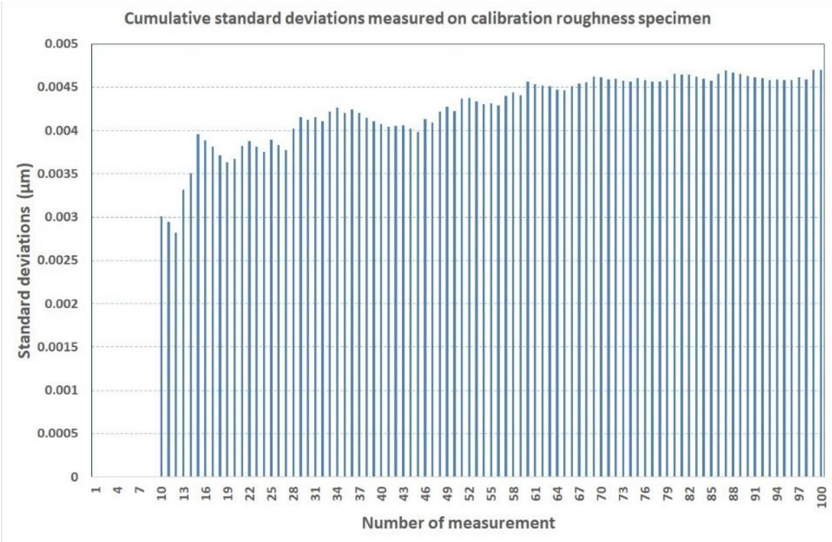

Figure 6. Cumulative standard deviations for 100 measurements at the same place under unchanged conditions (measured to standard - ISO1997 [18]; 0.25 mm/s; Lc=2.5 mm; X=5; Gauss).

5. Conclusions

From the stated values of standard deviations, it is possible to consider the maximum value *Zmax* = 0.005 µm for the standard uncertainty of measurement and evaluation of the quantity Ra for this device. However, the Secondary Surface Roughness Standard itself also contributes to this uncertainty. However, this uncertainty is still very small. This means that the device itself will not show a large measurement uncertainty, and the dispersion of the measured data will rather be related to the dispersion of values as a result of the implemented technology for the surface treatment of the component.

Acknowledgments: The authors would like to thank the Slovak Grant Agency - project VEGA 1/0191/24 and project KEGA 004TUKE-4/2024.

Conflicts of Interest: The authors declare no conflict of interest.

References

1. Kumar, S.P.L. Measurement and uncertainty analysis of surface roughness and material removal rate in micro turning operation and process parameters optimization. Measurement 2019, 140, 538–547. https://doi.org/10.1016/j.measurement.2019.04.029.
2. Beňo, J.; Maňková, I.; Vrabel, M.; Kottfer, D. Roughness measurement methodology for selection of tool inserts. Measurement 2013, 46, 582–592. https://doi.org/10.1016/j.measurement.2012.08.017.
3. Davinci, M.A.; Parthasarathi, N.L.; Borah, U.; Albert, S.K. Effect of the tracing speed and span on roughness parameters determined by stylus type equipment. Measurement 2014, 48, 368–377. https://doi.org/10.1016/j.measurement.2013.11.023.
4. Bhushan, B. Chapter: Surface Roughness Analysis and Measurement Techniques. In Modern Tribology Handbook, Two Volume Set, 1st ed.; CRC Press: Boca Raton, FL, USA, 2000; 1760p, ISBN 9780429126727. https://doi.org/10.1201/9780849377877.
5. Whitehouse, D.J. Surfaces and Their Measurement, 1st ed.; Butterworth-Heinemann: Oxford, UK, 2004; 432p, ISBN 9781903996607.
6. Leach, R. The Measurement of Surface Texture Using Stylus Instruments; NPL National Physical Laboratory, HMSO: Teddington, UK, July 2001.

7. Poon, C.Y.; Bhushan, B. Comparison of surface roughness measurements by stylus profiler, AFM and non-contact optical profiler. Wear 1995, 190, 76–88. https://doi.org/10.1016/0043-1648(95)06697-7.
8. Jester, W.; Klik, A. Soil surface roughness measurement—Methods, applicability, and surface representation. Catena 2005, 64, 174–192. https://doi.org/10.1016/j.catena.2005.08.005.
9. Stout, K.J. Surface roughness ~ measurement, interpretation and significance of data. Mater. Des. 1981, 2, 260–265. https://doi.org/10.1016/0261-3069(81)90069-8.
10. Verheijen, E. A survey on roughness measurements. J. Sound Vib. 2006, 293, 784–794. https://doi.org/10.1016/j.jsv.2005.08.047.
11. Chang, W.-R.; Kim, I.-J.; Manning, D.P.; Bunterngchit, Y. The role of surface roughness in the measurement of slipperiness. Ergonomics 2001, 44, 1200–1216. https://doi.org/10.1080/00140130110085565.
12. Whitehouse, D.J. Surface Characterization and Roughness Measurement in Engineering. In Photomechanics; Rastogi, P.K., Ed.; Topics in Applied Physics; Springer: Berlin/Heidelberg, Germany, 2000; Volume 77. https://doi.org/10.1007/3-540-48800-6_12.
13. Wieczorowski, M.; Cellary, A.; Majchrowski, R. The analysis of credibility and reproducibility of surface roughness measurement results. Wear 2010, 269, 480–484. https://doi.org/10.1016/j.wear.2010.05.003.
14. Farkas, G.; Drégelyi-Kiss, Á. Measurement uncertainty of surface roughness measurement. In Proceedings of the IOP Conference Series: Materials Science and Engineering, Volume 448, XXIII International Conference on Manufacturing (Manufacturing 2018), Kecskemét, Hungary, 7–8 June 2018; pp. 1–10. https://doi.org/10.1088/1757-899X/448/1/012020.
15. Rodriguez, F.V.; Sukumaran, J.; Ando, M.; De Baets, P. Roughness measurement problems in tribological testing. In Proceedings of the Sustainable Construction and Design 2011 (SCAD), Ghent, Belgium, 16–17 February 2011; Laboratory Soete, Ghent University: Ghent, Belgium, 2011; Volume 2, pp. 115–121.
16. Fedotkin, A.Y.; Akimchenko, I.O.; Tran, T.-H.; Shugurov, A.R.; Shesterikov, E.V.; Kozelskaya, A.I.; Rutkowski, S.; Tverdokhlebov, S.I. Improvement of the Surface Properties of Polyether Ether Ketone via Arc Evaporation for Biomedical Applications. Materials 2023, 16, 2990. https://doi.org/10.3390/ma16082990.
17. Podulka, P.; Macek, W.; Branco, R.; Nejad, R.M. Reduction in Errors in Roughness Evaluation with an Accurate Definition of the S-L Surface. Materials 2023, 16, 1865. https://doi.org/10.3390/ma16051865.
18. ISO 21920-2:2021; Geometrical Product Specifications (GPS)—Surface Texture: Profile—Part 2: Terms, Definitions and Surface Texture Parameters. European Committee for Standardization: Brussels, Belgium, December 2021.
19. ISO 5436-1:2000 Geometrical Product Specifications (GPS) — Surface texture: Profile method; Measurement standards — Part 1: Material measures. European Committee for Standardization. Brussels. March 2000.
20. Taylor, B.N. and Kuyatt, C.E., 1994, Guidelines for Evaluating and Expressing the Uncertainty of NIST Measurement Results, NIST Technical Note 1297.
21. [EA-4/02 1999] Expression of the Uncertainty of Measurement in Calibration. European co-operation Accreditation Publication Reference. December 1999.
22. [JCGM 100 2008] JCGM 100 – Evaluation of measurement data – Guide to the expression of uncertainty in measurement (ISO/IEC Guide 98-3). First edition September 2008. Available online: http://www.iso.org/sites/JCGM/GUM-JCGM100.htm.
23. [JCGM 104 2009] Evaluation of measurement data – An introduction to the "Guide to the expression of uncertainty in measurement" (ISO/IEC Guide 98-1). First edition July 2009. Available online: http://www.bipm.org/en/publications/guides/gum_print.html.

TECHNICKÁ UNIVERZITA V KOŠICIACH
Strojnícka fakulta

Analysis of selected psychoacoustic parameters in car interiors with binaural measuring equipment

Kristián Pástor [1,*] and Miroslav Badida [2]

[1] kristian.pastor@tuke.sk [2] miroslav.badida@tuke.sk
* Correspondence: kristian.pastor@tuke.sk; Tel.: 055 602 2721

Abstract: This article presents the results of the comparison of psychoacoustic parameters and sound pressure levels in the interior of hybrid and electric vehicles. The measurements were carried out using a binaural measuring device at vehicle speeds of 30 km/h, 50 km/h, 90 km/h and 130 km/h.

Keywords: hybrid vehicle; electric vehicle; psychoacoustics; sound quality;

1. Introduction

The basic concept of sound quality is the determination of human perception and was proposed by Blauert in 1994.[1] The character of the sound, which is related to how the sound is perceived by listeners, is called sound quality, which has played a large role in determining the satisfaction of listeners and customers. With the development of noise control technologies, sound quality research, which focuses on how people recognize, evaluate, and perceive sound, has gained attention, particularly in the automotive, transportation, and electrical appliance industries worldwide. [2][3]

Kousuke Noumura and Junji Yoshida talk about sound quality as an important factor that affects sales and customer interest. In the article Modeling the perception and quantifying the sound quality in the cabin, they write that to increase the overall marketability of the car, it is necessary to improve the sound quality. In this article, they talk about sensory evaluation tests performed on local residents in the USA, Germany, and Japan, and analyze the perception of vehicle interior sounds. [4]

But the psychoacoustic investigation of sound quality in the automotive industry concerns practically all sounds present in the acoustic environment of the vehicle, such as the sound of the door closing, the sound of the starter, engine noise, tire noise, wind noise, the sound of power windows, the noise of the air conditioning system and the sound produced by the car radio. [5]

Etienne Parizet, Erald Guyader and Valery Nosulenko focused on the sound of the door closing in the article Analysis of the quality of the sound of the car door closing. They analyzed the perception of the sound of a car door closing, focusing on the image of car quality that the listener might have in mind with this sound. [6]

2. Psychoacoustic measurements

Psychoacoustic sound quality based on the evaluation of binaural recordings is done using special measuring devices. These devices are called artificial heads and the subsequent software evaluation of the audio signal leads to the determination of various psychoacoustic parameters (sharpness, harshness, fluctuation, tonality, etc.). Sound recordings captured by conventional microphones are not suitable for accurate assessment of the acoustic environment and noise sources, as important acoustic information such as spatial and directional distribution of noise sources, masking effects, selective hearing, etc. is lost. Perceiving sound through two ears is called binaural hearing. It is the ability to hear sounds from the left ear and the right ear in parallel and the ability to locate the direction of the incoming sound. This type of hearing strongly depends on the geometric parameters of the human body (ears, head and trunk).

Binaural perception cannot be simulated simply by using two microphones. Such recordings can only be used after applying an acoustic filter that takes into account the characteristics and geometry of the human head, ears and shoulders. The artificial head is a simulation of the human head and shoulders, not only in terms of shape, but also in surface properties that correspond to the properties of human skin. This form of artificial head makes it possible to modify the sound field as in reality and thus recognize the differences like the human ear [7]. Microphones are placed in the ear, which are used to record sound signals. The artificial head enables the recording and subsequent playback of sounds as if listener was at the place where the artificial head is placed at the time of the measurement.

Various feelings or perceptions can be displayed using psychoacoustic parameters of perception, as well as using auditory thresholds of perception, which can be determined using psychoacoustic methods. Psychoacoustic parameters such as roughness, loudness, tonality, sharpness and fluctuation of strength are referred to as "classical" psychoacoustic parameters. Other parameters related to hearing are also known, such as height, color, subjective duration and others. [8][9]

3. Experimental measurements

The aim of the measurements carried out using a binaural measuring device, the so-called psychoacoustic head, was to determine the values of selected psychoacoustic parameters under conditions of different car speeds. The subjects of the research were Toyota Rav4 hybrid and Škoda Enyaq iv (Figure 1).

(a)

(b)

Figure 1. (a) Toyota Rav4 hybrid, (b) Škoda Enyaq iv

The psychoacoustic head was placed in the interior of the vehicle in the position of the passenger on the front seat. The location of the psychoacoustic head in the test vehicle is shown in Figure 2.

(a) (b)

Figure 2. Placement of the psychoacoustic head in vehicles, (a) Toyota Rav4 hybrid, (b) Škoda Enyaq iv

Measurements were performed at speeds of 30 km/h, 50 km/h, 90 km/h and 130 km/h. The section of the road where the measurements were taken is shown in Figure 3.

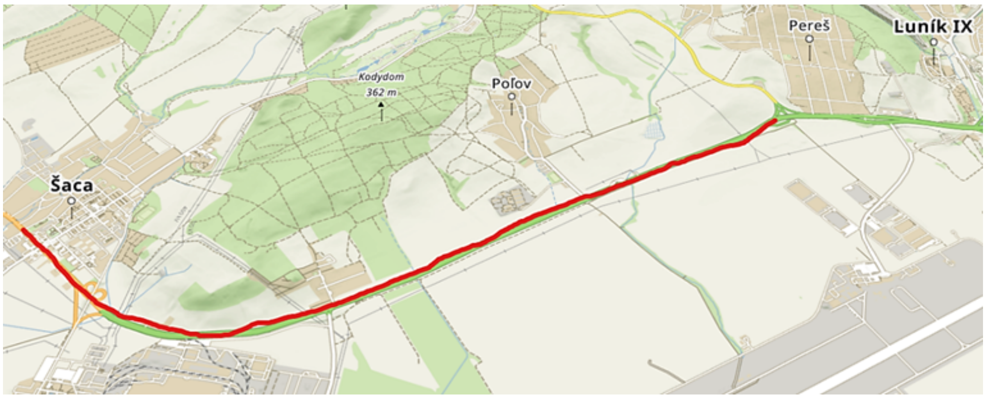

Figure 3. The section of the road where the measurements were taken

4. Measurement results

In Table 1, we can see a comparison of the sound pressure levels of both vehicles. A graphical comparison can be seen in figure 4. From the results we can see that, as expected, the electric vehicle achieved lower sound pressure values at all speeds. However, we can also see that the difference in these values decreases with increasing speed and at a speed of 130 km/h this difference is minimal.

Table 1. Sound pressure levels

Sound pressure values					
Speed	Microphone	Toyota Rav4 Hybrid		Škoda Enyaq iv	
			Average L-R		Average L-R
30 km/h	Left mic.	82,32	82,435	77,7	78,67
30 km/h	Right mic.	82,55		79,7	
50 km/h	Left mic.	83,28	83,19	77,4	78,01
50 km/h	Right mic.	83,1		78,7	
90 km/h	Left mic.	87,61	87,595	82,2	82,87
90 km/h	Right mic.	87,58		83,5	
130 km/h	Left mic.	91,9	91,975	90,6	90,89
130 km/h	Right mic.	92,05		91,2	

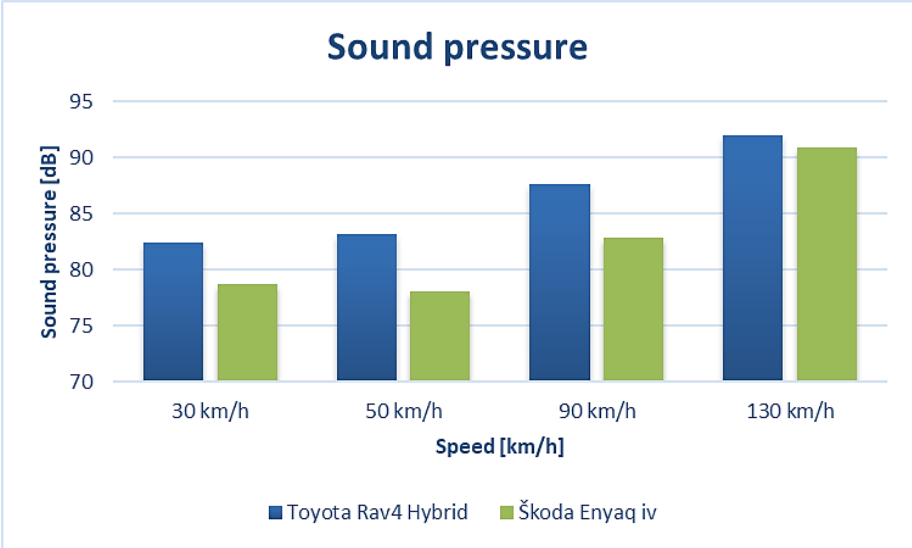

Figure 4. Graphical comparison of sound pressure levels

In Table 2 and Table 3, we can see the values of other examined psychoacoustic parameters. We can see the difference in the values for the left and right ear in the psychoacoustic parameter values but also in the sound pressure level values (Table 1). These differences can be caused by the placement of the psychoacoustic head in the vehicle, when one ear is closer to the surrounding environment and the other to the interior.

Table 2. Values of psychoacoustic parameters for Toyota Rav4 Hybrid

Toyota Rav4 Hybrid											
Speed	Microphone	Fluctuation Strength		Loudness		Roughness		Sharpness		Tonality	
			Average L-R		Average L-R		Average L-R		Average L-R		Average L-R
30 km/h	Left mic.	0,023	0,0235	8,34	8,915	0,0238	0,02505	0,614	0,5855	0,188	0,254
30 km/h	Right mic.	0,024		9,49		0,0263		0,557		0,32	
50 km/h	Left mic.	0,0221	0,0223	9,56	9,93	0,0272	0,0275	0,731	0,7335	0,173	0,1525
50 km/h	Right mic.	0,0225		10,3		0,0278		0,736		0,132	
90 km/h	Left mic.	0,0254	0,02555	16,6	17,6	0,0348	0,03585	1,13	1,145	0,085	0,11605
90 km/h	Right mic.	0,0257		18,6		0,0369		1,16		0,147	
130 km/h	Left mic.	0,0339	0,0333	28,2	29,4	0,0489	0,04955	1,41	1,435	0,095	0,1042
130 km/h	Right mic.	0,0327		30,6		0,0502		1,46		0,113	

Table 3. Values of psychoacoustic parameters for Škoda Enyaq iv

Škoda Enyaq iv											
Speed	Microphone	Fluctuation Strength		Loudness		Roughness		Sharpness		Tonality	
			Average L-R		Average L-R		Average L-R		Average L-R		Average L-R
30 km/h	Left mic.	0,0168	0,01845	7,9	8,415	0,0223	0,0238	0,783	0,769	0,633	0,6935
30 km/h	Right mic.	0,0201		8,93		0,0253		0,755		0,754	
50 km/h	Left mic.	0,0262	0,02725	8,03	8,465	0,0256	0,02775	0,831	0,8285	0,267	0,216
50 km/h	Right mic.	0,0283		8,9		0,0299		0,826		0,165	
90 km/h	Left mic.	0,0231	0,02435	14,8	15,55	0,0373	0,037	0,879	0,8895	0,333	0,2365
90 km/h	Right mic.	0,0256		16,3		0,0367		0,9		0,14	
130 km/h	Left mic.	0,0306	0,03105	23	24,05	0,0418	0,0431	1,24	1,27	0,295	0,2285
130 km/h	Right mic.	0,0315		25,1		0,0444		1,3		0,162	

A comparison of the average values of these parameters for both vehicles can be seen in the graphs in figure 5.

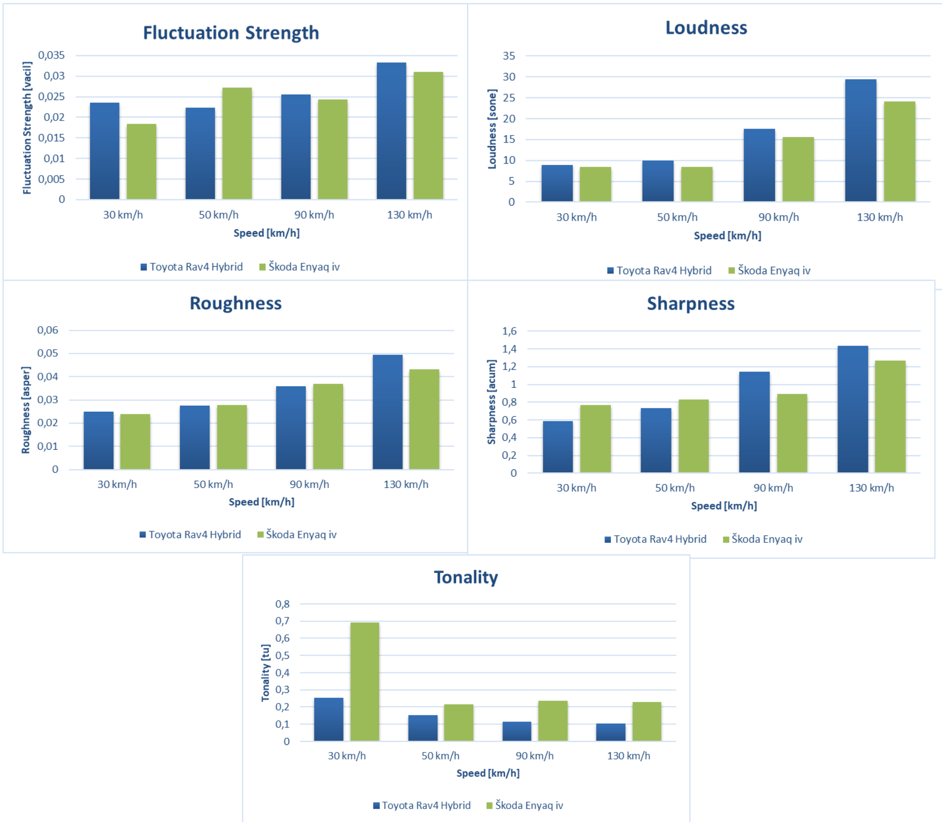

Figure 5. A comparison of the average values of psychoacoustic parameters

5. Conclusions

In this article, the results of the measurements of psychoacoustic parameters in the interior of a hybrid and electric vehicle were printed. During the experimental measurement, it was found that the psychoacoustic parameter values of the vehicles that were the subject of the research are affected by the speed of the vehicle. For most parameters, psychoacoustic parameter values increase with increasing speed. These values are also influenced by the location of the psychoacoustic head in the vehicle, when different values can be seen between the left and right ear. Also, when comparing both vehicles, we see that the electric vehicle reached lower values of both sound pressure and psychoacoustic parameters in most cases. However, this difference decreased until it was minimal for the acoustic pressure values with increasing speed. Also, the difference in the values of psychoacoustic parameters was small.

Acknowledgments: This contribution was created based on the solution of the project project KEGA 013TUKE-4/2022 and project VEGA 1-0485-2022.

References

1. Blauert J. Product-sound assessments: An enigmatic issue from the point of view of engineering. Proc internoise94, Yokohama, Japan, vol. 2; 1994. p. 857–62
1. Jekosch U. Meaning in the context of sound quality assessment. Acta Acustica 1999;85(5):681–4.
2. Jiguang J.; Yun L. Review of active noise control techniques with emphasis on sound quality enhancement, Applied Acoustics, Volume 136, 2018, Pages 139-148, ISSN 0003-682X, https://doi.org/10.1016/j.apacoust.2018.02.021.
2. Noumura K.; Junji Yoshida. Perception modeling and quantification of sound quality in cabin. SAE paper 2003;01:1514.
3. Miskiewicz A.; Letowski T. Psychoacoustics in the Automotive Industry, Acta Acustica United with Acustica, vol. 85, pp. 646 –649, Sept 1999.
4. Parizet E.; Guyader E. Valery Nosulenko. Analysis of car door closing sound quality. Applied Acoustics, Elsevier, 2008, 69, pp.12-22.
5. MORAVEC, M.; Sound quality subjective and objective assessment methods of domestic appliances: ANNALS of Faculty Engineering Hunedoara – International Journal of Engineering, 2019, p.91-94, ISSN 1584 – 2665
6. Badidová, A. 2011. Návrh metodiky posudzovania kvality zvuku v interiéri automobilu psychoakustickými metódami [Doctoral dissertation]. Košice: technická univerzita v Košiciach [s. n.], 2020. 187 p.
7. IPAR P.; et.al.: Psychoacoustic approach used for developing the model of sound pleasantness of vacuum cleaners and suction units based on objective and subjective analysis. In: 5th Congress of Alps-Adria Acoustics Association, September 2012,

Design of the mobility subsystem of a service robot designed for a contaminated environment

Patrik Pilát [1], Jozef Varga [2], Matúš Sabol [1] and Ján Semjon [1]

[1] Department of Production Technology and Robotics; patrik.pilat@tuke.sk; matus.sabol@student.tuke.sk; jan.semjon@tuke.sk
[2] Prototyping and Innovation centre, Faculty of Mechanical Engineering; jozef.varga.2@tuke.sk
* Correspondence: patrik.pilat@tuke.sk; Tel.: +421908443216

Abstract: The article deals with the the design of a mobile platform for a service robot intended for cleaning contaminated areas within the hot gas chamber of a reactor at a nuclear power plant. The use of service robotics in such environments is crucial for preventing human exposure to hazardous conditions. The mobile platform, a core component of the service robot, must meet high standards of robustness due to the demanding application requirements. The specific task involves the decontamination of a hot gas chamber, necessitating advanced maneuverability and specialized cleaning tools, including a rotating cylinder brush and an end effector gripper. The design also incorporates considerations for radiation resistance, temperature conditions, and the mechanical layout, ensuring the robot can navigate and operate effectively within the confined and obstacle-laden chamber. The resulting design features a four-wheel chassis with a divided frame connected by a pivot pin, driven and steered by servo motors, and equipped with various cleaning apparatus to handle different types of contamination. This development highlights the intersection of mechatronics and service robotics, contributing to safer and more efficient operations in nuclear facilities.

Keywords: service robot, cleaning, mechatronic system.

1. Introduction

The nuclear reactor KS-150 which was deployed in Jaslovské Bohunice represents the beginning of Czechoslovak nuclear energy. Construction and commissioning represented a major challenge for the industry at the time. This HWGCR type reactor moderated by heavy water for natural metallic uranium cooled by gaseous CO_2 had an electrical output of 127 MW. This project was interesting mainly for the possibility of using the unenriched uranium mined in Czechoslovakia.

Construction began in 1958, and in October 1972, the first controlled chain reaction was carried out in the reactor of the A1 nuclear power plant. Subsequently, two accidents occurred during the operation of the A1 power plant.

The first accident happened on 5 January 1976. When the fuel assembly was fired from one channel of the reactor during fuel exchange operation. By the end of the year, the reactor was repaired and put into operation.

The second accident occurred shortly after re-commissioning, on 22 February 1977. This resulted in contamination of the primary and secondary circuits. This serious accident made it impossible to put it back into service. In 1979, the government decided to decommission the A1 power plant. According to the international seven-level scale INES (International nuclear and radiological events scale), this accident was evaluated as level 4. Block A1, which also includes a hot gas chamber, is currently being liquidated [1].

Before disposing of the hot gas chamber, it is necessary to remove contaminated sediments. This process is challenging in terms of chamber access and environmental conditions. To fulfill this task, the use of a mobile service robot (hereinafter referred to as MSR) is essential.

The International Atomic Energy Agency (IAEA) recommends the use of MSR in nuclear power plants, mainly because of the benefits that can be achieved with this application. Among the main benefits are the replacement of people in the performance of tasks in a dangerous environment, an increase in efficiency and overall safety, and at the same time cost reduction [2].

Today, there are many universal MSRs, but their universality is not sufficient in many respects. In this case, it is necessary to design our own solution that will be suitable in all aspects.

Current MSRs have common features in the design and concept of the solution. The overall concept is further divided into sub-systems. Individual systems are functionally and structurally connected. These subsystems include: mobility subsystem, action superstructure subsystem – modules, subsystem of internal sensors, subsystem of external sensors, control and navigation subsystem, operator subsystem and energy support subsystem [3][4].

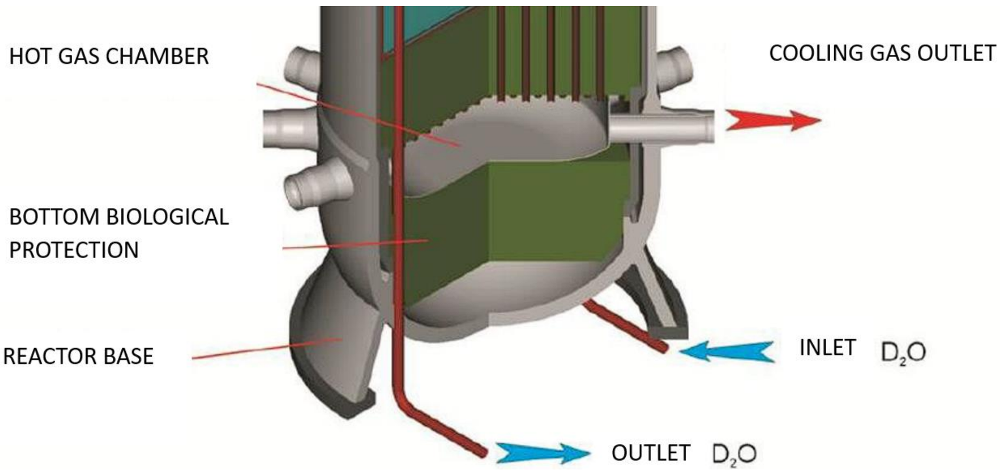

Figure 1. The lower part of the Czechoslovak heavy water reactor KS150.

2. Design of a mobility subsystem

The requirements for the mobility subsystem of the service robot are formulated by the environment in which it will be deployed and the service task it will perform.

The working environment of the MSR is represented by a hot gas chamber (Fig. 1). The lower part, that is, the bottom of the chamber, which is the object of cleaning, is turned at an angle of 34.2˚. The entrance to the chamber will be realized through the outlet of the cooling gas. This entry has a circular cross-section with a diameter 380 mm and length 8 m. Size of the MSR is limited by the diameter of the entry. Inside the hot gas chamber there are many obstacles in the hot gas chamber that the service robot must avoid, which increases the demands on its maneuverability.

In the area of the hot gas chamber, radiation is at the level of 2mSv/h. This data is key especially for the design of electronics. The temperature of the surrounding environment is approximately 20°C.

The task of the MSR is to decontaminate the hot gas chamber, three devices were designed for this purpose. The main cleaning tool will be a rotating cylinder brush that will be located in the front part of the service robot. By rotating this brush, sediments will be released, which will then be sucked out through the hose. This tool will be used for cleaning large surfaces.

The second tool is the end effector - gripper, which is used for collecting large pieces of deposits (Fig. 2) that would not pass through the suction hose. With the help of a gripper, these pieces will be placed in a removable container, which will be placed on the chassis. The third tool is a ball brush which is placed in a holder on the chassis. This brush represents a removable tool that can be grasped in the gripper. This tool will be used for cleaning hard-to-reach places where a rotary roller brush cannot reach.

Figure 2. Photo from the hot gas chamber of the KS 150 reactor.

Based on these facts, we will design of the chassis by choosing the servo motors that will ensure the movement of the MSR and the steering of the wheels. Subsequently, we will design the shape and material of the MSR wheels. Since the servo motors cannot be directly attached to the MSR frame, we will create motor mounts. The parts of the split front drive axle, so the left and right parts will be symmetrical, the same also applies to the rear drive steering axle. The front rigid axle will be anchored to the front of the frame and the rear steering axle will be attached to the rear of the split frame.

Servo motors are one of the most important parts of the chassis. For this reason, we use calculations according to which we determined output torque of the motors. Based on the calculated value we choose robot actuator. Robot actuator consists of frameless motor, high torque harmonic gearbox, encoder, brake and controller with canopen communication protocol. The torque from the robot actuator is transmitted to the wheels, which provide movement. The disc of these wheels will be made of aluminum. To enhance the traction of the robot, the circumference of the disc will be modified by applying a rubber coating. This layer will be applied to the aluminum disk through the vulcanization of the rubber compound.

The frame itself will consist of two parts that will be connected by a pivot pin. This solution results from the choice of chassis variant. The task of the frame is to connect all components and subsystems of MSR.

On one side, the pivot pin is stored in a hole that is part of the front part of the frame. The pin is inserted in a hole with a through fit and secured against movement with a lock nut. The second part of the frame is connected to the pivot pin by a bearing house that captures radial and axial forces. The pin against the bearing housing is secured by a locking screw.

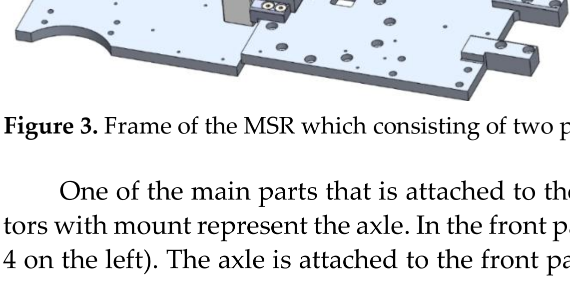

Figure 3. Frame of the MSR which consisting of two parts- bottom view.

One of the main parts that is attached to the frame are robot actuators. Robot actuators with mount represent the axle. In the front part of frame there is a split drive axle (Fig. 4 on the left). The axle is attached to the front part of the frame (Fig. 4 P4) using a mount

(Fig. 4 P3). Robot actuator (Fig. 4 P1), which rotates the wheel around the axis. The drive shaft has high strength in the radial and axial directions, therefore the wheel is attached directly to the motor shaft.

The rear split drive axle is also a directional axle, it is attached to the rear of the frame (Fig. 4 P4 on the right). Steering control is ensured by robot actuator (Fig. 4 P1) which rotates the wheel hinge (Fig. 4 P3). Robot actuator (Fig. 4 P2) which ensure wheel movements is attached to hinge (Fig. 4 P3). Turning the hinge around axis 2 provides steering control, turning the wheel around axis 1 provides movement.

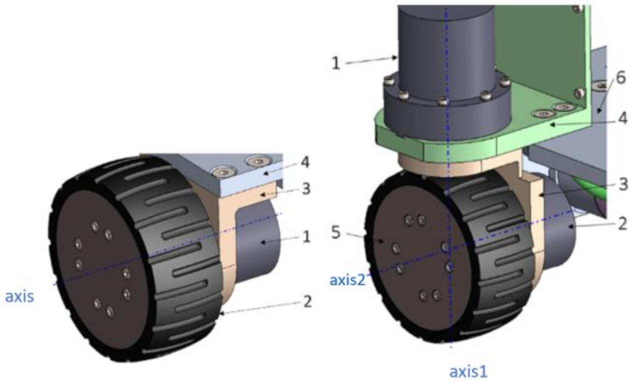

Figure 4. Split front drive axle pictured left, split rear drive axle with directional wheel pictured right.

By steering of rear wheel, we manage robot movement direction. By using a suitable way of steering, we prevent unwanted wheel slippage. In our case we will use Ackerman control which solves the difference in the steering angle of the directional wheels during movement. [3]

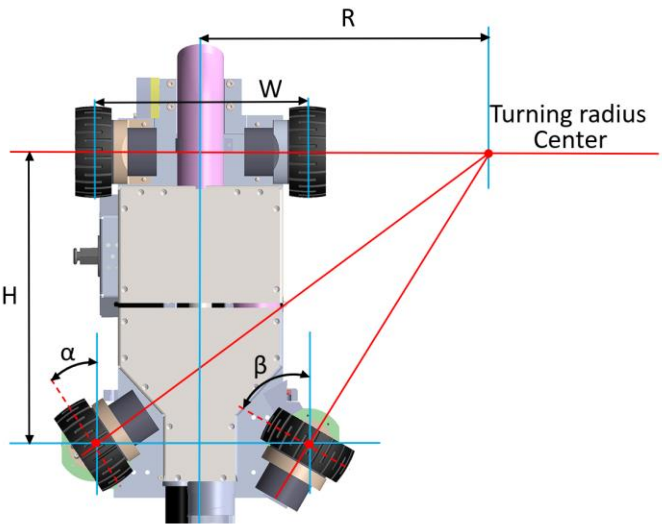

Figure 5. Rear axle steering

The individual steering angles can be expressed as:

$$= \arctan\left(\frac{}{+\ /2}\right) \tag{1}$$

$$= \arctan\left(\frac{}{-\ /2}\right) \tag{2}$$

The mobility subsystem serves as the base component of the entire MSR, to which other subsystems are connected. While the specifics of these subsystems are not detailed in this article, they are essential for consideration. For fixing of these subsystems, we modified the front and rear parts of the frame. Holes (Fig.6 P5) are intended for securing the front rotating cylindrical brush, while holes (Fig.6 P6) are designated for attaching the robotic arm. Removable container is located in the back of the MSR. A hose which is used for extracting deposits and transporting of contaminated waste outside the hot gas chamber is located inside the mobility subsystem. In the rear part, this hose connects to another one that goes outside the hot gas chamber (Fig.6 P9).

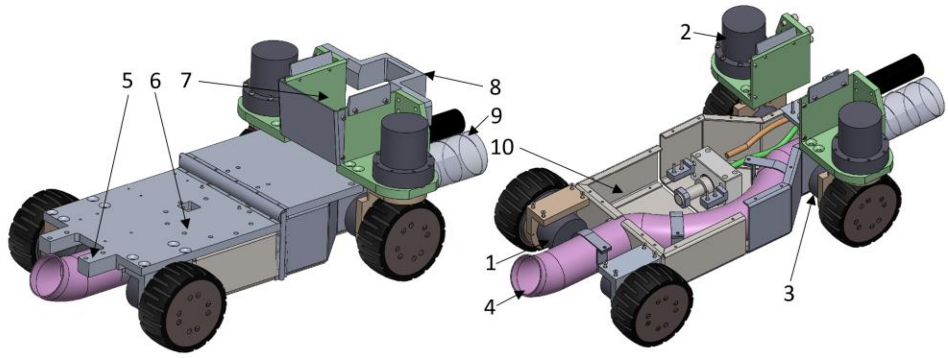

Figure 6. Three-dimensional model of the mobility subsystem

3. Conclusions

This article describes the design of a mobile platform of the for cleaning the contaminated space of the hot gas chamber. The result of this design is a four-wheel chassis whose frame is divided and connected by a pivot pin. All wheels are driven and steering control is provided by rear axle. The designed mobile platform will then be equipped with action superstructures: a robotic arm, a front brush and a removable container.

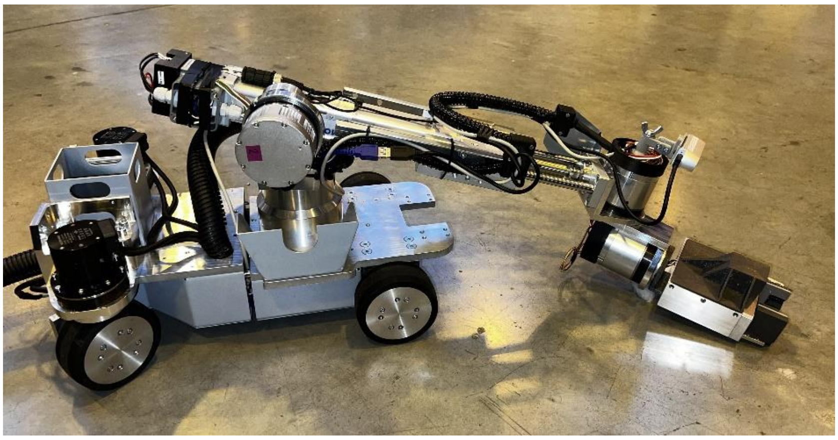

Figure 7. Mobility subsystem equipped with robotic arm and container.

Acknowledgments: This article was developed within the project KEGA: 020TUKE-4/2022 Development and implementation of new approaches in the teaching of industrial and collaborative robotics and the VEGA project: 1/0215/23 Research and development of robotic workplaces equipped with industrial and collaborative robots.

Conflicts of Interest: The authors do not declare any conflict of interest.

References

1. Kuruc, J.; Mátel, Ľ. *30. a 29. Výročie nehôd na reaktore jadrovej elektrárne A-1 Jaslovské Bohunice – rádioekologické a rádiobiologické následky*, https://inis.iaea.org/collection/NCLCollectionStore/_Public/37/110/37110257.pdf
2. Smith, R. J.; Cucco, E.; Fairbairn, C. Robotic Development for the Nuclear Environment: Challenges and Strategy, *Robotics 2020*, 9(4), 94; https://doi.org/10.3390/robotics9040094.
3. Smrček, J.; Kárník, L. *Robotika - servisné roboty. Navrhovanie, konštrukcia, riešenia*, Košice : Edícia vedeckej a odbornej literatúry - Strojnícka fakulta TU v Košiciach, 2008, 534 s., ISBN 80-7165-713-2.
4. Novák, P. *Mobilní roboty –pohony, sensory, řízení*, Praha: BEN - technická literatura, 256 s., ISBN 80-7300-141-1.
5. B.L. Luk, A.A. Collie, D.S. Cooke. Walking and climbing service robots for safeta inspection of nuclear reactor pressure vessels, https://journals.sagepub.com/doi/abs/10.1177/002029400603900201
6. Keiji Nagatani, Seiga Kiribayashi, Yoshito Okada, Kazuki Otake, Kazuya Yoshida, Takeshi Nishimura, Tomoaki Yoshida, Eiji Koyanagi. Emergency response to the nuclear accident at the Fukushima Daiichi Nuclear Power Plants using mobile rescue robots. https://onlinelibrary.wiley.com/doi/full/10.1002/rob.21439
7. Ata Jahangir Moshayedi, Atanu Shuvam Roy, Sithembiso Khaya Sambo, Yangwan Zhong, Liefa Liao. The Service Robot Mathematical Model. https://eudl.eu/pdf/10.4108/airo.v1i.20
8. Zhiping Liu, Yawen Wang. Trajectory Tracking of Mobile Service Robot. https://ieeexplore.ieee.org/stamp/stamp.jsp?tp=&arnumber=8833202

TECHNICKÁ UNIVERZITA V KOŠICIACH
Strojnícka fakulta

Modeling and 3D printing of scaffolds for tissue regeneration.

Piotr Szczygieł [1,*], Anna Kurowska[1], Adam Jabłoński [1] and Izabella Rajzer [1]

[1] Department of Mechanical Engineering Fundamentals, University of Bielsko-Biala, Willowa 2, 43-309 Bielsko-Biala, Poland
* Correspondence: ps000011@student.ubb.edu.pl

Abstract: Preparation and usage of scaffolds for tissue regeneration requires thorough knowledge of medical and biomaterial aspects. However, deep understanding of manufacturing process itself is also required to create an object, whose physicochemical parameters will correspond to creators' plans. It is therefore necessary to understand each step of manufacturing process, starting from the 3D modelling phase, to model conversion to G-code, which will eventually be used by 3D printer to create an object. During this process, unintended complications may occur that will affect the final result of the work, e.g. deterioration of mechanical parameters. Such problems might be solved either by preparing 3D model in a specific way, or by modification of printing parameters.

Keywords: 3D printing; 3D modelling; scaffold; tissue regeneration

1. Introduction

Tissue repair is still a demanding task for surgeons across the world [1]. Even though medicine has advanced significantly over the years, it is still necessary to master the technology of tissue repair. Depending on location, the effect of the injury may have a negative impact on the patient's life due to visual changes, that are clearly visible to other people. One of such examples is osteochondral tissue of the nose [2]. Advancement in 3D printing technology and biomaterials is a promising step toward improvement of quality of life and broader access to implantation of 3D printed tissue replacement objects [3]. However, possibility of using such implants depends on many aspects, including 3D modeling, appropriate printer hardware and setting printing parameters, selection of appropriate biomaterials etc. This is therefore a complex task that requires knowledge of issues in the field of medicine, but also of mechanical and materials engineering [4].

The main purpose of this work was to make scaffolds, that in the future could be used for tissue regeneration. Based on previous researches [2], an attempt was made to create scaffold with gradient structure, which would allow proper cell proliferation of different types.

2. Materials and Methods

For purpose of this research, FDM printing technique was used. Modeling of 3D scaffolds were performed using SolidWorks 2021 software, and complete models were exported as .STL files. Prusa Slicer software, which is dedicated for Prusa 3D printers was used to set all printing parameters, and to convert 3D objects into G-codes. Such G-code contains a set of instructions for 3D printer, on how to create an object. VarioStick [5] filament, which was made of Polycaprolactone (PCL, Sigma-Aldrich, Mw 80 kDa), was used for printing. Prusa i3 MK3S printer was used, with 0.25 mm nozzle diameter. For inspection and dimensions verification, optical microscope was used.

3. Results

Structure of scaffold was based on previous research carried out at the university, but was modified so that scaffold would allow proper regeneration of two types of tissues: bone and cartilage, that make up the human nose. These two types of tissues are characterized by different size of cells, and therefore different type of scaffold porosity is required to allow appropriate cells proliferation [6]. 3D model of scaffold was shown on Figure 1a, and dimensions of pores were shown on Figure 1b.

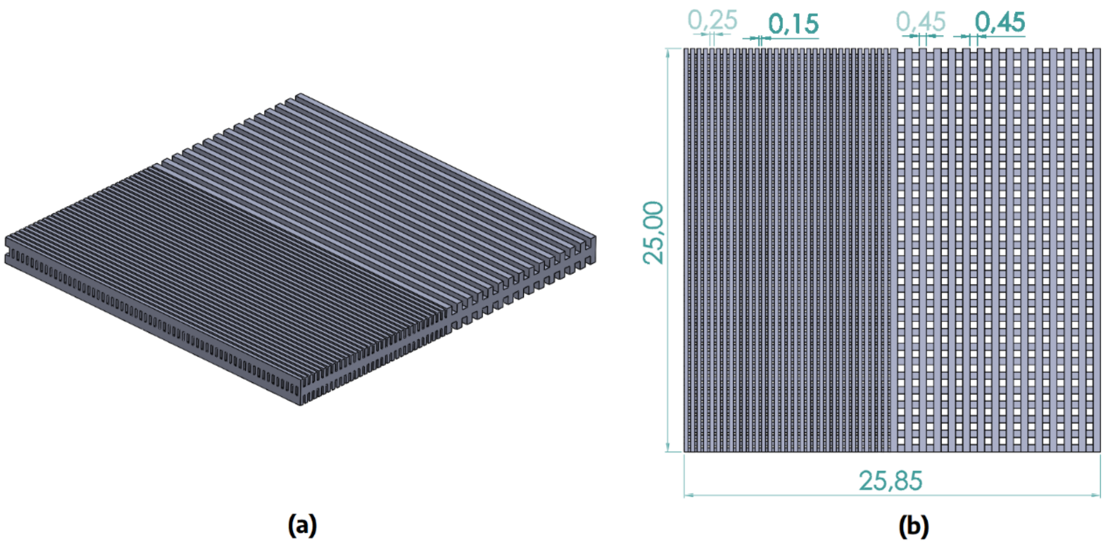

Figure 1. 3D model of scaffold with gradient structure: **(a)** isometric view; **(b)** dimensioned model.

Overall height of scaffold is 1.80 mm and consists of 3 layers. Compared to default printing settings, some parameters were changed. Optimization was necessary due to usage of filament made of PCL, which is more difficult to process with 3D printer, than rigid plastics like ABS. Such material is more flexible and rubber-like, causing extruder to jam, eg. while printing too fast.

When scaffold was printed, observations were made to verify, whether the dimensions are consistent with the model. Overall view of scaffold was shown on Figure 2a, and dimensions measured were shown on Figure 2b. The dimensions differ slightly, but the differences do not exceed a few percent of the model dimensions.

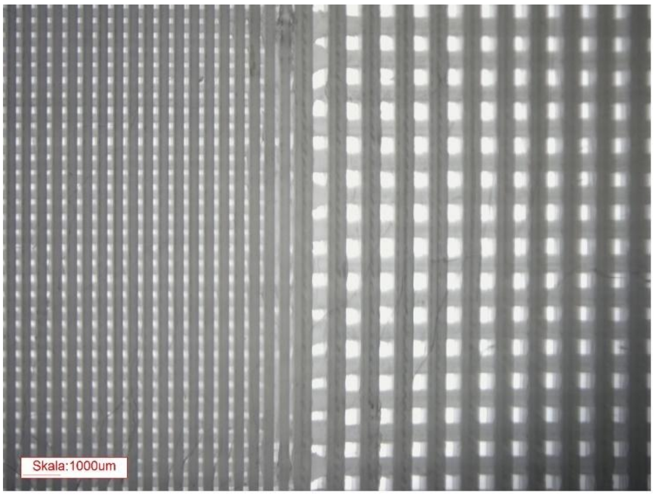

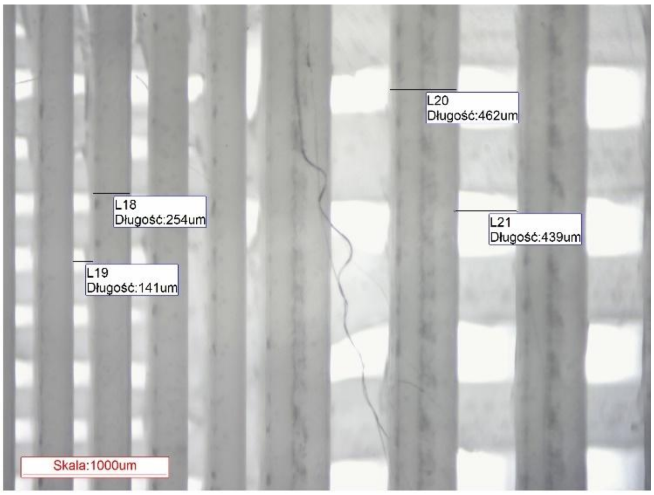

Figure 2. Pictures of scaffold taken with an optical microscope: (a) general view; (b) dimensioned side walls and gaps.

4. Discussion

3D model of scaffold with varying porosity was prepared and printed. Printing parameters optimization allowed to obtain object, whose dimensions are very close to prepared model. However printing of scaffolds with gradient structure causes additional issues, that did not occur while printing scaffolds with uniform structure. A place at the junction of two types of porosity deviates from the model, causing a deterioration of the mechanical properties at this place. This is the imperfection of transforming the 3D model into printer head movements. This issue could be resolved either by proper modeling of junction of two types of porosity, or by manually improving G-code. Further studies will be conducted to improve mechanical properties of gradient scaffolds, and to verify, which porosity structure will be appropriate in different cells proliferation process.

Acknowledgments: This work was supported by the National Science Centre, Poland in the frame of project: „3D and 4D printing of stimuli-responsive and functionally graded biomaterials for osteochondral defects regeneration", grant number: 2020/39/I/ST5/00569 (OPUS-LAP).

Conflicts of Interest: The authors declare no conflict of interest.

References

1. Mahyudin, F., Suroto, H. Tissue Bank and Tissue Engineering. Biomaterials and Medical Devices 2016, 58, DOI: 10.1007/978-3-319-14845-8_9
2. Rajzer I. et al. Biomaterials in the Reconstruction of Nasal Septum Perforation. The Annals of otology, rhinology, and laryngology 2020, 130 pp. 731–737, DOI: 10.1177/0003489420970589
3. Winarso R. et al. Application of fused deposition modeling (FDM) on bone scaffold manufacturing process: A review. Elsevier 2022, 8, DOI: https://doi.org/10.1016/j.heliyon.2022.e11701
4. Mohd Pu'ad N.A.S. et al. Review on the fabrication of fused deposition modelling (FDM) composite filament for biomedical applications. Materials Today: Proceedings 2020, vol. 29 part 1 pp. 228-232, DOI: https://doi.org/10.1016/j.matpr.2020.05.535
5. VarioStick project. Available online: https://variostick.pl/ (accessed on 15.12.2023)
6. Abbasi N., Hamlet S., Love R. M., Nguyen N. T. Porous scaffolds for bone regeneration. Journal of Science: Advanced Materials and Devices 2020, 5 pp.1-9, DOI: https://doi.org/10.1016/j.jsamd.2020.01.007

TECHNICKÁ UNIVERZITA V KOŠICIACH
Strojnícka fakulta

The relationship between psychological stress and musculoskeletal disorders

Denisa Porubčanová [1]*, Katarína Vaškovičová[2], Peter Darvaši[3] and Michaela Balážiková[4]

[1] Technical University of Košice, Faculty of Mechanical Engineering, Department of Safety and Quality; denisa.porubcanova@tuke.sk

[2] Technical University of Košice, Faculty of Mechanical Engineering, Department of Safety and Quality; katarina.vaskovicova@tuke.sk
[3] Technical University of Košice, Faculty of Mechanical Engineering, Department of Safety and Quality; peter.darvasi@tuke.sk
[4] Technical University of Košice, Faculty of Mechanical Engineering, Department of Safety and Quality; michaela.balazikova@tuke.sk

* Correspondence: denisa.porubcanova@tuke.sk

Abstract: Musculoskeletal disorders (MSDs) are now among the most prevalent occupational diseases worldwide. MSDs are diseases affecting bones, muscles, joints and connective tissues. Their onset and development is often attributed to inadequate physical stress, but genetic predispositions and general health are also partial influencing factors. In recent years, however, attention has also been drawn to the impact of psychological stress on the human body, and many authors believe that the onset and development of MSDs is also significantly influenced by the human psyche. This article discusses the possible influence of excessive psychological load at work on the development of MSDs and summarizes the various hypothesized mechanisms of psychological influences on the development of MSDs that have been reported in the literature. Although the exact mechanism of this action has not yet been clearly elucidated, there are a number of theories dealing with this topic.

Keywords: Musculoskeletal disorders, psychical load, working environment, prevention

1. Introduction

Musculoskeletal disorders (MSDs) are a worldwide problem that negatively impacts not only human health, but also the operation and economy of businesses and countries. These diseases are most often caused by excessive strain or overloading of body segments, repetitive, often unilateral strain, inappropriate working postures and other factors related to genetic predispositions and diseases as well as to work and working conditions. However, as in recent years attention has been drawn not only to physical stress and its prevention, but also to care and concern for the human psyche, speculations have arisen that the origin of MSD triggers may not be strictly physical [1]. Many publications point to links between the onset and development of MSDs and between psychological stress.

2. Musculoskeletal disorders

Diseases of the human musculoskeletal system, or musculoskeletal disorders, are diseases affecting bones, muscles, joints, nerves, tendons and other adjacent connective tissues. Work-related musculoskeletal disorders, often referred to as WRMSD/WMSD (work-related musculoskeletal disorders), have long had a high prevalence worldwide. The same trend is also indicated by Slovak statistics [1,2].

Such diseases are characterized by pain in the affected body area, and depending on the stage and severity of the disease, mobility of the body part may be limited, resulting in various limitations in work performance or complete incapacity for work. These conditions can occur in acute form, long term form or can progress to chronicity, which not only greatly affects mobility and physical dexterity of the person, but also affects the psyche and negatively affects psychosocial well-being [3].

2.1. MSD prevalence statistics

According to an analysis of 2019 Global Burden of Disease data, approximately 1.71 billion people across all ages suffered from musculoskeletal disorders. However, the prevalence of these diseases increases proportionally with age. Low back pain was the most commonly reported problem, with up to 570 million people reporting it. Further, among musculoskeletal disorders, fractures, osteoarthritis, neck pain and others were also frequently reported [3].

Slovak statistics also show that the prevalence of MSDs is significant. The overall trend in the incidence of occupational diseases in Slovakia is fluctuating, but the number is increasing during the last 3 years (2020-2022). In 2020 there were 254 recognized cases of occupational diseases, in 2021 there were 423 cases and in 2022 as many as 525 cases were recorded, which is also visible in Figure 1 [4].

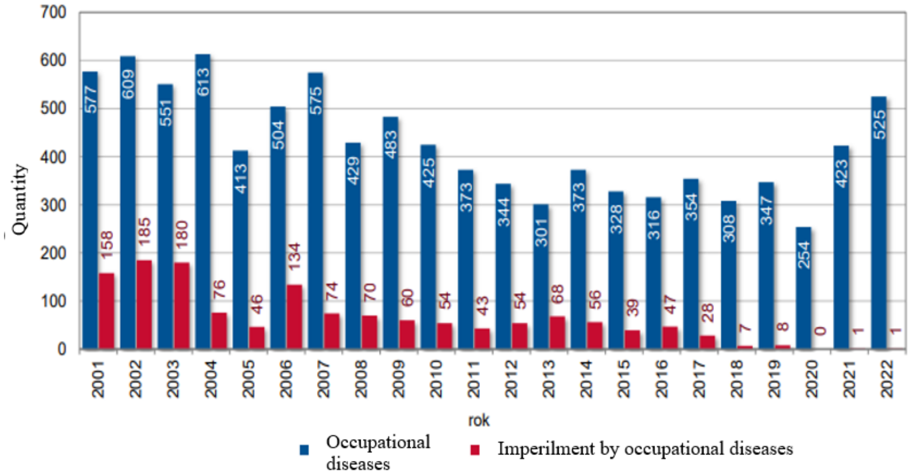

Figure 1 Occupational disease prevalence statistics in the Slovak Republic according to NCZI [4]

In 2022, 164 cases of MSDs were recorded out of a total of 525, accounting for more than 30% of the total number of recognised occupational diseases. Occupational diseases were most common in people working in the health and social care sectors, with those aged 55-59 years being the most affected group in terms of age [4].

3. Factors influencing the onset and development of musculoskeletal diseases

The human body is exposed to many factors throughout life that can be triggers for musculoskeletal and many other diseases. The following parameters are often evaluated in the assessment of physical stress, which has been shown to have an impact on the development of MSDs:

- Posture
- The force/weight of the load used
- Frequency of work
- Duration of work
- Work movements
- Speed of work
- Rest
- Anthropometric data/gender
- Worker's opinion/subjective perception - Other [1]

At the same time, environmental factors arising from the work environment and psychosocial factors are also taken into account to evaluate the workload as a whole. Often employees experience job dissatisfaction, lack of social support, high work demands, disproportionately low pay, disagreements within the team, ambiguous work organization and many other factors that affect the psyche, physical condition and overall functioning of the body [1,5].

Literature [6] reports that in the last two decades, a considerable amount of research has supported a complex and multifactorial etiology of work-related MSDs. Risk factors operating in the workplace can be divided into 3 broad categories:

1. Physical and biomechanical hazards related to physical activities or ergonomic characteristics in the workplace (e.g., loads, incorrect posture)
2. Psychosocial risks (e.g. high demands)
3. Individual risks (e.g. age, gender) [6]

According to research, the development of MSDs is also linked to sleep disturbances, which can develop as a result of physical and psychological workload. Since sleep is a very important physiological mechanism for the body to regenerate and recharge, disruption of its regularity, cycle and quality has an impact on the overall health of the person, on their sensitivity to pain and environmental influences, an overall decrease in energy and performance, as well as a negative impact on motivation. Sleep disturbances cause neuromuscular fatigue, causing a decrease in the rate of contraction and the extent of muscle relaxation, which in turn results in an increased risk of developing MSDs [7,8].

4. Relationship between psychological stress and musculoskeletal disorders

The mutual connection between psychological stress at work and the occurrence of MSD does not have an exact explanation of the mechanism of action. Many researches deal with this topic, but few cases investigate the detailed mechanism of action. Although there are several theoretical models, research is inconsistent in this regard. The reason may be the inaccuracy in defining and measuring the psychosocial aspects of work, which ultimately makes it difficult to evaluate the relative impact of stressors on the occurrence of MSD. Another problem is that most studies focus specifically on the interrelationship of these two quantities, instead of considering their functioning in a more complex framework. Since researching the human psyche is difficult, it is not possible to specify exactly which component or stimulus causing psychological stress has the most significant impact on the development of MSD [1].

Although the specific mechanism of action is not clarified, studies clearly demonstrate that long-term exposure to psychological stress contributes to the development of MSD. Research supports the hypothesis of synergistic effects between psychosocial factors and biomechanical factors that influence MSD [6].

The study of the interrelationship of MSD and psychological burden was already studied by researchers at the end of the last century, when they described the transactional approach. The transactional approach suggests that the work environment and its stressors cause stress reactions in the person, and these stress reactions have consequences for subsequent attitudes and behavior of workers. Long-term exposure to these stressors causes internal tension, which is involved in increasing the risk of developing MSD [1].

Another interconnection theory is the Sauter and Swanson model. This model is similar to the transactional model, but it also considers the opposite effect, i.e. the effect of the presence of MSD on the human psyche and its burden. He assumes that the presence of MSD, which is manifested by pain and restriction of mobility of the affected part, has a negative effect on the psyche of a person and contributes to a large extent to the psychological workload. The Sauter and Swanson model works with the theory of the physiological consequences of experiencing psychological stress [1].

According to the authors of the article [6], psychological stress triggers physiological reactions, including biochemical stress reactions, which lead to an increase in muscle tone, co-activation of the subsequent load on the musculoskeletal system, a decrease in the blood supply to the limbs and disrupt the ability to regenerate muscle tissues. There is also evidence of increased susceptibility of muscle tissues to injury due to psychosocial stressors, namely permanent activation of low-threshold motor units [6].

There is also a model that describes the effect of stress directly on muscle tissue. The functional integrity and quality of skeletal muscle is maintained by continuous protein exchange. This important remodeling process is regulated by hormones. Anabolic hormones such as growth hormone, insulin-like growth factor, and testosterone increase the rate of protein synthesis and decrease protein breakdown. Stress hormones cause catabolism of muscle proteins, reducing muscle strength. Other stress hormones cause oxidative damage in the skeletal muscle and thereby impair its quality and function. It has been proven that acute daily psychological stress induces atrophic gene expression and loss of muscle mass. Weakening of muscle tissue is a contributing factor to the development of MSD [9].

According to research [10], the occurrence of MSD is related not only to the biochemical cascades of the organism and their subsequent effect on the muscle fiber, but is also influenced by the inhibition of the ability to heal and regenerate. Acting psychological stressors are associated with disruption of the body's neuroendocrine and immune reactions, which leads to disruption of the healing process. An impaired healing response can result in reduced fatigue life of musculoskeletal tissues due to a reduced ability to keep up with accumulating damage and increased vulnerability of damaged tissue to further trauma due to a prolonged healing process. Research on engineered self-healing materials suggests that reduced healing kinetics in the presence of mechanical loading can substantially reduce the fatigue life of the materials, which can ultimately again lead to tissue damage and MSD [10].

5. Discussion

Research clearly proves that psychical stress has an impact on the development of musculoskeletal diseases. Although there are many theories describing the mechanism of their interaction, the exact cycle has not yet been revealed. Researchers work with theories of the connection between psychological tension and muscle tension, which can lead to muscle tissue damage, and also describe the connection between stress and internal biochemical processes and cascades that affect the overall functioning of the organism, its reactions and the ability to respond adequately. The effect of sleep disorders caused by psychical stress on the possibility of MSD is also described. However, all these theories unequivocally confirm the mutual connection between psychological stress and musculoskeletal diseases, both the impact of psychological stress on MSD and the presence of MSD on a person's psyche. Further research is needed to fully elucidate the mechanisms of action

The findings show that it is necessary to pay attention not only to the control and prevention of physical stress, but also to pay more attention to psychical stress.

Acknowledgments: The paper was prepared within the framework of the grant project of the Ministry of Education APVV-19-0367 Framework Integrated Process Safety Management Approach for Smart Enterprise.

Conflicts of Interest: The authors declare no conflict of interest.

References

1. Eatough, Erin M.; Way, Jason D.; Chang, Chu-Hsiang. Understanding the link between psychosocial work stressors and work-related musculoskeletal complaints. Online. Applied Ergonomics. 2012, Vol. 43, No.3, p. 554-563. ISSN 00036870. Available on the Internet: https://doi.org/10.1016/j.apergo.2011.08.009.
1. Onofrejová, Daniela; Balážiková, Michaela; Glatz, Juraj; Kotianová, Zuzana a Vaškovičová, Katarína. Ergonomic Assessment of Physical Load in Slovak Industry Using Wearable Technologies. Online. Applied Sciences. 2022, Vol. 12, No. 7. ISSN 2076-3417. Available on the Internet: https://doi.org/10.3390/app12073607.
2. World Health Organization. Musculoskeletal health. Online. 14.7.2022. Available on the Internet: https://www.who.int/news-room/fact-sheets/detail/musculoskeletal-conditions. [cit. 2023-11-28]
3. National Health Information Centre (NCZI). (10 May 2022). NCZI - Occupational diseases or risk of occupational disease. Available on the Internet: www.nczisk.sk: https://www.nczisk.sk/statisticke_vystupy/tematicke_statisticke_vystupy/choroby_povolania_alebo_ohrozenia_chorobou_povo lania/Pages/default.aspx
4. Chiasson, Marie-Ève; Imbeau, Daniel; Aubry, Karine a Delisle, Alain. Comparing the results of eight methods used to evaluate risk factors associated with musculoskeletal disorders. Online. International Journal of Industrial Ergonomics. 2012, Vol.42, No. 5, p. 478-488. ISSN 01698141. Available on the Internet: https://doi.org/10.1016/j.ergon.2012.07.003.
2. Afsharian, Ali; et al. Work-related psychosocial and physical paths to future musculoskeletal disorders (MSDs). Online. Safety Science. 2023, Vol.164. ISSN 09257535. Available on the Internet: https://doi.org/10.1016/j.ssci.2023.106177.
3. Heidarimoghadam, Rashid; Saidnia, Hamid; et al. Does mental workload can lead to musculoskeletal disorders in healthcare office workers? Suggest and investigate a path. Online. Cogent Psychology. 2019, Vol. 6, No.1. ISSN 2331-1908. Available on the Internet: https://doi.org/10.1080/23311908.2019.1664205.
4. Hämming, Oliver. Work- and stress-related musculoskeletal and sleep disorders among health professionals: a cross-sectional study in a hospital setting in Switzerland. Online. BMC Musculoskeletal Disorders. 2020, Vol. 21, No. 1. ISSN 1471- 2474. Available on the Internet: https://doi.org/10.1186/s12891-020-03327-w.

5. Poornima, K.N. Study of The Effect of Stress on Skeletal Muscle Function in Geriatrics. Online. JOURNAL OF CLINICAL AND DIAGNOSTIC RESEARCH. 2014. ISSN 2249782X. Available on the Internet: https://doi.org/10.7860/JCDR/2014/7014.3966.
6. Gallagher, Sean a Barbe, Mary F. The impaired healing hypothesis: a mechanism by which psychosocial stress and personal characteristics increase MSD risk? Online. Ergonomics. 2022, Vol. 65, No. 4, p. 573-586. ISSN 0014-0139. Available on the Internet: https://doi.org/10.1080/00140139.2021.1974103.

TECHNICKÁ UNIVERZITA V KOŠICIACH
Strojnícka fakulta

Non-contact temperature measurement of SMA materials

Jaroslav Romančík [1]*, Marek Vagaš [1]

[1] Technical University of Kosice, Faculty of Mechanical Engineering, Department of Industrial Automation and Mechatronics
* Correspondence: jaroslav.romancik@tuke.sk

Abstract: This article elucidates the application of the non-contact infrared sensor MLX90614 to measure dynamic temperature changes in a nitinol spring. Through a controllable external power source, the temperature of the material is elevated by modulating the current, and this change is detected and recorded by a system comprising a microcontroller and a temperature sensor. The experiment establishes the groundwork for elucidating the interdependencies between temperature and electrical parameters, offering valuable insights into the thermal behavior of nitinol springs for further research and exploration in this specific domain.

Keywords: nitinol spring, shape memory alloy, non-contact temperature sensor

1. Introduction

The utilization of materials and their physical characteristics constitute the cornerstone for addressing a broad spectrum of issues in various domains. In this article, our focus is directed toward shape memory alloys (SMAs), with specific attention given to the most prevalent among them, namely nitinol. At lower temperatures, this material is capable of undergoing plastic deformation, a property shared with various metallic alloys. However, unlike other alloys, nickel-titanium (nitinol) possesses the unique ability to revert to its original state through a specific internal temperature change; in other words, deformation can be restored by increasing the temperature. This phenomenon is referred to as the shape memory effect.

The material's capacity for this behavior is contingent upon an alteration in the internal structure of nitinol (**Figure 1.**). The temperature change induces a transition of the material between the austenite and martensite phases.

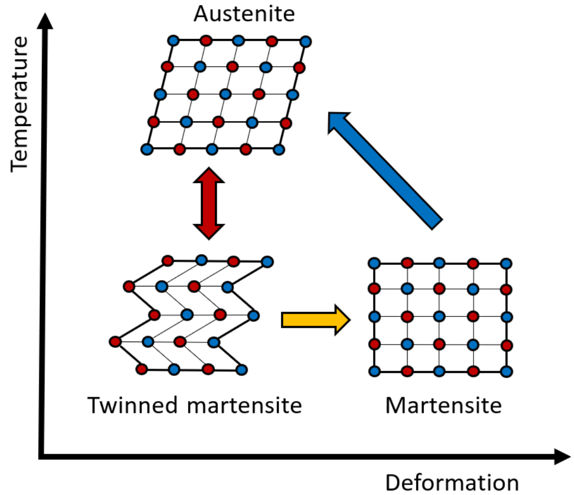

Figure 1. A change in the internal structure of the SMA material.

During the restoration of deformation, shape memory alloys generate force, transforming into actuators by converting heat into mechanical energy. Various methods, such as heat transfer, radiation, or electric Joule heating, can be employed to supply heat to the actuator [1-4].

Accurate measurement of the heat supplied to nitinol necessitates a reasonable approach. The most effective method involves the utilization of temperature sensors to capture the surface temperature of the material. For this purpose, we will employ the non-contact infrared sensor MLX90614.

2. Materials and Methods

2.1. SMA - Nitinol

In our experiment, we will use Shape Memory Alloy (SMA) material - nitinol in the form of a spring, wound from a 150 mm long wire with a thickness of 0.75 mm. In the austenitic phase (after heating), the spring contracts, shortening to a length of 20 mm with a diameter of 7 mm.

SMA materials can function as actuators in two ways:

- One-way SMA: The material can be deformed arbitrarily (**Figure 2. A**). Upon heating, it returns to its pre-trained shape (**Figure 2. B**). After cooling, it remains in the trained shape (**Figure 2. C**) [5].

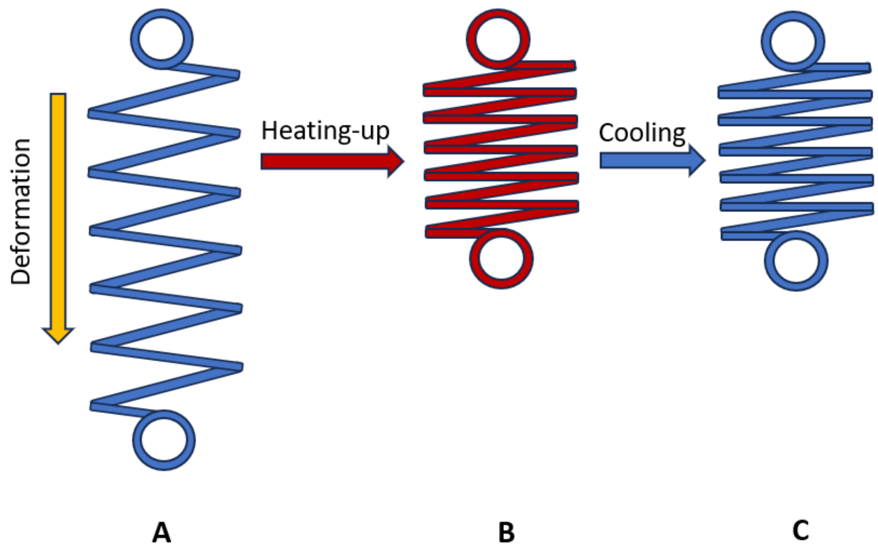

Figure 2. The behavior of a one-way nitinol spring.

- Two-way SMA: Similar to one-way SMA, the material can be deformed arbitrarily. Upon heating, the material assumes one of the pre-trained shapes. However, upon cooling, the material reshapes into the second pre-trained state [6].

We will use springs that operate as one-way SMA. We will induce spring shortening by heating it, but we will achieve deformation in the form of spring elongation using a weight attached to the end of the spring. This weight will exert a force in the opposite direction to the action of the SMA actuator force during heating.

2.2. Infrared non–contact temperature sensor MLX90614

Operating on the principle of infrared radiation, this sensor determines the temperature of objects by sensing electromagnetic waves emitted as light from the object. Equipped with a low-noise amplifier featuring a 17-bit ADC, it facilitates non-contact temperature measurement. Designed to accommodate diverse temperature conditions, it is effective within a range of -40 °C to 125 °C for ambient temperature and -70 °C to 380 °C for object temperature, all while adhering to a standard accuracy of ±0.5 °C [7,8].

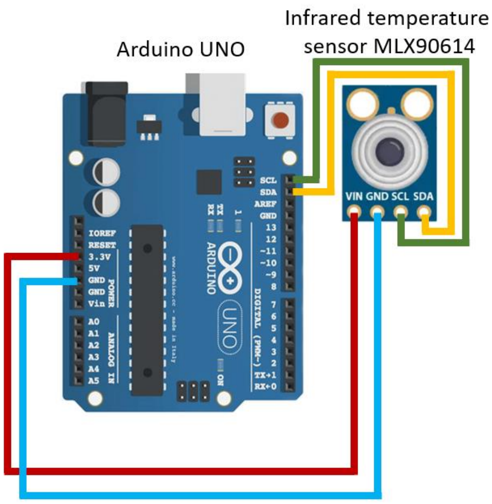

Figure 3. Connection of the Arduino Uno and the infrared temperature sensor MLX90614

This sensor is compatible with the Arduino microcontroller platform (**Figure 3.**), making it suitable for integration into our application.

3. Experiment

The experiment will be conducted in a workplace (**Figure 4.**) consisting of the following main components:

- Nitinol spring
- Infrared temperature sensor MLX90614
- Arduino UNO
- Programmable DC power supply
- Weight 500 g

The infrared non–contact temperature sensor MLX90614 is attached to the stand's structure using a bracket and is positioned behind the nitinol spring. The sensor is connected to the Arduino UNO microcontroller. This system measures temperature changes in the nitinol spring during the experiment with a sampling frequency of 2 Hz. One end of the spring is attached to a bracket on the stand's structure, and at the other end, a weight with a mass of 500 g is attached. Both ends of the nitinol spring are connected to the programmable power supply. This power supply will provide a constant current starting from 1.4 A for each measurement, increasing by 0.2 A up to the limit of 5.2 A.

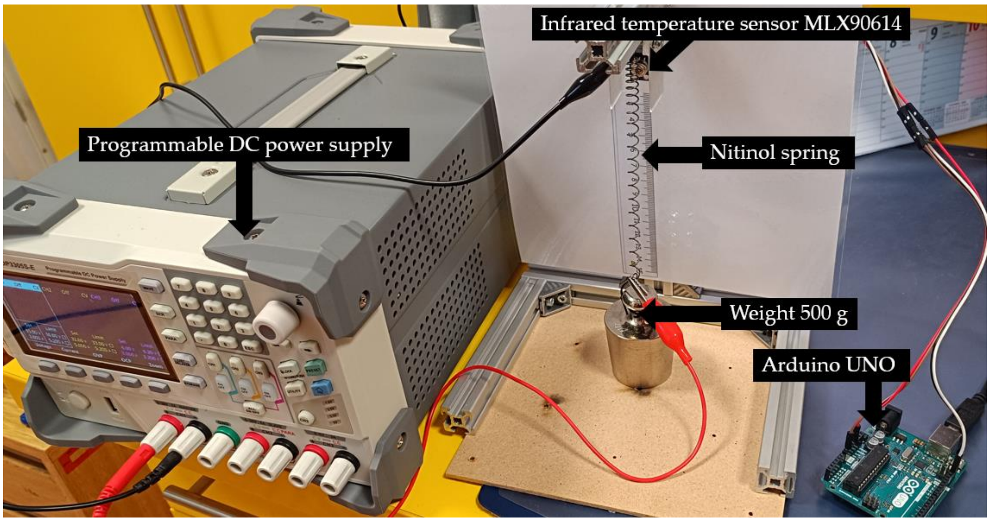

Figure 4. Experimental workplace

The lower limit of the current was determined experimentally as the minimum current at which it was possible to lift the 500 g weight using the nitinol spring.

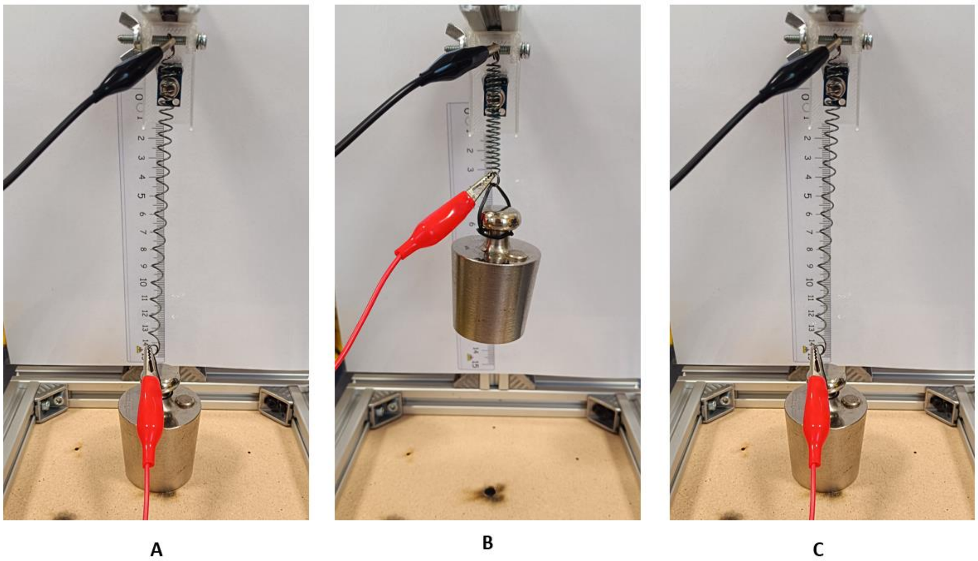

Figure 5. Experimental workplace.

In the first phase of the experiment (**Figure 5. A**), we will observe the increasing temperature of the stretched (deformed) nitinol spring as the weight is lifted from the base to a constant height for all measurements - maximum spring extension (**Figure 5. B**). This lift will be induced using the programmable power supply with a set constant current. In the second phase, we will observe the cooling of the nitinol spring until the weight returns, influenced by the gravitational force, back to the base-spring deformation (**Figure 5. C**).

4. Results

The collected data during our experiment were analyzed using graphs. From these data and graphs, we can deduce the following dependencies:

In the first phase, the nitinol spring exhibited exponential heating at each current setting. In the second phase, the nitinol spring cooled linearly during deformation caused by the weight (**Figure 6.**).

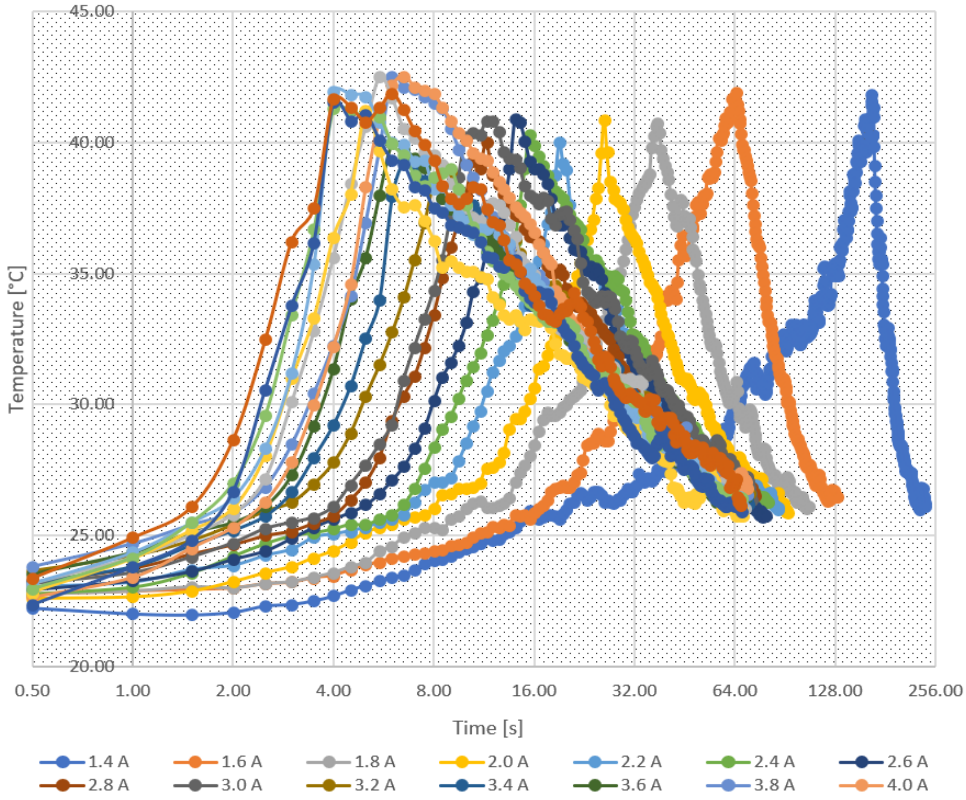

Figure 6. Experimentally obtain data, a graph of dependence of electric current and time.

The temperature of the nitinol spring, upon reaching maximum contraction and simultaneously lifting the weight, attains temperatures independent of the magnitude of the electrical current within the range of 39.11°C – 42.50°C (**Figure 7.**).

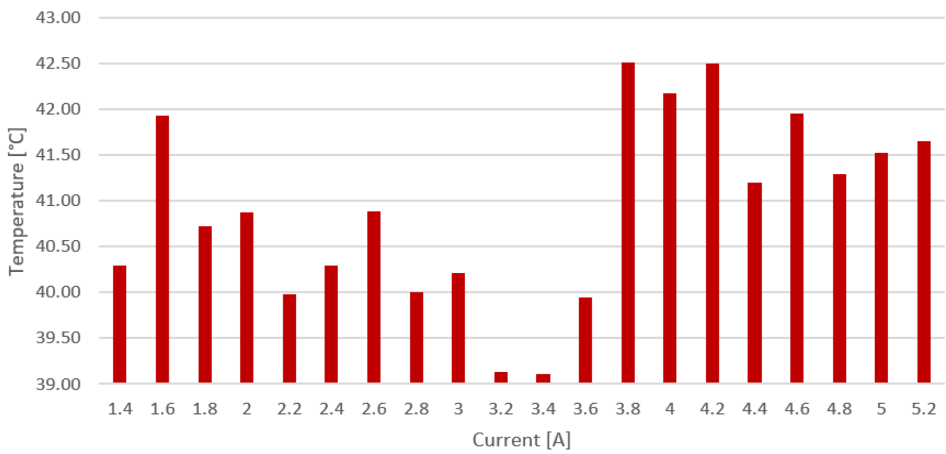

Figure 7. Experimentally obtain data, a graph of temperatures at different current sizes, at the point of greatest shortening of the spring.

With increasing current, the time of lifting a weight with a mass of 500 g decreases (**Figure 8.**). From the collected data, we can describe this change as a dependency between time and electrical current using the following power-law function:

$$= 151.83 * {}^{-1.25} \quad (1)$$

where:

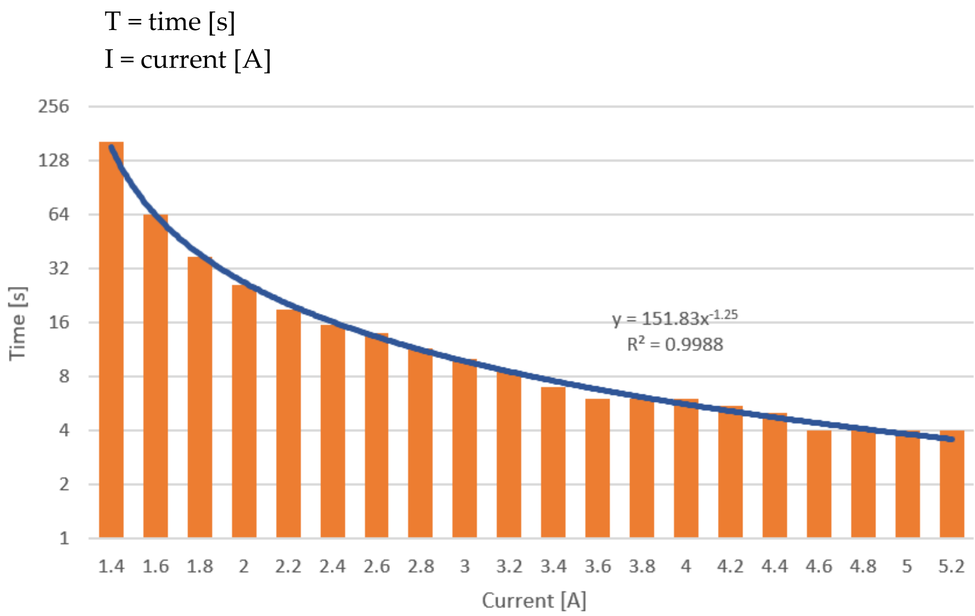

Figure 8. Experimentally obtain data, a graph of the dependence between the changing rate of electric current and the time to reach the maximum shortening of the spring.

5. Discussion

This article focuses on the experimental temperature measurement of a spring made of SMA material - nitinol using an infrared non–contact temperature sensor MLX90614. From our measurements and obtained data, we found that by increasing the rate of electric current, the shortening time of the spring decreases, which results in the lift of the load. The data obtained from this experiment form the basis for further work with nitinol springs at our department. Further experiments can focus on measuring the force that a nitinol spring can generate or on an effective way of cooling the SMA material.

Acknowledgments: This article was created thanks to the funds provided by the Tatra Bank Foundation project - the digital grant program for university students 2023, to support education and finance the implementation of research "Research and development of an adaptive soft effector".

Conflicts of Interest: The authors declare no conflict of interest.

References

1. C.H. Fu, M.P. Sealy, Y.B. Guo, X.T. Wei. *Austenite–martensite phase transformation of biomedical Nitinol by ball burnishing,* Journal of Materials Processing Technology, December 2014, Volume 214, Issue 12, pp. 3122-3130.
2. S. Chikkamaranahalli, R. R. Vallance, O. A. Rawashdeh, J. E. Lumpp, B. L. Walcott. *Precision instrument for characterizing contraction and extension of nitinol wire,* August 2015.
3. J.A. Shaw, S. Kyraiakides, *Thermomechanical Aspects of NiTi*, Journal of Mech.Phys Solids, 1995, Volume 43, No.8, pp.1243-1281.
4. I. Mihálcz, *Fundamental characteristics and design method for nickel-titanium shape memory alloy,* Periodica Polytechnica Mechanical Engineering, April 2000, Vol. 45, No.1, pp.75-86.
5. G. Costanza, M.E. Tata, C. Calisti. *Nitinol one-way shape memory springs: Thermomechanical characterization and actuator design,* Sensors and Actuators A: Physical, January 2010, Volume 157, Issue 1, pp. 113-117
6. O. M. A. Taha, M. B. Bahrom, O. Y. Taha, M. S. Aris, *Experimental study on two way shape memory effect training procedure for nitinol shape memory alloy,* ARPN Journal of Engineering and Applied Science, September 2015, Volume 10, No.17, ISSN 1819-6608.
7. A. Sudianto, Z. Jamaludin, A. A. A. Rahman, S. Novianto, F. Muharrom, *Smart Temperature Measurement System for Milling Process Application Based on MLX90614 Infrared Thermometer Sensor with Arduino,* Journal of Advanced Research in Applied Mechanics, 2020, Volume 72, Issue 1, pp. 10-24.
8. Datasheet, Melexis Data, *MLX90614 family, single and dual zone infrared thermometer in TO-39*, online, 2023.

The impact of annealing on the properties of packaging sheets.

Ing. František Ruda , Prof. Ing. Emil Spišák, CSc.

[1] frantisek.ruda@student.tuke.sk
[2] emil.spisak@tuke.sk
* Correspondence: frantisek.ruda@student.tuke.sk; Tel.: +421 910 947 185

Abstract: Packaging sheets are thin steel plates used in the production of cans, packaging, and other products. The properties of packaging sheets depend on their composition, thickness, surface treatment, and annealing process. Annealing is a crucial technological process affecting the structure, hardness, strength, corrosion resistance, reducing internal stress, and enhancing the ductility and toughness of sheets. This study aims to compare the impact of different annealing methods on the mechanical properties of packaging sheets. Two annealing methods are compared: batch annealing and continuous annealing. The goal is to identify the optimal annealing method that provides the best combination of properties for packaging sheets.

Keywords: Sheet, annealing, quality, temperature

1. Introduction

Packaging material is the most widely used material in the food industry, producing various cans, closures, lids, and beverage containers. It is also used for manufacturing cans for different colors, oils, aerosols, decorative containers, industrial containers, toys, and canisters.

Advantages of packaging material:

- Excellent recyclability – coated material can be continuously recycled, easy separation from other materials (can be separated by a magnet from various plastics). Therefore, this material will be used for a long time. As mentioned, it is recyclable, and it naturally decomposes in the environment after some time, unlike plastic that hardly decomposes in nature.
- In the past, a significant issue in tinplate production was the tin deficit. Manufacturers focused on reducing the thickness of the tin layer while maintaining sufficient protection. Over the last approximately 25 years, the tin layer has decreased from 11.2 g/m^2 to the current 1.0 to 1.5 g/m^2, depending on customer requirements.
- To reduce thickness and weight, a second reduction was introduced, resulting in the current thickness of packaging sheets being 0.13 to 0.14 mm. This fact significantly increased the surface area of manufactured packaging sheets from the same weight.

2. Current method of packaging sheet production

Due to the diversity of applications, steel sheets for packaging currently vary widely in thickness, mechanical properties, plastic properties, and corrosion resistance. The current production of packaging sheets involves a sophisticated process aiming to be largely independent of human factors. The current production of packaging sheets is illustrated in Figure 1.

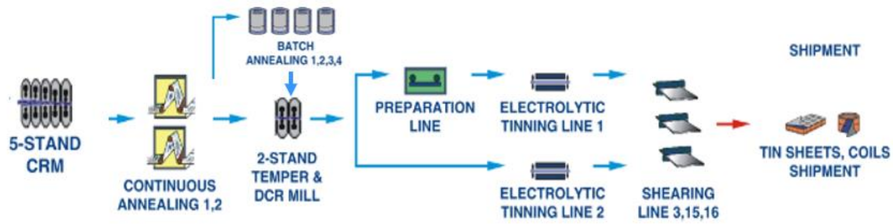

Figure 1: Packaging Sheet Production

One of the most important operations in packaging sheet production is annealing, performed after cold rolling on a five-stand tandem mill. There is a significant thickness change from 1.8 - 2.2 mm to a thickness of 0.18 - 0.45 mm. Recrystallization annealing is used to achieve optimal properties.

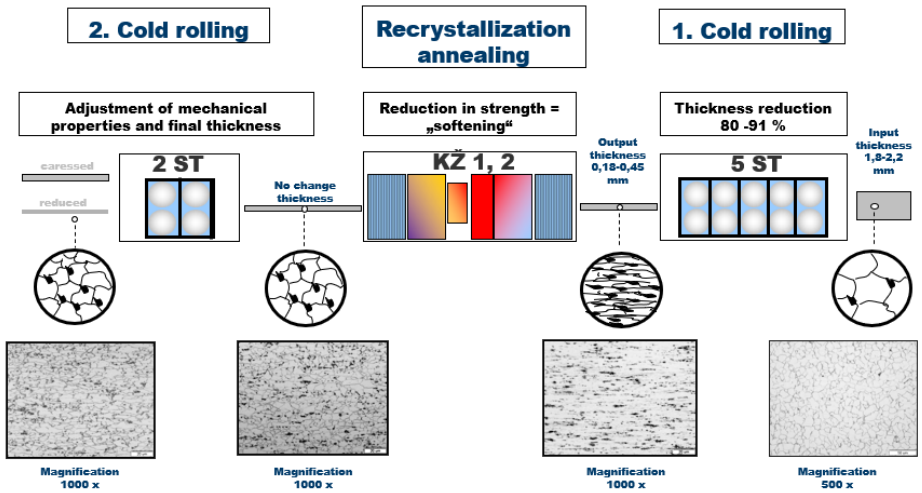

Figure 2 : Influence of rolling and annealing on ferritic lattice

Figure 2 illustrates the process of rolling, recrystallization annealing, and second cold rolling with the deformation and recovery of the ferritic grain through recrystallization annealing.

3. Recrystallization Annealing

Recrystallization annealing is a heat treatment process that leads to the formation and growth of new grains, resulting in complete restoration of the material's deformation structure. Factors controlling recrystallization are the degree of deformation (% reduction), temperature, and time. The course of recrystallization and its mechanical properties include:

Cold material deformation - High hardness, very low ductility hardness, very low ductility (deformed grains in the rolling direction)

Recovery - No change in mechanical properties (no change in microstructure).

Primary recrystallization: Hardness decrease and ductility increase (restoration of polyhedral structure).

Secondary recrystallization: Non-uniform sheet properties (local, enormous increase in some grains).

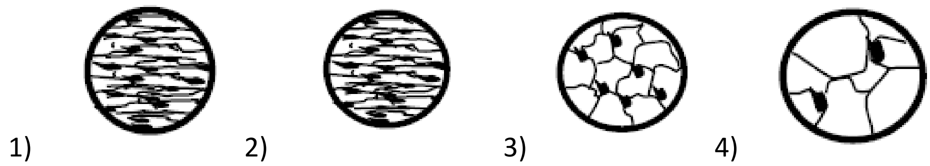

Figure 3: Types of microstructures

4 Annealing

The two most common annealing methods are :

- Batch annealing
- Continuous annealing

Equipment for each annealing method is shown in Figures 4 and 5.

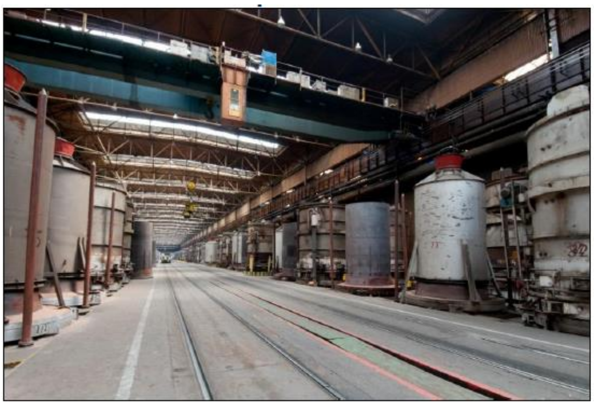

Figure 4: Batch annealing

Figure 5: Continuous annealing

4.1 Continuous Annealing

The continuous annealing line is designed for degreasing, cleaning, and recrystallization annealing of cold-rolled steel strip for packaging sheet production. The basic procedures and nodes of the continuous annealing line include.

The basic procedures and nodes of the continuous annealing line include:

1. Entry – trimming off out-of-tolerance sections, verifying the welding correctness of the strip pair.

2. Degreasing section - ensures degreasing of the strip, removal of impurities and residues of rolling emulsions, complete rinsing, and drying.
3. Annealing - this section is heated by radiant tubes to increase the temperature to the annealing temperature and maintain the strip temperature at the annealing temperature for a minimum of 10.5 seconds at a maximum speed of 420 m/min.
4. Rapid cooling and aging section - ensures rapid cooling of the strip from the holding temperature to the aging temperature at a high cooling speed (min. 50°C/sec) to the output temperature on the pyrometer - max. 470°C, optimum 450°C
5. Final cooling section - the strip is cooled by a stream of cooled protective gas from a temperature of 400-470°C, or 420-530°C to a maximum temperature of 130°C.
6. Water bath and drying section - in this section, the strip is cooled to a maximum temperature of 40°C and then immersed in demineralized water. Excess water is removed from the strip by squeezing rollers, and the strip is dried in a warm air dryer.
7. Output section - after annealing and cooling, the strip is wound onto a winder with a diameter of 500 mm.

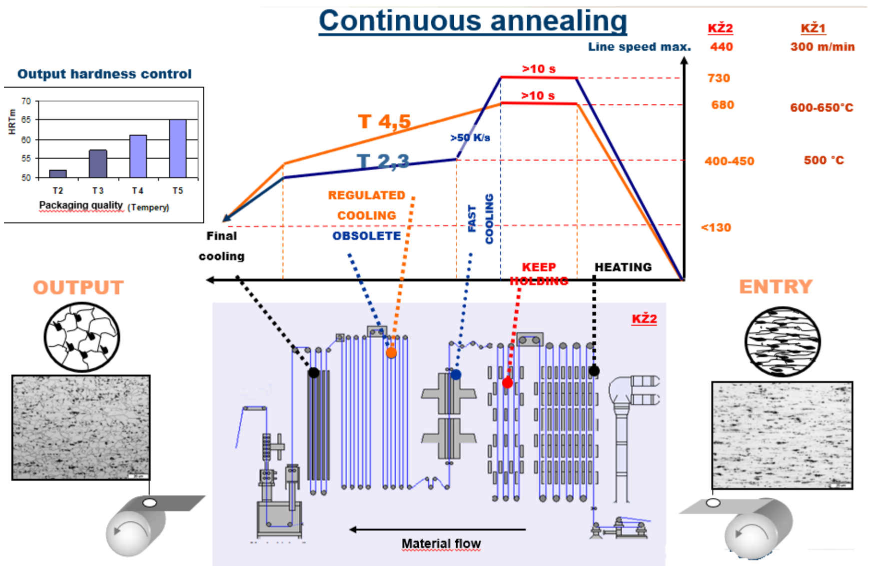

Figure 6: Continuous annealing scheme with temperature curve

Figure 6 shows the scheme of continuous annealing with temperature curves and the difference in the input material after cold rolling and the output of the material after annealing.

4.2 Batch Annealing

The task of batch annealing is to thermally process cold-rolled steel coils through recrystallization annealing to achieve the desired mechanical and physical properties while maintaining a glossy strip surface.

The production program of batch annealing consists of these main groups of steels:

- Drawing, cast for ZPO,
- Structural, and micro-alloyed cast for ZPO,
- Vacuum cast for ZPO

- Packaging (BA), cast for ZPO,
- Steels in the research stage.

The scheme of batch annealing is shown in Figure 7.

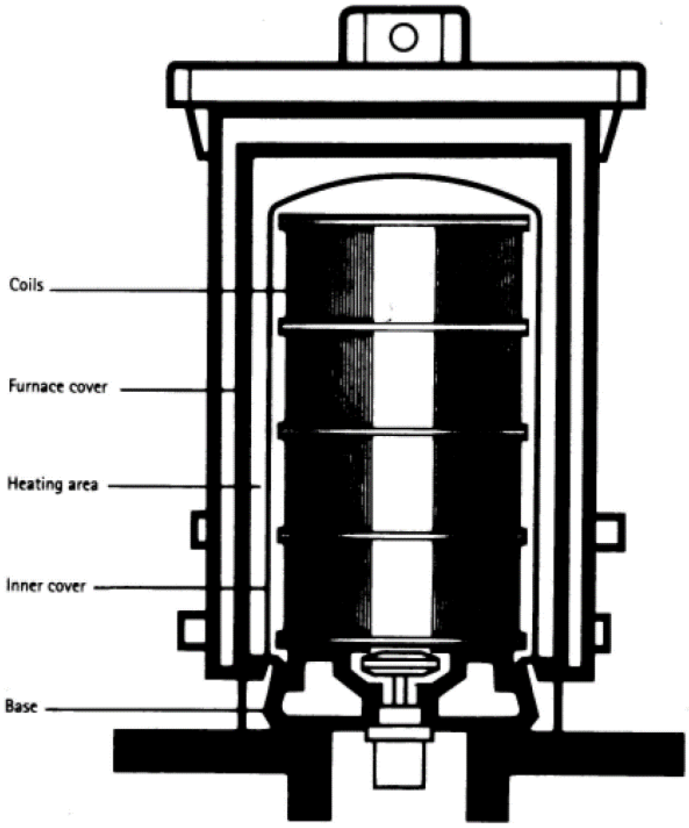

Figure 7: Batch annealing

Batch annealing is performed in the presence of a protective atmosphere consisting of 4-5% H_2 and 93-96% N_2. The protective atmosphere prevents the presence of oxygen during annealing (maximum 20 ppm). Hydrogen up to 99.98% and no nitrogen is used for the protective atmosphere on annealing furnaces 3 and 4. Nitrogen is only used for furnace purging during start-up and shutdown of annealing. Heating gas is mixed for annealing furnaces No. 1 and 2, and natural gas for furnaces No. 3 and 4. Figure 8 illustrates the flow of the protective gas in the cover.

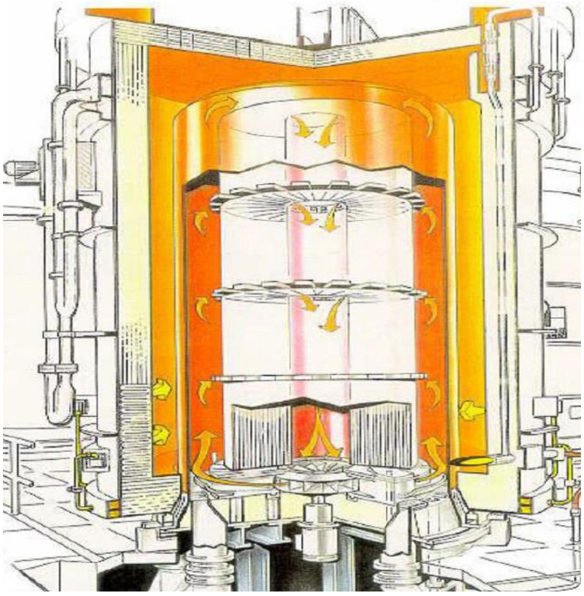

Figure 8: Flow of the protective atmosphere during annealing

The temperature and time dependence during cover annealing is shown in Figure 9.

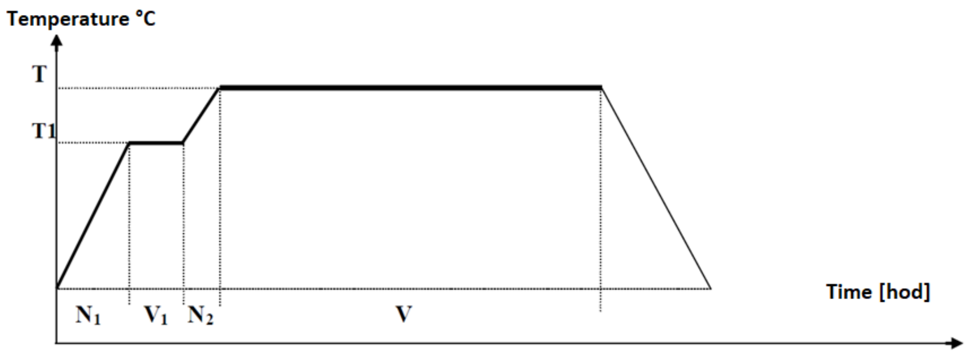

Figure 9: Annealing diagram

N1 – Ramp to 500°C - 9 hours.

T1 – Temperature of the 1st hold – 500°C.

V1 – Duration of the 1st hold – 6 hours at 500°C.

N2 – Ramp to the second annealing temperature - 6 hours at 710°C.

V – Overall hold duration, calculated based on the hold duration and charge parameters, ranging from 20 to 50 hours.

T – Hold temperature 710°C

After annealing, the operator removes the annealing cover, and the charge cools in the open air until the temperature of the protective atmosphere reaches 450°C. Then, it is necessary to put on the cooling cover. This cover is applied until the material reaches the unpacking temperature: 70°C for black charge, 60°C for BA material used for tinplating.

Figure 10 provides a comparison of continuous vs. cover annealing.

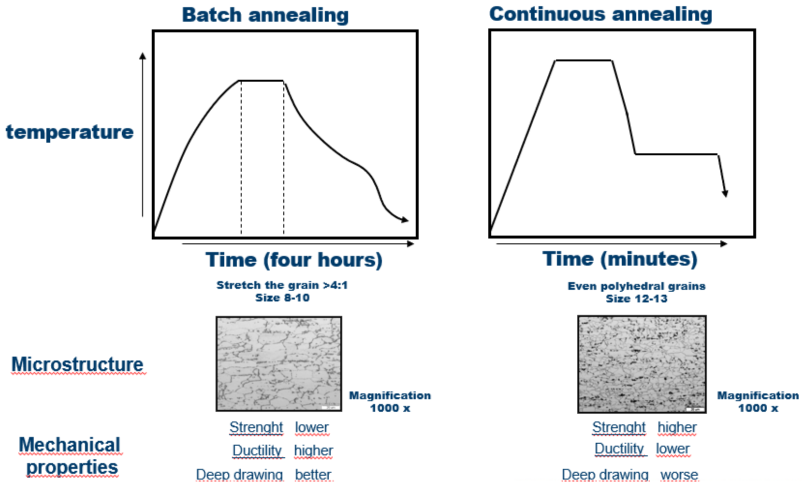

Figure 10: Continuous vs. cover annealing

Materials and their chemical elements influencing the annealing temperature and, consequently, mechanical properties, steel purity, and surface quality are listed in Table 1. The most important alloying elements for packaging steels are C, Mn, N, and Al (B)

Table 1: Chemical composition of packaging steels

Element	Designation	Production code					
		204	202	203	228	603	558 / 691 / 281 / 282
Uhlík	C	0,015-0,035	0,026-0,054	0,046-0,085	0,055-0,085	0,04	0,046-0,085
Mangán	Mn	0,175-0,284	0,246-0,354	0,246-0,354	0,346-0,454	0,246-0,354	0,330-0,454
Dusík	N	0,0065	0,0065	0,0074	0,0065	0,0045	0,0075-0,154
Hliník	Al	0,03-0,05	0,03-0,06	0,03-0,06	0,025-0,055	0,02-0,045	0,020-0,045
Bór	B	0,001	0,001	0,001	0,001	0,003-0,006	0,001
Síra	S	0,01	0,01	0,018	0,015	0,015	0,02
Fosfor	P	0,015	0,015	0,015	0,015	0,015	0,02
Kremík	Si	0,02	0,02	0,03	0,02	0,02	0,03
Meď	Cu	0,06	0,06	0,06	0,06	0,065	0,154
Nikel	Ni	0,03	0,03	0,05	0,04	0,035	0,105
Cín	Sn	0,02	0,02	0,02	0,02	0,02	0,05
Arzén	As	0,01	0,01	0,01	0,01	0,01	0,01
Molybdén	Mo	0,02	0,02	0,05	0,015	0,02	0,03
Chróm	Cr	0,045	0,045	0,08	0,06	0,045	0,105

Basic properties and their temperatures during cover annealing are described in Table 2.

Table 2: Annealing regimes and properties of the cover annealing furnace

P.č.	Quality	Thick [mm]	N_1 [hod]	T_1 [°C]	V_1 [hod]	N_2=N [hod]	T_2=T [°C]	V [hod]	TV_{aus} [°C]	K [/]	Leaving the furnace shut down (hour)	Prescription
1	777	Všetky	9	500	6	6	710	38	95	0,25	2	DTP
2	693, 473, 475, 630, 038, 420 221, 222, 223, 224, 225, 226, 248	Všetky	9	500	6	6	710	36	95	0,25	2	DTP
3	678, 398	Všetky	9	500	6	6	710	19	95	0,25	2	DTP
4	665, 669	Všetky	9	500	6	6	690	28	95	0,25	2	DTP
5	029, 194, 697	Všetky	9	500	6	6	690	25	95	0,25	2	DTP
6	674, 837	Všetky	9	500	6	6	690	23	95	0,25	2	DTP
7	694, 644, 459, 396, 676, 842	Všetky	9	500	6	6	690	18	95	0,25	2	DTP
8	360, 376, 395, 576, 653, 660, 673, 675	Všetky	9	500	6	6	670	19	95	0,25	2	DTP
9	247, 422, 463, 564, 655, 698	Všetky	9	500	6	6	670	14	95	0,25	2	DTP
10	141, 088, 591	Všetky	9	500	6	6	650	15	95	0,25	2	DTP

For some microalloyed qualities (395, 396, 398, 653, 674, 675, 676, 678, 837, 842), in case of coiling a coil with a weight over 20 tons onto the base, extend the annealing regime by 5 hours!

Table 3 provides qualities and their annealing temperatures for individual strip thicknesses and widths.

Table 3: Annealing regimes and qualities of the continuous annealing line.

Width (mm)	700-750				751-850				851-961				962-1050			
Thick od-do (mm)	T1 [°C]	v min m/min	v max m/min	T2 [°C]	T1 [°C]	v min m/min	v max m/min	T2 [°C]	T1 [°C]	v min m/min	v max m/min	T2 [°C]	T1 [°C]	v min m/min	v max m/min	T2 [°C]
0,170-0,179	715	180	360	715	715	180	360	715	715	180	365	715	*	*	*	*
0,18-0,185	715	180	365	715	715	180	365	715	715	180	365	715	715	180	360	715
0,186-0,22	715	180	365	715	715	180	365	715	715	180	365	715	715	180	360	715
0,221-0,24	715	180	360	715	715	180	360	715	715	180	360	715	715	180	340	715
0,241-0,26	715	180	330	715	715	180	330	715	715	180	330	715	715	180	330	715
0,261-0,28	715	180	300	715	715	180	300	715	715	180	300	715	715	180	260	715
0,281-0,32	715	180	285	715	715	180	300	715	715	180	285	715	715	180	285	715
0,321-0,36	715	180	250	715	715	180	250	715	715	180	250	715	715	180	250	715
0,361-0,39	715	160	205	715	715	160	205	715	715	160	205	715	715	160	195	715
0,391-0,42	715	150	175	715	715	150	180	715	715	150	175	715	715	150	175	715

Table 4 illustrates basic qualities for the annealing of packaging steels :

Table 4: Qualities of packaging steels.

Grades Designation in World Standards of Packaging Steel			Mechanical properties / Hardness 0,21<h≤0,28		Typical Usage
ASTM, JIS	European „old“ EN 10203:1991	European „New“ EN 10202:2001	Yield Strength $R_{p0,2}$ [MPa]	HR30Tm	
T1	T50BA	TS230	230±50	52±4	Drawing cans
T2	T52BA	TS245	245±50	55±4	Drawing cans
-	T55BA	TS260	260±50	57±4	Aerosol top
T3	T57BA	TS275	275±50	59±4	Ends, Aerosol top
T4	T59BA	TS290	290±50	61±4	Aerosol body
T4	T61CA	TH415	415±50	65±4	Crown corks, ends
T5	T65CA	TH435	435±50	70±4	Ends, aerosol bottom
T6	T70CA	-	530±50	-	Easy open ends
-	DR520CA	TH520	520±50	-	Ends, Drawing cans
DR8	DR550BA	TS550	550±50	-	Ends
DR8	DR550CA	TH550	550±50	-	Ends
-	DR580CA	TH580	580±50	-	Can body, Ends, TO closure
DR9	DR620CA	TH620	620±50	-	Ends, TO closure
DR9M	DR660CA	-	660±50	-	Twst-off closure

During tests of these materials, yield strength, tensile strength, and elongation are examined, representing the most crucial properties of packaging materials.

5. Conclusion :

The annealing process is determined based on the resulting properties of the packaging steel. As the analysis has shown, continuous annealing is a significantly shorter process lasting only a few minutes, whereas cover annealing is a process that takes tens of hours. Due to achieving specific properties of packaging steels, such as low yield strength and high elongation, cover annealing is currently an irreplaceable method for restoring the plastic properties of thin packaging steels after cold rolling.

References

1. Spišák, E., Slota, J., Majerníková, J.: Hodnotenie anizotropie tenkých obalových plechov. In: Visnik: Naukovo-mechničnij zbirnik. Kijev: Nacionaľnij transportnij univrsitet, 2006, p. 23-29
2. Majerníková, J.: Medzné deformácie tenkých obalových plechov pri rôznych napäťovo-deformačných stavoch. Dizertačná práca, Košice, 2008.
3. Spišák, E., Slota, J., Majerníková, J.: Anisotropy evaluation of tinplates. In. Pro-tech-ma ´07 : Progressive Technologies and Materials: International Scientific Conference: Rzeszów – Bezmiechowa, Poland, 28th June – 30th June 2007. Rzeszów . Politechnika Rzeszowska, 2007. ISBN 978-83-7199-443-2. p. 217-222
4. Spišák, E., Slota, J., Majerníková, J.: Analýza začiatku plastickej deformácie DR obalových plechov. In: Acta Mechanica Slovaca. roč. 10, č. 2b Pro-tech-ma (2006), s. 387-392. ISSN 1335-2393
5. Recommendation SEFL N0 7 Tinmil Products, Buxeles 1991
6. Rendek, F., a kol.: Výskum príčin starnutia obalových plechov a riešenie stability ich vlastností. [Výskumná správa] VaSÚ VSŽ, s.r.o. Košice, 1996
7. Oravec, K.: Mechanické vlastnosti plechov z IF ocele po vysokoteplotnom rekryštalizačnom žíhaní. Acta Met. Slovaca vol. 5, 1999, No. 5, pp. 348-351
8. Varga, A.: Tepelná technika v hutníctve. HF TU v Košiciach, 1999
9. Hašek, P.: Tabuľky pro tepelnou techniku. VŠB Ostrava, 1979
10. Hottel, H.C., Sarofim, A.F.: Přenos tepla zářením. SNTL Praha, 1979
11. Weber, F., Elzer, R., Knoche, H.: Durchlauf-Glühanlage für Feinst- und Feinbleche bei der Rasselstein AG. Stahl und Eisen 105, Nr. 6, 1985

Measurement of unindirectional pose accuracy and unindirectional orientation accuracy on collaborative robot

Matúš Sabol [1] and Ján Semjon [2*]

[1] Siemens Healthcare s.r.o., Lamačská cesta 3/B, 841 04 Bratislava; matus.sabol@siemens-healthineers.com
[2] Technical University of Košice, Faculty of Mechanical Engineering, Department of Production Technology and Robotics, Park Komenského 8, 042 00 Košice, Slovakia, jan.semjon@tuke.sk
* Correspondence: jan.semjon@tuke.sk; Tel.: +421 55 602 2625

Abstract: The article describes the measurement of one-way position accuracy and one-way orientation accuracy on the collaborative robot Dobot CR5. Dobot CR5 is a 6-axis robot manufactured by Dobot Robotics. The reason for carrying out the verification of the mentioned collaborative robot according to the relevant ISO 9283 standard was to find out whether it is possible to replace the standard collaborative robots in Slovakia with this robot.

Keywords: unindirectional pose accuracy; unindirectional orientation accuracy; collaborative robot; Dobot CR5

1. Introduction

Current demands of the market require the highest possible precision in production, efficiency and reliability of automated robotic lines, it is necessary to constantly improve the parameters of industrial robots. During designing a robot, it is necessary to think on several main aspects which include for example, the sensory apparatus, the motor system and the control architecture. These aspects interact and determine the behavior of the robot. The kinematics of the robot is also very important. Robot kinematics study robot movements and geometry. The kinematic chain of the robot is formed by the arms and joints of the robot. The joints can be revolve or prismatic. Revolving joints are joints that rotate around an axis, and prismatic joints act linearly along the axis of motion. Each of the joints adds one degree of freedom to the robot, six degrees of freedom are needed to control the end part of the robot freely in three-dimensional space, which ensures the positioning and orientation of the robot. Accuracy and repeatability are most important for industrial robots. Accuracy can be defined as the robot's ability to reach a set point in its workspace. Repeatability as the ability of the robot to reach a defined position, with each repeated request. Both accuracy and repeatability depend mainly on regular maintenance, static, dynamic and thermal loads, stiffness and various other factors. The international standard ISO 9283 describes the performance criteria and test methods of the performance characteristics of industrial robots [1-3]. The standard provide important role in the standardization of test methods and test conditions to ensure the same evaluation of individual characteristics and for the most accurate comparison of the measured parameters of individual robots. The standard does not specify which characteristics are required for testing robot. The individual methods are primarily aimed at developing and verifying robot specifications, but they can also be used for prototype testing. One-way positioning accuracy (AP) is, according to the ISO 9283 standard, the deviation between the desired position and the average value of the actual positions when reaching the desired position from the same direction [4-5]. The repeatability of the manipulator is the ability to move the end part of the effector to the same desired value in space. The repeatability of the robot is mainly limited by the resolution of the position reading system, i.e. the smallest possible value that this system can read [6-8].

2. Characteristics of measured Dobot CR5

Dobot CR5, Figure 1 is a collaborative robot with a maximum payload 5 kg. The reach of the robot is 900 mm, the maximum reach is 1096 mm. It has six joints that ensure rotation in 6 different axes, while the range of 1, 2, 4, 5 and the 6th axis is ± 360° and the 3rd axis is ± 160°. The maximum speed in all axes is equal to 180°/s. Repeatability is declared at the level of ± 0.02 mm. It is equipped with 5 levels of collision detection.

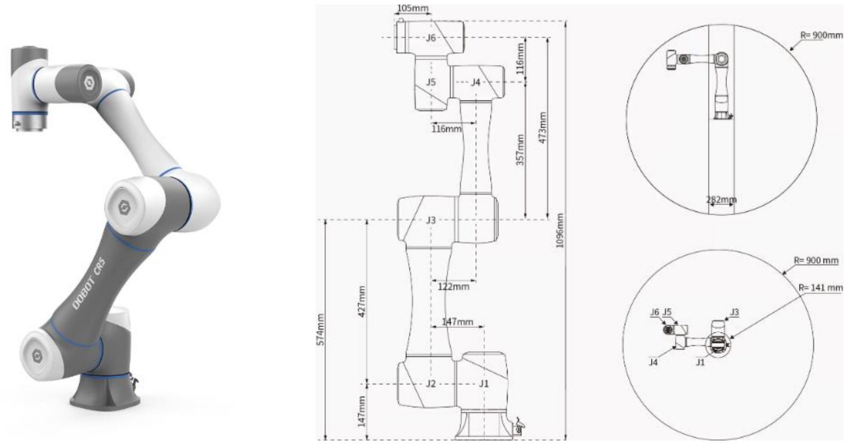

Figure 1. This is a figure. Schemes follow the same formatting [9].

More detailed parameters of the Dobot CR 5 robot are listed in Table 1.

Table 1. Selected parameters of the Dobor CR 5 robot [9].

Robot Type	DOBOT CR5		Maximum Speed	3m/s	
Weight(kg)	25kg		End-Effector I/O Interface	DI/DO/AI	2
Payload(kg)	5kg			AO	0
Reach(mm)	900mm		Communication Interface	Communication	RS485
Max. Reach(mm)	1096mm		Control Box I/O Ports	DO/DI	16
Rated Voltage	DC48V			AI/AO	2
Joint Ranges (°)	J1, J2, J4, J5, J6	±360°	Repeatability	±0.02mm	
	J3	±160	IP Classification	IP54	
Maximum Speed of Joints	J1/J2	180°/s	Temperature	0~45°	
	J3/J4/J5/J6	180°/s	Power	150W	

CR5 DOBOT is customizable with different applications, easy to use and quickly performs the desired movements. CR collaborative robots are recommended not only because of the extensive portfolio of arms end tools, but also because of the universal communication interfaces. With multiple I/O and communication interfaces, the CR series of collaborative robots is widely expandable and compatible with many arm tool end devices. In the basic version, the robot is supplied only with a robotic cabinet and the necessary cabling. As an option, it is possible to purchase a tablet, through which the robot can be programmed. The robot can be controlled with a computer or a tablet with installed the Dobot Studio program via an ethernet cable or Wifi.

3. Selection of suitable tests for measurement

In this method are measuring cube and weights mounted on the robot to simulate the robot's maximum load, Figure 2. The desired point in the robot's workspace is learned and a series of measurements are performed. Measurements consist of 3 sets of 35 repetitions. Each set of measurements is performed with a different robot speed. Measurements are performed at 50% and 100% robot speed. The purpose of the measurement is to determine the deviation between the programmed position and the actual position of the end part of the robot, i.e. to determine the deviation in the position of the measuring cube. The deviation is determined using six linear incremental sensors located in the programmed position, sensors from the manufacturer Heidenhain marked MT 25 and MT 12 with an accuracy of 0.004 mm were used, Figure 3.

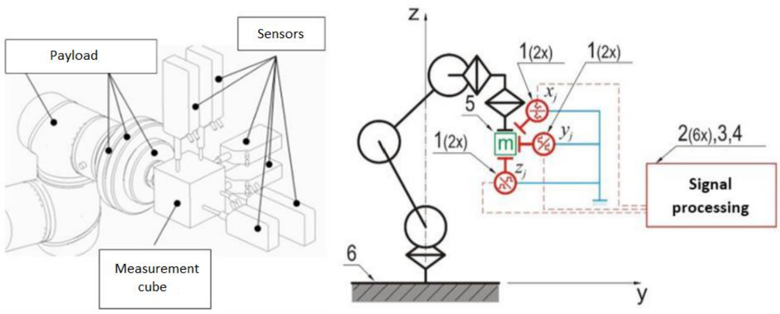

Figure 2. Location of sensors and measuring cube.

Figure 3. A real view of sensors during measurement.

Tests were selected from the ISO 9283 standard, the implementation of which ensures the identification and comparison of the required properties. The most important verification parameters were selected: Unindirectional pose accuracy and Unindirectional orientation accuracy. Before the actual measurement, the basic conditions must be met. The robot must be completely assembled and fully functional. The test must be preceded by a designated heating operation, if specified by the manufacturer. The ambient temperature during the tests should be kept within (20 ± 2) °C. The measured position and orientation data (coordinates xj, yj, zj, aj, bj, cj) must be expressed in a coordinate system whose axes are parallel to the axes of the coordinate system of the base of the measured robot [10-11].

Unindirectional pose accuracy (AP_{xyz}) - represents a deviation between the programmed position and the average of the positions achieved when moving to the programmed position from the same direction. Unindirectional pose accuracy (mm) is calculated according to:

$$= (\bar{\ } - \ ) \qquad = (\bar{\ } - \ ) \qquad = (\bar{\ } - \ ), \tag{1}$$

where, (x_c, y_c, z_c) are the programmed values and (x_j, y_j, z_j) are the actual (measured) values (mm). While:

$$\bar{\ } = - \ \frac{1}{\ }\sum_{=1} \qquad \bar{\ } = - \ \frac{1}{\ }\sum_{=1} \qquad \bar{\ } = - \ \frac{1}{\ }\sum_{=1} \ . \tag{2}$$

The resulting value of "unindirectional pose accuracy" wrist precision is based on the relationship (mm):

$$xy \quad = \sqrt{(^{-} - \quad)^2 + (^{-} \; - \quad)^2 + (^{-} - \quad)^2}. \tag{3}$$

Unidirectional orientation accuracy (AP$_{abc}$) - represents the deviation between the programmed position and the average of the positions reached when orienting around the tool position to the programmed position from the same direction. Unidirectional orientation accuracy (mm) is calculated according to:

$$= (^{-} \; - \quad) \qquad = (\bar{\;} \; - \quad) \qquad = (^{-} - \quad), \tag{4}$$

where, (a_c, b_c, c_c) are the programmed values and (a_j, b_j, c_j) are the actual (measured) values (mm). While:

$$^{-} \;\; = - \; \frac{1}{}\sum_{=1} \qquad\qquad ^{-} \;\; = - \; \frac{1}{}\sum_{=1} \qquad\qquad ^{-} = - \; \frac{1}{}\sum_{=1} \quad , \tag{5}$$

The resulting value of "unindirectional orientation accuracy" wrist precision is based on the relationship (mm):

$$abc = \sqrt{(^{-} \; - \quad)^2 + (\bar{\;} \; - \quad)^2 + (^{-} - \quad)^2}. \tag{6}$$

4. Measurement results and discussion

The first measurement was carried out at half load, as defined by the ISO 9283 standard. The half load capacity of the Dobot CR5 robot is 2.5 kg. Table 2 shows the measured data of the first ten measurements at a load capacity of 50%. The table on the left represents the measured data at 50% of the robot's movement speed, and the table on the right represents the measured data at the full 100% of the robot's speed.

Table 2. Measured data at 50% of the robot's load capacity (2.5 kg).

No. / axis	Xj (mm)	Aj (mm)	Yj (mm)	Bj (mm)	Zj (mm)	Cj (mm)
1	0,005	0,004	0,000	0,000	-0,007	-0,007
2	0,007	0,006	0,001	0,001	-0,009	-0,009
3	0,007	0,007	-0,003	-0,003	-0,010	-0,011
4	0,008	0,008	-0,002	-0,002	-0,013	-0,014
5	0,005	0,006	-0,005	-0,005	-0,006	-0,007
6	0,006	0,006	-0,004	-0,004	-0,008	-0,008
7	0,006	0,006	0,000	0,001	-0,008	-0,010
8	0,006	0,006	0,003	0,005	-0,008	-0,011
9	0,010	0,010	-0,003	0,000	-0,014	-0,018
10	0,011	0,011	-0,004	-0,001	-0,015	-0,019

No. / axis	Xj (mm)	Aj (mm)	Yj (mm)	Bj (mm)	Zj (mm)	Cj (mm)
1	0,015	0,015	-0,001	-0,001	-0,017	-0,017
2	0,015	0,015	-0,001	-0,001	-0,014	-0,015
3	0,017	0,016	0,000	0,001	-0,017	-0,018
4	0,017	0,016	-0,003	-0,002	-0,019	-0,020
5	0,017	0,016	-0,001	0,000	-0,017	-0,018
6	0,015	0,015	-0,002	-0,001	-0,015	-0,016
7	0,015	0,015	0,001	0,003	-0,016	-0,019
8	0,019	0,018	-0,002	0,000	-0,021	-0,023
9	0,021	0,019	0,002	0,003	-0,023	-0,025
10	0,019	0,019	-0,005	-0,003	-0,020	-0,022

The second measurement was carried out when the robot was fully loaded. The full load capacity of the Dobot CR5 robot is 5 kg. Table 3 shows the measured data of the first ten measurements at a load capacity of 100%. The table on the left represents the measured data at 50% of the robot's movement speed, and the table on the right represents the measured data at the full 100% of the robot's speed.

Table 3. Measured data at 100% of the robot's load capacity (5 kg).

No. / axis	Xj (mm)	Aj (mm)	Yj (mm)	Bj (mm)	Zj (mm)	Cj (mm)
1	0,008	0,008	-0,003	-0,005	-0,014	-0,016
2	0,008	0,009	-0,003	-0,005	-0,016	-0,017
3	0,005	0,007	-0,009	-0,011	-0,012	-0,012
4	0,003	0,004	-0,012	-0,012	-0,006	-0,006
5	0,000	0,000	-0,013	-0,002	0,000	0,000
6	-0,002	-0,002	-0,012	-0,001	0,005	0,004
7	-0,002	-0,001	-0,015	0,001	0,004	0,003
8	-0,001	-0,001	-0,014	-0,002	0,004	0,003
9	-0,003	-0,002	-0,014	-0,003	0,005	0,004
10	0,000	0,000	-0,014	-0,001	0,000	0,000

No. / axis	Xj (mm)	Aj (mm)	Yj (mm)	Bj (mm)	Zj (mm)	Cj (mm)
1	0,002	0,003	0,008	-0,007	-0,003	-0,003
2	0,000	0,001	0,015	-0,010	-0,001	-0,001
3	0,007	0,009	0,019	-0,020	-0,017	-0,016
4	0,008	0,009	0,017	-0,011	-0,017	-0,017
5	0,008	0,009	0,015	-0,017	-0,015	-0,014
6	0,009	0,011	0,013	-0,018	-0,017	-0,016
7	0,008	0,009	0,011	-0,012	-0,016	-0,015
8	0,008	0,008	0,010	-0,013	-0,017	-0,016
9	0,007	0,007	0,006	-0,014	-0,014	-0,013
10	0,007	0,007	0,003	-0,012	-0,014	-0,013

After inserting the measured data into relations (1-4) and (5-8) and calculating them according to ISO 9283, the following conclusions can be drawn:

1. Verification results with 50% payload and 50% speed;

   Unindirectional pose accuracy (50%; 50%)

   $= 0.00946\text{mm} \qquad = 0.00943\text{mm} \qquad AP \ = 0.00090\text{mm}$

   $AP = 0.013387 < 0.02\text{mm}$

   Unindirectional orientation accuracy (50%; 50%)

   $= 0.00054\text{mm} \qquad = 0.01210\text{mm} \qquad AP \ = 0.01440\text{mm}$

   $AP = 0.018816 < 0.02\text{mm}$

2. Verification results with 50% payload and 100% speed;

   Unindirectional pose accuracy (50%; 100%)

   $= 0.01980\text{mm} \qquad = 0.01891\text{mm} \qquad AP \ = 0.00090\text{mm}$

   $\boldsymbol{AP = \ .027394 > \ .02\text{mm}}$

   Unindirectional orientation accuracy (50%; 100%)

   $= 0.00020\text{mm} \qquad = 0.02150\text{mm} \qquad AP \ = 0.02240\text{mm}$

   $\boldsymbol{AP = \ .031049 > \ .02\text{mm}}$

3. Verification results with 100% payload and 50% speed;

   Unindirectional pose accuracy (100%; 50%)

   $= 0.00311\text{mm} \qquad = 0.00317\text{mm} \qquad AP \ = 0.00286\text{mm}$

   $AP = 0.00528 < 0.02\text{mm}$

   Unindirectional orientation accuracy (100%; 50%)

   $= 0.00046\text{mm} \qquad = 0.00049\text{mm} \qquad AP \ = 0.00055\text{mm}$

   $AP = 0.000868 < 0.02\text{mm}$

4. Verification results with 100% payload and 100% speed;

   Unindirectional pose accuracy (100%; 100%)

   $= 0.00357\text{mm} \qquad = 0.00471\text{mm} \qquad AP \ = 0.05091\text{mm}$

   $\boldsymbol{AP = \ .051252 > \ .02\text{mm}}$

   Unindirectional orientation accuracy (100%; 100%)

   $= 0.02569\text{mm} \qquad = 0.01377\text{mm} \qquad AP \ = 0.01263\text{mm}$

   $\boldsymbol{AP = \ .031766 > \ .02\text{mm}}$

Based on the calculated data for two load sizes and two speed values, as recommended by the ISO 9283 standard, it can be concluded that the verified Dobot CR5 robot does not reach the manufacturer's guaranteed parameters. The verified robot was able to reach the required parameters only at half the movement speed. At maximum speed, values higher than guaranteed by the manufacturer (0.02 mm) were calculated.

5. Conclusion

The verified robot Dobot CR5 was subjected to measurement of accuracy of positioning and orientation. The measurement took place in the laboratory, under laboratory conditions, consisting of 4 measurements at different robot loads and different robot speeds. The seller states the positioning accuracy at the level of ± 0.02 mm, this value was confirmed at 50% load of the robot, at the maximum 100% load of the robot, this value was exceeded up to the level of 0.05 mm. Based on these findings, an analysis was carried out under which conditions the verified robot worked and what activities it performed. It was found that the robot was used as a demonstration, that means often transportation to various events, transportation in the trunk of a passenger car, various service personnel. For this reason, we can conclude that the aforementioned non-standard use of the robot could have had an impact on its results during the measurement and it would be appropriate to carry out a comparative measurement on other robots of this type.

Acknowledgments: This article was created thanks to the support of the VEGA project: 1/0215/23 Research and development of robotic workplaces equipped with industrial and collaborative robots.

References

1. Thesis. Available online: https://core.ac.uk/download/pdf/158311062.pdf (accessed on 20-03-2024).
2. Semjon, J.; Janos, R.; Sukop, M. et al. Verification of the UR5 robot's properties after a crash caused by a fall of a transferred load from a crane. International Journal of Advanced Robotic Systems. 2020;17(1). doi:10.1177/1729881420904209
3. Płaczek, M. and Piszczek, L. Testing of an industrial robot's accuracy and repeatability in off and online environment. Eksploatacja i Niezawodnosc - Maintenance and Reliability (2018).
4. ISO 9283:1998. Manipulating industrial robots. Performance criteria and related test methods. International Organization for Standardization. Geneva.
5. Slamani, M.A. et al. Assessment of the positioning performance of an industrial robot. Ind. Robot 39 (2012): 57-68.
6. Pollák, M.; Kočiško, M.; Paulišin, D.; Baron, P. Measurement of unidirectional pose accuracy and repeatability of the collaborative robot UR5. Advances in Mechanical Engineering. 2020;12(12). doi:10.1177/1687814020972893.
7. ISO 8373:2012. Robots and robotic devices – Vocabulary. International Organization for Standardization. Geneva.
8. Onderová, I. and Kolláth, L. Testing and verification of selected technological parameters of the PKS. Proceedings of the 2014 15th International Carpathian Control Conference (ICCC) (2014): 398-402.
9. Dobot. Available online: https://www.dobot-robots.com/products/cr-series/cr5.html (accessed on 21-03-2024).
10. ISO 9787:2013. Robots and robotic devices – Coordinate systems and motion momenclatures. International Organization for Standardization. Geneva.
11. ISO 9787:2013. Robots and robotic devices – Coordinate systems and motion momenclatures. International Organization for Standardization. Geneva.

TECHNICKÁ UNIVERZITA V KOŠICIACH
Strojnícka fakulta

CRITERIA FOR THE ASSESSMENT OF LOW-FREQUENCY NOISE EMISSIONS

Lukáš Salaj [1], Michaela Balážiková,[2], Mária Hlinková [3],

[1] Technical University of Košice, Faculty of Mechanical Engineering, Department of Production Safety and Quality, Slovakia, lukas.salaj@ student.tuke.sk
[2] Technical University of Košice, Faculty of Mechanical Engineering, Department of Production Safety and Quality, Slovakia, michaela.balazikova@tuke.sk
[3] Technical University of Košice, Faculty of Civil Engineering, Department of Environmental Engineering, maria.hlinkova@student.tuke.sk

Abstract: The article analyses the assessment of vibro-acoustic risks in mechanical engineering by evaluating the impact of vibrations on humans in the working process in the mechanical engineering industry. Within the working environment and the individual factors that affect the performance and safety of workers in the work process, it is most important to monitor their health. Worker health is seen as a set of factors interacting within the work environment, the environment, genetics and lifestyle. It is therefore very important to evaluate and assess the risks present in the working environment, since workers are more likely to be exposed to concomitant health effects given the relatively long periods of time that they carry out their work activities. These co-morbidities are also directly related to vibration and noise.

Keywords: low-frequency noise, noise measurement, measurement evaluation

1. Introduction

There are many times when the terms sound and noise are confused, and these are different terms. Sound is defined as a form of energy that is propagated and transmitted by a change in pressure, which the human ear picks up and can recognize. Noise is defined as unwanted sound that has a clearly negative connotation when compared to sound. The best person who can tell whether it is sound or noise is the human being himself. At work, where workers are exposed to low frequency noise, a higher degree of annoyance and annoyance has been reported in many studies to be associated with subjective symptoms such as fatigue, dizziness, feeling of pressure in the head and on the eardrum, mood swings, which affects people in their work performance by reducing their attention and concentration. Speech intelligibility is significantly affected by low frequencies such as 20 Hz. Disruption of the vestibular system results in disorientation, nausea, or disturbed balance. [1] It can be argued that this type of noise increases occupational stress, increasing cognitive load and therefore increasing the likelihood of errors and increasing the likelihood of workplace accidents. The effects of extra-occupational low-frequency noise on work and the employer include a negative impact on work performance (reduced quality, increased errors), an overall reduction in work efficiency, and an increase in employer costs associated with increased employee sickness and the occurrence of work-related injuries and accidents. [2]

Many researchers [4,5,6] have pointed out the inaccuracies associated with measuring noise using dB(A), as this method involves an over-reliance on the average hearing sensitivity curve and associated loudness functions as predictors of noise annoyance.

2. Materials and Methods

The aim of the experimental measurements in this paper is to confirm or exclude the exceedance of L_{Zeq} over L_{Aeq} [3] values in the selected work activity (CNC Milling) by measuring the A equivalent sound pressure level L_{Aeq} and the Z equivalent sound pressure level L_{Zeq}.

The main reason for these measurements is to show the difference between the L_{Aeq} and L_{Zeq} values (the influence of acoustic energy not only on auditory, but mainly on extra-auditory effects in employees exposed to this type of noise).

Measurements of low-frequency noise at the engineering workplace - CNC Milling, when they were measured with the instrument designed for this purpose:
- equivalent sound pressure level A L_{Aeq} [dB],
- equivalent sound pressure level Z L_{Zeq} [dB].

3. Results

The CNC milling operation takes place in a room, Fig.1, where in addition to the equipment, there are worktables with a computer with special software for programming the equipment. In addition to the tables, there is also a storage area.

There is one window in the room, which is the only source of ventilation, as the workplace does not have a ceiling fan or an air conditioning unit. The source of light, apart from natural light, is neon lights placed lengthwise on the ceiling, 6 in number. The dimensions of the room are 11,5 m in length and 4,5 m in width. The ceiling height is 3 m, the floor is tiled. A schematic representation with a floor plan of the workplace and the location of the measuring equipment is shown in Fig. 2.

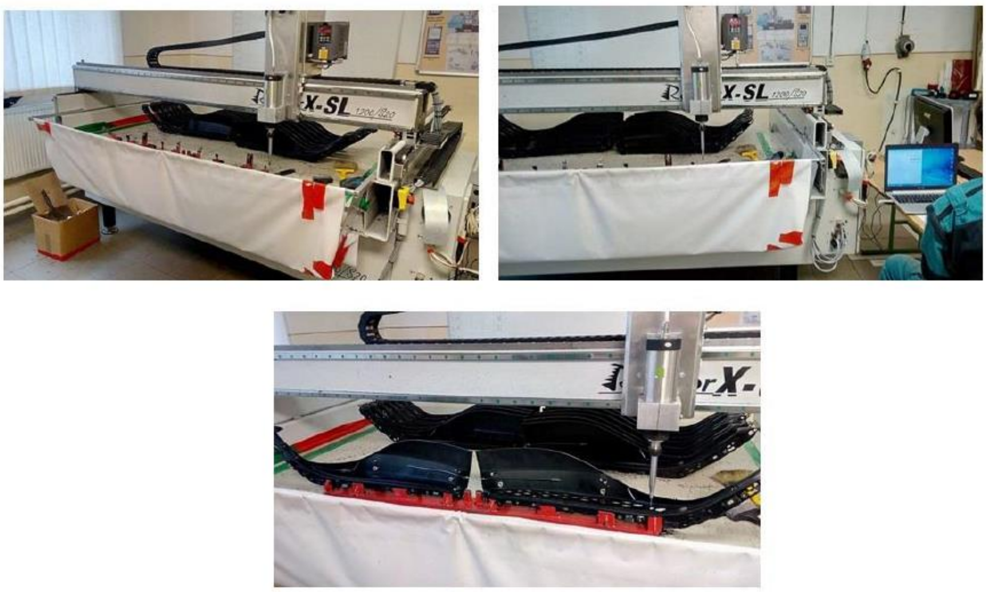

Figure 1. CNC machining workplace

The measurement time of L_{Aeq} and L_{Zeq} was 5 minutes, which represents the machining time of a specific single plastic part for automobiles. The application range of the machine is extremely wide due to the adjustable height of the working surface.

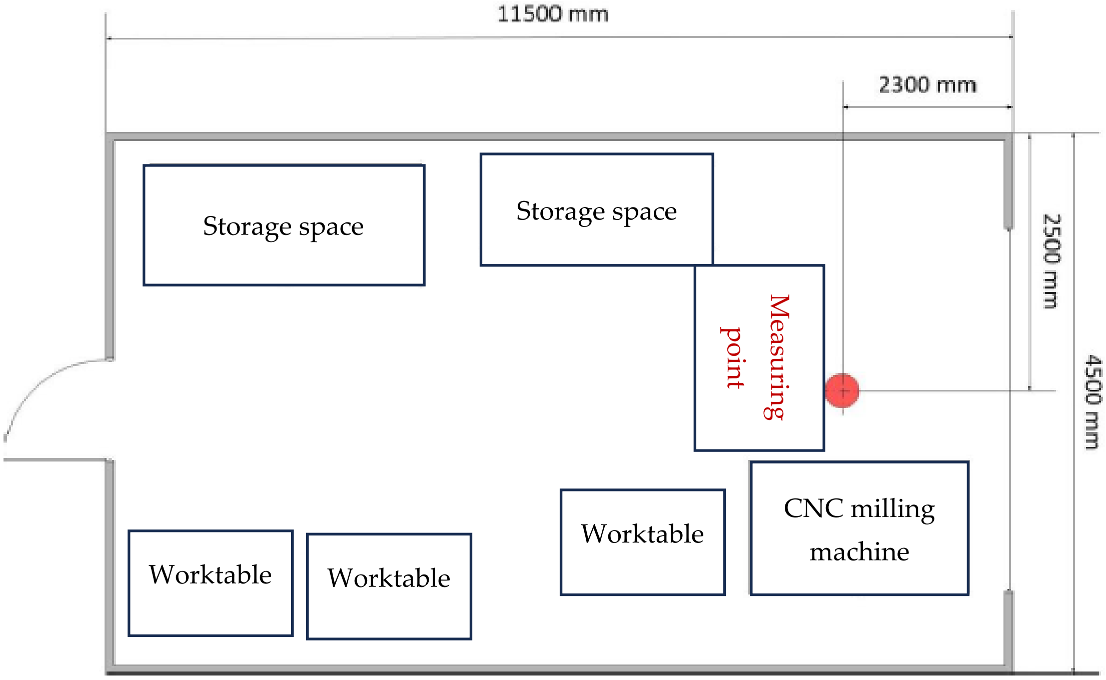

Figure 2. Plan of the CNC machining workplace.

As described in the previous sections, the measurement at workstation during the work activities were carried out twice, the first time the sound analyzer was set to measure with the A weighting filter and then the measurement was carried out with the Z weighting filter. In the individual measurement records, the A and Z sound pressure levels at low frequencies, namely from 12.5 Hz to 125 Hz, are specified for the evaluation of the measured parameters; for comparison, the frequency of 1 kHz is also evaluated. This is due to the fact that the aim of the experimental measurement is to show the different values of noise exposure using the A-weighting filter and the Z-weighting filter. The 1 kHz frequency is compared because the subjective loudness in phonons is identical to the objective loudness in decibels at this frequency.

Table 1 shows the measured L_{Aeq} and L_{Zeq} levels during the work activity.

Table 1. Measured L_{Aeq} and L_{Zeq} at the sites.

Work activities		L_{Aeq}	L_{Zeq}
Activities	CNC machining	81,54	84,32

Fig.3 show the frequency analysis of machining using CNC milling machine shows the sound pressure levels A at frequencies from 8 Hz to 16 kHz. For frequencies of 25 Hz, the values of L_{AFmin} = -12.8 dB, L_{AFmax} = 26.8 dB and L_{Aeq} = 2.5 dB, Fig.3.

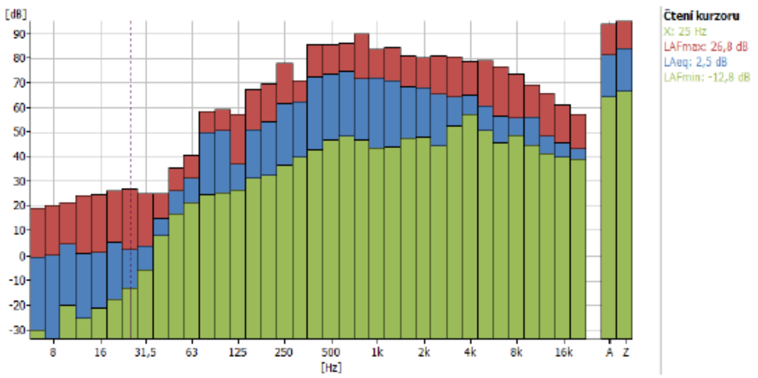

Figure 3. 1/3 octave frequency analysis when measured with weighted filter A at 25 Hz.

For comparison of the measurements with the A-weighted filter, the values of L_{ZFmin} = 31.8 dB, L_{ZFmax} = 52.8 dB, and L_{Zeq} = 41.7 dB at a frequency of 25 Hz, Fig. 4.

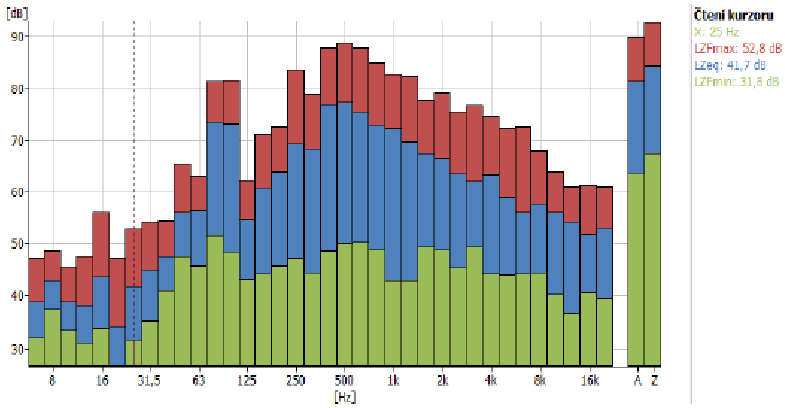

Figure 4. 1/3 octave frequency analysis when measured with weighted filter Z at 25 Hz.

Based on the recorded L_{Aeq} and L_{Zeq} values for low frequencies from 12.5 Hz to 125 Hz and at 1 kHz in the time-course measurement with the A and Z weighting filters, the individual measured L_{Aeq} values and L_{Zeq} values are graphically processed in Fig. 5 and Fig. 6, respectively. Comparing the figures, it is evident that the L_{Aeq} levels at low frequencies are lower compared to the measured L_{Zeq} levels.

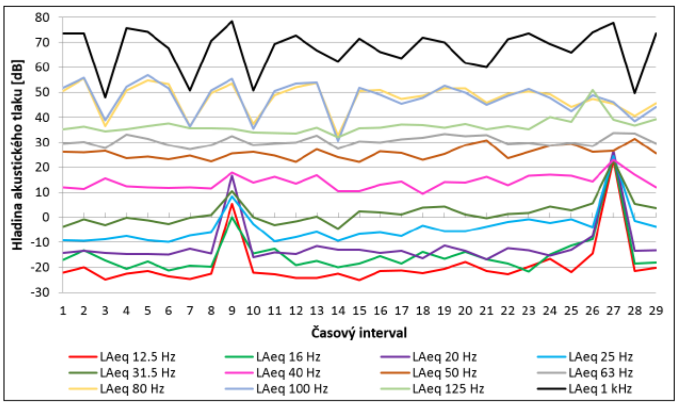

Figure 5. Time history of sound pressure levels L_{Aeq} at the considered frequencies with weighting filter A.

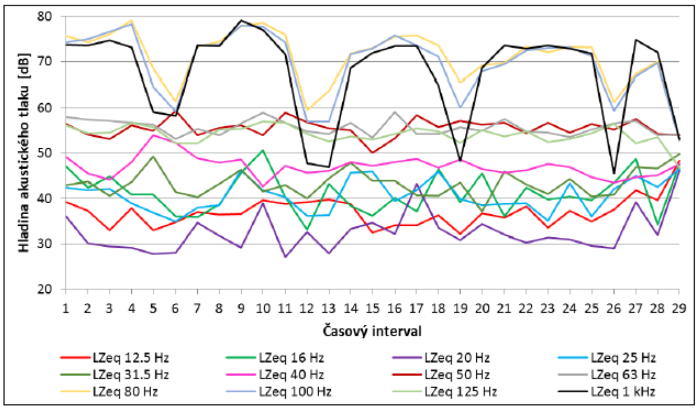

Figure 6 Time history of sound pressure levels L_{Zeq} at the considered frequencies with weighting filter Z.

4. Discussion

The comparison and difference of the measured values of the sound pressure levels L_{Aeq} and L_{Zeq} are described in Table 2. The most noticeable difference is 42 dB at a frequency of 16 Hz. The difference decreases with increasing frequency.

Measurement with weighing filter A		Measurement with weighing filter Z		Difference $L_{Zeq} - L_{Aeq}$ [dB]
L_{Aeq}	[dB]	L_{Zeq}	[dB]	
12.5 Hz	1,16	12.5 Hz	38,44	37,28
16 Hz	1,54	16 Hz	43,54	42
20 Hz	5,78	20 Hz	34,33	28,55
25 Hz	2,49	25 Hz	41,7	39,21
31.5 Hz	4,17	31.5 Hz	44,92	40,75
40 Hz	14,8	40 Hz	47,68	32,88
50 Hz	26,09	50 Hz	56,06	29,97
63 Hz	30,93	63 Hz	56,44	25,51
80 Hz	49,97	80 Hz	73,58	23,61
100 Hz	50,63	100 Hz	73,2	22,57
125 Hz	37,01	125 Hz	54,62	17,61
1 kHz	71,86	1kHz	72,32	0,46

Table 2. Difference between measured values of L_{Aeq} and L_{Zeq} levels

From the following Fig. 7, the difference between the noise exposure measurements using the A and Z weighting filters can be seen by means of graphical processing. The biggest difference is at low frequencies. The sound pressure levels equalize to merge at 1 kHz.

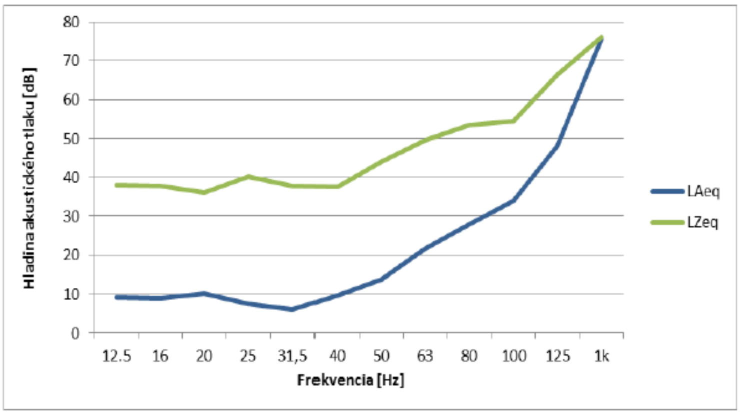

Figure 7. Comparison of L_{Aeq} and L_{Zeq} levels at frequencies from 12.5 Hz - 125 Hz and at 1 kHz

The difference between L_{Zeq} and L_{Aeq} decreases with increasing frequency, as demonstrated by the resulting differences. The primary aim of the noise exposure measurements was to draw attention to the fact that, although legislative regulations stipulate noise measurements in workplaces together with sound pressure limits and also specify noise protection options, employees are also exposed to a different type of noise at work, namely low frequency noise.

5. Conclusions

Low-frequency noise is ubiquitous in modern society and yet existing legislation in this area is inadequate. Not only are they expressed only in dB(A) units, which do not reflect the assessment of low-frequency noise, but no specific measures are prescribed when excessive low-frequency noise is identified. Although this noise is inaudible to human hearing, it is nevertheless understood and perceived as a mixture of stimuli and is one of the risk factors for health damage in workplaces. As the values of low-frequency noise using the Z-weighting filter are not legislated, the measurement and assessment of this noise is not mandatory for employers and therefore does not have to be carried out. However, these values highlight the need to address the issue of assessment and measurement of low-frequency noise at work in indoor environments, which is not adequately described.

Acknowledgments: The paper was prepared within the framework of the grant project of the Ministry of Education APVV-19-0367 Framework Integrated Process Safety Management Approach for Smart Enterprise.

Conflicts of Interest: The authors declare no conflict of interest.

References

1. ŽIARAN, S., CHLEBO, O.: Expozícia človeka nízkofrekvenčnému hluku. In Životné podmienky a zdravie: zborník vedeckých prác. 1. vyd. Bratislava: Úrad verejného zdravotníctva SR, 2016, S. 52-58. ISBN 978-80-7159-225-9.
2. PRASHANTH, M., VENUGOPALACHAR, S.: The possible influence of noise frequency components on the health of exposed industrial workers, In: NOISE & HEALTH, Volume:13, Issue:50,2011,16-25.
3. DIRECTIVE 2003/10/EC OF THE EUROPEAN PARLIAMENT AND OF THE COUNCIL of 6 February 2003 on the minimum health and safety requirements regarding the exposure of workers to the risks arising from physical agents (noise).
4. RASMUSSEN, G., NIELSON, K. M.: Technical Note Low Frequency Calibration of Measurement Microphones. In: Journal of low frequency noise, vibration and active control, roč. 28, č. 3, 2009. s. 223-228.
5. MOORHOUSE, AT., WADDINGTON, DC., ADAMS: Procedure for the assessment of low frequency noise disturbance. In: The Journal of the Acoustical Society of America. 2009 roč. 126, 2009, č.3, s. 1131-1141. doi: 10.1121/1.3180695.
6. PERSSON WAYE, K.: Noise and Health - Effects of Low Frequency Noise and Vibrations: Environmental and Occupational Perspectives. In: Encyclopedia of Environmental Health. Vol 2, 2011. Publisher: Burlington, Editors: Nriagu JO, s.240-253.

TECHNICKÁ UNIVERZITA V KOŠICIAH
Strojnícka fakulta

Overview of Currently Used Techniques and Innovative Alternatives with the Use of 3D Printing in Orthodontic Treatment of Patients with Cleft Palate

Natalia Savkova [1], Jozef Zivcak [2] and Marek Schnitzer [3,*]

[1] Technical University of Kosice, Department of Biomedical Engineering, Automation and Measurement; dr.nataliasavkova@gmail.com
[2] Technical University of Kosice, Department of Biomedical Engineering, Automation and Measurement; jozef.zivcak@tuke.sk
[3] Technical University of Kosice, Department of Biomedical Engineering, Automation and Measurement; marek.schnitzer@tuke.sk
* Correspondence: dr.nataliasavkova@gmail.com

Abstract: Cleft lip and/or palate is the most common congenital maxillofacial anomaly, which has functional and aesthetic implications for the individual. These patients require lengthy orthodontic treatment, often from infancy to adulthood. Increased caries risk, dystopically erupted teeth, decreased patient motivation due to the length of the treatment, as well as the possible presence of oro-nasal communication, require a specific approach. The aim of this article is to present orthodontic treatment using 3D printing alternatives to achieve personalized, more precise, and easily reproducible appliances.

Keywords: 3D printing; cleft palate; NAM; aligners

1. Introduction

Cleft lip (with or without cleft palate) occurs in approximately 1 in 700 live births in Europe. [1] In Slovakia, according to the Health Yearbook, there were 1.52 cases per 1000 live births. [2] Cleft lip and palate is a congenital defect where during facial development, there is a disruption in the growth and fusion of five facial prominences between the 4th and 10th week of gestation. [3] The result is incomplete fusion of the lips and/or palate, which requires long-term interdisciplinary care. The treating team includes pediatricians, pediatric dentists, orthodontists, maxillofacial surgeons, otolaryngologists, geneticists, speech therapists, psychologists/psychiatrists, and others depending on associated conditions. Treatment of these patients must occur at recommended intervals to prevent early mortality and long-term problems with feeding, speech, hearing, self-esteem, and interpersonal relationships. [4–6]

The main objective of this article is to review current techniques and explore innovative alternatives, with a particular focus on the use of 3D printing in the orthodontic treatment of patients with cleft palate.

2. Materials and Methods

Electronic databases including PubMed, MEDLINE, and Web of Science were used to search for current articles using the following keywords: "cleft lip/palate" OR "orofacial cleft", AND "biomaterials" OR "biocompatible", AND "3D printing" OR "4D printing" OR "additive manufacturing" OR "3D bioprinting". Only articles with full text written in Slovak, English, French, or Spanish were considered. Further manual searching was conducted based on relevant citations.

3. Results

3.1 Current orthopedic treatment of patients with cleft palate

The first postnatal procedure performed in the first weeks after birth is preparation for surgery, characterized as pre-surgical orthopedic treatment (PSIOT) through nasoalveolar molding (NAM), facial taping, or Latham appliances. [7] These therapeutic approaches have been used for many years and exist in either active or passive forms. [8]

The aim of passive methods is to separate the oral from the nasal cavity, prevent tongue insertion into the cleft gap, and thereby normalize intraoral forces, while the aim of active methods is to approximate individual skeletal, cartilaginous, and soft tissue parts to improve the outcomes of subsequent surgeries. [9]

NAM is the most popular for shaping the nasal wings and dental arch, and in the case of cleft palate, it requires taking an impression of the jaw for NAM plate fabrication. The NAM plate is accompanied by taping various parts of the nose and lip.

Taking an impression from a newborn poses certain risks, especially due to possible aspiration of the impression material, requiring the presence of an anesthesiologist.

The second orthopedic phase of treatment is typically performed during the mixed dentition period, aimed at ensuring proper access for the surgeon (to prevent collapse of the maxillary segments) and addressing deviations such as anterior or posterior crossbite, which if persistent into later ages, may worsen jaw development.

In this phase, removable appliances are often used, causing slow expansion of the jaw, or fixed appliances such as the bihelix, quadhelix, or Haas/Hyrax. [7,10,11]

The third step of orthodontic treatment involves functional and aesthetic correction of orthodontic deviations using fixed appliances attached directly to the teeth. This treatment lasts an average of 3.4 years. [12] Worth's meta-analysis showed that patients with clefts had a higher prevalence of dental caries than those without clefts. [10,13] Prolonged orthodontic treatment also increases the risk of dental caries. [14]

3.2 Proposed orthodontic treatment approach for patients with cleft palate using 3D printing

In the first presurgical phase, a non-invasive intraoral scan (IOS) can be performed to mitigate the risk of impression material aspiration, making it safer and allowing for intraoral device printing. An extraoral scan (FS) can also be used to aid in planning extraoral appliance retention parts. Additionally, it allows for data acquisition and storage for comparison of individual improvements and subsequent research. An active appliance can be produced, gradually bringing individual parts closer together, or a passive one, primarily aimed at separating the nasal cavity from the oral cavity, thus preventing tongue insertion into the cleft space.

A similar procedure was carried out in patients with unilateral cleft lip and palate. Prenatal DICOM (Digital Imaging and Communications in Medicine) data were obtained using 3D ultrasound and low-dose CT scanning. This resulted in the creation of a 3D-printed PCAM PNAM-JUSCHI device coated with silicone to reduce mucosal irritation, ensuring maximum comfort. One of the advantages of this approach was that the patient had the device placed into the oral cavity immediately after birth, allowing for breastfeeding. Several patents are associated with this device, including Slovak (PP 8-2020) and European ones (EP4021342A1). [15–17]

In the second and third orthodontic phases, which vary for each patient, a removable aligner prepared by 3D printing can also be used. Removable aligners are currently a common part of almost every orthodontic practice. Their main advantages include aesthetic appearance and the ability to remove them for eating and hygiene. Several studies indicate that compared to fixed appliances, they facilitate oral hygiene for the patient. [18–20] Another advantage is the possibility of combining CBCT and .stl files for precise treatment planning and tooth movement as needed.

However, conventional removable aligners have certain limitations, such as not including ectopically erupted teeth, which are very common in patients with clefts. Figure 1 shows the omission of an ectopically erupted lateral incisor in a patient without a cleft. They are also limited in terms of the dental arch, meaning they do not cover the palate.

Despite surgeries, many patients at this age fail to achieve complete separation of the oral and nasal cavities and are expected to undergo them again at a later age. Oro-nasal communication, among other things, causes hypernasal speech, which can be difficult to understand. [21]

3.3 Design and the material of 3D printed aligners

With directly printed aligners, the orthodontist can design them using 3D software, control their strength and flexibility, and most importantly, customize everything to the patients' needs. Direct printing of aligners can reduce production time and increase productivity. It is actively used not only in Korea but also on the international market, showing much better results than conventional methods. [22]

One specific material with potential in orthodontic treatment of patients with Cleft Lip/Palate (CLP) is Tera Harz TC-85. It is a bio-compatible photopolymer that has already obtained global certifications for medical devices, including CE, FDA, and KFDA. It is currently available in transparent (TC-85DAC) and white (TC-85DAW).

The directly printed aligner has a uniform thickness designed to be 0.5 mm, but the thickness and shape of the aligner can be customized as needed. Tera Harz TC-85 is a shape memory polymer (SMP), so it regains its shape at human body temperature. [22,23] After one week of wearing the aligners, they exhibited the same mechanical properties as at the beginning, which is not the case with conventional aligner appliances. [24]

In the case of conventional thermoformed aligners created from 3D printed models, complete deformation occurs in boiling water. However, in the case of directly printed aligners, even if contaminated by long-term use and foreign object debris, they can be restored to a clean state and their original shape and mechanical properties through temperature disinfection up to 100°C. Directly printed aligners are resistant to color changes and easily regain transparency through simple cleaning with toothpaste, whereas existing materials are weak to color changes and never able to regain their original color. [22,23]

In patients with CLP, aligner designs may have higher edges to achieve greater control over tooth movement. The maxillary aligner may also cover the palate in cases of oro-nasal communication to improve speech. Teeth in the cleft gap area should have fewer or no attachments designed to minimize trauma to the periodontium during appliance insertion and removal, as in patients with periodontal diseases.

Figure 1. Limitation of conventionally used aligners.

4. Discussion

Among the advantages of using 3D printing in patients with cleft palate are individualization, higher accuracy, reproducibility, fewer appliance adjustment visits, and data storage for scientific research.

Currently, the method of newborn digital scanning and subsequent 3D printing of appliances is increasingly used, as documented by Zarean et al., who make passive presurgical orthopedic plates with stereolithography. They use a biocompatible photopolymer resin called BioMed Clear from Formlabs Inc. (Somerville, MA, USA) for plate fabrication. They note that using this plate resulted in passive reduction in the size of the cleft defect, with patients wearing the same plate for three to four months with significantly fewer adjustments and therefore fewer visits. [25]

Ahmed also recommends using the SLA method to create NAM appliances from biocompatible resins but does not specify which were utilized in their study. [26]

In another study by Xepapadeas and colleagues from Germany, they focus on printing the Tübingen Palatal Plate (TTPP), which in addition to covering the palate also includes a velar flap, which may be defective in patients affected by Pierre Robin sequence, along with cleft palate. This flap prevents tongue fall-back, thereby reducing the likelihood of airway obstruction. [27]

Batra used 3D printing as an intermediate product to create 3D models of the jaw and subsequently thermoformed aligners to create a series of active appliances, with movement between the aligners limited to 1 mm. Their goal was to align and approximate the alveolar segments, using 15 aligners for all four patients with an average treatment duration of 16 weeks. [28]

5. Conclusions

The use of intraoral scanners reduces the risk of impression material aspiration. Digitization of this process thus allows for a less stressful record of the palate for the entire team, parents, and patients. The record is retainable and usable for creating a 3D-printed device, which according to various studies, is more accurate, although further research is necessary.

The use of 3D printed aligners in later stages of treatment may bring various benefits, including increased aesthetics, comfort, reproducibility, palate coverage during speech, and potentially reduced dental caries.

Conflicts of Interest: The authors declare no conflict of interest.

References

1. Leslie EJ, Carlson JC, Shaffer JR, Feingold E, Wehby G, Laurie CA, et al. A multi-ethnic genome-wide association study identifies novel loci for non-syndromic cleft lip with or without cleft palate on 2p 24.2, 17q23 and 19q13. Hum Mol Genet. 2016;25(13):2862–72.
2. Národné centrum zdravotníckych Informácií. Zdravotnícк ročenka [Internet]. Bratislava; 2022. Available from: https://www.nczisk.sk/Documents/rocenky/2021/Zdravotnicka_rocenka_Slovenskej_republiky_2021.pdf
3. Langman J, Sadler TW. Langman's Medical Embryology. 7th ed. Wilkins W&, editor. 1995. 460, 69–92 p.
4. Hunt O, Burden D, Hepper P, Johnston C. The psychosocial effects of cleft lip and palate: a systematic review. Eur J Orthod [Internet]. 2005 [cited 2024 Jan 30];27:274–85. Available from: https://academic.oup.com/ejo/article/27/3/274/457476
5. Hocevar-Boltezar I, Jarc A, Kozelj V. Ear, nose and voice problems in children with orofacial clefts. J Laryngol Otol [Internet]. 2006 Apr [cited 2024 Jan 30];120(4):276–81. Available from: https://www.cambridge.org/core/journals/journal-of-laryngology-and-otology/article/abs/ear-nose-and-voice-problems-in-children-with-orofacial-clefts/B057285216F047207D62591F4431BDAD
6. Nowak AJ, Christensen JR, Mabry TR, Townsend JA, Wells MH. Pediatric Dentistry: Infancy Through Adolescence. Elsevier, editor. 2019. 634 p.
7. Yates D, Allareddy V, Caplin J, Yadav S, Markiewicz MR. An Overview of Timeline of Interventions in the Continuum of Cleft Lip and Palate Care. Oral Maxillofac Surg Clin North Am. 2020 May 1;32(2):177–86.
8. Gong X, Dang R, Xu T, Yu Q, Zheng J. Full Digital Workflow of Nasoalveolar Molding Treatment in Infants With Cleft Lip and Palate. J Craniofac Surg [Internet]. 2020 [cited 2024 Jan 30];31(2):367–71. Available from: https://journals.lww.com/jcraniofacialsurgery/fulltext/2020/04000/full_digital_workflow_of_nasoalveolar_molding.13.aspx
9. Nalabothu P, Benitez BK, Dalstra M, Verna C, Mueller AA. Three-Dimensional Morphological Changes of the True Cleft under Passive Presurgical Orthopaedics in Unilateral Cleft Lip and Palate: A Retrospective Cohort Study. J Clin Med [Internet]. 2020 Apr 1 [cited 2024 Jan 30];9(4). Available from: /pmc/articles/PMC7230798/
10. Gillgrass T. The orthodontic management of patients with cleft lip and palate: from birth to the late mixed dentition. [cited 2024 Jan 30]; Available from: https://doi.org/10.1038/s41415-023-5955-x
11. Allareddy V, Bruun R, MacLaine J, Markiewicz MR, Ruiz R, Miller MA. Orthodontic Preparation for Secondary Alveolar Bone Grafting in Patients with Complete Cleft Lip and Palate. Oral Maxillofac Surg Clin North Am. 2020 May 1;32(2):205–17.
12. Hameed O, Amin N, Haria P, Patel B, Hay N. Orthodontic burden of care for patients with a cleft lip and/or palate. J Orthod. 2019;46(1):63–7.
13. Worth V, Perry R, Ireland T, Wills AK, Sandy J, Ness A. Are people with an orofacial cleft at a higher risk of dental caries? A systematic review and meta-analysis. Br Dent J [Internet]. 2017;223(1):37–47. Available from: http://dx.doi.org/10.1038/sj.bdj.2017.581
14. Choi YY. Relationship between orthodontic treatment and dental caries: results from a national survey. 2019;
15. Zivcak J. Material development in personalized implantology. 1st ed. Kosice; 2023. 116–130 p.
16. Juhas M, Zivcak J, Hudak R, Schnitzer M, Stefanovic B. Personalizovaná zdravotnícк pomôcka a spôsob jej prí ravy [Internet]. Slovakia; 2020. Available from: https://wbr.indprop.gov.sk/WebRegistre/Patent/Detail/8-2020?csrt=6167676377133915492#
17. Juhas M, Zivcak J, Hudak R, Schnitzer M, Stefanovic B. PERSONALIZED MEDICAL DEVICE AND METHOD OF ITS PREPARATION [Internet]. 2022. Available from: https://worldwide.espacenet.com/patent/search/family/086055678/publication/EP4021342A1?q=EP21716564
18. Azaripour A, Weusmann J, Mahmoodi B, Peppas D, Gerhold-Ay A, Van Noorden CJF, et al. Braces versus Invisalign®: Gingival parameters and patients' satisfaction during treatment: A cross-sectional study. BMC Oral Health [Internet]. 2015 Jun 24 [cited 2021 May 24];15(1):1–5. Available from: https://bmcoralhealth.biomedcentral.com/articles/10.1186/s12903-015-0060-4
19. Rouzi M, Zhang X, Jiang Q, Long H, Lai W, Li X. Concise Review Impact of Clear Aligners on Oral Health and Oral Microbiome During Orthodontic Treatment. 2023 [cited 2024 Jan 31]; Available from: https://doi.org/10.1016/j.identj.2023.03.012
20. Jiang Q, Li J, Mei L, Du J, Levrini L, Marco Abbate G, et al. Systematic Review Periodontal health during orthodontic treatment with clear aligners and fixed appliances A meta-analysis. 2018 [cited 2024 Jan 31]; Available from: https://doi.org/10.1016/j.adaj.2018.04.010
21. Leturc T, Chaux-Bodard A-G, Paulus C. Up-to Date Review And Case Report Oronasal fistula as a cleft palate sequela : closure with tongue flap. Case report with review of the literature. [cited 2024 Jan 30]; Available from: www.mbcb-journal.org
22. Graphy- 3D printing materials [Internet]. Available from: http://www.itgraphy.com/ENG/bbs/content.php?co_id=sub0201_1
23. Kim KB, Graf S. Direct printing of clear aligners. J Clin Orthod [Internet]. 2023 Aug [cited 2023 Dec 22];57(8):450–8. Available from: https://pubmed.ncbi.nlm.nih.gov/37778119/
24. Can E, Panayi N, Polychronis G, Papageorgiou SN, Zinelis S, Eliades G, et al. In-house 3D-printed aligners: effect of in vivo ageing on mechanical properties. [cited 2024 Jan 31]; Available from: https://academic.oup.com/ejo/article/44/1/51/6265460
25. Zarean P, Zarean P, Thieringer FM, Mueller AA, Kressmann S, Erismann M, et al. A Point-of-Care Digital Workflow for 3D Printed Passive Presurgical Orthopedic Plates in Cleft Care. Child (Basel, Switzerland) [Internet]. 2022 Aug 1 [cited 2023 Sep 17];9(8). Available from: https://pubmed.ncbi.nlm.nih.gov/36010151/

26. Ahmed MK, Ahsanuddin S, Retrouvey JM, Koka KS, Qureshi H, Bui AH, et al. Fabrication of Nasoalveolar Molding Devices for the Treatment of Cleft Lip and Palate, Using Stereolithography Additive Manufacturing Processes and Computer-Aided Design Manipulation Software. J Craniofac Surg [Internet]. 2019 Nov 1 [cited 2023 Oct 9];30(8):2604–8. Available from: https://journals.lww.com/jcraniofacialsurgery/fulltext/2019/12000/fabrication_of_nasoalveolar_molding_devices_for.85.aspx
27. Xepapadeas AB, Xepapadeas AB, Weise C, Frank K, Spintzyk S, Poets CF, et al. Technical note on introducing a digital workflow for newborns with craniofacial anomalies based on intraoral scans - Part II: 3D printed Tübingen palatal plate prototype for newborns with Robin sequence. BMC Oral Health [Internet]. 2020 Jun 16 [cited 2023 Sep 17];20(1):1–7. Available from: https://bmcoralhealth.biomedcentral.com/articles/10.1186/s12903-020-01159-7
28. Batra P, Gribel BF, Abhinav BA, Arora A, Raghavan S. OrthoAligner "NAM": A Case Series of Presurgical Infant Orthopedics (PSIO) Using Clear Aligners. Cleft Palate-Craniofacial J [Internet]. 2020 May 1 [cited 2023 Sep 11];57(5):646–55. Available from: https://journals.sagepub.com/doi/10.1177/1055665619889807?url_ver=Z39.88-2003&rfr_id=ori%3Arid%3Across-ref.org&rfr_dat=cr_pub++0pubmed

TECHNICKÁ UNIVERZITA V KOŠICIACH
Strojnícka fakulta

The impact of monitoring the light spectrum with a smart bracelet on the circadian rhythm

Veronika Sedláková [1]*, Petra Kolembusová [2] Norbert Ferenčík [3] Radovan Hudák [4] Jana Hlubeňová [5] and Zuzana Naďová[6],

[2] Affiliation 2; petra.kolembusova@tuke.sk
[3] Affiliation 3; norbert.ferencik@tuke.sk
[4] Affiliation 4; radovan.hudak@tuke.sk
[5] Affiliation 5; jana.hlubenova@tuke.sk
[6] Affiliation 6; zuzana.nadova@tuke.sk
* Correspondence: veronika.sedlakova@tuke.sk; Tel.: +421 556 022 044

Abstract: This study explores the influence of light spectrum on sleep quality using the Xiaomi Mi Band 6 wristband for sleep quality measurement and an LED strip with diverse color spectrums. The research highlights the nuanced relationship between color spectrum and sleep quality, concluding with illustrative graphs offering insights into optimizing sleep environments.

Keywords: Circadian Rhythm; LED strips; Sleep quality measurement; Sleep quality light sleep; Xiaomi Mi Band 6

1. Introduction

In this study, we delve into the impact of light spectrum on sleep, focusing on the nuanced relationship between color spectrum and sleep quality. The investigation utilizes the Xiaomi Mi Band 6 wristband for sleep quality measurement and an LED strip with diverse color spectrums as interventions before sleep initiation. By exploring the influence of light spectrum, particularly on light sleep, this study contributes valuable insights into optimizing sleep environments.

2. Circadian Rhythm

Circadian Rhythm is a natural internal process that regulates the sleep-wake cycle. This process repeats approximately every 24.2 hours (see Figure 1). Each organism has its own internal body clock, which in humans is located in the suprachiasmatic nucleus (SCN) in the hypothalamus [1,2].

Melatonin signals the time of day through a secretion pattern that defines the so-called biological night. The secretion of melatonin is not influenced by wakefulness or sleep; instead, it depends on the level and intensity of light reaching the retina. Secretion increases with decreasing light intensity and increasing wavelength. Visible light for the human eye is electromagnetic radiation with a wavelength of 390-790 nm [3].

Typically, melatonin peaks between 3:00 and 5:00 a.m., triggering sleep-inducing reactions via receptor binding in the suprachiasmatic nucleus [3,4,5].

Exposure to evening light delays melatonin release, potentially leading to insufficient production until morning and elevated illumination levels. Blue light, with a maximum response around 440-500 nm, most disrupts melatonin secretion [6,7,8].

Light exposure at night suppressing melatonin has negative health consequences, impacting both physical and mental well-being. Circadian-related sleep disorders are common in mental illnesses, particularly mood disorders [9].

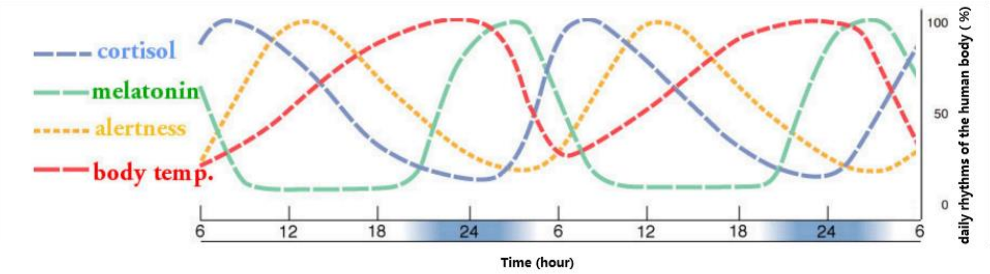

Figure 1. Percentage Performance of Sleep-Influencing Attributes [4]

The opposite process occurs in the morning when the eyes begin to perceive the first light. The central clock receives a signal from the retina that daylight is approaching, and circadian rhythms synchronize. Melatonin production stops, and the body begins to produce the hormone cortisol [10,11].

Cortisol, also known as the stress hormone, induces wakefulness in humans. The highest cortisol levels are typically produced in the early morning [10,11,12].

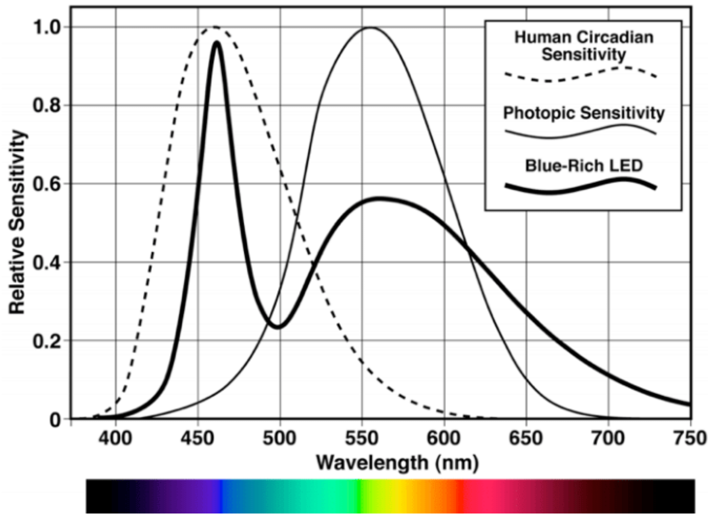

Figure 2. Graph depicting the relationship between the relative sensitivity of the eye and the wavelength of light [13]

In Figure 2, where the human visual sensitivity is represented in the green and yellow parts of the spectrum, it is depicted by a thin line. Circadian rhythms are influenced by light emitted in a broken curve. The light color emitted by a typical cool-white 5500 Kelvin LED is represented by a bold line [13].

A significant portion of light emitted by this light source falls outside the range of human photopic vision and aligns with the circadian rhythm curve. The International Dark-Sky Association (IDA) recommends limiting the emission of blue light below 500 nm, as indicated in the shaded part of the graph [13].

Light plays a crucial role in synchronizing circadian rhythms. One treatment for many circadian disorders is light therapy, which involves sitting close to a bright light at scheduled times to exercise the body's internal clock. A powerful lamp is designed to mimic natural daylight and is often used in the morning to normalize circadian timing[14].

3. The Impact of Light Spectrum on Sleep

From the medical field and various studies, it is evident that, in addition to light intensity, light color also plays a significant role in the impact on the organism. The organism is most sensitive to the blue component of light, as it resembles natural daylight. Light sources such as LED with a cool or neutral shade predominantly emit in the blue region. Therefore, it is advisable to prefer types with a warmer light tone [15].

The color of emitted light is expressed in Kelvins (K). The color spectrum ranges from warm tones to cooler ones (refer to Figure 3). The American Medical Association recommends staying away from light above 5,700 K, as it may be harmful to the human circadian rhythm and affect sleep patterns [16,17].

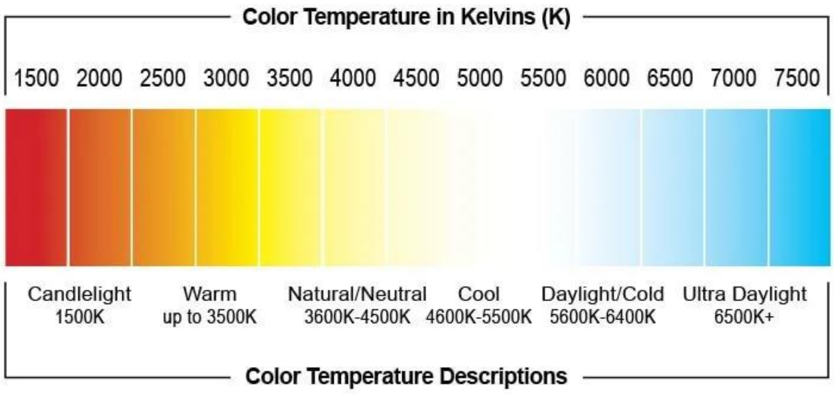

Figure 3. Percent Color Temperature (Light Color Temperature) [18].

According to a study by Peter Studer et al. at the University Hospital Erlangen in Germany, measuring the time it takes for typically developing adolescents (11–17 years) to fall asleep, they found that with blue light, participants experienced a delay of 12-13 minutes in falling asleep, while with red light, the delay was only 6 minutes [19].

The Lighting Research Center, a part of the Rensselaer Polytechnic Institute in New York, conducted a study on the potential therapeutic effects of blue light. Over four weeks, seniors were exposed to LED lighting every day from 4:30 PM to 6:30 PM. The participants, all of whom had individuals with AD in both groups, were observed [20].

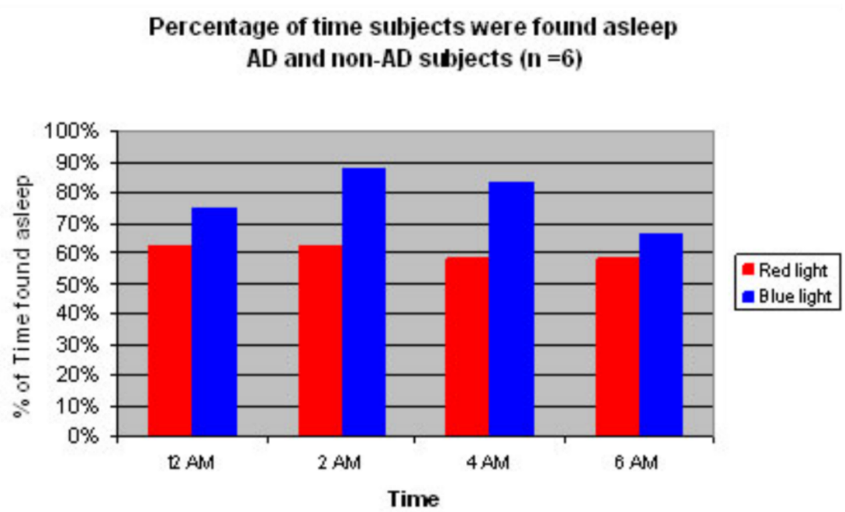

Table 1. Percentage of time subject were found asleep AD and non-AD subject [20].

One group was exposed to blue LED lights during the first two weeks, and the other group to red LED lights (necessary control for the placebo effect). During the second two weeks, the groups were switched. The study demonstrated a statistically significant extension of sleep duration after exposure to blue light during this period in all subjects [20].

In Table 1, the percentage share of nighttime sleep after exposure to red and blue light combined is depicted for individuals without and with AD [20].

3. Proposal for Sleep Quality Measurement

Quality of sleep was assessed using the intelligent Xiaomi Mi Band 6 wristband, while, prior to sleep, an LED strip with various color spectrums was activated.

3.1. Xiaomi Mi Band 6

The Xiaomi Mi Band 6, a leading global fitness tracker, boasts a sleek design with a compact display, touch screen, and AMOLED technology. Weighing 12.7 g, it features a comfortable replaceable polyurethane material [21].

Figure 5. Xiaomi Mi Band6 [21]

Monitored by the new-generation BioTracker sensor, the device's fitness functions encompass heart rate (automatic 24/7), sleep (automatic 24/7), and SpO2 (manual start) [21].

3.2. RGB LED strip

LED strips come in 60 LEDs/m or 30 LEDs/m configurations, with SMD5050 being a highly versatile option. Available in single-color (cool white) and RGB (R=red, G=green, B=blue) versions, SMD5050 combines three chips in one package, also known as tri-chip LED strips. These powerful light sources enable the creation of various colors and shades through a control unit, typically operated by remote controllers [22].

Figure 6. Controller for LED strip and power supply

3.3. Sleep quality and lighting

The box graph illustrates statistics on the duration of awake time in relation to different light colors.

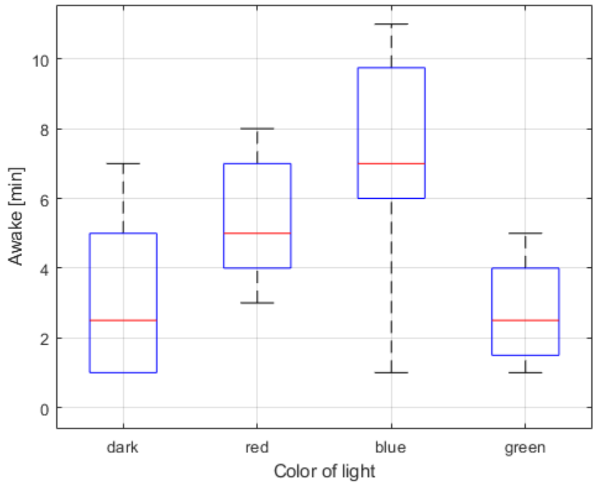

Graph 1. Graph of awake time dependence on light color

The average duration of awakening time without light is 3.17 ± 2.56 min, reflecting a larger dataset without light compared to other categories. With red light exposure, awakening time extends to an average of 5.3 ± 1.88 min, as indicated by the awakening time versus light color graph. It suggests a longer awakening time than with green; however, certainty is limited due to wider variance in data without light.

For blue light, the average awakening time is 6.91 ± 3.45 min, with the awakening time versus light color graph showing a negative impact on sleep quality. The subject experienced the longest time of wakefulness compared to others.

Green light shows an average awakening time of 2.75 ± 1.49 min, slightly longer than without light. This difference may be attributed to green light containing less of the blue spectrum, the primary disruptor of melatonin.

4. Discussion

This study sheds light on the nuanced relationship between light spectrum and sleep quality, emphasizing the impact of different colors on awakening time. Notably, our findings indicate that exposure to blue light had a significantly negative influence on sleep quality, leading to prolonged awakening times. On the other hand, both green light and the absence of light did not show a substantial impact on awakening time. The Xiaomi Mi Band 6 proves to be a valuable tool for sleep quality measurement, providing continuous monitoring alongside the intervention of an RGB LED strip. The observed effects underscore the importance of considering not only light intensity but also color in designing environments conducive to healthy sleep patterns.

5. Conclusions

In conclusion, our study illuminates the intricate interplay between light spectrum and sleep quality, with a specific focus on their impact on awakening time. Leveraging the Xiaomi Mi Band 6 for comprehensive sleep quality assessment, in tandem with interventions using an RGB LED strip, reveals valuable insights. It underscores the necessity of considering color, not just intensity, when designing environments that foster healthy sleep patterns.

References

1. DRAKE, Christopher L. The characterization and pathology of circadian rhythm sleep disorders. Journal of Family Practice, 2010, 59.1: S12-S12.
2. KOVACIC, Peter; SOMANATHAN, Ratnasamy. Cell signaling, receptors, electrical effects and therapy in circadian rhythm. Journal of Receptors and Signal Transduction, 2013, 33.5: 267-275.
3. ARENDT, Josephine. Melatonín a ľudské rytmy. Chronobiology international , 2006, 23.1-2: 21-37.
4. DROUYER, Elise, et al. Responses of suprachiasmatic nucleus neurons to light and dark adaptation: Relative contributions of melanopsin and rod–cone Inputs. Journal of Neuroscience, 2007, 27.36: 9623-9631.
5. BRITANNICA, Encyclopaedia. Available online: https://www. britannica. com/science. Geophone (accessed on 10 March 2021), 2021.
6. JONES, Therésa M., et al. Melatonin: a possible link between the presence of artificial light at night and reductions in biological fitness. Philosophical Transactions of the Royal Society B: Biological Sciences, 2015, 370.1667: 20140122.
7. FALCHI, Fabio, et al. Limiting the impact of light pollution on human health, environment and stellar visibility. Journal of environmental management, 2011, 92.10: 2714-2722.
8. STEVENS, Richard G., et al. Breast cancer and circadian disruption from electric lighting in the modern world. CA: a cancer journal for clinicians, 2014, 64.3: 207-218.
9. MOHD AZMI, Nor Amira Syahira, et al. Consequences of circadian disruption in shift workers on chrononutrition and their psychosocial well-being. International journal of environmental research and public health, 2020, 17.6: 2043.
10. VAN BOMMEL, W. J. M.; VAN DEN BELD, G. J. Lighting for work: a review of visual and biological effects. Lighting research & technology, 2004, 36.4: 255-266.
11. LEGATES, Tara A.; FERNANDEZ, Diego C.; HATTAR, Samer. Light as a central modulator of circadian rhythms, sleep and affect. Nature Reviews Neuroscience, 2014, 15.7: 443-454.
12. VAN BOMMEL, Ir WJM; VAN DEN BELD, Ir GJ. Lighting for work: visual and biological effects. Philips Lighting, The Netherlands, 2003, 1-17.
13. DE ALMEIDA, Aníbal, et al. Solid state lighting review–Potential and challenges in Europe. Renewable and Sustainable Energy Reviews, 2014, 34: 30-48.
14. BARION, Ana; ZEE, Phyllis C. A clinical approach to circadian rhythm sleep disorders. Sleep medicine, 2007, 8.6: 566-577.
15. MICHALSKI, Stefan. Agent of deterioration: light, ultraviolet and infrared. Canadian Conservation Institute, 2018, 17.
16. ALAASAM, Valentina J., et al. Light at night disrupts nocturnal rest and elevates glucocorticoids at cool color temperatures. Journal of Experimental Zoology Part A: Ecological and Integrative Physiology, 2018, 329.8-9: 465-472.
17. ZAUNER, Johannes; PLISCHKE, Herbert. Designing light for night shift workers: application of nonvisual lighting design principles in an industrial production line. Applied Sciences, 2021, 11.22: 10896.
18. MCCAMY, Calvin S. Correlated color temperature as an explicit function of chromaticity coordinates. Color Research & Application, 1992, 17.2: 142-144.
19. STUDER, Petra, et al. Effects of blue-and red-enriched light on attention and sleep in typically developing adolescents. Physiology & behavior, 2019, 199: 11-19.
20. FIGUEIRO, M. G.; REA, M. S. New research in the light and health field is expanding the possibilities for LED lighting in healthcare environments. In: CIE Midterm Meeting Conference Proceedings, Leon, Spain. 2005.
21. POLANSKÝ, Ondřej. Chytrý náramek pro snímání fyziologických a environmentálních dat. 2021.
22. IBRAGIMOV, Matkarim; KUSHNAZAROV, Firdavs; KUSHNAZAROV, Farrukh. Použitie pulzno-expanzného modulu na zvýšenie efektivity prirodzeného kŕmenia rýb lietajúcim hmyzom na umelých rybníkoch. In: Web konferencií E3S . EDP Sciences, 2023. s. 03017.

TECHNICKÁ UNIVERZITA V KOŠICIACH
Strojnícka fakulta

Effect of 3D arch support on foot rotation during walking

Jan Sekac[1], Radovan Hudak[2]

1 Movement laboratory, Orthopedic clinic, Kosice; laboratorium.pohybu@gmail.com
2 Technical University of Kosice; radovan.hudak@tuke.sk
* Correspondence: MUDr. Jan Sekac, Movement laboratory, Orthopedic clinic, Marsala Koneva 1, 040 22, Kosice, laboratorium.pohybu@gmail.com

Abstract: We decided to study the effects of longitudinal and transverse arch support on foot rotation. The rotation of the foot affects the biomechanical load of all passive and active movement structures of the foot and other structures proximal to the ankle. In this work, we evaluated the change in foot rotation using Diers pedogait analysis using a moving belt, a camera with light and a special program that evaluates the data obtained from the participants.

Keywords: 3D foot orthosis, foot rotation, Diers pedogait

1. Introduction

When analyzing the foot during walking, many factors come into play, which is why comparing the results of individual studies is difficult. Distance errors of 2.7-14.9mm [1,2] and angle errors > 10°[3] arise when foot mobility is measured during walking based on markers.

In order to eliminate such errors, standard methods for motion analysis of the foot have been developed [4-10]. Analysis of the foot with the Diers pedogait diagnostic system while walking is fairly repeatable, not complicated. Of course, specialist knowledge and relatively expensive technical equipment are required. Clinical examination, implementation of movement analysis, visualization of results is undemanding. As part of the prevention of possible disorders in the area of the foot, weight-bearing joints and the spine, consistent patient education is essential. Many studies have been devoted to analyzing the motion of the foot with and without an orthopedic insole using biplanes [5-8]. Longitudinal and transverse arch support is primarily used for compensation forces acting on the longitudinal arch on the redistribution of foot pressures, which causes a symmetrical distribution of forces in the articular apparatus of the foot and ankle [7-8]. Some published work confirmed that longitudinal arch support positively affects foot motion, subtalar joint kinematics, and ankle [6], indicating that the longitudinal arch of the foot is a very important component of foot and ankle motion. In addition, when the medial longitudinal arch decreases, pronation of the foot occurs, the height of the tuberculus naviculare decreases [10] (i.e., it affects the talonavicular joint and other joints of the foot). Different types of foot orthoses, different analytical procedures and systems were used in the published studies, and there remains for discussion and further research regarding the analysis of the longitudinal and transverse arch of the foot and their influence not only on the foot and ankle, but also on other parts of the locomotor apparatus of the lower limbs and the axial skeleton.

2. Materials and Methods

We evaluated the effect of longitudinal and transverse arch support on foot rotation in ten female volunteers with planovalgus position of the feet without clinical complaints in the area of the feet. A 4D analysis of the feet was performed using the Diers pedogait system. Movement along the Diers pedogait strain gauge trail was realized at a speed of 3 km/h. first without and then with midfoot support with a 3D orthopedic insole without forefoot and heel guidance. The impact of midfoot support on the change in foot rotation was evaluated.

Figure 1: *3D foot orthosis (part of the orthopedic insole) in lateral projection, used orthosis sample.*

Figure 2: *3D foot orthosis (part of the orthopedic insole) in posteroanterior projection, used orthosis sample.*

Diers pedogait is a diagnostic system used to analyze a patient's gait. The following steps describe the procedure for this examination**:**

1. The patient walks on a special flat, tight pad that is equipped with pressure sensors.
2. Pressure sensors capture the individual points of contact of the feet with the mat and record the distribution and time of the load at each point.
3. The computer software subsequently processes the obtained data and creates a 2D and 3D representation of the patient's gait.
4. The examining physician or specialist evaluates these data and can identify various gait errors or dysfunctions, such as uneven loading, unequally divided gait or irregular movement [11-13].

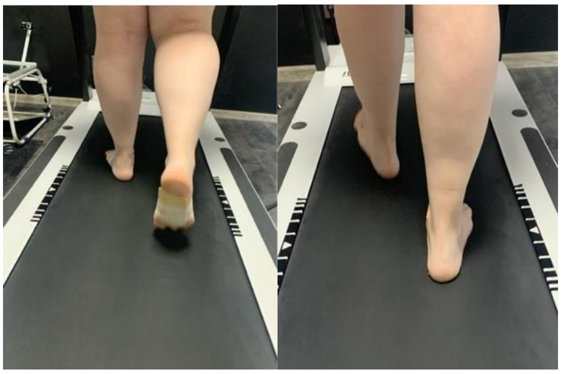

Figure 3: *Walking on the Diers pedogait tensometric moving walkway (in posteroanterior view without orthosis on the left, with orthosis on the right).*

Figure 4: *Walking on the Diers pedogait tensometric moving walkway (in side view without orthosis on the left, with orthosis on the right).*

3. Results

Ten individuals (10 women) participated in the study. The average age, height and weight of the participants were 48.6 ± 13.54 years, 164 ± 11.40 cm, 63.5 ± 14.0 kg. The average foot length was 216 ± 4.36 mm. When comparing walking without midfoot support and with 3D orthopedic insole support, differences in foot rotation during walking were observed. Physiological extrarotation of the foot during walking is considered 10-15°. The average extrarotation during walking without orthosis was 16.3°. During walking with an orthopedic insole, the average extrarotation of the feet was 14.1°. The differences specifically related to the correction of pathological extrarotation of the foot by supporting the longitudinal and transverse arches.

The results of the work pointed to the correction of pathological extrarotation of the foot when walking barefoot on a flat hard surface by supporting the longitudinal and transverse arch with an orthopedic insole. Our study pointed out the suitability of walking with midfoot support by an individual 3D foot orthosis on a flat hard surface.

It is also necessary to take into account the subjective point of view of the probands. They all unanimously agreed that when walking with midfoot support using a 3D individual orthosis, they walked more stably, subjectively better than without shoes, or with the entire insert.
The test subjects positively evaluated the direct contact of the fingers, thumb and heel

with the surface when walking with a minimalistic 3D insole. Subjectively, the sensory perception of the surface was positive when stepping on the heel and when rolling off the big toe and toes.

Figure 5: Parameters obtained *during the examination of Diers pedogait (The examined foot rotation parameter marked with a blue arrow).*

4. Discussion

Using gait analysis with the Diers pedogait system, we can obtain data on the rotation of each foot separately, a pressure map of the foot, and indicate the production of personalized orthoses with the intention of improving the walking stereotype, axial symmetry of the lower limbs, improving the patellofemoral, tiobiofemoral and femoroacetabular articulation.

In real life, a natural walking surface is rather an exception. The evaluation of the leg support by the 3D orthosis by the probands on a flat hard surface, the stability of walking and the sensory contact of the toes and heels when in contact with the mat was positive. Minimalistic 3D leg support, or midfoot, it brings with it several positives, in addition to the subjective satisfaction of the perception of the surface and stability, improvement of the symmetry of the load of the foot and axial correction, as well as an economic and ecological point of view [7-10].

5. Conclusions

The outcome of the Diers pedogait examination provide valuable information about the patient's posture and gait, which can be useful in the treatment and rehabilitation of patients with spine, leg or foot problems. The participants signed an informed consent about the purpose and method of the examination - gait analysis using the Diers pedogait system.

Acknowledgments: This work was supported by the entity: Foundation for better care, Klimentská 1746/52, Prague 1, IČO: 106 97 331 110 00 in accordance with the Regulation of the European Parliament and the Council (EU) 2016/679 of April 27, 2016 on the protection natural persons in connection with the processing of personal data and on the free

movement of such data and on the repeal of Directive 95/46/EC (General Regulation on the Protection of Personal Data).

Conflicts of Interest: The author declared no potential conflicts of interest.

References

1. MacWilliams, B. A., Cowley, M., & Nicholson, D. E. (2003). Foot kinematics and kinetics during adolescent gait. *Gait & posture*, *17*(3), 214–224.

2. Maslen, B. A., & Ackland, T. R. (1994). Radiographic study of skin displacement errors in the foot and ankle during standing. *Clinical biomechanics (Bristol, Avon)*, *9*(5), 291–296..

3. Nichols, J. A., Roach, K. E., Fiorentino, N. M., & Anderson, A. E. (2016). Predicting tibiotalar and subtalar joint angles from skin-marker data with dual-fluoroscopy as a reference standard. *Gait & posture*, *49*, 136–143.

4. Peltz, C. D., Haladik, J. A., Hoffman, S. E., McDonald, M., Ramo, N. L., Divine, G., Nurse, M., & Bey, M. J. (2014). Effects of footwear on three-dimensional tibiotalar and subtalar joint motion during running. *Journal of biomechanics*, *47*(11), 2647–2653.

5. Lenz, A. L., Strobel, M. A., Anderson, A. M., Fial, A. V., MacWilliams, B. A., Krzak, J. J., & Kruger, K. M. (2021). Assignment of local coordinate systems and methods to calculate tibiotalar and subtalar kinematics: A systematic review. *Journal of biomechanics*, *120*, 110344.

6. Hoffman, S. E., Peltz, C. D., Haladik, J. A., Divine, G., Nurse, M. A., & Bey, M. J. (2015). Dynamic in-vivo assessment of navicular drop while running in barefoot, minimalist, and motion control footwear conditions. *Gait & posture*, *41*(3), 825–829.

7. Chen, Y. C., Lou, S. Z., Huang, C. Y., & Su, F. C. (2010). Effects of foot orthoses on gait patterns of flat feet patients. *Clinical biomechanics (Bristol, Avon)*, *25*(3), 265–270.

8. Hollander, K., Zech, A., Rahlf, A. L., Orendurff, M. S., Stebbins, J., & Heidt, C. (2019). The relationship between static and dynamic foot posture and running biomechanics: A systematic review and meta-analysis. *Gait & posture*, *72*, 109–122.

9. Wang, B., Roach, K. E., Kapron, A. L., Fiorentino, N. M., Saltzman, C. L., Singer, M., & Anderson, A. E. (2015). Accuracy and feasibility of high-speed dual fluoroscopy and model-based tracking to measure in vivo ankle arthrokinematics. *Gait & posture*, *41*(4), 888–893.

10. Brown, J. A., Gale, T., & Anderst, W. (2020). An automated method for defining anatomic coordinate systems in the hindfoot. *Journal of biomechanics*, *109*, 109951.

11. Kim, K., Mullineaux, D. R., & Jeon, K. (2019). A Comparative Study of Spinal Deformity and Plantar Pressure according to the Static Standing Posture of Female Adolescents with or without Idiopathic Scoliosis. *Iranian journal of public health*, *48*(2), 345–346.

12. De Cock, A., De Clercq, D., Willems, T., & Witvrouw, E. (2005). Temporal characteristics of foot roll-over during barefoot jogging: reference data for young adults. *Gait & posture*, *21*(4), 432–439.

13. Hallemanns, A.; D´Aouť, K.; De Clercq, D.; Aerts, P.

Pressure Distribution Patterns Under the feet of new walkers: the first two month of independent walking. Foot Ankle International; 24(5), 444-445 (2003).

Additively manufactured auxetic metamaterials and their application in biomedical engineering

Barbara Schürger [1,*] and Peter Paličká [1]

[1] Technical University of Košice, Faculty of Mechanical Engineering, Department of Applied Mechanics and Mechanical Engineering, Letná 9, 042 00 Košice, Slovak Republic; barbara.schurger@tuke.sk
[1] Technical University of Košice, Faculty of Mechanical Engineering, Department of Applied Mechanics and Mechanical Engineering, Letná 9, 042 00 Košice, Slovak Republic; peter.palicka@tuke.sk
* Correspondence: barbara.schurger@tuke.sk; Tel.: +421910116236

Abstract: This paper present properties and review of modern metamaterials used in biomedical engineering. In the recent years, there has been an increased interest in the design, manufacturing and testing of 3D printed metamaterials due to their unique properties and application in healthcare. The future of auxetic metamaterials in healthcare is promising, with opportunities for continues advancements.

Keywords: metamaterials; 3D printing; biomedical engineering; polymers; additive technology; auxetic; healthcare

1. Introduction

A metamaterial is a material that has been designed to exhibit properties that do not occur in nature. The term metamaterial was introduced already in 1999 by Rodger W. Walters from the University of Texas at Austin. It was originally defined as an artificial macroscopic composite material, characterized by a three-dimensional periodic cellular structure. In today's well, however, the cell structure does not have to be strictly periodic. Its periodicity is only related to the homogeneity of the given material [1,2].

Metamaterials can currently be divided into 4 categories based on their properties, namely electromagnetic metamaterials (EMM), acoustic metamaterials (AMM), thermal metamaterials (TMM) and mechanical metamaterials (MMM). In this article, we will only discus mechanical materials, because they are used for application in the biomedical industry [3].

Mechanical metamaterials are able to convert mechanical energy from one direction to another, compressive force to torque, or absorb energy as, for example, auxetic structures.

2. Auxetic metamaterials

Auxetic metamaterials are materials that exhibit a negative Poisson's ratio, hence their counterintuitive behavior. Poisson's ratio is defined as the negative ratio of transverse strain (lengthening/shortening) to longitudinal strain [4]:

$$\nu = -\frac{\varepsilon_y}{\varepsilon_x}. \tag{1}$$

The main feature of auxetics is their behavior during deformation, especially under uniaxial loading. Conventional materials expand (contract) under compression (tension) loading, while auxetics contract (expand) under compression (tension) loading as seen in Figure 1 [4].

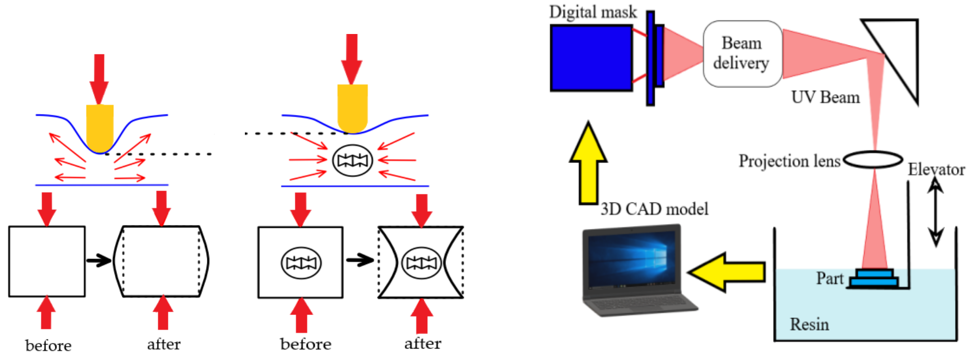

(**a**) (**b**) (**c**)

Figure 1. The difference between standard and auxetic material: (**a**) Behavior of standard material under applied load; (**b**) Behavior of auxetic material under applied load. (c) Additive manufacturing process used for metamaterial fabrication.

Additive manufacturing processes, which are based on the gradual controlled addition of the given material, are mostly used for the production of auxetic structures. These are projection micro-stereo-lithography (PmSL) as seen in Figure 1 (c), liquid polymerization (SLA), direct laser writing (DLW), powder melting techniques (SLM, SLS, EBM) or selective electron beam melting (SEBM) [4]. With the help of optimization in the metamaterial design process, we can achieve the ideal distribution of the material for the given application.

3. Application in biomedical engineering

Metamaterials have a wide range of applications due to their unusual properties. Thanks to these properties, they are suitable candidates for use in the field of biomedical engineering. Of all types of metamaterials, mechanical metamaterials are mainly used in biomedical engineering for the purpose of manufacturing bone implants, vascular stents, healthcare applications etc. [5].

The inspiration for the usage and production of metamaterials in biomedicine was the fact that even some naturally occurring materials exhibit properties such as negative Poisson's number, such as cancellous bone, embryonic epithelial tissues [5,6], the nuclei of embryonic stem cells arteries [7], tendons [8], and the annulus fibrosis of the intervertebral disc [9], which are all natural tissues.

3.1. Bone implants

Mechanical metamaterials have properties such as low weight, adjustable stiffness, auxeticity, which makes them a great candidate for bone implants. Thanks to their structure, they are suitable for the transmission of tensile and compressive loads, energy dissipation and they also show a high level of resistance to shear [9-10].

3.1.1. Bone screw

One of the most used bone implants is bone screw. The principle of auxetic bone screw is simple. When the bone screw is loosened there is a noticeable pullout force, at which the radial expansion of the auxetic bone screw expand the mechanical interaction between the screw and the bone, hence improving the anti-pullout effect. When pulled, the bone screw will expand transversal making a screw body of itself, so the fixation is enforced like in Figure 3 [10].

In the research [10], the research team designed auxetic bone screws with different unit cells (chiral, re-entrant and rotating). Computationally and experimentally, the re-entrant structure performed the best results and was considered to have the greatest strength and stiffness out of all designs.

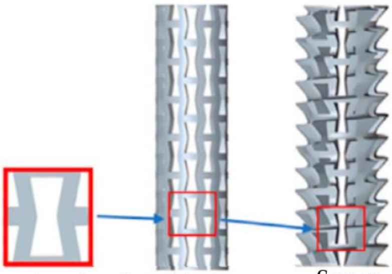

Figure 3. Bone screw with its auxetic unit cell structure [10].

3.1.2. Hip implants

The implementation of auxetic metamaterials for hip implants are relatively early. The lightweight properties of metamaterials have drawn the attention of the researchers all around the world. For example, the triply periodic minimal surface (TPMS) structures are widely applied in bone scaffolds [11]. The applications of TPMS structures guarantee that the bone scaffolds are both lightweight and meet the required biomechanical properties. This is also like the properties of natural human bone.

Authors [12] designed acetabular cup-shaped socket based on six different auxetic unit cells and showed after series of bionic compression tests that metamaterial implants with functional gradient had the best space-filling behavior as seen in Figure 4.

(**a**) (**b**)

Figure 4. Hip implant: (**a**) 3D printed titanium auxetic hip implants; (**b**) Concept of auxetic hip implant [12].

However, stress shielding and micro motions are two of the most serious problems in the stem of artificial joints [13]. To solve these problems, auxetic mechanical metamaterials are used to design hip implants. Therefore, different types of meta-biomaterials are also designed and additively manufactured with a rational distribution of positive and negative Poisson’s ratios, thereby improving the contact between implant and bone, increasing the implant longevity [14]. In addition, heterogeneous structural hip implant stems with the positive and negative Poisson’s ratio are effective in preventing bone implant failure [15]. Furthermore, fatigue performance and fatigue crack initiation and propagation are investigated in auxetic implants [15].

3.2. Intervertebral discs

3D printed mechanical metamaterials can not only have been used in bone screws and hip implants but also on intervertebral discs. The lumbar spine with its intervertebral discs is very important part of the body to carry loads. That’s why lumbar disc herniation is a restriction on mobility for all group of ages. There is research that shows that polymeric auxetic intervertebral disc implant can be used as a replacement for natural disc. [16]. The negative Poisson´s ratio of this structure can provide great compression stability and energy absorption. When compressed, the metamaterial disc will decrease in the transverse plane, and so the nerves will not be compressed [16].

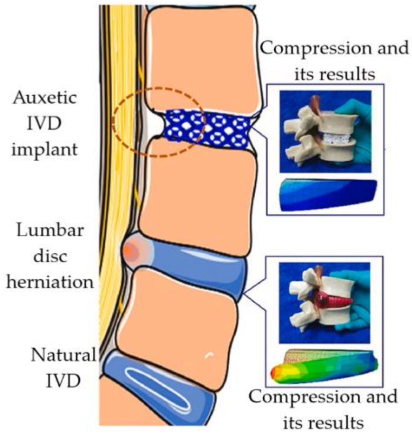

Figure 5. Difference between natural IVD and auxetic IVD implant [18].

Metamaterial intervertebral discs can be made of re-entrant cellar structures in the form of auxetic foam [17]. Finite element analysis has shown that the use of artificial auxetic disc with negative Poisson´s ratio is a solution to the problem due to eradication of damage to the spinal nerves [18]. In Figure 5, authors compared natural intervertebral disc, conventional widely produced 3D implants, and new designed auxetic polymeric implant and the results showed that the auxetic implant had more compelling stress transfer and devitalization under physical loading conditions [18].

3.3. Vascular stents

Vascular stents are small tubular scaffolds widely used in the treatment of arterial stenosis (narrowing of the vessel) to prevent acute vessel closure and late restenosis in a variety of vessels such as coronary arteries [19]. In the clinic, the shape-shifting or reconfigurable behavior of vascular stents is essential for the successful implantation. The inner radius of blood vessel is so small and varies from location to location, requiring vascular stent to be miniature and can be moved to the target location and fixed at that location. The reconfigurable behavior of auxetic mechanical metamaterials exactly matches this possibility [19].

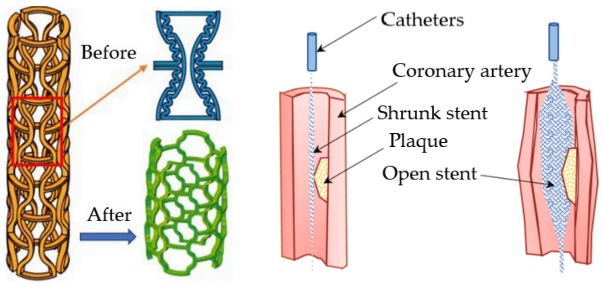

Figure 6. Auxetic vascular stents: (**a**) Behavior of vascular stent after activation [19]; (**b**) Process of transfer to the target region [20].

The vascular stent is shrunk and placed into the target location through minimally protruding surgery, and then opened out in the target location to secure that region. The shape-shifting metamaterial will change their structure and dimension upon activation via external stimuli (e.g., light, heat, magnetism, electricity, etc.), as shown in Figure 6 [20]. For the example, the auxetic 3D polymers are temporarily frozen and deformed, and are transferred to the target location. When the temperature increases, they expand and fill the inside of the vessel. [21]. The shape-shifting auxetic polymers have characteristics such as elasticity and deformability, excellent biocompatibility, and controlled degradation properties, making them one of the most optimal vascular stent materials.

3.4. Other healthcare application

Mechanical polymeric metamaterials can be used in impact protector devices, like pads, gloves, helmets, and mats, to utilize greater conformability for comfort, support, and protection. A cylinder-ligament honeycomb structured metamaterial with synclastic curvature was reported, which made this system a candidate core material in sports helmet applications [22].

Polymeric metamaterials have compelling potential for textile applications [23]. In the biomedical engineering fields, the fiber or yarn form of metamaterial textiles can be developed in different ways. For example, smart bandage is one, as shown in Figure 7. The bandage was made of auxetic fibers with wound-healing agents. When swelling appeared in the wound, the bandage would open and release the agents. When the wound healed, the bandage closed and stopped releasing the agents.

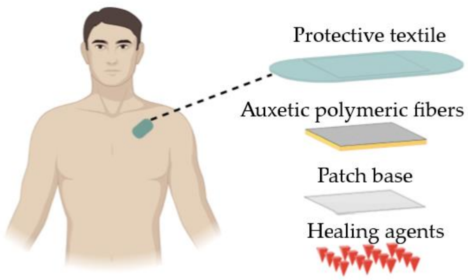

Figure 7. Structure of smart bandage [23].

3. Results and future trends

In summary, mechanical metamaterials have been more and more commonly used in the biomedical engineering field. Due to their specific and unique behaviors, they have been used to strengthen the fixation of bone screws, reduce weight and increase strength in hip implants, can provide great compression stability and energy absorption in intervertebral discs, allow for the minimally invasive implantation of vascular stents, increase the resilience of running shoes, etc.

However, the research maximum has not been reached and further efforts should be made to improve the performance of biomedical products:

- Optimization: the metamaterial structure need to be optimized for unique application, so the optimal structure can maximize the product performance;
- Minimizing product defects: the complex integrated design-manufacturing process should be used to minimize inaccuracy using additive manufacturing;
- Efficient assessment: the assessment of the performance of metamaterials used in biomedical engineering is essential using numerical and musculoskeletal modeling techniques;

Conflicts of Interest: The authors declare no conflict of interest.

References

1. Greaves, N.; Greer, A.; Lakes, R. Poisson's ratio and modern materials. *Nature Materials*, **2011**, *12*, 823-837.
2. Zhao, Y.; Belkin, M.; Alu, A. Twisted optical metamaterials for planarized ultrathin broadband circular polarizers. *Nature Communications*, **2012**, *4*, 870.

3. Kadic, M.; Buckmann, T.; Stenger, T.; Thiel, M. On the practicability of pentamode mechanical metamaterials. *Applied Physics Letters,* **2012**, *18*, 100-110.
4. Kadic, M.; Buckmann, T.; Wegener, N.; Schitty, M. Elastic measurements on macroscopic three-dimensional pentamode metamaterials. *Applied Physics Letters,* **2013**, *1*, 103-105.
5. Wiebe, C.; Brodland, G. Tensile properties of embryonic epithelia measured using a novel instrument. *Journal of biomechanics*, **2005**, *38*. 2087-2094.
6. Chen, X.; Brodland G. Mechanical determinants of epithelium thickness in early-stage embryos**.** *The Journal of the Mechanical Behavior of Biomedical Materials*, **2009**, *5*, 494-501.
7. Pagliara, S.; Franze, K.; McClain, C. Auxetic nuclei in embryonic stem cells exiting pluripotency. *Nature Materials,* **2014**, *13*, 638–644.
8. Gatt, R.; Mizzi, L.; Azzopardi, J. Hierarchical Auxetic Mechanical Metamaterials. *Scientific Reports,* 2015, *5*, 8395.
9. Derrouiche, A.; Zaouali, A.; Zaïri, F. Osmo-inelastic response of the intervertebral disc. *Proceedings of the Institution of Mechanical Engineers,* **2019**, *233*, 332-341.
10. Yao, Y. et al. A novel auxetic structure based bone screw design: Tensile mechanical characterization and pullout fixation strength evaluation. *Materials & Design*, **2020**, *188*, 264-271.
11. Huo, Y.; Yongtao, L.; et al. A Critical Review on the Design, Manufacturing and Assessment of the Bone Scaffold for Large Bone Defects. *Frontiers in Bioengineering and Biotechnology*, **2021**, *9*, 155-168.
12. Kolken, H.M.A.; Fontecha Garcia, A.; Du Plessis, C. Fatigue performance of auxetic meta-biomaterials. *Acta Biomaterialia*, **2021**, *126*, 511-523.
13. Ghavidelnia, N.; Hedayati, R.; Sadighi, M. Development of porous implants with non-uniform mechanical properties distribution based on CT images. *Applied Mathematical Modelling*, **2020**, *83*, 801-823.
14. Kolken, H.M.A.; Janbaz, S.; Leeflang, S.M.A.; Lietaert, K. Rationally designed meta-implants: a combination of auxetic and conventional meta-biomaterials. Materials Horizons, **2018**, *5*, 28-35.
15. Yu, A.; Zhang, C.; Xu, W.; Zhang, Y. Additive manufacturing of multi-morphology graded titanium scaffolds for bone implant applications. Journal of Materials Science & Technology, **2023**, *139*, 47-58.
16. Martz, E.O.; Lakes, R.S.; Goel, V.K.; Park, J.B. Design of an Artificial Intervertebral Disc Exhibiting a Negative Poisson's Ratio. *Cellular Polymers*, **2005**, *24*, 127-138.
17. Maerz, T.; Herkowitz, H.; Baker, K. Molecular and genetic advances in the regeneration of the intervertebral disc. *Surgical Neurology International*, **2013**, *4*, 94-105.
18. Tian, S.X.; Xu, T.; Shi, R.Y. Analgesic effect of electro acupuncture on bone cancer pain in rat model: the role of peripheral P2X3 receptor. *Purinergic Signalling*, **2022**, *19*, 13–27.
19. Wang, S.B.; Cheng, Y.N.; Cui, S.X. Des-γ-carboxy prothrombin stimulates human vascular endothelial cell growth and migration. *Clinical and Experimental Metastasis*, **2009**, *26*, 469–477.
20. Wan, T.; Jing, T.; Zhang, H. Adoption of Novel Nano Bio-vascular Stent in Carotid Artery Stenosis Stent Intervention and Perioperative Nursing Analysis: Adoption of Novel Nano Bio-vascular Stent in Carotid Artery Stenosis Stent. *Cellular and Molecular Biology*, **2022** , *68*, 114–121.
21. Solis, D.M.; Czekanski, A. 3D and 4D additive manufacturing techniques for vascular-like structures – A review. *Bioprinting*, **2022**, *25*, 251-263.
22. Sanami, M.; Ravirala, N.; Alderson, K.; Alderson, A. Auxetic Materials for Sports Applications. *Procedia Engineering*, **2014**, *72*, 453-458.
23. Wang, Z.; Hu, H. Auxetic materials and their potential applications in textiles. *Textile Research Journal*. **2014**, *84*, 1600-1611.

TECHNICKÁ UNIVERZITA V KOŠICIACH
Strojnícka fakulta

Steel structure design with the support of mathematical optimization procedures

Marián Siman [1], Jozef Kuľka [2,*]

[1] Faculty of Mechanical Engineering, Technical University of Košice, Slovakia; marian.siman@tuke.sk
[2] Faculty of Mechanical Engineering, Technical University of Košice, Slovakia; jozef.kulka@tuke.sk
* Correspondence: jozef.kulka@tuke.sk;

Abstract: The article deals with the use of modern calculation and optimization methods in the optimization of load-bearing nodes of steel constructions of manipulation devices. It proposes a comprehensive methodology enabling the generation of optimal dimensions of already conceptually designed supporting nodes of steel constructions of handling equipment. The proposed methodology is made up of a set of sub-methods, the gradual application of which leads to the optimal dimensional configuration of the solved node of the structure with respect to the chosen criterion. The article describes mathematical optimization methods (5 methods - Analytical methods of mathematical analysis, Numerical gradient methods, Heuristic algorithms, Sequential quadratic programming and Genetic algorithms) modern optimization schemes based on gradient and heuristic basis.

Keywords: steel structure; optimization methods; objective function

1. Introduction

In the last twenty years, the construction process has gone through a number of fundamental methodological changes connected mainly with the deployment of computer technology and CAx technologies. CAD systems brought better visualization possibilities and increased productivity of designers' work. CAEA (Computer Aided Engineering Analysis) systems complement CAD systems with the possibility of creating calculation models of various types, which serve to predict the behaviour of the proposed product in various configurations and under various conditions. From a structural point of view, it is necessary to design and dimension the structure in such a way that it meets all strength, legislative, technological and functional requirements. The highly competitive environment brings economic criteria to the fore, which demands the lowest possible costs in order to increase competitiveness and maximize profit. When designing a product, some parameters are always fixed and some can be changed by the designer. The effort of the developers is to find the optimal arrangement of constructions that minimize the price while simultaneously meeting all other requirements. This work focuses on the use of mathematical optimization methods in the field of steel supporting structures of handling equipment and specializes in the design of a methodology that will allow finding the optimal arrangement of load-bearing nodes made of composite cross-sections, which are used in a wide range of handling equipment. The optimization criterion is often the weight of the structure, which is directly related to the price of the material and the cost of operation. A lighter construction means not only a saving of material, but also a reduction of moving masses and thus a saving of operating energy.

Some publications such as [1] mathematically describe the optimization of welded bridge crane girders. Pavlović et al. [1] describe in detail the analytically performed optimization of the box girder of the bridge crane for the two most important variables (height and width of the girder) by the method of Lagrange multipliers, taking into account the limitation on tilting and buckling of the walls.

The methodology focused on mass optimization of the bridge crane beam with consideration of stiffness and stress limitations is described in detail [2]. In their work, optimization is solved numerically using simple nonlinear programming. However, the stability of the beam itself is not considered at all in the limiting conditions. Objective functions and limiting conditions are formulated in their work using analytical equations. Mass optimization of a bridge crane girder using a point cloud is described in [3]. 10 limiting conditions and 6 design variables are included in the calculation. These are calculated and formulated analytically. In total, 400040 variations of the limiting conditions and the objective function were needed to find the solution. A relatively high number of calculations is characteristic of all heuristic optimization methods. A direct link to the finite element method is practically impossible due to the high number of analyses. Mass optimization [4] is solved using MS Excel software. Verification is provided by ANSYS software using direct optimization solvers. With the help of FEM, stability limitation is not solved, only voltage deflections. The resulting optimization is solved for 11 design variables. The stability of the beam is analyzed analytically.

Mathematical optimization methods are rarely used in the design of steel structures. Empirical approach, experience, trial-and-error method, or comparison of several analyzed scenarios prevails in the actual design and construction. Although this procedure is called optimization, it is not optimization in the mathematical sense. A typical example is the optimization of the thicknesses of the flanges and the stays of the beams of the bridge crane [5]. The above-mentioned works use either an analytical form of description of the function and limiting conditions, or a direct connection of the optimization solution and the finite-element system. None of the mentioned approaches solves the stability constraints using the Finite Element Method, and even rounding to the available sheet thicknesses can cause a significant deviation from the optimal solution. None of the mentioned works take into account material fatigue. Published publications define sheet metal thickness to whole decimal numbers. However, it should be emphasized that rounding to whole numbers can cause a significant deviation [2], [4]. When dealing with the stability of steel structures, standards are always used that include rules that take into account the influence of imperfections.

2. Materials and Methods

2.1 Optimization

Optimization is the process of finding the extremum of the objective function while observing the given limiting conditions [6]. The objective function is a suitably formulated dependence of the optimized quantity on design (design) variables. The purpose function can be, for example, the weight of the structure, the price or the movement time of the mechanism.

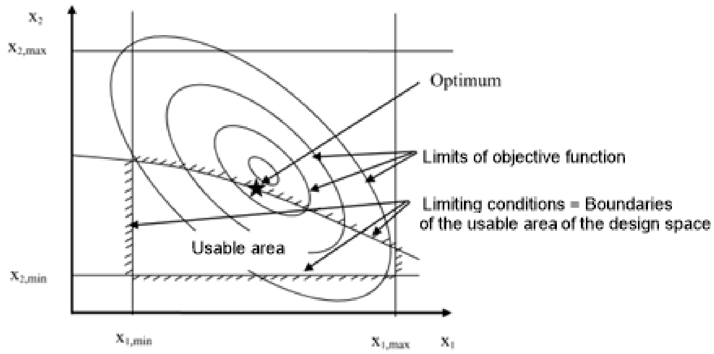

Figure 1. Delimitation of the objective function, display of limiting conditions and bounded optimum.

2.2 Defining the optimization problem

The optimization problem can be formulated as finding a combination of values of design variables

$$_{opt} = \begin{pmatrix} x_{1,opt} \\ x_{2,opt} \\ \cdot \\ \cdot \\ x_{n,opt} \end{pmatrix} \tag{1}$$

from an n-dimensional design space such that the objective function reaches a minimum. In many practical examples, the values of design variables cannot be chosen arbitrarily, but must meet certain conditions. These conditions enter the optimization problem as so-called limiting conditions and take the form of equations and inequalities:

$$g_i(\ ) = 0, \qquad i = 1,2,\dots,m \tag{2}$$

$$h_j(\ ) \leq 0, \qquad j = 1,2,\dots,p \tag{3}$$

$$x_k \in \langle x_{k,min} | x_{k,max} \rangle \qquad = 1,2,\dots, \tag{4}$$

Where:

x_k – design variables,
g – limiting conditions in the form of equality,
h – limiting conditions in the form of an inequality,
X - design vector consisting of n design variables.

In the theory of mathematical optimization, we almost always talk about the minimum. This is because any search for the maximum of the function f (X) can be converted to the search for the minimum of the function –f (X).

Condition (4) defines an n-dimensional design space. By applying (2) and (3), the design space is reduced and the minimum of the objective function is sought only on this subset.

The minimum of the function on this subset of the design space can be located either inside (the so-called free minimum) or on its edge (the so-called bound minimum, Fig. 2). When formulating limiting conditions (e.g.: limit states) in the field of load-bearing structures of handling equipment, it is advisable to take into account the normative recommendations given in standards for steel structures (e.g.: [7], [8]).

The optimization problem can be formulated using multiple objective functions whose minima do not have to lie at a single point.

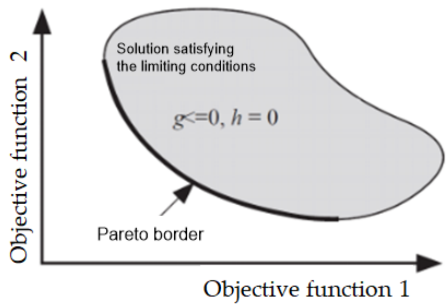

Figure 2. Pareto optimum [9]

It is often a matter of meeting conflicting requirements and finding a compromise. The Pareto optimum principle applies here, which defines Pareto-optimal points in such a way that when one criterion improves, another one worsens. The result of the process is a set of points in the criterion space (Fig. 2) referred to as the Pareto frontier, from which the solver chooses based on the preferences of a certain criterion [9]. A multi-criteria optimization problem is often described using a single objective function, where individual criteria are assigned weights expressing the importance of the given criterion.

$$F(\ ) = \sum_{i=1}^{k} W_i f_i(\ ) \tag{5}$$

where:
F( ) - set objective function,
W_i-weight coefficients of individual criteria,
k- number of purpose functions,
$f_i(\mathbf{X})$ - individual objective functions (often in normalized form),
X – design vector.

3. Mathematical optimization methods

Methods of mathematical solution of optimization problems are developed for solving a narrower class of problems with a special structure. When choosing a mathematical optimization method, we must take into account the following facts in particular:

- The spatial dimension of the design space
- Purpose function type:
  - continuous, continuous in parts, discrete
  - linear, quadratic, non-linear
- Type of restrictive conditions (if formulated)
  - in the form of equality or inequality
  - continuous, continuous in parts, discrete
  - linear, non-linear
- Type of minimum sought
  - local or global.

Since the methodology proposed in this work only uses continuous metamodels, only methods for continuous functions will be mentioned in the following text. The methods of mathematical solution of optimization problems with continuous functions can basically be divided as follows:

- According to the type of algorithm
  - *Analytical methods of mathematical analysis*

Classical differential calculus methods are used, which require double differentiability of the objective function and limiting conditions with respect to all design variables and the continuity of these derivatives. For problems with limiting conditions in the form of equalities, the method of direct substitution or the method of Lagrange multipliers can be used. For problems with constraint conditions in the form inequality, the Kuhn–Tucker condition can be used. The advantage of the methods is the speed of finding the optimum by analytical means. The disadvantage is the requirement for differentiability [10].

- *Numerical gradient methods*

This group of methods is based on the fact that the gradient of a function at a point indicates the direction of the greatest slope of this function at that point. It proceeds from the starting point from the design space to the optimal point, while three basic questions are solved in each iteration:

a) Is the current point the optimal point?

b) In which direction to go in the design space?

c) How far to move in a given direction?

Once these questions are answered, basically two cases can arise. If the answer to the first question is positive, we have found the minimum and the algorithm ends. In the second case, the algorithm moves to the next point given by the relation:

$$_{+1} = \quad + \propto \cdot \tag{6}$$

Where:

$_k$ – the current point in the design space,

$_{k+1}$–next progress point in the design space,

$\propto_k$- step size within the current iteration,

$_k$- vector determining the direction of further progress,

k – iteration number.

The advantage of this approach is the speed of convergence. The disadvantage is the tendency to "slip" into a local minimum. The main groups of methods falling into this category include Linear Programming, Quadratic Programming and Non-Linear Programming.

- *Heuristic algorithms*

These methods belong to the so-called global optimization methods. The design space is systematically searched in its entire volume using heuristics given by a specific algorithm. The advantage of the approach is not using derivatives and a strong tendency to find a global minimum. The disadvantage is the computational complexity of the algorithm due to the large number of computations of the objective function needed to find the optimum. The main groups of methods falling into this category include Genetic Algorithms, Simulated Annealing and methods using swarm intelligence.

Due to the fact that in optimization problems focused on the optimization of load-bearing nodes of steel structures of handling equipment there are always limiting conditions in the form of inequalities (e.g. conditions defining the design space, maximum stress in the structure, etc.) the selection of optimization methods is limited to methods that take into account the limiting conditions in the form of inequalities. Another fact that complicates the chosen approach is the general non-linearity of the objective function and/or the limiting conditions. Based on professional studies literature focused on mathematical optimization methods, a combination of two methods, one gradient and the other heuristic, is chosen for the methodology proposed in this dissertation. The use of two fundamentally different methods is appropriate for the purpose of mutual verification of the result. The inclusion of a heuristic method also ensures that the minimum found is not only a local minimum. Sequential quadratic programming (SKP) is chosen from gradient methods and genetic algorithm (GA) is chosen from heuristic methods. Both methods can be implemented within Matlab.

- *Sequential quadratic programming*

Sequential quadratic programming (SKP) represents one of the best modern methods of nonlinear programming [10], [11]. SKP is an iterative method that, within each iteration, approximates the objective function by the first three terms of the Taylor series (up to the quadratic term) developed at the current iteration point. In case the left sides of the limiting conditions are nonlinear, they are linearized using the first two terms of the Taylor series (up to the linear term) developed at the current iteration point [12]. In each iteration, a partial optimization sub problem (7) is defined, which is solved using the quadratic programming method.

(7)

$$\min - \quad + \nabla \mathrm{f}(\quad)^{\mathrm{T}} \quad + \mathrm{f}(\quad)$$

$$\begin{aligned} \nabla \mathrm{g_i}(\quad)^{\mathrm{T}} \quad + \mathrm{g_i}(\quad) = 0, \qquad \mathrm{i} = 1,2,\dots,\mathrm{m} \\ \nabla \mathrm{h_j}(\quad)^{\mathrm{T}} \quad + \mathrm{h_j}(\quad) \leq 0, \qquad \mathrm{j} = 1,2,\dots,\mathrm{p} \end{aligned}$$

The Lagrange function of the quadratic sub problem at the current point $\boldsymbol{Xk}$ has the form:

$$\begin{aligned} & \mathrm{L}_{\mathrm{X_k}}(\ ,\lambda) = \\ & = \frac{1}{2} \qquad + \nabla \mathrm{f}(\quad)^{\mathrm{T}} \quad + \sum_{=} \lambda\, (\nabla \mathrm{g_i}(\quad)^{\mathrm{T}} \quad + \mathrm{g_i}(\quad)) + \\ & + \sum_{=} \lambda_{\ +}\, (\nabla \mathrm{h_j}(\quad)^{\mathrm{T}} \quad + \mathrm{h_j}(\quad)) \end{aligned} \tag{8}$$

Where:
 - vector determining the direction of further progress through the design space from the current point ,
 - positive definite approximation of the Hessian matrix at the point ,
( )- limiting conditions in the form of equality calculated at the point ,
( )- limiting conditions in the form of an inequality calculated at the point ,
$\nabla(\ )$, $\nabla h(\ )$, $\nabla(\ )$ – gradients of limiting conditions and objective functions at point ,.
$L_k(\ ,\lambda)$– Lagrangian function of the quadratic optimization sub problem,
 - Lagrange multipliers.

The Hessian matrix is represented in each iteration by its positive definite approximation, which is computed using the Broyden–Fletcher–Goldfarb–Shann (BFGS) variant of the quasi-Newton method. The Kuhn–Tucker optimality conditions are applied to the Lagrange function (8), which are sufficient conditions for the positive definite form of the matrix . The solution to each quadratic subproblem is the vector , which determines the direction of further progress through the design space within the current iteration. The step length (parameter $\propto$ in equation (6)) is determined using one of the step length optimization methods [11], [9]. SKP has the following advantages:

- Problems with limiting conditions in the form of equalities and inequalities can be solved;
- Optimization problems with constraint conditions require fewer iterations than problems without constraints (a set of active constraint estimates is generated and renewed in each iteration);
- Only active constraint gradients are calculated;
- The Hessian matrix is approximated based on a sequence of gradients across iterations (second derivatives are not calculated).

SKP is part of the MATLAB optimization toolbox. The FMINCON algorithm is used for implementation.

➢ *Genetic algorithms*

Genetic algorithms (GA) represent mathematical models of the biological evolutionary process that enable the solution of optimization problems. GAs are implemented using an iterative a process that differs in many ways from traditional optimization approaches. Major differences include:

- GAs within one iteration (generation) do not work only with one value of the

objective function, but with a whole group of values called the population.
- GAs do not use the derivative of the objective (fitness) function to find a better solution.
- GAs systematically search the design space in its entire volume, which (with some probability) leads to finding a global extremum.
- GAs use random number generation at their core.

Typically, at the beginning of the simulation, the population is composed of completely random members. As part of the creation of a new generation, the value of the fitness function is calculated for each individual, which expresses the quality of the solution represented by this individual. According to this quality, individuals are stochastically selected that will remain unchanged in the population, with the remaining individuals being modified by mutation and crossing, resulting in a new generation of individuals. This procedure is repeated iteratively, thereby gradually improving the quality of the solution in the population. The algorithm usually stops when sufficient solution quality is achieved, or after a predetermined time [13].

From a mathematical point of view, optimization is the process of finding the extremum of an objective function while observing the given limiting conditions. The objective function is a suitably formulated dependence of the optimized quantity on design (design) variables. In our case, the objective function could be the weight of the crane's main girder. Since a continuous beam metamodel is used for the optimization, it is of course clear that only the mathematical solution method with continuous functions can be used. According to the type of algorithm, it can be analytical methods of mathematical analysis, numerical gradient methods or heuristic algorithms. When considering limiting conditions in the form of inequalities, our radius of action is narrowed only to methods that can work with such conditions. For criteria constructed in this way, they can be used in the Matlab environment from the gradient tasks of the linear programming method, sequential quadratic programming and from heuristic methods, e.g. genetic algorithm.

The goal of the design can be the lightest possible variant of the welded beam, but which meets the strength requirements given by valid standards. The optimization problem solves only basic parameters. The objective function will be the volume of material used to construct the crane girder. Limiting conditions are formulated with regard to the selection of beam cross-section parameters, strength and stability conditions.

If we had the main beam of the box structure with a rectangular cross-section according to Fig. 3, the parameters L, L_1, h_1 and d would be given in advance (they do not represent design variables).

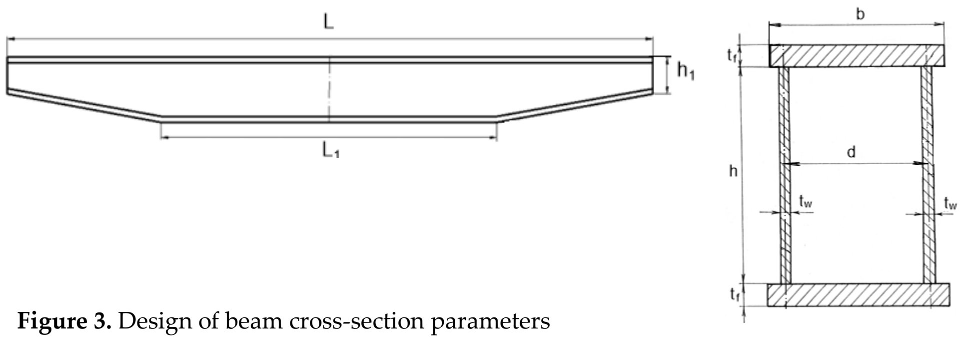

Figure 3. Design of beam cross-section parameters

According to practical experience, the height of the beam h is recommended to vary depending on the width in the ratio h = 3.5d. The racks are thin-walled. In the case of full-wall beams, the local stability of the wall is achieved by increasing the thickness of the wall, exceptionally by welding reinforcements. The straps are thicker. For better welding, the flanges on both sides extend over the webs. The cross-section, in order to withstand twisting, is reinforced inside with transverse partitions - diaphragms, in our case they could be separated by 100% of the height of the beam, i.e. at a distance h, and they will have the same thickness as the webs.

The subject of the optimization will be the search for optimal values of the dimensions of the cross-section at the minimum weight of the beam. In general, it is possible to choose seven design variables describing the box cross-section, if different thickness and width of flanges in the upper and lower part of the beam were considered. This number can be reduced to four design variables for practical reasons. The stanchion spacing d is set to the largest possible value in order to maximize the torsional stiffness and thus the resistance to tipping. The width of the flanges b is derived from the parameter d so that there is enough space for the weld on the edges.

It is not advisable to choose the ranges of individual design variables unnecessarily large, because large ranges of design variables generally lead to lower quality metamodels due to the creation of an approximation over a larger design space. If we do not know the approximate position of the optimum, it is possible to perform the optimization in two or more steps, where in each subsequent step we reduce the design space depending on the indicated position of the optimum.

Conclusion

Fulfilment of the indicated requirements requires the deployment of complex approaches that can simultaneously take into account all requirements and generate the resulting solution. Since we are looking for an optimal solution with respect to the chosen optimization criterion(s), the possibility of using the theory of mathematical optimization is offered, when the solver formulates a so-called optimization problem. In this problem, everything that the designer can change appears as a design (design) variable, the optimization criterion takes the form of an objective function, and all other requirements are formulated as limiting conditions. As a result, it is often a set of equations and inequalities that are solved on a previously defined definition field, which in this case we call the design space. Optimization is more demanding compared to the classical approach, because relatively complex mathematical methods are applied, in contrast to the prevailing empiricism in the classical approach.

Acknowledgments
This paper was prepared within the solution of the grant project KEGA 044TUKE-4/2024.

Conflicts of Interest

The authors declare no conflict of interest."

References

1. Pavlovic, G. V., Savkovic, M., Gašic, M., Bulatovic, R., Zdravkovi, N. *Optimization of the box section of the main girder of the double beam bridge crane according to the criteria of lateral stability and local stability of plates*. Machine Design. 2012, Vol.4, No.4, pp. 197-204.
2. Tian, G., Zhang, S., Sun, S. *The Optimization Design of Overhead Traveling Crane's Box Girder.* Advanced Materials Research. 2012.
3. Chaoli, S., Ying, T., Jian-chao, Z., Jeng-Shyang, P., Yuanfang, T. *The Structure Optimization of Main Beam for Bridge Crane Based on An Improved PSO*. Journal of computers. 2011, Vol.6, No.8.
4. Zuberi, R., Long, K., Zuo, Z. *Design Optimization of EOT Crane Bridge.* International Conference on Engineering Optimization. 2008.
5. Becirovic, A., Vukojevic, D., Hadžikadunic, F. *Optimization of double box girder overhead crane in function of cross section parameter of main girders.* 15th International Research/Expert Conference „Trends in the Development of Machinery and Associated Technology". 2011.
6. Belegundu, A.D.; Chandrupatla, T.R. *Optimization concepts and application in engineering. 2nd edition:* Cambridge University press, 2011. ISBN 978-0-521-87846-3.
7. STN EN 1993-1-5 ed.2 Eurokód 3: Navrhovanie oceľových konštrukcií - Časť 1-5: Búlenie stien. 2013.
8. STN EN 1993-1-1 Eurokód 3: Navrhovanie oceľových konštrukcií - Časť: 1-1: Všeobecné pravidlá a pravidlá pre budovy. 2006.

9. Adora, J.S. Introduction to Optimization. Optimization of Structural and Mechanical Systems. : World Scientific Publishing, 2007, chapter 1, pp. 1-34.
10. Rao, S.S. *Engineering Optimization*: Theory and Practice. 4rd edition. : John Wiley & Sons, 2009. ISBN: 978047018352-6.
11. Constrained Nonlinear Optimization Algorithms. Documentation Center. [Online], MathWorks. [Citácia: 8. 3. 2024.] http://www.mathworks.com/help/optim/ug/constrained-nonlinear-optimization-algorithms.html#f26965.
12. Mareš, T. *Základy konstrukční optimalizace*. Praha : Vlastním nákladem, 2006. Sv. 2. ISBN: 8023965085.
13. Genetický algoritmus. Wikipédia-Otvorená encyklopédia. [Online]. [Citácia: 8. 3. 2024.] http://cs.wikipedia.org/wiki/Genetick%C3%BD_algoritmus.

Positional data collection for continuum robot dataset

Peter Jan Sincak [1]*, Ivan Virgala [2]

[1] ARM lab, Faculty of Mechanical Engineering, Technical University of Kosice
* Correspondence: peter.jan.sincak@tuke.sk

Abstract: The main inspiration for continuum robots is nature, these robots are inspired by various snakes, trunks and tentacles. They can be classified into three main groups: tubular, soft and cable driven continuum robots. Due to their specific kinematic structures the control of these robots is a challenging task. The classical model based approaches rely on mathematical models that can be distant from the real robot and hard to compute. The newer model free approaches rely on machine learning techniques like reinforcement learning or supervised learning. The supervised learning techniques however require data to be trained on. In this paper, an automated data collection method is presented. In the presented experiment, a continuum robot prototype was used for executing large amounts of actions so that appropriate positions of end point of the robot could be measured with a MOCAP system. The gathered data are forming a workspace of the robot, representing reaching capabilities of the used prototype. The created dataset will be a valuable source in the future development and research of the machine learning based controllers at the ARM laboratory.

Keywords: continuum robots, data collection, positional data

1. Introduction

The concept of continuum robots is inspired by nature from all sorts of snakes, tentacles and trunks. Thanks to their unique capabilities like great dexterity and maneuverability in complicated environments, robots that are inspired by these features are trying to mimic them and use them for precise manipulation [1], inspection and minimally invasive surgeries like in [2]. Continuum robots can be classified into three main groups. First are the soft continuum robots like in [3], [4]. These robots are made of soft deformable materials, which makes them suitable for grasping and maneuvering around fragile objects. Another group of robots are tubular continuum robots [5], [6]. They are composed of multiple curved concentric tubes with progressively smaller diameters towards the end of the robot. The tubes are rotated and pushed in and out in order to navigate the robot to the desired coordinates. The last group of continuum robots are cable driven continuum robots [7], [8]. These robots use cables or tendons to steer the robot in its workspace. When it comes to the control of continuum robots, it is divided into two main groups. One of the groups is so called model-based methods. These methods use classical analytical methods, that are based on mathematical models. The other group are model-free methods, which employ machine learning algorithms to figure out the control of the robot. One of these methods is based on supervised learning. The supervised learning method is dependent on the data from the robot, so that a model can be trained to steer the robot. One of the ways to gather such data is presented in this paper. The use of a prototype continuum robot is presented for gathering the positional data of the end tip of the robot.

The paper is structured as follows. First, a brief introduction of the used robot is presented along with the measurement apparatus used for positional measurements. Further, the scheme of the experiment is shown with the pseudocode of the Matlab algorithm responsible for the measurement and robot control. Finally, the measured data are presented with the workspace of the robot and the conclusion is drawn.

2. Methods

In this paper it was decided to use a prototype of continuum robot developed in our ARM lab for creating a dataset of all possible actions and the achieved positions of the endpoint of the robot. This prototype can be seen in figure 1. It's manufactured by using 3D printers using soft material TPU and rigid parts are made of PLA. This robot is controlled by three tendons that are routed through the kinematic structure to the tip of the robot. The tendons are equally placed around the central axis of the robot. Each of the tendons is controlled by a separate motor, that is responsible for shortening and extending the tendons depending on the given actions. The soft TPU parts are orange color and green parts are rigid PLA. The flexible segments are stacked on top of each other forming a single segment continuum robot controlled by three tendons. The robot is placed parallel to the ground and moving

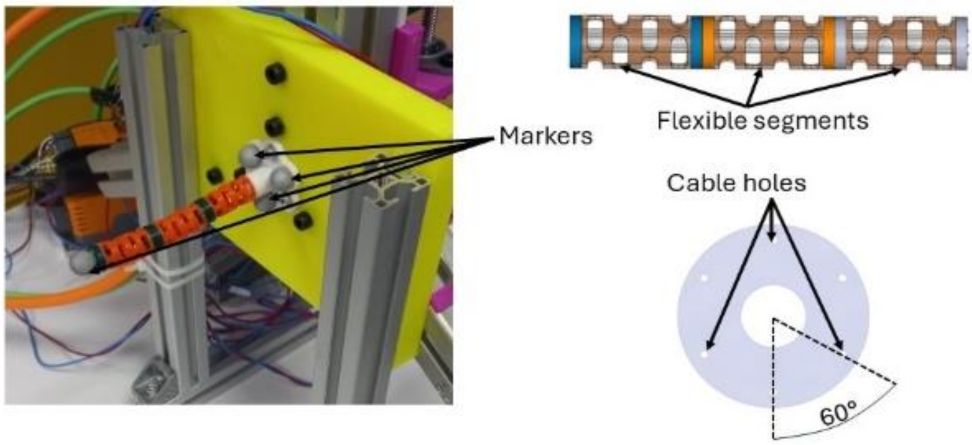

Figure 1. This is a figure. Schemes follow the same formatting.

For positional measurements, a motion capture system (MOCAP) was utilized. This system consists of 6 cameras (Prime13x, Optitrack) with the objective to track reflective markers. The basic principle of the MOCAP system is based on radiating infrared light with a specific wavelength. This light is being reflected by the reflective markers and is detected by the cameras. The coordinates of these reflective markers are then triangulated by using multiple cameras. The cameras are positioned in the U shape around the robot on the ceiling, so that the robot is visible to all the cameras. The workspace of the MOCAP system is roughly a 3x3x3 m cube, where the robot is placed in the center on top of a table. At the endpoint of the robot, a reflective marker is placed which is being tracked with the respect to the base of the robot. For the dataset, the appropriate action is paired with the XYZ coordinate of the endpoint of the robot which is tracked by the cameras. Before the measurement, the calibration of the MOCAP is done based on the system requirements. The resultant accuracy shown in the MOCAP software is 0.268 mm.

2.1. The experiment and the measurement algorithm

The goal of this paper is to create a dataset from an actual prototype of a continuum robot. The scheme of the measurement can be seen in figure 2. The experiment consists of sending 30250 generated actions and measuring their corresponding achieved positions with the tip of the robot. The actual robot consists of three servomotors, where each motor is controlling one cable. Each cable is responsible for steering the robot and controls the direction and position of the robot. The motors are connected to lead screws so that the rotational movement is changed to translational and the runner is moving back and forth based on the rotation of the motor. The runners are connected to the cables, which control the movement of the robot. This way it is easier to track the changes in the lengths of the cables. The servomotors are controlled by plc controller which communicates by serial communication with the pc. The pc controls both the robot and the MOCAP system.

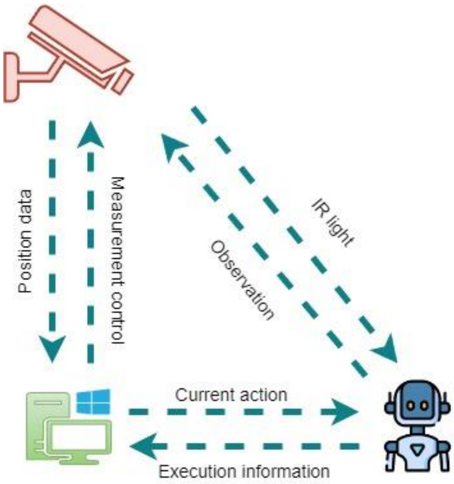

Figure 2. Measurement scheme

The measurement algorithm is written in Matlab. This code is connected by serial communication with the plc that controls the robot, as well as with the MOCAP software that runs on the same pc and streams the measured data upon request from the Matlab. This algorithm can be seen in algorithm 1. First, all possible actions are calculated. The robot is controlled by three cables, so either one or two cables at the same time can be shortened and the other cable/ cables are fixed in the zeroth position. The range of shortening of each cable is between 0 and 1 cm with a step of 0.01 cm. This way 30250 possible actions are calculated, all of which operate within the workspace of the robot. Next, the communication between the robot and MOCAP software is initialized.

Algorithm 1 Measurement algorithm

```
Calculate all possible actions N
Initialise communication with the robot and with the MOCAP software
for Action = 1, 2, ..., N do
    Read single action
    Home the robot
    if The robot is home then
        Execute the current action
        if The robot reached its position then
            Measure the current position
            Save the action and position
            The robot is not home
        end if
    end if
end for
Save the measured data to dataset
```

Algorithm 1. Matlab algorithm

If this is done, the main for loop is cycling through all the calculated actions, it reads the current action, homes the robot to the initial straight position, if the robot is homed the action is executed. The algorithm waits for the robot to reach the position (the plc sends the info that the robot has finished the movement) and then it triggers the MOCAP system to capture the XYZ coordinates and save them. The plc sends the information that the robot is not homed. The main cycle repeats itself until all the actions and appropriate coordinates are saved. After the cycle is finished, the data are saved to text file.

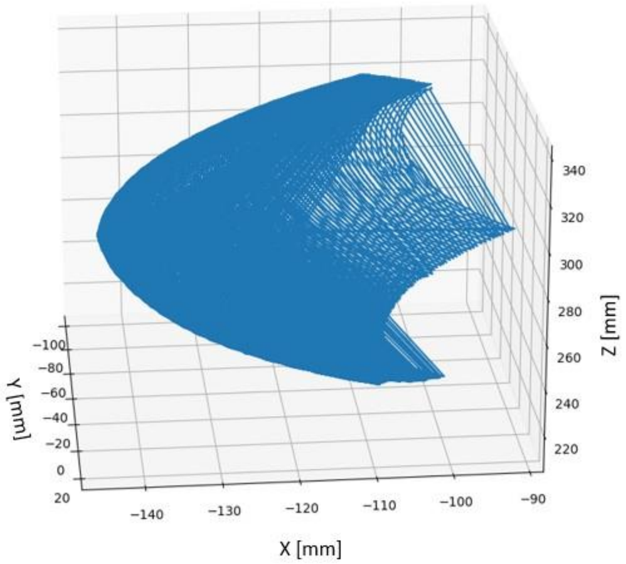

Figure 3. Measured data

In figure 3, the measured positional data can be seen. This figure represents the actual workspace of the robot consisting of 30250 XYZ coordinates of the endpoint of the robot. The total experiment time was roughly four continuous 24-hour days. It can be observed that the resultant workspace has the shape of a half eggshell. This is caused by the construction limitations of the kinematic structure and the bending limitation of 90 degrees. Overall, the resultant dataset will be beneficial in further research of control algorithms for continuum robots.

5. Conclusions

The area of continuum robots is an innovative and progressive area. The need for the development of new kinematic structures and their control is increasing. The goal of this paper is to create a dataset of positional data and appropriate action that could be used for further research of the supervised learning control algorithm of continuum robots. In this paper a brief introduction to used continuum robot prototype, that was made by ARM lab. Further, the MOCAP system was described along with the basic principle that is used by this system to measure the coordinates of the reflective markers. The introduction of the experiment was shown as well as the measurement scheme. The Matlab algorithm that was controlling the experiment was also described. It was shown that the algorithm sends actions to the robot and when it executes the action, the MOCAP system measures the position of the endpoint. This data is then saved to the dataset together with the action values that caused the robot's movement. The experiment altogether took roughly four full days and measured 30250 different positions of the robot. This dataset will be used in further research of control algorithms for training models. The expected result of these models will be the ability of controlling continuum robots with higher precision than regular model based control algorithm that are based on mathematical models.

Acknowledgments The authors would like to thank to the Slovak Grant Agency VEGA 1/0201/21, VEGA 1/0436/22 and KEGA 030TUKE-4/2020. This research was also funded by Research grant for young researchers at TUKE Control of kinematically redundant robots for minimally invasive surgeries.

Conflicts of Interest: The authors declare no conflict of interest.

References

[1] O. Fischer, Y. Toshimitsu, A. Kazemipour and R. K. Katzschmann, "Dynamic Task Space Control Enables Soft Manipulators to Perform Real-World Tasks," *Advanced Intelligent Systems,* vol. 5, p. 2200024, January 2023.

[2] L. Wu, S. Song, K. Wu, C. M. Lim and H. Ren, "Development of a compact continuum tubular robotic system for nasopharyngeal biopsy," *Medical & Biological Engineering & Computing,* vol. 55, p. 403–417, March 2017.

[3] Y. Kim, G. A. Parada, S. Liu and X. Zhao, "Ferromagnetic soft continuum robots," *Science Robotics,* vol. 4, p. eaax7329, August 2019.

[4] N. El-Atab, R. B. Mishra, F. Al-Modaf, L. Joharji, A. A. Alsharif, H. Alamoudi, M. Diaz, N. Qaiser and M. M. Hussain, "Soft Actuators for Soft Robotic Applications: A Review," *Advanced Intelligent Systems,* vol. 2, p. 2000128, 2020.

[5] J. Burgner-Kahrs, "Task-specific Design of Tubular Continuum Robots for Surgical Applications," in *Soft Robotics*, Berlin, 2015.

[6] L. G. Torres, A. Kuntz, H. B. Gilbert, P. J. Swaney, R. J. Hendrick, R. J. Webster and R. Alterovitz, "A motion planning approach to automatic obstacle avoidance during concentric tube robot teleoperation," in *2015 IEEE International Conference on Robotics and Automation (ICRA)*, 2015.

[7] S. Geng, Y. Wang, C. Wang and R. Kang, "A Space Tendon-Driven Continuum Robot," in *Advances in Swarm Intelligence*, Cham, 2018.

[8] S. Bhattacherjee, S. Chattopadhayay, V. Rao, S. Seth, S. Mukherjee, A. Sengupta and S. Bhaumik, "Kinematics and Teleoperation of Tendon Driven Continuum Robot," *Procedia Computer Science,* vol. 133, p. 879–886, January 2018.

TECHNICKÁ UNIVERZITA V KOŠICIACH
Strojnícka fakulta

The Biomechanisms and Links between Abdomino-Pelvic Vascular Compression Syndromes and Symptomatic Joint Hypermobility Syndromes

Silvia Šišková [1]*, Jozef Živčák[2], Ricardo Gil Sánchez [3] and Talal Ali [4]

[1] Technical University of Košice, Faculty of Mechanical Engineering, Department of Biomedical Engineering, Letná 1/9 | 042 00 Košice-Sever; silvia.siskova@student.tuke.sk
Asociácia Vaskulárnych Kompresívnych Syndrómov a Ehlers-Danlos, o.z., Balkánska 110/108, 851 10 Bratislava, Slovakia, silvia.siskova.phd@gmail.com
[2] Technical University of Košice, Faculty of Mechanical Engineering, Department of Biomedical Engineering, Letná 1/9 | 042 00 Košice-Sever; jozef.zivcak@tuke.sk
[3] Dr. Ricardo Gil Sánchez, Internal medicine, Rare disease speciality, Calle del Doctor Zamenhof 29 Bajo, 46008 Valencia, Spain; Hospital La Fe, Valencia, consulta@dricardogil.com
[4] National Institute of Cardiovascular Diseases, Pod Krásnou hôrkou 1/7185, 833 48 Bratislava; dr.talal.ali8@gmail.com
* Correspondence: silvia.siskova@student.tuke.sk

Abstract: The link between Abdomino-Pelvic Vascular Compression Syndromes (APVCS) and Symptomatic Joint Hypermobility Syndromes (SJHS) highlights the need for a better understanding of the biomechanisms involved in the pathogenic processes of these disorders. This paper discusses 41 patient cases from Slovakia and Czech Republic primarily diagnosed with APVCS, but not eval- uated further. Within the investigation process, these patients were clinically assessed for SJHS, in particular the hypermobile type of Ehlers Danlos Syndrome and Hypermobility Spectrum Disorder. The results point out the need to acknowledge the link between these two conditions and call for further research to better understand the biomechanisms involved in these pathogenic processes.

Keywords: Abdomino-Pelvic Vascular Compression Syndromes (APVCS); Median Arcuate Ligament Syndrome (MALS, Dunbar Syndrome); Left Renal Vein Compression Syndrome (NCS, Nutcracker Syndrome); Superior Mesenteric Artery Syndrome (SMAS, Wilkie Syndrome); Iliac Vein Compression Syndrome (MTS, May-Thurner Syndrome); Pelvic Venous Insufficiency (PVI); Pelvic Congestion Syndrome (PCS); Symptomatic Joint Hypermobility Syndromes (SJHS); Ehlers-Danlos Syndrome (EDS); Hypermobility Spectrum Disorder (HSD)

1. Introduction

Abdomino-Pelvic Vascular Compression Syndromes are currently defined as rare conditions, where vessels in the abdomen and pelvis are compressed by other vessels or other structures and organs, or where vessels compress other structures and organs. These include Median Arcuate Ligament Syndrome, Left Renal Vein Compression Syndrome, Superior Mesenteric Artery Syndrome, Iliac Vein Compression Syndrome, Pelvic Venous Insufficiency, and Inferior Vena Cava Syndrome [1-3,5,8-11,16]. These described syndromes present with a wide variety of clinical symptoms as well as anatomic variations. Moreover, the symptomatology frequently also overlaps with many other conditions. Thus, the diagnostic process is often very demanding and unclear, as well as the patient treatment management [5,8,9,16]. Most affected seem to be patients of young age and these conditions have a significant impact on their quality of life.

Recently, a few studies have pointed out the link between Abdomino-Pelvic Vascular Compression Syndromes and Symptomatic Joint Hypermobility Syndromes and their co-existing conditions [8-11]. SJHS are a group of connective tissue disorders, which present with joint laxity, hypermobility and tissue fragility. They are defined as spectrum disorders, and thus manifest on different scales of comorbidity combinations as well as their varied severities in each individual [4,6,12-15]. However, a more in-depth research in this field is lacking. Therefore, the objective of this study is to further build on this emerging knowledge in order to allow for a better understanding of the pathogenic mechanisms as well as the interplay involved in these conditions.

2. Materials and Methods

A combination of retrospective data collection and a prospective diagnostic analysis was utilized in order to carry out this research study. The investigated patient population consisted of 41 patients from Slovakia and Czech Republic, who are members of the patient assistance group under the Association of Vascular Compression Syndromes and Ehlers-Danlos for Slovakia and Czech Republic. All of these 41 patients were diagnosed with one or more APVCS prior to joining the patient assistance group. They were diagnosed in different centers around Slovakia and Czech Republic. However, none of these patients were further investigated for all APVCS comprehensively or for the possibility of having a genetic connective tissue disorder, such as hypermobile Ehlers-Danlos Syndrome or Hypermobility Spectrum Disorder, which both belong under the umbrella condition Symptomatic Joint Hypermobility Syndromes.

Therefore, this study focused on the investigation and evaluation of possible hEDS or HSD in these patients. Since the molecular basis for the hypermobile type of EDS has not been uncovered yet globally, the diagnostic is based on clinical assessment according to the latest version of Diagnostic Criteria for Hypermobile Ehlers-Danlos Syndrome (hEDS) updated by The International Consortium in 2017 [6,7,14,15]. Out of these 41 pa- tients, so far 17 were assessed in cooperation with Dr. Ricardo Gil, a specialist in rare dis- eases; including Ehlers-Danlos Syndrome; and 24 patients have so far undergone a pre- liminary evaluation with the study lead author, waiting to be assessed in cooperation with Dr. Ricardo Gil.

3. Results

A total of 41 patients previously diagnosed with one or more APVCS from Slovakia and Czech Republic were clinically evaluated for hEDS and HSD. The evaluation was carried out according to the Diagnostic Criteria for Hypermobile Ehlers-Danlos Syndrome 2017 [15] as well as The Beighton Scoring System [14].

As seen in Table 1 and Table 2, out of the 17 patients evaluated in cooperation with Dr. Ricardo Gil, 8 (47.06%) patients met the diagnostic criteria of hEDS, 5 (29.41%) patients met the diagnostic criteria of HSD, and 4 (23.53%) patients did not meet hEDS or HSD criteria. The mean Beighton score was 5.76. Beighton score of 5 and higher indicates a positive result for joint hypermobility [14]. Hence, this group of patients, on average, met the diagnostic criteria for SJHS. Additionally, more than half (n = 9, 52.94%) of these patients have already undergone a surgery for APVCS, while the lesser half (n = 8, 47.06%) have not, as shown in Table 3.

Table 1. 17 patients with APVCS evaluated for hEDS and HSD in cooperation with Dr. Ricardo Gil

Patients	Beighton score	hEDS / HSD	AVCS surgery
Patient no. 1	5	HSD	no
Patient no. 2	3	no hEDS, no HSD	no
Patient no. 3	6	HSD	yes

Patient no. 4	6	hEDS	no
Patient no. 5	4	no hEDS, no HSD	yes
Patient no. 6	5	HSD	no
Patient no. 7	9	hEDS	yes
Patient no. 8	5	hEDS	yes
Patient no. 9	2	no hEDS, no HSD	yes
Patient no. 10	7	hEDS	yes
Patient no. 11	5	hEDS	no
Patient no. 12	4	HSD	yes
Patient no. 13	9	hEDS	no
Patient no. 14	8	hEDS	yes
Patient no. 15	8	HSD	yes
Patient no. 16	9	hEDS	no
Patient no. 17	3	no hEDS, no HSD	no
Average	**5,76**		

Table 2. Evaluation of results from Table 1

Type	Amount	%
hEDS	8	47.06
HSD	5	29.41
no hEDS, no HSD	4	23.53
Sum	**17**	**100**

Table 3. Surgery for APVCS

Surgery	Amount	%
yes	9	52.94
no	8	47.06

In addition, the results of 24 more patients, who have undergone a preliminary evaluation of hEDS and HSD with the study lead author, were summarized. Table 4 and Table 5 show that 9 (37.50%) patients did not meet the diagnostic criteria of hEDS or HSD, 8 (33.33%) patients met the diagnostic criteria of HSD, and 6 (25.00%) patients met the diagnostic criteria of hEDS. In addition, 1 (4.17%) patient met the diagnostic criteria of hEDS, but at the same time has already performed and received results from molecular genetic analysis, which showed a variant of unknown significance NM_000093.5 (COL5A1): c.3023C>T p.(Thr1008Met), possibly related to the classical type of EDS. The patient is currently awaiting results from additional molecular screening as are the rest of the patients. The mean Beighton score in this group of patients was 3.83. Additionally, in this group, exactly half (n = 12, 50.00%) of these patients have already undergone a surgery for APVCS, and the other half (n = 12, 50.00%) has not, as shown in Table 6.

Table 4. 24 patients with APVCS preliminarily evaluated for hEDS and HSD

Patients	Beighton score	hEDS / HSD	AVCS surgery
Patient no. 1	1	no hEDS, no HSD	no
Patient no. 2	5	hEDS, susp. cEDS (VUS)	yes
Patient no. 3	1	HSD	yes
Patient no. 4	1	HSD	yes

Patient no. 5	0	no hEDS, no HSD	no
Patient no. 6	4	hEDS	no
Patient no. 7	6	hEDS	no
Patient no. 8	4	hEDS	no
Patient no. 9	1	hEDS	yes
Patient no. 10	4	no hEDS, no HSD	yes
Patient no. 11	5	HSD	no
Patient no. 12	5	HSD	yes
Patient no. 13	6	hEDS	no
Patient no. 14	1	no hEDS, no HSD	no
Patient no. 15	3	no hEDS, no HSD	yes
Patient no. 16	0	no hEDS, no HSD	yes
Patient no. 17	5	HSD	yes
Patient no. 18	9	hEDS	no
Patient no. 19	8	HSD	yes
Patient no. 20	8	HSD	no
Patient no. 21	2	no hEDS, no HSD	no
Patient no. 22	2	no hEDS, no HSD	yes
Patient no. 23	2	no hEDS, no HSD	yes
Patient no. 24	9	HSD	no
Average	**3.83**		

Table 5. Evaluation of results from Table 4

Type	Amount	%
no hEDS, no HSD	9	37.50
HSD	8	33.33
hEDS	6	25.00
hEDS, susp. cEDS (VUS)	1	4.17
Sum	**24**	**100**

Table 6. Surgery for APVCS

Surgery	Amount	%
yes	12	50.00
no	12	50.00

Finally, the combined results of these two patient groups are summarized in Table 7 and Table 8 below. Out of the total of 41 patients, 14 (34.15%) patients met the diagnostic criteria of hEDS, 13 (31.71%) patients met the diagnostic criteria of HSD, 13 (31.71%) patients did not meet the diagnostic criteria of hEDS or HSD, and 1 (2.44%) patient met the diagnostic criteria of hEDS, but at the same time showed a genetic mutation potentially linked with cEDS, awaiting further genetic evaluation. A combined (hEDS + HSD + hEDS, susp. cEDS) total of 28 (68.29%) patients met the diagnostic criteria of Symptomatic Joint Hypermobility Syndromes. This makes up more than half and almost three quarters of the studied patient group. In addition, 21 (51.22%) patients have already undergone a surgery for APVCS, while the lesser half, 20 (48.78%) patients have not.

Table 7. Combined results from both patient groups (combined Table 2 and Table 5)

Type	Amount	%
hEDS	14	34.15

HSD	13	31.71
no hEDS, no HSD	13	31.71
hEDS, susp. cEDS (VUS)	1	2.44
Sum	**41**	**100**
Sum SJHS	**28**	**68.29**

Table 8. Surgery for APVCS – combined results from both patient groups

Surgery	Amount	%
yes	21	51.22
no	20	48.78

Graph 1. Patients with APVCS evaluated for hEDS and HSD

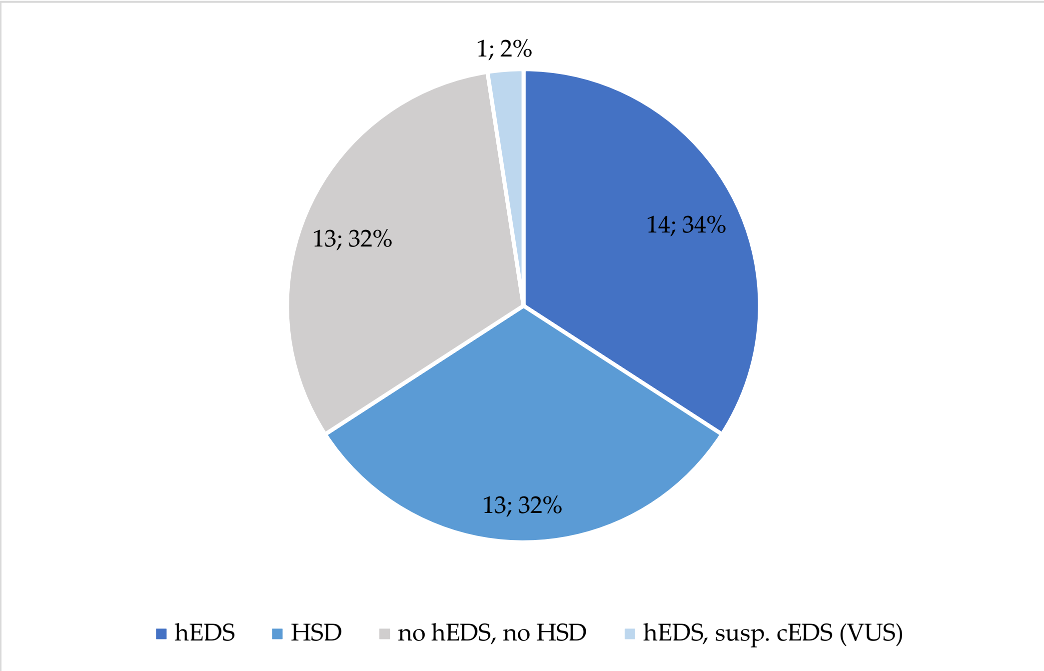

4. Discussion and Conclusion

Patients diagnosed with Abdomino-Pelvic Vascular Compression Syndromes often show signs of joint hypermobility and, after a careful evaluation, many of them even meet the clinical requirements of either Hypermobility Spectrum Disorder or Hypermobile Ehlers-Danlos Syndrome, falling under the umbrella term Symptomatic Joint Hypermobility Syndromes, a group of connective tissue disorders. This study showed that out of 41 patients initially diagnosed with APVCS, after a detailed clinical analysis for HSD and hEDS, a significant portion of 68.29% met the clinical criteria of these conditions.

Since these connective tissue disorders are associated with a broad variety of comorbid conditions, further supported by the prevalence of wide spectrum and overlap of patient symptomatology, these findings emphasize the need for further detailed investigation and a multidisciplinary patient diagnostic and treatment approach. Only through engaging in aforementioned practice can we allow to facilitate a better understanding of the biomechanisms and pathogenic processes involved in the interplay of these complex conditions.

Disclosures: All data and information were obtained directly from patients, with their approvals to be used in this study.

Acknowledgements: This paper was written with the financial support from the KEGA granting agency within the project solutions No. 050TUKE-4/2022 and No. 021TUKE-4/2022, and with financial support from the APVV granting agency within the project solutions No. APVV-20-0068 and No. SK-CZ-RD-21-0056.

References

1. Ali T., Tomka J., Bakirli I., Bakirov I. Surgical Treatment of Wilkie's Syndrome by Vascular Transposition. Cureus. 2022 Apr 18;14(4):e24251. doi: 10.7759/cureus.24251. PMID: 35475250; PMCID: PMC9018456.
2. Barbati, M. E. Vascular Compression Syndromes - What You Need to Know. Self-published. 2023 May 17. ISBN-13 979-8394995682
3. Barbati, M. E. Pelvic Congestion Syndrome - Beyond Menstrual Cramps. Self-published. 2023 May 17. ISBN-13 979-8215002322
4. Daylor, Victoria & Gensemer, Cortney & Norris, Russell & Bluestein, Linda. (2023). Hope for Hypermobility: Part 1—An Integrative Approach to Treating Symptomatic Joint Hypermobility. Topics in Pain Management. 38. 1-9. 10.1097/01.TPM.0000924780.91929.b3.
5. D'Oria M, Zlatanovic P, Anthony A, Dua A, Flores AM, Tanious A, Rodríguez Morata A, Scerrati A, Baccellieri D, Biscetti F, Baldazzi G, Mantovani G, Sen I, Peinado Cebrian J, Rocha-Neves J, Sousa J, Davidovic L, Juszynski M, Markovic M, Oller Grau M, Tessari M, Hynes N, Gloviczki P, Shaw P, Zamboni P, Hinchliffe R, Ricci R, Sultan S, Acharya Y, Troisi N, Antignani PL, Mansilha A, Komlos PP. International Union of Angiology consensus document on vascular compression syndromes. Int Angiol. 2023 Aug;42(4):282-309. doi: 10.23736/S0392-9590.23.05100-3. Epub 2023 Jul 27. PMID: 37498053.
6. Gensemer C, Burks R, Kautz S, Judge DP, Lavallee M, Norris RA. Hypermobile Ehlers-Danlos syndromes: Complex phenotypes, challenging diagnoses, and poorly understood causes. Developmental Dynamics. 2021; 250:318–344. https://doi.org/10.1002/dvdy.220
7. Gil R. (2024) El Síndrome de Ehlers Danlos. Accessed 11 March 2024. https://dricardogil.com/sindrome-ehlers-danlos/
8. Kim, K. International Foundation of Abdominal Vascular Compression Syndromes, Baltimore, MD. Abdominal Vascular Compression Syndromes: Current and Future of Management of Abdominal Vascular Compression Syndromes that Includes Median Arcuate Ligament Syndrome, Nutcracker Syndrome, Superior Mesenteric Artery Syndrome, May-Thurner Syndrome, and Associated Pelvic Venous Insufficiency.
Journal of Vascular Surgery. April Supplement 2023. PIIS074152142300201X
9. Kim, K. & International Foundation of Abdominal Vascular Compression Syndromes. (2023, April 15). Abdominal Vascular Compression Syndromes: AVCS: Relationship & Interconnectivity of May-Thurner, Nutcracker, Median Arcuate Ligament, Superior Mesenteric Artery Syndromes, & Associated Pelvic Venous Insufficiency [Presentation]. II Venous Summit CCEV 2023 Endovascular Surgery Chapter, Malaga, Spain. https://venous-summit.com/VENOUS-SUMMIT2023
10. Ormiston CK, Padilla E, Van DT, Boone C, You S, Roberts AC, Hsiao A, Taub PR. May-Thurner syndrome in patients with postural orthostatic tachycardia syndrome and Ehlers-Danlos syndrome: a case series. Eur Heart J Case Rep. 2022 Apr 9;6(4):ytac161. doi: 10.1093/ehjcr/ytac161. PMID: 35620060; PMCID: PMC9131024.
11. Sandmann, W., Scholbach, T., & Verginis, K. (2021). Surgical treatment of abdominal compression syndromes: The significance of hypermobility-related disorders. American Journal of Medical Genetics Part C: Seminars in Medical Genetics, 1–9. https://doi.org/10.1002/ajmg.c.31949
12. Seneviratne SL, Maitland A, Afrin L. Mast cell disorders in Ehlers-Danlos syndrome. Am J Med Genet C Semin Med Genet. 2017 Mar;175(1):226-236. doi: 10.1002/ajmg.c.31555. Epub 2017 Mar 6. PMID: 28261938.
13. Tinkle B, Castori M, Berglund B, Cohen H, Grahame R, Kazkaz H, Levy H. 2017.Hypermobile Ehlers–Danlos syndrome (a.k.a. Ehlers–Danlos syndrome Type III and Ehlers–Danlossyndrome hypermobility type): Clinical description and natural history. Am J Med Genet Part C SeminMed Genet 175C:48–69.
14. The Ehlers Danlos Society. (2024). Assessing joint hypermobility. Accessed 18 March 2024. https://www.ehlers-danlos.com/assessing-joint-hypermobility/
15. The Ehlers Danlos Society. (2024). hEDS Diagnostic Checklist. Accessed 19 March 2024. https://www.ehlers-danlos.com/heds-diagnostic-checklist/
16. Živčák, J., Tóth, T., & Trebuňová, M. (2013). Meranie intraabdominálneho tlaku. Technická Univerzita, Košice. ISBN 978-80-553-1602-4

TECHNICKÁ UNIVERZITA V KOŠICIACH
Strojnícka fakulta

Exploring the Transformative Potential of Microsoft Power BI in Scientific Research and Data Analysis

Dominika Sukopová [1,*], Jaroslava Kádárová [1], Laura Lachvajderová [1] and Lenka Vyrostková [1]

[1] Technical University of Kosice, Faculty of Mechanical Engineering, Department of Business Management and Environmental Engineering
* Correspondence: dominika.sukopova@tuke.sk

Abstract:
This article examines the capabilities of Microsoft Power BI as a key tool for data analysis and visualization in research. Power BI offers a comprehensive platform that integrates data extraction, transformation, and visualization. The study highlights Power BI's ability to connect to various data sources, use advanced analytical functions with DAX, and perform data transformations using Power Query Editor. A practical example demonstrates how Power BI visualizes research data on the development and impact of Business Intelligence (BI) between 2018 and 2022. The results show that Power BI is an indispensable tool for researchers and analysts, despite some limitations such as data size constraints and dependence on the Microsoft ecosystem. Power BI allows for ease of use, cost-effectiveness, and high customizability, opening up new possibilities and innovations in the field of research.
Keywords: Microsoft Power BI, Data Analysis, Data Visualization, Analytics Tools, Business Intelligence

1. Introduction

In today's rapidly evolving world of information and data, organizations and researchers are harnessing new technological tools as crucial instruments for efficiently processing, analyzing, and presenting vast amounts of data. In this digital era, where data represents a goldmine for understanding patterns and trends, we delve into the realm of Microsoft Power BI. This article focuses on how Power BI is not merely another tool for data analysis and visualization but is becoming an indispensable companion for researchers seeking dynamic and interactive solutions for their analytical needs [1].

Developed by Microsoft, Power BI brings with it a broad array of features that enable not only the swift and effective management of data from various sources but also the creation of insightful visualizations with remarkable ease. It is precisely in this combination of capabilities that Power BI's potential for research lies, where high-quality analytical tools can be decisive in comprehending complex research questions and effectively presenting results [2].

Imagine Power BI as the key that unlocks the doors to analytical minds, enabling those who seek a deeper understanding of their data to bring new dimensions to the world of research. Our exploratory journey with Power BI allowed us to comprehend its advantages, disadvantages, and a wide range of applications across various domains. The article provides a comprehensive view of how this tool becomes an indispensable partner in the analytical environment, paving the way for new possibilities and innovations in the field of research and data analysis [3].

2. Decoding Power BI: In-Depth Exploration

When delving deeper into the Microsoft Power BI software, numerous possibilities for data analytics and visualization unfold. Power BI represents a sophisticated solution for business analytics, seamlessly integrating into contemporary research projects [4].

2.1. Data Integration and Processing

At its core, Power BI functions as a platform that facilitates the extraction, transformation, and visualization of data from diverse sources. Its exceptional capabilities lie not only in its ability to connect to various databases, Excel files, and cloud storage but also in its capacity to process and cleanse raw data directly within the tool. This capability empowers researchers to leverage the potential of diverse data sources, enabling the creation of sophisticated analytical models [5].

2.2. Advanced Analytical Functions Using DAX

The transformative capabilities of Power BI extend to the realms of modeling and visualization. By utilizing a powerful language known as Data Analysis Expressions (DAX), researchers can formulate intricate calculations and metrics, surpassing the boundaries of conventional data operations. This feature opens pathways for in-depth analysis, facilitating the identification of patterns and trends crucial to the research process [5].

2.3. Power Query Editor for Data Transformation

Power Query Editor within Power BI allows for extensive data transformation and cleaning operations. Researchers can use it to combine, reshape, and refine data from multiple sources, enabling more accurate and insightful analyses [6].

2.4. Visualization Capabilities and Relational Modeling

Power BI stands out for its compelling visualization capabilities. Going beyond static graphs and tables, Power BI offers a multitude of customizable visual elements, allowing for the creation of dynamic and interactive dashboards. Researchers can create and manage relationships between different data tables, which enhances data integrity and the ability to perform complex queries and analyses. This not only enhances the interpretability of results but also elevates the communication of complex research insights.

Navigating through the nuances of Power BI reveals that this tool significantly surpasses common data analysis tools. It emerges as a strategic partner for researchers navigating the vast sea of data, transforming it into a comprehensible landscape of insights [7].

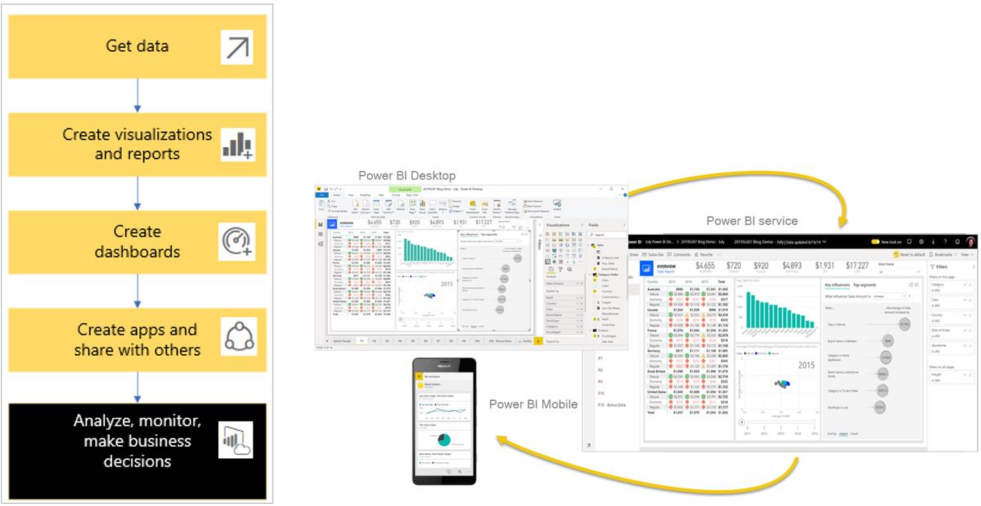

(a) **(b)**

Figure 1. (a) Power BI progress; (b) The components of Power BI

3. Advantages and Disadvantages of Power BI: A Critical Perspective

When examining Microsoft Power BI, its substantial advantages naturally come to the forefront, but so do certain limitations. A critical overview of these aspects provides a holistic understanding of how Power BI can integrate into the analytical environment. For better clarity and systematic comparison of these aspects, we have created the following table.

Table 1 Advantages and Disadvantages of Power BI

Advantages of Power BI	Disadvantages of Power BI
• Integration with Various Data Sources • ETL Capability - Extract, Transform, Load • High Customizability of Visualizations • Ease of Use and Cost-Effectiveness	• Limited Size of Data Sets (Depending on the License) • Dependence on the Microsoft Ecosystem • Advanced Features Require a Certain Level of Expertise

4. Areas of Application: Leveraging Power BI Across Industries

The following table highlights the diverse applications of Power BI across various industries and sectors. From financial analysis to healthcare, manufacturing, research, education, and more, Power BI's versatility is showcased through its ability to address specific needs and provide valuable insights. This table offers a glimpse into the expansive reach of Power BI, demonstrating its effectiveness in enhancing decision-making processes and driving analytical solutions in different domains.

Table 2. Application Areas and Characteristics in Power BI

Areas of Application	Characteristics
• Business and Marketing	• Financial Analysis: Power BI enables in-depth analysis of financial data, budget creation, and performance monitoring. • Economic Trend Forecasting: The robust tools within Power BI assist in predicting economic trends and supporting strategic decision-making.
• Healthcare and Biomedicine	• Patient Data Analysis: Power BI provides tools for analyzing patient data, monitoring treatment outcomes, and creating visualizations for healthcare reports. • Biomedical Research: In the realm of research, Power BI enables the analysis and visualization of data to support biomedical studies.
• Manufacturing and Logistics	• Supply Chain Management: Power BI is utilized for monitoring and optimizing the supply chain, including inventory management and deliveries. • Production Monitoring: The creation of visualizations enables

	managers to monitor and optimize manufacturing processes.
• Research and Development	• Management of Research Projects: Power BI is employed for tracking the progress of research projects, allocating resources, and predicting research outcomes. • Data Visualization for Research: Power BI facilitates the visualization of complex scientific data, aiding in pattern recognition and trend analysis.
• Education and Training	• Analysis of Student Performance: Power BI can be used to track and analyze student results, aiding in evaluating the effectiveness of teaching and identifying areas for improvement. • Employee Training and Development: Monitoring the effectiveness of employee training and development through visualizations.

5.Practical Application Example: Visualization of BI Research Data

In addition to the previously discussed applications, we utilized Microsoft Power BI Desktop to visualize data from a simple research example, demonstrating the versatile use of Power BI in the academic field. This research example includes analyzing the development and impact of Business Intelligence (BI) between 2018 and 2022 by examining articles published in five major journals in the field of Business Information Systems.

5.1. Methodology

The following Figure 2 illustrates the steps to visualize data in Power BI Desktop.

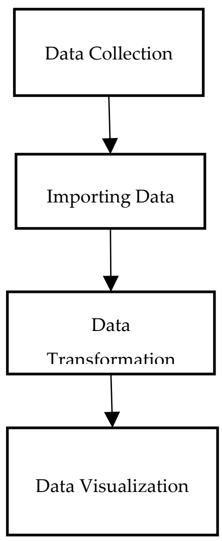

Figure 2. Main Steps for Data Visualization

The process begins with the collection of necessary data. This data is gathered in a suitable format, such as CSV files, from relevant and reliable sources. It is important to ensure that the data is comprehensive and accurate to facilitate meaningful analysis and visualization.

Once the data is collected, it is imported into Power BI Desktop using the "Get Data" function. This function allows for seamless integration of various data sources into the Power BI environment. Importing the data correctly ensures that it is available for subsequent transformation and analysis.

In the Power Query Editor, essential transformations are performed to clean and reshape the data. This step is crucial as raw data often contains inconsistencies, errors, and irrelevant information. Transformations may include removing duplicates to prevent data redundancy, filtering rows to focus on the desired timeframe, and splitting columns to separate combined data points into individual components. These transformations enhance the quality and usability of the data.

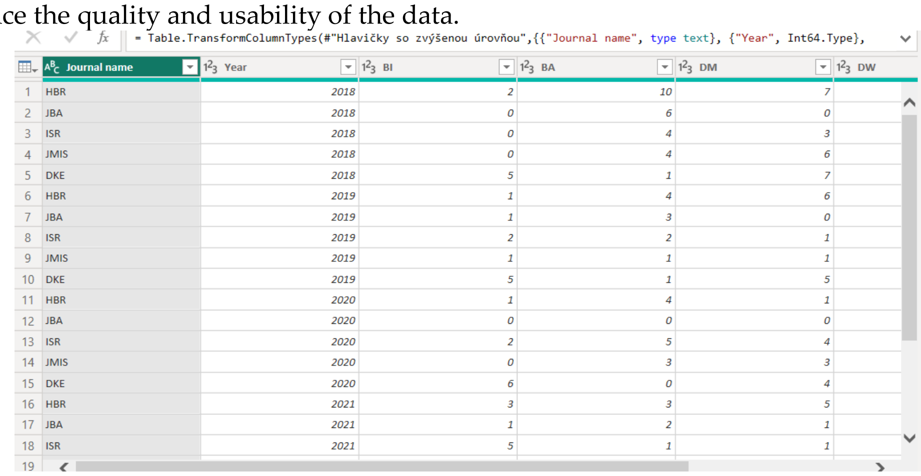
= Table.TransformColumnTypes(#"Hlavičky so zvýšenou úrovňou",{{"Journal name", type text}, {"Year", Int64.Type},

	Journal name	Year	BI	BA	DM	DW
1	HBR	2018	2	10	7	
2	JBA	2018	0	6	0	
3	ISR	2018	0	4	3	
4	JMIS	2018	0	4	6	
5	DKE	2018	5	1	7	
6	HBR	2019	1	4	6	
7	JBA	2019	1	3	0	
8	ISR	2019	2	2	1	
9	JMIS	2019	1	1	1	
10	DKE	2019	5	1	5	
11	HBR	2020	1	4	1	
12	JBA	2020	0	0	0	
13	ISR	2020	2	5	4	
14	JMIS	2020	0	3	3	
15	DKE	2020	6	0	4	
16	HBR	2021	3	3	5	
17	JBA	2021	1	2	1	
18	ISR	2021	5	1	1	
19						

Figure 3. Data Transformation Process

After the data has been appropriately transformed, various visualizations are created using Power BI tools. Visualization is a critical component of data analysis as it allows for the graphical representation of data, making it easier to identify patterns, trends, and insights. Examples of visualizations include line charts to display trends over time, bar charts to compare different categories, and pie charts to show the distribution of key themes. These visualizations are interactive and customizable, enabling users to explore the data from multiple perspectives.

Finally, perform final adjustments to the visualizations to enhance readability and aesthetics. This includes formatting charts, adding labels and legends, and ensuring the overall visual appeal. These adjustments help in effectively communicating the insights derived from the data analysis.

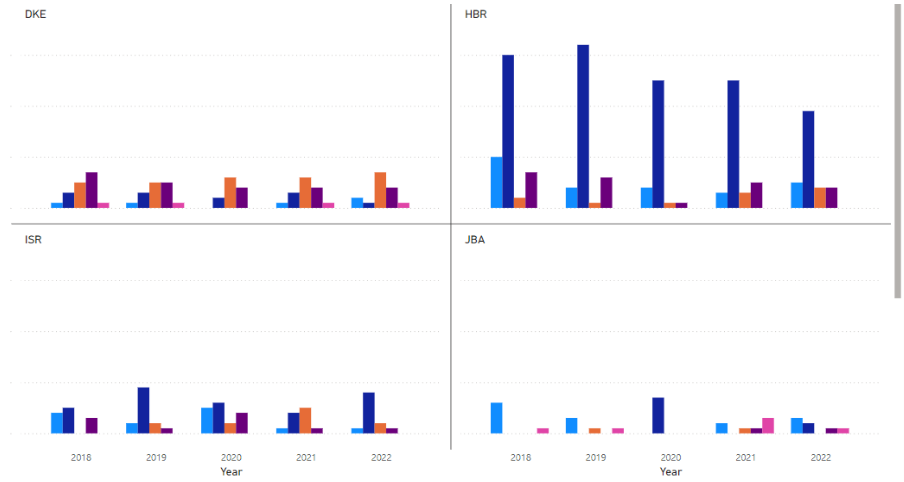

Figure 4 Example of Research Data Visualization Using MS Power BI Desktop

As shown in Figure 3, one of the resulting visualizations for our research is tailored for easy understanding and comparison of results. This visualization serves as a clear example of using MS Power BI Desktop for effective and comprehensive data presentation.

6. Conclusions

Microsoft Power BI has proven to be a versatile and powerful tool for data analysis and visualization in research and academic studies. It offers an integrated platform for data extraction, transformation, and visualization, going beyond traditional data analysis tools. Key capabilities include integration with various data sources, advanced data transformations using Power Query Editor, and complex analytical models with DAX. Its extensive visualization options allow researchers to present data intuitively and interactively, enhancing result interpretability and insight communication. The practical application example demonstrated Power BI's potential to simplify complex data sets and reveal meaningful patterns and trends. Dynamic dashboards and customizable visual elements help researchers gain deeper insights and make data-driven decisions efficiently. Despite limitations such as data size constraints and dependence on the Microsoft ecosystem, Power BI's advantages make it indispensable for modern researchers and analysts. Its ease of use, cost-effectiveness, and high customizability add to its appeal. In conclusion, Microsoft Power BI exceeds contemporary data analysis and visualization needs, opening new possibilities and innovations in research. As data grows in volume and complexity, tools like Power BI will be crucial in unlocking the full potential of data-driven research and decision-making.

Acknowledgments: This article was created with the support of project: VEGA 1/0340/21 “The impact of a pandemic and the subsequent economic crisis on the development of digitization of enterprises and society in Slovakia.”

References

1. Ali, S. M., Gupta, N., Nayak, G. K., & Lenka, R. K. (2016). Big data visualization: Tools and challenges. 2016 2nd International Conference on Contemporary Computing and Informatics (IC3I)
2. Becker, L. T., & Gould, E. M. (2019). Microsoft power BI: extending excel to manipulate, analyze, and visualize diverse data. Serials Review, 45(3), 184-188.
3. Doko, F., & Miskovski, I. (2020). Advanced analytics of big data using power BI: credit registry use case.
4. “Powe BI”, from https://www.microsoft.com/en-us/power-platform/products/power-bi/, 16.11.2023
5. Aspin, A. (2021). Classic Chart Visual Styles. In Pro Power BI Theme Creation: JSON Stylesheets for Automated Dashboard Formatting (pp. 125-164).
6. Wright, C.Y.; Wernecke, B. Using Microsoft© Power BI© to visualise Rustenburg Local Municipality's air quality data, 2020.
7. Muhammad F., 10 Best Power BI Reports Examples, from https://hevodata.com/learn/10-best-power-bi-reports-examples/,17.11.2023

TECHNICKÁ UNIVERZITA V KOŠICIACH
Strojnícka fakulta

Adaptive slicing for robotic additive manufacturing

Pavol Štefčák [1]*, Ivan Gajdoš [2]*, Ján Slota [3]*

[1] pavol.stefcak@tuke.sk [2]
ivan.gajdos@tuke.sk [3]
jan.slota@tuke.sk
* Slovakia, Technical University of Košice, Department of Technology, Materials and Computer Supported production, Mäsiarska 74,040 01 Košice

Abstract: The use of multi-purpose and gantry robots with 5 or more axes in large format additive manufacturing (LFAM) presents many opportunities and challenges. The ability to process large volumes of material and rapidly produce products of significant dimensions requires the formulation of an appropriate manufacturing strategy. This includes setting production parameters and selecting the right software to generate toolpath movements, considering the limitations of the technologies used. There are many companies on the market that offer multi-axis LFAM cutting software, but prices above €6,000 per year per machine could be limiting for some users. To overcome this limitation, this paper explores the use of parametric modelling and visual programming as a powerful tool in planar, non-parallel, angular and adaptive additive manufacturing at a fraction of the cost, approximately €1,000 for a one-off payment. This paper discusses use of non-planar adaptive printing in applications as manufacturing composites, repairing of complex parts and how it can reduce overall fabrication times. As alternative to expensive pieces of software, an adaptive slicing script in relatively cheap software Rhino grasshopper was made and tested by printing test samples. In conclusion the possibilities offered by the Rhinoceros Grasshopper software in the design of toolpath strategies were discussed.

Keywords: LFAM, Grasshopper, slicing, parametric design, visual scripting

1. Introduction

Advanced Design for Additive Manufacturing (ADfAM) requires Advanced slicing capabilities which is a key process in generating a set of flat or curved layers [1]. The use of 6-axis robots makes it possible to overcome the limitations of product design in additive manufacturing processes by using planar horizontal material deposition and brings with it an extension of the possibilities of applying materials to complex non-planar surfaces that can be used in a variety of applications such as:

1. Manufacturing of composites where achieving the correct fiber orientation is crucial for the proper functioning of these parts. The conventional planar-layer material deposition process often results in undesirable fiber orientation as it orients fibers in the plane of the layer. To overcome this issue, the ability to position fibers along a 3-dimensional curve is required. To meet this requirement, the ability to deposit material along non-planar layers is necessary.
2. Reducing Overall Fabrication Time in Large Part Printing: Many part geometries require a specific build direction to minimize the staircase effect in a conventional planar layer-based process. However, this can result in printing a large number of layers, which is time-consuming. Non-planar layers offer more options for minimizing the staircase effect. Several types of geometries can be printed faster using non-planar layers, minimizing staircase effects on curved surfaces. This can significantly reduce build time for large parts and reducing the need for post processing by minimizing the staircase effect.
3. Repairing of complex parts what involves depositing material on non-planar surfaces and shaping it accordingly. Robotic 3D printing has the potential to enable near-net deposition, simplifying the overall process by allowing the same robot to be used for material deposition, grinding, and sanding. The ability to deposit material on curved surfaces will also increase automation in the repair of complex parts. Robots can

be used for material deposition, allowing for in-situ additive manufacturing on prefabricated structures [2,3,4]. With the help of 6-DOF robot arms, it is now possible to fabricate 3D parts at various angles, which overcomes the limitations of conventional 3D printing methods. Recently, there has been growing interest in the use of industrial robots for additive manufacturing in both academia and industry [5,6].

The aim of our research was to create a viable trajectory for adaptive printing using non-planar material deposition. The feasibility of the planned trajectory was validated through robotic simulation. The proposed trajectory planning was implemented on the robotic AM system, which was built at our department. The system comprises a 6-DOF robot arm manipulator, FANUC M-20iB/25 robot equipped with an MDPH2 pellet extruder. Our paper focuses on trajectory planning for non-planar layered printing and its feasibility. The trajectory is generated using a nonplanar planes intersection method in Visual programming software Rhino Grasshopper and process parameters are determined through empirical experiments.

2. Materials and Methods

To generate a path on a non-planar surface, a grasshopper script of planes intersection method we used instead of a common slicing algorithm that transforms 3D objects into individual layers. The main objective was to create sequences of positions and orientations of the tool center point (TCP). This is a crucial aspect of the adaptive printing process and greatly affects design possibilities. The grasshopper adaptive slicing script (fig. 1) was developed to generate G-code for a simple B-rep geometry which represent curved surface to verify its functionality. To achieve this, several integrated function blocks and special position obtaining blocks of Rhino Grasshopper software were used. The experiment was conducted on a FANUC M-20iB/25 robot equipped with an MDPH2 pellet extruder.

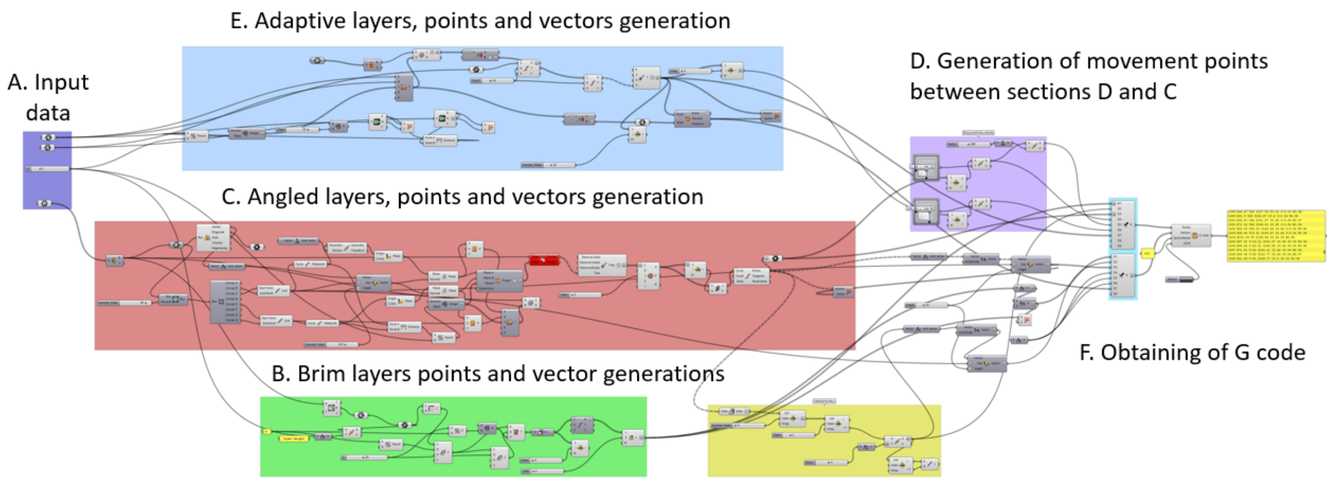

Figure 1. *Grasshopper adaptive slicing script scheme*

The Grasshopper adaptive slicing script consist of 6 sections which are parametrically connected and converts Input data into printable G code. Section A (fig. 1) collects input data as B-rep geometry to slice, layer height and surfaces which defines start and end of adaptive slicing. Section B (fig. 1) is generating build plate adhesion related feature to secure faultless creation of nonplanar surface. In the section C (fig. 1) layers, points and vectors for of B-rep geometry representing nonplanar surface are generated. The intersection curves generated serve as layer indicators and are displayed in Figure 2. The points and vectors determine the motion and adaptive orientation of the extruder relative to the current extruder position.

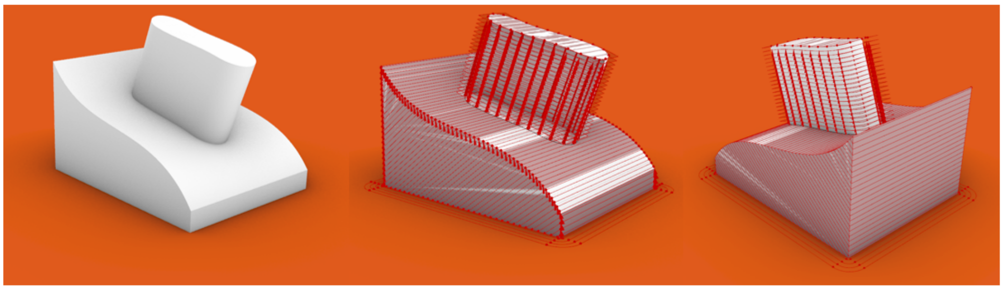

Figure 2. B-rep geometry (from left) and generated layers,points and vectors

To avoid collision between already printed part and ready to print start point on curved surface, movement for the extruder is settled in section D (fig.2). Adaptive layers, points and vectors generation in section E (fig. 2) are representing experimental part of this paper to prove it’s functionality. Finally, the process of obtaining coordinates of points and vectors can be found in section F. The results of the grasshopper script (fig. 3) can then be exported in G-code format. Once the G-code has been generated, it must be uploaded into the robot simulating software RoboDK. This is where the robot's movement is programmed and the G-code is translated into the robot's movement language. The final steps of the preprocessing of robotics 3D printing include setting up start/end procedures, final checking for possible collisions, and uploading the program to the robot.

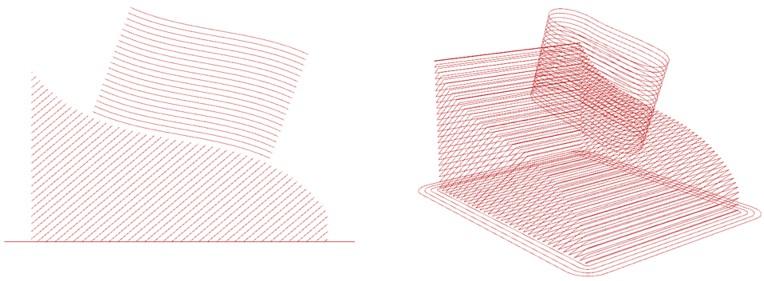

Figure 3. Preview of generated layers angled (bottom section) and addaptive top section of the part

3. Results

Offline programming and simulation of the robot’s movements was done in specialized RoboDK software for industrial robots with 3D printing plugin. Translated robot language was transferred to the control system of the robot and then executed (fig. 4). The script tests the adaptive printing options on curved surface and their impact on the design limitation for non-planar additive manufacturing. Several samples were printed for validation of method functionality and used for further analyze.

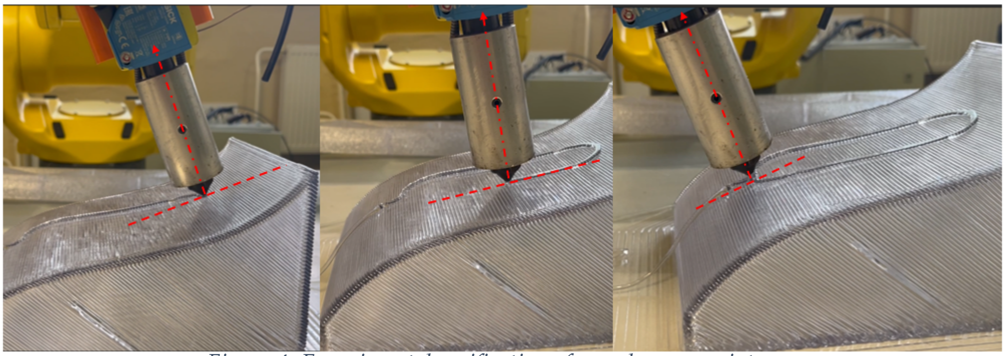

Figure 4. Experimental verification of grasshopper script

In this process, angled printing was used to create nonplanar surface to test adaptive printing with minimal material consumption due to the ability to hollow print without the need for infill (fig. 5). Manufacturing parameters were settled accordingly:

- Temperature: 200°C
- print speed: 20 mm/s
- nozzle diameter: 3mm
- layer height: 2 mm
- layer width: 5 mm
- material: PETG

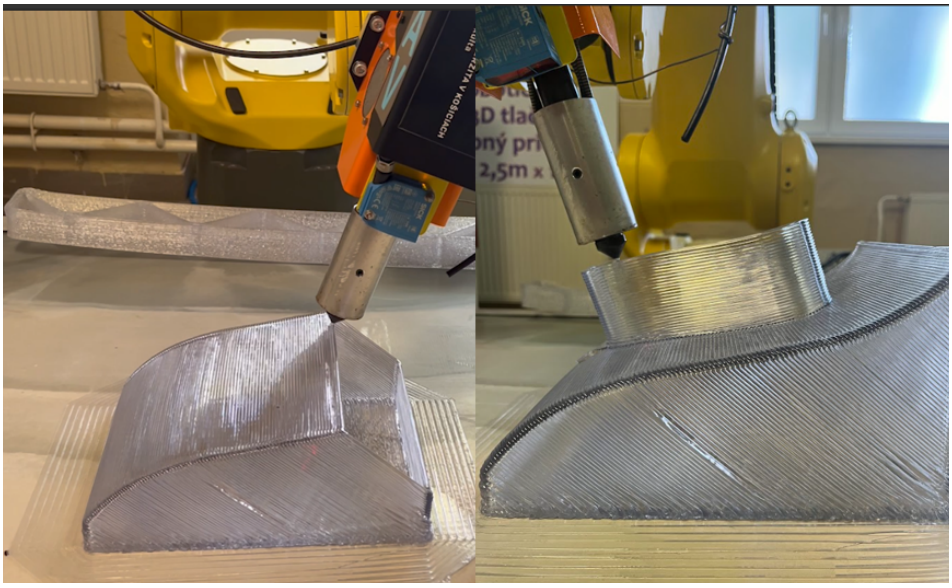

Figure 5. Preview of manufacturing proces of experimental verification

5. Conclusions

The printed samples proved that the designed script works and 3 samples were printed without problems. The use of the Rhinoceros Grasshopper software extends the possibilities of designing the toolpath and due to its cost it can significantly reduce production costs. Further research will focus on optimizing the speed of the Grasshopper script and creating clusters that allow the user to slice segments faster and easier and combine different settings for different segments.

Acknowledgement: This work was supported by projects: „Research on the possibilities of forming and joining innovative metal-plastic composites in the production of light- weight thin-walled structures”, project number: SK-PL-23-0040 & BPN/BSK/2023/1/00038/U/00001, VEGA -1/0539/23 and KEGA 050TUKE-4/2023.

References

1. Donghua Zhao, Weizhong Guo. Mixed-layer adaptive slicing for robotic Additive Manufacturing (AM) based on decomposing and regrouping. Journal of Intelligent Manufacturing 2020; 31:985–1002. https://doi.org/10.1007/s10845-019-01490-z
2. Shembekar, Aniruddha & Yoon, Yeo Jung & Kanyuck, Alec & Gupta, Satyandra. (2018). Trajectory Planning for Conformal 3D Printing Using Non-Planar Layers. V01AT02A026. 10.1115/DETC2018-85975.
3. Campbell, I., Bourell, D., and Gibson, I., 2012. “Additive manufacturing: rapid prototyping comes of age”. Rapid Prototyping Journal, 18(4), pp. 255–258
4. Gao, W., Zhang, Y., Ramanujan, D., Ramani, K., Chen, Y., Williams, C. B., Wang, C. C., Shin, Y. C., Zhang, S., and Zavattieri, P. D., 2015. “The status, challenges, and future of additive manufacturing in engineering”. ComputerAided Design, 69, pp. 65–89
5. Zhang, G. Q., Li, X., Boca, R., Newkirk, J., Zhang, B., Fuhlbrigge, T. A., Feng, H. K., and Hunt, N. J., 2014. “Use of industrial robots in additive manufacturing - a survey and feasibility study”. In ISR/Robotik 2014; 41st International Symposium on Robotics; Proceedings of, VDE, pp. 1–6.

6. Bhatt, P. M., Peralta, M., Bruck, H. A., and Gupta, S. K., 2018. “Robot assisted additive manufacturing of thin mul tifunctional structures”. In ASME 2018 13th International Manufacturing Science and Engineering Conference collo cated with the 46th NAMRI/SME North American Manu facturing Research Conference, American Society of Me chanical Engineers.

Advanced combustion chamber and mixture stratification

Pavol Tarbajovský [1*], Michal Puškár [2], Matúš Lavčák [3]

[1] Faculty of Mechanical Engineering, TU Košice, Letná 9, 040 01 Košice, Slovak Republic; pavol.tarbajovsky@tuke.sk
[2] Faculty of Mechanical Engineering, TU Košice, Letná 9, 040 01 Košice, Slovak Republic; michal.puskar@tuke.sk
[3] Faculty of Mechanical Engineering, TU Košice, Letná 9, 040 01 Košice, Slovak Republic; matus.lavcak@tuke.sk
* Correspondence: e-mail@e-mail.com: pavol.tarbajovsky@tuke.sk; Tel.: +421 55 602 2355

Abstract: Combustion of lean fuel mixture dramatically influences its flow in the combustion chamber which triggered the design of a new „Combustion chamber implementing homogenization and controlled fuel mixture self-ignition by compression" granted a patent. The design was based on the idea that an engine with a layered charge creates a richer fuel mixture close to the spark and a leaner fuel mixture in the rest of the combustion chamber. The richer mixture is easier to ignite which subsequently ignites the lean mixture in the rest of the combustion chamber. In summary, this phenomenon enables the engine to use a lean mixture which improves efficiency and at the same time secures complete combustion. Simulation results approved the benefit of this design for emission reduction.

Keywords: combustion chamber, fuel stratification, homogenous mixture

1. Introduction

In recent years, the automotive industry has been going through a turning point due to the industrial policy of the EU member states. The goal of this effort is to transition to a clean, renewable and low-carbon economy. The goal is also to reduce the amount of emissions produced by transport and increase the share of industrial production as an important part of the overall economy of EU countries. Digitization, the transition to electromobility, new drive technologies and the transition to alternative energy sources are also important challenges that require considerable attention.

The current emission standards are so strict that car companies often struggle to comply with them. They have to invest large amounts of money to develop new power units and measures to reduce emission production, while the results are often uncertain. Therefore, current research and development is focused on technology that would preserve the efficiency of combustion engines and significantly reduce emissions of nitrogen oxides. One such technology is SPCCI, which uses the principle of spark-controlled homogeneous combustion of a fuel mixture using compression and spark. Combustion of a homogeneous mixture takes place simultaneously in the entire volume of the combustion space of the cylinder, which leads to efficient use of fuel, more perfect fuel combustion and, as a result, cleaner emissions.

2. Structural design of an internal combustion engine using SPCCI technology

There are currently several different approaches to controlling HCCI combustion timing. One of these approaches is to change the mixture temperature parameters to achieve control over combustion timing. This change can be achieved in a variety of ways, such as variable valve timing, residual exhaust gas capture, variable compression ratio, variable EGR method, fixed in-cylinder injection timing, intake temperature modulation, water injection or coolant temperature adjustment. Another possible approach to control the ignition timing is to control the reactivity of the mixture, which can also be achieved in a variety of ways, including fuel modulation, fuel stratification, fuel additives, and controls [1, 2, 5].

Various mechanisms have been proposed to solve this problem. One option is to initialize the engine in conventional mode and then switch to SPCCI mode after a short warm-up. Other proposed solutions include different fuel or fuel additives and increasing the compression ratio.

The development of SPCCI technology is also the subject of investments by several automotive companies, and the current problems associated with combustion engines confirm the importance of this direction. When combined with state-of-the-art technologies such as direct injection, electronic camshaft timing, variable valve lift, and cylinder pressure measurement, SPCCI should theoretically deliver significant fuel savings while meeting future emission standards. SPCCI makes it possible to achieve high combustion efficiency like diesel engines and the high performance of gasoline engines.

In classical combustion, fuel reacts with oxygen in the air. The oxidation of fuel by air can be expressed as:

$$el + (\ _2 + 3{,}76\ _2) \rightarrow yC\ _2 + \ \ _2 \qquad \ldots$$

where $(\ _2 + 3{,}76\ _2)$ represents air, which consists of roughly 21% oxygen and 79% nitrogen. The coefficients x, y ,and depend on the particular fuel and the fuel/air equivalence ratio in the reaction. The equivalence ratio is defined as:

$$\emptyset = \frac{/}{(\ \ /\ \ )_{EC}} = \frac{1}{\ } \qquad [2]$$

where the denominator corresponds to the stoichiometric ratio of fuel and air when the correct ratio of both is available to completely consume all the fuel and oxygen mole-cules. ø = 1 corresponds to the stoichiometric ratio, if ø < 1 it is a lean mixture (excess air) and if ø > 1 the mixture is rich (excess fuel). The air-fuel equivalence ratio λ (lambda) is the ratio of the actual AFR value to the stoichiometric value for a given mixture. λ = 1.0 is for a stoichiometric mixture, for rich mixtures λ < 1.0 and lean mixtures λ > 1.0. [4,6]

$$= \frac{AFR}{AFR_{STEC}} \qquad [3]$$

The stoichiometric air-fuel ratio λ for several common fuels is given in Table 1.

Table 1. Air-fuel stoichiometric ratios of common fuels

Fuel	AFR
Methane	17,2
Propane	15,7
Butane	15,5
Gasoline	14,5
Ethanol	9,0

In classical combustion of a stoichiometric mixture, the flame spreads, so the combustion energy is converted into heat and the work required to push the piston. Lean combustion contains significantly more air in the same amount of fuel, so diatomic molecules that move easily, such as N2 and O2, are used relatively more than before. Consequently, burning the same amount of fuel increases the rate of pressure rise and increases the amount of work that can be extracted, leading to a higher thermal efficiency of this concept.

The effects of lean combustion can be summarized as follows:

- Lean combustion, in which the ratio of air and fuel increases, increases the ratio of specific heat.
- As the combustion temperature decreases, the difference between the gas temperature and the wall temperature decreases, reducing the amount of heat transfer and cooling loss.
- Compared to λ=1 operation, lean combustion reduces throttle loss due to more intake air at the same torque value. In this way, the synergistic effect dramatically improves the thermal efficiency.

The combustion of a lean mixture is fundamentally affected by its flow in the combustion chamber, therefore a "Combustion chamber with the implementation of homogenization and controlled self-ignition of the fuel mixture using compression" (Fig. 1) was designed, for which a patent was granted [3]. The design was based on the assumption that a stratified charge engine creates a richer fuel mixture near the spark and a leaner mixture throughout the rest of the combustion chamber. The rich mixture ignites easily and subsequently ignites the lean mixture throughout the rest of the chamber; ultimately allowing the engine to use a leaner mixture, improving efficiency while ensuring complete combustion. [6,7]

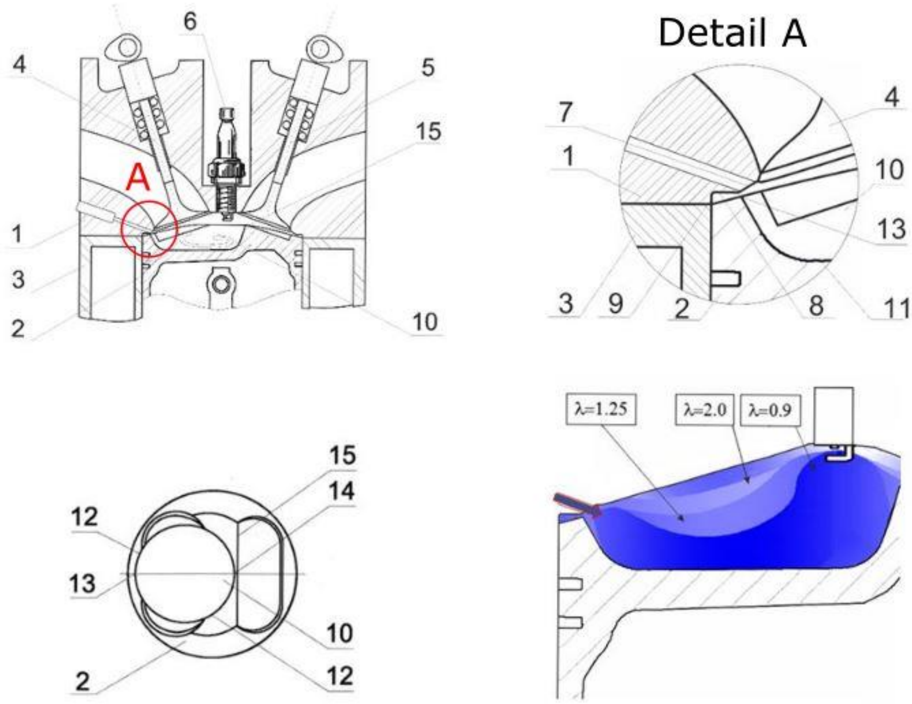

Figure 1. Combustion chamber with the implementation of homogenization and controlled self-ignition of the fuel mixture using compression

Fig. 1 also outlines the method of stratification of the mixture during lean combustion based on the shape of the homogenizing part and the injection angle. The homogenizing part of the piston acts as a chamber and is located on the side of the inlet channel. The geometry of the homogenizing part of the piston is designed so that the injected fuel falling on the homogenizing curve of the piston goes under the spark plug. It is believed that the high pressure of the injected fuel prevents the formation of a fuel film on the bottom of the piston during breakage and ensures the supply of a sufficiently rich dose of fuel under the spark plug. The stratification of the mixture was chosen so that several zones of different coefficients of excess air λ occur. [5]

3. Simulation Results

The proposed solution was implemented and analyzed using 3D simulation software. At the same time, a simulation of the standard solution took place, and the achieved results were compared in terms of the course of work characteristics and benefits in the emission area. Temperature analysis was chosen for the analysis of the processes taking place in the combustion chamber. Fig. 2 presents the temperature analysis in the combustion chamber with the implementation of homogenization and controlled self-ignition of the fuel mixture using compression, which was designed and a commonly used piston.

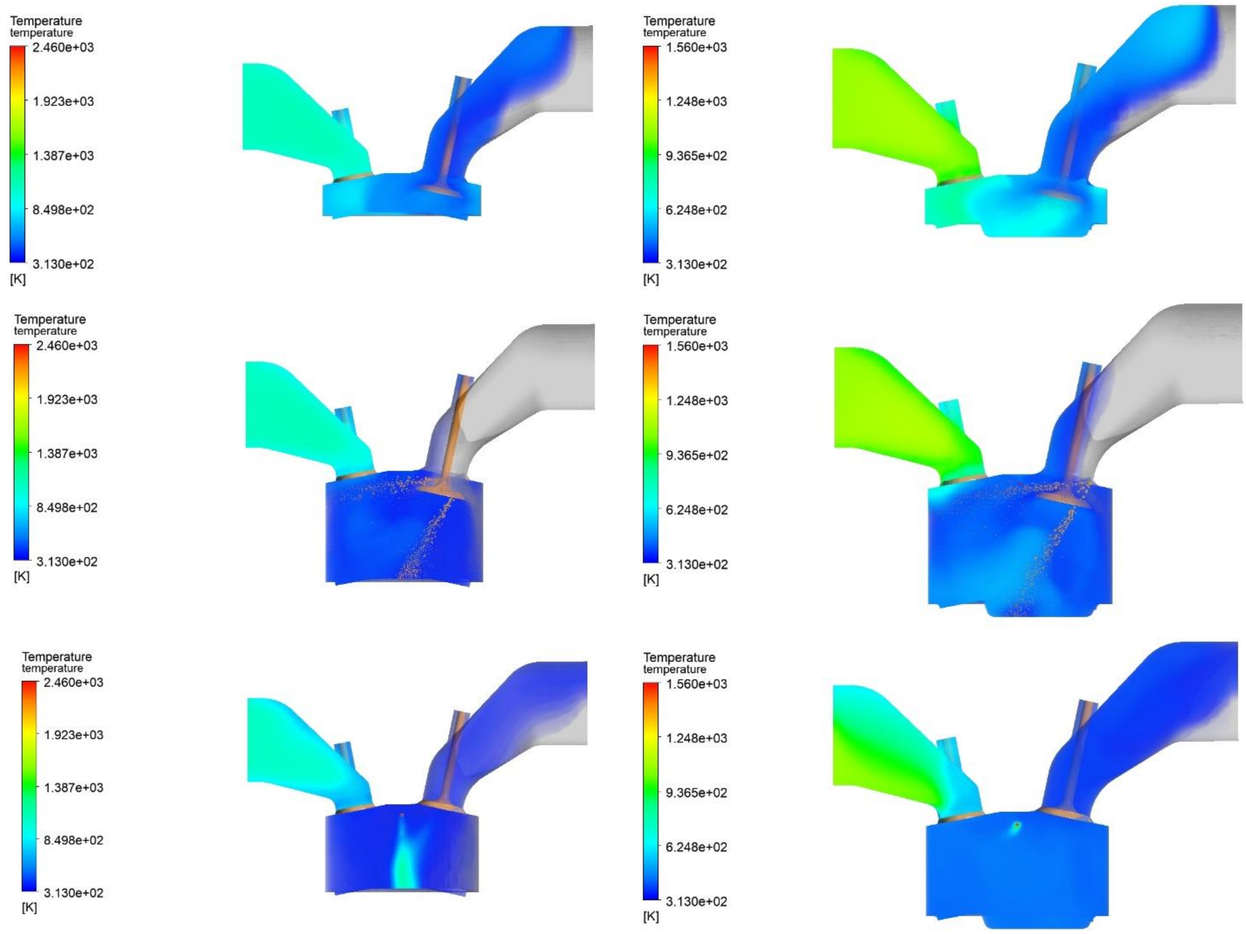

Figure 2. Analysis of the working temperature in the combustion chamber using a standard piston (left); Analysis of the working temperature in the combustion chamber with the implementation of homogenization and controlled self-ignition of the fuel mixture using compression and spark-plug (right)

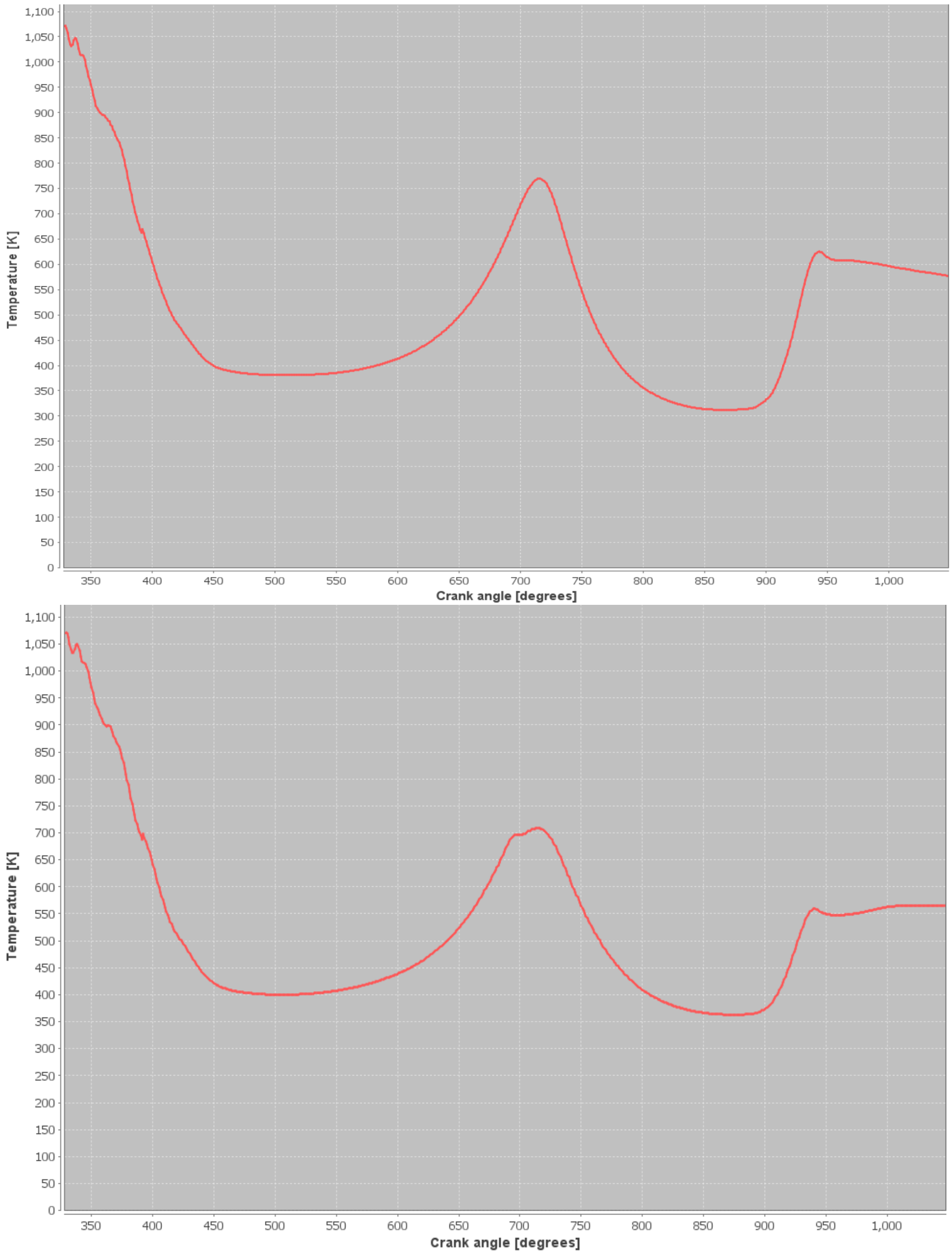

Figure 3. The course of the working temperature in the combustion chamber depending on the position of the crankshaft (upper curve - standard solution, lower curve - designed combustion chamber)

The analysis of the solution shows that there was a significant reduction in the working temperature in the combustion chamber, which is one of the prerequisites for the application of SPCCI, the characteristic feature of which is that energy is obtained by a low-temperature process. This fact has a fundamental impact on the production of NOX emissions, which should be almost negligible, as confirmed by the simulation results.

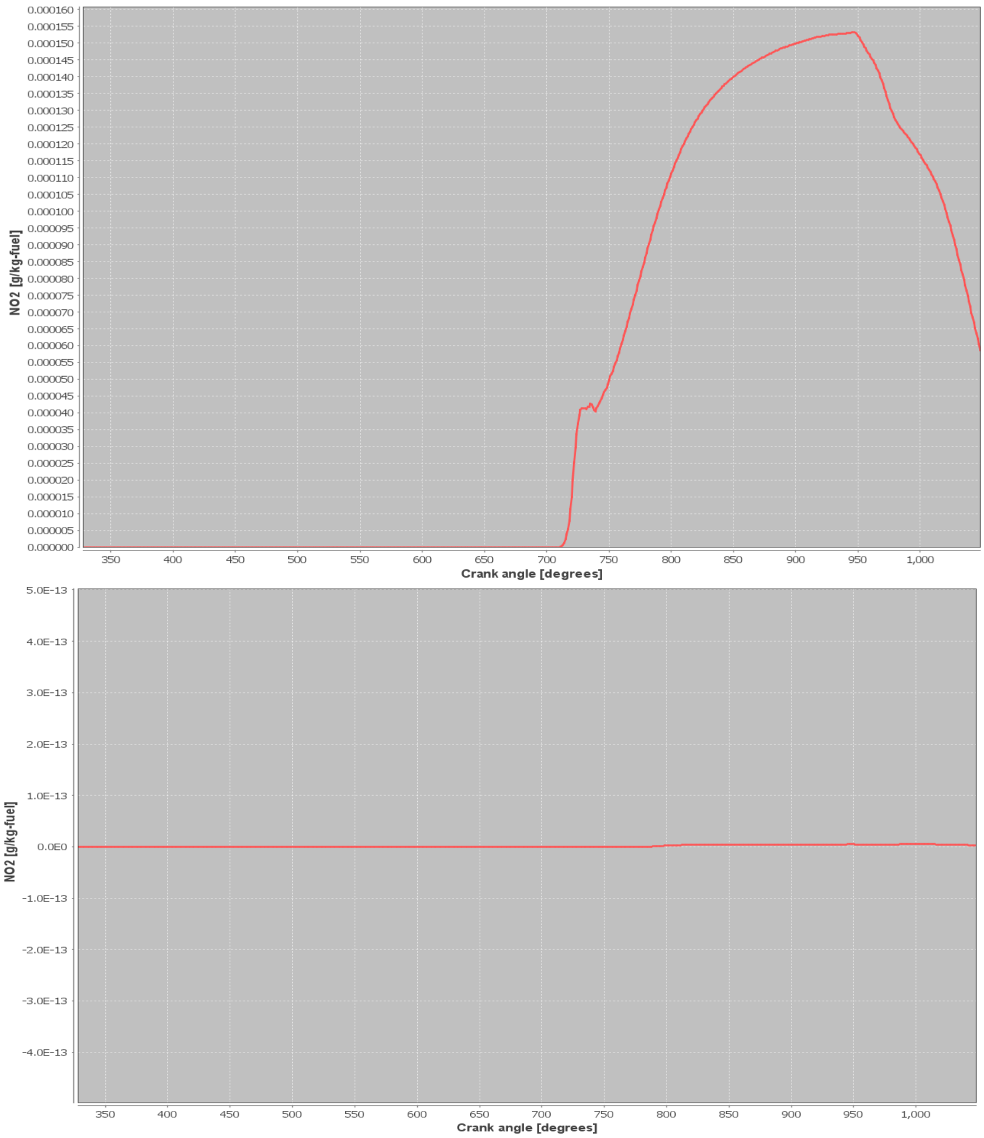

Figure 4. Analysis of the production of nitrogen oxides depending on the position of the crankshaft (upper curve - standard solution, lower curve - designed combustion chamber)

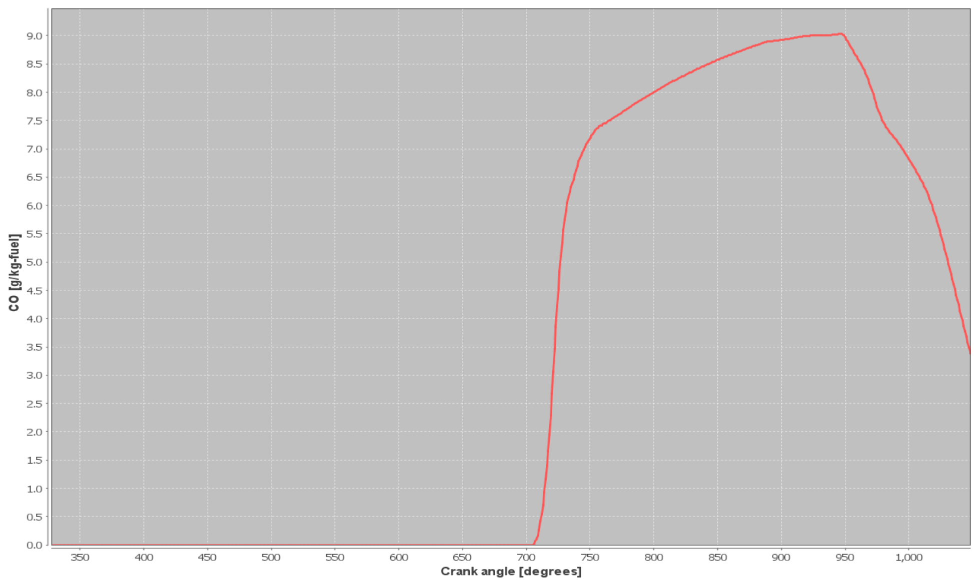

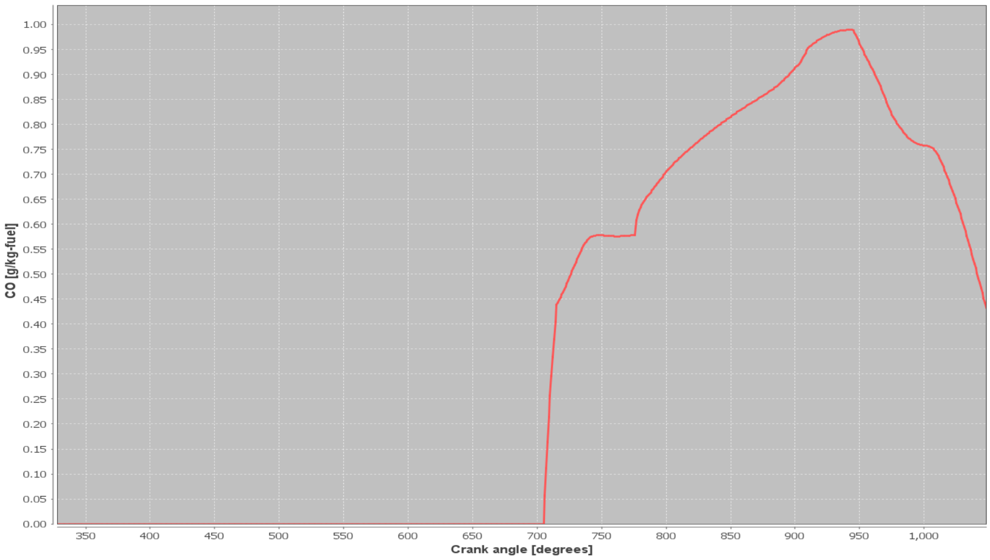

Figure 5. Analysis of CO emission production depending on the position of the crankshaft (upper curve - standard solution, lower curve - designed combustion chamber)

5. Conclusions

Despite the rapidly developing electric mobility, vehicles with internal combustion engines are still the most popular choice from the point of view of customers. Therefore, research and development in the field of new engine technologies will continue to be essential from an ecological point of view. In addition, the internal combustion engine is an important element in hybrid drives and diesel drives have a great advantage mainly about the parameters achieved. The SPCCI technology needs to be tested more but the results so far indicate the use of this type of combustion as promising and applicable to motor vehicles.

Acknowledgments: This work was supported by the Slovak Research and Development Agency under the Contract no. APVV-19-0328. The article was written in the framework of Grant Projects: VEGA 1/0318/21 "Research and development of innovations for more efficient utilization of renewable energy sources and for reduction of the carbon footprint of vehicles" and KEGA 007TUKE-4/2023 "Transfer of innovations and advanced technologies, determined for more ecological and more efficient vehicle drive systems, into the educational process."

Conflicts of Interest: The authors declare no conflict of interest.

1. PUŠKÁR, M: Pokročilé technológie spaľovania a emisná problematika vozidiel. Prvé vydanie. Košice: Technická univerzita v Košiciach. 2023. 63 s. ISBN 978-80-553-4196-5
2. PUŠKÁR, Michal – TARBAJOVSKÝ, Pavol: Spaľovacie motory a možnosti redukcie emisií. Košice: Technickí univerzita v Košiciach, 2022. 123 s. ISBN 978-80-553-4152-1
3. GE, Y., CHEN, L. AND FENG, H. (2022) 'Optimal piston motion configuration for irreversible Otto cycle heat engine with maximum ecological function objective', Energy Reports, 8, pp. 2875–2887. doi:10.1016/j.egyr.2022.01.220.
4. LAVČÁK, M., ŠOLTÉSOVÁ, M., PUŠKÁR, M.: Automobilový priemysel a emisná problematika. In: KOKA 2022 Scientific Proceedings.- Bratislava (Slovensko): Spektrum STU s. 201-206 . - ISBN 978-80-227-5215-2, [Online].
5. OLSSON JO, TUNESTÅL P, HARALDSSON G, JOHANSSON B. A turbo charged dual fuel HCCI engine. SAE Technical paper; 2001.
6. STANGLMAIER RH, LI J, MATTHEWS RD. The effect of in-cylinder wall wetting location on the HC emissions from SI engines. SAE Technical Paper; 1999.
7. JENNISCHE M. Closed-loop control of start of combustion in a homogeneous charge compression ignition engine (MSc Thesis). Lund Institute of Technology; 2003.

TECHNICKÁ UNIVERZITA V KOŠICIACH
Strojnícka fakulta

Standardization as a lean production tool indicating the direction of influence on the basic attributes of Industry 4.0

Martin Trebuňa [1,*]

[1,*] Technical University of Kosice, Faculty of Mechanical Engineering. Hlavna 9, 042 00 Kosice; martin.trebuna@tuke.sk

Abstract: Lean Manufacturing (LM) is considered a production philosophy that has been adapted for several decades in the conditions of many world-renowned industrial and other enterprises with the aim of continuous improvement of processes and their outputs with a primary focus on the customer. Its basic principles are focused on activities that add value, continuous improvement, and the elimination of all forms of waste from production and administrative processes.

In the field of industrial production, the term "Industry 4.0" or, in other words, the "fourth industrial revolution" has been used relatively recently. It is not based on exact methods; it focuses on bridging the physical and cyber world through the most modern technologies.

In a more detailed analysis of the essence of the above-mentioned concepts, the question arises whether and how these two areas can co-exist and complement each other. One of the key answers that could provide space for revealing the mutual compatibility of the mentioned principles, especially in connection with the premise of continuous improvement, is the answer hidden under the term standardization.

Keywords: keyword LEAN manufacturing (LM), Industry 4.0 (I 4.0), 5S, Standardization of work

1. Introduction

In real conditions, there are and are constantly being created many lean tools (5S, SMED, Kanban, Kaizen, Jidoka, etc.), which by their nature and with correctly implemented procedures in terms of substantive content and temporal continuity can significantly influence the fulfillment of the strategic goals of the production of the enterprise.

In addition to this fact, it is widely known that the fourth industrial revolution changes conventional industrial enterprises into "smart industrial enterprises" due to the influence of development, which are characterized, among others, by the following features:

- the ubiquity of digital devices and computing technology, which minimizes the intervention of human capital in processes,
- connecting global demand and supply in real time,
- high-speed collection, analysis and sharing of data in real time,
- interweaving of the virtual and real world.

Over the last three decades, the field of LM has emerged as one of the supporting alternatives in correspondence with an effective and strategically oriented way of managing companies and appears as one of the most progressive methodologies that represents the best choice for navigation for the new - digitally integrated industrial platform. In other words, the principles of lean production form an ideal basis for the further application and development of I 4.0.

One of the primary and relatively frequently applied basic methods of lean production, the conditional basis of which is precisely standardization, is the "5S" method.

The goal of standardization is sustainable achievement of process stability, continuous increase of productivity, quality, and efficiency of work. Standardization can be seen as one of the conditions in connection with automation, or digitization.

2. Definition of terms – lean production, Industry 4.0, 5S, standardization

2.1 Lean Manufacturing

Kiichiro Toyoda, Taiichi Ohno and other Japanese engineers tried to implement a series of simple "quick win" improvements in the production process of the Toyota Motor Company in order to optimize the process flows in correspondence with the critical situation after the end of the Second World War in the automobile industry in Japan. They tried to revise Henry Ford's original ideas related to the production of the Ford Model T car in the twenties of the last century and jointly developed the Toyota Production System (TPS), better known as Lean Produktion [2, 4].

In the following overview, I will try to describe the concept of lean production in a simplified and brief way [1].

Lean means:

1. Constant improvement, which consists in daily elimination of errors!
2. Problem areas are eliminated through continuous improvement (Kaizen).
3. Lean is about eliminating 8 problematic details:

- Overproduction
- Excessive processing
- Movement
- Waiting
- Transportation
- Inventory
- Fixing errors
- Untapped potential of employees

Important lean principles:

- People who think "lean" support the creativity of other people, thereby showing respect for them.
- People who think "lean" are not owners of ideas, it's always a team effort.
- People who think "lean" say they are wrong at least twice a day.
- The improvements are endless because waste in the broadest sense of the word is like gravity.
- 90% of everything you do is useless.
- Never look at the problem areas of others, you will always have enough of your own around you!
- Lean is not about working fast, but rather about work well done.

Of course, other typical positive effects of building LM in the conditions of a production company are: lower probability of process failure, or technological equipment, lower volume of stock, space savings, higher efficiency, higher employee morale, etc. [5].

2.2 Industry 4.0

The term Industry 4.0 (I 4.0) was first used in 2013 by the German Hanover (Industrie 4.0) and was created at the instigation of the German government at the time of analyzing the impact of new technologies on the country's economy. In short, the term I 4.0 refers to the process of optimizing production procedures using the most modern technological knowledge with the aim of increasing production.

The goal of this process is to return industrial production back to Europe naturally at a technological level that can compete with other countries in terms of productivity [12].

I 4.0 will ultimately lead to a pull economy built on real-time demand research and highly automated and flexible manufacturing, fully connected. The result will be the ubiquitous use of automation, robotics, and intelligent machines to supplement human labor, resulting in a dramatic change in workforce engagement along with new forms of skills.

I 4.0 is a continuation of LM using digitization elements. Businesses today are full of software and data islands that hardly communicate directly with each other or at all. The solution is to connect them and achieve a smooth flow of information. The collection of new data and the accumulation of information can achieve previously unimaginable effects. An example is a digital twin - one of the technological tools of I 4.0, built on a digital copy of a real process. Digital optimization improves existing processes with minimal investment.

Technological changes in the spirit of I 4.0 are a response to market demands. For businesses, the transition to the I 4.0 concept certainly does not mean huge investments or throwing away what works. Implementation processes take place in parallel, and therefore it is essential to have a quality team, a well-thought-out procedure, a sequence of steps that will map out strategic opportunities and set up the processing of the pilot project. After its evaluation, they set the implementation program for the next period. This will bring effects in the form of increasing productivity, flexibility, quality, or reducing costs.

2.3 What is 5S?

5S is a system with which we can organize the workspace so that the activity performed in it is performed more efficiently and safely [13].

This method is a simple, low-cost solution that requires a relatively low proportion of special knowledge when deciding on its implementation. Although the 5S methodology has been known for more than 30 years, many companies have not been able to understand how to use this methodology to its full potential, or to support a broader picture of the principles of lean production.

The name of the method itself is derived from five words of Japanese origin, where this method was introduced and developed. Each of the letters "S" represents one of the five stages of the process, which ultimately, with correct implementation, can help to make the functionality of the processes as such more efficient.

5S was introduced by the management apparatus of the Toyota Motor Company in the first half of the twentieth century at its inception as part of the "Toyota Production System" (TPS).

The goal of the system was to ensure an increase in the consumer/utility value of produced goods or services for customers. This model was also aimed at the elimination of undesirable elements from the production process.

Figure 1. Model 5S Source: https://www.5stoday.com/what-is-5s/.

Among the basic benefits that the methodology in question provides when properly applied within the processes include, among others:

- cost reduction,
- higher quality,
- increase in labor productivity indicators,
- employee satisfaction,
- safer working environment.

I provide a more detailed description of the individual steps (activities) in the following overview:

Table 1. Description of 5S model activities Source: [13].

Activity*	Description	Corresponding questions
Sort	Keep only the necessary tools and objects close at hand, remove everything else.	What is the purpose of this item? When was this item last used? How often is it used? Who uses it? Does he really have to be here?
Set in order	Make sure everything around is organized and has its own space.	Which people (or workstations) use which items? When are items used? Which items are used most often? Should items be grouped by type? Where would it be most logical to place the items? Would some locations be more ergonomic for workers than others? Would some placements restrict unnecessary movement?
Shine	Clean the workplace regularly.	
Standardize	Establish standards for maintaining activities 1 through 3.	
Sustain	Follow and review activities 1 to 4..	

With the correct application of the 5S model in the workplace, it is much easier in the perspective of time to identify a potential problem before this problem manifests itself as a serious complication.

Figure 2. Output of the 5S method application.

A simplified view of the output of the model implementation is shown in fig. no. 2.

2.4 Standardization

Standardization is considered a key element of lean production, or it represents a fundamental attribute of a continuous and never-ending improvement process (Kaizen). The goal of the implementation is to ensure the correct course of work performance without the occurrence of errors, negative effects on the executors and the environment as such [6, 8].

The use of standards in practice could be summarized in the following points [7]:

- reduction of variability and corrections associated with error rate,
- improving work safety,
- facilitating communication,
- making problem areas visible,
- assistance in training and educational activities,
- increasing discipline in the performance of work,
- simplifying reactions when challenges occur,
- clarification of production procedures.

Standardization is also one of the effective application solutions for the exchange and sharing of important information in the production process. Visual standardization of processes can help guarantee the identical performance of a work task within several production employees.

3 Standardization as a tool of lean production vs. Industry 4.0 paradigms

While the field I 4.0 is by its nature considered to be the fourth industrial revolution and directly or indirectly includes the redefinition of individual production processes, sub-processes and technological units are the result of theories and innovative procedures that were implemented in the previous period.

Professor Amrik Sohal from Monash University in Melbourne, Australia, has been working on the implementation of lean manufacturing principles in practice for more than 30 years.

He says: "What has happened over the last half century in the industrial environment is that the principles of lean manufacturing have not only focused on simple, understandable tools and techniques, but have evolved into a phase of perceiving these principles as a specific philosophical field. Companies use this philosophy within the management of their business activities as a whole, they do not narrow it down to the area of the production process as such."

With the arrival of I 4.0, it seems at first glance that the LM era is slowly coming to an end. However, it is necessary to fully realize that focusing only on the field of automation and digitization and their outputs in the form of data is quite dangerous from the point of view of process management, as we must take into account that the data output is only as good as it can inform a competent person about the given phenomenon.

"It is really great if we can be recipients of data generated by technical equipment, but the question is what this data can tell us in correspondence with the process of continuous process improvement. In my opinion, IIoT (Industrial Internet of Things) is the next evolutionary wave of lean manufacturing. It's all about how we can leverage all these new technologies to build leaner processes...," said Terri Hiskey, vice president of software company Epicor, Austin, Texas.

A particularly significant fact that underlines the importance of work standardization as one of the important elements of the interconnection of lean production management models when using I 4.0 elements is a detail related to the overall value of the impact rate of the standardization tool in the matrix of the impact of I 4.0 tools on the management of lean production in a manufacturing company [11].

After a more detailed analysis of the report, it is clear that the LM - standardization tool has one of the highest shares in the overall evaluation in terms of the power of influence/synergistic effect [9]. with I 4.0 attributes ("+" - weak influence, "++" - stronger influence, "+++" - strongest influence). Similarly, this fact can be observed and subsequently stated with tools such as Kaizen (philosophy of continuous improvement) and Takt (time required to implement an activity at a pace aligned with the customer's request), that is, with tools that are closely related to the standardization tool.

Table 2. Matrix of the influence of Industry 4.0 on Lean Manufacturing tools Source: [11].

	Data Acquisition and Data Processing				Machine to Machine Communication (M2M)		Human-Machine Interaction (HMI)	
	Sensors and Actuators	Cloud Computing	Big Data	Analytics	Vertical integration	Horizontal integration	Virtual Reality	Augmented Reality
5S	+	+	+	+	+	+	++	+++
Kaizen	+	++	+++	+++	+++	+++	+++	+++
Just-in-Time	++	++	+++	+++	+++	++	+	++
Jidoka	+	+++	+++	+++	++	++	+	+
Heijunka	++	++	+++	+++	+++	++	++	+
Standardisation	++	+++	+++	+++	++	++	+++	+++
Takt time	+	+	+++	+++	+++	+++	+	+
Pull flow	++	+	+	+	+++	+++	+	+
Man-machine separation	+	+	+	+	+	+	+++	+++
People and teamwork	+	+	+	+	+	+	+++	+++
Waste reduction	+	+	++	+++	+++	+++	+	+

As M. Imai (1986) explained in his outstanding book on continuous improvement "Kaizen", it is impossible to improve any process without first stabilizing it and then standardizing it [3].

5. Conclusions

The question of the interrelationship of process standardization and quality is the subject of other contexts, so I will not focus on this area, even though it is important to mention this area due to its complexity.

Conflicts of Interest: “The author declares no conflict of interest.”

References

1. Akkers, P. *2 Second Lean: How to Grow People and Build a Lean Culture*, FastCap Press 2019, p. 150.
2. Holweg, M. The genealogy of lean production, In. *Journal of Operations Management*, 2007, *Vol. 25,* pp. 420-437.
3. Ima,i M. *Gemba Kaizen. Management and quality improvement in the workplace.* Brno: Computer Press; 2005. 314 p.
4. Liker, J.K. *The Toyota Way*, McGraw-Hill, New York (2004).
5. Kadarova, J., Demecko, M. New Approaches in Lean Management. In. *Procedia Economics and Finance.* 2016, *39.* p. 11-16. 10.1016/S2212-5671(16)30234-9.
6. Košturiak, J., Frolík, Z. *Lean and innovative company.* Praha: Alfa Publishing, s. r. o.; 2006.
7. Košturiak, J, Boledovič, Ľ., Kriťak, J., Marek, M. *Kaizen, The proven of practice Czech and Slovak companies,* Computer Press, a.s.; 2010.
8. Ohno, T. *Toyota Production System.* Portland: Productivity Press; 1998.
9. Pekarčíková, M., Trebuňa, P., Kliment, M. Digitalization effects on the usability of lean tools. In. *Acta logistica.* 2019, *6.* 9-13. 10.22306/al.v6i1.112.
10. Shingo, S. *A Study of the Toyota Production System: From an Industrial Engineering Viewpoint,* New York, Productivity Press (newly translated by Dillon A. P.), 1989.
11. Wagner, T., Herrmann, Ch., Thiede, S.: Industry 4.0 Impacts on Lean Production Systems, In. *Procedia CIRP*, 2017, *Vol. 63*, pp. 125-131.

12. http://priemyselstyrinula.sk/.
13. https://www.5stoday.com/what-is-5s/.

Technology in sport: A review of biofeedback and neurofeedback as forms of psychological skills training.

Radovan Hudak [1*], Mojmir Trebunak[2]

[1]Technical university of Kosice, Faculty of Mechanical Engineering, Department of Biomedical Engineering, Slovakia
*Corresponding authors: radovan.hudak@tuke.sk, mojmir.trebunak@gmail.com

Abstract: Biofeedback training (BFT) is an emerging technique gaining traction in sports psychology. It capitalizes on the idea that physiological changes reflect mental and emotional states. By providing real-time feedback on physiological responses (e.g., heart rate, muscle tension), BFT helps athletes develop self-regulation strategies for optimal performance. This article reviews the theoretical underpinnings of BFT and its application in sports. BFT can be used to manage arousal levels, improve cognitive function, enhance emotional well-being, and combat mental fatigue. However, limitations exist, including the need for more research in real-world sports settings and personalization of BFT programs for individual athletes. Overall, BFT offers a promising tool for athletes seeking to optimize their training and performance.

Keywords: biofeedback, neurofeedback, sport performance, psychological skills training

1. Introduction

The brain is the core of athletic performance, where physical and mental aspects converge for success [1]. Notably, mental factors are widely seen as key – especially in those crucial pre-performance seconds [2]. Athletes excel by strategically switching mental approaches to meet performance demands. Optimizing this allocation of neurocognitive resources is critical for peak performance [3].

This article explores brain function across athlete expertise levels. We examine how to control brain activity for superior performance, acknowledging limitations in current research. Finally, we propose future research directions to create a more unified approach.

Biofeedback is a way to adjust physical function and train step science. The information that biofeedback can provide mainly includes skin surface temperature, blood pressure, and muscle tension. This technology uses electronic facilities to selectively process information related to physiological and psychological processes in the body, so that it can be displayed in the instrument in auditory and visual ways. Individuals gradually learn to control and correct these activities to the maximum extent according to changes by controlling and learning the external feedback signals provided by the instrument, and then can achieve the purpose of self-regulating internal physiological and psychological changes and cultivating good physical and mental conditions.

2. Theoretical background of BFT

Biofeedback (BFT) and Neurofeedback (NFT) capitalize on the idea that physiological changes mirror mental and emotional shifts [4]. Drawing from operant learning [5], positive reinforcement through feedback helps athletes self-regulate targeted responses, potentially improving performance. This is why BFT and NFT are popular tools for psychological skills training (PST) in sports [6].

PST encompasses various techniques to enhance emotional control, cognitive skills, and mental toughness, ultimately leading to better athletic performance [7]. PST is particularly valuable when integrated into pre-performance routines [6].

The Wingate five-step approach (W5SA) exemplifies PST using BFT. W5SA outlines five stages: introduction, identification, simulation, transformation, and realization. Building on W5SA, proposed the learning-modification-application (LMA) approach, focusing on tailoring psychological strategies for stressful situations [8].

Another BFT periodization approach is the integrated psychological skills training program (IPSTP) by Beauchamp et al. [9]. IPSTP aims to train athletes in recognizing and monitoring their performance states through BFT. The program includes seven phases: orientation, observation, analysis, assessment, concept utilization, intervention, and evaluation.

3. Literature review

Biofeedback helps individuals become aware of internal processes typically beyond conscious control [10]. By providing feedback on physiological responses (heart rate, breathing), biofeedback allows individuals to develop self-regulation strategies. The goal is to identify suboptimal physiological states and train individuals to self-regulate towards optimal responses. Ultimately, the aim is to integrate these learned strategies into real-world situations without relying on the technology [11].

Research on biofeedback's effectiveness in sports remains limited since its initial proposal by Zaichkowsky [12]. Early studies explored using biofeedback for performance enhancement. Gracz found poor tennis serves were linked to suboptimal skin conductance levels, suggesting a link between arousal and performance [13]. Similarly, Zaichkowsky et al. investigated using EMG biofeedback to reduce stress in gymnasts, with mixed results [12].

Other studies focused on relaxation techniques. Peper and Schmid-Shapiro used biofeedback to reduce anxiety in rhythmic gymnasts, leading to positive experiences and improved performance [14]. Costa et al. applied relaxation techniques via biofeedback to decrease pre-competition anxiety in handball players [15].

Blumenstein and colleagues took a multi-modality approach, combining biofeedback with relaxation and imagery. They reported reduced pre-competition stress and improved performance in judo and canoeing/kayaking athletes [16].

While neurofeedback has been explored in non-sport domains [17], Landers et al. is the only known neurofeedback study in sports [18]. They found that correct feedback improved shooting performance in archers, while incorrect feedback hindered it.
Heart rate variability research has yielded mixed results. Lagos et al. [19] and Strack [20] reported performance improvements in golf and baseball with biofeedback training, while Tanis observed no improvement in volleyball [21].

4. Procedure of BFT

Commonly biofeedback experiments have a similar plan. Athletes first complete a pre-training skill test while their physical responses are monitored (using telemetry). This is followed by several biofeedback sessions where they learn to control their arousal levels through biofeedback-assisted self-regulation techniques. Finally, they perform a post-training skill test with physical monitoring again.

4.1. BFT in practice

Biofeedback training utilizes specialized equipment to create a feedback loop between the body and mind (Figure 1). It measures physiological signs (muscle tension, brainwaves, heart rate, etc.) and converts them into visual or auditory signals. This allows athletes to objectively perceive their internal state and, with professional guidance, learn to consciously control these responses. Through repeated training, they can develop conditioned reflexes to regulate physiological activity, promoting optimal performance and correcting imbalances. Common biofeedback tools include EEG, EMG, and heart rate variability feedback.

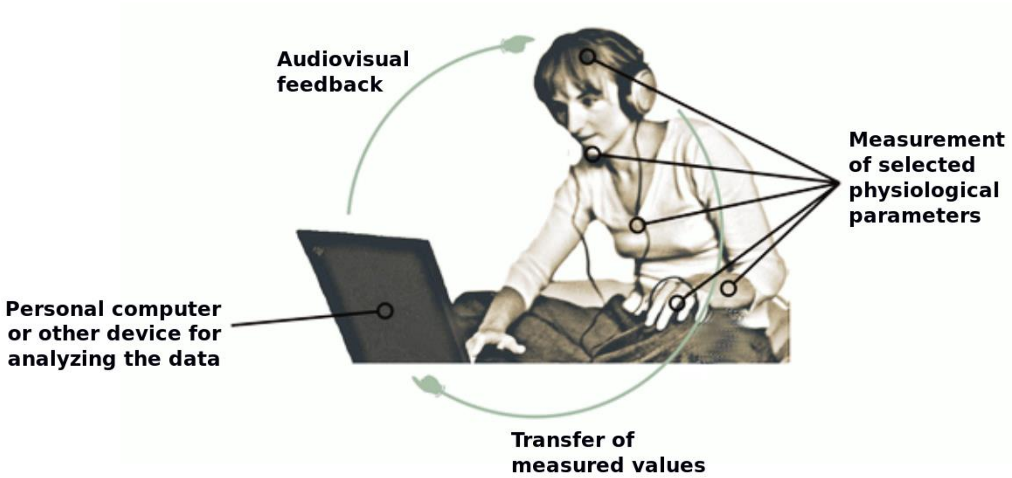

Figure 1: "Biofeedback process with physiological parameter measurement and audiovisual feedback"

5. Application of BFT in sport

Peak athletic performance hinges on optimal arousal levels before competition (Yerkes-Dodson Law). Arousal initially improves performance as it rises but exceeding a critical point led to performance decline. Biofeedback training can effectively address this by helping athletes manage arousal.

Studies have shown that high muscle tension and excessive pre-competition arousal hinder performance [22]. EMG biofeedback, for example, helps athletes relax and reduce muscle tension [23]. This training can also be applied to involuntary muscles controlled by the autonomic nervous system, including blood vessel tension and respiration rate.

Biofeedback allows athletes to identify their optimal arousal point by monitoring various indicators (Figure 2). This information can then be used to transform excessive arousal into energy, ultimately guiding athletes into a competitive peak state.

Biofeedback offers a range of benefits for athletes, enhancing both cognitive function and emotional well-being.

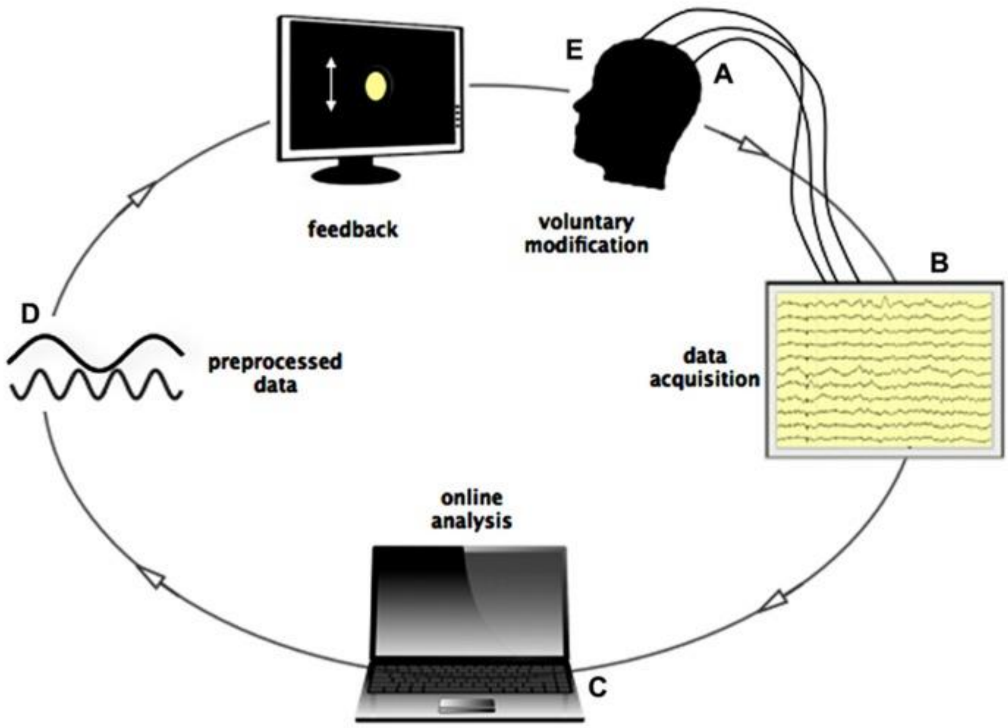

Figure 2 : “Process of biofeedback: data acquisition, online analysis, and real-time feedback”

5.1. *Improved Cognitive Function and Performance*

Studies by Shen H. et al. and Wang Y. et al. demonstrate biofeedback's effectiveness in improving concentration and relaxation [24]. Biofeedback training, particularly focusing on alpha waves in the left temporal lobe, has been shown to significantly improve shooting performance. This is attributed to enhanced focus and efficient neural circuits, leading to quicker entry into an optimal execution state. Additionally, Chang S. et al. found that biofeedback, through breathing and attention training, can improve gymnasts' independent relaxation skills, aiding in completing difficult movements and boosting overall performance [25].

5.2. *Mood Stabilization and Combating Mental Fatigue*

Research by Raymond et al. suggests that EEG biofeedback can effectively manage emotional fluctuations in athletes, reducing negativity and promoting positive emotions, leading to better rhythmic sensitivity [16]. Xu Zhao's work highlights how heart rate variability biofeedback can enhance emotional stability, relaxation, and self-regulation [26]. This training alleviates physiological symptoms of mental fatigue like nervousness and sleep disorders, ultimately improving performance by reducing negative physical reactions. Other studies indicate that EEG biofeedback can adjust individual consciousness through brainwave stimulation, accelerating entry into a work-adapted brain state. This heightened focus not only improves athletic performance but also plays a role in eliminating mental fatigue.

6. Challenges and Future Directions of BFT

BFT currently faces limitations in its application. Most research is conducted in controlled laboratory settings, focusing on experimental procedures and ideal training environments. This raises concerns about the "ecological validity" of these studies – can the observed benefits translate to real-world sports situations? While some research has explored training in sports fields, it remains limited and requires further investigation.

Another challenge is tailoring biofeedback to specific sports. Judo and taekwondo benefit from EMG and skin conductivity training due to their emphasis on strength and muscle control. Conversely, shooting and archery prioritize mental preparation and focus, making EEG feedback more suitable. Additionally, athletes, especially high-level competitors, have diverse psychological needs and performance characteristics. Personalized biofeedback programs that consider athletes' sports specialties, training methods, and individual psychology will likely yield better results.

7. Conclusions

Biofeedback technology offers a game-changing advantage for athletes by providing immediate feedback on physiological changes during training and competition. It acts as a window into the workings of the autonomic nervous system, the body's "fight-or-flight" system. By monitoring physiological indicators through biofeedback instruments, athletes gain a deeper, more objective understanding of their internal state.

This real-time data empowers athletes to tailor their training activities based on feedback information. This personalized approach not only significantly improves their ability to self-regulate their nervous system but also promotes overall health. Biofeedback training, in essence, lays the foundation for achieving optimal results from training activities by ensuring athletes train within healthy parameters.

Furthermore, biofeedback acts as a catalyst for accelerating the scientific process of training control. Traditionally, gauging training effectiveness relied heavily on measuring external factors like performance outcomes. Biofeedback allows for a more nuanced understanding by revealing the internal physiological mechanisms at play. By monitoring how the body adapts to different training stimuli through biofeedback data, coaches and athletes can refine training programs with greater precision and efficiency, ultimately leading to faster progress.

References

1. Krane, V., & Williams, J. M. (2006). Psychological characteristics of peak performance. In J. M. Williams (Ed.), *Applied sport psychology: Personal growth to peak performance* (5th ed., Vol. 5, pp. 207–227). McGraw-Hill, New York.
2. Bertollo, M., Di Fronso, S., Filho, E., Conforto, S., Schmid, M., Bortoli, L., & Robazza, C. (2016). Proficient brain for optimal performance: The MAP model perspective. *PeerJ*, 4, e2082. doi: 10.7717/peerj.2082
3. Hatfield, B. D. (2018). Brain dynamics and motor behavior: A case for efficiency and refinement for superior performance. *Kinesiology Review*, 7(1), 42–50. doi: 10.1123/kr.2017-0022
4. Levy, J. J., & Baldwin, D. R. (2019). Psychophysiology and biofeedback of sport performance. In M. H. Anshel, T. A. Petrie, & J. A. Steinfeldt (Eds.), *APA handbook of sport and exercise psychology* (pp. 745-758). Washington, DC: American Psychological Association. doi: 10.1037/0000123-037
5. Skinner, B. F. (1963). Operant behavior. *American Psychologist*, 18(8), 503–515. doi: 10.1037/h00445185
6. Blumenstein, B., & Orbach, I. (2018). Periodization of psychological preparation within the training process. *International Journal of Sport and Exercise Psychology*, 18, 1-11. doi: 10.1080/1612197X.2018.1478872
7. Vealey, R. S. (2012). Mental skills training in sport. In G. Tenenbaum & R. C. Eklund (Eds.), *Handbook of sport psychology* (pp. 285–309). Routledge. doi: 10.1002/9781118270011.ch13
8. Blumenstein, B., & Orbach, I. (2012). *Psychological skills in sport: Training and application*. Hauppauge, NY: Nova Science.
9. Beauchamp, M. R., Beauchamp, G. T., & Thatcher, P. E. (2012). An integrated biofeedback and psychological skills training program for Canada's Olympic short track speed skating team. *Journal of Clinical Sport Psychology*, 6(1), 67-84. doi: 10.1123/jcsp.6.1.67
10. Zaichkowsky, L. D., & Fuchs, C. Z. (1988). Biofeedback applications in exercise and athletic performance. *Exercise and Sport Science Reviews*, 16(1), 381–421. doi: 10.1249/01.ESSR.16.1.381
11. Blumenstein, B., Bar-Eli, M., & Tennenbaum, G. (1997). A five-step approach to mental training incorporating biofeedback. *The Sport Psychologist*, 11(4), 440–453.
12. Zaichkowsky, L. D. (1975). Combating stress: What about relaxation training and biofeedback? *Mouvement*, October, 309–312.
13. Gracz, J. (1977). The cutaneous galvanic reaction as an indicator of prestart emotional intensity. *Przeglod Psycholic*, 20, 117–129.
14. Peper, E., & Schmid-Shapiro, A. (1997). The use of electrodermal biofeedback for peak performance training. The Biofeedback Foundation of Europe. Retrieved May 1, 2010, from http://www.bfe.org/protocol/pro12eng.htm
15. Costa, A., Bonaccorsi, M., & Scrimali, T. (1984). Biofeedback and control of anxiety preceding athletic competition. *International Journal of Sport Psychology*, 15(2), 98–109.
16. Blumenstein, B., & Bar-Eli, M. (1998). Self-regulation training with biofeedback in elite canoeists and kayakers. In V. Issurin (Ed.), *Science and practice of canoe/kayak high performance training* (pp. 124–132). Elite Sport Department of Israel, Wingate Institute, Tel Aviv, Israel.
17. Raymond, J., Sajid, I., Parkinson, L. A., & Gruzelier, J. H. (2005). Biofeedback and dance performance: A preliminary investigation. *Applied Psychophysiology and Biofeedback*, 30(1), 65–73. doi: 10.1007/s10484-005-8000-2
18. Landers, D. M., Petruzzello, W. S., Crews, D. J., Kubitz, K. A., Gannon, T. L., & Han, M. (1991). The influence of electrocortical biofeedback on performance in pre-elite archers. *Medicine and Science and Exercise*, 23, 123–129.
19. Lagos, L., Vaschillo, E., Vaschillo, B., Lehrer, P., Bates, M., & Pandina, R. (2008). Heart rate variability biofeedback as a strategy for dealing with competitive anxiety: A case study. *Biofeedback*, 36, 109–115.

20. Strack, B. (2003). The effect of heart rate variability biofeedback on batting performance in baseball [Unpublished doctoral dissertation]. Alliant International University, San Diego, CA.
21. Tanis, C.J.. (2013). Performance enhancement and stress reduction using biofeedback with women collegiate volleyball players. Athletic Insight's Writings of 2012. 129-143.
22. Wang, H., & Cui, Q. (1991). Research on psychological control training with EMG feedback technology (in Chinese). *Sports Science*, 4, 84–87.
23. Song, S., Tian, Y., & Ren, W. (1994). Research on improving archers' movement consistency with EMG feedback (in Chinese). *Sports Science*, 5, 78–81.
24. Shen, H., Zhang, Z., & Pang, J. (2011). Biofeedback intervention training for improving psychological adjustment in Jiangsu men's epee team. *Journal of Nanjing Institute of Physical Education*, 25(5), 121–125.
25. Chang, S., Ji, C., Zhou, Y., et al. (2011). Study on the influence of biofeedback training on gymnasts' independent relaxation ability (in Chinese). Ninth National Sports Psychology Conference.
26. Xu, Z. (2009). Effect of HRV feedback training on sportsmen's mental fatigue. *Journal of Shandong Institute of Physical Education*, 25(11), 46–48.

Analysis of joining FRC and light metal alloys by flowdrilling

Nikita Veligotskyi * and Anna Guzanová

Technical University of Košice, Faculty of Mechanical Engineering, Department of Technology, Materials and Computer Supported Production; nikita.veligotskyi@tuke.sk, anna.guzanova@tuke.sk
* Correspondence: nikita.veligotskyi@tuke.sk

Abstract: The paper deals with the analysis of the behaviour of a composite material reinforced with continuous fibers in the process of joining with a metal sheet by flow drilling without using a bolt. It presents the concept of fiber continuity on the preservation of the mechanical properties of the composite. When the composite is heated locally, the fibers are not broken when flowdrill tool is passing through the composite, but they are deflected from their position to flow around the resulting bushing. According to the diameter of the tool used, it is necessary to determine the diameter of the heated zone of the composite so that the mechanical properties of the fibers are not exceeded when the fibers are deflected.

Keywords: flowdrill, multimaterial joint, FRP (Fiber Reinforced Polymer) composite

1. Introduction

Nowadays, there is no doubt that the way to develop different types of structures, especially in automotive, aerospace, implantology, toolmaking, power generation, or marine structures, is through the design of multi-material structures. This is motivated not only by the desire to achieve an overall weight saving of the structure, but more importantly to achieve optimum properties in the individual zones of the structural units, to achieve savings in critical material types and thus to ensure the sustainability of production. The different properties of the materials used synergistically ensure the necessary product properties. Multimaterial concepts bring with them challenges in the form of optimization of material selection, design of their geometry and technology of their combination in the final structure [1].

The Joining subgroup of the EU Manufuture Technology Platform defines joining as: "The creation of a particular type of connection between materials or components to achieve a specific physical performance". It is important whether it is the joining of different materials from the same material group (joining dissimilar metals and alloys together, e.g. different grades of steel, steels and alloys of light non-ferrous metals, etc., which was the first stage in the development of multi-material joints), or the joining of materials from different material groups - e.g. metals and polymers, or polymer composites. Whether materials from the same or different material groups are joined, their joining can be accomplished by mechanical, chemical, thermal processes, or a combination of these [1].

The same is true for joining polymers and metals. This task is challenging because of the completely different chemical and physical properties that are responsible for the poor adhesion between polymer and metal. To overcome this problem, various methods of joining metals to polymers have been developed, which can be divided into three main categories: (a) mechanical joining; (b) chemical modification of the polymer or metal to improve adhesion; and (c) the use of a third member, the fastener. [2]

2. Joining of dissimilar materials

The topicality of joining metals and composites is documented by the following list of existing or expected applications: Joining of composites to metal in the manufacture of turbine blades in power generation, joining of lightweight structures made of metals and composites for solar panels, joining of fuel cell components and ceramics, the aerospace sector needs to innovate in joining polymer composites with refractory metals, the construction and transport sectors face challenges in joining dissimilar/hybrid materials including aluminium, steel, high strength steel, polymer fibre composites and thermoplastics. Electronics and nanotechnologies are focusing on the production of printed circuit boards and joining processes such as miniaturised soldering and bonding, joining copper to aluminium and metals to polymers. [1,3]

Mechanical methods of forming multi-material joints include the use of threaded fasteners, flow drilling, clinching, friction stir blind riveting, self piercing riveting, and many other modifications of joining, providing form mechanical wedging of the materials being joined. Chemical bonding mainly includes adhesive bonding with possible surface preparation by chemical modification on different basis [2,4]. Thermal processes include electric arc welding, spark plasma sintering processes, high-energy beam welding [5], brazing and soft soldering, resistance welding, FSW, friction welding, ultrasonic or microwave welding, many of them combinable with adhesive bonding. If one selects from the above list the technologies applicable to joining metals and polymer composites, the possibilities narrow down considerably - mechanical joining with threaded fasteners, flow drilling, clinching [6], resistance welding with a metallic element [7], adhesive bonding. Mechanical joining of metal-polymer composite using controlled texturing of the metal surface and the creation of geometrically defined protrusions that wedge into the polymer composite surface [8,9] has also proven successful.

Authors were attracted by the mention in the publication [10], which focuses on the application of flowdrill (FD) technology for joint formation. Although the main objective of this technology is to create a hole in hollow thin-walled sections without chip formation by locally heating the material, plasticising it and moving the volume of material from the location of the future hole in the direction and against the direction of movement of the flowdrill tool. The material displaced in the direction of tool movement will form a bushing of up to three times the thickness of the original material, allowing more than one thread to be formed and enabling a secure bolted joint to be formed. Material repositioned against the movement of the tool will form a rim, which is usually compressed and retained or cut off with the same tool. However, Schmerler [10] introduces the idea of using FD technology to join multiple overlapped materials just by flow drilling alone, without subsequent thread formation and without bolt, Fig. 1 in the middle. The possibility of joining two different materials (different steels, steel-aluminum alloy) by FD was verified in work [11], and it was determined that this technology is particularly suitable for joining steel-aluminum alloy material combinations, with the principle that the aluminum should always be in the bottom position in the pair when joining, Fig. 1, left. Should it be in the upper position, the frictional heat generated leads to a more pronounced softening of the aluminium and instead of forming a bushing, the aluminium is simply pushed sideways out of the hole location, the aluminium bushing and therefore the joint is not formed, Fig. 1, right.

The heat generated by friction, expressed as homologous temperature, is significantly higher in aluminum than in steel. However, if the aluminum is in the bottom position, the frictional heat heats the steel, which plasticizes and forms a solid bushing by the movement of the tool, the aluminum lying below the steel is heated not directly by friction but by conduction of heat from the steel and also a bushing is formed by copying the shape of the steel bushing being formed. This results in the formation of two concentric nested bushings which, when the joint is subsequently loaded, are broken by shearing of the inner bushing formed from the top material of the joined pair, Fig. 1 left.

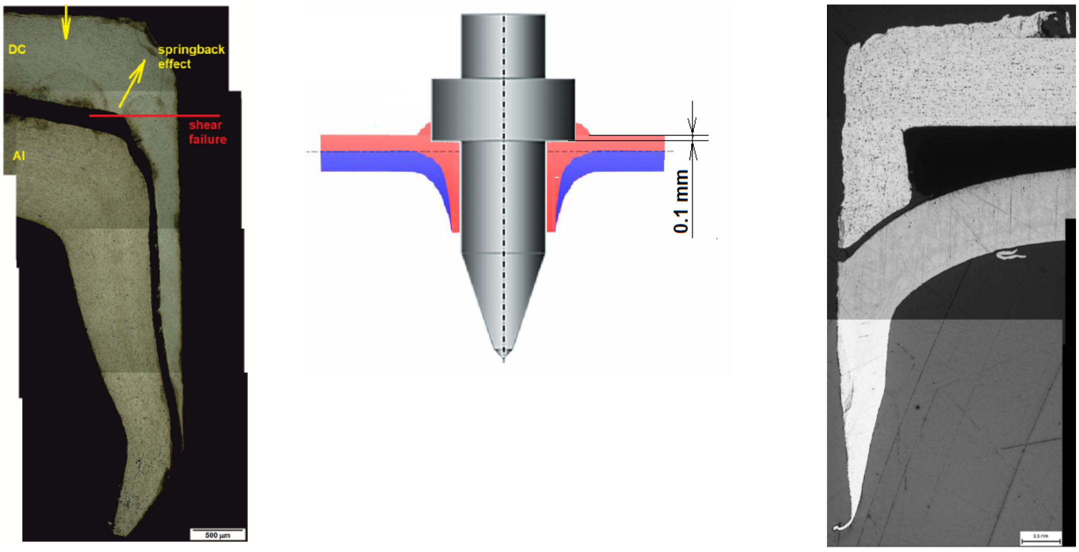

FD joint (Al in bottom position) FD joint scheme FD joint (Al in upper position)

Figure 1. Influence of the position of steel-Al alloy materials in the FD joint (DC - DC04, Al - EN AW 6082 T6) [11]

The combination of FD with adhesive bonding was also proved as very promising, there was an increase in the maximum load on the joint and an increase in the energy absorbed before the joint failed. However, authors of [10] and [11] cosistently found that the formed metal rim, otherwise unused, can also play a role in the creation of multi-material joints - it can mechanically clinch into the softer material lying above it - which can be, for example, a fiber reinforced polymer composite (FRC), Fig. 2.

Schmerler [10] provides schematically the possibility of forming multi-material joints of thin sheets/materials in the combination of Al-steel-Al, steel-FRC-steel, Al-FRC-Al or steel-FRC-Al. In these joints where one of the materials is FRC, the frictional heat generated from tool – metal sheet friction is expected to heat the thermoplastic-based FRC, the FRC will soften, and the drilling will only deflect the fibers away from the drilling location without disturbing their continuity. Heating can also be provided by external heating on a defined area of the composite at the future joint location. Confirmation of this hypothesis would be a significant advantage of this technology over clinching or other joining technologies where fiber continuity is disturbed.

3. Joining of metals with FRP reinforced with bidirectional long fibers

The concept of preserving the continuity and integrity of materials is also found in nature. For example, if there is a defect in a tree, which means a local weakness of the structure, there is a stress concentration in the area around the defect. Surrounding structures are strengthened in the vicinity of the defect, fiber girdling of the defect occurs in order to maintain an even distribution of stresses in the wood mass, Fig. 3a). The same reason causes the higher load carrying capacity of rolled threads over threads produced by machining, Fig. 3b).

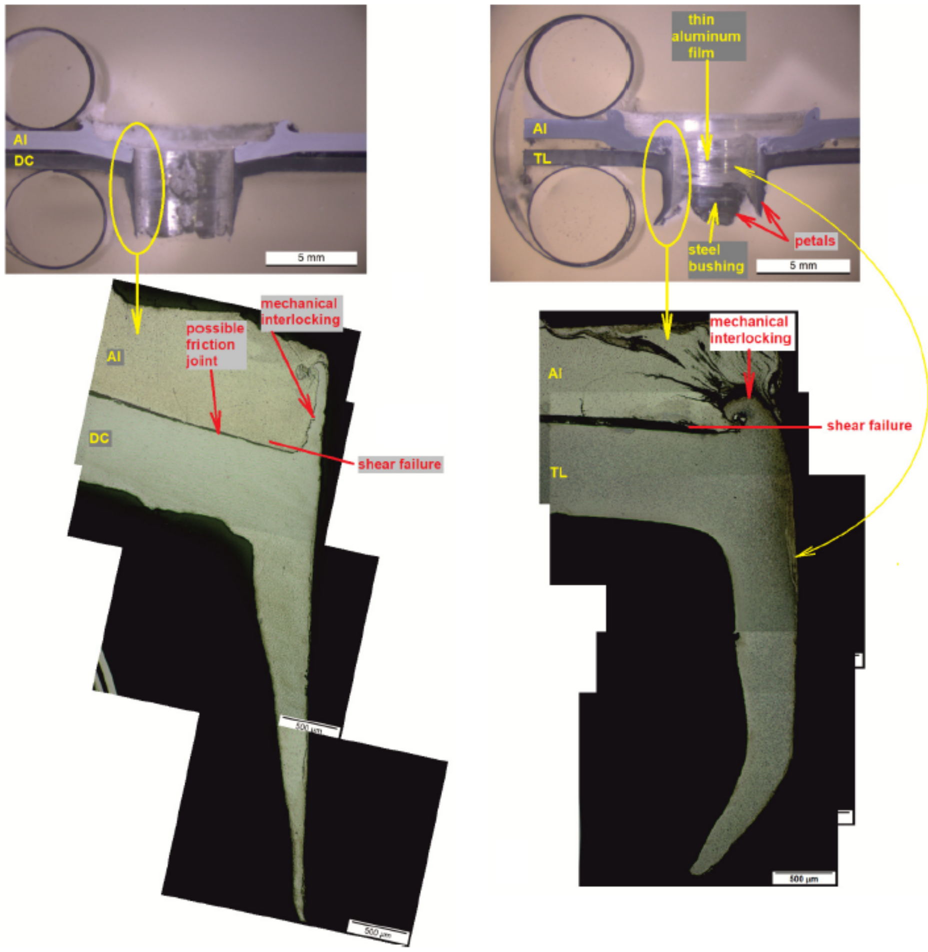

Figure 2. The rim of the DC04 deep-drawing steel is mechanically clinched into the Al alloy placed in the upper position (left), the same effect occurs with the HSLA steel (TL) (right). If we replace the Al alloy with a composite, we expect the same interlocking mechanism [11]

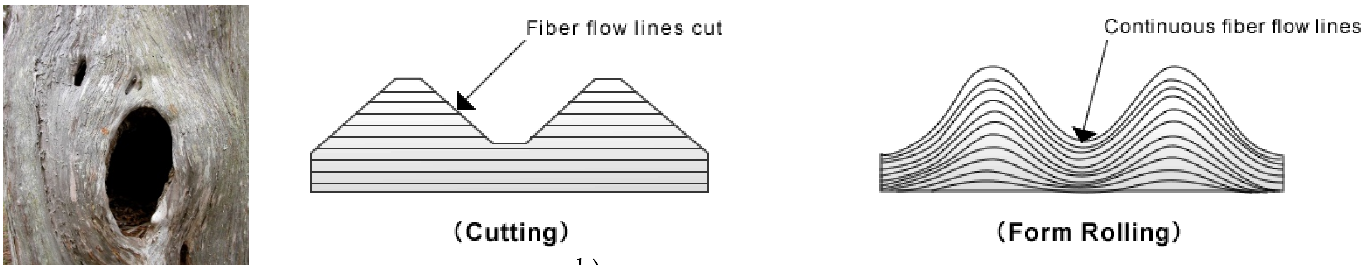

a) b)

Figure 3. Preserving the continuity of the structure of a) the tree, b) the material in the production of the thread, as a prevention of damage

If this concept is applied to the processes of joining metals and thermoplastic FRP composites by FD technology, it is required to maintain the continuity of the fibers for higher load carrying capacity of the joints. For thermoplastic FRP composites, this can be achieved by local heating of the composite followed by flow drilling. The FD tool can penetrate the composite, whereby the fibers are relocated instead of breaking. However, the deformability of the fibers is obviously limited, and the resistance of the fibers to breakage will depend on the diameter of the FD tool. The authors [12] defined the geometry of the joint with respect to fiber deflection caused by the flow drilling, Fig. 4.

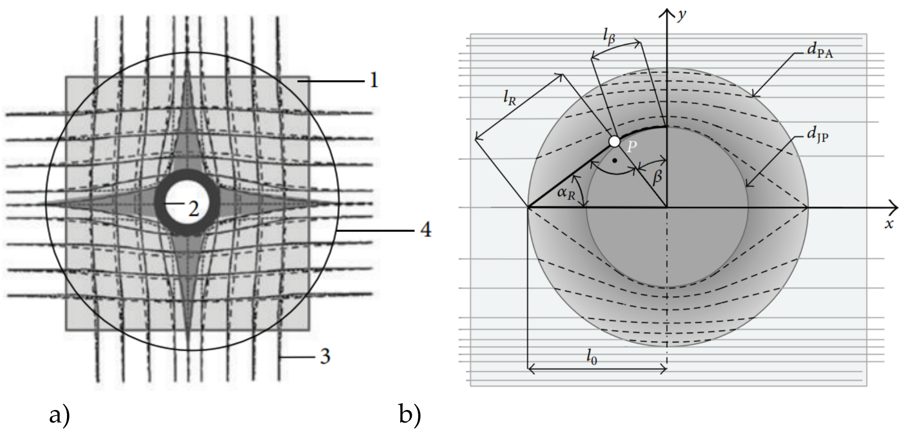

Figure 4. a) Fiber realignment near the metal-composite FD joint: 1 - metal sheet, metal bushing, 3 - fibers of FRP, 4 - area of realignment, b) geometric model of fiber realignment with unidirectional fiber deposition: d_{PA} - diameter of the plasticized zone of the joint, d_{JP} - diameter of the metal bushing after flow drilling, l_0 - original fiber length, P - intersection of tangent, l_R - length of the relocated fiber to the P point, l_β - length of the fiber wrapped around the bushing, α_R - angle of fiber relocation, β - angle of fiber wrapping around the metal bushing [12].

From Fig. 4, it can be seen that the fibers that originally led through the origin of the coordinate system are the most relocated after joining, therefore the stress level in them will also be the highest. To maintain the integrity of the fibers, it is necessary that the stress in the most stressed fibers does not overcome their tensile strength. The diameter of the heated zone will be directly proportional to the diameter of FD tool used, Fig. 5b).

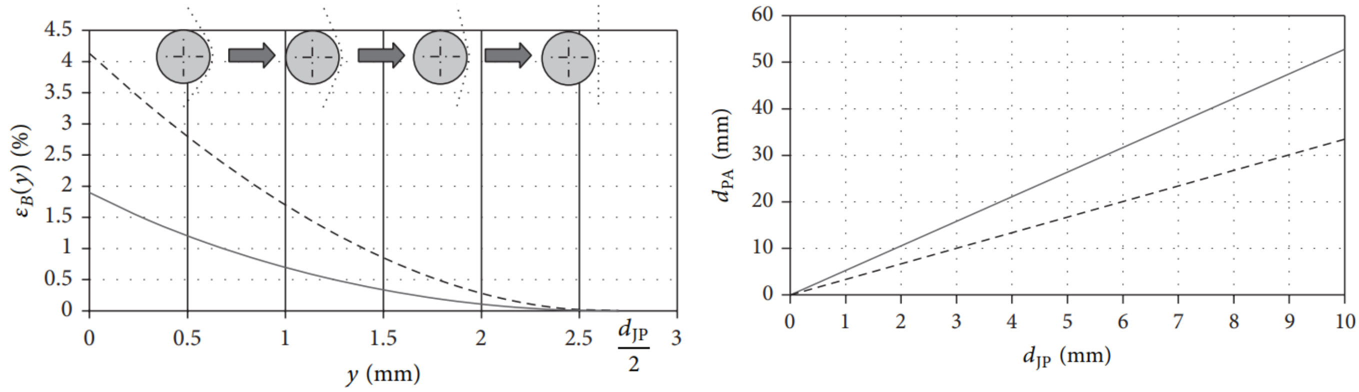

Figure 5. a) Strain ε in fibers with different relocation y, b) diameter of the plasticized zone d_{PA} depending on FD tool diameter d_{JP} for the maximum strain level in carbon fibers (ε_{CF}= 1.8%) and glass fibers (ε_{GF}= 4.5%) [12]

From Fig. 5a) it can be seen that the lowest strain ε is in the fibers distant from the hole by $d_{JP}/2$, i.e., which are only tangentially contacting the metallic bushing. The highest stress is in the fibers that originally crossed the axis of the future hole (y=0) and are the most relocated from their original position. The maximum strain ε_{GF} in the glass fibers, for FD tool diameter of 5.3 mm, is 4.5%, in the carbon fibers ε_{CF} = 1.8%. The required minimum diameter of the plasticized area d_{PA} for glass (dashed line) and carbon fibers (solid line) at which the stresses in the most relocated fibers would not exceed tensile strength of fibers can be determined from Fig. 5(b).

Due to the way the joint is stressed, it is advisable to test the joints by lap-shear tensile test as well as cross-tension test, the first mentioned test focuses on the shear capacity of the joint, while the second one on the resistance of the joint against to opening. In order to increase the resistance of the joint against to opening, it is advisable to make closing head of joint by reforming bushing, Fig. 6.

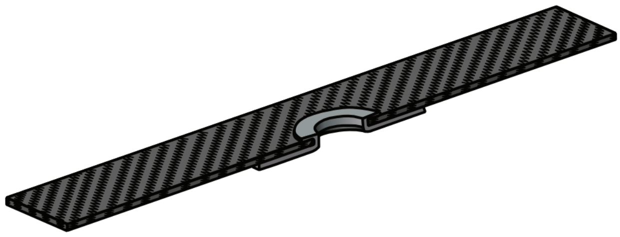

Figure 6. Flowdrill metal-composite joint with closed head by bushing reforming

The metal bushing must protrude at least 1mm through the FRP composite to enable make a closed head.

4. Conclusions

Joining of continuous fiber reinforced composites with 0°/90° fibers alignment and metal sheets, either steel or light non-ferrous metal based, is proving to be a promising alternative to riveting, bolting or clinching of these materials. By properly designing the diameter of the plasticized zone, it is possible to optimize the joint to achieve the necessary fiber displacement without disrupting the integrity of the fibers, thus allowing the flowdrill tool to perforate the composite, form a bushing, and introduce it into the composite, with possible subsequent hemming and closing of the joint.

Acknowledgments: Authors are grateful for funding support within project VEGA 1/0229/23: Research on the applicability of thermal drilling technology for the creation of multi-material joints in the automotive industry.

Conflicts of Interest: The authors declare no conflict of interest.

References

1. Martinsen, K.; Hu, S.J.; Carlson, B.E. Joining of dissimilar materials. *CIRP Annals - Manufacturing Technology* **2015**, *64*, 679–699. http://dx.doi.org/10.1016/j.cirp.2015.05.006
2. Izadi, O.; Mosaddegh, P.; Silani, M.; Dinari, M. An experimental study on mechanical properties of a novel hybrid metal–polymer joining technology based on a reaction between isocyanate and hydroxyl groups. *Journal of Manufacturing Processes* **2017**, *30*, 217–225. http://dx.doi.org/10.1016/j.jmapro.2017.09.022
3. Jahna, J.; Weeber, M.; Boehner, J.; Steinhilper, R. Assessment strategies for composite-metal joining technologies –A review. *Procedia CIRP* **2016**, *50*, 689 – 694. doi: 10.1016/j.procir.2016.05.034
4. Guzanová, A.; Draganovská, D.; Brezinová, J.; Viňáš, J.; Janoško, E.; Moro, R.; Szelag, P.; Vojtko, M.; Tomáš, M. Application of organosilanes in the preparation of metal surfaces for adhesive bonding. *Journal of Adhesion Science and Technology* **2022**, *36*, 1153-1175. https://doi.org/10.1080/01694243.2021.1962078
5. Markovits, T.; Bauernhuber, A. Comparing adhesive bonding and LAMP joining technology in case of hybrid material combination. *Physics Procedia* **2014**, *56*, 818 – 823. doi: 10.1016/j.phpro.2014.08.094
6. Krassmann, D.; Moritzer, E. Development of a new joining technology for hybrid joints of sheet metal and continuous fiber-reinforced thermoplastics. *Welding in the World* **2022**, *66*, 45–60. https://doi.org/10.1007/s40194-021-01194-0
7. Troschitz, J.; Vorderbrüggen, J.; Kupfer, R.; Gude, M.; Meschut, G. Joining of Thermoplastic Composites with Metals Using Resistance Element Welding. *Appl. Sci.* **2020**, *10*, 7251. https://doi.org/10.3390/app10207251
8. Rodríguez-Vidal, E.; Sanz, C.; Lambarri, J. Quintana, I. Experimental investigation into metal micro-patterning by laser on polymer-metal hybrid joining. *Optics and Laser Technology* **2018**, *104*, 73–82. https://doi.org/10.1016/j.optlastec.2018.02.003
9. Ukar, E.; Liébana, F.; Andrés, M.; Marcos, I.; Lamikiz, A. Laser Texturing and Dissimilar Material Joining. *Procedia Manufacturing* **2017**, *13*, 671-678. https://doi.org/10.1016/j.promfg.2017.09.142
10. Schmerler, R.; Rothe, F.; Grunert, M. Hybrid Joining Using the Flow Drill Technology. Available online: https://www.researchgate.net/ publication/341616091_Hybridfugen_durch_Fliesslochformen_Hybrid_joining_using_the_flow_drill_te chnology (accessed on 17 January 2022).
11. Guzanová, A.; Janoško, E.; Draganovská, D.; Vrabeľ, M.; Tomáš, M.; Horňak, P.; Vojtko, M.; Veligotskyi, N. Investigation of Applicability Flowdrill Technology for Joining Thin-Walled Metal Sheets. *Metals* **2022**, *12*, 540. https://doi.org/10.3390/ met12040540

Seidlitz, H.; Ulke-Winter, L.; Kroll, L. New Joining Technology for Optimized Metal/Composite Assemblies. *Journal of Engineering* **2014**, *Article ID 958501*, 11 pages. http://dx.doi.org/10.1155/2014/958501

Deep-drawing evaluation of HX420 using Simufact Forming

Samuel Vilkovský [1]*. Janka Majerníková [1]

[1] Technical University of Košice, Department of Technology, Materials and Computer Aided Production
* Email: Samuel.vilkovsky@tuke.sk

Abstract: This study involves an experimental investigation of the HX420 sheet for the formation of ears using a cupping test on a metal sheet with a diameter of 63 mm. The comparison of experimental results was validated through the utilization of Simufact software. An HX420 metal sheet, measuring 0.7 mm in thickness, was employed in the simulations. The modeling of the manufacturing process holds significance in engineering production. Deep drawing is an intricate procedure influenced by various factors. The objective of this work is to verify the formability of the HX420 material for earing formation and compare experimental results with simulations using yield criteria models based on Hill and Barlat, as well as hardening models according to Hollomon and Krupkowski.

Keywords: Deep-drawing, anisotropy, earing, Simufact Forming

1. Introduction

The process of deep drawing, which involves forming sheet metal, finds extensive use in various industries. Examples of its diverse applications include shaping automotive parts, arms industry products, aerospace components, as well as forming medication and perfume tubes, pots, pans, and various kitchen appliances. Deep drawing is based on production parts with simple or complex shapes through large plastic deformation [1,2]. During the deep drawing process, several defects can occur such as surface scratches, wall, and flange wrinkling, tearing, or earing [3].

The deep drawing process is significantly influenced by material properties, as well as geometric and technological parameters. Key material factors include elasticity, plasticity, and anisotropy. Additionally, parameters such as punch velocity, blank holding pressure, and lubrication play a substantial role, along with the radius of the punch and die, blank thickness, and the clearance between the punch and die. Improper definition of these parameters can lead to various defects [5,6].

Earing, characterized by the development of a wavy edge at the open end of the cup, stands out as a prevalent defect in the deep drawing process. Numerous studies addressing earing defects have been published in recent years [6,7].

The widespread adoption of computer-aided engineering has led to the extensive utilization of numerical simulation in the metal plastic forming process [7]. This study focuses on investigating the prediction of earing in HX420 material, which has a thickness of 0.7 mm. The investigation is carried out through experimental research and finite element method (FEM) simulation using different yield criteria and hardening models, utilizing Simufact forming software.

2. Materials and Methods

In the experiment, a steel sheet made of micro-alloyed steel HX420 with a thickness of 0.7 mm was used. The mechanical properties of the material are shown in Table. 1.

Table 1 Mechanical properties of HX420 (input data for both hardening models)

RD (°)	Yield strength (MPa)	Ultimate Tensile strength (MPa)	Elon-ga-tion (%)	r (-)	r_m (-)	Δr (-)	n (-)	K (MPa)	ε_0 (-)
0	468.0	521.5	22.2	0.790			0.143		
45	465.1	511.7	24.0	1.096	0.895	-0.402	0.142	791	0.01
90	453.5	522.0	18.8	0.599			0.151		

Strengthening Models

In numerical simulation, input data includes the Hollomon or Krupkowski hardening curves. The Hollomon hardening curve describes material behaviour under plastic deformation between the yield point and tensile strength. The specific index n is the strain hardening exponent characterizing hardening processes initiated during cold plastic deformation. The Hollomon hardening curve is defined by the equation:

$$\sigma= K(\varepsilon_p+\varepsilon_0)^n \tag{1}$$

Simulation programs also use the Krupkowski hardening curve condition, defined by the following equation:

$$\sigma= K(\varepsilon_p+\varepsilon_0)^n \tag{2}$$

where:
ε_p – plastic deformation,
ε_0 – offset deformation,
n – strain hardening exponent,
K – material constant [4].

Plasticity condition

Considering the advantages and disadvantages of various plasticity conditions, recommendations for industrial application of these programs are provided. Both groups must be familiar with the state–of-the-art in this field and the theory of plasticity: the first group (Hill) uses more efficient plasticity conditions, while the second group (Hosford) chooses the most suitable criteria offered by commercial programs for material parameters used as input data and for understanding the physical significance [5,6].

Cupping test

The study involves a cupping test performed using the ZD-40 hydraulic press (Figure 1a). To evaluate the anisotropy indicated by earing on the cups, a dedicated deep drawing tool was developed (Figure 1b). The blank is drawn radially into a forming die by the punch, with a mechanical blank holder applying pressure to prevent wrinkling of the sheet.

Dimensions of the experimental tool are shown in Table 2.

Table 3 Deep-drawing tool dimensions

Parameters	Dimensions (mm)
Punch diameter	31.71
Die diameter	33.46
Punch radius	4.5
Die radius	5.5

Clearence between punch and die	1.75

Figure 1. a) Hydraulic press ZD-40, b) experimental deep-drawing tool for cupping test

According to the value of Δr, it is possible to determine the susceptibility of the sheet to earing formation during deep drawing. Ears are formed in the directions of the sheet where the value of the coefficient of normal anisotropy r is maximum, as follows:

If Δr > 0, ears will be formed in the directions 0 ° and 90 ° to the rolling direction.
If Δr = 0, ears will not be formed.
If Δr < 0, ears will be formed in the direction of 45 °.

The ears are larger as the absolute value of Δr increases.

Experimental material was used to create circular blanks with a diameter of 63 mm. These blanks were used to deep-draw three cylindrical flat-bottomed cups. The height of each cup (Figure 2a) was measured at eight points around their circumference, as illustrated in Figure 2b.

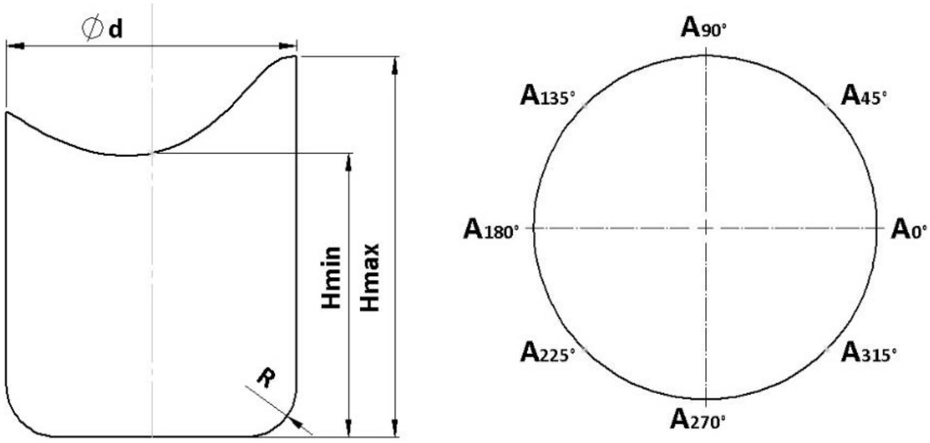

Figure 2. **a)** Earing on the cylindrical cup **b**) the principle of height measurement

Based on the measured values of ear heights in different directions, average heights were calculated for all measured directions. Table 3 presents the average measured height values of cups when using lubricant. In the experiment, microthin foil was employed as a lubricant to minimize friction between the puller and the tested material.

Table 4 Average heights of the cups made from HX420 material

RD	0 °	45 °	90 °	135 °	180 °	225 °	270 °	315 °
Average height (mm)	22.459	24.789	22.235	24.578	22.246	24.801	22.257	24.673

Deep-drawing numerical simulations were executed through Simufact Forming, a CAE forming software. The role of tool geometry in sheet metal forming is significant, underscoring the need for precise modeling of forming tools for seamless integration into CAE software. Figure 4 displays the imported CAD model of the experimental tool used in the numerical simulation. The CAD model's geometry and dimensions for both the tool and materials aligned with those employed in the experiment (refer to Table 2).

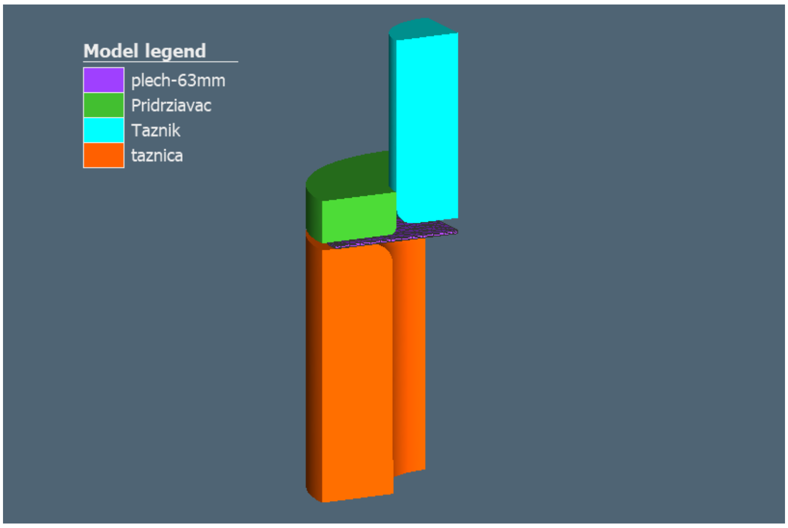

Figure 4. Experimental tool in Simufact Forming

Following the importation of the CAD model into the CAE environment, hexahedral solid elements were employed to mesh the blank sheets required for simulation, as showcased in Figure 5.

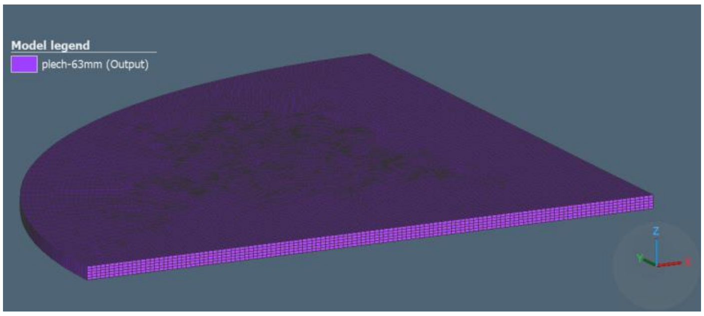

Figure 5. Hexahedral elements using in the simulation

The main objective of this simulation was to assess earing values for cups produced from experimental material by employing various yield criteria's and strain hardening models. Subsequently, these values were to be compared with experimental results. The focus parameter in this investigation was the ear height of the cups. The simulations utilized yield criteria, namely Hill48 and Barlat, along with isotropic hardening models based on Holomon and Krupkowski. A numerical simulation was carried out with a friction coefficient set at 0.05, applying the Coulomb friction law. The numerical simulation results are shown in Figures 6-9. Simulation results were compared with average height values in the directions 0 °, 45 ° and 90 ° obtained during the experimental test (Figure 10).

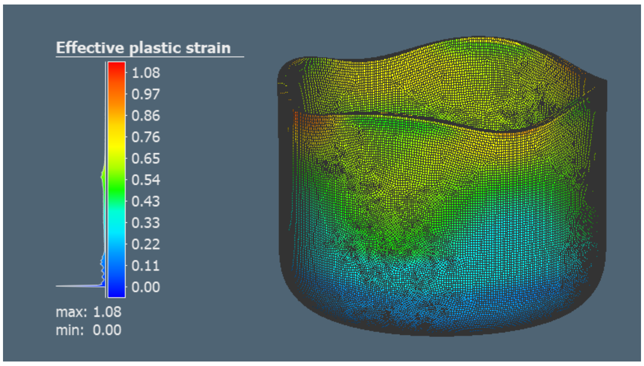

Figure 6. Simulation of deep-drawing using Hill-Hollomon models

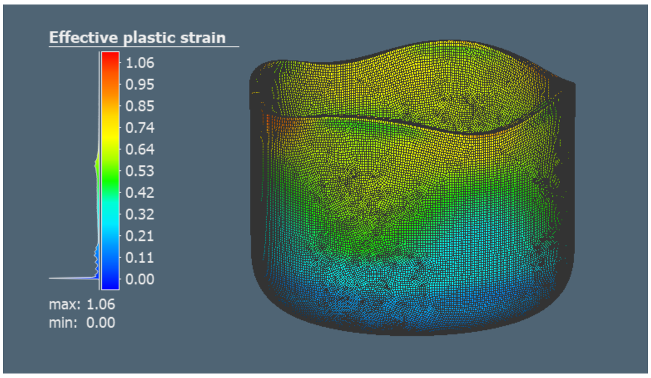

Figure 7. Simulation of deep-drawing using Hill-Krupkowski models

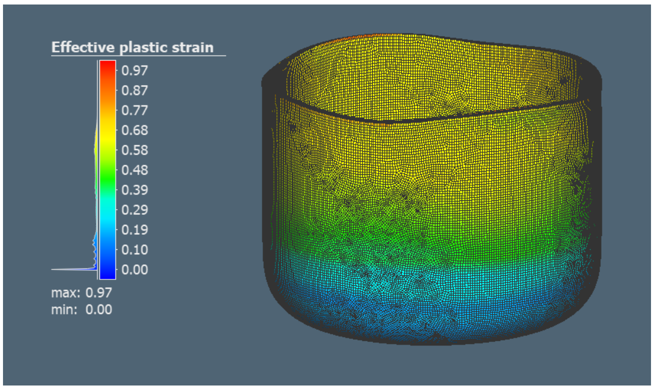

Figure 8. Simulation of deep-drawing using Barlat-Hollomon models

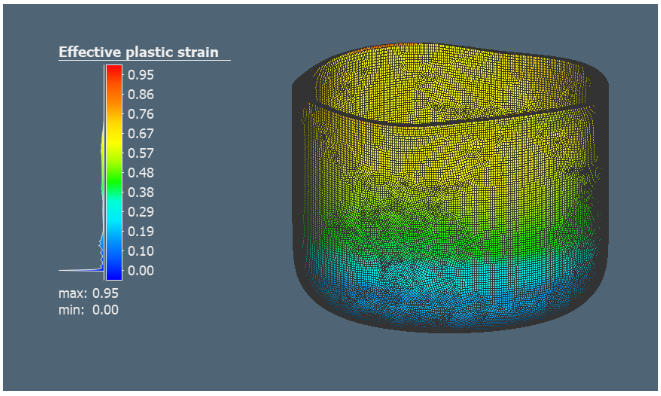

Figure 9. Simulation of deep-drawing using Barlat-Krupkowski models

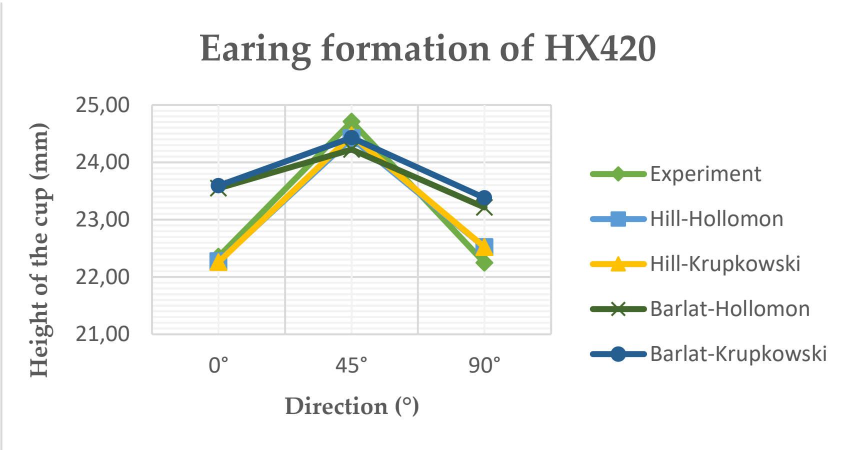

Figure 10. Comparison of experimental results with simulations

3. Results

In conclusion, the formability of the HX420 material and its susceptibility to earing were examined in this paper. It was found that ears on material HX420 are formed at a 45 ° direction, as predicted based on planar anisotropy. Experimental results from the cupping test were verified through simulations using the Simufact Forming software. In the simulations, hardening models according to Hollomon and Krupkowski were employed, along with yield criteria based on Hill and Barlat. It can be stated that simulations utilizing Barlat's yield criteria were more conservative in predicting the earing of the HX420 material compared to Hill's yield criteria. In terms of the accuracy of earing prediction, the combination of Hill-Hollomon models proved to be the most effective variant.

Acknowledgments: The authors are grateful to VEGA -1/0539/23 and KEGA 050TUKE-4/2023.

References

1. Spišák, E., et al. : Strojárske technológie. Košice: Strojnícka fakulta TU v Košiciach, 2011. Edícia vedeckej a odbornej literatúry. Strojnícka fakulta TU v Košiciach. ISBN 978-80-553-0820
2. Rong, Yi et.al.: Structural topology optimization with an adaptive design domain. In: Computer Methods in Applied Mechanics and Engineering. Vol.389, (2022), ISSN: 0045-7825
3. Dwivedi, R., Agnihotri, G.: Study of Deep Drawing Process Parameters. In: Materials Today: Proceedings. Vol. 4, Issue 2. (2017), p. 820-826, ISSN: 2214-7853
4. Semiatin, S.L.: Introduction to Sheet-Forming Processes. In: Metalworking: Sheet Forming 9th edition,Vol.14 B. Ohio:ASM International, 2006 pp 319-33. ISBN electronic: 978-1-62708-186-3
5. Joshi, A.R. et al.: Effects Of Different Parameters On Deep Drawing Process: Review. In: International Journal of Engineering Research & Technolog. Vol. 2, Issue: 3. (2013). ISSN: 2278-0181

6. Benke, M.; Schweitzer, B.; Hlavacs, A.; Mertinger, V. Prediction of Earing of Cross-Rolled Al Sheets from {h00} Pole Figures. Metals 2020, 10, 192. DOI: https://doi.org/10.3390/met10020192
7. Hlavacs, A.; Szucs, M.; Mertinger, V.; Benke, M. Prediction of Earing of Hot-Rolled Al Sheets from Pole Figures. Metals 2021, 11, 99. DOI: https://doi.org/10.3390/met11010099
8. Weiping, D. et al.: Stress analysis of cylindrical parts during deep drawing based on Dynaform. 2018 IOP Conf. Ser.: MaterSci. Eng. 423 012166

Generative design and Automated modeling in Fusion 360

Matúš Virostko [1]*, Martin Mantič [2] and Samuel Sivák [3]

[1] Faculty of Mechanical Engineering, Technical university of Košice, Slovakia; matus.virostko@tuke.sk
[2] Faculty of Mechanical Engineering, Technical university of Košice, Slovakia; martin.mantic@tuke.sk
[3] Faculty of Mechanical Engineering, Technical university of Košice, Slovakia; samuel.sivak@tuke.sk
* Correspondence: matus.virostko@tuke.sk; Tel.: +421 55 602 2354

Abstract: The article deals with a basic comparison of two modern technologies implemented in Autodesk's Fusion 360 CAD software. These are generative design and automated modelling. Compared are the part shapes created in these modules and the basic differences in input data entry for generating outputs. Based on the optimum part shapes thus generated with respect to the input constraints, two shapes from these modules are selected for comparison with each other These shapes are compared both in terms of their shape and strength at the end of the paper.

Keywords: optimalization; simulation, generative design

1. Introduction

The design process is currently developing dynamically , CAD systems are being updated with new functions and modules. Their aim is to obtain the ideal shape of the body with respect to predefined boundary conditions and loads. The process of building models is accelerated by using Automated Modeling (Figure 1), which provides a variety of geometric shapes that you can utilize as inspiration or to finish your design. It provides fast design alternatives to connect the geometries that are already present in your design. When you incorporate one of the options into your design, a parametric solid is produced that can be further edited with the timeline. You can quickly adjust the final model in the menu with regard to the amount of material used in a particular alternative. We can then manually alter the generated geometry on the model in post-editing. [1][3][4]

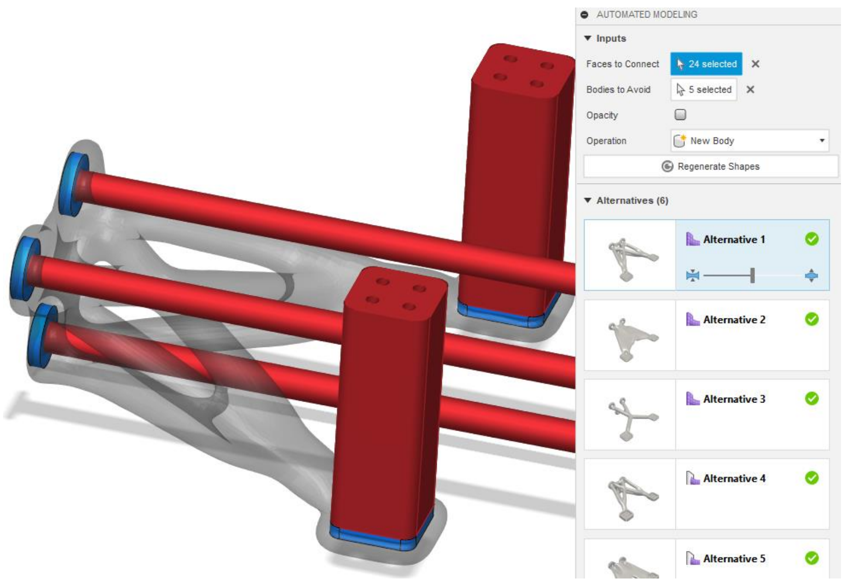

Figure 1. Automated modeling in Fusion 360

The design process of generative design (Figure 2) is inspired by nature's evolutionary process. Design goals and other parameters, like materials, manufacturing processes, and budgetary restrictions, are entered by designers or engineers into generative design software. In contrast to topology optimization, the program swiftly produces design alternatives by investigating every possible combination of a solution. With every iteration, it tests and discovers what functions and what doesn't. Four categories make up product design: the part's function, the materials used, the manufacturing process, and the way it has to operate. [2] [5]

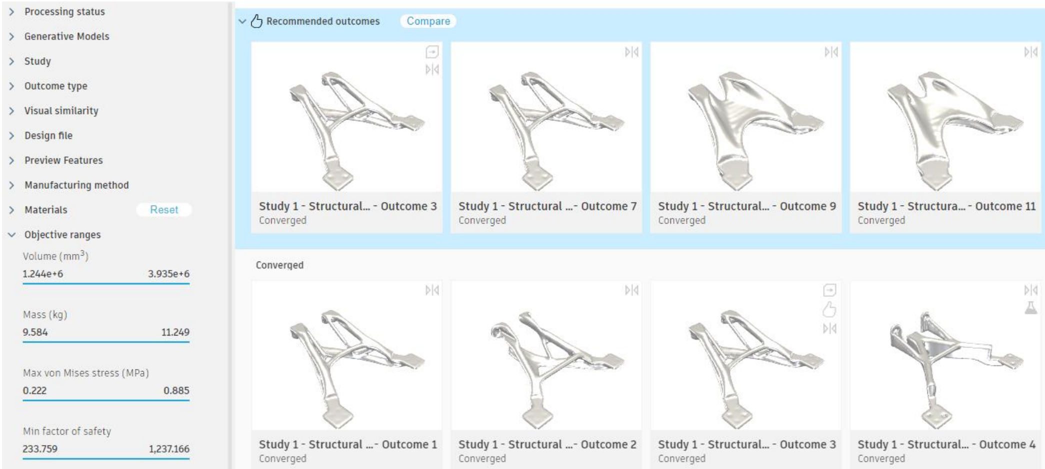

Figure 2. Generative design in Fusion 360

2. Model optimization using input data by generative design and automated modeling in Fusion 360

To generate the shape, it was necessary to create five basic geometric te-lies representing the connection surfaces (Figure 3A), from which the system will start when creating the actual shape of the part. In the case of the generative design, the input parameters also included boundary conditions in the form of a fixed fit (red marks) and the definition of a loading force of magnitude 50N (blue marks).

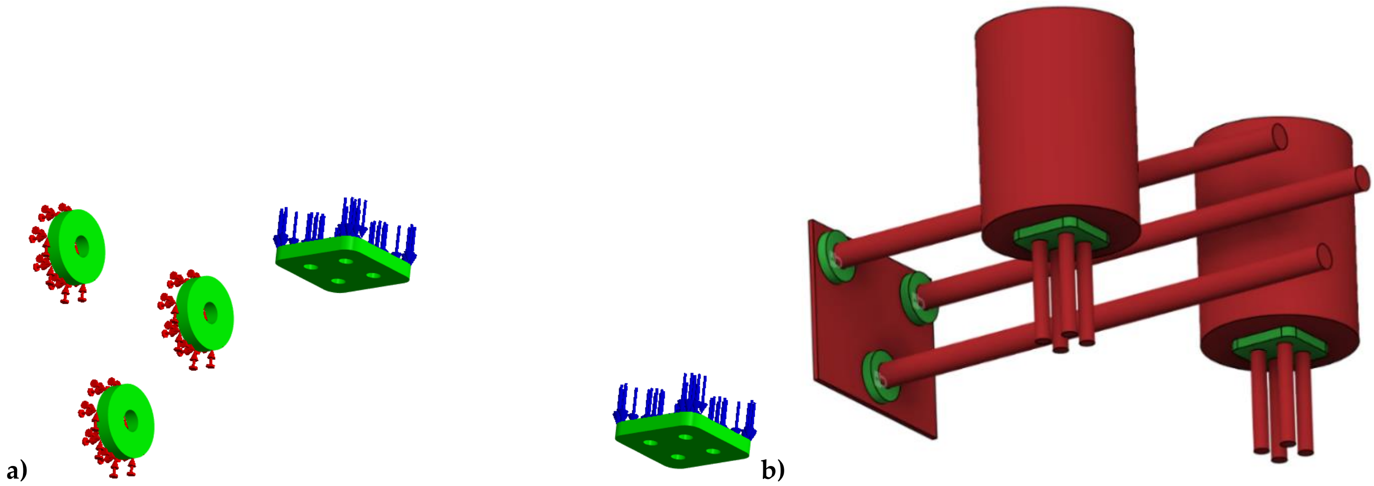

Figure 3. Modelling the input parameters
a) creating bodies for optimization, b) creating obstacle geometry

The specified material for the analysis was AISI 1050 (yeld strength 580MPa, tensile strength 690MPa) with chemical composition Fe=98.46-98.92%, C=0.47-0.55%, Mn=0.6-0.9%, S=≤ 0.050%, P=≤ 0.040%.In the second part, the spatial constraints (red solids in Figure 3B) were modelled , which the system must respect when generating the optimal shape. [6]

In the next step before the actual process, the objects to be preserved during the optimization have to be determined, they are marked in blue in Figure 4a. For the two shape generation processes being compared, the second step is to determine the spatial constraints to be avoided. For this purpose, geometric shapes representing mainly holes and space for attachments are modelled. These are the 22 solids marked in blue in Figure 4b.

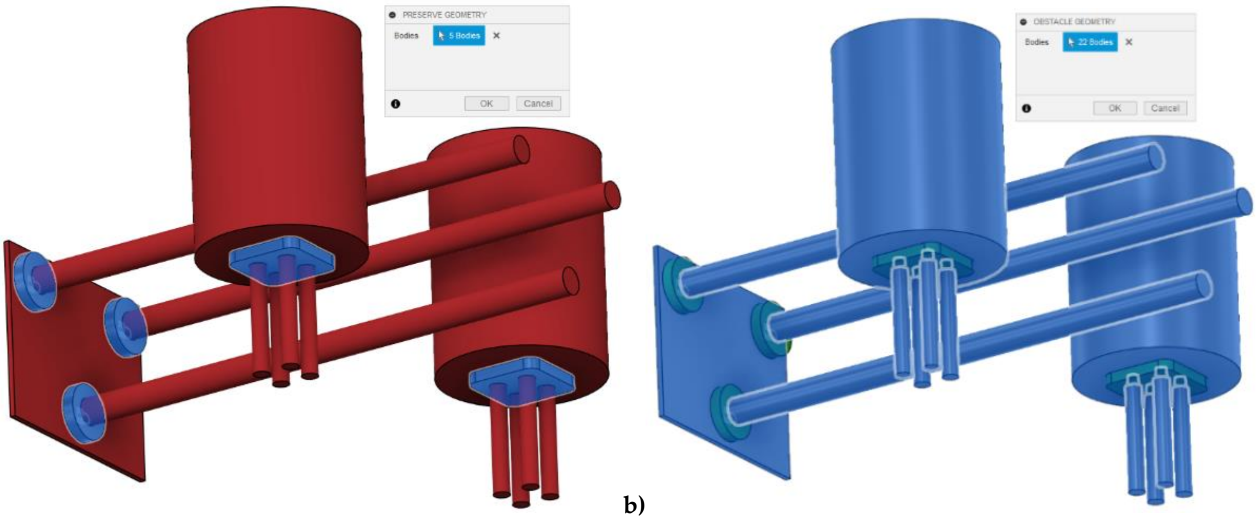

a) b)

Figure 4. Modelling constraints
a) objects to preserve in optimization, b) obstacle geometry

Each of the presented optimizations will generate several kinds of different shapes of the resulting model. For this reason, we selected the optimal shapes from both the generative design process and the automatic modeling process for further comparisons. In the automatic modelling process, the first variant suggested by the system was selected (Figure 5).

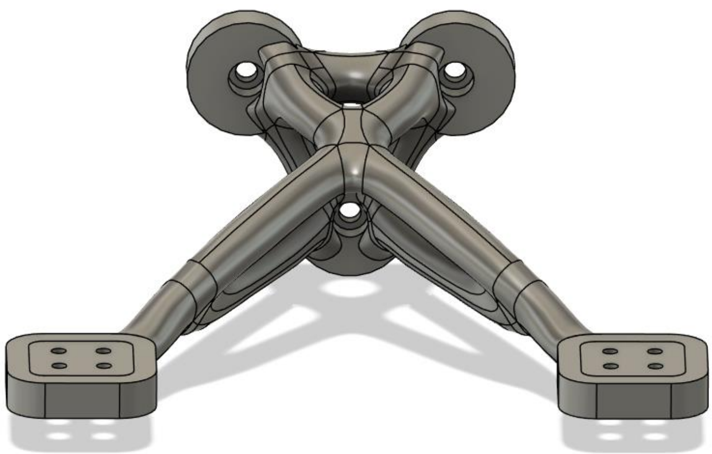

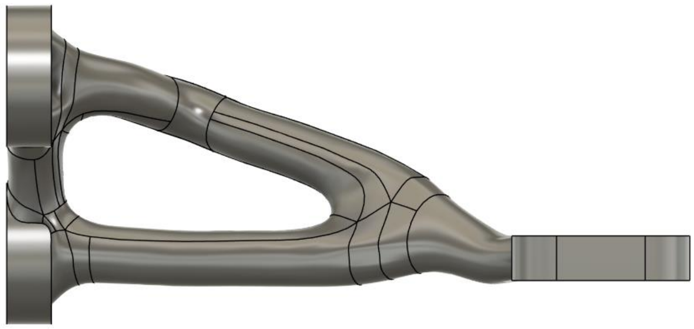

Figure 5. Generated model using Automatic Modelling

For the outputs from the generative design process, we also considered the lowest weight and manufacturing method when selecting the final shape of the part to match the selection we made in the output from the automated optimization. The shape of the part selected from the generative design is shown in Figure 6.

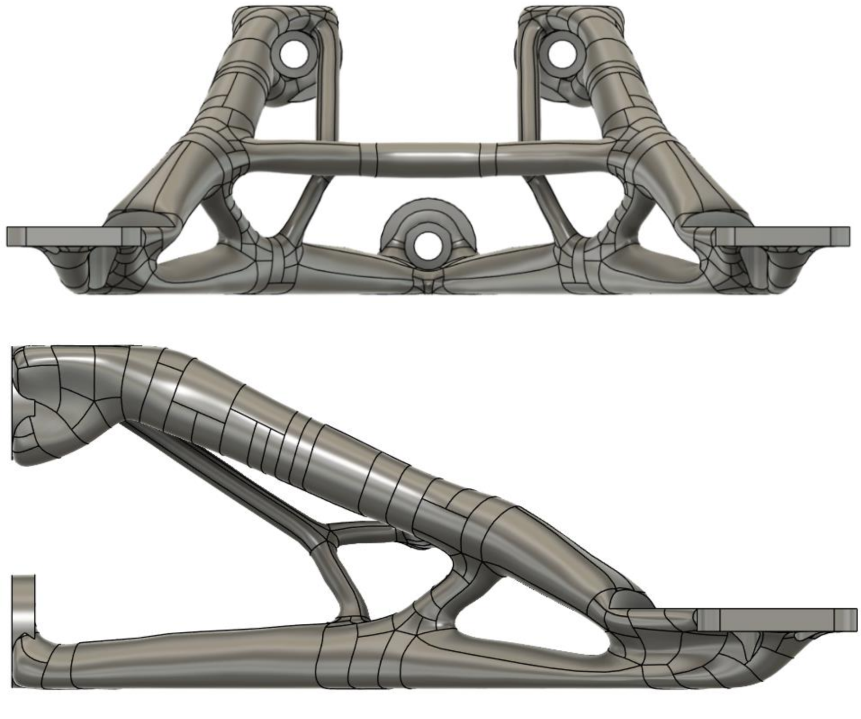

Figure 6. Generated model using Generative Design

In terms of comparing the shapes obtained by these modern technologies, it can be stated that the output from automatic modelling postulates a simpler appearance compared to generative design, which produced more complex shapes given the input data.

3. Strength analysis of the outputs of generative design and automated modeling

For comparison of the results, a strength check of the components was also carried out. A loading condition was simulated when the component is firmly anchored through 3 circular holes and loaded through the connection plates with a perpendicular force of 100 N. The maximum displacement and maximum stress were investigated. At the output of the automatic modelling, the maximum displacement was 0.019 mm and the maximum stress was 4.99 MPa (Fig. 7).

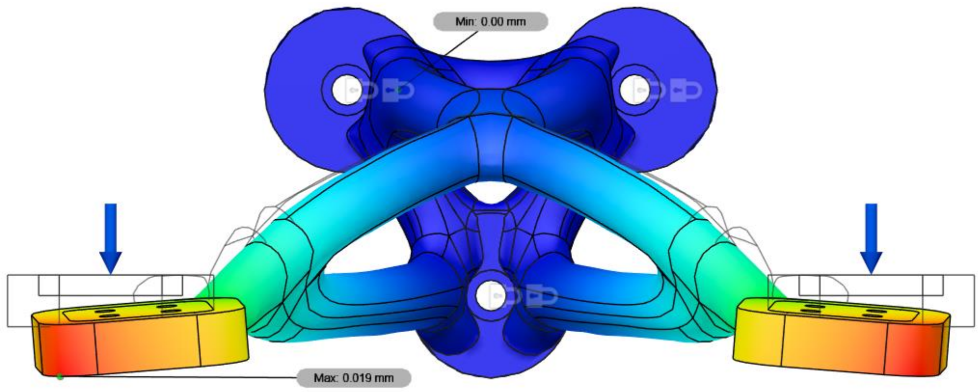

Figure 7. Simulating the output from Automatic Modelling

The model from the generative design performed significantly better after simulation, where the maximum displacement was 0.003 mm and the maximum stress was almost half as high at 2.85 MPa (Fig. 8). These differences are mainly due to the larger number of inputs required by the generative design system before the actual design process.

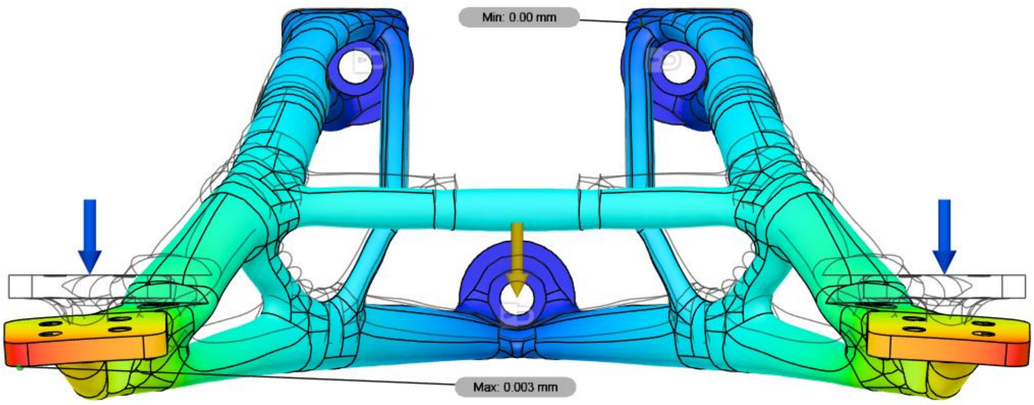

Figure 8. Simulation from the output of Generative Design

5. Conclusions

Modern technologies implemented in CAD systems are designed as a tool for the rapid creation of optimal part shapes, taking into account input parameters and constraints. In terms of rapid design of the appearance of a part, automatic modelling serves the purpose, requiring only basic input data for their creation. However, if the optimization also needs to consider functionality , manufacturing method at known load values, generative design is a better choice. This technology, however, already requires more precise input parameters with which the system will generate several different designs through iterations. These designs can then be retrofitted as required. Thus, if the goal is only an interesting appearance without precise input data, automatic modelling will be sufficient, otherwise generative design will have to be used. It should also be noted that both of these methods preferentially generate shapes more suitable for additive manufacturing. However, generative design also provides in its settings the possibility to take into account some conventional manufacturing technologies.

Acknowledgment

The contribution was created within the framework of the solution of the projects VEGA 1/0528/20 and KEGA 029TUKE-4/2021.

References

1. Autodesk. (2022) Product Documentation – Automated modeling. Available online: https://help.autodesk.com/view/fusion360/ENU/?guid=SLD-AUTOMATED-MODELING (accessed on 6.12.2023)
2. Autodesk. (2023) Fusion 360 Introduction to Generative design. Available online: https://www.autodesk.com/autodesk-university/article/Fusion-360-Introduction-Generative-Design (accessed on 5.12.2023)
3. Chad Jackson. (2017) Empowering engineers with generative design and facet modeling. Available online: https://static.sw.cdn.siemens.com/siemens-disw-assets/public/2dhrNXsZVjzFCb94OnAO9D/en-US/eBook--Empowering-Engineers-with-Generative-Design-and-Facet-Modeling_tcm27-12349.pdf (accessed on 5.12.2023)
4. Vectornator, What Is Generative Design ? A Full Guide. Available online: www.vectornator.io/blog/generative-design/ (accessed on 6.12.2023)
5. All3dp, The Best Generative Design Software od 2022. Available online: all3dp.com/1/the-best-generative-design-software-of-2022/ (accessed on 6.12.2023)
6. AZO Materials, AISI 1050 Carbon Steel. Available online: https://www.azom.com/article.aspx?ArticleID=6526 (accessed on 1.7.2024)

TECHNICKÁ UNIVERZITA V KOŠICIACH
Strojnícka fakulta

Solving intense abrasive wear by optimizing the structure of the coating transferred by the MOG and plasma system

Doc. Ing. Milan ČOMAJ CSc.[1], Ing. Jozef ZOHN, PhD.,IWE.[1]; Ing. Jozef VÝBOCH, IWE.[2,*]; prof. Ing. Ján VIŇÁŠ, PhD., IWE.[2]

[1] ASKOZVAR s.r.o.. Hraničná 2, 040 01 Košice, Slovakia; j.zohn@askozvar.sk
[2*] Department of Technology, Materials and Computer Aided Production, Faculty of Mechanical Engineering,Technical University of Košice, 042 00 Košice, Slovakia; vyboch.jozef@gmail.com;

Abstract: Abrasive wear of the C-Cr-Mo-Nb-W-V surfacing system. Wear resistance, electron beam investigation of carbide phases, thermal effect of the surfacing system on the hardness of the layers. Implementation of MOG and plasma cladding system. The paper presents the results of the evaluation of the influence of the change of the cladding parameters on the resulting quality of the newly formed cladding layers.

Keywords: cladding, plasma, hardness, structure, SEM microscopy

1. Introduction

Cladding of abrasive stressed parts is one way of extending their service life Surface renovaration can be carried out on non-alloyed but also on high-alloyed types of manganese, Hadfield and maraging steels [1]. Conventional arc methods can be used to produce functional layers, but increasingly in practice beam methods are being used for surface formation [2]. As presented in [3], procedures for the recovery of dimensional parts for steel production and processing are particularly topical. These extremely stressed parts after renovation by cladding allow to minimize the cost of renovation in the metallurgical and heavy engineering industries [4]. Modern MOG tubular wire and plasma welding systems allow the composition of the welding system to be optimised. In this work, the effect of cycling of the winding caterpillars and thus, among other things, achieving an improvement in the morphology of the carbide of the weld will be assessed [5]. Abrasive wear is characterized by the separation of particles from the functional surface by the effect of abrasive particles. Hard mineral particles are formed into the surface of the components when they move relative to each other. When the elastic deformations are exceeded, plastic deformations occur to form microparticles separated from the surface of the body. As the body continues to deform, material loss occurs, up to and including failure of the functionality of the device. It is known from the theory of abrasive wear that the amount of wear is affected by the hardness, grain size of the abrasive. Further, the hardness and structural structure of the worn surface. The body material is characterized by the so-called relative abrasion resistance Ψ, which determines at a plus value the multiple of the abrasion resistance to ethanol. Since carbon ferritic-perlitic steel has low resistance to abrasive wear, these problems are solved by hard martensitic surface coatings based on chromium (e.g. 2% C, 15% Cr) or with the addition of boron. These surfacing systems for extreme abrasive wear, even at elevated temperatures, are now obsolete. Dimensional chromium carbides (or carboborides) are distributed in the martensitic matrix, and these are abraded and broken out by the abrasive in the matrix.

2. Materials and Methods

In work [6], experiments were carried out, a series of laboratory tests, where the best result was achieved by a coating system characterized by the guideline chemical composition (%) with the designation SKA-45-0, EN ISO 14175, see Table 1.

Table 1. Chemical composition SKA-45-0, EN ISO 14175 (% in. wt.)

C	Mn	Si	Cr	Mo	Nb	W	V	Fe
4,5-5,3	0,7	0,8	20-21	6,1-6,3	6,1	1,8	1,8	Bal.

With hardnesses according to the RD (tubular wire) manufacturer, see Table 2.

Table 2. Hardness RD (tubular wire)

20°C	550°C	600°C
63HRc	54HRc	50HRc

When the abrasive is pressed into the austenitic matrix of this system (Table 2), which is reinforced with fine precipitates - carbides NbC, Mo2C, WC, VC, there is no stripping and breaking of the dimensional chromium carbides. The austenitic matrix accumulates a greater amount of energy, it is secondarily solidified (up to 100Hv) by the resulting fine NbC precipitates.

In classical MOG or plasma welding, the deposition of individual caterpillars produces loosened areas of reduced hardness in the overlapping area of the so-called heat-affected zone, acting as wear centers.

Therefore, we have investigated the diverging wire winding, see. Figure 1, where we achieve:

- wider weld caterpillars with less mutual influence

- less mixing with the base material

- improved morphology of the welding carbides

- increased welding productivity

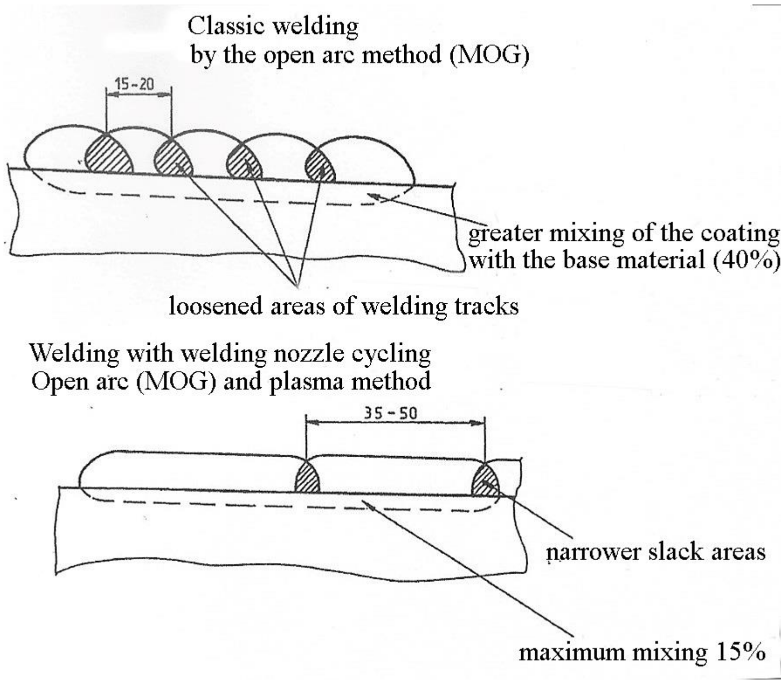

Figure 1. Classical cladding with OPEN ARC (MOG) method, cladding with cycling of the cladding nozzle with OPEN ARC (MOG) method or with plasma.

Cladding with cycling is controlled electronically, the winding head performs a perpendicular swing to the winding direction.

3. Results

SEM analysis

The C-Cr-Mo-Nb-W-V based deposit with the specific composition given in Section 2, its SEM analysis was carried out using carbon extraction replicas on a Tesla BS 450 transmission electron microscope, directly from the deposit samples on a JSM-U3 line scanning microscope. The bloom was double-layered.

The nature of the excluded carbide phases was monitored (by electron diffraction).

Sample No. 1 was cooked with the MOG system without swaging with A-45-0 tubular wire with a change in ferroniobes ranging from 0.18 to 0.30 mm, which is commonly supplied.

Sample No. 2 was cooked with the MOG system with a swing (cycling) with A-45-0 tubular wire where a ferroniobic grain size below 0,18 mm was required.

The grain structure of both samples is austenitic with the exclusion of dimensional primary chromium carbides, eutectic chromium carbides of M_7Cr_3,Cr_3C_2, and NbC type, see Figure 2.

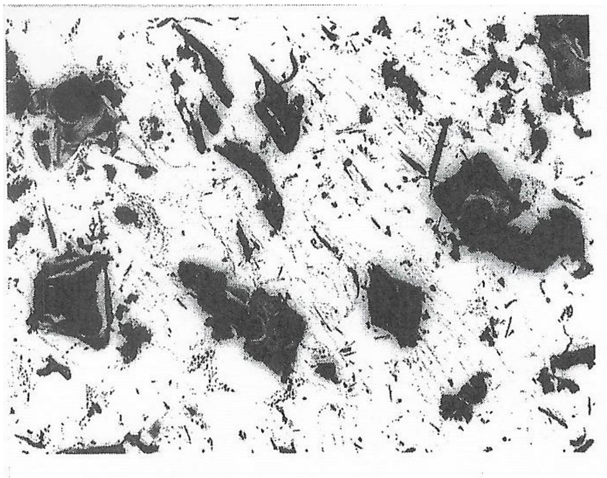

Figure 2. The grain structure of both samples (1500x mag.)

The fine carbide phases reinforcing the matrix are mainly composed of niobium carbides (sample 2), molybdenum, tungsten and vanadium. The nature of the excluded particles - see Figure 3 is mainly Mo_2C and NbC.

For sample No.2, the orientation of the primary chromium and niobium carbides is more favorable.

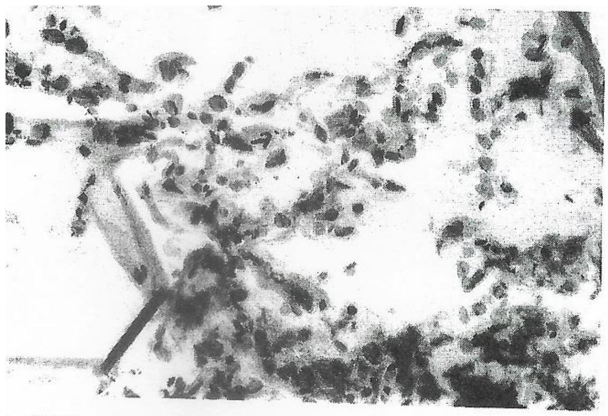

Figure 3. Detail of chromium and niobium carbide particles in the cladded layers (60 000x mag.)

The results of the SEM analyses of the evaluated claddings of samples 1 and 2 are presented in Table 3.

Table 3. Results of the SEM analysis of the claddings of samples 1 and 2

Filler material type	Type of particles - precipitates determined by electro diffraction and microanalysis	Area fraction of carbide particles %	Resistance to abrasive wear Ψ 2
A-45-0 č.1 cladded without cycling	fine 7,1. 10-5 mm MoC, W_2C,VC medium 5. 10-4 mm Cr_7C_3 large 6,3. 10-3 mm Cr_7C_3, NbC	16,5	3,5

A-45-0 č.2 cladded with cycling	fine NbC,MoC, W_2C,VC medium Cr_7C_3, NbC large Cr_7C_3, NbC	35,4	4,4

We also tested resistance to abrasive wear at elevated temperatures.
The measured results of the hardness of samples 1 and 2 are shown in Table 4, with a tempering time of 1h.

Table 4. Measured results of the hardness of samples 1 and 2

Samples / layers		Temperature of tempering °C						
		30	300	450	500	600	700	750
Sample No.1	1.Layer Hardness HV10	673	675	670	665	622	724	675
	2.Layer Hardness HV10	821	862	870	874	826	907	807
Sample No. 2	1.Layer Hardness HV10	826	847	841	873	807	947	695
	2.Layer Hardness HV10	875	876	886	894	912	1006	815

Abrasion resistance tests

The tests of abrasive wear resistance were carried out on a laboratory testing machine type WPM, on a grinding screen according to STN 01 5084.
Conditions: sandpaper Globus 120, dimensions 10x10x12, load 0,2 MPa, sanding path 45m.
For each type of pattern 3 samples were used. The weight losses were measured on an analytical balance with a precision of 10-4 (g).
; The so-called relative abrasion resistance Ψ2 was evaluated.

$$2 = \frac{Wh\ \ etal\,on}{Wh\ \ samp\,le}\ \ \frac{\gamma\ \ sam\,ple}{\gamma\ \ etal\,on} \qquad (1)$$

Etalon structural steel S235
Wh - weight loss (g)
γ – specific weight (g/cm^3)

The measured and calculated values are shown in Table 3.

Evaluation of measured results and requirements for cladding additive

Cladding with A-45-0 tubular wire with the required ferroniob grain size confirmed the electron microscopic findings and the favourable orientation of the primary carbides for the swirl welding by ether tests.
The weld has a favourable austenitic structure reinforced by fine precipitates of carbides mainly MbC and also M02C. This is manifested by an increase in hardness of 12% up to a depth of 0.1 mm.

In this austenitic hardened matrix, the breakage of large primary chromium carbides, niobium. In cycled cladding we have wide areas of good orientation of the primary carbides, which is reflected in an increase in abrasion resistance characterized by an increase in Ψ2 from 3.5 to 4.4. I.e. an increase in abrasion resistance of 25%. tempering curves, the wax maintains a high hardness up to 750°C.

Plasma cladding

Plasma cladding using powder additive materials (PPMs) is advantageous for solving diverse tribological requirements. The advantage over the MOG system with tubular wire, lower heat input and thus less mixing of the filler with the base material and thus the desired properties in smaller filler thicknesses.
Therefore, ASKOZVAR s.r.o. purchased a modern plasma welding system type Eutronic Gap 3511 DC with the possibility of applying the welds in a 5-axis environment, rotation and selection of pitch parameters.
Using PPM based on Ni-Cr-C-B-Si + WC + VC, NbC, MoC (2) austenitic matrix, the dimensional chromium carbides and borides are protected against delamination by pre-preparation of said carbides by sintering at the required grain size according to the required tribological system. We are currently optimizing the use of PPM for the diverse requirements of the practice.

Figure 4. Plasma cladding workplace of the company. ASKOZVAR s.r.o

4. Conclusions

Knowing the tribological conditions of individual friction systems, we can optimize the structure of the welding system by using the MOG system with the use of tubular wires and especially by plasma, where we have wider possibilities of optimizing the welding system. The technological measures - the divergence as mentioned above allow us to minimize the adverse effects of the transition layers between the caterpillar clusters.

Acknowledgments: This contribution is the result of the project implementation: Innovative approaches of the restoration of functional surfaces by laser weld overlaying APVV-20-0303, supported by the Slovak Research and Development Agency and supported by the Ministry of Education of Slovakia Foundation under grant projects VEGA No. 1/0597/23, and KEGA No. 046TUKE-4/2022.

Conflicts of Interest: - The authors declare no conflict of interest.

References

1. Pan, Z.; Dong, X.; Cao, H.; Huang, Q. *The Role of Distribution Forms of Fe-Cr-C Cladding Layer in the Impact Abrasive Wear Performance of Hadfield Steel*. Materials (Basel). 2020, doi:10.3390/MA13081818.
2. Bai, Q.; Ouyang, C.; Zhao, C.; Han, B.; Liu, Y. *Microstructure and Wear Resistance of Laser Cladding of Fe-Based Alloy Coatings in Different Areas of Cladding Layer*. Materials (Basel). 2021, doi:10.3390/ma14112839.
3. Blaškovitš, P.; Čomaj, M.; Malik, J. P*resent state and future perspective of surfacing rolling mill rolls in Czechoslovakia*. Alfa, 1986; pp.67-92..
4. Blaškovitš, P.; Čomaj, M. *Surfacing and Thermal Spraying in Slovak Heavy Metallurgy*. In Proceedings of the Welding in the World; 16.11.2005; pp. 112-156..
5. Blaškovitš, P.; Čomaj, M.; Malik, J. *Present State and Future Perspective of Surfacing Rolling Mill Rolls in Czechoslovakia*. In. First Int. Conf. Surf. Eng. (BRIGHTON, U.K. JUN. 25-28, 1985) 1985.

6 Blaškovitš, P., Čomaj, M.: *Renovácia naváraním a žiarovým striekaním*. STU Bratislava, 204 s. ISBN, 80-227-2482-3, 2006.

Thermovision Analysis of Heat in Pneumatic Flexible Coupling

Lucia ŽUĽOVÁ [1]*, Robert GREGA [2] and Matúš Kačír [3]

[1] Faculty of Mechanical Engineering, Technical University of Košice, Slovakia; lucia.zulova@tuke.sk
[2] Faculty of Mechanical Engineering, Technical University of Košice, Slovakia; robert.grega@tuke.sk
[3] Faculty of Mechanical Engineering, Technical University of Košice, Slovakia; matus.kacir@tuke.sk
* Correspondence: lucia.zulova@tuke.sk; Tel.: +421 55 602 2354

Abstract: The mechanical drive possesses lot of thermal energy transformations in its individual parts. In this article, the research is focused on a heat of pneumatic flexible coupling, which properties significantly affects the smooth operation of the drive. Its thermovision diagnostics includes thermographic images with temperature information of the pneumatic flexible coupling in various modes, their analysis, and recommendations for operation with less affected thermal zones.

Keywords: thermovision, pneumatic flexible coupling, mechanical drive

1. Introduction

Thermovision is used more and more often in the evaluation of technical condition and maintenance of machines and equipment, as well as in industrial processes. It allows us to take thermal imaging measurements, which are carried out either once or repeatedly and indicate the current state of the operated object. This fact brings the possibility of detecting the incipient damage of the machine or its individual parts, and in some cases, it can assess the degree of damage after failure. The relative ease of use and technological progress of thermal imaging cameras allows its application for continuous monitoring of the condition of the machine during its entire operation [1-3].

In concept of thermal imaging diagnostics that is used in the research presented in this article, the aim of which is to observe the spread of heat in a pneumatic flexible coupling in a mechanical drive [4-7]. This pneumatic flexible coupling (Fig. 1) was the basic observed element of the thermal camera. The resulting images enabled the observation and subsequent analysis of the distribution of heat on its surface and the thermal influence of the surrounding members of the drive.

2. Materials and Methods

The basis of the measuring part of the proposed monitoring system was a thermal camera (Fig. 1), which enabled the observation of the temperature distribution on the surface of the pneumatic flexible coupling in the range of the determined field of view. The experiment was carried out in the Laboratory of Torsional Oscillations of Mechanical Systems including a mechanical drive containing the devices listed in the description in fig. 1. The main part of the interest of the observation was the pneumatic flexible coupling shown in the detailed picture in Fig. 1.

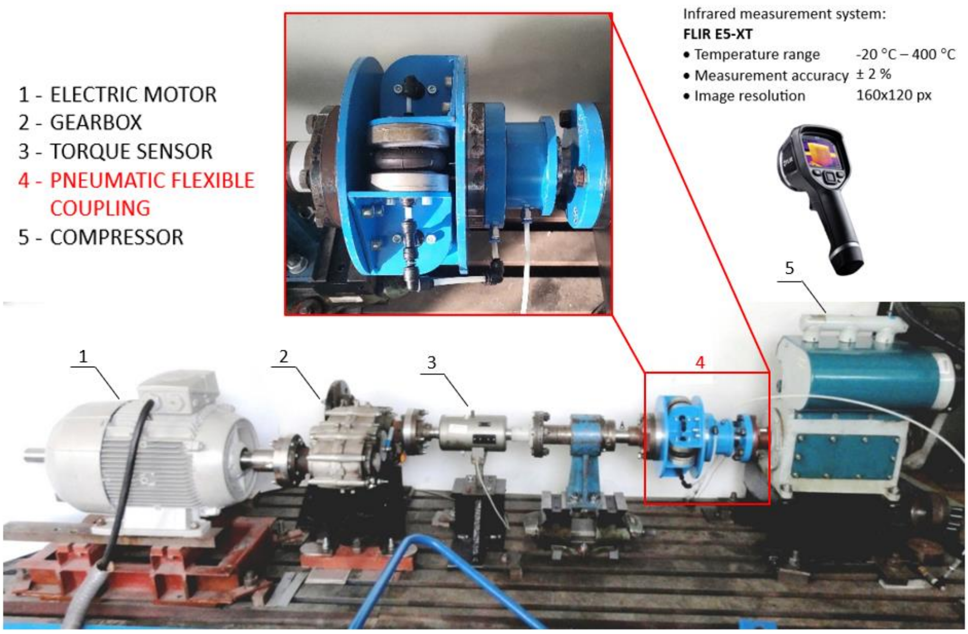

Figure 1. Investigated pneumatic flexible coupling and applied infrared camera.

3. Results

The pneumatic flexible coupling´s properties can smoothly influence the operation of mechanical drives and provide tuning the mechanical drive so that it reaches the lowest possible values of dangerous torsional vibrations [8-10]. By changing the pressure of the gas medium in its compression spaces, its stiffness changes and thus also the stiffness of the entire drive [11-15]. During the experiment, the stiffness of the pneumatic flexible coupling corresponds to air pressure 200 kPa. Thermal changes in the individual parts of the drive are also an inseparable part of this tuning of mechanical drives, namely the change in the operating speed of the drive. Operating range were set from 500-800 rpm during the recording of temperature changes, due to the occurrence of resonances at these working speeds]6], [7]. Thermovision images from individual speed modes are shown in Fig. 2.

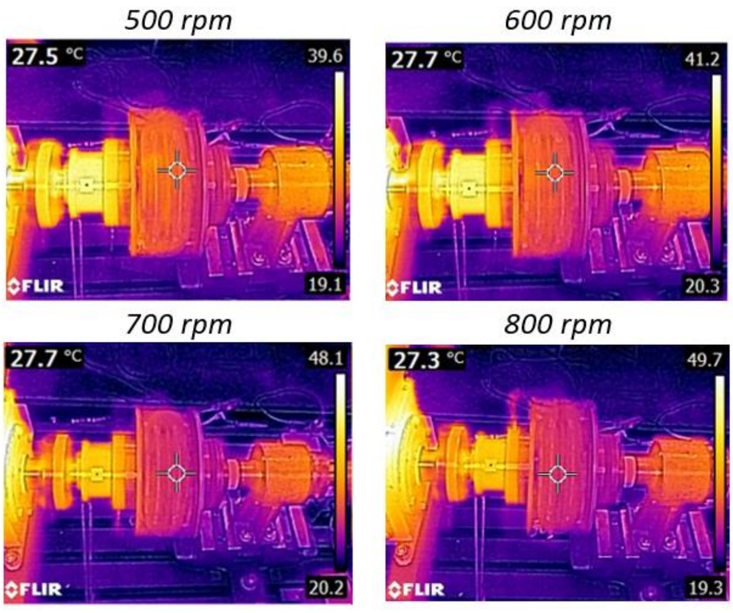

Figure 2. Thermovision images of a pneumatic flexible coupling in different speed modes of the drive.

Thermographs recorded temperature changes during 4 speed modes. From them, it is possible to observe the range of temperatures in the measured field from 20 °C - 49.7 °C. With increasing revolutions, the temperature difference in the investigated part of the drive was 29.7 °C. The temperature change is in the range of 0.2 °C, which can be ignored from the point of view of measurement uncertainty. This leads to the conclusion that pneumatic flexible coupling in this drive does not change its temperature under these operating parameters. However, as can be seen in fig. 3, its part in which the air is supplied is thermally affected by another part of the drive, in our case the compressor. From the comparison of thermal images in fig. 3, the temperature difference of the coldest and hottest place in the pneumatic flexible coupling is up to 17.6 °C. Such a temperature difference can already affect the properties of the pneumatic flexible coupling, and therefore further research with applied technical measures should be applied.

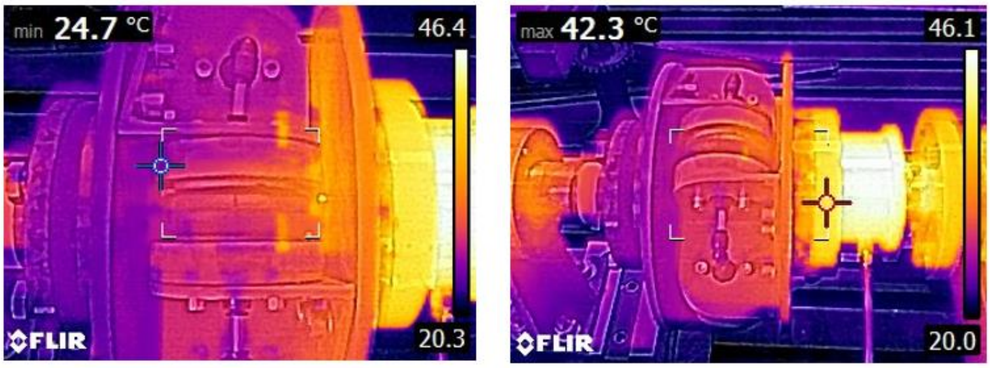

Figure 3..

5. Conclusion

Thermovision images and their analysis were presented in the research results of this article, the aim of which was the temperature analysis of heat spreading in the pneumatic flexible coupling of the mechanical drive. The result of the analysis are thermovision images from four operating modes of the mechanical drive, in which a constant, unchanging temperature of the surface of the pneumatic flexible coupling was demonstrated, and two images of a temperature comparison in the examined field of view of the thermal camera, a significant temperature change of the surface of the pneumatic flexible coupling and an obvious influence on it were demonstrated temperature from the compressor located in the drive. The concept of thermovision in such an analysis of heat spreading in mechanical drives is suitable. The result of the thermal imaging showed that it is possible to apply such a pneumatic flexible coupling even in a machine with higher temperature changes, but with the necessary modification of its parts to achieve the smallest possible temperature influence. Precautions as well as possible design changes will be the basis for further research in this issue.

Acknowledgments: This paper was written in the framework of Grant Project VEGA: „1/0528/20"

Conflicts of Interest: The authors declare no conflict of interest.

References

1. FIDALI, M.: An idea of continuous thermographic monitoring of machinery. Silesian University of Technology, Gliwice, Poland, 9th International Conference on Quantitative InfraRed Thermography doi: 2008 10.21611/qirt.2008.02_08_14.
2. LEPIARCZYK D et.al.: Usage of thermovision in research concerning kinematic pair of friction in machines and mechanical devices, AGH University of Science and Technology, Krakow, Poland, 2012.
3. LIEVIN, Boris A.; INKOV, Yuri M.; OVCHAROV, Igor V.: On the history of thermovision monitoring of ground environment. World of Transport and Transportation, 2014, 12.3: 230-237.

4. KRAJNAK, J.; HOMISIN, J.; GREGA, R.; KASSAY, P.; URBANSKY, M. The failures of flexible couplings due to self-heating by torsional vibrations - validation on the heat generation in pneumatic flexible tuner of torsional vibrations. Engineering Failure Analysis, 2021, Volume119, DOI10.1016/j.engfailanal.2020.104977
5. KRAJŇAK J, GREGA R: Analysis of external temperature in flexible element at various speed levels. Projektowanie, badaniaieksploatacja Tom 1. - Bielsko-Biała: AkademiaTechniczno-Humanistyczna w Bielsku-Białej (2018) 191-198 ISBN 978-83-65182-93-7
6. GREGA, R., KRAJNAK, J., ŽUĽOVÁ, L., KAČÍR, M., KAŠŠAY, P., & URBANSKÝ, M. (2023). Innovative solution of torsional vibration reduction by application of pneumatic tuner in shipping piston devices. Journal of Marine Science and Engineering, 11(2), 261.
7. ŽUĽOVÁ, L., GREGA, R., KRAJŇÁK, J., FEDORKO, G., & MOLNÁR, V.: Optimization of noisiness of mechanical system by using a pneumatic tuner during a failure of piston machine. Engineering Failure Analysis, 2017, 79, 845-851.
8. Robert GREGA, Jozef KRAJŇÁK, Lucia ŽUĽOVÁ, Gabriel FEDORKO, Vieroslav MOLNÁR: Failure analysis of driveshaft of truck body caused by vibrations, Engineering Failure Analysis,Volume 79,2017, Pages 208-215, ISSN 1350-6307, https://doi.org/10.1016/j.engfailanal.2017.04.023.
9. URBANSKÝ, Matej: Comparison of piston and tangential pneumatic flexible shaft couplings in terms of high flexibility. Zeszyty Naukowe. Transport/Politechnika Śląska, 2018, 99: 193-203.
10. HOMISIN, Jaroslav: Pneumatic flexible shaft couplings. Transport Problems, 2007, 2.3: 63-71.
11. KAŠŠAY, P., GREGA, R., URBANSKÝ, M., KRAJŇÁK, J., KAČÍR, M., & ŽUĽOVÁ, L.: Novel Design of Variable Stiffness Pneumatic Flexible Shaft Coupling: Determining the Mathematical-Physical Model and Potential Benefits. Machines, 2023, 12(1), 28.
12. URBANSKÝ, Matej; GREGA, Robert: Contactless Measuring Device for Flexible Shaft Coupling Twist Angle. Current Methods of Construction Design: Proceedings of the ICMD 2018, 2019, 193-200.
13. GREGA, Robert; KRAJŇÁK, Jozef; HARACHOVÁ, Daniela: Comparation of the impact of selected technical gases on properties of a pneumatic flexible coupling. In: MATEC Web of Conferences. EDP Sciences, 2018. p. 03008.
14. KRAJŇÁK, Jozef; GREGA, Robert: Comparison of three different gases and their influence on dynamic properties one-bellow and two-bellows flexible pneumatic coupling. Zeszyty Naukowe. Transport/Politechnika Śląska, 2013.
15. GREGA, Robert: Examination of applicated pneumatic flexible coupling and its effect on magnitude of vibrations in drive of belt conveyer. Zeszyty Naukowe. Transport/Politechnika Śląska, 2014.

TECHNICKÁ UNIVERZITA V KOŠICIACH
Strojnícka fakulta

Topology Optimization for Solid Gear Wheel Body

Samuel Sivák [1, *], Silvia Maláková [1], Matúš Virostko [1]

[1] Faculty of Mechanical Engineering, Technical University of Košice, Letná 9, 042 00 Košice, Slovakia; saumel.sivak@tuke.sk , silvia.malakova@tuke.sk , matus.virostko@tuke.sk
* Correspondence: samuel.sivak@tuke.sk

Abstract: Advancements in technology have revolutionized the field of intelligent design automation systems, driven by the integration of high-performance computing, machine learning, and additive manufacturing. This paper explores the intersection of Computer-Aided Design, Topology Optimization, and Generative Design in the context of product development. The study delves into prominent topology optimization techniques, the evolving landscape of generative design, and the utilization of these methodologies in the design process. Practical applications are demonstrated through a case study involving SolidWorks software, emphasizing the significance of topology optimization in achieving lightweight, efficient designs. The research highlights the potential for further growth in topology optimization technology and its broader adoption in product design.

Keywords: design; topology optimization; gear body; SolidWorks, gear wheel

1. Introduction

Advancements in technology, particularly in processing power, machine learning, and associated algorithms, have played a crucial role in the development of intelligent design automation systems. The utilization of high-performance computing capabilities from the cloud has made previously impractical complex optimization computations and iterations feasible. This allows designers to swiftly conduct intricate simulations to assess various product configurations in diverse scenarios, providing crucial insights for selecting optimal design choices. Concurrently, the rapid progress in additive manufacturing technology is bringing about notable transformations in component production and design, enabling the creation of intricate geometries that were previously unattainable through conventional production methods [1].

The integration of Computer-Aided Design (CAD) systems into the design process is becoming increasingly prevalent, supported by the expanding capabilities of these systems [2]. Engineers have developed CAD-based topology optimization (TO) software to generate optimal designs for specific structures. However, this has primarily gained recognition among designers and engineers rather than the broader field of product design [3]. To address this, generative design (GD) algorithms have been incorporated into CAD software, aiming to stimulate designers' creativity by generating a diverse array of design solutions.

Prominent TO techniques include Solid Isotropic Material with Penalization, Evolutionary Structural Optimization, its enhanced version of Bi-directional Evolutionary Structural Optimization, and Level Set [4]. Deaton and Grandhi's article [5] provides a comprehensive analysis of various techniques, while alternative methods employing components or voids have also gained popularity [6]. TO components have been integrated into commercial products like ANSYS and ABAQUS. The information presented indicates that TO technology has made significant strides and suggests potential for further growth in the future.

2. Materials and Methods

In contrast to the traditional design approach, which relies on CAD systems to create precise geometry according to user specifications, the incorporation of TO and GD shifts the designer's focus from the form to the function of the product. In these methods, optimization programs are employed to generate various design alternatives. Both approaches share a common initial stage, where the CAD system is used solely for defining functional surfaces. Furthermore, the final stage is uniform in both methods, involving the utilization of Computer-Aided Manufacturing (CAM) systems to ensure accurate manufacturing.

Diverging from the previously mentioned CAM systems, those specific to Additive Manufacturing (AM) are tailored to enhance printing capabilities. They optimize the part's orientation, determine the optimal number and type of supports, and, more recently, predict part deformation resulting from the substantial stress gradient during the printing process [7].

2.1. Generative design

GD research began in the 1980s, initially focusing on theoretical concepts without real-world applications. Initially rooted in architecture [8], interest expanded to various domains exploring the convergence of computer and evolutionary theory parallels. Vajna et al. [9] introduced autogenetic design theory, drawing parallels between product creation and natural evolution.

GD, a transformative paradigm in computational design and engineering, integrates advanced algorithms, artificial intelligence, and parametric modeling. This approach enables the efficient generation of complex, optimized designs through algorithmic processes, iterative refinement, and multi-objective optimization. With applications in architecture, aerospace engineering, product development, and urban planning, GD promotes sustainability by managing resources, reducing material consumption, and improving environmental impact. It produces aesthetically compelling and functionally efficient designs, challenging traditional paradigms.

Characterized by automated and semi-autonomous features, GD simultaneously generates multiple design iterations, simulating evolutionary processes observed in nature. Starting with initial designs, it iteratively refines them to align with pre-established requirements and specific constraints. Designs failing to meet criteria or constrained by unsuitable parameters are eliminated, guiding the evolutionary search process toward novel trajectories.

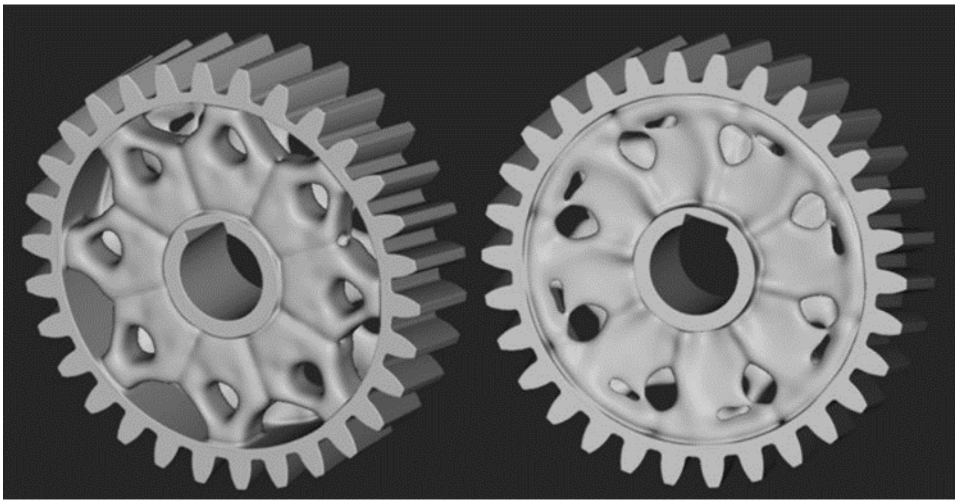

Figure 1. Two solutions of generative design on a gear wheel

2.1. Topology optimization

The method called topological optimization aims to optimize the arrangement of materials within a designated space, taking into account factors such as load and boundary conditions. Typically utilized in the early design phase, this technique analyzes and assesses various design alternatives based on predefined criteria, including reducing weight, increasing stiffness, lowering stress, and minimizing strain [3].

Topological optimization software is designed to streamline the efforts of individuals engaged in iterative design processes and complex analytical tasks. These programs not only facilitate creativity by presenting unconventional solutions that may be overlooked but also constitute a fundamental aspect of design optimization. Unlike shape optimization, which focuses on meeting predefined criteria and goals, such as stress reduction and fatigue resistance improvement, contour optimization considers specific contour attributes influenced by node positioning. This computational approach not only helps users refine their designs but also stimulates innovative thinking by revealing non-traditional solutions (Figure 2).

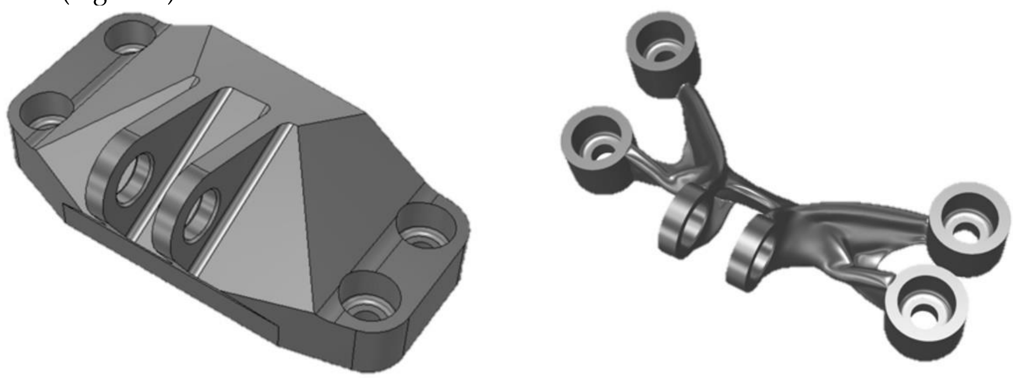

Figure 2 Topology optimization before/after

3. Utilization of topology optimization

SolidWorks, a software equipped with advanced 3D modeling capabilities and robust design automation tools, was employed to digitize the model. The designer considered that the optimized model should remain a single, unified entity due to the limitation of SolidWorks' TO module, which doesn't support simultaneous optimization of multiple components or assemblies. It's noteworthy that certain elements, such as holes and feature profiles, had to retain their original geometry, necessitating well-defined boundaries.

External loads and intrusions were defined following principles similar to finite element simulations, with the distinction of applying force loads to individual gear teeth to ensure a consistent, patterned shape for the optimized gear and eliminate areas with inadequate or no support.

Subsequently, optimization objectives and topological criteria were established. For material reduction, the goal was to minimize the body's volume while maximizing stiffness. These objectives influenced the extent of material reduction, determining the final shape of the optimized solid by balancing material loss and stiffness. Constraints were introduced to set upper and lower bounds for maximum displacement within the 3D model or specify limitations on mass removal.

In the TO process, the material was adjusted to align with optimization objectives based on specified geometric criteria. However, traditional manufacturing processes like casting or forging could pose challenges for creating the 3D model. To address this, appropriate manufacturing control criteria were applied to avoid issues like undercuts and hollow sections, ensuring the optimized 3D model could be correctly molded or extracted from a mold. SolidWorks simulation offered four different manufacturing conditions:

- Thickness criterion: This criterion fine-tuned the model's topology to avoid excessively thin or thick sections, improving manufacturability.

- Surface Preservation: This added preserved components (surfaces) to the 3D model, which remained unchanged during TO, preserving the crucial geometry for the model's functionality.
- Symmetry criterion: It achieved symmetry in the optimized 3D model concerning predetermined planes. Depending on the design layout, a planar symmetry option could be selected, such as half, quarter, or eighth symmetry.
- Form criterion: This feature simulated the extraction of the optimal 3D model from a mold.

After defining the optimization criteria and setting boundary conditions, the automated optimization process is initiated, governed by algorithms. However, it was recommended to predetermine the number of iterations before commencement. Iterations constituted sub-simulations of modified volumes, each striving to generate a more optimized shape than the previous one. While a greater number of iterations produced superior results, it extended the optimization time. The optimization result was visualized as a color-coded model, akin to finite element analysis, categorizing volumes as "excessive," "suitable to keep," or "necessary to keep".

The generated models were exported in either volume or area formats, necessitating additional refinement to achieve a smoother representation, given their association with the geometry of the finite element mesh.

The main goal was to create a gear with minimal mass, emphasizing gearing rigidity. The thickness of the rim beneath the gear teeth was consistently maintained across all newly designed variations. The altered wheel stand shapes took on their revised appearance after these adjustments.

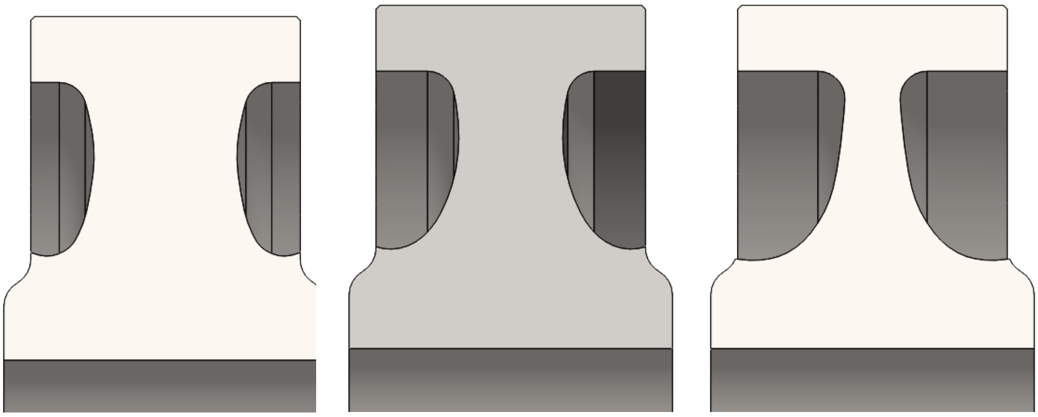

Figure 3 Results of optimization shown in cross-sections

The analysis concluded that for the wheel shape of variant 3, which consisted mainly of the yellow parts of the optimized wheel, it had the highest measured strain values and therefore the lowest stiffness while the volume loss was the highest. However, despite the level of volume reduction achieved, the value of the resulting gear stiffness was insufficient. In terms of deformation, variants 1 and 2 showed the lowest values. At the same time, these variants had a very similar shape and volume of the gear body. The stiffness condition implies that the optimized gear would be for variant 2. However, all of the mentioned wheels had a very specific shape of the gear body surface, which can be seen in the cross-sections of the variants. Results are shown in figures 3 to 5.

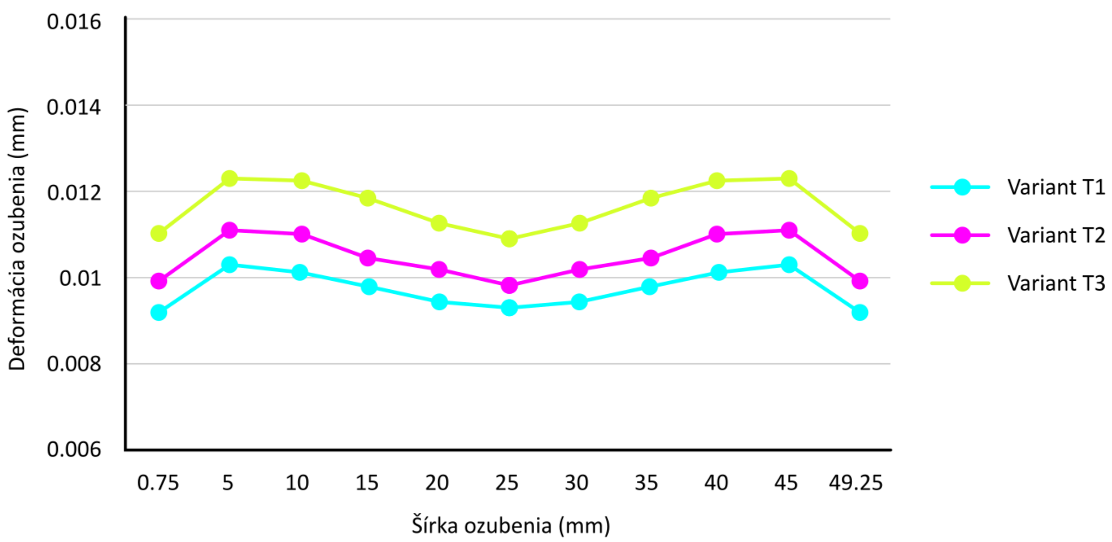

Figure 4. Deformation of variants

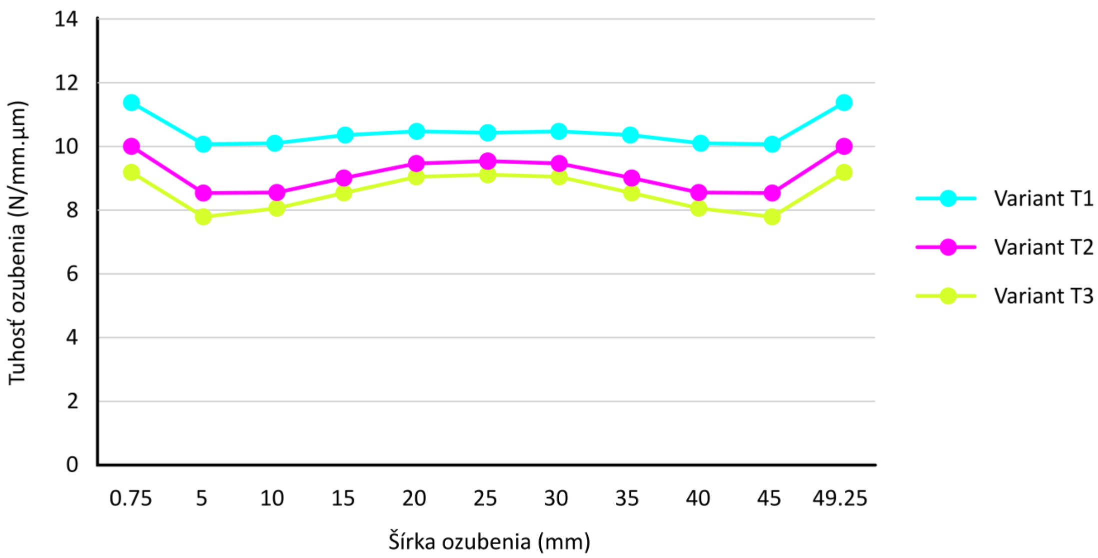

Figure 5. Stiffness of variants

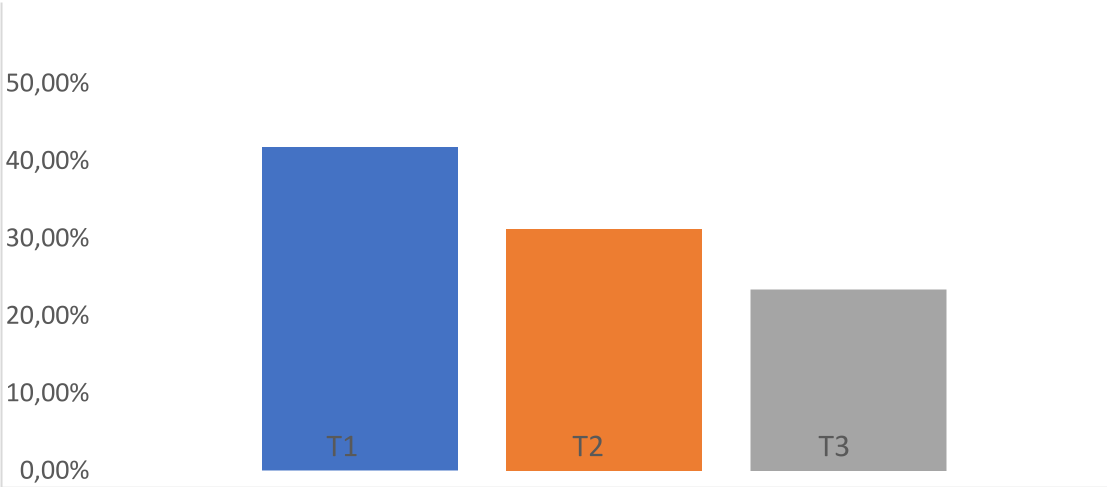

Figure 6. Comparison of weight reduction of variants

Conclusions

This study underscores the transformative impact of topology optimization and generative design on the product development landscape. By shifting the focus from traditional CAD-centric approaches to function-oriented design, these methodologies enable the generation of innovative and efficient designs. The integration of topology optimization techniques with advanced 3D modeling tools, exemplified through SolidWorks, showcases the practical application of these concepts in real-world scenarios. The optimization criteria, manufacturing control, and iterative refinement processes contribute to the creation of designs with minimal mass and enhanced structural integrity. The color-coded visualization of optimization results aids in decision-making and provides insights into material distribution. As technology continues to advance, the potential for further optimization and refinement in design processes is promising, opening new avenues for creativity and efficiency in product development.

Future works will be performed not only in SolidWorks software but also in other ones such as Fusion 360. This will be done to ensure and choose in need of the best software to optimize the gear wheel body. One of the missing features of SolidWorks software is also a lack of generative design options. This will be addressed in future works alongside the comparisons of software capabilities and optimized shapes.

Acknowledgments: This paper was written in the framework of Grant Project VEGA: „1/0528/20 and KEGA 029TUKE-4/2021.

Conflicts of Interest: The authors declare no conflict of interest.

References

1. Bici, M., Broggiato, G. and Campana, F. Topological Optimization in Concept Design: starting approach and a validation case study. *Lecture Notes in Mechanical Engineering* 2016, pp.289-299.
2. Horváth, I. On some Crucial Issues of Computer Support of Conceptual Design. *Product Engineering* 2004, pp.123-142.
3. Querin, O. Topology design methods for structural optimization. 2017. London, United Kingdom: Academic Press.
4. Zhu, J., H. Zhou, C. Wang, L. Zhou, S. Yuan, and W. Zhang. 2021. “A Review of Topology Optimization for Additive Manufacturing: Status and Challenges.” Chinese Journal of Aeronautics 34 (1): 91–110.
5. Deaton, J. D., and R. V. Grandhi. 2014. “A Survey of Structural and Multidisciplinary Continuum Topology Optimization: Post 2000.” Structural and Multidisciplinary Optimization 49 (1): 1–38. doi:10.1007/s00158-013-0956-z.
6. Wein, F., P. D. Dunning, and J. A. Norato. 2020. “A Review on Feature-Mapping Methods for Structural Optimization.” Structural and Multidisciplinary Optimization 62 (4): 1597–1638.

7. Pagac, M., Hajnys, J., Halama, R., Aldabash, T., Mesicek, J., Jancar, L. and Jansa, J. Prediction of Model Distortion by FEM in 3D Printing via the Selective Laser Melting of Stainless Steel AISI 316L. *Applied Sciences* 2021, 11(4), p.1656
8. Vajna, S. et al. The Autogenetic Design Theory: An evolutionary view of the design process. *Journal of Engineering Design* 2005, 16(4), pp. 423-440.
9. Krish, S. A practical generative design method. *Computer-Aided Design* 2011, 43(1), pp. 88-100.

Novus Scientia 2024

Zborník príspevkov z XXI. Medzinárodnej vedeckej konferencie doktorandov strojníckych fakúlt technických univerzít a vysokých škôl

Názov:	Novus Scientia 2024
Editor:	© prof. Ing. Ján Slota, PhD.
	© Ing. Lucia Žuľová
	© Ing. Jaroslav Melko
Vydavateľ:	Technická univerzita v Košiciach,
	Strojnícka fakulta, Letná 1/9, 042 00 Košice-Sever
Rok:	2024
Náklad:	75 výtlačkov
Rozsah:	444 strán
Miesto konania:	Strojnícka fakulta, Technická univerzita v Košiciach
Dátum konania:	25.01.2024

ISBN 978-80-553-4690-8